INFLUENCE OF LOCAL STRESS AND STRAIN ON INTERGRANULAR CRACKING OF 316L STAINLESS STEEL IN SUPERCRITICAL WATER

by

Elaine Ann West

A dissertation submitted in partial fulfillment
of the requirements for the degree of
Doctor of Philosophy
(Nuclear Engineering and Radiological Sciences)
In The University of Michigan
2010

Doctoral Committee:

Professor Gary S. Was, Chairman
Professor Michael Atzmon
Professor Tresa Pollock
Professor Lumin Wang

To my family

ACKNOWLEDGMENTS

I would like to first thank my advisor, Dr. Gary S. Was, for his guidance and support throughout my time in graduate school, and for his dedicated assistance in completing this work. I would also like to thank the members of my dissertation committee, Dr. Atzmon, Dr. Pollock, and Dr. Wang for their valuable insight.

I would like to thank my colleagues for their encouragement, many helpful discussions, and assistance in the laboratory, Deepak Kumar, Pantip Ampornrat, Anne Campbell, Micah Hackett, Gaurav Gupta, Cheng Xu, Mike McMurtrey, Janelle Penisten, Gokce Gulsoy, Kale Stephenson, and Tyler Moss. Special thanks go to Zhijie (George) Jiao for sharing his knowledge in many important areas, and for his assistance with TEM analysis. I would also like to thank Sebastien Teysseyre for his consistent encouragement, support, and laboratory assistance during our time together at Michigan.

For their assistance during my many proton irradiations at the Michigan Ion Beam Laboratory, I would like to thank Ovidiu Toader, Fabian Naab, and Victor Rotberg. Alex Flick also deserves many thanks for his help with my numerous CERT tests in the Irradiated Materials Testing Laboratory. I am also grateful to the staff at the Electron Microbeam Analysis Laboratory, John Mansfield, Kai Sun, and Haiping Sun for their laboratory assistance.

Last, but far from least, I would like to express my heartfelt gratitude to my parents (Robert and Janet West), siblings (Erin Farrell, Paul West, and Adrienne West),

and husband (Sean Lemecha) for their constant support and patience over the years. Their encouragement and optimism have helped me in all of my endeavors.

This work was supported by the U.S. Department of Energy under award number DE-FC07-05ID14664. Fellowship support was provided through a Rackham Merit Fellowship from the University of Michigan.

TABLE OF CONTENTS

LIST OF FIGURES

LIST OF TABLES

LIST OF APPENDICES

ACRONYMS

AFM	Atomic Force Microscopy
AOI	Area Of Interest
BPM	Beam Profile Monitor
BWR	Boiling Water Reactor
CERT	Constant Extension Rate Tensile (test)
CGR	Crack Growth Rate
CLT	Constant Load Test
CNS	Critical Normal Stress
CSL	Coincident Site Lattice
CSS	Critical Shear Stress
CSLB	Coincident Site Lattice Boundary
CW	Cold work
DI	DeIonizing
DO	Dissolved Oxygen
DSC	Displacement Shift Complete
EBSD	Electron BackScatter Diffraction
EBSP	Electron BackScatter Pattern
ECT	EquiCohesive Temperature
EDM	Electrical Discharge Machining
EELS	Electron Energy Loss Spectroscopy

EGBD	Extrinsic Grain Boundary Dislocations
EMAL	Electron Microbeam Analysis Laboratory
FCC	Face-Centered Cubic
FM	Ferritic-Martensitic
FWHM	Full Width at Half Maximum
GBC	Grain Boundary Channel (crack type)
GBCD	Grain Boundary Character Distribution
GBE	Grain Boundary Engineering
GBS	Grain Boundary Sliding
HTCL	High Temperature Corrosion Laboratory
IG	InterGranular
IASCC	Irradiation Assisted Stress Corrosion Cracking
IGSCC	InterGranular Stress Corrosion Cracking
LAB	Low Angle Boundary
LVDT	Linear Variable Differential Transformer
LWR	Light Water Reactor
MSCW	Multi-sample SuperCritical Water (system)
NS	Normal Stress (crack type)
NWC	Normal Water Chemistry
ODS	Oxide Dispersion Strengthened
OIM®	Orientation Imaging Microscopy
PWR	Pressurized Water Reactor
RHAB	Random High Angle Boundary
RIS	Radiation Induced Segregation

SCC	Stress Corrosion Cracking
SCW	SuperCritical Water
SCWR	SuperCritical Water Reactor
SEM	Scanning Electron Microscope/Microscopy
SFE	Stacking Fault Energy
SMGBS	Schmid-Modified Grain Boundary Stress (model)
STEM	Scanning Transmission Electron Microscopy
TD	Tensile Direction
TEM	Transmission Electron Microscope/Microscopy
TGSCC	Transgranular Stress Corrosion Cracking
XEDS	X-ray Energy Dispersive Spectroscopy

ABSTRACT

INFLUENCE OF LOCAL STRESS AND STRAIN ON INTERGRANULAR CRACKING OF 316L STAINLESS STEEL IN SUPERCRITICAL WATER

by

Elaine Ann West

Chair: Gary S. Was

The objective of this study was to determine how the deformation propensities of individual grains of 316L stainless steel influence intergranular cracking behavior in supercritical water (SCW). The grain-to-grain variations in deformation propensities were estimated from the Schmid and Taylor factors of grains. Resulting stress inhomogeneities and strain incompatibilities which were evaluated to determine the conditions that promoted intergranular cracking in SCW.

Proton irradiation of 316L caused hardening and radiation induced depletion of chromium at grain boundaries and was found to increase intergranular cracking severity. The SCW environment increased the crack density on the gage surfaces of the specimen by a factor of 18 compared to a 400˚C argon environment. Intergranular cracks preferentially occurred along grain boundaries oriented perpendicular to the tensile axis and adjacent to grains with low Schmid factors. The Schmid-Modified Grain Boundary Stress (SMGBS) model was developed to analyze local grain boundary stresses. The

model was validated by showing that the Schmid factor dependence of cracking in SCW could be predicted from the trace inclination distribution, and confirmed that cracking was driven by the normal stresses acting on grain boundaries.

The similar dependencies of slip discontinuity and intergranular cracking on trace inclination, Schmid factor, Taylor factor, and grain boundary character suggest that slip discontinuity contributes to intergranular cracking. Grains with low Taylor factors decreased slip discontinuity propensity at grain boundaries with trace inclinations >50˚ because they provided multiple favorably oriented slip systems on which deformation could occur.

Grain boundary engineering reduced the intergranular cracking propensity of 316L stainless steel in SCW by virtue of the fact that special grain boundaries were more resistant to intergranular cracking in SCW than random high angle grain boundaries.

The findings of this study indicate that the intergranular cracking resistance of 316L stainless steel in a SCW environment would be greatest for a microstructure with a large population of grains with high Schmid factors (for a specified stress state), a high frequency of grain boundaries oriented nearly parallel to the tensile direction, and a large fraction of special grain boundaries.

CHAPTER 1

INTRODUCTION

Nuclear power is an integral component of the world's energy portfolio. It accounts for 15% of the electrical production in the world, with the US responsible for over 27% of the worldwide generating capacity. The groundwork is currently being established for the next generation of nuclear reactors (Generation IV), which were designed with the goals of improved nuclear safety, proliferation resistance, minimization of waste, and decreased cost. The Supercritical Water Reactor (SCWR) is one of the six most promising Gen IV concepts.

The SCWR is a logical progression from the current Light Water Reactors (LWRs) whose thermal efficiencies are limited to ~33% by the low pressure and temperature of the steam generated. The SCWR combines existing LWR technologies with knowledge of supercritical fossil-fueled power plants, which have been operating since 1957 and have efficiencies of 47-49%. The resulting SCWR is designed to operate above the thermodynamic critical point of water (374˚C, 22.1 MPa) and offers many advantages over current LWRs. The operating pressure and outlet water temperature are anticipated to be 25 MPa and ~500˚C [1], respectively, which will yield a thermal efficiency of ~44%. The single phase of the coolant also allows for considerable plant simplification by eliminating the need for steam generators, separators and dryers.

These advantages, however, come at the cost of a severe reactor environment. In addition to withstanding this high temperature and pressure environment, the internal core components in the SCWR will be exposed to neutron doses as high as 30 dpa. The classes of alloys selected for the reactor concept include austenitic stainless steels, ferritic-martensitic steels, Ni-base alloys, and Ti-base alloys. Each alloy class is susceptible to some form of degradation in the SCWR environment as indicated in Table 1.1. In general, the austenitic stainless steels and Ni-base alloys have sufficient resistance to general corrosion, but are susceptible to irradiation induced swelling and stress corrosion cracking (SCC). The ferritic-martensitic alloys are resistant to SCC and perform well under irradiation, but they have high corrosion rates and poor high temperature mechanical integrity. This study will focus on the SCC behavior of irradiated 316L stainless steel in a SCW environment.

Austenitic stainless steels are widely used for the core components of current LWRs, and their susceptibility to intergranular stress corrosion cracking (IGSCC) is well documented [2]. While the database on IGSCC in LWR environments has been built through decades of research, the IGSCC behaviors of candidate alloys for the SCWR are a critical issue that has yet to be fully addressed. Stainless steels and nickel base alloys have been shown to be susceptible to IGSCC in SCW at temperatures from 400-500˚C [3], and proposed IGSCC mechanisms include selective internal oxidation [4], and slip-oxidation or dissolution mechanism [4, 5].

Irradiation damage is known to enhance IGSCC, with irradiation assisted (IA)SCC being a frequent problem with stainless steels in boiling water reactor (BWR) environments and also occurs in pressurized water reactor (PWR) environments at higher

threshold neutron doses. Although correlations exist between irradiation hardening and radiation induced segregation (RIS) and cracking propensity, there is evidence that some other irradiation-induced change contributes to irradiation assisted stress corrosion cracking (IASCC) [6]. A growing body of literature is examining the role of the localization of deformation in irradiated materials [6-16].

The mode by which deformation is accommodated in or near grain boundaries is believed to influence the cracking propensity of the boundary [17]. Researchers have shown that grain boundary deformation in the form of sliding is a precursor to cracking of Ni-16Cr-9Fe in high temperature water [18]. Other researchers have shown that the cracking susceptibility of the grain boundary depends on the propensities of the adjacent grains to deform via crystallographic slip [19-21]. This suggests that parameters that describe the relative propensity of a grain to deform, such as the Schmid and Taylor factors of the grains, may correlate with the cracking susceptibility of the adjacent boundary. In irradiated alloys, deformation becomes localized to slip channels that induce high levels of strain at grain boundaries [14], strain hardening is low, and the intergranular cracking propensity is often high for irradiated steels [15]. Therefore, irradiated stainless steel provides an excellent means to study the relationship between deformation and cracking propensity because,

(1) Crystallographic slip and grain boundary strain incompatibilities can be quantified because deformation occurs via slip channeling.

(2) The incidence of cracking is high, providing for statistically significant measurements.

To date, no study has demonstrated the ability to predict the cracking propensity of the boundary based on deformation parameters with statistically significant results. The objective of this study is to determine whether intergranular cracking of 316L in SCW is influenced by the propensity for deformation in the grains adjacent to the crack, as determined via Schmid factor and Taylor factor analysis.

Chapter 2 of this thesis provides relevant background information, and then describes the objective of the current study and experimental approach. Chapter 3 describes the systems used in the study, the experimental procedures, and the analysis techniques. Chapter 4 presents the results of the cracking and localized deformation measurements on the 316L specimens. Chapter 5 discusses the reasons for the observed relationships between the deformation parameters and the cracking propensity. Finally, Chapter 6 states the conclusions of this study.

Table 1.1 Degradation modes relevant to SCWR candidate materials

Alloy class	Corrosion resistance		Radiation damage resistance		High Temp mechanical integrity
	General corrosion	SCC	Swelling	Embrittlement	
Austenitic stainless steel	High	Low	Low	High	Medium
Ferritic-Martensitic steel	Medium	High	High	High	Low
Ni-base	High	Low	Low	Medium	High
Ti-base	Medium-High	Limited data			Medium-High

CHAPTER 2

BACKGROUND

This chapter provides a review of published literature that yields insight into the deformation and intergranular cracking behavior of alloys in high temperature environments. The first section describes the properties of SCW and their strong dependencies on pressure and temperature. The second section focuses on the corrosion behavior of stainless steels in a SCW environment. The third section provides a more in depth review of the intergranular cracking behavior of stainless steels in SCW and dependencies on several variables including temperature, chemical additions, and irradiation dependence, and concludes with a review of proposed cracking mechanisms. The fourth section discusses the nucleation and growth of intergranular (IG) creep cracks. The fifth section describes the deformation behavior of crystalline materials and introduces the Schmid and Taylor factors which are used as indicators of the deformation behaviors of individual grains. The sixth section describes the geometries of grain boundaries and their influence on IG degradation. The seventh section reviews the findings of previous SCW experiments that led to the selection of the current thesis topic and experimental parameters. The final section states the objective of this work and the experimental approach through which it is met.

2.1 Supercritical water environment

The critical point of water is 374˚C and 22.1 MPa, and the fluid is in the supercritical phase at all temperatures and pressures above this point as illustrated in Figure 2.1. Supercritical water has both liquid and gas-like characteristics, and is a very responsive medium with respect to pressure and temperature. Due to the property changes that occur as either is altered, the corrosion phenomena in SCW can vary dramatically. While the adaptable properties of SCW make it possible to "tune" the environment to desired conditions, the SCWR coolant will range from temperatures in the subcritical regime to temperatures as high as 620˚C [22]. Therefore, it is imperative to understand how the properties of supercritical water evolve in this temperature regime, and how those changes influence corrosion behavior.

Metallic corrosion reactions in aqueous environments require the mass transport of ions to and from a metal surface. Parameters that influence corrosion behavior include density, dielectric constant, and ionic product of the water. All three of these parameters generally decrease with increasing temperature and increase with pressure in the supercritical regime. The density of the SCW is important because it affects the polarity of the fluid and influences the hydrogen bonding behavior. When density increases, the polarity increases, and ionic reactions become more prevalent due to the greater solubility and dissociation of ionic species in the fluid. When density decreases, the polarity decreases, and ionic reactions are suppressed. The degree of hydrogen bonding appears to decrease at lower densities, which leads to a lower dielectric constant [23]. The dielectric constant determines the extent to which ions are stable in the environment, and is one of the key parameters that determines the solubility of metal

oxides [24]. The dielectric constant of water at ambient temperature and pressure is ~78, and it can drop to values below 5 in the supercritical regime depending on pressure and temperature [25]. The ionic product of water is an equilibrium constant for the H_3O^+ and OH^- reactions;

$$2H_2O(l) \leftrightarrow H_3O^+(aq) + OH^-(aq),$$

the reactions through which water undergoes an acid-base reaction with itself. Although the ionic product increases with temperature throughout most of the subcritical regime, it decreases dramatically near the critical temperature, and decreases gradually thereafter. Therefore, although water remains neutral as temperature increases because the hydroxide (OH^-) and hydronium ion concentrations (H_3O^+) remain balanced, the pH increases as temperature is increased in the supercritical regime due to the lower concentration of hydronium ions. Graphs illustrating the temperature and pressure dependence of each parameter are shown in Figure 2.2.

The corrosion behavior of SCW changes dramatically with density, and may be separated into regimes where the SCW acts as (a) a non-polar solvent (low density), and (b) a polar-solvent (higher density). In high density SCW, >0.2-0.3 g/cc, acids readily dissociate, and the addition of even small amounts of acid can result in a dramatic decrease in pH. Both high and low pH values can cause chemical dissolution of a protective oxide layer [26]. Gases are also less soluble in high density SCW. Low density SCW is generally a less corrosive environment. Low density SCW has a low solvency for ionic compounds, however, most gases and organic compounds are completely miscible in SCW. In high temperature aqueous environments at electrochemical potentials between the transpassive and active states, oxide films form on

metals surfaces to yield a passive state [26]. The high solubility of gases in SCW holds the potential for high partial pressures of oxygen even at moderate concentrations to yield an aggressive oxidizing environment.

2.2 Corrosion in SCW

As discussed in the previous section, the corrosion behavior of metals in SCW can vary dramatically depending on the pressure, temperature, and chemistry of the fluid. While the dominant corrosion mechanism in lower density SCW may be based on the molecular interactions between oxygen (or H_2O) and the metal and the transport of cation and anion species in the oxide, corrosion in high density SCW with higher dielectric constants is expected to occur via an electrochemical mechanism based on the formation and dissolution of a surface film [26-28]. The studies discussed in this review fall in the lower density, low conductivity SCW regime.

The growing database on corrosion of alloys in SCW includes five classes of alloys with temperatures up to 650˚C, exposure durations of 24 to 3,000 hours, and dissolved oxygen (DO) concentrations of <10 ppb to 8,000 ppb. Corrosion in SCW is highly alloy dependent, and experiments have been performed on ferritic-martensitic (FM) alloys, nickel-base alloys, and austenitic stainless steels in SCW. A limited number of experiments have also been performed on titanium alloys [29] and zirconium alloys [30-34]. A comparison of the weight gains experienced by several candidate alloys in 500˚C SCW following 3,000 hours of exposure is shown in Figure 2.3. The weight gains of the FM alloys are several times greater than that of the austenitic stainless steels, and the weight gain of nickel-base alloy 625 is lower still. While the weight gain of all three

alloy classes increases with temperature, the weight gain of the FM alloys and austenitic stainless steels show stronger time dependence in SCW than Ni-base alloy 625 in 500-600˚C SCW [28]. The dissolved oxygen (DO) content of the SCW also appears to influence the weight gain of some alloys, although a clear correlation has yet to be established for nickel-base alloys and austenitic stainless steels [28].

This study will focus on 316L stainless steel, and so the corrosion behavior of the austenitic stainless steels will be reviewed here in more detail. The compositions of all alloys discussed in Sections 2.2 and 2.3 are given in Table 2.1. Only a single composition is listed for each alloy, and slight heat to heat variations in compositions exist between different institutions. Within the category of austenitic stainless steels, there is substantial variation in the oxidation behaviors of various alloys. The weight gains of alloys 316, D9, and 800H following exposure to 600˚C SCW are shown as a function of time in Figure 2.4. In this study, 316 had greater weight gain than D9 or 800H for exposure times ranging from approximately 330-1025 hrs. For studies in 8 ppm dissolved oxygen (DO) SCW at 550˚C, the weight gain of 304 was slightly greater than 316L and 310 had the lowest weight gain of the three following a 500 hr exposure [29, 35]. Experiments performed in 400-550˚C deaerated SCW, however, indicated that the weight gain of 316L was generally greater than that of 304 following exposures of 419-578 hours [36, 37]. Despite the relatively high tendency of the 316L to oxidize compared to the other alloys mentioned, it has been reported that 316 exposed to 400˚C SCW for 7 days “showed no visible oxidation or pitting effects” when viewed in cross section [38].

While the weight gain of some austenitic stainless steels increases steadily with time, D9 and 800H may become susceptible to oxide spallation [39, 40]. The spalling

tendency of D9 was observed when the DO content of 500˚C SCW was increased from 25 ppb to 2 ppm. Possible reasons included formation of voids in the oxide, lattice parameter mismatch between the oxide layers or substrate, or cracking of the oxide induced by high expansion coefficient of D9 during subsequent heating or cooling [40]. The spallation observed for 800H in 500˚C SCW was apparently greater than that of the D9, but it was discovered that thermomechanical processing treatments could be applied to improve oxide adherence [39].

Oxidation rates generally follow Arrhenius behaviors, where the parabolic rate constant of oxidation, k_p, is expressed as a function of temperature,

$$k_p = k_o \times e^{\frac{-E_A}{RT}}, \tag{2.1}$$

where k_o is a pre-exponential factor, E_A is the apparent activation energy of the oxidation reaction, R is the gas constant, and T is the temperature. The oxide thickness, x, is given as,

$$x^n = k_p \times t, \tag{2.2}$$

where t is time and n is the oxide growth exponent. This equation may also be used for weight gain calculations, by substituting weight gain measurements, w, for x. By substituting equation (2.1) into equation (2.2), the oxide thickness can be expressed as,

$$x = k_{eff} \times e^{\frac{-E_A}{nRT}} \times t^{1/n}, \tag{2.3}$$

where $k_{eff} = k_o^{1/n}$. By analyzing the oxide thickness as a function of time, n can be determined. For example, in the absence of spallation, Chen et al. [40] found that D9 followed a parabolic growth rate law in 500˚C SCW with 1/n=0.54,0.53, or 0.52 depending on the environmental conditions and whether the oxide thickness or weight gain measurements were used for the calculation. Was et al. [36] used weight gain measurements to calculate the activation energies for the oxidation of 304 and 316L stainless steel as 210 kJ/mol and 214 kJ/mol, respectively. This was performed by plotting ln(w) vs. 1/T, the slope of which is equal to $-E_A/2R$ when the oxide growth exponent is taken as n=2. The dramatic increase in weight gain and oxide thickness with temperature for 316L and 304 stainless steel exposed to deaerated SCW is shown in Figure 2.5. With further increases in temperature, the 316 oxide morphology changes dramatically. Betova et al. exposed 316 to deoxygenated SCW at temperatures of 500˚C, 600˚C, and 700˚C for 100 hours [41]. They found that the crystallite size of the outer oxide on 316L increased with temperature, and following a 100 hour exposure at 700˚C, the oxide thickness was approximately 27 μm.

The oxides formed on stainless steel in low DO SCW generally form a duplex structure that consists of an outer layer of Fe rich oxide, and an inner layer of Cr rich oxide [36, 37, 40-42]. The outer layer is magnetite (Fe_3O_4) or a mixed magnetite-hematite layer, and the inner layer has a mixed-spinel structure [28, 36, 37]. These inner and outer layers have been observed to have a roughly 1:1 thickness ratio for 316L and 304 stainless steel [36]. Electron backscatter diffraction (EBSD) analysis has shown that

the crystallographic orientation of the oxide growth of both the inner and outer oxide layer on 304 and 316L stainless steel generally match that of the underlying grain [36].

An oxidation mechanism for austenitic stainless steels in SCW has been proposed by Was et al. based on both quantitative and qualitative analysis of the oxide layers formed on 316L and 304 in 400-550˚C SCW [36]. The inner oxide layers of both alloys were dense and had orientations identical to the metal substrate, and the interface between the two oxide layers was observed to be very even. This indicated that the interface may have been the original location of the metal surface. The approximately 1:1 thickness ratio between the inner and outer oxide layers (after accounting for the porosity in the outer oxide of 304) oxide indicated that they grew at the same rate. The inner layer appeared to grow via inward anion diffusion of oxygen into the base metal to form a protective oxide, while the outer layer grew via outward cation diffusion of iron to form a non-protective oxide. Crouch and Robertson [43] calculated an oxygen diffusion coefficient of 264 kJ/mol for the activation energy of oxygen diffusion. While this activation energy is comparable to the activation energies for oxide growth in 316L (214 kJ/mol) and 304 (210 kJ/mol), the resulting diffusion coefficient proposed by Crouch and Robertson falls 2 orders of magnitude short in predicting the thickness of oxide measured. By considering a short-circuit path of grain boundary diffusion, however, Was [36] was able to demonstrate that a diffusion depth comparable to the oxide thickness could be achieved. In summary, the oxidation of 316L and 304 stainless steels in SCW appears to occur through the inward diffusion of oxygen along short-circuit paths such as grain boundaries to form a protective inner oxide layer with a mixed-spinel structure, and

an outer non-protective layer of magnetite (Fe_3O_4) forms due to the outward diffusion of iron.

2.3 Intergranular cracking in supercritical water

The growing database on the cracking behaviors of candidate alloys for the SCWR concept includes data collected from constant extension rate tensile (CERT), constant load tests (CLT), and crack growth rate (CGR) tests on austenitic stainless steels (nine alloys), nickel-base alloys (eight alloys), FM steels (6 alloys), one titanium alloy, and one FM oxide dispersion strengthened (ODS) alloy. The temperatures of the experiments ranged from 288˚C to 732˚C, DO contents ranged from <10 ppb to 8000 ppb, pressures as high as 60 MPa were used, and chemical additions included HCl, NaCl, H_2SO_4, and H_2O_2. While the severity of cracking varied considerably between alloy classes and with environmental parameters, all except the titanium and ODS alloys displayed susceptibility to IG cracking. The austenitic stainless steels and nickel-base alloys generally exhibited greater cracking propensities than the FM steels. The only FM alloy that showed susceptibility to IG cracking was HT9. A summary of the experimental parameters and results of the studies are given in Table 2.2 and Table 2.3.

This review will focus on the IG cracking behavior of stainless steels in SCW and inert high temperature environments. The austenitic stainless steels analyzed included 304, 316, 316L, 316NG, 310, 347, 347H, 1.4970, BGA4, 31266, D9, and 800H. The alloys were evaluated in a variety of conditions – sensitized, solution annealed, grain boundary engineered, fine grain, and cold-worked. The different alloy conditions, combined with the varied experimental parameters, made for a challenging comparison

between data sets. Within specific institutions, however, common parameters were used, and these results will be used to evaluate the relationship between cracking and temperature, environment, and microstructure.

2.3.1 Temperature dependence

There is no universal acceptance of a single type of experiment or analysis method for quantifying cracking susceptibility, and so it is often explored through CERT, CLT, or CGR experiments. Following CERT experiments, the gage surfaces of the specimens can be analyzed to determine the crack densities, depths, and lengths, or their fracture surfaces can be analyzed to determine the %IG if the specimen are strained to failure. CLT experiments involve applying a specified load for a given period of time, and inspecting the specimen afterwards for signs of crack initiation or failure. CGR experiments measure the lateral growth rate of cracks, often at a constant stress intensity factor,

$$K = \sigma\sqrt{\pi a}, \tag{2.4}$$

where K is the stress intensity, σ is the stress, and a is half of the crack length. Unfortunately, not all experimental and analysis methods lead to the same conclusions regarding cracking susceptibility. In this section, it will be shown that CGR testing and fracture surface analysis of stainless steel specimens in SCW indicate that IG cracking susceptibility generally decreases with temperature in the SCW regime, whereas crack depth and sometimes gage surface crack density measurements indicate that cracking susceptibility increases with temperature. The temperature dependence of cracking will be divided into 2 categories, (1) temperature near or below the phase transition to

temperatures in the supercritical regime (360˚C to 400˚C), (2) increases in temperature within the supercritical regime (400˚C to 550˚C).

Studies performed on sensitized stainless steels 304 and 316 in pure water indicated a significant increase in the strain to failure as the temperature was increased from either 360˚C or 380˚C to 400˚C [44-47]. They observed that this increase in strain to failure correlated with a decrease in %IG on the fracture surface. Watanabe et al. strained non-sensitized 316L in a 800 ppm DO, 0.01M H_2SO_4 environment, however, and demonstrated that a substantial decrease in strain to failure occurred when the temperature was increased from 360˚C to 400˚C [48]. Experiments on neutron irradiated, modified 316 stainless steel demonstrated that the %IG on the fracture surface increased with temperature from 385˚C to 400˚C for both solution annealed and (CW) specimens. Although the water density was three times greater at 385˚C due to greater system pressure, Teysseyre and Was determined that the difference in cracking could be explained by temperature alone [49]. These studies provide strong evidence that both acid additions and irradiation damage may alter the temperature dependence of IG cracking near the phase transition.

Crack growth rate studies performed by Peng et al. [50] and Arioka et al. [51]indicate that the crack growth rate in high temperature water initially increases, but then rapidly decreases as the temperature is increased to or near the supercritical regime, as shown in Figure 2.6. Both researchers analyzed cold-worked 316 and witnessed this temperature dependence of the CGR despite substantial differences in the extent of cold work and water chemistries. The work performed by Arioka et al. indicated that crack growth rates peaked at temperatures between 320˚C and 340˚C for 20%-50% CW316 in a 500 ppmB +

2 ppm Li + 30cc/DH_2 / kgH_2O environment and then decreased. Peng et al. attributed the decrease in crack growth rate from 360˚C subcritical water to 400˚C supercritical water to crack blunting due to rapid oxidation in SCW.

Although the CGR values measured from *CGR experiments* decrease as the temperature is increased further into the SCW regime, the crack depth into *CERT-evaluated* tensile specimens and crack lengths on the gage surfaces have been shown to increase as a function of temperature [4]. Stainless steel 304 and 316L specimens were strained in deaerated SCW at temperatures ranging from 400-550˚C and the crack depth increased by a factor of 21 while the average crack length increased by roughly a factor of 3 with the temperature increase. The crack densities on the gage surfaces of the 304 and 316L, however, decreased with temperature by 70% and 72%, respectively. Tsuchiya et. al. analyzed the cracking behavior of sensitized 304 in 8 ppm DO water at temperatures ranging from 290˚C to 550˚C and witnessed a transition in the %IG on the fracture surface from 100% at 290˚C to 0% at temperatures of 400˚C and above [45]. They noted that there were a considerable number of cracks on the gage surfaces of the specimens, however, and that the density increased with temperature [46]. Therefore, opposite trends in cracking susceptibility are measured under these conditions for %IG on fracture surface analysis vs. crack density measurements on the gage surface as shown in Figure 2.7.

2.3.2 Chemical additions and property changes

As discussed in the SCW environment section, acids can readily dissociate in SCW if the density is sufficiently high, and the addition of even small amounts of acid can

dramatically decrease the pH of the environment. Both high and low pH values can cause chemical dissolution of a protective oxide layer. Similarly, higher dielectric constants and ionic products that can result from an increase in pressure cause metals to ionize more readily, and solubility of metal oxide increases. Therefore, anodic dissolution of metals increases with higher dielectric constants. The chemical additions and variance in the dielectric constant discussed in this section, therefore, were anticipated to significantly alter the cracking behaviors of stainless steels in SCW.

Additions of HCl and H_2SO_4 both increased the cracking propensities of stainless steels in SCW. Fujisawa et al. [5], observed that while 316 stainless steel did not crack in pure 400˚C water at 25 MPa. An addition of 0.001 mol/l HCl, however, resulted in a reduction in the strain to failure from 38% to approximately 21% and was accompanied by intergranular facets on the fracture surface. Additions of 0.01 mol/l HCl further decreased the strain to failure. Bosch and Delafosse also observed an increase in cracking propensity with the addition of 1 g/l HCl [52]. Their estimated crack growth rate for 31266 in a 400˚C SCW environment with 1 g/l HCl, at a loading of 100% of the yield strength, was over an order of magnitude greater than that estimated for a 10wt% H_2O_2 + 1.6 g/l NaCl SCW environment [52]. The IG cracks were observed to initiate at the sites of precipitate dissolution, and had a deep and narrow morphology. Watanabe et al. [48] evaluated the impact of H_2SO_4 on the cracking susceptibility of 316L in 400˚C SCW. They found that the addition of 0.01 M H_2SO_4 in 8ppm DO SCW at 60 MPa resulted in a dramatic decrease in the strain to failure from approximately 48% to 12%. The cracks appear to have a narrower morphology than the cracks observed by Teysseyre and Was on 304 and 316L in pure deaerated SCW [4].

Watanabe et al. [48] also altered the pressure of the SCW to evaluate the effect of the dielectric constant on the cracking behavior, and did not see much change in the strain to failure of the 316L in this very aggressive environment. In a separate study [24], however, they analyzed the cracking behavior of sensitized 316 in pure 400˚C SCW and witnessed a dramatic decrease in the strain to failure as the pressure was increased from 25 MPa to 60 MPa. This was attributed to the increase in the dielectric constant that resulted from the pressure increase.

The influence of hydrogen addition on cracking propensity has also been analyzed in SCW [5, 49]. In BWR environments, cracking propensity is known to decrease with the addition of hydrogen due to a decrease in corrosion potential. Fujisawa et al. varied the H_2 partial pressure from 0.05 MPa to 3.6 MPa in 400˚C SCW at 25 MPa pressure containing 0.01 mol/l HCl, and analyzed the cracking behavior of 316 stainless steel. They found that the strain to failure and maximum stress generally increased with increasing H_2 partial pressure. Teysseyre and Was [49] found that the cracking propensity of neutron irradiated modified 316 stainless steel dramatically decreased with the addition of 500 ppb H_2 in both the solution annealed and CW conditions.

2.3.3 Irradiation dependence

Irradiation damage has been demonstrated to increase the cracking propensities of 316L, modified 316, D9, and 800H in a SCW environment at temperatures of 400-500˚C [49, 53-56]. Zhou et al. [53] evaluated the cracking propensities of proton irradiated 316L, 800H, and D9 at temperatures of 400˚C and 500˚C. They found that the cracking propensity of 316L, as quantified by %IG on fracture surface, crack length per

unit area on the gage surface, and crack depth all increased with dose from 2 to 7 dpa as shown in Figure 2.8. Previous work had also shown that the cracking propensities of 316L, 800H, and D9 increased substantially in the 7 dpa proton irradiated condition compared to the unirradiated condition as shown in Figure 2.9. It can be seen from the figure that the normalized crack length per unit area on the irradiated regions of the specimens was greater than that on the unirradiated portions. Teysseyre and Was evaluated modified 316 stainless steel that had been neutron irradiated to 26.9-43.9 dpa, in both hydrogenated and deaerated SCW at temperatures ranging from 385-500˚C. The irradiation temperatures ranged from 390-520˚C, and the alloy was evaluated in both the solution annealed and CW conditions, which resulted in hardness values ranging from 296-368 kg/mm^2. While IG cracking was not observed in a 400˚C argon environment, it did occur in the SCW environment, and exhibited dependence on hardness, temperature (previously discussed), and hydrogen additions (previously discussed).

The increase in cracking propensity with irradiation damage was expected, as it is commonly known to enhance cracking of austenitic alloys in LWR environments. While IASCC is often correlated with irradiation induced hardening, RIS, or the formation of dislocation loops, the IASCC mechanism has yet to be fully explained. The proton irradiation studies did address the irradiation induced microstructure and microchemistry of the irradiated stainless steels, but no decisive conclusions could be reached regarding the reason for the increase in cracking propensity. Irradiation induced microstructure analysis of the dislocation loops and voids in 316L indicated both temperature and dose dependence [53-56]. In general the size of the dislocation loops increases with temperature at the expense of the loop density, and void densities became significant as

the temperature was increased from 400˚C to 500˚C. Radiation induced segregation at grain boundaries reduced chromium to levels of 11-14 wt% compared to the unirradiated 19.1%, and occurred by the purported inverse Kirkendall mechanism [57]. The grain boundary chromium depletion at 7 dpa broadened with a temperature increase from 400˚C to 500˚C as shown in Figure 2.10[53]. These moderate levels of depletion coupled with the likely low potential deaerated SCW environment, make chromium depletion an unlikely candidate to explain the increase in cracking propensity of stainless steels in the irradiated condition [55]. The cracking propensity of 316L does correlate with hardening, however, at both 400˚C and 500˚C [53].

In the neutron irradiation study [49], Teysseyre et al, showed that cracking propensity increased with hardening regardless of whether the hardness was due to irradiation alone, or a combination of CW and irradiation. From this it was suggested that the irradiation induced features of the microstructure which determine the hardness, and/or the resulting heterogeneity in the deformation behavior may be affecting the cracking behaviors of the alloys. The neutron irradiation induced microstructure was not analyzed, however, and so a full interpretation of the IASCC behavior was not possible.

2.3.4 Cracking mechanism in SCW

The mechanism of IG cracking of stainless steels in SCW has been discussed by several researchers, and it is possible that the operating mechanism may change depending on the environment and condition of the alloy [3, 28, 44, 48, 49]. Abe et al. witnessed a pressure dependence of the cracking behavior of sensitized 316 stainless steel in 400˚C SCW, where the enhancement in cracking at higher pressures was attributed to a

higher dielectric constant [44]. They claimed that this observation was evidence of a dissolution mechanism driving the IG cracking, as higher dielectric constants enhance anodic dissolution of the metal. In the same study, however, they found that non-sensitized 316L cracked readily in 400˚C SCW with 0.01 M H_2SO_4 + 0.05 M H_2O_2 even at the lowest pressure of 25 MPa, and further increases in pressure to 60 MPa did not appear to increase the crack density. Cross sectional analysis revealed networks of sharp IG cracks with oxides along the grain boundaries. Therefore, the operation of a dissolution mechanism was deemed unlikely, and an internal oxidation-type mechanism was proposed [44]. It was impossible to determine if the internal oxidation occurred pre- or post-cracking, however, and it was concluded that additional analysis would be required to verify this hypothesis. Fujisawa et al. also studied the effect of acid additions by evaluating the cracking behavior of 316 in 400˚C SCW. While no cracking on the fracture surfaces was found following straining to failure in deionized water, the additions of 0.001 and 0.01 mol/l HCl to the SCW resulted in IG cracking on the gage and fracture surfaces of the specimens. It was stated that the IG cracking was likely caused by a dissolution mechanism, an oxidation mechanism, or a combination thereof.

Cracking in low density, pure SCW is simpler to discuss, because corrosion has been suggested to be chemically rather than electrochemically driven [49] and the pH is generally more neutral. Teysseyre and Was [4] analyzed the cracking behaviors of unirradiated 304 and 316L in 400-550˚C SCW and estimated the crack growth rate from the maximum crack depth and time under load. The crack growth rate is generally expected to be thermally activated, and so it often follows an Arrhenius behavior with temperature. Therefore, the crack growth rate, da/dt, can be described as,

$$\frac{da}{dt} = Ae^{\frac{-Q}{RT}}, \tag{2.5}$$

where A is a pre-exponential factor, Q is the activation energy, R is the gas constant, and T is the temperature. They plotted the calculated crack growth rate versus inverse temperature as shown in Figure 2.11. Given the expected crack growth rate behaviors of the alloys, the apparent activation energy for crack growth can be estimated by taking the slope of ln(da/dt) vs 1/T, which is equal to –Q/R. From these calculations, Teysseyre and Was calculated activation energies of 105 and 85 kJ/mol for 304 and 316L, respectively [4]. These activation energies are lower than the previously discussed activation energy for oxide growth on stainless steels (210-214 kJ/mol). Therefore, they suggested that a short-circuit growth path for the IG cracking may exist due to either a slip-oxidation type mechanism or selective internal oxidation [4, 28].

As discussed previously, however, dramatic decreases in crack growth rate have been measured with temperature increases near and into the SCW regime [50, 58]. Peng et al. [50] addressed this apparent discrepancy by noting that oxidation rates increase dramatically with temperature in the SCW regime, which may have caused crack blunting under constant K condition. During the CERT experiments, however, constant straining would continually rupture the oxide film to increase the crack depth. A separate study by Arioka et al. [59] evaluated the creep behavior of CW 316 in air under a constant load with an initial stress intensity of 40 MPa $m^{1/2}$. They used the maximum crack depth and exposure time to calculate the creep CGR, and observed a strong temperature dependence with the CGR increasing with temperature from 380-475˚C as shown in Figure 2.12. From this data, they determined that the activation energy for IG

creep crack growth was ~100 kJ/mol, which is consistent with the activation energies of 304 (105 kJ/mol) and 316L (85 kJ/mol) in 400-550˚C SCW measured by Was and Teysseyre [4]. An earlier study by Arioka et al. [60] analyzed the creep behavior of solution-treated and sensitized 316 in high temperature air at a constant load of 343 MPa for 13,150 hours, and observed IG cracking at temperatures of 500- 550˚C. They attributed the IG cracking to a GB sliding mechanism because sliding and cavities were observed at grain boundaries, and the %IG on the fracture surface was reduced in the sensitized alloy that contained grain boundary carbides that suppressed GB sliding. They also calculated the activation energy of the creep behavior in the 380-500˚C regime to be 110 kJ/mol [60], which is also consistent with that measured for IG cracking in SCW by Teysseyre and Was [4].

The previously discussed results lend strong support for a creep based mechanism for IG cracking in low density SCW. In addition to Arioka's observations of IG creep cracking in high temperature air, Teysseyre and Was [4] observed apparent creep cracking of 304 stainless steel in a 500˚C argon (99.998% pure) environment. IG facets were observed on the fracture surface at an area fraction of 5-10% near the center of the specimens, indicating that environmental influence on the cracking was unlikely. IG facets around the perimeter of the fracture surface would have been more indicative of environmental influence, as that region of the specimen is in contact with the environment for the duration of the experiment. The much higher IG cracking propensity in SCW, however, indicated that the environment greatly influenced the cracking behavior. Evaluation of a 316L specimen under the same conditions showed completely ductile rupture, however [4]. Gupta et al. [61] also observed IG cracking of 7 dpa proton

irradiated FM alloy HT9 in a 500˚C argon environment. The maximum crack length and crack densities, however, were 51% and 87% less than those observed in a SCW environment, respectively. These findings support an environmentally assisted creep cracking mechanism for SCW environments.

2.4 Creep cracking

It is recognized that an equicohesive temperature (ECT) exists at which the matrix and grain boundaries have equal strength [62]. Below the ECT, the grain boundaries are stronger than the matrix, and above the ECT, the grain boundaries become relatively weak. The ECT is not fixed, however, and is known to decrease with strain rate [62]. Therefore, a transition occurs from transgranular cracking to intergranular cracking as temperature increases for a sufficiently low strain rate. This transition may be attributed to the occurrence of grain boundary sliding (GBS), which is often stated to play a key role in the initiation of intergranular cavitation at elevated temperatures [63]. The morphologies of creep cracks are highly dependent on temperature and strain rate. At high stresses and intermediate temperatures, fracture often occurs in the form of wedge cracks which are believed to form due to the inability to accommodate grain boundary sliding driven by shear stresses as illustrated in Figure 2.13 [62-64]. They are generally stated to occur preferentially along boundaries aligned for maximum shear [62]. As temperature is increased and/or applied stress is decreased, grain boundary cavity nucleation, growth, and coalescence become the dominant mode for IG creep fracture. This type of creep fracture is known as r-type, and such cavities are frequently reported to form along boundaries oriented perpendicular to the tensile axis [58, 65, 66]. Therefore,

the inclination of the cracks with respect the tensile axis can vary dramatically as experimental parameters are altered. It has been shown that relatively high strain rates result in preferential cavity formation on boundaries inclined at a true angle of ~45˚ with respect to the tensile axis, whereas lower strain rates result in cavity formation on boundaries normal to the tensile axis as shown in Figure 2.14 [67].

While there is nearly universal support for the nucleation of wedge type cracks due to the inability to accommodate grain boundary sliding, the mechanism for the nucleation of the r-type cavities is still a subject of debate. It has been suggested, however, that given the various creep mechanisms and temperature, stress, and alloy dependencies, perhaps it is not realistic to assume that a single mechanism is operating in all conditions [64]. Nucleation of cavities may occur thermally via condensation of vacancies on stressed surfaces if the homologous temperature is high enough for substantial vacancy concentrations and mobility. Cavities have also been suggested to nucleate as a result of elevated stresses at grain boundary irregularities or as a result of dislocation pile up at grain boundary particles.

Elevated levels of stress may develop around geometrical or structural irregularities along grain boundaries such as grain boundary particles which resist sliding [68], or at grain boundary ledges, cusps at triple junctions, athermal decohesion sites, or at sites of slip band intersection with grain boundaries [63]. GBS is often stated to be a key contributor to cavity formation, although in a more localized region for r-type cavities [64]. GBS is expected to occur preferentially along boundaries oriented for maximum shear. Therefore, the consistent observations of r-type cavity (and sometimes wedge-type) formation along boundaries perpendicular to the tensile axis, appears to

contradict this postulation. While no consensus has been reached on this apparent discrepancy, some potential reasons have been discussed. Courtney [64] argued that the crack growth rates of wedge cracks are greater along boundaries perpendicular to the tensile axis. Therefore, although, sliding may occur preferentially along boundaries oriented for maximum shear, the only nucleated wedge cracks that will grow to detectability may be those that have the greatest propensity to grow.

Similar arguments have been made for the r-type cavities, in that these cavities may form along all grain boundaries, but only those which are able to grow to eventually lead to intergranular creep failure [64]. Dyson and McLean [69] proposed a theory of cavity nucleation and growth that was later built upon by Dyson [70], that decohesions nucleate athermally by dislocation pile up at grain boundary particles (rather than GBS). They postulated that each incremental strain, $\delta\varepsilon$, results in the formation of spherical decohesions with a distribution of radii, r. The only decohesions that develop into cavities by vacancy absorption are those that satisfy the equation,

$$r > \frac{2\gamma_S}{\sigma_{n^*}}, \tag{2.6}$$

where σ_{n^*} is the local steady state tensile stress. This is illustrated in Figure 2.15 where the cavity radius distribution is shown as well as the critical radius, r_C, above which cavities are stable. The boundaries with the greatest normal stress will be those that are oriented perpendicular to the tensile axis. Therefore, although the distribution of decohesion sites may be random, cavities will preferentially develop on boundaries perpendicular to the tensile axis.

As alluded to in the previous paragraph, crack growth mechanisms may dominate the observed cracking behavior, and may not be reliable indicators of the nucleation mechanism. Therefore, it is imperative to understand the potential errors in cavity nucleation measurements to prevent erroneous interpretation of crack nucleation versus growth mechanisms. Dyson [70] argued that cavity nucleation measurements will usually be influenced by the growth of the cavity due to the small scale of the initiation event versus the limited resolution of most analytical instruments. The cavities that nucleate at stresses equal to or greater than the nucleation stress are generally about 2 to 5 nm in size [63], whereas the diameter of the voids reported in most cavity nucleation studies are 200 nm or larger, and therefore such measurements are likely influenced by growth [70, 71].

Void growth can occur through several modes including surface diffusion, grain boundary diffusion, and power-law creep. The controlling mechanism depends on the temperature and applied stress, and may change as the void grows. In general, grain boundary diffusion controls void growth at low stresses, and surface diffusion or power law creep controls growth at higher stresses [64]. The shape of a void is often indicative of its growth mechanism. Spherical voids are often controlled by surface diffusion, and grain boundary diffusion may limit their growth. Voids may take on an elliptical shape when grain boundary diffusion is faster, and they may form a wedge-type shape when surface diffusion is low.

It is perhaps most realistic to assume that both diffusion and dislocation creep may influence the growth of cavities. Beeré and Speight [72] introduced a schematic that illustrates the combined influence of diffusional and dislocation creep on cavity growth,

as shown in Figure 2.16. A cavity with initial radius, a, is surrounded by material that generates vacancies which diffuse towards the cavity (region I). The vacancies that diffuse into the cavity cause an outward flow of atoms which plate into the grain boundary, and the resulting wedge at the cavity edge create a wedge force in this region. This wedge stress is accommodated by dislocation power law creep in region 2, which is bounded by b, the intercavity half spacing. While this idealized schematic illustrates how both grain boundary diffusion and dislocation creep can influence crack growth, the existence of such discrete regions is unlikely. Needleman and Rice [73] also considered the coupled influence of diffusion and dislocation creep on cavity growth. They calculated a characteristic diffusion length, L, that expresses the coupling between dislocation creep and diffusion on cavity growth,

$$L = \left(\frac{D_B \delta_B \Omega \sigma_\infty}{kT \dot{\varepsilon}_\infty} \right)^{1/3}, \tag{2.7}$$

where σ_∞ is the remotely applied equivalent tensile stress, and $\dot{\varepsilon}_\infty$ is the associated creep strain rate. Therefore, L decreases with increasing temperature and has values of 0.25 to 25 μm for metals when stressed to 10^{-3} σ_n/E at a homologous temperature of 0.5. When L is much smaller that the cavity diameter, a, grain boundary diffusion has little impact on the cavity growth rate. When L is less than the intercavity half spacing, b, the coupling of the diffusion and dislocation creep is significant and the cavity growth rate is substantially higher than that expected from diffusion alone. When L>b, however, the influence of dislocation creep is negligible. By comparing the results of Beeré and Speight [72] to those of the rigid grain approximations, which neglect the effects of

dislocation creep, it can be seen that for cavities with radii much smaller than the intercavity spacing (low a/b), the effects of dislocation creep can often be neglected, but they become important as the cavities get larger (greater a/b) as shown in Figure 2.17.

2.5 Deformation in crystalline materials

Deformation in crystalline materials occurs primarily through crystallographic slip along the most densely packed planes and directions in the lattice. Although the deformation mechanism is the same in both single and polycrystalline materials, slip in single crystals is simpler to describe because the constraints on deformation are fewer than for polycrystals. Deformation in single crystals is often analyzed using Schmid's law, where the tensile yield strength of a grain can be calculated from its most favorably oriented slip system.

In polycrystalline materials, deformation is restricted by surrounding grains, and multiple slip systems must become active in order to satisfy the imposed shape change. Deformation in polycrystalline materials can be studied using either upper or lower-bound analyses. Upper-bound approaches assume geometrically self-consistent deformation fields, while lower-bound approaches assume self-consistent internal stress fields [74]. Neither one of these approaches is completely accurate, however, because the upper-bound models violate equilibrium of stress across neighboring grains and lower-bound models do not account for strain compatibility between grains.

The first attempt at describing the deformation behavior of polycrystals was made by Sachs in 1928 with a method similar to treating single crystals [75]. Sachs assumed that only one slip system was active in each grain, and estimated the tensile strength as an

average of the yield strengths of the individual crystals. The limitation of slip to one system in a polycrystalline material, however, would give rise to strain incompatibilities between grains. In 1938, Taylor pointed out this weakness, stating that "All attempts made so far to correlate the mechanical properties of crystal aggregates with those of single crystals rest on the same fallacy, namely that each crystal grain can be treated as though its neighbors did not exist." [76]. Taylor proposed an alternative upper-bound approach whereby all grains undergo the same shape change as the entire polycrystal [76, 77]. He assumed that 5 slip systems were active according to the von Mises criterion [78], and that all plastic deformation occurred via crystallographic slip.

Since the introduction of Taylor's model, various other attempts have been made at modeling grain interaction during deformation. In 1951, Bishop and Hill [79, 80] investigated the stress states required to simultaneously activate 5 or more slip systems, and found 28 compatible states. Several other models of polycrystalline plasticity are shown in Figure 2.18. Figure 2.18(a) illustrates a lower bound model where all stress components are identical, but strain varies from grain to grain. Figure 2.18(b) illustrates Sachs model (1928) [75] where each grain is loaded proportionally, and neither strain compatibility or stress equilibrium is achieved. The upper-bound Taylor model is illustrated in Figure 2.18(c) where each grain undergoes uniform shape change. Figure 2.18(d) illustrates Kochendörfer's [81] modification of the Sachs model to account for bending stresses near grain boundaries. Ashby [82] showed that geometrically necessary dislocations could be responsible for alleviating strain incompatibilities as illustrated in Figure 2.18(e). A lower-bound model developed by Chastel and Dawson [83] is illustrated in Figure 2.18(f) where each individual grain deforms when the critical

level of stress is reached. In materials where strain is more heterogeneous and mean-field strain assumptions may not hold, more rigorous finite element modeling calculations may provide the best means of describing local response.

In the current study, the need to analyze large areas of the polycrystal to obtain statistically significant cracking results outweighed the need to study how the detailed influence of neighboring grain geometries on the response of an individual grain. The Schmid factor is widely accepted as a valid predictor of the slip system most likely to activate, and the Taylor model's requirement of multiple slip and its reasonable texture predictions have caused it to be favored by material scientists [84]. Therefore, the Schmid factor and Taylor factor will be utilized throughout this study.

2.5.1 Schmid's Law

As stress is applied to a crystal, the resolved shear stress, τ_{RSS}, acting on a slip system increases until it reaches the critically resolved shear stress, τ_{CRSS}. Then slip occurs by the movement of dislocations through the lattice as the grain plastically deforms. This requirement for crystallographic slip is known as Schmid's Law,

$$\tau_{RSS} = \tau_{CRSS}, \tag{2.8}$$

or,

$$\tau_{CRSS} = \sigma_y \cos\lambda \cos\phi, \tag{2.9}$$

where σ_y is the yield stress, λ is the angle between the slip direction and the tensile axis, and ϕ is the angle between the slip plane normal and the tensile axis as shown in Figure 2.19.

The Schmid factor, m, is equal to the quantity $\cos\lambda\cos\phi$. Therefore, in a single crystal, the tensile yield stress, σ_y, can also be expressed as,

$$\sigma_y = \frac{\tau_{CRSS}}{m}. \tag{2.10}$$

Greater values of m indicate that less applied stress will be required to activate the slip system. In a face-centered cubic (FCC) material, the favored slip directions and planes are the $\langle 110 \rangle \{111\}$ families, respectively, amounting to 12 independent slip systems. When a single value of m is reported for a grain, it corresponds to the most favorably oriented slip system, i.e. the one that requires the least amount of applied stress to undergo crystallographic slip.

The orientation of the slip planes, and therefore m, is determined by the orientation of the grain. Therefore, the orientation dependence of m for an FCC material can be visualized on a basic stereographic triangle as shown in Figure 2.20. Crystals with [111] orientations have the lowest Schmid factors and require the greatest amount of applied stress to deform, and crystals with λ=45˚, ϕ=45˚ have the greatest Schmid factors and require the least amount of applied stress to deform.

2.5.2 Taylor factor

The Taylor model [76, 77] describes the deformation of polycrystalline materials through the slip behavior of the individual crystals. The key assumptions of the Taylor model are,

(1) all crystals undergo the same shape change as the entire polycrystal,

(2) five slip systems are active in each crystal,

(3) the critically resolved shear stress, τ_{CRSS}, is the same for all active slip systems, and

(4) all deformation occurs via crystallographic slip.

Hosford [74] provides an excellent description of the Taylor factor calculation for a single grain orientation, and his formulas will be used here.

When a specimen is strained in uniaxial tension, the external strain is axially symmetric. The imposed deformation is achieved, however, through crystallographic slip driven by shear stresses on several slip systems in the crystal. The orientations of the slip systems, in turn, depend on the crystallographic orientation of the grain. Therefore, it is convenient to describe the external normal ($d\varepsilon_{xx}$, $d\varepsilon_{yy}$, $d\varepsilon_{zz}$) and shear ($d\gamma_{yz}$, $d\gamma_{zx}$, $d\gamma_{xy}$) strains in relation to the three cubic axes of the crystal as, $d\varepsilon_1$, $d\varepsilon_2$, $d\varepsilon_3$, $d\gamma_{23}$, $d\gamma_{31}$, $d\gamma_{12}$. Then, the imposed shape change can be described by the crystallographic shear strains, $d\gamma_i$, from the reference frame of the cubic crystal. The orientation of the specimen axes (x,y,z) can be described in relation to the cubic axes (1,2,3) of the crystal by two angles, ψ and χ as shown in Figure 2.21.

As discussed previously, FCC crystals have 12 independent slip systems, and the external strain must be accommodated through the activation of some combination of these slip systems. The slip systems and the notation that will be used to designate each system are given in Figure 2.22. Using these slip system designations and the direction cosines between the slip elements and cube axes given in Table 2.4, the external principle external strains, $d\varepsilon_i$, and external shear strains, $d\gamma_{ij}$, can be expressed relative to the cube axes in terms of the crystallographic shear strains, $d\gamma_{ai,}$- $d\gamma_{di}$, as follows,

$$
\begin{aligned}
d\varepsilon_1 &= (-d\gamma_{aII} + d\gamma_{aIII} - d\gamma_{bII} + d\gamma_{bIII} - d\gamma_{cII} + d\gamma_{cIII} - d\gamma_{dII} + d\gamma_{dIII})/\sqrt{6} \\
d\varepsilon_2 &= (+d\gamma_{aI} - d\gamma_{aIII} + d\gamma_{bI} - d\gamma_{bIII} + d\gamma_{cI} - d\gamma_{cIII} + d\gamma_{dI} - d\gamma_{dIII})/\sqrt{6} \\
d\varepsilon_3 &= (-d\gamma_{aI} + d\gamma_{aII} - d\gamma_{bI} + d\gamma_{bII} - d\gamma_{cI} + d\gamma_{cII} - d\gamma_{dI} + d\gamma_{dII})/\sqrt{6} \\
d\gamma_{23} &= (+d\gamma_{aII} - d\gamma_{aIII} - d\gamma_{bII} - d\gamma_{bIII} + d\gamma_{cII} - d\gamma_{cIII} - d\gamma_{dII} + d\gamma_{dIII})/\sqrt{6} \\
d\gamma_{31} &= (-d\gamma_{aI} + d\gamma_{aIII} + d\gamma_{bI} - d\gamma_{bIII} + d\gamma_{cI} - d\gamma_{cIII} - d\gamma_{dI} + d\gamma_{dIII})/\sqrt{6} \\
d\gamma_{12} &= (+d\gamma_{aI} - d\gamma_{aII} + d\gamma_{bI} - d\gamma_{bII} - d\gamma_{cI} + d\gamma_{cII} - d\gamma_{dI} + d\gamma_{dII})/\sqrt{6},
\end{aligned}
\tag{2.11}
$$

where the subscripts that each of the shear strains refers to are defined in Figure 2.22. Since the volume of the crystal will be conserved as it deforms, the sum of the normal strains must equal zero,

$$d\varepsilon_1 + d\varepsilon_2 + d\varepsilon_3 = 0. \tag{2.12}$$

This relationship indicates the shows that the principle strains are not independent, resulting in a system of 5 independent equations with 12 unknowns. This system of equations can only be solved if certain assumptions are made. Taylor considered the work expended in slip,

$$\Sigma_i(\tau_i d\gamma_i), \tag{2.13}$$

and assumed that crystallographic slip would occur in a way that would minimize the required energy for the crystal to deform. Because it was also assumed that the critically resolved shear stress was the same for all active slip systems, this is equivalent to minimizing the total amount of shear strain, $d\gamma = \Sigma_i |d\gamma_i|$, required for the shape change. To accommodate an arbitrary shape change, a minimum of 5 of the slip systems have to

be active. Therefore, Taylor proposed that 7 of the 12 shear terms in equation (2.11) could be set equal to zero to solve for the remaining 5. Whichever combination of 5 active slip systems required the least amount of plastic work can then be used to calculate the Taylor factor which is given as the ratio of the shear strain, $d\gamma$, to the uniaxial strain ($d\varepsilon_x$ for a tensile direction along the x-axis),

$$M = \frac{d\gamma}{d\varepsilon_x}. \tag{2.14}$$

Therefore, the Taylor factor is a parameter that describes the amount of shear strain required in a grain to satisfy a prescribed shape change. Greater values of M imply that more shear strain is required, and that greater amounts of energy would be expended to deform the grain. The value of M is shown as a function of crystallographic orientation in a stereographic triangle in Figure 2.23. It can be seen that the [111] and [110] orientations have the highest Taylor factors.

2.5.3 Lattice rotation

A consequence of restricted crystallographic slip is the occurrence of lattice rotation. This is illustrated in Figure 2.24 where crystals are strained without and with constraints along the tensile axis. Without constraints, the crystal elongates from the applied stress with no change in slip plane or direction, but the orientation of the tensile axis changes with respect to the crystal orientation. When the orientation of the tensile axis is constrained, the crystal again elongates from the applied stress, but the individual elements within the crystal are forced to rotate with respect to the tensile axis.

When a volume of material is deformed, the strain can be described by normal (ε_{xx}, ε_{yy}, ε_{zz}) and shear displacements (ε_{xy}, ε_{yx}, ε_{xz}, ε_{zx}, ε_{yz}, ε_{zy}) in tensor form. The

expressions for the infinitesimal strains, $\frac{\partial u}{\partial x}$ though $\frac{\partial w}{\partial z}$, may be used for small strains,

where $\varepsilon_{xx} = \frac{\partial u}{\partial x}$ etc.,

$$\begin{vmatrix} \varepsilon_{xx} & \varepsilon_{xy} & \varepsilon_{xz} \\ \varepsilon_{yx} & \varepsilon_{yy} & \varepsilon_{yz} \\ \varepsilon_{zx} & \varepsilon_{zy} & \varepsilon_{zz} \end{vmatrix} = \begin{vmatrix} \frac{\partial u}{\partial x} & \frac{\partial u}{\partial y} & \frac{\partial u}{\partial z} \\ \frac{\partial v}{\partial x} & \frac{\partial v}{\partial y} & \frac{\partial v}{\partial z} \\ \frac{\partial w}{\partial x} & \frac{\partial w}{\partial y} & \frac{\partial w}{\partial z} \end{vmatrix}, \tag{2.15}$$

where the mathematical shear displacements are equal to half of the engineering shear displacements, γ_{ij},

$$\begin{aligned} \varepsilon_{yz} = \varepsilon_{zy} &= \frac{1}{2}\gamma_{yz} = \frac{1}{2}\left(\frac{\partial v}{\partial z} + \frac{\partial w}{\partial y}\right) \\ \varepsilon_{zx} = \varepsilon_{xz} &= \frac{1}{2}\gamma_{zx} = \frac{1}{2}\left(\frac{\partial w}{\partial x} + \frac{\partial u}{\partial z}\right) \\ \varepsilon_{xy} = \varepsilon_{yx} &= \frac{1}{2}\gamma_{xy} = \frac{1}{2}\left(\frac{\partial u}{\partial y} + \frac{\partial v}{\partial x}\right). \end{aligned} \tag{2.16}$$

While the normal displacements result in only strain, the shear displacements lead to both strain and rigid-body rotation. Consider the two dimensional shearing of a rectangle as shown in Figure 2.25. Shearing in the x,y plane can result in both pure shearing of an area element, or pure rotation. Therefore, it is helpful to separate the displacement tensor into a strain tensor, ε_{ij}, and a rotation tensor, ω_{ij},

$$\varepsilon_{ij} = \begin{vmatrix} \varepsilon_{xx} & \varepsilon_{xy} & \varepsilon_{xz} \\ \varepsilon_{yx} & \varepsilon_{yy} & \varepsilon_{yz} \\ \varepsilon_{zx} & \varepsilon_{zy} & \varepsilon_{zz} \end{vmatrix} = \begin{vmatrix} \frac{\partial u}{\partial x} & \frac{1}{2}\left(\frac{\partial u}{\partial y} + \frac{\partial v}{\partial x}\right) & \frac{1}{2}\left(\frac{\partial u}{\partial z} + \frac{\partial w}{\partial x}\right) \\ \frac{1}{2}\left(\frac{\partial u}{\partial y} + \frac{\partial v}{\partial x}\right) & \frac{\partial v}{\partial y} & \frac{1}{2}\left(\frac{\partial v}{\partial z} + \frac{\partial w}{\partial y}\right) \\ \frac{1}{2}\left(\frac{\partial u}{\partial z} + \frac{\partial w}{\partial x}\right) & \frac{1}{2}\left(\frac{\partial v}{\partial z} + \frac{\partial w}{\partial y}\right) & \frac{\partial w}{\partial z} \end{vmatrix} \tag{2.17}$$

$$\omega_{ij} = \begin{vmatrix} \omega_{xx} & \omega_{xy} & \omega_{xz} \\ \omega_{yx} & \omega_{yy} & \omega_{yz} \\ \omega_{zx} & \omega_{zy} & \omega_{zz} \end{vmatrix} = \begin{vmatrix} 0 & \frac{1}{2}\left(\frac{\partial u}{\partial y} - \frac{\partial v}{\partial x}\right) & \frac{1}{2}\left(\frac{\partial u}{\partial z} - \frac{\partial w}{\partial x}\right) \\ \frac{1}{2}\left(\frac{\partial v}{\partial x} - \frac{\partial u}{\partial y}\right) & 0 & \frac{1}{2}\left(\frac{\partial v}{\partial z} - \frac{\partial w}{\partial y}\right) \\ \frac{1}{2}\left(\frac{\partial w}{\partial x} - \frac{\partial u}{\partial z}\right) & \frac{1}{2}\left(\frac{\partial w}{\partial y} - \frac{\partial v}{\partial z}\right) & 0 \end{vmatrix}. \quad (2.18)$$

Note that these tensors show that whenever corresponding displacement gradients are not equal, there will be a rigid body rotation about the perpendicular axis. For example, if $\partial u / \partial y \neq \partial v / \partial x$, there will be a clockwise rotation around the z axis in the amount of ω_z radians,

$$\omega_z = \frac{1}{2}\left(\frac{\partial u}{\partial y} - \frac{\partial v}{\partial x}\right). \quad (2.19)$$

The resulting rotations cause the primary slip direction to rotate towards the tensile direction. In reality, such rotations are restricted and occur heterogeneously throughout the grain, with orientation gradients often developing near grain boundaries.

2.5.4 Relationship between deformation parameters and cracking

The Schmid and Taylor factors provide means of predicting the deformation propensities of grains based on their crystallographic orientations. It can be argued that Taylor factor analysis is generally more applicable than Schmid factor analysis because the stress field in a polycrystalline material will always be multiaxial even when a uniaxial load is applied to the specimen due to deformation restrictions by surrounding grains. It has been shown, however, that Schmid factor analysis is generally a good predictor of the primary slip plane in polycrystalline materials. Wang et al. [85, 86]

demonstrated that approximately 70% of the grains in fatigue-evaluated polycrystalline 316NG had only one active slip plane, and therefore a maximum of only 2 independent active slip systems. Researchers have evaluated cracking propensities through both Schmid and Taylor factor analyses of individual grains, and both will be discussed here.

Intergranular crack initiation and growth are highly dependent on stress, which has previously been discussed in the context of the normal stress acting on grain boundaries. As discussed in the previous sections, the accumulation of stress and strain in grains is not uniform, and therefore heterogeneities in cracking behaviors are also expected. This section will review the state of current knowledge on the relationship between Schmid and Taylor factors and cracking propensity.

A number of studies have been conducted to analyze the relationship between the orientation of slip systems and both transgranular and intergranular cracking, often through Schmid and Taylor factor analysis of the surrounding grains [19-21, 86-89]. These studies have included investigations of fatigue cracks [20, 21, 90], IGSCC [87, 89], and apparent creep cracking [19]. Most have focused on the potential for crack initiation at sites where differing deformation propensities in adjacent grains may result in strain incompatibilities at their common boundary.

Kim and Laird [20, 90] performed high strain fatigue testing on oxygen free high conductance (OFHC) copper to evaluate crack nucleation. They did not determine the Taylor or Schmid factors of the grains, but they did observe substantial inhomogeneities in the deformation both within individual grains and between grains. They observed that grain boundary steps formed and increased in height with progressive cycling until a critical step height of 1-2 μm was reached, and a crack became visible. These steps were

observed to form due to inhomogeneity of slip between adjacent grains. The development of slip traces directed at grain boundaries that proved vulnerable to cracking supported their theory that crack initiation was driven by the interaction of a dominant slip system (over a long distance) with the grain boundary on the sample surface to form a step. Although the compatibility in slip between adjacent grains was discussed, it was noted that their results indicated that "dominant, directed slip" in one of the two adjacent grains was sufficient for crack development. In a separate high-temperature (650˚C) low-cycle fatigue experiment on alloy A286, Rho et al. [21] analyzed grain boundary cavitation in the context of slip behavior and Schmid factor. They witnessed intergranular cavitation at the intersection of slip traces with grain boundaries as shown in Figure 2.26, and attributed the cracking to the discontinuity in slip across the boundary. To further investigate the role of strain incompatibility at the grain boundary, they determined the Schmid factors of 8 grains and analyzed the cavitation behavior at their adjacent grain boundaries. At random high angle grain boundaries, they observed that higher propensities for cavitation occurred at the boundaries between adjacent grains with large differences in Schmid factors.

The influence of relative grain orientation on the SCC propensity of Alloy 182 weld metal was evaluated by Alexandreanu et al. through CGR experiments in a simulated PWR environment [87, 89]. It was argued that grains with very different orientations likely have different Taylor factors, and because high Taylor factor mismatch should increase the propensity of the grain boundary to deform and crack, the relative orientations of adjacent grains should be a good predictor of the cracking susceptibility of the boundary. It was found that 87% of the cracks that developed occurred along grain

boundaries separating dissimilarly oriented grains. It is worthwhile to note, however, that grains with different orientations may have similar Taylor factors. For example, it can be seen from Figure 2.23 that grains with [111] and [110] orientations both have Taylor factors of 3.67.

A recent study by Lehockey et al. [19] indicated that apparent IG creep cracking in low carbon steel feeder piping may be explained by a loss of texture symmetry and differences in the Taylor factors of adjacent grains. The nominal texture of the steel was highly symmetrical with a $\langle 100 \rangle + \langle 111 \rangle$ double fiber texture. This texture was not present, however, in the susceptible material. It was suggested that this absence of symmetry made it difficult for the material to accommodate residual plastic strain fields. It was also stated that the strain intensity at grain boundaries and triple junctions was higher if the adjacent grains had large differences in Taylor factors. A dislocation gradient developed near the grain boundaries of the material, and it was determined that the nature of these dislocations was such that it minimized the difference in Taylor factor between the two adjacent grains. The cracked and uncracked portions of the feeder piping were analyzed to determine the Taylor factor distributions. The grains in the cracked region had a bi-modal Taylor factor distribution, while the uncracked region did not as shown in Figure 2.27. It was noted that a bi-modal distribution would increase the likelihood of having adjacent grains with large differences in Taylor factors.

Wright and Field investigated the fatigue pre-cracking behavior of a nickel superalloy [91]. They found that the path of the crack changed direction abruptly to follow the path of a Σ3 twin boundary. They found that the Taylor factors of the grains

adjacent to the cracked boundary had a high mismatch, and therefore suggested that a strong Taylor factor mismatch could lead to the development of strain incompatibilities that could lead to fracture.

An important downfall in each of these studies, however, is the lack of one or both of necessary elements to make an argument for why deformation parameter mismatch leads to cracking,

(1) a quantitative argument that the parameter (Schmid or Taylor factor) used accurately describes the deformation behavior in the material, and

(2) statistically significant measured correlations between the parameter and the cracking behavior.

If cracking is indeed a stochastic process, analysis of a great number of cracked grain boundaries would be required to confirm the relationship between a deformation parameter and cracking propensity.

2.5.5 Localized deformation

2.5.5.1 Dislocation channeling

While deformation of alloys in the annealed condition is relatively homogenous and characterized by high densities of slip lines along the primary slip planes, the deformation behavior in an irradiated microstructure can be altered dramatically where dislocation motion is restricted by black dot damage (small defect clusters that cannot be resolved in the TEM [92]), dislocation loops, and voids. Deformation often becomes highly localized to narrow channels in which slip deformation clears away dislocation loops and black dot damage to subsequently enhance deformation in the region. This

process has been termed “dislocation channeling” by Wechsler in 1971, although the formation of dislocation channels had been predicted in the late 1950s and observed in the early 1960s [93]. In 1968, Sharp [94] demonstrated that slip step formation in irradiated copper occurred at dislocation channel sites. This dislocation channeling behavior has been observed in a variety of materials including aluminum, iron, molybdenum, niobium, vanadium, rhenium, stainless steels, and zirconium alloys, thus encompassing fcc, bcc, and hcp materials.

The formation of the dislocation channels is driven by the shear stresses acting on the primary slip planes, as indicated by the formation of channels and resulting surface steps along planes inclined to the tensile axis for maximum shear stress [95]. Analysis by Hashimoto and Byun [96] has shown that the dislocation channel width, increases with the resolved shear stress level for neutron irradiated 316 stainless steel as shown in Figure 2.28. Based on these observations, it was hypothesized that the channel width may be limited by the shear stress level. Therefore, the Schmid factor of the grain may be important in characterizing the dislocation channeling behavior.

Temperature appears to influence the width and step height of the channels, as they have both been observed to increase with increasing temperature in the range of -196˚C to 200˚C for neutron irradiated copper [93]. The level of irradiation damage also appears to have an important impact on the localized deformation behaviors of materials. At lower temperatures and/or faster strain rates, deformation twinning may occur in irradiated alloys. Byun et al. [12] analyzed the deformation behavior of 360 keV He+ irradiated 316LN at room temperature by a transmission electron microscopy (TEM) disk bend method at doses ranging from 0.0015 to 15 dpa and witnessed a dramatic evolution

in the deformation behavior. At low doses, ordinary dislocation interaction was observed as well as small stacking faults. As the dose increased, the width of the stacking faults increased and the dislocation glide became increasingly confined to the $\{111\}$ planes. By 0.15 dpa, cross slip was severely restricted and thin twin layers were formed by partial dislocations. Irradiation to still higher doses and subsequent straining resulted in the formation of twin bands, and dislocation glide concentration on the $\{111\}$ planes resulted from restriction of cross-slip. Therefore, the transition to localized deformation along the $\{111\}$ planes was observed to be dose dependent. Dislocation channels in neutron irradiated 316 stainless steel have been found to form following neutron irradiation to doses as low as 0.1 dpa [96]. The spacing of the dislocation channels has also been observed to be dependent on dose for 304 and 316 stainless steel irradiated with 200 keV He+ ions to doses of 0.1 to 20 dpa [95]. While in this study, the increase in channel spacing with dose was attributed to the decreasing ability of slip to penetrate through the ion damage region, the step height has also been observed to increase with dose by other researchers [15], indicating that deformation becomes more heterogeneous with increasing dose. The number of slip systems activated also appears to depend on dose and temperature. Byun [12] analyzed the plastic deformation behavior of unirradiated and neutron irradiated 316LN and observed that deformation in the unirradiated materials at -100 and -150˚C occurred on at least 2 slip systems, while deformation was strongly confined to a single slip system for the irradiated specimens at room temperature.

2.5.5.2 Role of localized deformation in IASCC

There is growing evidence that the localized deformation that occurs in irradiated metals may play a key role in the mechanism of IASCC. IG cracking, microcracking, or grain boundary separation has been observed by several researchers at the intersection of dislocation channels with grain boundaries [8, 9, 11, 14, 15, 97]. In fact, Onchi has gone so far as to say that, by a mechanistic consideration of IASCC initiation, the high stress and strain concentrations created by deformation along the $\{111\}$ planes is more essential than the corrosive environment [8]. This is supported by the observations of several researchers that IG cracking can occur in irradiated metals in inert environments [9, 97, 98]. The environment, however, has been demonstrated to influence the cracking behavior. Jiao and Was [15] analyzed the deformation and cracking behavior of a 5 dpa proton irradiated austenitic 15Cr12Ni alloy through CERT experiments, and found that no cracking occurred in an argon environment at 288˚C, but cracking was observed in the simulated BWR environment at strains as low as 1%. Onchi et al. [9] evaluated the cracking behavior of neutron-irradiated sensitized 304 stainless steel and found that the %IG on the fracture surface was 8% following straining to failure in inert gas at 290˚C and 33% in an oxygenated water environment. Therefore, although mechanical deformation appears to play a key role in the IASCC mechanism, environmental effects are still considered important.

It was previously discussed that the nucleation of intergranular cavities requires levels of stress ($\sim 10^{-2}\ \sigma_n/E$) that greatly exceed the normal stress levels for creep experiments ($\sim 10^{-4}\ \sigma_n/E$). While stress concentrations at ledges and other grain boundary features were discussed in this context, dislocation channeling in irradiated materials can

also lead to high strain incompatibility between channels and surrounding grains and therefore to high microscopic internal stresses [99]. The increase in yield strength of the alloy, $\Delta\sigma$, due to the irradiation induced defects can be calculated using the dispersed barrier hardening model [100],

$$\Delta\sigma = \overline{M}\rho\mu b(Nd)^{1/2}, \tag{2.20}$$

where $\overline{M}$ is the average Taylor factor (3.06), μ is the shear modulus, b is the Burgers vector of the glide dislocation, N is the atomic density, d is the obstacle diameter, and ρ is the average barrier strength of the defect. The strength of the barrier depends on the type of the defect, i.e. void or dislocation loop, and can have values as high as 1 which indicates a perfectly hard obstacle [92].

The high amounts of stress in irradiated alloys cause strain in dislocation channels that can exceed 100% [92], and so the accommodation of such large amounts of strain at the grain boundary requires consideration. The strain induced by slip channels can be accommodated through multiple routes, (1) dislocations can be transmitted directly across grain boundaries, (2) dislocations pile ups can induce the activation of dislocation sources in a neighboring grain, (2) the dislocations can be absorbed into the grain boundary and dissociate to become mobile, or (3) grain boundary fracture may occur.

The pile-up of dislocations at a grain boundary leading to IG crack formation suggests the type of cracking mechanism proposed by Zener in 1947, where edge dislocations are piled up at an obstacle such as a grain boundary and coalesce to form a crack nucleus as shown in Figure 2.29 [101]. In 1954, Stroh [102] independently analyzed this type of crack to predict the number of dislocations required in the pileup to form a crack. This cracking mechanism has since become known as the Zener-Stroh

mechanism. Stroh stipulated that, in addition to the requirement that the stress normal to the plane of the crack approach the fracture stress of the material, the formation of the crack could only occur if the energy of the system decreased as a result [102]. Stroh expressed the energy of the crack as,

$$-\frac{1}{8}\pi(1-\nu)\sigma_n{}^2 r_\ell{}^2 / G + 2\gamma r_\ell, \tag{2.21}$$

where v is Poisson's ratio, σ_n is the normal stress, r_ℓ is the crack length, G is the rigidity modulus, and γ is the surface energy per unit area. This expression is negative when,

$$\sigma_n{}^2 r_\ell > \frac{16\gamma G}{\pi(1-\nu)}. \tag{2.22}$$

Stroh considered the stresses generated by the dislocations piled up at the obstacle and determined that the resulting normal stress, σ_n, acting on the obstacle was,

$$\sigma_n = \frac{3}{2}(L_0 / r_\ell)^{1/2}\sigma_0 \sin\theta\cos\frac{1}{2}\theta, \tag{2.23}$$

where L_0 is the length of the slip plane occupied by the pileup, σ_0, is the stress holding the dislocations in equilibrium, and θ is the angle between the obstacle plane and the slip plane. By differentiating equation (2.13) with respect to θ, it can be shown that the maximum normal stress occurs when θ=70.5˚, and can be calculated as follows,

$$\sigma_{\max} = \frac{2}{\sqrt{3}}\left(\frac{L_0}{r_\ell}\right)^{1/2}\sigma_0. \tag{2.24}$$

Stroh showed that by combining equations (2.22) and (2.24), and expressing L_0 as,

$$L_0 = \frac{Gbn}{\pi(1-\nu)\sigma_0}, \tag{2.25}$$

where n is the number of dislocations in the pileup, the condition for crack nucleation can be expressed as,

$$n > \frac{12\gamma}{b\sigma_0}. \tag{2.26}$$

Using this criterion, Stroh demonstrated that a pileup on the order of 1000 dislocations would be required to initiate a crack in work-hardened copper.

2.6 Grain Boundary Geometry

A grain boundary is the surface between two dissimilarly oriented crystal lattices, and may be regarded as a narrow region of lattice disruption. In 1950, Read and Shockley [103] demonstrated that a grain boundary can be modeled as an array of dislocations. Although the average grain boundary width is less than two atomic diameters [104], these dislocations cluster in grain boundaries, and create excess free volume. This excess free volume and resulting stress fields differentiate the properties of the grain boundary from those of the undisturbed matrix. Grain boundaries are recognized to have stronger propensities for elemental segregation, diffusion, accommodation of defects and strain, and nucleation phenomena [104]. Not all grain boundaries are equally susceptible to these phenomena, however. The degree of alignment, and therefore the excess free volume, between the two lattices varies as their orientations change. This difference in orientation is referred to as misorientation.

2.6.1 Misorientation

Misorientations can be described in two ways (1) through the description of an angle/axis pair, (2) with a misorientation matrix, and both will be described. The

angle/axis pair is simpler to visualize, while the misorientation matrix is most often used in practice for misorientation computations. The misorientation between two lattices can be described by defining an axis of misorientation (UVW) and a misorientation angle, θ. Imagine that two interpenetrating lattices exist, one is rotated about an axis (UVW) by angle θ as shown in Figure 2.30. These lattices represent two adjacent grains, and the misorientation between their lattices is fully described by indicating the θ/UVW pair.

Alternatively, the misorientation may be described as a misorientation matrix. Euler angles are a convenient way to express a crystal orientation in a different frame of reference as a sequence of rotations. In the context of misorientation, the orientation of a grain with respect to its neighboring grain can be expressed through three sequential rotations about specified axes. Two different crystal orientations are represented in Figure 2.31 with their axes given by $x_1y_1z_1$ and $x_2y_2z_2$. In order to make the axes of crystal 2 coincide with crystal 1, three rotations are required (1) crystal 2 must be rotated by angle φ_1 about axis z_2, (2) crystal 2 must be rotated by angle φ_2 about axis x'_2, and (3) crystal 2 must be rotated by angle φ_3 about axis z_1. Each of these rotations can be expressed in the form of a matrix, m_1, m_2, m_3, and the final misorientation matrix can be expressed as,

$$M_M = m_3 m_2 m_1 = \begin{vmatrix} a_{11} & a_{12} & a_{13} \\ a_{21} & a_{22} & a_{23} \\ a_{31} & a_{32} & a_{33} \end{vmatrix}, \tag{2.27}$$

or in terms of the Euler angles as,

$$M_M = \begin{vmatrix} \cos\varphi_1 \cos\varphi_3 - \sin\varphi_1 \cos\varphi_2 \sin\varphi_3 & \sin\varphi_1 \cos\varphi_3 + \cos\varphi_1 \cos\varphi_2 \sin\varphi_3 & \sin\varphi_2 \sin\varphi_3 \\ -\cos\varphi_1 \sin\varphi 3 - \sin\varphi_1 \cos\varphi_2 \cos\varphi_3 & -\sin\varphi_1 \sin\varphi_3 + \cos\varphi_1 \cos\varphi_2 \cos\varphi_3 & \sin\varphi_2 \cos\varphi_3 \\ \sin\varphi_1 \sin\varphi_2 & -\cos\varphi_1 \sin\varphi_2 & \cos\varphi_2 \end{vmatrix}. \tag{2.28}$$

It should be noted, however, that symmetry in cubic systems results in 24 routes of achieving a specified misorientation. Therefore, it is common to choose the misorientation matrix that corresponds to the smallest value of θ, the disorientation angle, from the angle/axis pair approach.

2.6.2 Coincident Site Lattice Boundaries (CSLBs)

The previous section described the misorientation relationship between two crystal lattices. Misorientation measurements can be used to define the character of a grain boundary. Boundaries with misorientations of <15˚ are called Low Angle Boundaries (LABs), and boundaries with misorientations of >15˚ are often referred to as High Angle Boundaries (HABs). Certain misorientations within the category of HABs, however, result in a high degree of alignment between the adjacent lattices. Therefore, the category of HABs can be subdivided into Random High Angle Boundaries (RHABs) and Coincident Site Lattice Boundaries (CSLBs).

The CSL model [105] is commonly used to characterize the geometry of grain boundaries. Certain angle/axis combinations between lattices result in periodicities that result in low excess free volume at their interface. The grain boundary that such an interface represents is assigned a number corresponding to the reciprocal density of the coinciding lattice sites. For example, consider a FCC structure lattice in the [100] orientation as shown in Figure 2.32. If one lattice is rotated by disorientation angle/axis pair, 36.9˚/[100] , and the two lattices are overlapped, one in every five lattice sites is coincident. Therefore the interface between the two lattices represents a Σ5 CSLB. There are a large number of angle/axis pairs for CSLs, and those that result in CSLs of up

to Σ35 are listed in Table 2.5. It can be seen from this table that several CSLs can be created through multiple angle/axis pairs, and such CSLs are designated a, b, etc..

One special consequence of twinning in low stacking fault energy FCC materials is the relatively high frequencies of Σ3, Σ9, and Σ27 boundaries. This is a result of the interactions that occur between twin boundaries as they migrate, termed $\Sigma 3^n$ interactions. When two migrating Σ3 boundaries combine, they can form either a Σ1 (LAB) or a Σ9 boundary. Similarly, when a Σ3 and Σ9 interact, they can form either a Σ3 or Σ27 boundary. Therefore, due to the high frequency of Σ3 twin boundaries in low stacking fault materials, the presence of $\Sigma 3^n$ boundaries is higher than would be expected in a random misorientation distribution.

It is unlikely that the grain boundary misorientation will exactly match a specific CSL geometry. Therefore, a tolerance must be set for the degree of allowed deviation from exact coincidence. Although stricter criterion exist [106], the most commonly used is the Brandon criterion [107],

$$v_m = v_0 \Sigma^{-1/2}, \tag{2.29}$$

where, v_m is maximum allowed deviation from exact coincidence, v_0 is a proportionality constant equal to the maximum allowed deviation for a Σ1 boundary, 15˚. Therefore, the allowed deviation decreases with increasing Σ; while the allowed deviation for a Σ3 boundary is 8.66˚, and that for a Σ27 boundary is only 2.89˚.

2.6.3 Influence of grain boundary structure on intergranular cracking

Grain boundary misorientation has been argued and demonstrated to influence various modes of degradation including intergranular cracking [89, 106, 108-120], creep [106, 119, 121-123], elemental segregation at grain boundaries [124-128], and intergranular and general corrosion [106, 109, 123, 129-136] through both experimental and modeling work. Intergranular cracking, and especially IGSCC, are often influenced by creep, segregation, and intergranular corrosion, and so the exhibited resistance of CSLBs to all four phenomena is logical. Several researchers have argued and demonstrated that fracture stress is highly dependent on grain boundary misorientation [120, 137-139]. Tsurekawa et al. [138] analyzed molybdenum bicrystals through TEM analysis and calculated fracture stress from the dihedral angles of the grain boundary grooves. They found that LABs, Σ3, Σ17b have much higher fracture strength than other boundaries as shown in Figure 2.33. It has also been shown that the fracture stress of CSLBs in Mo, Si, Zn, and Al with sigma values of 1-11 have fracture stresses 2 to 18 times that of random boundaries [120].

The resistance of CSLBs and LABs to intergranular degradation has earned them the frequent designation of “special boundaries”. The criterion for a boundary to be considered “special”, however, has been the subject of debate. Some have argued that Brandon’s criterion is too lenient and erroneously includes susceptible boundaries in the special category [106]. Others have pointed out that the crystallographic orientation of the grain boundary plane likely influences cracking propensity, which is not considered in misorientation calculations [116]. Lim and Raj [140] showed that intergranular cavitation in polycrystalline nickel did not occur along Σ3 boundaries along the $\{111\}$

planes, but did occur at other boundaries with the same misorientation. There is also debate over the level of periodicity required for the boundary to exhibit special properties. While special boundaries are generally assumed to be roughly <Σ29, Gertsman and Bruemmer [111] argued that only coherent Σ3 boundaries in austenitic alloys could be considered resistant to IGSCC in complex high-temperature water environments and stress states. Similarly, in other studies, coherent Σ3s [89], LABs [116], or both Σ3 and LABs [118] have shown zero cracking frequency. It is likely that the resistance of the boundary to a particular type of degradation depends on the aggressiveness of the environment. This is supported by observations by Crawford and Was [116] that the CSLBs in pure Ni-16Cr-9Fe are more resistant to cracking in argon than in deaerated high purity water at 360˚C despite their superior behavior in both environments. There is reason to believe that while CSLBs are resistant to cracking, they too will eventually degrade. Lim and Raj [140] performed low cycle fatigue experiments on polycrystalline nickel and observed that RHABs and boundaries with >Σ75 cavitated first, but lower Σ boundaries developed cavities after further deformation eventually including all but the coherent twin boundaries, as previously discussed. Kane and McMahon [110] conducted 4 point bend experiments on bicrystals of IN718 at 650˚C, and loaded the samples until a crack propagated. They found that the LAB and Σ3 boundaries required higher stress intensities to crack than Σ19, Σ31, and RHABs, and they observed that the crack velocities were slow, but both ultimately cracked.

Some studies have argued that coherent Σ3 boundaries should be excluded from the grain boundary character measurements because they do not crack [89, 109, 141,

142]. Such considerations are critical for modeling studies where crack blunting is assumed to occur at randomly distributed resistant boundaries. If the resistant boundaries include coherent twin boundaries that are confined to the grain internals, modeling predictions will be inaccurate due to their inclusion. Lehockey et al. [109] demonstrated that the exclusion of such "neutral twins" improved the accuracy of a stochastic model developed by Palumbo [112] by factors ranging from 2 to 6 for low stacking fault FCC materials. Yi and Kim also found that the probability of crack arrest was unaffected by the population of coherent twins, and recommended they be excluded from the measured CSLB fraction [141]. Alexandreanu also noted that their inclusion in the Σ3 category simply enhances the apparent differences in cracking susceptibilities of special boundaries and RHABs [89]. By considering the $\Sigma 3^n$ interactions that occur in low SFE fcc materials, it has been shown that the effective twin fraction, $f_{\Sigma 3}^{eff}$, which excludes the fraction of neutral twins, can be calculated excluding the fractions of Σ9 boundaries, $f_{\Sigma 9}$, and Σ27 boundaries, $f_{\Sigma 27}$, present [109],

$$f_{\Sigma 3}^{eff} = -\frac{f_{\Sigma 27} + f_{\Sigma 9}}{2} \pm \sqrt{\left(\frac{f_{\Sigma 27} + f_{\Sigma 9}}{2}\right)^2 - 2\left(f_{\Sigma 1} f_{\Sigma 9} + f_{\Sigma 1} f_{\Sigma 27} - f_{\Sigma 27} - f_{\Sigma 9}\right)}. \tag{2.30}$$

The effective special boundary fraction, f_{sp}^{eff}, is then given as,

$$f_{sp}^{eff} = f_{\Sigma 1} + f_{\Sigma 3}^{eff} + f_{3<\Sigma\leq 29}. \tag{2.31}$$

There are other persuasive arguments, however, for including coherent twin boundaries in the special boundary fraction. Apparent coherent twin boundaries can crack [91], despite the observations that they are immune to cracking in many alloy/environment combinations. It may also be difficult distinguish an apparent

coherent twin boundary from a true one. Qualitative observations of the boundary, such as recognizing curvature in the boundary can definitively *exclude* such boundaries from the coherent population, but serial sectioning methods and detailed analysis would be required to confirm coherency along the $\{111\}$ plane. Therefore, such qualitative exclusions of apparent coherent twin boundaries are inherently subjective. It is also known that although coherent twin boundaries generally do not crack, their intersection with a susceptible boundary can reduce the likelihood of a crack propagating [112, 143]. Gertsman and Bruemmer have observed frequent crack arrest at RHAB/twin intersections [111]. It should be considered, however, that twin boundaries separate dissimilarly oriented lattices which may have very different deformation characteristics as indicated in Figure 2.34. Therefore, crack arrest at the intersection of a coherent twin with a RHAB could either be an indication of the dependence of cracking on grain orientation, deformation behavior, or on the localized grain boundary structure at the site of crack arrest. The resistance of special boundaries to intergranular degradation has encouraged many researchers to focus on developing thermomechanical processing treatments to increase the CSLB fraction in the alloy; a process termed grain boundary engineering (GBE) by Watanabe in 1984 [144].

Lehockey and Palumbo [122] were able to increase the CSLB fraction in polycrystalline nickel from 13% to as high as 66% through a one-step recrystallization thermomechanical treatment. Subsequent creep evaluation in air at 450˚C revealed a 16-fold reduction in the steady-state creep rate and a 6-fold reduction in the primary creep strain under a load due to the enhanced CSLB fraction. With a special boundary fraction of 45%, the polycrystalline nickel was observed that cavitation was only observed at 8%

of the special boundaries, while 70% of the RHABs had cavitated. The improvement in the creep behavior was attributed to the reduced susceptibility of the special boundaries to cavitation. In a later study, Lehockey et al. [123] performed proprietary thermomechanical treatments on alloys 625, V-57, and 738. While no degradation in tensile strength or ductility were witnessed, improvements in corrosion, creep, and fatigue resistance of 50%, 90%, and 50%, respectively were observed when the microstructures contained special grain boundary fractions greater than 50%.

Crawford and Was [116] applied iterative thermomechanical processing treatments to pure Ni-16Cr-9Fe to increase the CSLB fraction from 12-20% to 27-44%. They subsequently strained the specimens in argon and deaerated high-purity water at 360˚C. It was determined that the CSLB enhancement reduced the cracked boundary fractions to 0.01 to 0.08 compared to 0.07 to 0.10 for the annealed samples. The resistance of the special boundaries to IG cracking was discussed in the context of the relative ability of the grains boundaries to allow slip continuity. It was suggested that the LABs, which were found to be immune to cracking, and the CSLBs were more capable of allow slip continuity across the boundary to accommodate more strain before cracking. They also discussed the relative sensitivities of crack initiation and propagation to the grain boundary character distribution. They determined that the %IG fracture on the fracture surface was not influenced by the GBE treatment whereas the cracking on the gage surfaces were reduced by the GBE treatment, which is consistent with later observations by Was et al. [119]. They discussed that crack propagation may be less sensitive to the increased CSLB fraction because the relative probability of encountering a RHAB was almost as high in the GBE sample as the annealed. This emphasizes the

importance of disturbing the connectivity of the network of RHABs in addition to simply increasing the fraction of special boundaries during thermomechanical processing, which has been recognized by many researchers [114, 117, 120]. If the connectivity of the RHABs is disturbed significantly, as they were in GBE alloy 690 for West and Was [108] in Figure 2.35, crack propagation becomes difficult due to the high probability of the crack encountering a crack resistance CSLBs.

The impact of GBE on the creep and IGSCC behavior of Ni-16Cr-9Fe in argon and deaerated high-purity water at 360˚C was evaluated by Was et al. [119]. Iterative thermomechanical processing was applied to increase the special boundary fraction in the alloy from 16-20% to 26-43%, which resulted in a creep rate reduction by a factor of 10-30 and a shortened primary creep regime. They found that in high purity water, 2.9% of the special boundaries and 7.7% of the RHABs cracked, whereas in argon, 1.2% of the special boundaries cracked and 4.3% of the RHABs, thus indicating both the influence of the environment and boundary character on IG cracking susceptibility. They emphasized the influence of mechanical creep on IGSCC susceptibility by pointing out the strong correlation between the steady state creep rate and percent cracked boundaries as a function of the fraction of CSLBs as shown in Figure 2.36. They noted that others have shown that grain boundary cavitation [145] and GBS [146] preferentially occur along RHABs, and argued that differences in dislocation behaviors at RHABs and CSLBs could be responsible for the superior behavior of the CSLBs.

The IGSCC behavior of GBE Ni-16Cr-9Fe-xC alloys was investigated by Alexandreanu and Was in simulated primary water at 360˚C. The iterative thermomechanical processing treatments increased the special boundary fraction (which

excluded coherent twins) from 20-25% to 30-40%. They determined that, the total IG cracked fraction in all alloys evaluated decreased with increasing CSLB fraction regardless of the microstructure or strain. While the total fraction of grain boundaries cracked increased steadily with strain, the ratio of the CSLB cracked fraction to the HAB cracked fraction was always less than 1 and generally less than 0.5.

Research on the performance of GBE alloys in SCW is limited. Tan et al. [135, 136] applied GBE treatments to alloys 800H and 617 prior to exposure in 500 and 600˚C SCW. Compared to their annealed conditions, the GBE specimens had more compact and continuous oxide scales. This was attributed to the lower diffusivity of the low-Σ boundaries compared to the RHABs which made the grain boundary diffusivity as a whole closer to the bulk diffusivity. The only study to date on IGSCC of GBE alloys in SCW was done by Gupta et al. [61] on FM alloy HT-9. In this study the observed mitigation of IGSCC was attributed to a reduction in precipitate coarsening at the CSLBs and LABs due to the lower diffusivities along these boundaries.

From the previous discussion, it is apparent that CSLBs are resistant to cracking in a variety of alloys and environments. The reason for this resistance has often been discussed in the context of the increased structural order at CSLBs which decreases the propensity for absorption, mobility, and dissociation of dislocations in the boundary [122]. Dislocations impinging upon a grain boundary have the potential to be absorbed into the grain boundary, subsequently dissociate, and become mobile to cause GBS. Whether or not this occurs, or the extent to which it occurs likely depends on the grain boundary structure.

Lim and Raj pointed out that grain boundaries are energetically favorable sinks, as the Burgers vectors for grain boundary dislocations are smaller than those for crystallographic slip in the lattice [140]. Dingley and Pond [147] have witnessed dislocations and linear structures in both CSLBs and RHABs, and observed that the dissociation of some of the dislocations entering the CSLBs resulted in perfect dislocations with Burgers vectors of the displacement shift complete (DSC) lattice. The DSC lattice is the set of all displacement vectors which preserve the CSL structure. The mobility of the dissociated grain boundary dislocations, was found to depend on the grain boundary misorientation and grain boundary plane [147]. As reduced mobility would oppose the absorption of subsequent dislocations into the grain boundary region, long range internal stresses may develop as the dislocations pile up at the grain boundary to decrease the effective stress [119]. This hypothesis is supported by the TEM analysis of Was et al. [119] on deformed ultrahigh-purity Ni-16Cr-9Fe. It was shown that that the EGBDs, created when the lattice dislocation interacts with the grain boundary, had densities at the CSLBs that were three times higher than in RHABs.

Lim and Raj [140] showed that the different behavior of the dislocations at the CSLBs may be a result of the magnitude of the DSC vector at the boundaries. As the Σ value of boundary decreases, or the coincidence between the adjacent lattices increases, the magnitude of the DSC vector increases which increases the energy of the dissociated lattice dislocations in the boundary. This longer range strain field was argued to be stronger than that at a RHAB, and may be more likely to induce secondary slip in adjacent grains to relieve the misfit dislocations in the grain boundary. The idea of CSLBs and LABs being more capable of transmitting dislocations, or absorbing them and

re-emitting dislocations into adjacent grains to reduce the high strain energies at boundaries has the support of other researchers [116]. Although mobile dissociated dislocations may enter an adjacent grain with a different Burgers vector from which they originated to induce secondary slip [147], it has been recognized that slip in the two adjacent grains may not be entirely compatible, leading to an increased density of grain boundary dislocations with strain [140].

2.7 Previous Experiments

Several experiments were conducted to evaluate the IG cracking behavior of austenitic alloys prior to the development of the objective and approach for this thesis [53, 54, 56]. The findings from those experiments will be discussed in this section to address the influence of alloy, irradiation, and SCW temperature on the IG cracking propensity. These are important parameters that are not discussed in depth in this dissertation because the alloy, condition, and environment were fixed in order to isolate the influence of local stress and strain on intergranular cracking propensity. This background information will be used to explain how the final thesis topic was chosen and to justify the final selection of alloy and experimental parameters.

Previous experiments evaluated the cracking susceptibilities of four austenitic alloys (316L, D9, 690, and 800H) in 400˚C and 500˚C SCW in the unirradiated conditions and for doses ranging from 2-7 dpa [53, 54, 56]. The results indicated that each of the alloys was susceptible to IG cracking under certain experimental conditions. Several different measures of IG cracking susceptibility will be discussed including the

crack depth into the sample substrate, the %IG fracture on the fracture surface, crack density on the gage surface, and crack length per unit area on the gage surface.

It was found from these experiments that the cracking severity of alloy 690 increased with temperature [53], which was expected because intergranular cracking often exhibits an Arrhenius behavior. The maximum crack depths into the irradiated surfaces of the specimens of alloys 316L and 800H also increased slightly with temperature, although these cracks penetrated through the irradiated depth into the unirradiated material and are therefore not indicative of the maximum crack depth expected in a fully irradiated specimen [53]. The cracking severity of D9 and 316L, as measured by the crack length per unit area, decreased with increasing temperature [53, 56]. While this behavior was unexpected, it is consistent with the observation that the crack growth rate of 316 stainless steel decreases as the temperature of the water approaches the critical point [50, 51].

It was also observed that irradiation increased cracking propensity regardless of the alloy or temperature. It is therefore instructive to consider the microstructural changes that occurred in the alloys as a result of irradiation. The irradiation damage created high densities of dislocation loops in the alloys with densities on the order of 10^{21}-10^{22} m^{-3} depending on the irradiation temperature and the energy of the protons (2 MeV vs. 3 MeV) [53, 56]. The sizes of the dislocation loops increased with dose and temperature. Voids were observed in all alloys except for the D9, which was cold worked. The void densities were lower than that of the dislocation loops, and did not exceed 1.63×10^{21} m^{-3}. These dislocation loops and void populations contributed to the irradiation induced hardening which ranged from 84-266 Hv at 400˚C and 84-121 Hv at 500˚C. The

irradiation induced hardness values for each alloy were consistently lower at 500˚C than 400˚C.

The grain boundary concentration of chromium was also of interest because the intergranular cracking in irradiated alloys is often attributed to radiation induced depletion of chromium at grain boundaries. Chromium is well known to increase the corrosion resistance of iron-base austenitic alloys through the formation of protective chromium-rich oxides[53]. The depletion of chromium at grain boundaries as a result of RIS is analogous to the chromium depletion that occurs adjacent to grain boundaries in thermally sensitized alloys, which has been shown to promote intergranular cracking [148]. The chromium concentration at the grain boundary decreased for in the 7 dpa irradiated conditions of D9, 316L, and 690 compared to the unirradiated conditions. The chromium concentrations at the grain boundaries of 316L, following a 7 dpa proton irradiation at 400˚C and 500˚C, were depleted to 14.4 wt% and 13.13 wt%, respectively, compared to a bulk concentration of 16.62 wt%. The composition change at the grain boundaries of the 690 was more dramatic. The concentrations were depleted to 24.4 wt% and 15.2 wt%, respectively, compared to a bulk concentration of 29.4 wt%. The depletion zones around the grain boundaries broadened with increasing temperature.

The increase in cracking susceptibility, as measured by the crack length per unit area, for all alloys as a function of dose at both 400˚C and 500˚C is shown in Figure 2.37 [149]. Other measures of cracking susceptibility including the crack density, crack length, and % IG on fracture surface also generally indicated increased cracking propensity with irradiation damage. There were two exceptions. Once was that the crack density of the 316L at 400˚C was lower in the irradiated condition. The total number of

grain boundaries that cracked was still greater in the irradiated condition, but there was a lower density of longer cracks than found on the unirradiated specimens. The other exception was a small decrease in the average crack length from 0 to 7 dpa for the 800H specimen at 400˚C.

The enhancement of intergranular cracking as a result of irradiation damage is often attributed to the hardening of the alloy or the depletion of chromium at the grain boundaries. As both of these changes generally increase with irradiation damage, however, it is often difficult to distinguish the influence of each parameter. The intergranular cracking susceptibility, as characterized by the crack length per unit area normalized to %strain, is shown as a function of hardness and grain boundary chromium concentration in Figure 2.38 and Figure 2.39, respectively. It can be seen that the cracking severity consistently increases with hardness and decreasing chromium concentration for each alloy/temperature combination. While these results cannot be used to definitively determine the influence of each parameter on cracking propensity, qualitative arguments may be used to discuss the possible influence of each parameter. It can be seen from Figure 2.38 that the increases in cracking severity with hardness are similar (as indicated by the slopes of the lines) for all alloy/temperature combinations except 690 at 500˚C. Interestingly, despite the dramatic increase in the cracking severity of the 690 in the irradiated condition, the irradiation induced hardening was relatively low. While the hardness of the irradiated 690 was higher at 400˚C, the cracking severity was much lower than at 500˚C suggesting that irradiation induced hardening may not be the primary reason for the increased cracking susceptibility. The RIS data indicate that chromium was depleted to 24% at the grain boundary following the 400˚C, 7 dpa

irradiation. At this chromium level, however, the formation of a passive oxide film is still possible and such chromium depletion is unlikely to result in a change in the cracking severity. At 500˚C, however, the 7 dpa irradiation resulted in additional chromium depletion to 15% chromium which is roughly only 50% of the bulk chromium concentration. Once the chromium has depleted to a level that prevents the formation of a passive oxide film, the cracking propensity should increase dramatically. Based on these arguments, it is likely that the depletion of chromium at the grain boundaries of the 500˚C irradiated 690 played an important role in the dramatic increase in cracking severity.

While the previous discussion suggests that both hardening and RIS may influence cracking severity of austenitic alloys in SCW, the influence of each parameter could not be isolated from the data available. Post-irradiation annealing experiments performed by Busby et al.[6], however, which removed virtually all of the dislocation loops while leaving the RIS virtually unchanged, have been used to isolate the role of RIS. Those results demonstrated that chromium depletion is not the primary determinator for IASCC susceptibility of 304 stainless steel in normal water chemistry. Thus, the mechanism of IASCC and the roles of hardening and RIS are complex, and despite decades of research this mechanism is still not fully understood in subcritical water. This irradiation induced enhancement or cracking, therefore, presents an important challenge for the design of the SCWR.

In addition to the aforementioned influence of irradiation induced hardening and RIS on IASCC, a growing body of literature is discussing the role of localized deformation in the cracking mechanism [7-9, 11-16]. As discussed in Section 2.5, the

strain incompatibilities that develop at grain boundaries due to the differences in the orientation of the slip systems in neighboring grains have been argued to lead to intergranular cavitation and cracking [19-21, 90]. These findings indicate that the deformation mode and propensity of individual grains may influence the cracking behavior of the adjacent grain boundary. While the degree of localized deformation may increase with dose [150], just as RIS and hardening are observed to evolve, the influence of localized deformation and strain incompatibilities are readily seen through visual inspection on the SEM. Therefore, if the environment, alloy, and irradiation conditions are fixed, the role of local stress and strain on the cracking behavior of 316L stainless steel can be isolated by evaluating how the grain to grain variations in stress and strain influence cracking propensity.

The selection of alloy and experimental parameters for this thesis required careful consideration of the type of data desired. The influence of strain incompatibilities on cracking can be best determined from a material where the deformation can easily be characterized. In unirradiated materials, slip lines are often hard to discern in the SEM and characterizing their interactions with grain boundaries is not possible on a highly oxidized surface. In irradiated materials, however, deformation is localized to dislocation channels that are readily visible through SEM analysis. This enables analysis of the strain compatibilities or incompatibilities that exist where dislocation channels intersect grain boundaries. Furthermore, irradiation was shown to enhance the cracking propensities of austenitic alloys in SCW. While this behavior is undesirable from a materials performance standpoint, it is very desirable for the current study which requires analysis of a large number of cracked boundaries to achieve sufficient cracking statistics.

The results of the previous studies also demonstrated that the alloy and temperature influence cracking propensity. To achieve a high propensity for IG cracking, alloy 316L was selected and evaluated in the irradiated condition in a 400˚C SCW environment, as it was shown to induce more cracking than 500˚C SCW. These experimental conditions and alloy selection enabled analysis of a large number of cracked grain boundaries where the influence of local stress and strain on cracking propensity was evaluated.

2.8 Objective and Approach

The objective of this work is to determine whether intergranular cracking of 316L stainless steel in SCW is influenced by the propensity for crystallographic slip in the grains adjacent to the crack, as determined via Schmid and Taylor factor analysis. The approach in this study is to use the Schmid and Taylor factors of grains as a means of determining the influence of strain incompatibilities and local stresses on the relative cracking propensities of grain boundaries in 316L stainless steel in SCW. Therefore, the two critical aims of this study will be,

(1) To determine if the Schmid and Taylor factors of individual grains in polycrystalline 316L stainless steel correlate with their deformation behaviors, and

(2) To determine if the Schmid and/or Taylor factors of grains correlate with the cracking propensities of their adjacent grain boundaries.

As previously discussed, irradiation damage results in a transition in the deformation behavior of metals from relatively homogenous slip to heterogeneous deformation along

dislocation channels. The dislocation channels that form in irradiated materials can be analyzed via scanning electron microscopy (SEM) and atomic force microscopy (AFM) analysis. Such analysis can be applied to determine if there is a relationship between the dislocation channeling behavior and the Schmid or Taylor factors of the individual grains. The extent of lattice rotation of the grains will also be analyzed via EBSD analysis to determine if the rotation is influenced by the deformation parameters. While local grain boundary stresses cannot be directly measured, the Schmid factors of grains will be used as an indicator of their strengths to discuss the stress dependence of IG cracking behavior.

The cracks that form in the specimens following straining in SCW will be analyzed to determine if they exhibit a tendency to occur at grain boundaries adjacent to grains with specific Schmid or Taylor factors. If they do, the cracking behavior of the boundary may be attributed to the deformation behavior of one or both of the adjacent grains. The grain boundary misorientation is also recognized to influence the propensity of the grain boundary to deform and crack due to the absorption and mobility of dislocations in the boundary. Therefore the strain incompatibility, in terms of slip continuity, will be analyzed to determine if it is influenced more by the grain boundary misorientation or the bulk deformation propensities of the adjacent grains. The cracking behavior of the irradiated alloy will also be evaluated in argon to isolate the role of the environment on the intergranular cracking behavior.

An additional study will also be described that was used to determine the role of grain boundary engineering on the performance of unirradiated 316L stainless steel in SCW. The objective of this study was to evaluate the ability to reduce intergranular

cracking propensity of 316L in SCW and determine the relative propensities of different grain boundary characters to crack.

Table 2.1 List of alloy compositions from corrosion and intergranular cracking studies performed in SCW environments. [4, 5, 24, 45, 47, 52, 53, 151-156]

Alloy Class	Alloy	Fe	Cr	Ni	C	Si	Mn	P	S	Mo	Cu	N	Co	Other
Austenitic Stainless Steels	304	Bal.	18.3	8.5	0.035	0.65	1.38	0.02	0.03	0.37	NM	0.068	NM	
	304L	Bal.	18.34	9.9	0.019	0.51	0.011	0.025	0.001	NR	NR	0.036	NR	
	316	Bal.	17.46	12.35	0.03	0.58	0.82	0.032	0.002	2.07	NR	NR	NR	
	316L	Bal.	16.62	10.12	0.022	0.65	1.86	0.03	0.001	2.06	0.24	0.02	0.05	
	347	Bal.	17-19	9-12	0.08	1	2	NR	NR	NR	NR	NR	NR	Nb 10 x C (min)
	347H	Bal.	17.58	10.7	0.048	0.29	1.84	0.026	0.013	NR	NR	NR	NR	0.56 Nb
	316NG	Bal.	16.6	11.3	0.014	0.42	0.8	0.032	0.001	2.11	0.23	NR	0.07	0.007 Al, 0.01 Nb, 0.004 Ti, 0.04 V, 0.02 W
	1.497	Bal.	15	15.3	0.095	0.53	1.68	0.007	0.001	1.18	NR	NR	0.03	0.05 Al, 0.45 Ti, 0.02 V, <0.01 W
	BGA4	Bal.	22.9	15.4	0.11	0.49	6.1	0.02	0.024	0.14	NR	NR	NR	
	S31266	41.87	23.9	21.9	0.014	NR	3	NR	0.001	5.4	1.54	0.47	NR	1.9 W
	D9	Bal.	13.95	15.12	0.043	0.66	2.03	<0.005	<0.005	2.2	0.005	NR	0.014	0.014 Al, <0.02 Nb, 0.26 Ti
	800H	Bal.	20.42	31.59	0.069	0.13	0.76	0.014	0.001	NR	0.42	NR	NR	0.5 Al, 0.57 Ti
Ni-base	600	9.77	14.63	74.79	0.07	0.19	NR	NR	NR	NR	0.22	NR	NR	
	625	0.89	22.03	Bal.	0.01	0.08	0.01	0.004	0.001	8.99	0.02	NM	0.03	3.48 Nb
	690	10	29.4	Bal.	0.03	0.03	0.18	NM	0.001	0.01	0.01	NM	NM	0.22 Al, 0.34 Ti
	718	Bal.	17.95	53.67	0.033	0.07	0.04	0.006	0.002	2.98	0.1	NR	0.04	0.52 Al, 0.005 B, 5.27 Nb, 0.92 Ti
	C276	5	16	Bal.	<0.1	<0.1	NR	NR	NR	16	NR	NR	NR	4 W
	MC	NR	45	Bal.	NR	NR	NR	NR	NR	1	NR	NR	NR	
	N06030	14.9	29.5	Bal.	0.01	0.26	1.1	0.013	0.002	4.9	NR	NR	2.5	0.81 Nb, 2.8 W
F/M	12Cr-1Mo-1WVNb	Bal.	12	NR	0.11	0.23	0.48	0.017	0.001	NR	NR	NR	NR	0.25 V, 1 W
	T91	Bal.	8.37	0.21	0.1	0.28	0.45	0.009	0.003	0.9	0.17	0.048	NR	0.022 Al, 0.076 Nb, 0.216 V
	HCM12A	Bal.	10.83	0.39	0.11	0.27	0.64	0.016	0.002	0.3	1.02	0.063	NR	0.001 Al, 0.054 Nb, 0.190 V, 1.89 W
	HT-9	Bal.	11.63	0.5	0.2	0.22	0.52	0.02	0.006	1	0.04	0.047	0.08	<0.01 Al, <0.01 Ti, 0.300 V, 0.52 W
Ti-base	Ti-15Mo-5Zr-3Al	0.03	NR	NR	NR	NR	NR	NR	NR	14	NR	0.01	NR	3.3 Al, 0.01 H, 0.12 O, Bal. Ti, 5.0 Zr
ODS	PM2000	Bal.	20.1	0.03	0.005	0.02	0.08	0.007	0.001	0.09	<0.01	NR	0.04	5.5 Al, 0.03 Nb, 0.43 Ti, 0.03 V, <0.01 W
	19Cr	Bal.	18.37	NR	0.05	0.041	0.06	<0.005	0.002	NR	NR	0.014	NR	<0.01 Al, 0.014 N, 0.28 Ti, 0.29 W, 0.29 Y, 0.368 Y_2O_3
	19Cr-4.5Al	Bal.	18.85	NR	0.09	0.039	0.06	<0.005	0.002	NR	NR	0.005	NR	4.61 Al, 0.28 Ti, 1.83 W, 0.29 Y, 0.368 Y_2O_3

NM = Not Measured
NR = Not Reported

Table 2.2 Summary of experiments and results for austenitic alloys evaluated for the SCWR concept. [28]

Alloy Class	Alloy	Temp. (°C)	Water chemistry	Loading mode	Results	Ref.
Austenitic SS	304, 316L (sensitized)	290–550	8000 ppb DO*, 0.06 µS/cm, 25 MPa	SSRT** 4 x 10^{-7} s^{-1}	IG*** 304 below 400°C	[45-47, 157]
	310S (fine grain)	290, 550	8000 ppb DO, 25 MPa	SSRT 4 x 10^{-7} s^{-1}	No IGSCC	[152]
	316L	400	8000 ppb DO, 25 MPa, up to 0.01 mol/l HCl, up to 3.6 MPa H_2	SSRT 2.78 x 10^{-6} s^{-1}	IGSCC	[5]
	304L, 316L	400-550	Deaerated (<10 ppb DO), non-deaerated (~8000 ppb DO), <0.1µS/cm, 25 MPa	SSRT 3 x 10^{-7} s^{-1}	IG at all temperatures	[4]
	316 (sensitized)	360, 400	8000 ppb DO, 25-60 MPa, 2.4-13.4 dielectric constant	SSRT 2.78 x 10^{-6} s^{-1}	IG, pressure dependent	[24]
	347H, 316NG, 1.4970, BGA4	500,650	100-150ppb, <0.1µS/cm, 25 MPa	SSRT 3 x 10^{-7} s^{-1}	IGSCC 316NG and BGA4	[154]
	316	288-500	non-deaerated (2000 ppb DO), deaerated (<10 ppb DO), 0.1-0.5 µS/cm 10.3-24.8 MPa	CGR****	CGR temperature dependent	[50]
	316L, 316LGBE	500	<10 ppb DO, <0.1 µS/cm, 25 MPa	SSRT 3 x 10^{-7} s^{-1}	IG reduced in GBE condition	[108]
	316 (sensitized)	360,400	8000 ppb, 25-60 MPa, 2.4-13.4 dielectric constant	SSRT 2.78 x 10^{-6} s^{-1}	IG, strong dependence on pressure	[44]
	316L (SA)	360, 400	8000 – 800,000 ppb, up to 0.01M H_2SO_4, 30 – 60 MPa,	SSRT 2.78 x 10^{-6} s^{-1}	IG, strong dependence on pressure, H_2SO_4	[44, 48]
	S31266	400-500	5-25 MPa, 10wt% H_2O_2, up to 1.6 g/l NaCl, up to 1 g/l HCl	SSRT 10^{-3} s^{-1}, 5 x 10^{-7} s^{-1} Constant load - 87%σ_y, 100% σ_y	IG crack under certain condition	[52]
	316, 347	732	Deaerated, 34.5 MPa	Constant load 103, 83 MPa for 168hr	TG crack in 316	[153]
	316L, D9 (0, 7 dpa)	400, 500	<10 ppb DO, <0.1 µS/cm, 25 MPa	SSRT 3 x 10^{-7} s^{-1}	IG at both temperatures	[53]
	316L (0, 7 dpa)	400, 500	<10 ppb DO, <0.1 µS/cm, 25 MPa	SSRT 3 x 10^{-7} s^{-1}	IG at both temperatures	[55]
	316L (SA and CW, 27-44 dpa)	400, 500	<10 ppb DO, hydrogenated, <0.1 µS/cm, 24-27.6 MPa	SSRT 3 x 10^{-7} s^{-1}	IGSCC correlates w/ hardening and hydrogen	[49]
	800H	500	400-600 ppb DO, <0.2 µS/cm, 25 MPa	SSRT 0.8 x 10^{-7} s^{-1} or 1.5 x 10^{-7} s^{-1} (conflicting rates given)	No SCC	[158]
	800H (0, 7 dpa)	400, 500	<10 ppb DO, <0.1 µS/cm, 25 MPa	SSRT 3 x 10^{-7} s^{-1}	IG at both temperatures	[53, 56]

*DO = Dissolved Oxygen
**SSRT = Slow Strain Rate Test
***IG = Intergranular
****CGR = Crack Growth Rate Test

Table 2.3 Summary of experiments and results for nickel-base, FM, titanium-base, and ODS alloys evaluated for the SCWR concept. [28]

Alloy Class	Alloy	Temp. (°C)	Water chemistry	Loading mode	Results	Ref.
Nickel-base	600	290–550	8000 ppb DO, 0.06 µS/cm, 25 MPa	SSRT 4 x 10^{-7} s^{-1}	No IGSCC	[46]
	625, C276, MC	400	8000 ppb DO, 25 MPa, up to 0.01 mol/l HCl, up to 3.6 MPa H_2	SSRT 2.78 x 10^{-6} s^{-1}	IGSCC for 625, C276	[5]
	600, 690, 625	290-550	8000 ppb DO, <0.1 µS/cm, 25 MPa	SSRT 4 x 10^{-7} s^{-1}	IGSCC 625 at 550°C	[47]
	625, 690	400–550	Deaerated (<10 ppb DO), <0.1µS/cm, 25 MPa	SSRT 3 x 10^{-7} s^{-1}	IG at all temperatures	[157]
	690, 690GBE	500	<10 ppb DO, <0.1 µS/cm, 25 MPa	SSRT 3 x 10^{-7} s^{-1}	IG reduced in GBE condition	[108]
Nickel-base	690, 718	400	Aerated SCW, 25 MPa	SSRT 1 x 10^{-6} s^{-1}	IGSCC in 718	[158]
	N06625, N06030	390-500	22.5-25 MPa, 10wt% H_2O_2, up to 1.6 g/l NaCl	SSRT 10^{-3} s^{-1}, 5 x 10^{-7} s^{-1} Constant load - 100% σ_y, 140% σ_y	IGSCC in 625	[52]
	690 (0, 7 dpa)	400, 500	<10 ppb DO, <0.1 µS/cm, 25 MPa	SSRT 3 x 10^{-7} s^{-1}	IG at both temperatures	[53, 56]
	690 (0, 7 dpa)	400, 500	<10 ppb DO, <0.1 µS/cm, 25 MPa	SSRT 3 x 10^{-7} s^{-1}	IG at both temperatures	[55]
Ferritic-Martensitic	12-Cr-1Mo-1WVNb	290,550	8000 ppb DO, <0.1 µS/cm, 25 MPa	SSRT 4 x 10^{-7} s^{-1}	No IGSCC	[47]
	T91, T92	370-600	<10-600ppb, <0.1-171.1 µS/cm, 25 MPa	SSRT 0.8-3 x 10^{-7} s^{-1}, fatigue CGR	No SCC	[159-161]
	T91, T91 CSL HCM12A, HT-9 (0-10 dpa)	400	<10 ppb DO, <0.1 µS/cm	SSRT 3 x 10^{-7} s^{-1}	IG in HT-9 only	[162]
	T91, T91 CSL, HCM12A, HT-9 (0, 7 dpa)	400, 500, 600	10, 100, 300 ppb DO, 25 MPa	SSRT 3 x 10^{-7} s^{-1}	IG in HT-9 only, increase with irradiation, temp, DO	[163, 164]
	T91	370, 500	<10 ppb DO, <0.1 µS/cm inlet, 25 MPa	corrosion fatigue	Fatigue CGR increased due to fatigue-oxidation interaction	[165]
	HT-9, HT-9 CSL (0,7 dpa)	400, 500	<10 ppb DO, <0.1 µS/cm inlet, 25 MPa	SSRT 3 x 10^{-7} s^{-1}	IG cracking in all conditions	[61]
Ti Alloy	Ti-15Mo-5Zr-3Al	290,550	8000 ppb DO, <0.1 µS/cm, 25 MPa	SSRT 4 x 10^{-7} s^{-1}	TGSCC	[47]
ODS	PM2000	500,650	100-150ppb, <0.1µS/cm, 25 MPa	SSRT 3 x 10^{-7} s^{-1}	No SCC	[154]
	19Cr, 19Cr-4.5Al	288	8000 ppb DO, 7.8 MPa	SSRT 10^{-4} to 3 x 10^{-7} s^{-1}	No SCC	[151]

Table 2.4 Direction cosines between slip systems and crystal axes [74]

	1 = [100]	2 = [010]	3 = [001]
a = (111)	$1/\sqrt{3}$	$1/\sqrt{3}$	$1/\sqrt{3}$
I = $[01\bar{1}]$	0	$1/\sqrt{2}$	$-1/\sqrt{2}$
II = $[\bar{1}01]$	$-1/\sqrt{2}$	0	$1/\sqrt{2}$
III = $[1\bar{1}0]$	$1/\sqrt{2}$	$-1/\sqrt{2}$	0
b = $(\bar{1}\bar{1}1)$	$-1/\sqrt{3}$	$-1/\sqrt{3}$	$1/\sqrt{3}$
I = $[0\bar{1}\bar{1}]$	0	$-1/\sqrt{2}$	$-1/\sqrt{2}$
II = [101]	$1/\sqrt{2}$	0	$1/\sqrt{2}$
III = $[\bar{1}10]$	$-1/\sqrt{2}$	$1/\sqrt{2}$	0
c = $(\bar{1}11)$	$-1/\sqrt{3}$	$1/\sqrt{3}$	$1/\sqrt{3}$
I = $[01\bar{1}]$	0	$1/\sqrt{2}$	$-1/\sqrt{2}$
II = [101]	$1/\sqrt{2}$	0	$1/\sqrt{2}$
III = $[\bar{1}\bar{1}0]$	$-1/\sqrt{2}$	$-1/\sqrt{2}$	0
d = $(1\bar{1}1)$	$1/\sqrt{3}$	$-1/\sqrt{3}$	$1/\sqrt{3}$
I = $[0\bar{1}\bar{1}]$	0	$-1/\sqrt{2}$	$-1/\sqrt{2}$
II = $[\bar{1}01]$	$-1/\sqrt{2}$	0	$1/\sqrt{2}$
III = [110]	$1/\sqrt{2}$	$1/\sqrt{2}$	0

Table 2.5 Disorientation angle/axis pairs for CSLs with reciprocal densities up to 35. (reproduced from [166])

Σ	**θ**	**UVW**	**Σ**	**θ**	**UVW**
3	60	111	23	40.5	311
5	36.9	100	25a	16.3	100
7	38.2	111	25b	51.7	331
9	38.9	110	27a	31.6	110
11	50.5	110	27b	35.4	210
13a	22.6	100	29a	46.3	100
13b	27.8	111	29b	46.4	221
15	48.2	210	31a	17.9	111
17a	28.1	100	31b	52.2	211
17b	61.9	221	33a	20.1	110
19a	26.5	110	33b	33.6	311
19b	46.8	111	33c	59	110
21a	21.8	111	35a	34	211
21b	44.4	211	35b	43.2	331

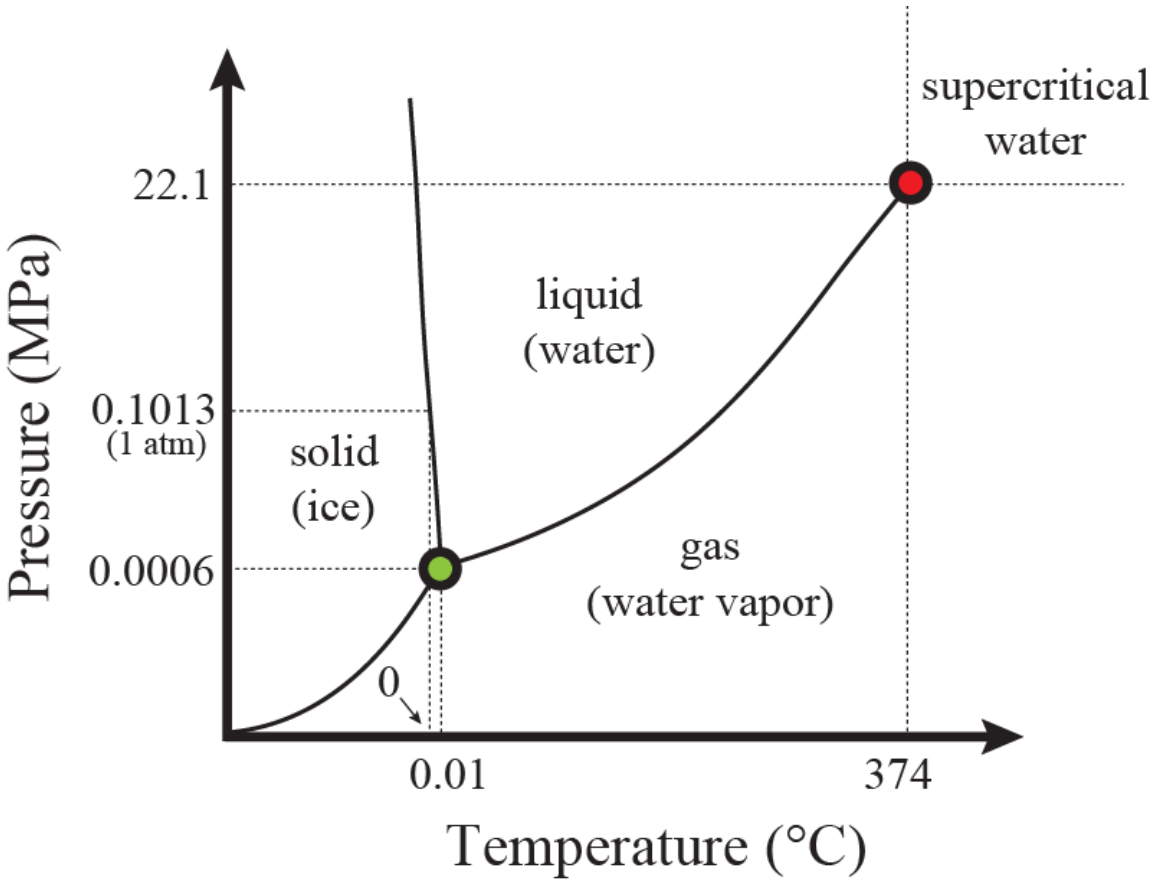

Figure 2.1 Phase diagram for water. Above temperatures of 374˚C and pressures of 22.1 MPa, water exists in the supercritical phase.

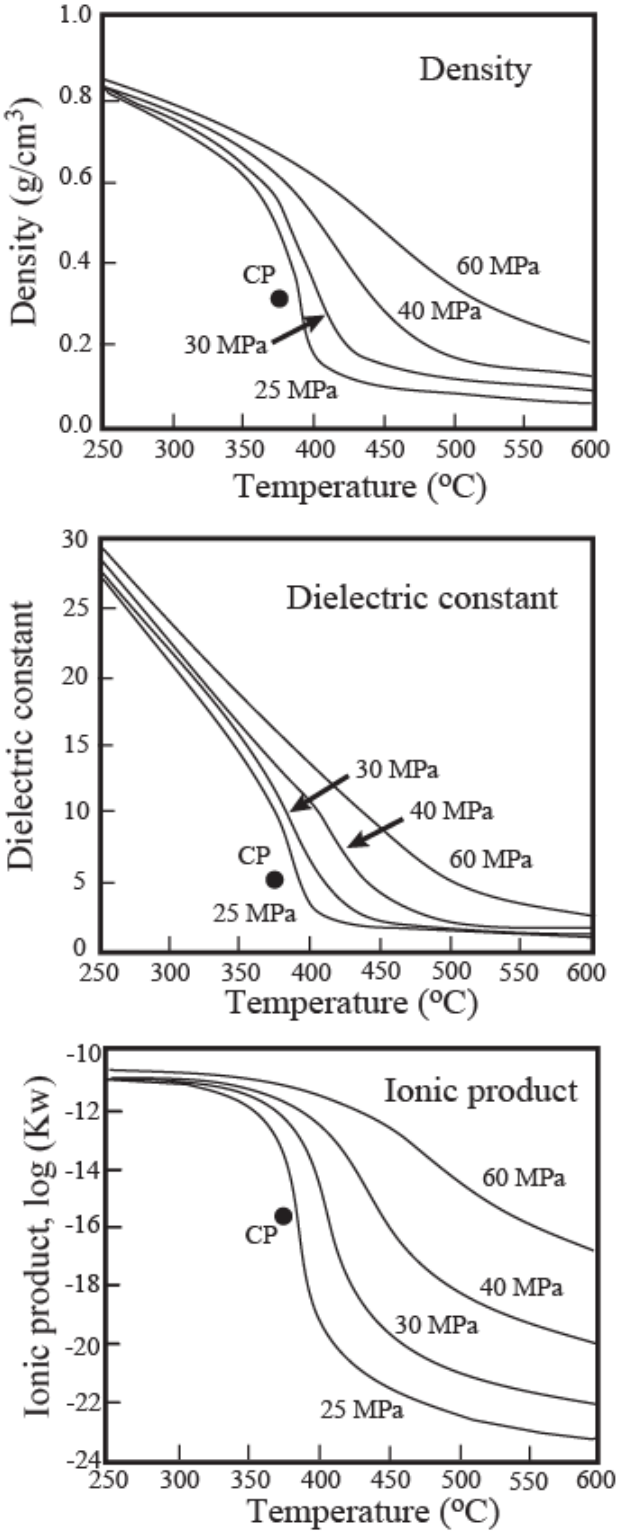

Figure 2.2 Temperature and pressure dependence of SCW density, dielectric constant, and ionic product. The CP abbreviation indicates the critical point. (reproduced from [24]).

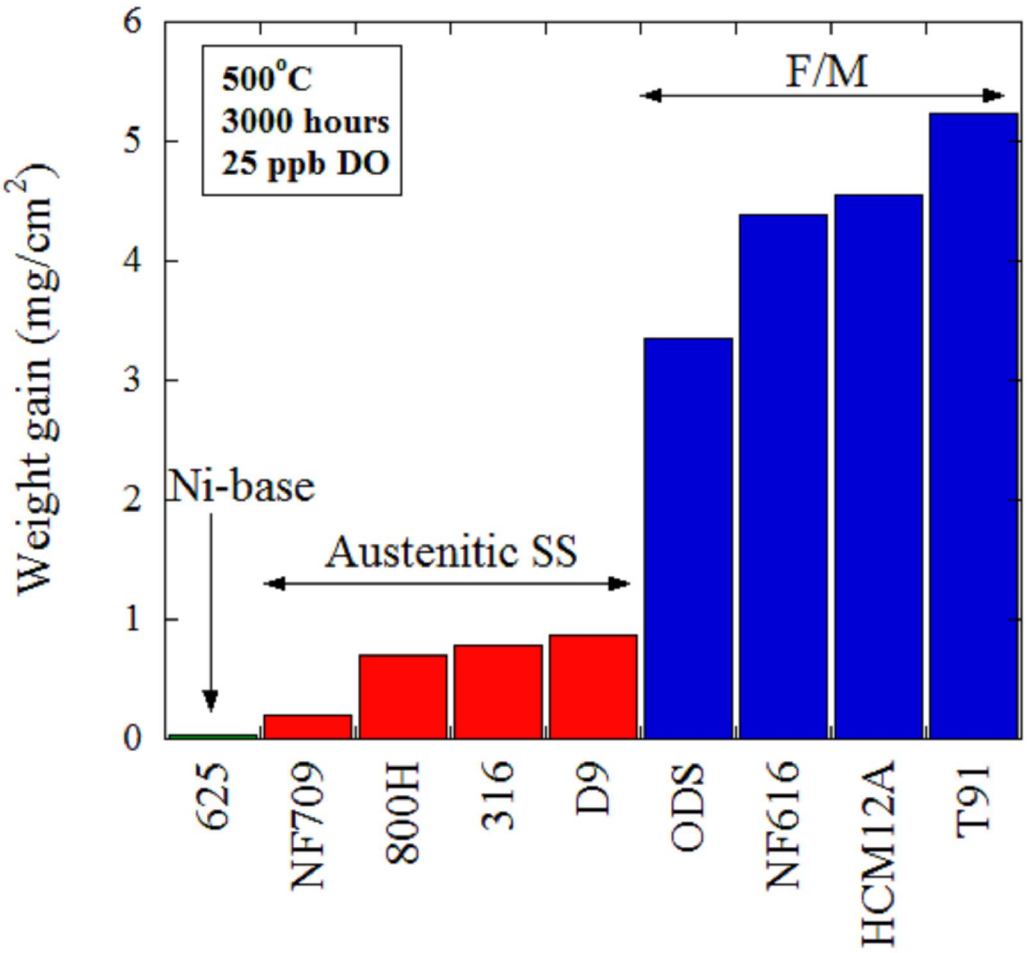

Figure 2.3 Weight gain comparison for 3 different alloy classes exposed to 500˚C SCW for 3000 hours with 25 ppb DO. The F/M abbreviation indicates ferritic-martensitic alloys. (reproduced from [28])

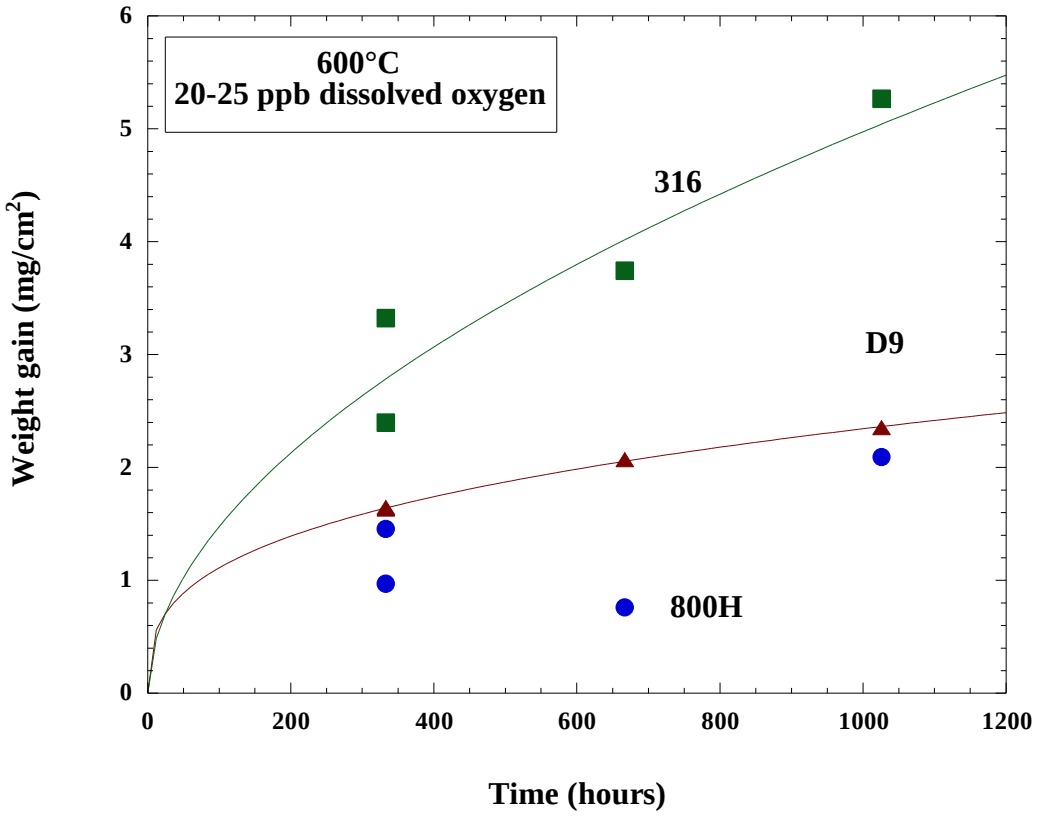

Figure 2.4 Weight gain as a function of time for austenitic stainless steels 316L, D9, and 800H in 20-25 ppb DO SCW at 600˚C. Substantial variation in oxidation behaviors of alloys is evident. [28]

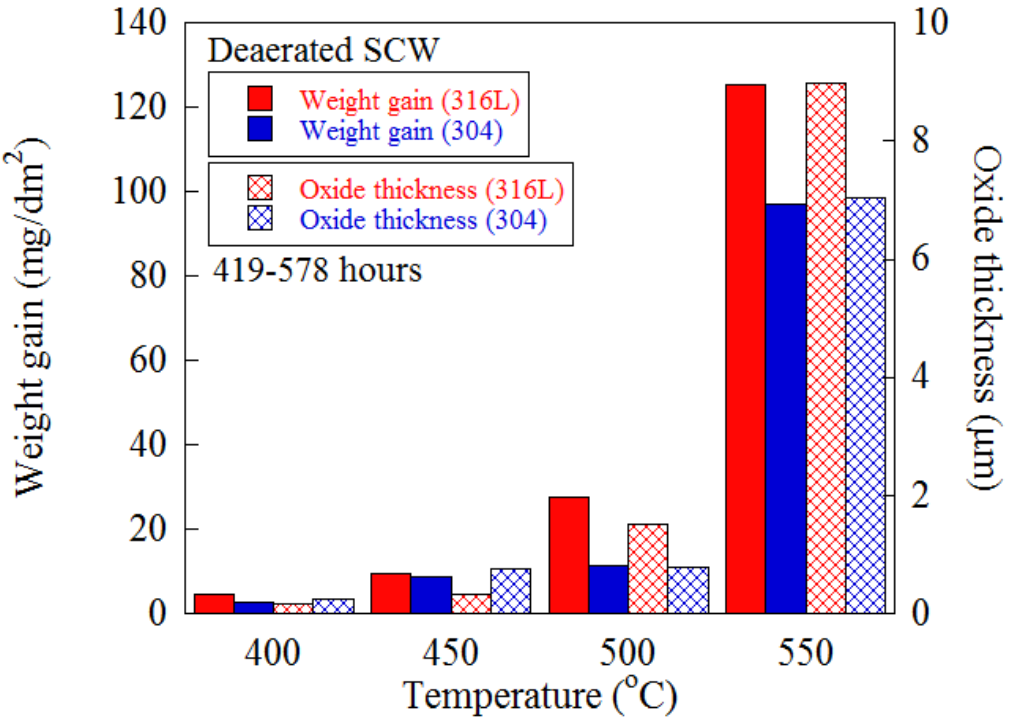

Figure 2.5 Temperature dependence of weight gain and oxide thickness for 316L and 304 stainless steel exposed to deaerated SCW for 419-578 hours. (modified from [36])

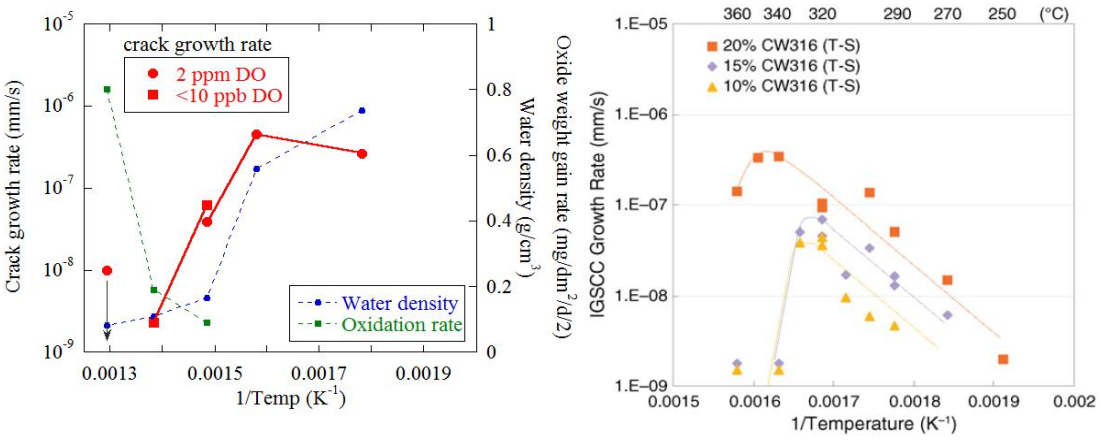

(a) (b)

Figure 2.6 Crack growth rate of CW 316 stainless steel as a function of temperature in the subcritical and supercritical water. The crack growth rate decreases as the temperature approaches or reaches the phase transition in the studies performed by (a) Peng et al. [50] and (b) Arioka et al.[51].

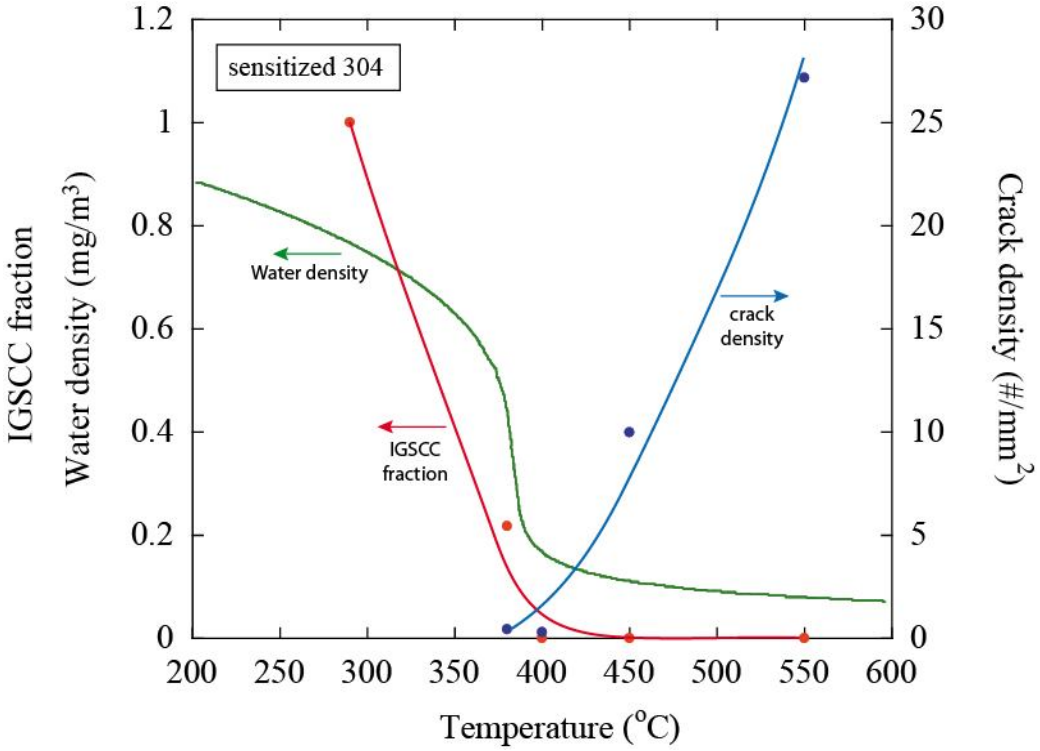

Figure 2.7 IGSCC fraction and crack density on sensitized 304 stainless steel strained to failure in 8 ppm DO SCW as a function of temperature [28]. The unit #/mm^2 indicates the number of cracks per unit area on the gage surface of the specimen.

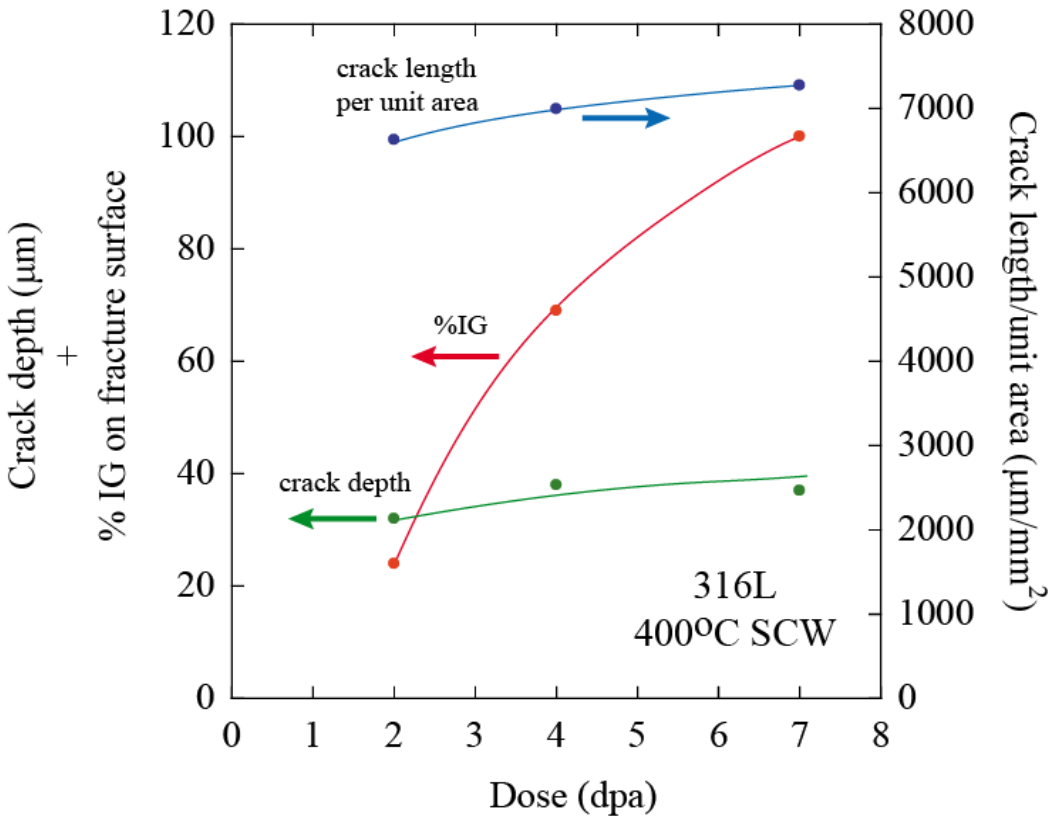

Figure 2.8 Dose dependence of intergranular cracking propensity for 316L strained to failure in deaerated 400˚C SCW [28, 53].

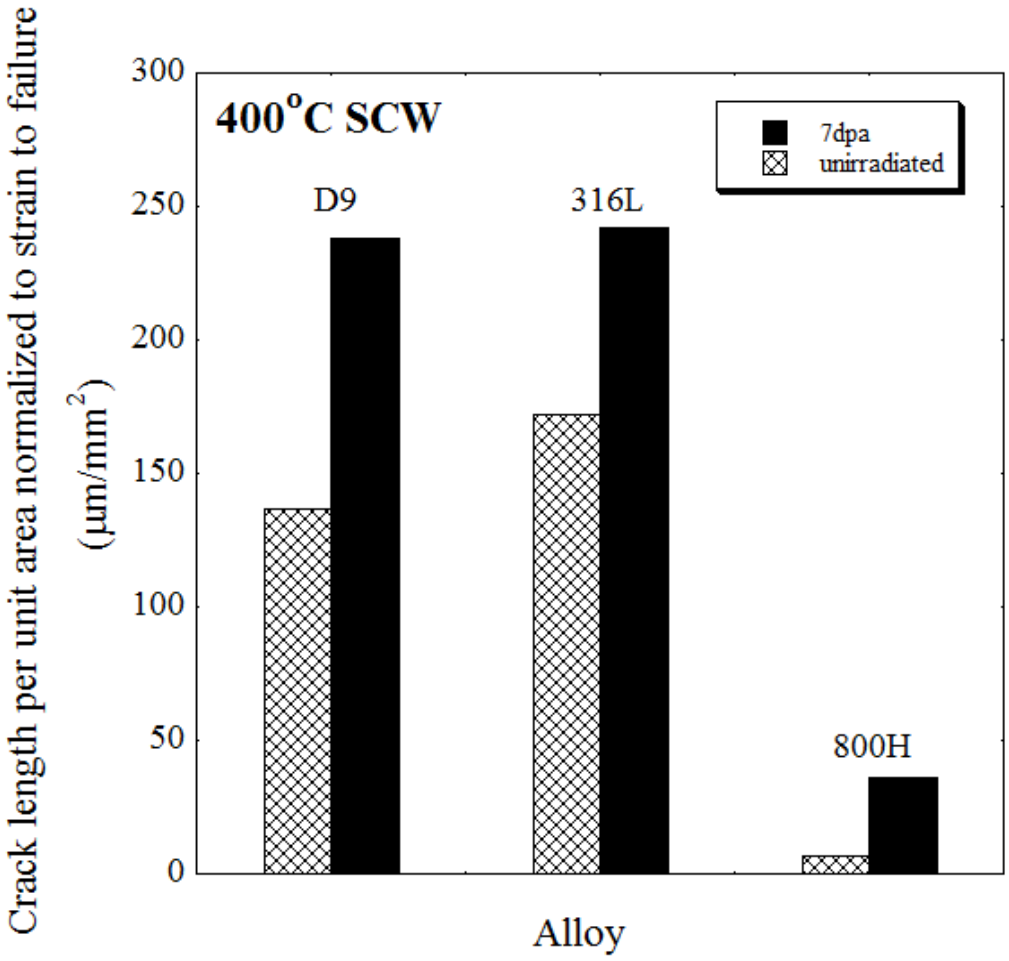

Figure 2.9 Crack length per unit area on gage surface of tensile specimens strained in deaerated 400˚C supercritical water. Solid bars indicate cracking on the irradiated section of the specimens, while hatched bars indicate cracking on the unirradiated section [56].

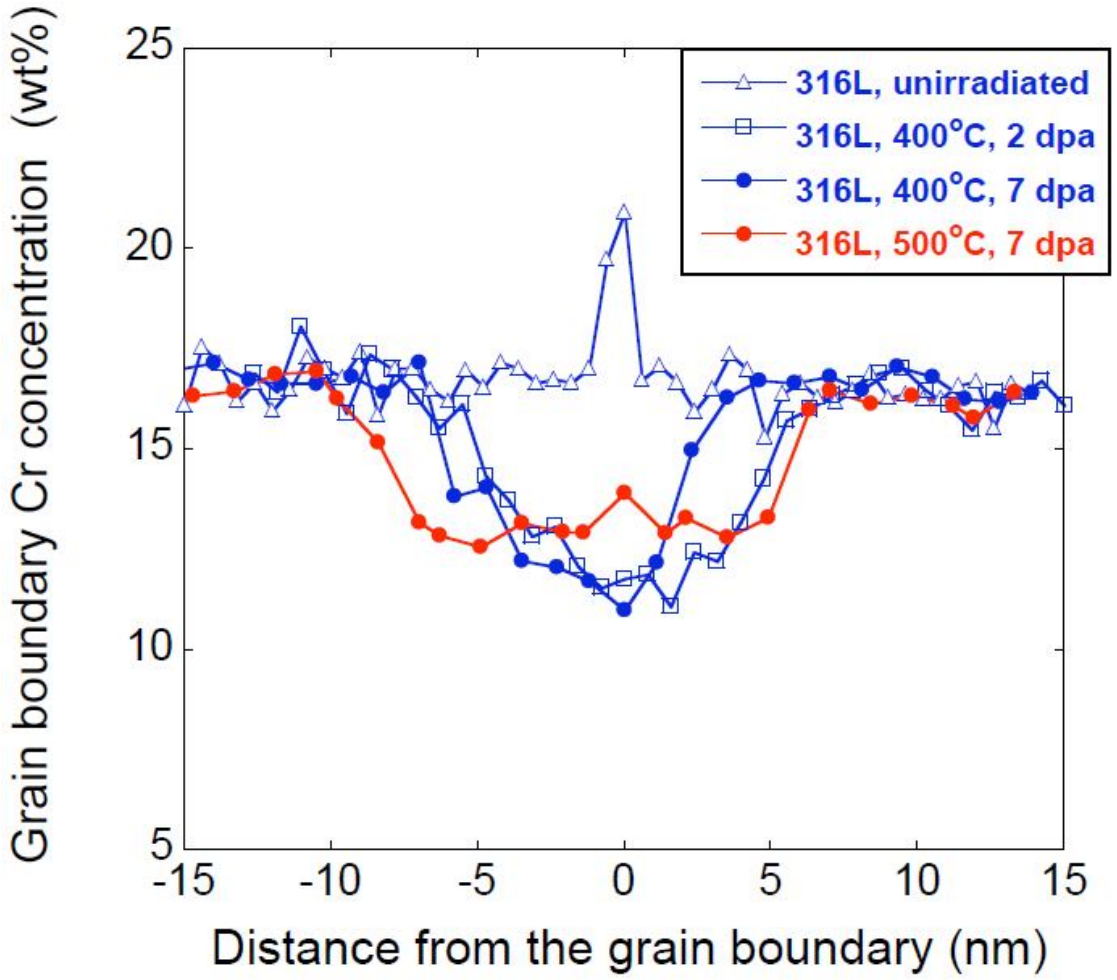

Figure 2.10 Grain boundary chromium composition profile for 316L in the unirradiated and proton irradiated conditions at 400˚C and 500˚C [53].

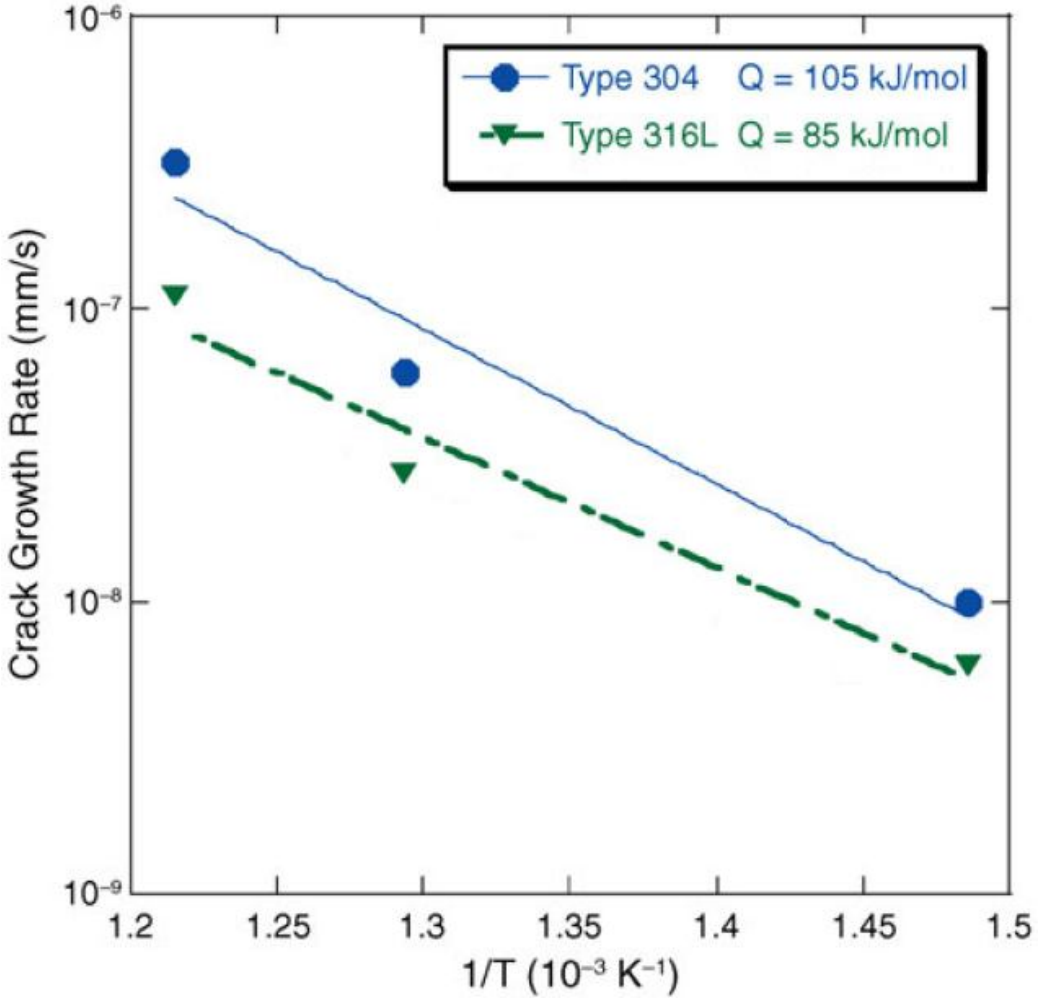

Figure 2.11 Calculated crack growth rates of 304 and 316L as a function of inverse temperature in 400-550˚C SCW. (modified from [4])

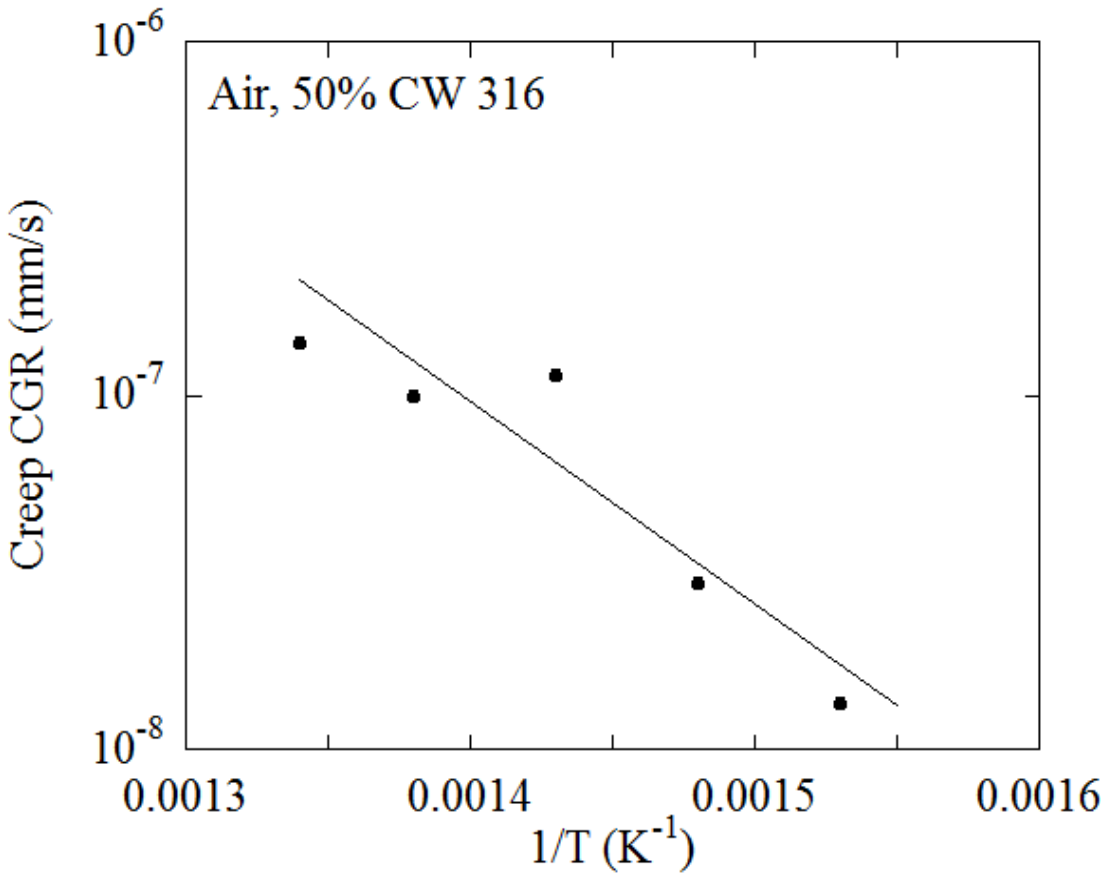

Figure 2.12 Creep crack growth rate versus inverse temperature for non-sensitized 50% CW 316L in air. (data taken from [59])

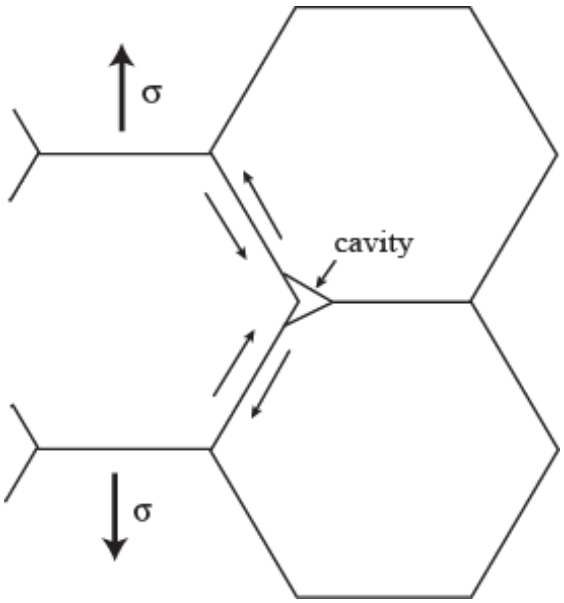

Figure 2.13 Wedge shaped cavity formed at triple junction due to inability to accommodate grain boundary sliding caused by shear stresses along grain boundaries.

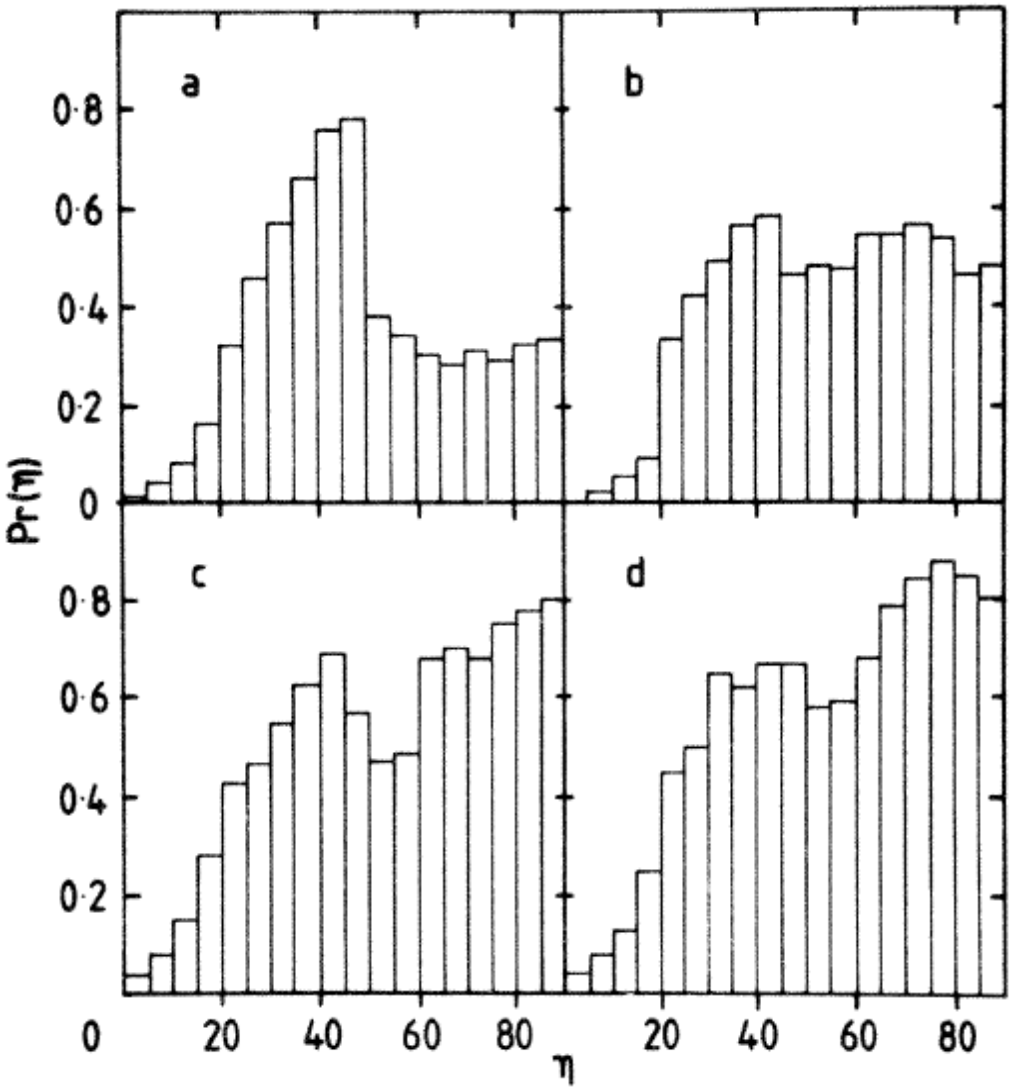

Figure 2.14 Distribution function, Pr(η), for cracked boundaries with respect to the angle they make with the tensile axis, η. Each plot indicates the distribution for a given temperature compensated strain rate, $\dot{\varepsilon}=\dot{\varepsilon}_0 e^{Q/RT}$, where Q=243 kJ/mol. The temperature compensated strain rates are (a) $\dot{\varepsilon} = 6.7 \times 10^{12}$, (b) $\dot{\varepsilon} = 1.5 \times 10^{11}$, (c) $\dot{\varepsilon} = 4.6 \times 10^{9}$, and $\dot{\varepsilon} = 2.2 \times 10^{8}$ [67].

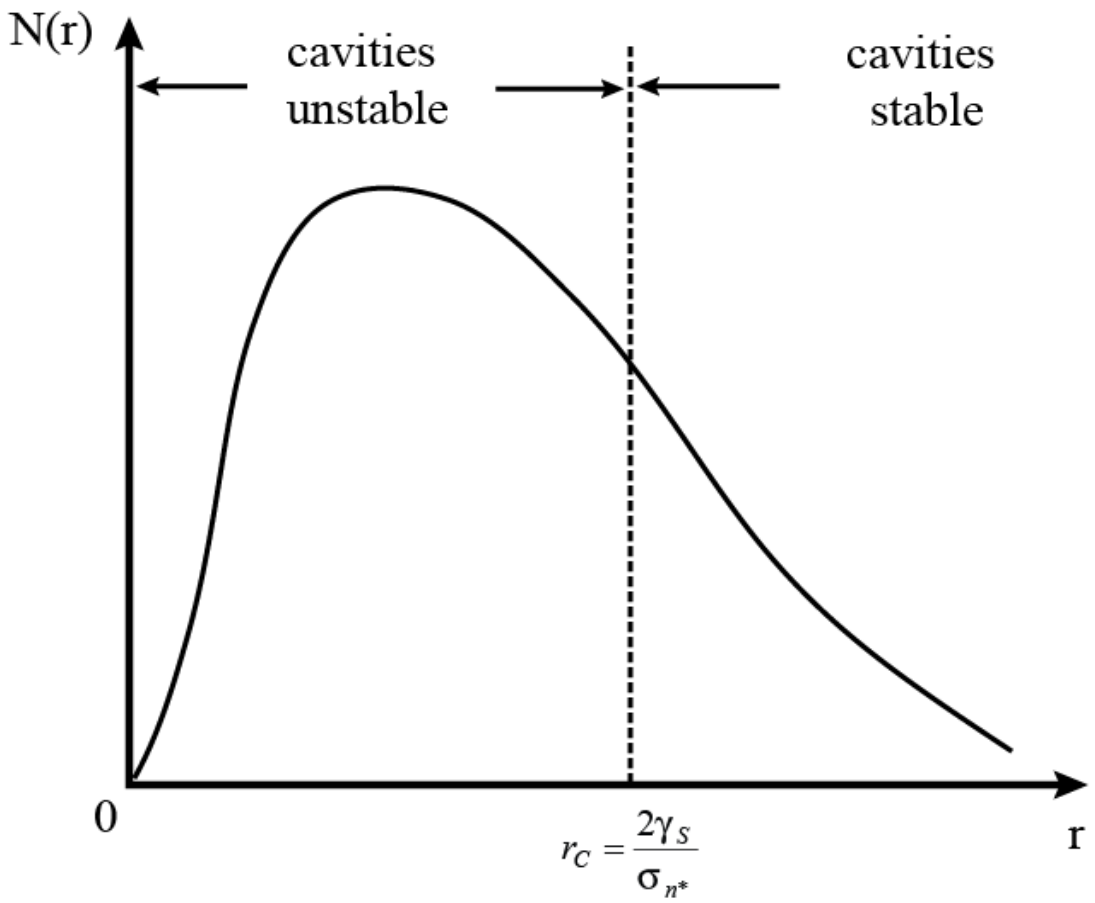

Figure 2.15 Distribution of radii of voids formed due to matrix creep. Only voids with radii exceeding the critical radius, r_C, will grow by into stable cavities. (modified from [70])

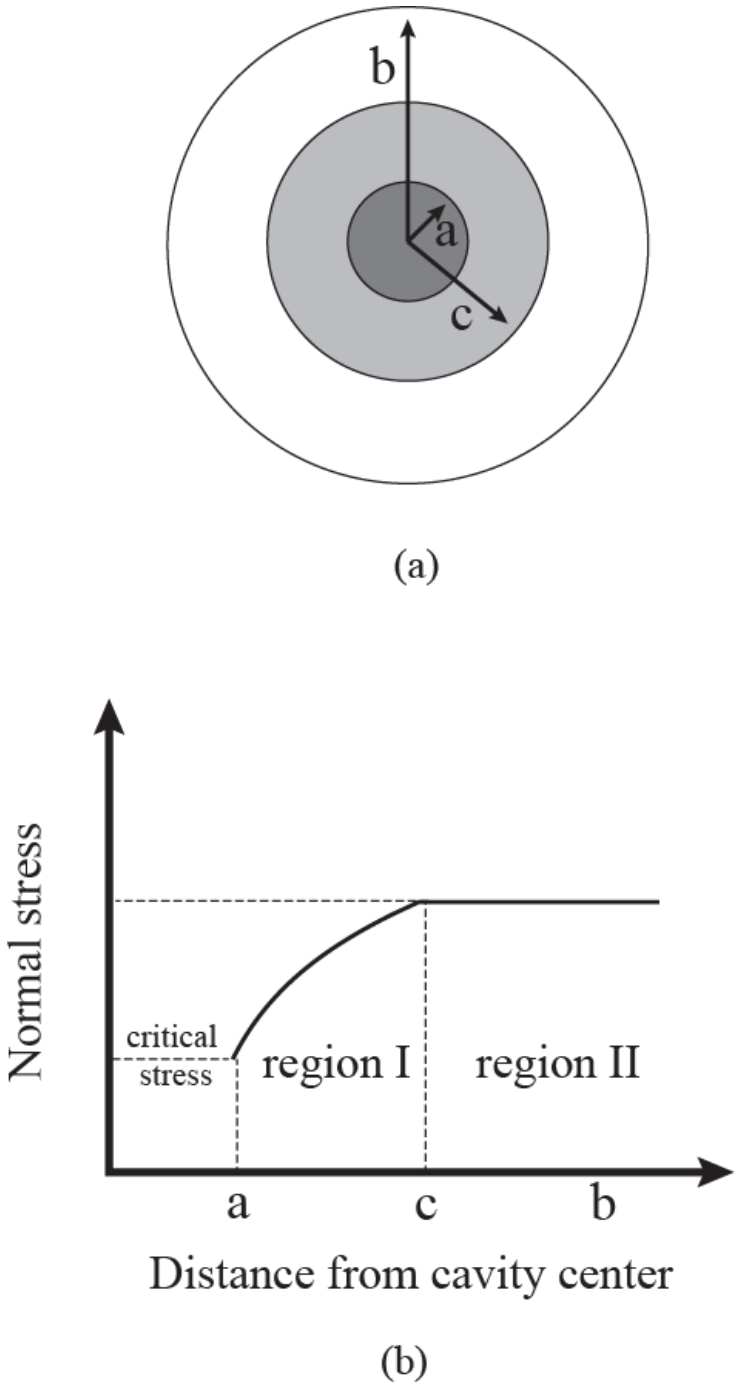

Figure 2.16 (a) Schematic of regions surrounding cavity that dictate growth. The region with radius a indicates the initial cavity, the next outer region extending to radius c indicates the region of the material that generates vacancies that diffuse into the cavity, and the outer region undergoes power-law dislocation creep. (b) The normal stress gradient as a function of the distance from the center of the cavity with radius a. (modified from [72])

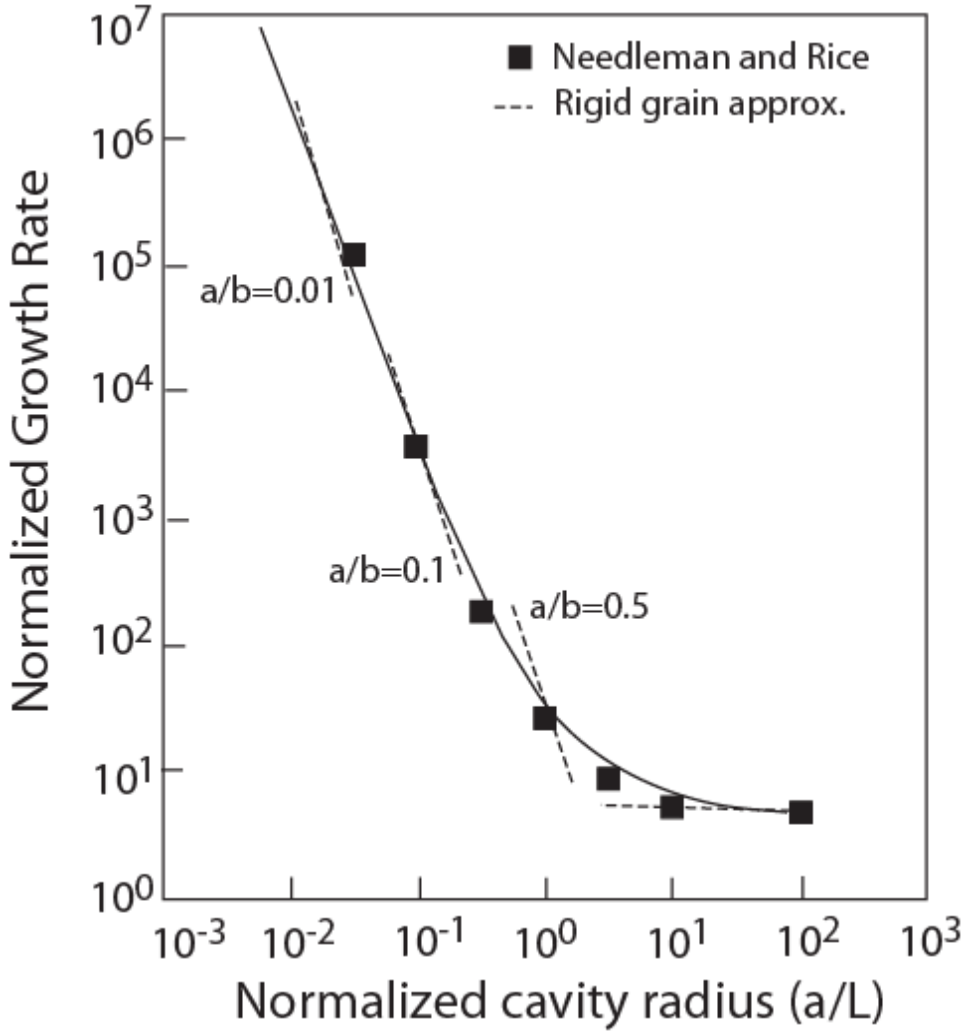

Figure 2.17 Normalized cavity growth rate versus normalized cavity radius for Needleman and Rice's model which considers the coupling between diffusion and dislocation creep, and for rigid body approximations of cavity growth. Agreement is seen only when the cavity radius, a, is small compared to the intercavity half spacing, b. L is the characteristic diffusion length. (modified from [63])

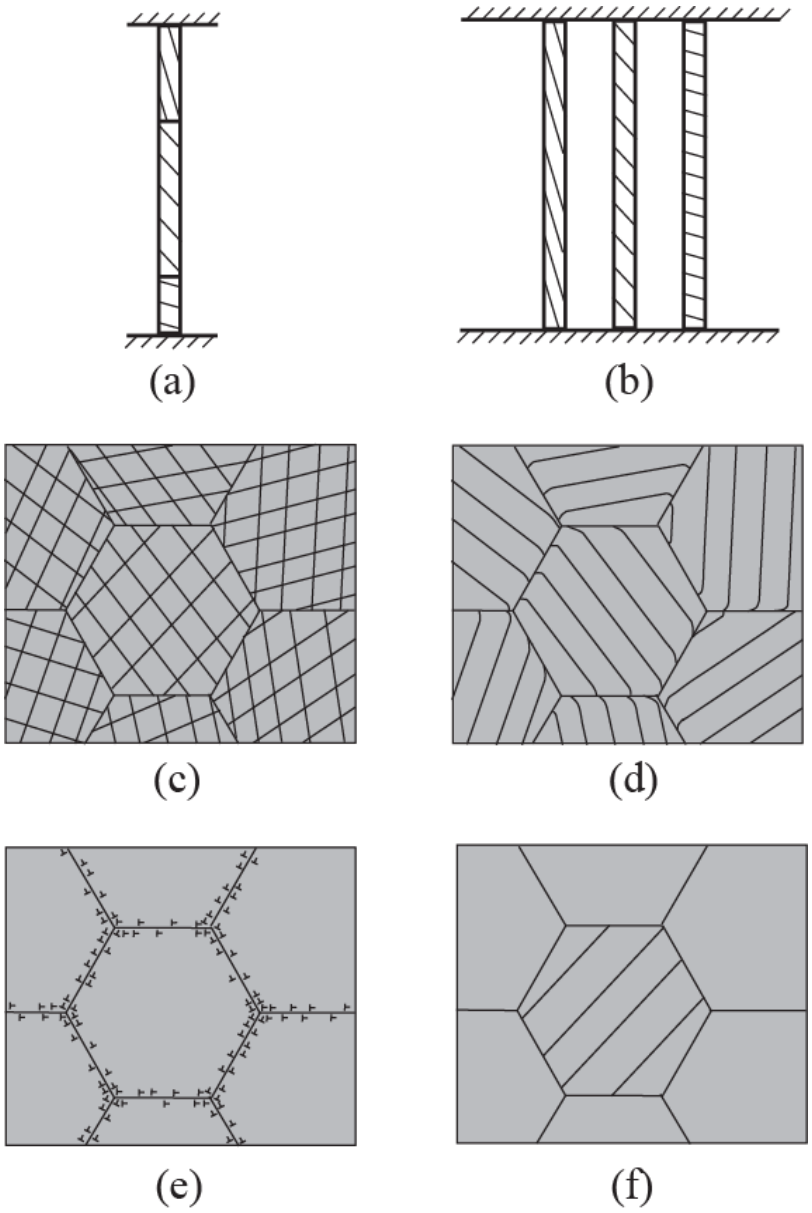

Figure 2.18 Illustrations of several polycrystal plasticity models, (a) lower bound model for a linear serial polycrystal, (b) Sachs model, (c) Taylor's upper bound model, (d) Kochendorfer's model incorporating bending stresses, (e) Ashby's model incorporating geometrically necessary dislocations, (f) Chastel and Dawson's lower bound model for a 3-D polycrystal. (modified from [84])

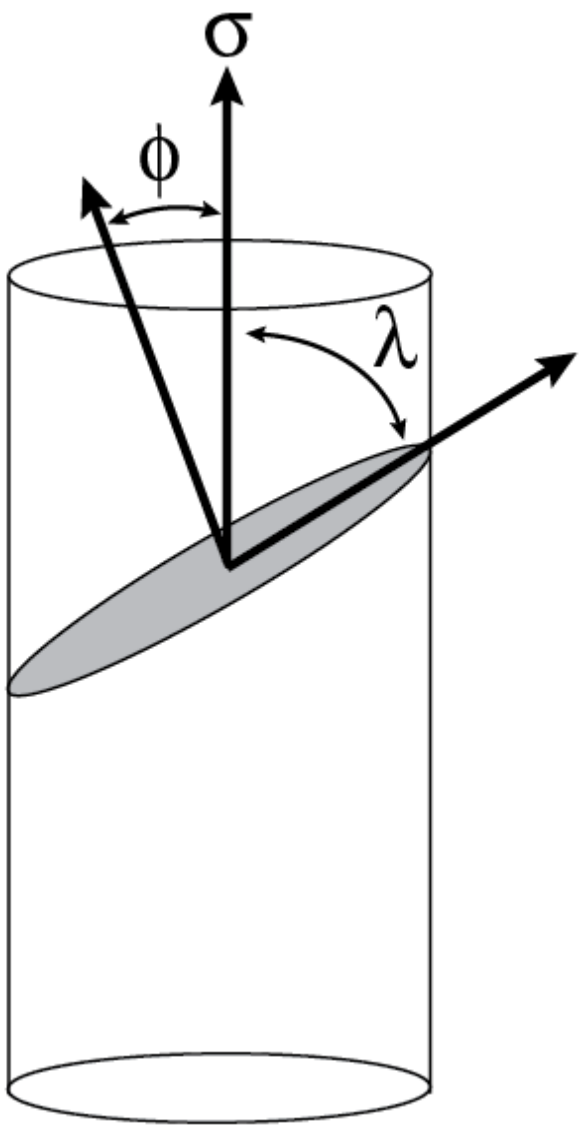

Figure 2.19 Illustration of variables in Schmid factor calculation for a crystal in uniaxial tension.

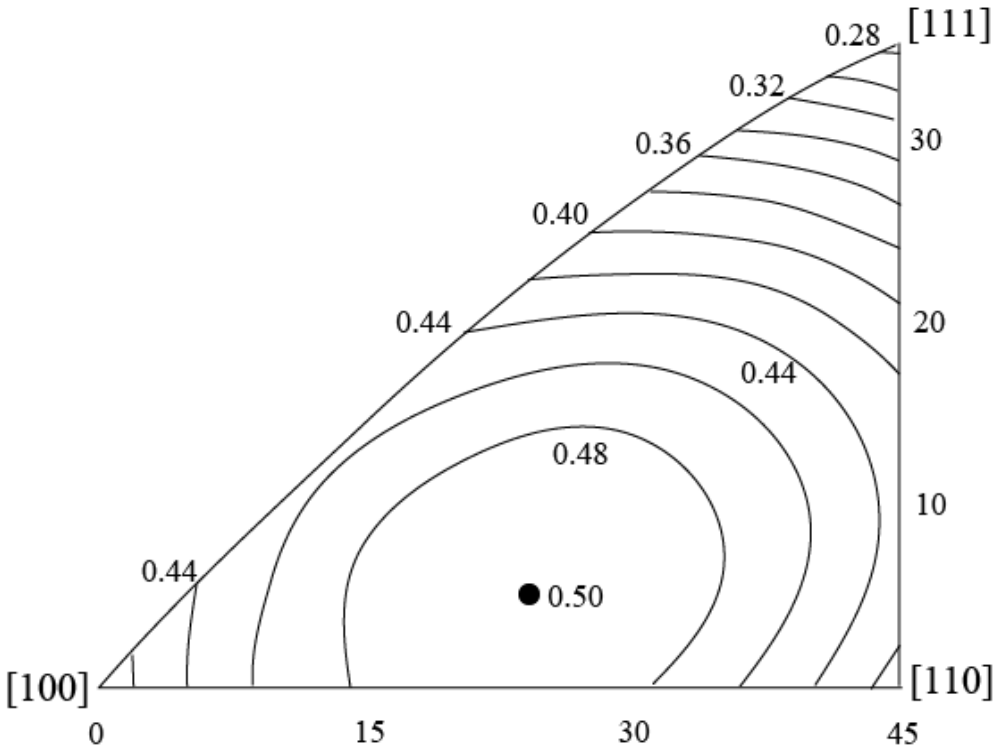

Figure 2.20 Relationship between Schmid factor and crystal orientation for FCC materials. (reproduced from [74])

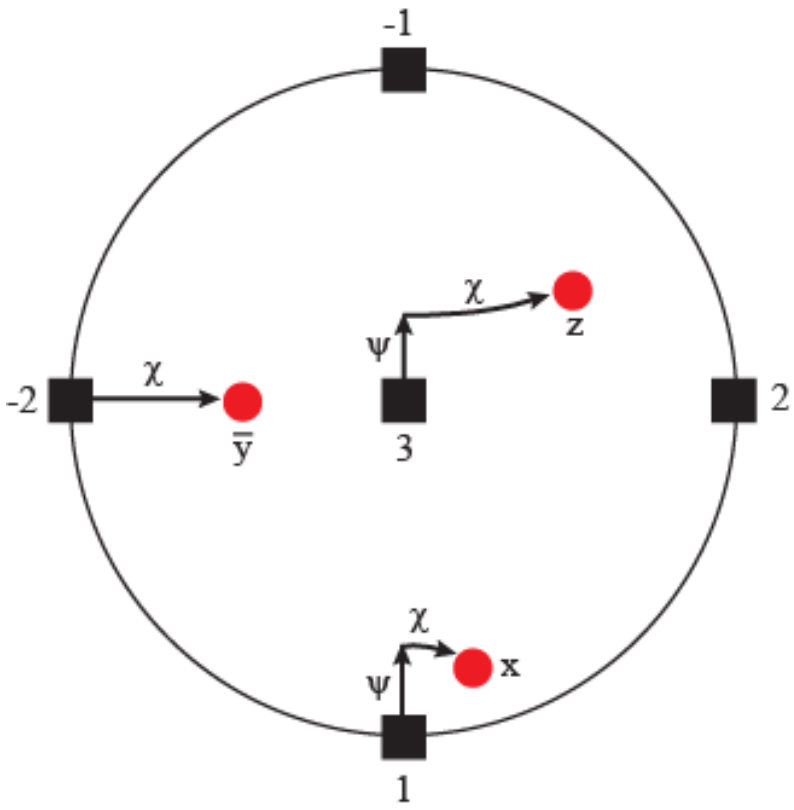

Figure 2.21 Stereographic diagram relating the specimen axes x, y, and z (red dots) to the crystallographic axes 1, 2, and 3 (black squares). (reproduced from [74])

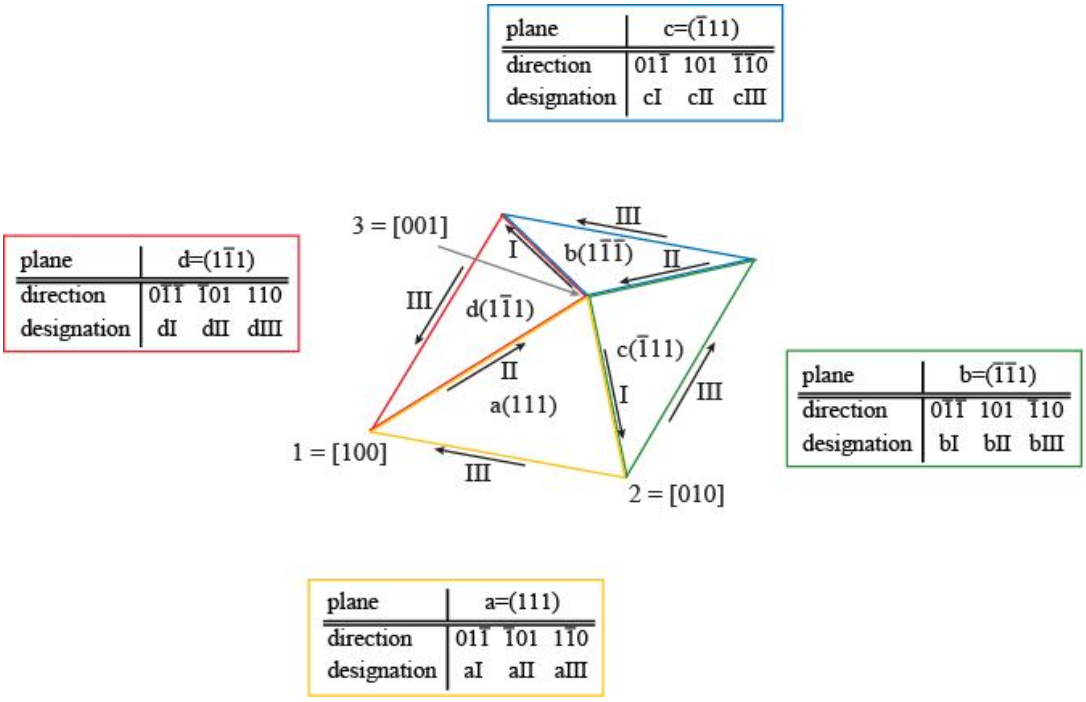

Figure 2.22 Diagram of 12 slip systems in fcc crystals. The four slip planes are designated as a, b, c, and d, and the three slip directions are designated as I, II, and III. (reproduced from [74])

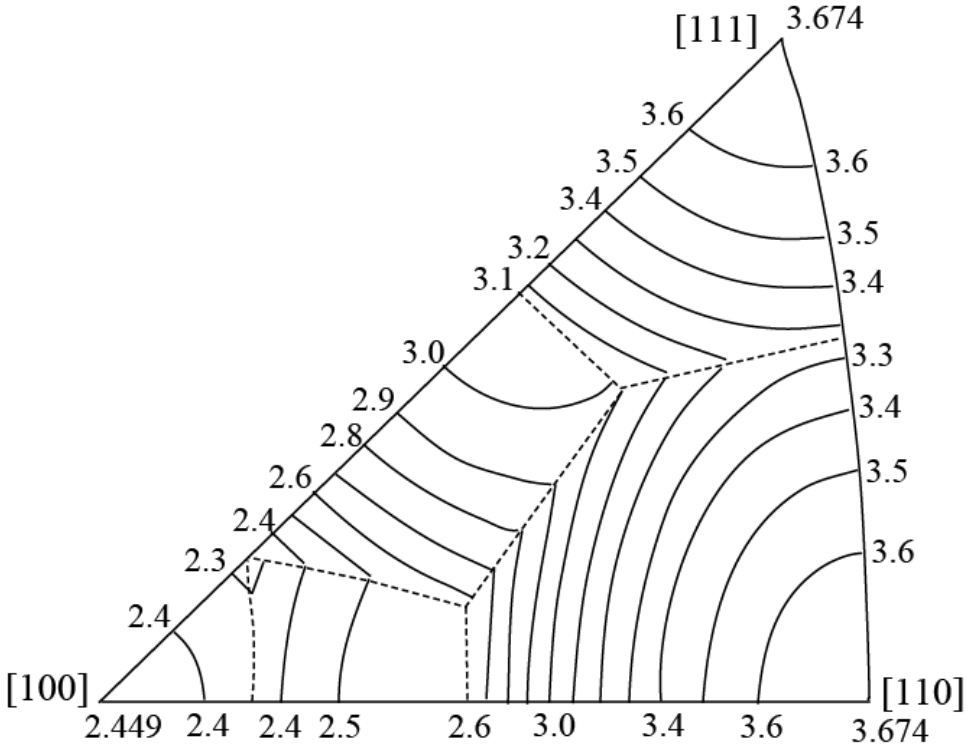

Figure 2.23 Relationship between Taylor factor and crystal orientation for FCC materials. (reproduced from [74])

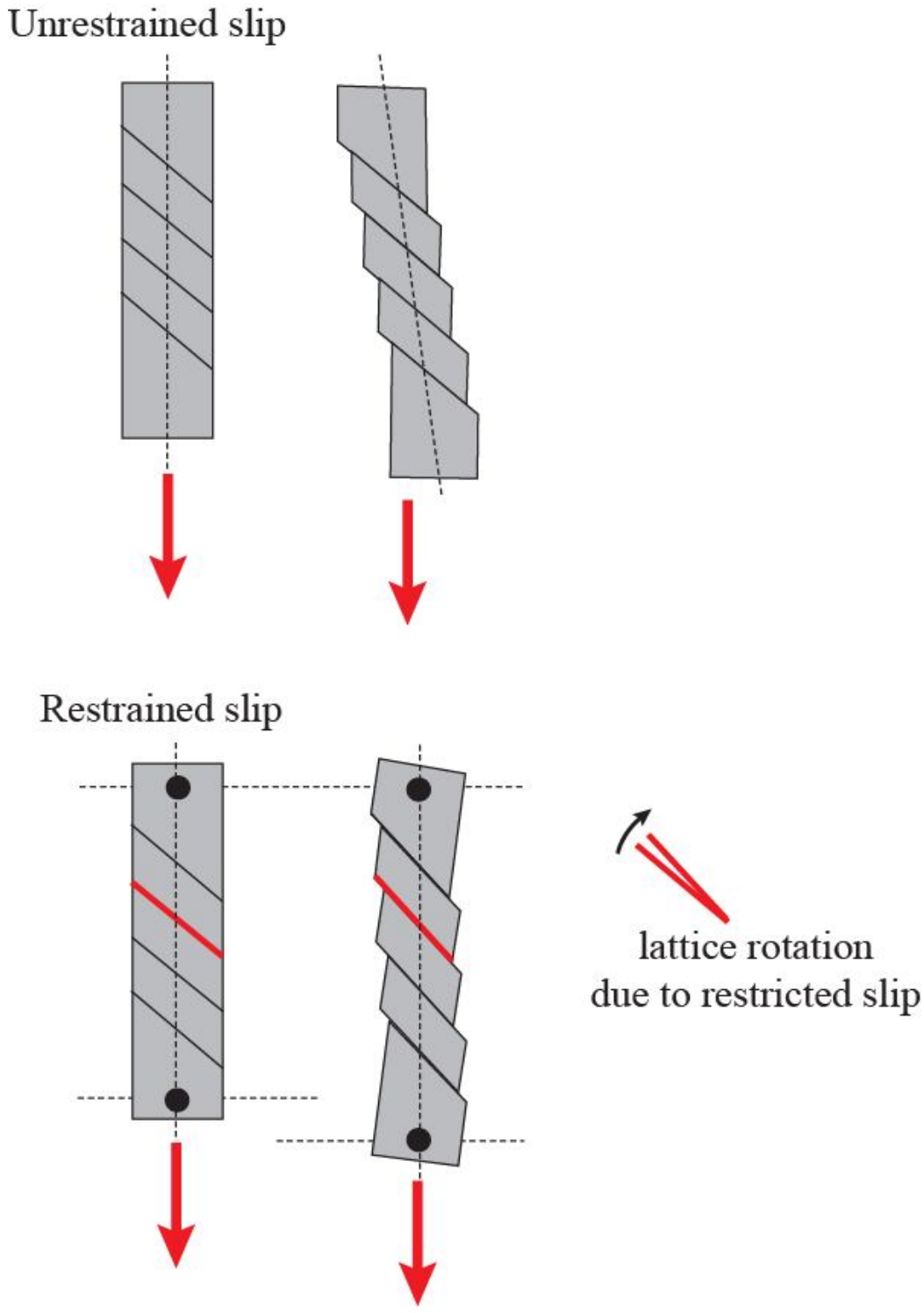

Figure 2.24 Unrestrained slip versus restrained slip behavior. Restrained slip results in rotation of the crystal lattice.

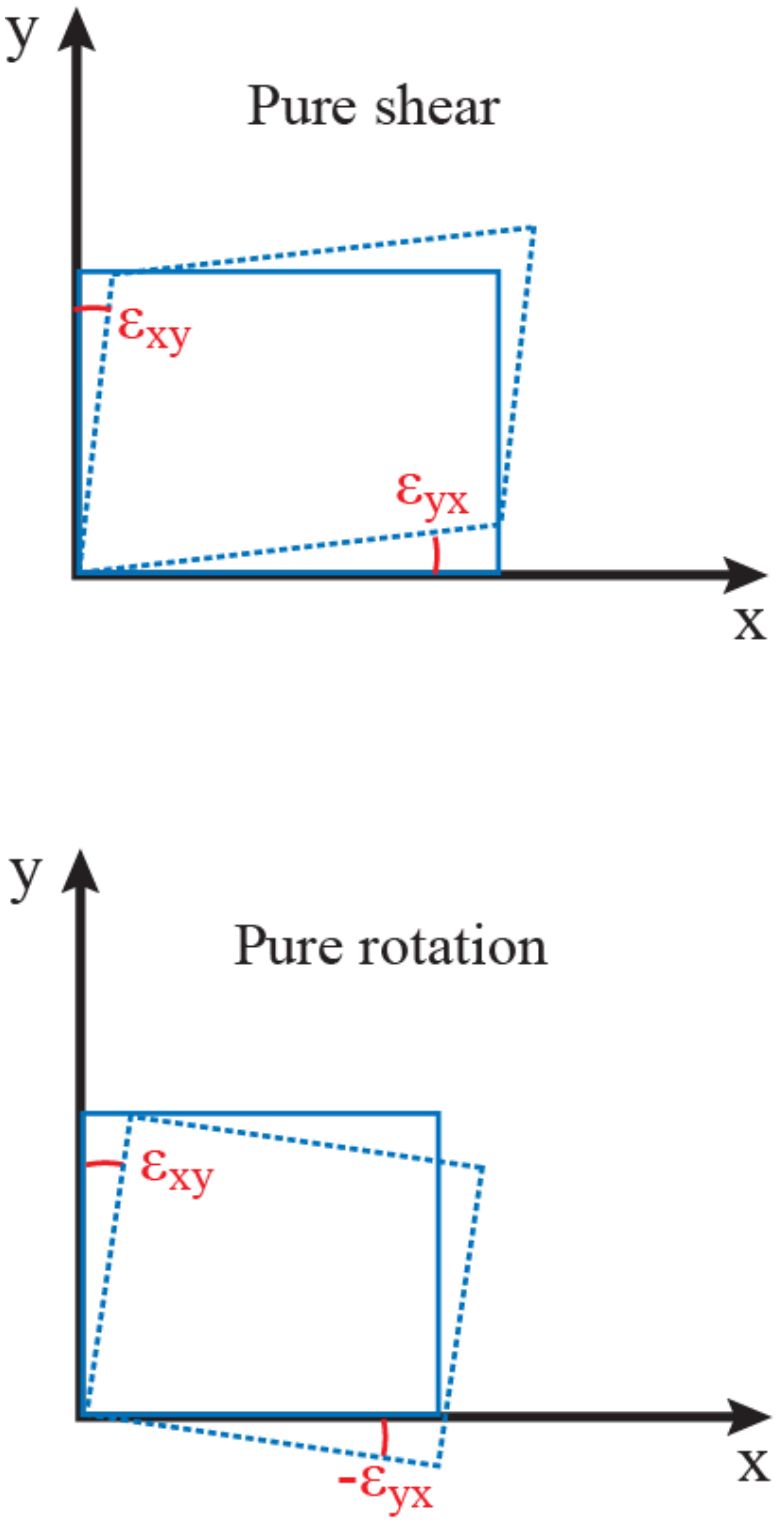

Figure 2.25 Shear strain and rigid-body rotation resulting from shear displacements. (reproduced from [62])

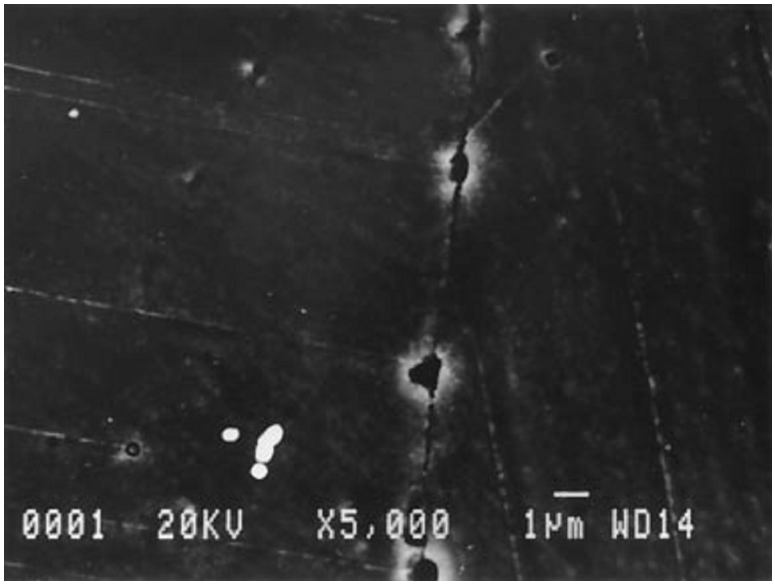

Figure 2.26 Slip induced cavitation at grain boundary of alloy A286 subjected to high-temperature low-cycle fatigue testing [21].

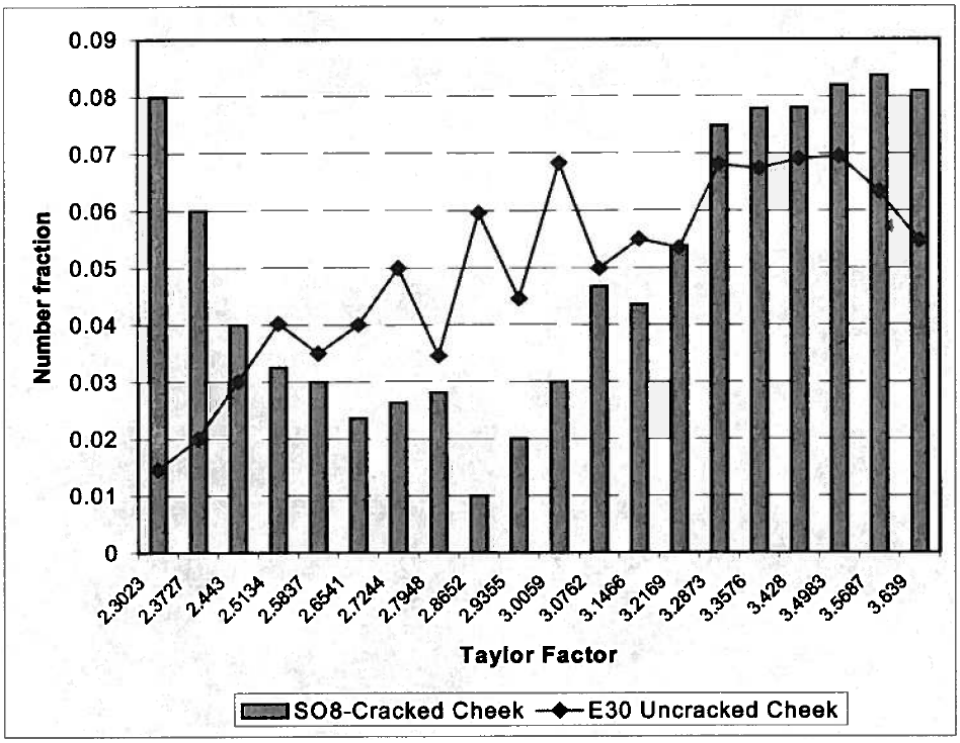

Figure 2.27 Taylor factor distributions in cracked and uncracked portions of feeder piping. The bimodal distribution of Taylor factors in the cracked cheek increases the likelihood of adjacent grains having high Taylor factor mismatch [19].

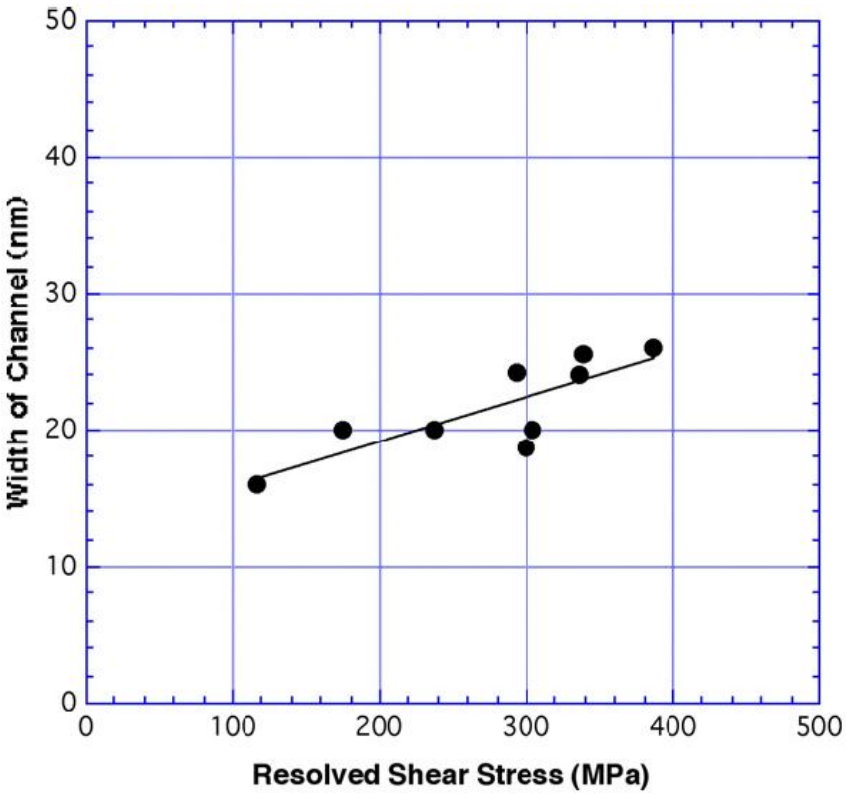

Figure 2.28 Width of dislocation channels in neutron irradiated 316 stainless steel strained at room temperature [96].

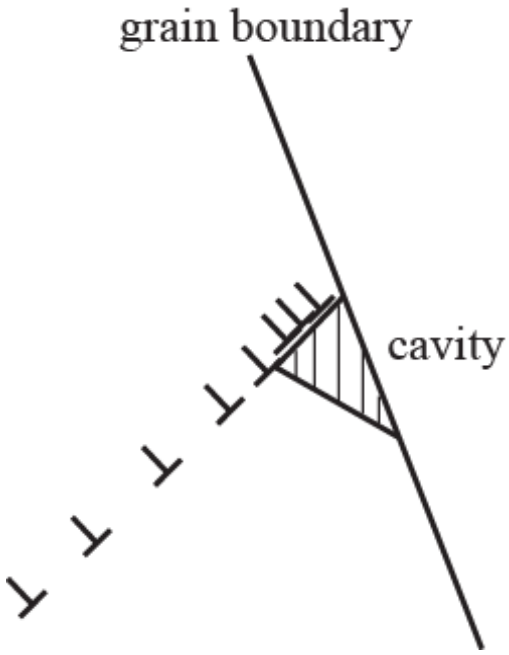

Figure 2.29 Illustration of Zener-Stroh cracking mechanism due to dislocation pile up at grain boundaries. Once a critical stress is achieved, dislocations coalesce to form a cavity.

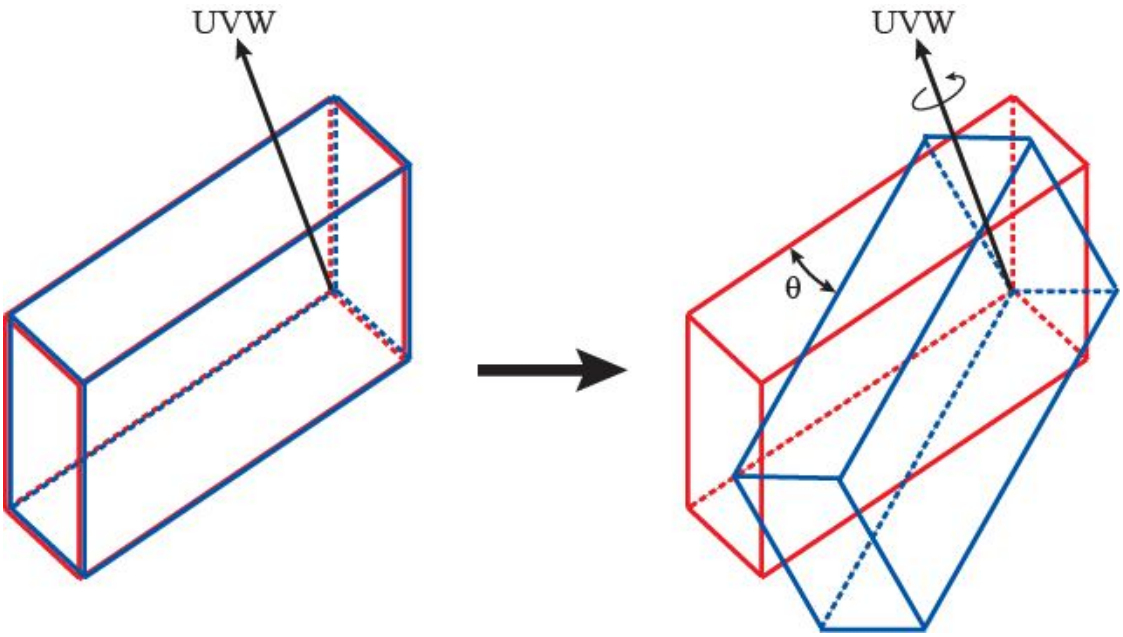

Figure 2.30 A misorientation between two lattices can be described by an angle/axis pair, in this example, θ/UVW.

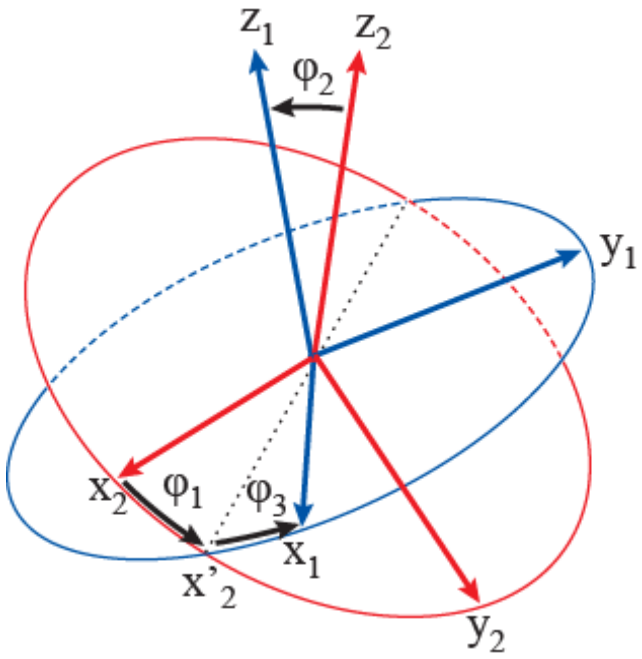

Figure 2.31 Illustration of Euler angles (φ_1, φ_2, φ_3) describing misorientation between two crystal lattices with axes $x_1y_1z_1$ and $x_2y_2z_2$. (modified from [104])

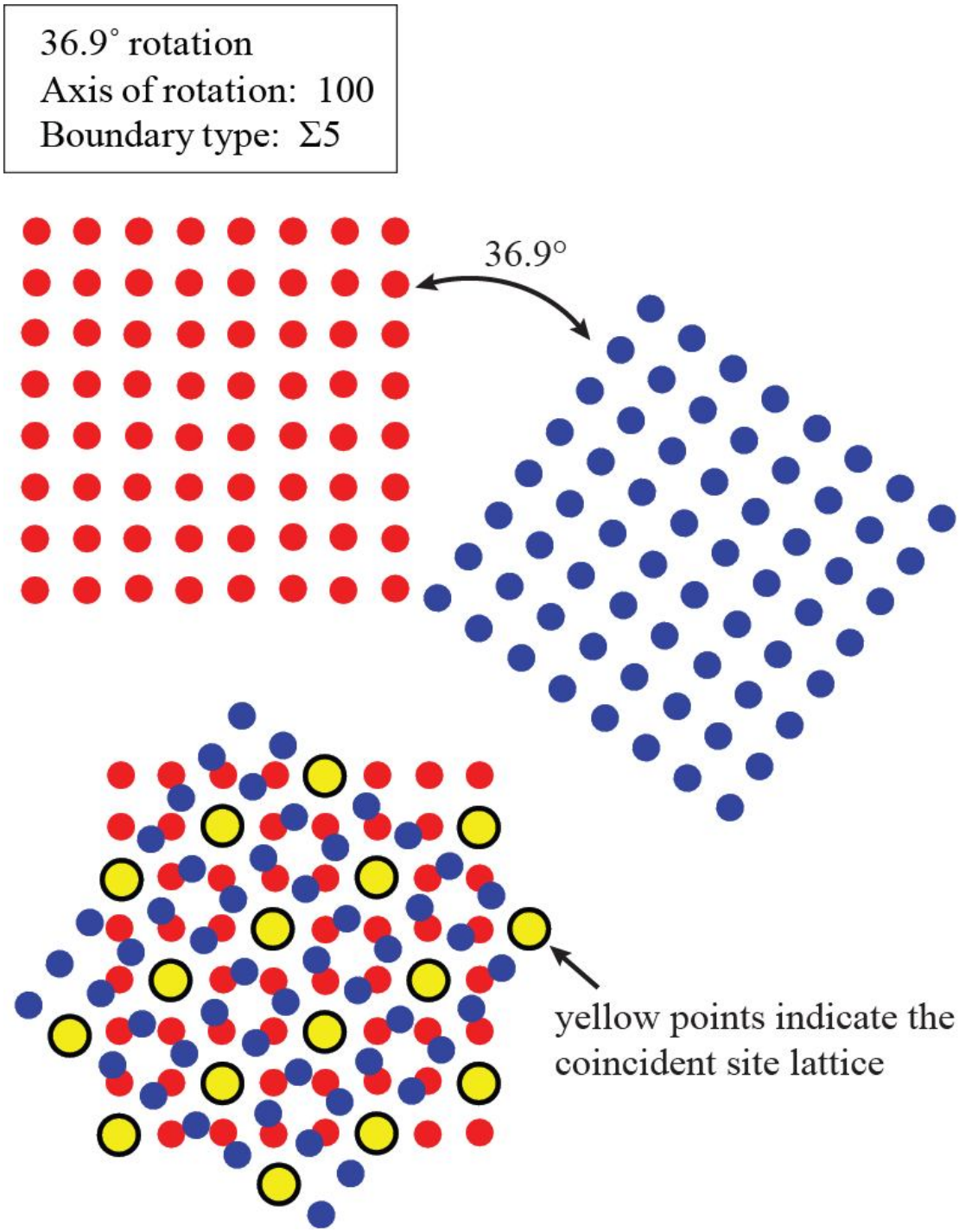

Figure 2.32 Illustration of a Σ5 CSL. Both lattices are viewed from the 100 direction. The blue lattice is rotated about the 110 direction by 36.9˚. When the two lattices overlap, one in every 5 lattice sites is coincident. These yellow coincident sites comprise the CSL.

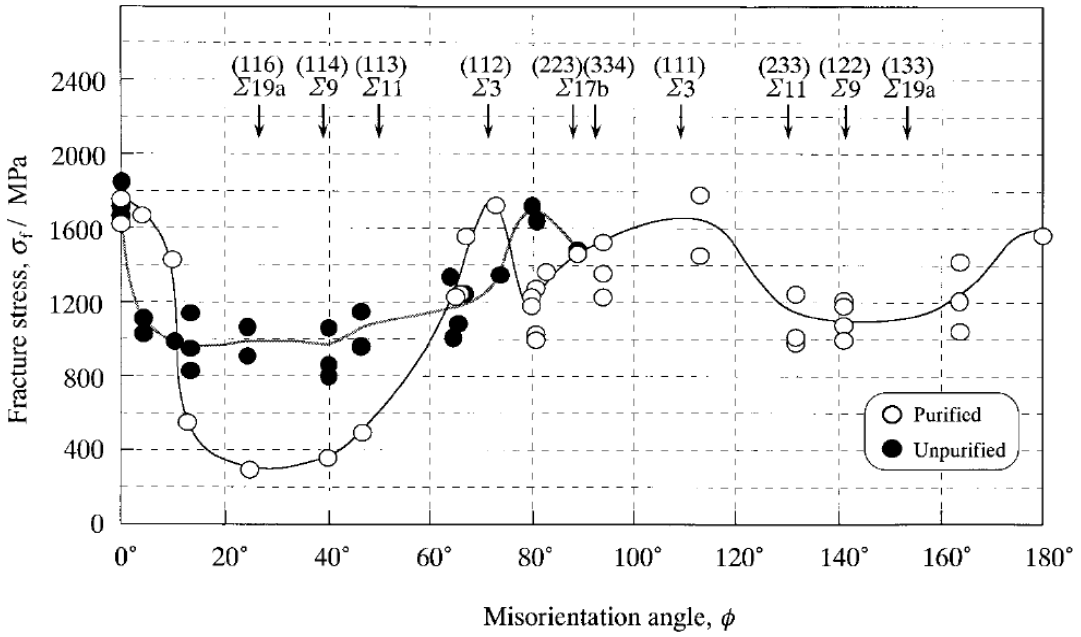

Figure 2.33 Misorientation dependence of fracture stress in molybdenum bicrystals with <110> twist boundary [138].

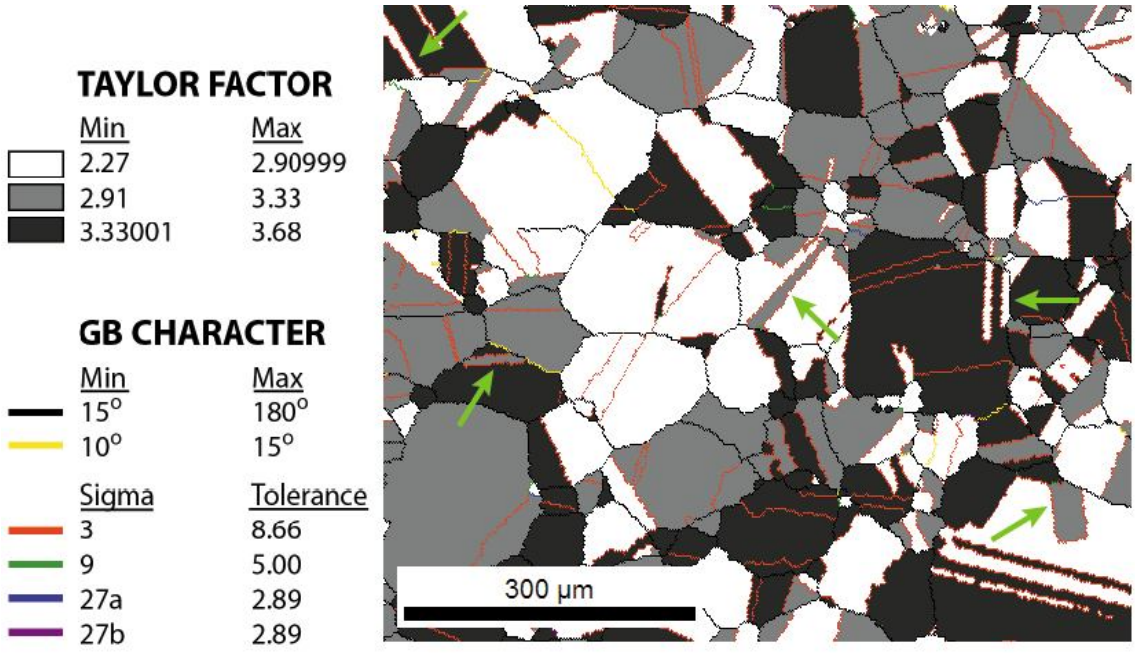

Figure 2.34 EBSD map of 316L stainless steel indicating grain boundary characters and Taylor factors of the grains. Twinned regions of 316L stainless steel represent often have different Taylor factors than the bulk grain.

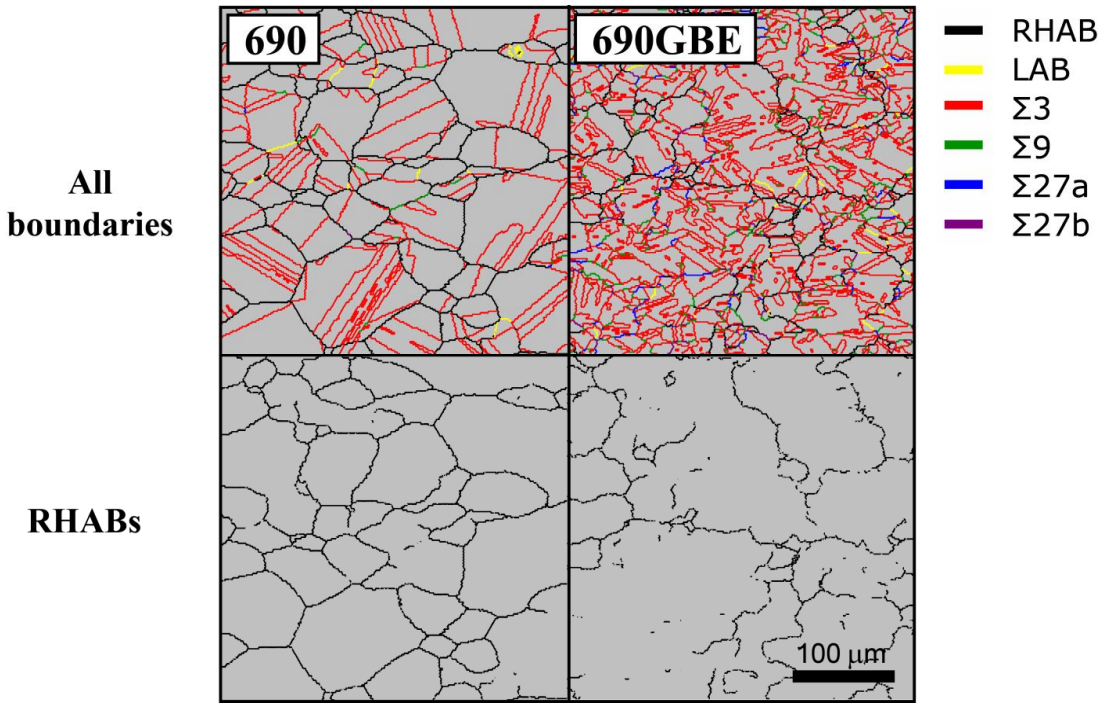

Figure 2.35 Grain boundary character maps for 690 and 690GBE. The top maps show all grain boundaries present in the alloy, while the bottom maps only show the RHABs. The connectivity of the RHABs has been disturbed in the GBE specimen [108].

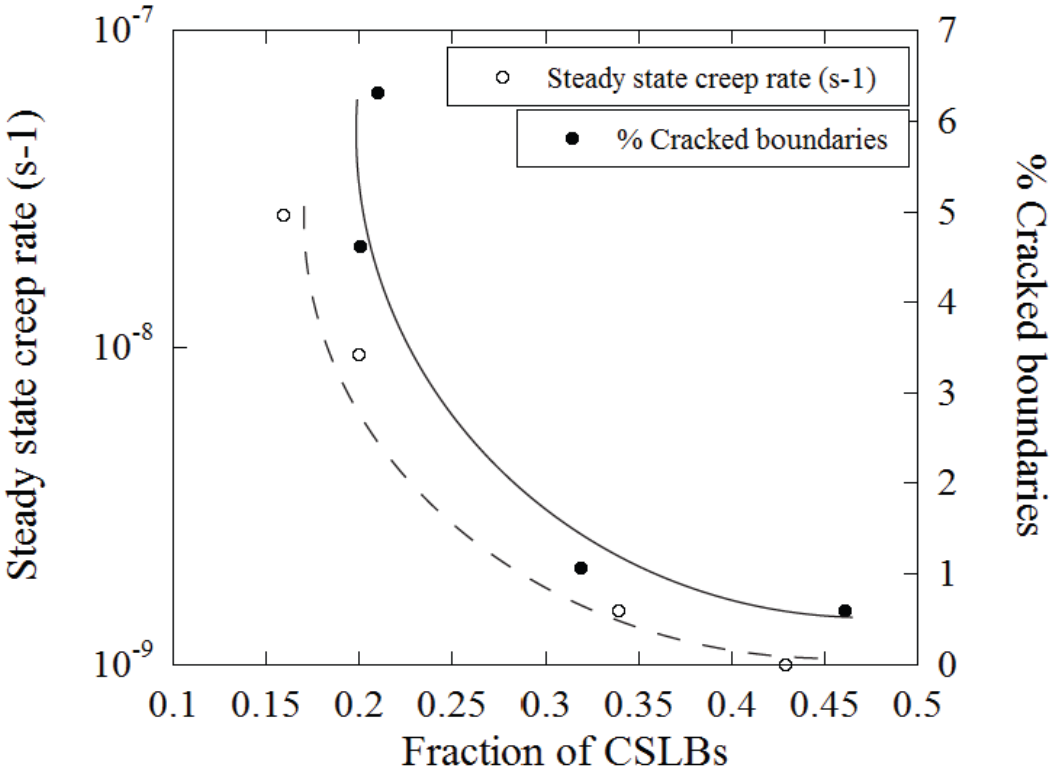

Figure 2.36 Steady state creep rate and percent cracked boundaries as a function of the fraction of CSLBs in coarse grained Ni-16Cr-9Fe in argon at 360˚C [119].

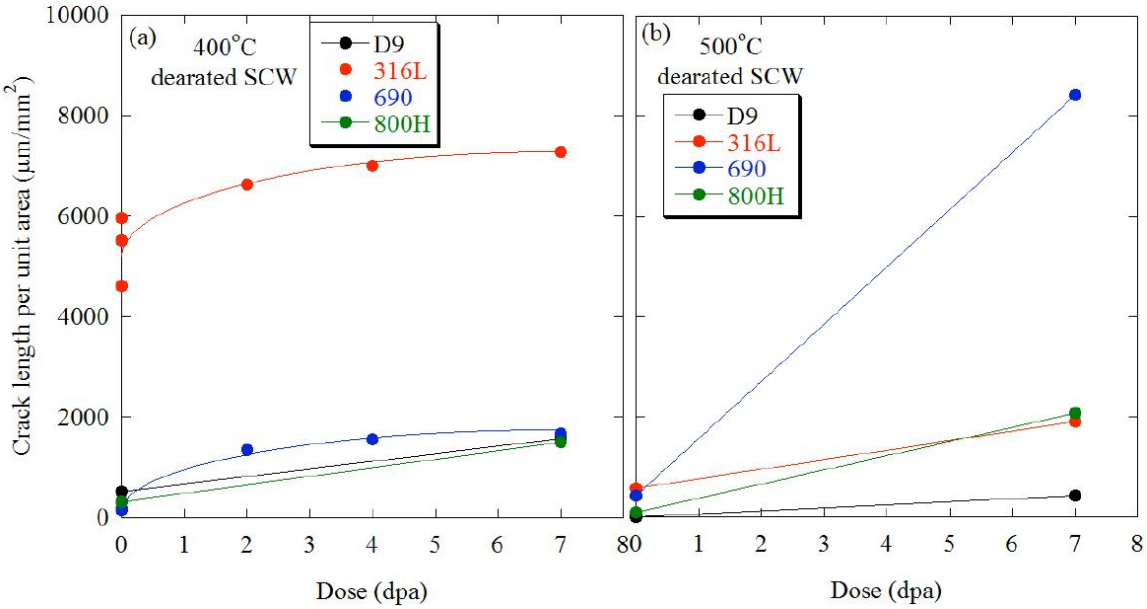

Figure 2.37 The crack length per unit area on the gage surfaces of specimens as a function of dose following straining to failure in (a) 400˚C and (b) 500˚C SCW [149].
**The cracking data for alloys 316L and 690 exclude the 3 MeV proton irradiated specimens.*

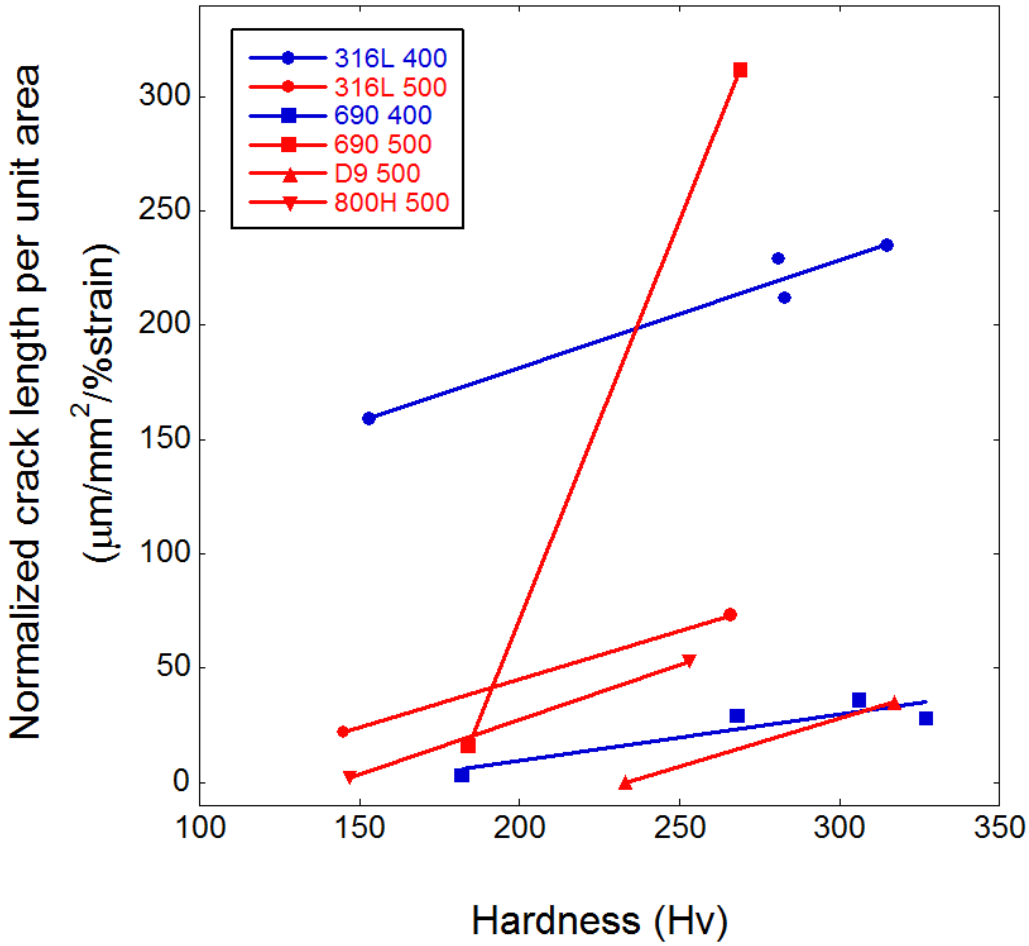

Figure 2.38 Cracking severity as measured by the normalized crack length per unit area vs. hardness for all alloys and temperatures [53].

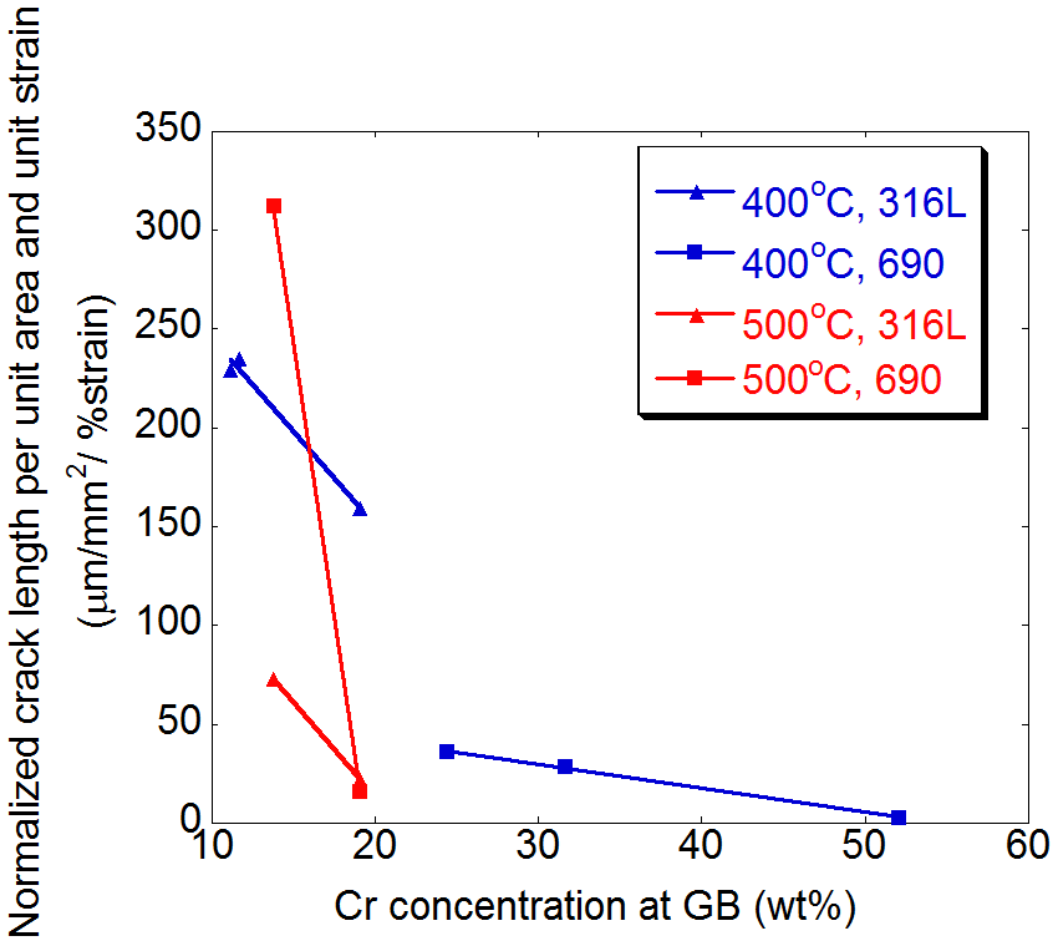

Figure 2.39 Cracking severity as measured by normalized crack length per unit area vs. grain boundary chromium concentration for alloys 316L and 690 at temperatures of 400˚C and 500˚C [53].

CHAPTER 3

EXPERIMENTAL PROCEDURES

3.1 Alloy description

The alloy selected for this study was required to exhibit susceptibility to IASCC in SCW and have a high fraction of $\Sigma 3^n$ CSLBs to ensure sufficient cracking for statistically significant results. Based on these criteria, 316L stainless steel was chosen for evaluation. The metal plate was supplied by Metal Short Incorporated from heat# 80601. The plate dimensions were 1.27 × 15.25 × 30.50 cm and the composition is given in Table 3.1.

The as-received plate was solution annealed at 1100˚C for 20 min and immediately water quenched. The resulting grain sizes on the rolled face and transverse face of the 316L plate varied but were an average of 81 μm and 58 μm, respectively, as indicated in Figure 3.1. To produce a higher CSLB fraction, the GBE specimens received an additional thermomechanical processing treatment, originally developed by Michiuchi et al. [132], following electrical discharge machining (EDM). The specimens were compressed by 5% using an Instron® machine and then annealed in a Lindberg Model 54232 furnace for 72 hours at 967˚C under flowing argon. The samples were packed in alumina powder and wrapped in stainless steel foil to minimize oxidation. This treatment resulted in a final 316LGBE grain size of 170 μm.

The grain boundaries were carbide free for both alloy conditions. Ferrite banding was present in the plate, as shown in Figure 3.2 and the chemical composition of the delta ferrite as measured by electron microprobe analysis (EMPA) is given in Table 3.2. Ferrite is commonly found in cast austenitic stainless steels, but thermomechanical processing treatments generally reduce its content in the bulk. Area fraction measurements indicated that the ferrite content was <2%. Optical microscopy inspection showed that the ferrite content varied across the plate and was distributed in thin bands parallel to the rolling direction.

3.2 Specimen geometry

Two types of specimens were used in this study, tensile specimens and TEM bars. The specimens were machined via EDM because the spark erosion results in reduced mechanical damage to the specimen surface as a result of the low amount of force required to EDM machine conductive materials [167]. The geometries of the specimens are shown in Figure 3.3 and Figure 3.4. The tensile specimens had 2 mm × 2 mm square cross sections, a gage length of 23 mm, and 5/40 threaded ends. They were machined parallel to the rolling direction of the plate and the specimen face parallel to the rolling surface was tracked during the machining process and indicated with the orientation mark shown in Figure 3.3. The TEM bars were also machined in the rolling direction, had square 2 mm × 2 mm cross sections, and were 20 mm in length. The TEM specimen face parallel to the rolled surface was also tracked during the machining process to ensure that the rolled surface was irradiated.

3.3 Specimen preparation techniques

The specimens were mechanically polished with SiC abrasive paper. Mechanical polishing began with 500 grit paper and continued successively with 800, 1200, 2400, and 4000 grit papers. At each transition between papers, it was verified that all scratches created by the previous paper were ground away by polishing in perpendicular directions with sequential grinding papers.

The specimens were then electropolished in a 10% perchloric in methanol solution at -50˚C. A 304 stainless steel cathode was used to polish the specimens with an applied voltage of 30 V, and resulted in a current of 0.1 – 0.2 A. The removal rate was determined by masking a portion of the specimen with stop-off lacquer prior to electropolishing. Following electropolishing, a Dektak 3® precision profilometer was used to measure the surface step created at the interface between the masked and unmasked regions of the specimen. The resulting measurements indicated the thickness of the specimen that was removed during the electropolishing, and they are plotted in Figure 3.5. It can be seen from the figure that the removal rate was approximately 1 μm every 15 s. The mechanical polishing removed the 25-38 μm recast layer from the EDM machining, but the 4000 grit paper creates scratches with a maximum depth of 2.5 μm in stainless steel. The specimens were electropolished for the period of time required to remove the damage induced by the mechanical polishing, with the duration ranging from 15-60 seconds depending on the type of specimen and the quality of the ground surfaces. The unirradiated specimens were lightly electro-etched in a 10% oxalic acid solution for 15 s at 4 volts to verify that no grain boundary chromium carbides were present. This etching treatment was demonstrated to reveal grain boundary chromium carbides when

present, but it did not compromise the mirror finish of the specimens. SEM analysis following etching showed no visible signs of surface degradation.

Oxide stripping was performed on specimens that had been exposed to supercritical water to reveal slip channels and fine cracks on the surfaces of the specimens. The oxidized specimens were first submerged in a 100 g/l sodium hydroxide, 30 g/l potassium permanganate solution at 95˚C for 5 minutes and then submerged in a 100 g/l ammonium oxalate solution at 95˚C for an additional 5 minutes. This stripping treatment was repeated three times, and the sample was ultrasonically cleaned in distilled water following each treatment. The amount of metal lost from the surface of the samples was determined by removing the oxidation from a corrosion coupon following a 400˚C exposure in SCW for approximately 326 hrs. The mass of the specimen prior to exposure was compared to that following exposure and three oxide stripping treatments as shown in Figure 3.6. The metal loss was determined from the surface area and density of the corrosion coupon and the difference in mass before exposure and following the third stripping treatment. It was determined that between 0.07 and 0.17 μm of metal had been lost due to the incorporation of the metal atoms into the oxide structure and loss of the metal substrate during the oxide stripping treatment,

$$\frac{0.00044 \pm 0.00020 g \times 10^7 \, \mu m / cm}{4.6 cm^2 \times 8.02 g / cm^3} = 0.12 \pm 0.05.$$

3.4 Orientation Imaging Microscopy

Orientation Imaging Microscopy (OIM)^{TM} is an analysis technique whereby automatically indexed electron backscatter diffraction patterns (EBSPs) are used to map

the orientations of grains on specimen surfaces. This orientation information can be processed to generate various visualizations of the sample surfaces including grain boundary misorientation, Schmid factor, and orientation deviation maps.

3.4.1 OIM™ system

The OIM™ system used in this study consisted of a silicon intensified camera, amplifier, phosphor screen, image processor, and a workstation. This system worked in conjunction with a PHILIPS® XL30FEG SEM, and a schematic of the system is shown in Figure 3.7. The electron beam exits the pole piece and strikes a specimen that is tilted to an angle of 70˚. The electrons disperse beneath the specimen surface and diffract off of the crystallographic planes in the specimen. Some of the diffracted electrons satisfy the Bragg criterion in that their difference in path length is equal to an integer number of wavelengths so that they remain in phase,

$$\lambda = 2d \sin\theta \ , \tag{3.1}$$

where λ is the wavelength, d is the spacing of the atomic planes, and θ is the incident and reflected angle. The initial dispersion of the electrons occurs in all directions, therefore, the subsequent Bragg diffracted electrons form Kossel cones as shown in Figure 3.8. The intersection of the Kossel cones with a surface creates a set of lines called Kikuchi lines, and this set of lines forms a diffraction band. The patterns of intersecting diffraction bands from the actively diffracting families of $\{hkl\}$ planes create an electron backscatter pattern (EBSP) on the phosphor screen. The EBSP is averaged over 32 frames, background corrected, and then digitized into the computer memory. The angles between

the diffraction bands are measured, and these angle measurements are compared to a table of known inter-planar angles for a given material to determine the crystallographic orientation [168].

In this way, orientation data can be collected over large areas of the specimen surface. The collimated beam scans over the specimen, and the computer software automatically indexes the EBSP at each point of interest. At each position, the three Euler angles defining the crystal orientation are recorded as well as the (x,y) coordinates of the beam position on the specimen surface. Additional parameters are collected at each point defining (a) the sharpness of the EBSP termed the Image Quality factor, and (b) the degree of confidence that the EBSP is correctly indexed, termed the Confidence Index (CI).

3.4.2 Orientation Imaging Microscopy (OIM ™) procedure

The tensile specimen was inserted into the Philips® XL30FEG SEM, tilted to 70˚, and the area of interest on the specimen surface was located. The gage surfaces of the irradiated 316L tensile specimens were marked with 2 sets of 6 parallel micro-indentations as indicated in Figure 3.9. These indents spanned 3.5 mm in the tensile direction, and 1.5 mm in the transverse direction. The indents on the unirradiated specimens spanned the same distance, but only a single line of indents was created on the center line of the specimens. These indents were necessary for two reasons, (1) to serve as placemarkers during OIM ™ and cracking characterization, and (2) to align the electron beam to correct for distortion that occurred due to tilting. After the specimen

was tilted, the sample rotation and scan rotation settings were adjusted to align the indents in the horizontal and vertical directions.

The initial scans on the unstrained specimens were performed over 1500 μm x 700 μm areas with an accelerating voltage of 20 kV, spot size 5, step size 2.5 - 5 μm, and 15 mm working distance at a magnification of 200x. These settings varied for the post-straining scans, with the accelerating voltage ranging from 20-30 kV, step sizes of 0.1-2.5 μm, and magnifications of 100x – 4000x. The optimal settings depended on the quality of the specimen surface and the feature of interest. Increasing the accelerating voltage improved the quality of the EBSP because the yield of backscattered electrons increased, and the sampling depth increased. Therefore, increasing the accelerating voltage was beneficial when analyzing strained and oxide stripped specimens where the quality of the surface had degraded. The step size and magnification were adjusted according to the degree of resolution required for the type of analysis being performed. For example, if information regarding the lattice rotation around a cracked grain boundary was required, only the area immediately surrounding the crack would be analyzed (high magnification), but at high resolution (small step size).

Through this analysis technique, 3 of the 5 macroscopic degrees of freedom of the grain boundary geometry were determined as indicated in Figure 3.10. The degrees of freedom shown in Figure 3.10 (d) and (e) can only be determined through serial sectioning and analysis of the surface trace of the grain boundary plane, respectively. The grain boundary characters reported in this study are, therefore, determined from 3 degrees of freedom based on the crystallographic misorientation between adjacent grains.

3.4.3 Orientation Imaging Microscopy (OIM ™) analysis

The data obtained from the OIM ™ scans were analyzed using the TSL OIM Analysis Version 5 software. Four different types of OIM ™ maps were generated from the orientation data, (1) Schmid factor maps, (2) Taylor factor maps (3) grain boundary character maps, and (4) orientation deviation maps.

3.4.3.1 Schmid Factor

The Schmid factors of grains were determined through a three step process with the TSL software. The first step was to define the slip systems, and describe the stress state with a 2nd rank tensor. As discussed in Chapter 2, the slip systems in FCC crystals are given as $\{1,1,1\}\langle 1,\bar{1},0\rangle$. The specimens were scanned with the tensile direction in the transverse direction according to the coordinates of the OIM ™ software as shown in Figure 3.11. The transverse direction corresponds to the normal stress in the y-direction, σ_{yy}, and the stress state for uniaxial tension is simply given as,

$$\begin{vmatrix} 0 & 0 & 0 \\ 0 & 1 & 0 \\ 0 & 0 & 0 \end{vmatrix}.$$

Recall from Chapter 2 that the Schmid factor is simply a geometrical factor that determines the resolved shear stress acting on a slip system from the orientation of the system with respect to the tensile axis. Thus, this simple expression for the stress state is adequate.

The second step is to calculate the Schmid factor for each of the 12 slip systems. As described in Chapter 2, the Schmid factor, m, is equal to the quantity $\cos\ \lambda \cos\ \phi$,

where λ is the angle between the slip direction and the tensile axis, and ϕ is the angle between the slip plane normal and the tensile axis. The crystallographic orientation of the grain, and therefore the orientation of the slip systems, is known through the indexing of the EBSPs. The resolved shear stress on a slip system can range anywhere from 0 to 50% of the applied stress, therefore the Schmid factor for a given slip system can range from 0 to 0.50.

The final step in calculating the Schmid factor is to determine the most favorably oriented slip system, which is the system with the greatest resolved shear stress. The Schmid factor for that system is reported as the Schmid factor for the grain. Because the slip system geometries are fixed relative to one another, the resolved stress on the most favorably oriented slip system is always finite, and Schmid factors of grains range from 0.27-0.50.

3.4.3.2 Taylor Factor

A detailed description of the calculation of the Taylor factor is given in Chapter 2. This section will describe the procedure for calculating the Taylor factor using the TSL software. The Taylor factors of the grains were generated by defining two input parameters, (1) the slip systems, $\{1,1,1\}\langle 1,\bar{1},0\rangle$, and (2) the displacement tensor as determined from the orientation of the specimen with respect to the tensile axis. The specimens were scanned with the tensile direction (TD) in the transverse direction. Therefore, the sample extends in the transverse direction and constricts in the two perpendicular directions (ND and RD), and the deformation tensor is,

$$\begin{vmatrix} -0.5 & 0 & 0 \\ 0 & 1 & 0 \\ 0 & 0 & -0.5 \end{vmatrix}.$$

By referring back to Chapter 2, it can be seen that the diagonal terms, -0.5, 1, and -0.5 correspond to the external normal strains, $d\varepsilon_{xx}$, $d\varepsilon_{yy}$, $d\varepsilon_{zz}$, respectively. The zero terms correspond to the shear strains.

The Taylor's theory assumes that the external strain is accommodated through crystallographic shear strains on 5 of the 12 slip systems in a way that minimizes the expended work. Because τ_{CRSS} is the same for each slip system, this amounts to minimizing the required crystallographic slip. The system of 6 equations used to express the external strain, equation (2.11), can therefore be solved by setting 7 of the 12 crystallographic shear strains to zero and determining which combination of 5 active slip systems minimizes the required slip. This would require solving the equations 792 times if it were not for geometrical considerations that show that the majority of these combinations of slip do not produce 5 independent strains. For example, each slip plane contains 3 slip directions, so there can be only 2 independent slip directions active for a single slip plane. Through this and similar considerations, the number of combinations can be reduced to 96. Each combination of slip systems is evaluated, and the combination that requires the least amount of crystallographic slip is chosen to calculate the Taylor factor, M, as the ratio of the required crystallographic slip to the uniaxial strain as indicated in equation (2.14).

3.4.3.3 Grain Boundary Character

Grain boundary character maps were also generated from the grain orientation data. The boundary between any two adjacent points in the scan with a misorientations of >10° was regarded as a grain boundary. A lower limit on misorientation must be set for a grain boundary, as the measured misorientation between adjacent data points within a single grain is often finite. Defining the minimum grain boundary misorientation as 10° eliminated erroneous subgrain LABs that appeared at defect sites. The character of the boundary was determined from the misorientation matrix, M_M, between adjacent grains, which describes the rotations required to align the crystallographic axes of the grains as described in Chapter 2. The OIM™ software then compares the misorientation matrix to user defined boundary types. In this study, the special boundaries included LABs (misorientation of 10°-15°), Σ3, Σ9, and Σ27 boundaries. All other boundaries having misorientations of >15° are referred to as RHABs. A tolerance must be prescribed for the allowed deviation of the CSLBs from exact coincidence as explained in Chapter 2. In this study, the Brandon criterion was applied [107] which states that the maximum allowed deviation from exact coincidence, v_m, is given by,

$$v_m = v_0 \Sigma^{-1/2}, \tag{3.2}$$

where Σ is the reciprocal density of coincidence sites, and v_0 is 15˚.

The OIM™ software compiles the misorientation data to generate 2D maps of the grain boundary network. The software reports the grain boundary character distribution (GBCD) in terms of total length fraction of each boundary character, while the Taylor and Schmid factor data are reported in terms of area fractions. These length and area

fraction values are not conducive to performing the cracked boundary analysis where the *number* of cracked boundaries is of interest. Therefore, manual measurements of the number fraction distributions of the Taylor factors and Schmid factors were made with the OIM™ software, and number fraction measurements of the GBCD were performed using Scion Image software. The Taylor factor and Schmid factor distributions were generated from 6,000 grains from representative OIM™ scan areas, and all grains with a minimum diameter of 5 μm in the areas analyzed were counted. Four 0.7 mm × 1.5 mm grain boundary maps were analyzed with the Scion Image® software to measure the GBCD, and all grain boundary segments with lengths greater than 3.5 μm were counted and the character recorded. This resulted in the tabulation of over 6,000 grain boundaries, including Σ3 coherent twin boundaries for the GBCD measurements. The number fractions, F_i, were calculated as follows,

$$F_i = \frac{N_i}{N}, \tag{3.3}$$

where N_i is the number of boundaries or grains of type i, and N is the total number of boundaries or grains counted.

3.4.3.4 Localized lattice rotation

As described in Chapter 2, when crystallographic slip is restricted, rotation of the lattice results. This rotation of the lattice can be captured through EBSD analysis, by performing post-strain analysis on the gage surfaces of specimens. When performing an OIM™ scan, orientation data is collected over the entire surface of a grain. By comparing the rotation matrix of each data point to the rotation matrix of the average orientation of the grain, a misorientation matrix, M_M, can be generated for each

individual data point within the grain in the same way as it was determined for the misorientation between adjacent points at a grain boundary. The angular deviation from the reference average orientation can then be used to assign a color to the data point depending on the extent of the deviation.

When analyzing the lattice rotation, a smaller step size is often used for the scan to ensure that the lattice rotation is captured. The greatest deviation from the average grain orientation often occurs in the region adjacent to grain boundaries, and the collection of a large number of data points in this region aids in visualizing the lattice rotation gradient.

3.4.4 OIM™ cleanup procedures

OIM™ scans were processed through 2-3 cleanup procedures prior to analysis, and the procedures served two different purposes. The first two cleanup procedures that will be described removed potentially erroneous data to improve the quality of the grain boundary character maps, and the third procedure was used when it was necessary to make a representative measurement of a specific grain because the parameter of interest was not constant throughout the grain.

The first cleanup procedure identified points having a low confidence of being correctly indexed (CI<0.1) and assigned those points the orientations of their neighboring points with the highest confidence indexes. Orientation measurements with CI=0.1 are indexed correctly approximately 90-95% of the time, with the accuracy increasing thereafter. Therefore, eliminating all data points with CI<0.1 ensures that well over 90% of the scan data originated from points that were accurately indexed.

The second procedure was used to restrict the minimum grain size to 5 μm for the 316L specimens, and 10 μm for the 316LGBE specimens. All grains below this size, and points that could not be indexed, were incorporated into surrounding grains. This prevented single points that were erroneously indexed from being regarded as grains. The 316L grains analyzed in this study had an average size of 81 μm on the rolled face. Therefore, the minimum grain size is a factor of 16 lower than the average grains size. Therefore, no grain of substantial size was excluded from the final grain map.

The final cleanup procedure identified the perimeter of the grain based on the criterion of >10° misorientation, determined the average orientation of all indexed points within the grain, and assigned each point within the grain this grain average orientation. This cleanup procedure was only performed when a grain averaged parameter was required, such as the Schmid or Taylor factor, and the lattice rotation in the grain was not of interest.

3.5 Proton irradiations

Proton irradiations were performed using the 1.7 MV Tandetron accelerator at the University of Michigan Ion Beam Laboratory. Tensile and TEM bars were loaded onto a custom designed stage and irradiated to a dose of 7 dpa with either 2 or 3 MeV protons at 400±10°C. This section will describe the unique stage design, loading and alignment procedures, temperature control, dose determination, and post-irradiation analysis of the activity and hardness of the specimens.

3.5.1 Stage design

The execution of a successful irradiation requires, (1) secure specimen mounting, (2) proper beam alignment, (3) dose uniformity, (4) temperature uniformity and control. The proton irradiation stage designed and built at the University of Michigan satisfied all of these requirements.

A schematic of the stage is shown in Figure 3.12. The base of the stage was a block of copper with penetrations for the resistive cartridge heater and air cooling loop which control the temperature of the specimens. The specimens were secured to the stage with hold-down bars that were tapered to decrease the amount of thermal reflection onto the stage. The hold-down bars were held in place using four screws. Immediately underneath the specimens was a shim that was mounted onto the copper block. The shim provided a reservoir beneath the specimens which was filled thin sheets of indium that were molten during the irradiation. This solid/liquid/solid interface between the copper block, indium, and specimens ensured excellent contact between all three layers and maintained temperature uniformity across the specimens. An example of a built stage is shown in Figure 3.13.

As shown in Figure 3.13, four J-type (iron/constantine) thermocouples were spot welded onto the TEM specimens. The 0.005" iron and constantine wires were threaded through insulating sheaths to prevent shorts caused by contact between crossed wires. Two of the thermocouples were welded to the guide bars, and the other two were on inner TEM bars to verify temperature uniformity. The placement of the thermocouples is critical, as they must not be in contact with either the irradiated region of the specimens or the hold-down bars. This will be explained in greater detail in Section 3.5.2.

Above the stage was a set of four tantalum apertures. The apertures were used to select the 10 mm × 18 mm area of the specimens that was irradiated, and they were electrically isolated from the copper stage. The apertures were aligned using a benchtop laser that was diffused using a plastic film. The focused laser was first adjusted on its translating stage as shown in Figure 3.14(a) so that the laser point lied directly in the center of the specimens. The laser light was then dispersed using a plastic film, so that the area of the specimen that will be irradiated was illuminated. The apertures were adjusted vertically and horizontally until the illuminated area fell on the center of the specimens as shown in Figure 3.14(b) with a precision of greater than 2 mm. In this way, the inner 8 samples were evenly irradiated, and half of the guide bars on each end were irradiated.

3.5.2 Proton irradiation procedures

The built proton stage was loaded into the 15° beamline of the Tandem accelerator, and was isolated from the rest of the beamline with the ceramic isolator shown in Figure 3.12(a). The chamber pressure was maintained at approximately $<1 \times 10^{-7}$ torr to 5×10^{-8} torr for the duration of the irradiation in an effort to prevent oxidation of the specimens.

3.5.2.1 Temperature calibration and control

The stage was heated with the cartridge heater to the irradiation temperature of 400°C as measured by the spot-welded J-type thermocouples. The pyrometer of the IRCON® Stinger thermal imaging system was then properly positioned to measure the thermal radiation from the stage. Three areas of interest (AOIs) were created on each

specimen where the temperatures were recorded during the irradiation. The temperature spread of the four thermocouples was typically ~3 degrees indicating excellent uniformity. The emissivity value of each AOI was determined by adjusting the value until the AOI temperature matched the average thermocouple temperature. The AOI temperature data was collected through the Stinger software and averaged over a period of 15-60 seconds. By adjusting the heater voltage and air pressure, the temperature was maintained at 400 ± 10°C. Alarms were set to alert the individual monitoring the irradiation as soon as the temperature of the AOI reached ± 9°C of the target temperature.

When the proton beam was incident on the specimens, the spot welded thermocouple readings were no longer accurate indications of the temperature in the irradiated region of the specimens. As mentioned previously, the thermocouples were spot welded outside of the irradiated region, and so their proximity to the irradiated region dictated the temperature measurement. The temperature readings of the thermocouples were always lower than the irradiation temperature, typically by about 80-140°C. A fifth thermocouple was inserted into the base of the stage to measure the back temperature. The purpose of this thermocouple was to ensure that the stage temperature never approached the melting temperature of indium (156°C) which would cause the indium to solidify and temperature uniformity would be compromised.

Following the irradiation, the AOI temperatures of each specimen were plotted to verify that the temperature was maintained within the ± 10°C bounds. An example of such a profile is shown in Figure 3.15. It can be seen that the large majority of the data falls in the range of 390-410°C, with an average temperature of 399°C and 2σ of 7.3°C.

3.5.2.2 Beam alignment

The proton beam size was verified to be a maximum of 3 mm at full width half maximum (FWHM) using a Beam Profile Monitor (BPM) which measured the intensity distribution of the proton beam. The beam was then rastered across the stage and apertures in the pattern shown in Figure 3.16. The horizontal and vertical scanning frequencies were 255 and 2061 Hz, respectively, with a total scan cycle occurring over a period of 3.9 ms. Because the ratio of the horizontal and vertical scanning frequencies is not an integer (8.08), each beam path was offset from that of the previous cycle. This ensured spatial uniformity in addition to dose uniformity amongst the specimens.

In order to uniformly irradiate all of the specimens, it would be necessary for the proton beam to scan completely off of the stage and onto the apertures with each horizontal and vertical pass. This would mean that a 3 mm width of the inner perimeter of the apertures would be irradiated. It is shown in Figure 3.17 that the ratio of the proton irradiated stage area to the aperture surface area is,

$$\frac{18mm \times 10mm}{(24mm \times 16mm) - (18mm \times 10mm)} = \frac{180mm^2}{204mm^2} = 0.9.$$

Therefore, roughly a 1:1 ratio between the stage and aperture currents would be required to evenly irradiate this entire region. In practice, however, a stage to aperture ratio of 2:1 was used, which was shown to uniformly irradiate the inner 8 specimens on the stage. The reason that this ratio provides even irradiation is due in part to the positioning of the 2 guide bars on either ends of the stage, which were not used for analysis and therefore were not required to be uniformly irradiated.

This positioning of the raster-scanned area was made possible by recording the proton beam current on each of the individual apertures and the stage using a PC based monitoring system. The size of the area scanned by the proton beam was adjusted by controlling the amplitude of the scanning in the horizontal and vertical directions until the stage to aperture current ratio was 2:1. Then the beam steerer controls were used to center this rectangular scanning area over the apertures. If the beam alignment was disturbed, causing the aperture currents to become unbalanced, an alarm would sound, immediately alerting the individual monitoring the irradiation.

3.5.3 Calculating irradiation dose

The damage profiles created by the 2 MeV and 3 MeV protons in 316L stainless steel were analyzed using SRIM 2006™ [169]. The average number of displacements generated per ion density, per unit volume of material, as a function of ion range was calculated. A displacement energy, E_d, of 40 eV was used for the Fe, Cr, and Ni content of the alloy as recommended by ASTM E 521-89 [170]. The detailed SRIM™ calculations were performed with full damage cascades using a minimum of 500,000 ions. These calculations generated smooth damage profiles that extended to depths of 20 μm and 37 μm for the 2 MeV and 3 MeV protons, respectively, as shown in Figure 3.18. A nearly uniform region of damage exists up to depths of 15 μm and 30 μm for the 2 MeV and 3 MeV protons, respectively.

The displacement damage increases with depth up to the damage peak as shown in Figure 3.18. Therefore, it was necessary to pick a point along the profile that most closely represented the volume of the specimen analyzed to calculate the dose. The point

chosen was at 60% of the maximum damage depth, which was 12 μm for the 2 MeV specimens, and 22.2 μm for the 3 MeV specimens. The corresponding displacement damage values were 5.8×10^{-5} displacments/ion-Å and 8.58×10^{-5} displacments/ion-Å, respectively.

As previously described, the proton irradiation stage was electrically isolated from the rest of the beam line with a ceramic stand-off, and the apertures were electrically isolated from the rest of the stage. Therefore, the recorded stage current reflected only the beam current incident upon the specimens. This beam current was integrated over a period of time to determine the μC of charge that resulted from the incident protons. Each μC of charge was recorded as a count, and these counts were tabulated by the PC-based monitoring system. The counts required per dpa were calculated as follows,

$$\frac{counts}{dpa} = \frac{N\left(\frac{atoms}{cm^3}\right) \times A\left(cm^2\right) \times q\left(\frac{C}{proton}\right) \times \left(\frac{counts}{C}\right)}{displacement\_rate\left(\frac{displacements}{proton \cdot \mathring{A}}\right)}, \tag{3.4}$$

where N is the atomic density of 316L (8.72×10^{22} cm^{-3}), q is the coulomb charge per proton (1.6×10^{-19} C), and A is the surface area of the samples that was irradiated (1.8 cm^2). Using equation (3.4), it can be shown that the number of counts required per dpa during the 2 MeV and 3 MeV irradiations were 4.33×10^6 and 2.93×10^6, respectively.

3.5.4 Radioactivity and beta counting

Post-irradiation β counting measurements were made of the residual activities of the proton irradiation 316L specimens. The purpose of the measurements was to ensure that the samples were uniformly irradiated. When the 316L stainless steel specimens were irradiated with high energy protons, many nuclear reactions occurred. Table 3.3 lists the possible (p,n) interactions that can occur in the alloy when irradiated with 2 MeV and 3 MeV protons along with the threshold energies and cross sections for the reactions. A previous study used 3.2 MeV protons to irradiate stainless steels and determined that four isotopes had been produced, Cu-61, Cu-64, Co-57, and Mn-54 through (p,n) interactions with Ni, Cr, and Fe [171]. While the production of all of these isotopes is possible with 3 MeV protons, the threshold energies of the (p,n) reactions with Ni and Cr are greater than 2 MeV. Therefore the residual radioactivity of the 2 MeV irradiated specimens was lower than that of the 3 MeV protons as shown in Table 3.4 where the beta counting was performed 231.2 hours after the irradiation ended.

The β counting measurements were performed using an Alpha/Beta Scalar (Model # 2929) produced by Ludlum Measurements Inc.. Each specimen was loaded, with the irradiated face up, into a small metal tray and the β particles were detected over a period of 5 minutes. Measurements were normalized to time and the irradiated surface area of the specimen. As can be seen from Table 3.4, the measurements indicated excellent uniformity in residual activation. If non-uniformity had been detected, this would have been an indication of insufficient beam overscan, a defocused beam, shielding by the apertures, or misalignment of the beam.

3.6 Vickers microhardness measurements

The pre-irradiation and post-irradiation hardness of the specimens was measured using a Micromet®-II Vickers Microhardness tester. A calibration block was used first to ensure that the indenter was working properly. A minimum of 5 indents were made on a 338 Hv (kgf/mm^2) block with a 25 g load, and it was verified that the error was <5%. Then, 30 hardness measurements were made on each TEM specimen with a minimum center-to-center spacing of 100 μm. Only indents that showed a proper diamond shape were measured and recorded. The light 25 g load was used to ensure that the sampling volume of the indenter tip was confined to the irradiated region of the material. The indent depth, D, as a function of hardness is shown in Figure 3.19, and can be calculated as follows,

$$D = \frac{d}{2\sqrt{2}} \times \tan(22°), \tag{3.4}$$

where,

$$d = \sqrt{\frac{2 \times l \times \sin\left(\frac{136°}{2}\right)}{HV}}, \tag{3.5}$$

where d is the arithmetic mean of the two diagonals of the indent, l is the applied load (.025 kg), and HV is the Vickers Hardness.

It can be seen from Figure 3.19 that the indent depth in the 400°C, 7 dpa proton irradiated 316L was 1.6 μm. The irradiated region of the specimens irradiated with 2 MeV protons extended 20 μm into the sample substrate. Therefore, the sampling volume

of the indenter tip was confined to < 1/10 of the irradiated depth, and the measurements were not influenced by the underlying unirradiated material [172].

3.7 Post-irradiation sample preparation

TEM and SCC specimens were prepared post-irradiation through series of mechanical grinding and polishing, electrochemical polishing, and ion milling techniques. This section will describe the procedures used to prepare both types of specimens for TEM analysis and CERT experiments.

3.7.1 TEM specimen preparation

Both unirradiated and irradiated TEM specimens were prepared using the same techniques, but it was necessary to track the irradiated face of the irradiated TEM specimens to ensure that this layer was not removed during the thinning processes. The TEM bar was mounted irradiated face down on an aluminum polishing block and polished sequentially with SiC abrasive paper from 500 – 4000 grit to achieve a final thickness of roughly 300 μm. The thinned bar was then mounted face down on a graphite block and loaded into a South Bay Technologies Slurry Core Cutter. A dollop of 600 grit SiC powder slurry was placed on the area being drilled, and a 3 mm brass bit was used to drill three TEM specimens from the 10 mm irradiated length of the specimen as illustrated in Figure 3.20. Because the TEM specimens were only 2 mm wide, the TEM discs were not full 3 mm diameter disks.

The discs were mounted, with the irradiated face down, into a Gatan® 623 sample polishing unit. The unit was carefully calibrated and capable of thinning samples to

precise thicknesses with a reproducibility of 5 μm. Discs were thinned with 2400 and then 4000 grit SiC abrasive paper to approximately 75 μm.

The specimens were then thinned electrochemically using a South Bay Model 550B single jet polisher. A 5% perchloric acid and methanol solution was cooled with either liquid nitrogen or dry ice to a temperature of -55°C. The voltage was adjusted to yield a current of 15-20 mA, and the specimen was thinned from the irradiated face for 25 seconds. The specimen was then removed from the system, cleaned in acetone and then methanol, and reloaded in the system. The specimen was then thinned to perforation from the unirradiated side over a period of 7-9 minutes. The resulting hole was positioned approximately 4 μm beneath the original surface of the specimen.

3.7.2 SCC specimen preparation

The residual indium on the SCC bars had to be removed following the irradiation in preparation for tensile testing. The first step in preparing the specimen was to coat the irradiated face of the specimen with stop-off lacquer to prevent this face from being scratched or removed during subsequent mechanical and electrochemical polishing. All three unirradiated faces of the specimens were sequentially polished with SiC abrasive paper from 1200-4000 grit. The specimens were then electropolished in the manner described in Section 3.3. The stop-off lacquer was finally removed with Strip C (n-methyl-2-pyrrolidone).

The cross-sectional dimensions of the gage sections of the specimens were measured using a digital micrometer in three positions along the length of the bar. The minimum cross sectional area was used when calculating the stress on the specimen

during the CERT experiments. The total lengths of the specimens were also measured, and it was verified that the specimens were machined with a 23 mm gage length.

3.8 TEM analysis of microstructure and microchemistry

The microstructure and microchemistry analyses of the irradiated and unirradiated 316L specimens were performed using the JEOL^{TM} 2010F analytical TEM at the North Campus Electron Microbeam Analysis Laboratory (EMAL) at the University of Michigan. The microscope had a zirconated tungsten thermal field emission tip and operated at an accelerating voltage of 200 kV. It was equipped with x-ray energy dispersive spectroscopy (XEDS) and electron energy loss spectroscopy (EELS) systems, and a Gatan double-tilt sample holder was used. Each specimen was cleaned with a FISCHIONE^{TM} 1020 plasma cleaner prior to being analyzed to ensure that any organic contamination present on the surfaces of the specimens was removed.

3.8.1 Dislocation loop imaging and measurements

The dislocation loops were imaged using the rel-rod dark field technique which is better for imaging small loops (<10 nm) than other dislocation loop imaging techniques. The dislocation loops in FCC materials form on the four $\{111\}$ planes of the lattice. These planar defects create "spikes" (reciprocal-space lattice-points) oriented perpendicular to the defect plane. Additional spots in the diffraction pattern are created as a consequence of these reciprocal-space lattice rods (rel rods) reflections intersecting the reflecting sphere as shown in Figure 3.21.

These excited rel-rods were viewed by tilting 5-10° off the <011> zone axis to form a g=[113] 2-beam condition. The rel-rod spots appear along the g=[113] reflection

between the [111] and [200] spots. The excited rel-rod was centered on the viewing screen, and then the smallest objective aperture was placed over the spot to create a dark field image over a relatively long exposure time. While a long exposure time was necessary to image the loops, excessive exposure times would cause the loops to blur due to sample drift. Generally an exposure time of approximately 15 seconds was optimal for imaging the loops and minimizing blurring due to drift. In this dark-field imaging mode, the faulted dislocation loops then appear as white streaks against the black background of the specimen.

Although a rel-rod reflection is present for each of the four {111} planes, only two are visible for each 2-beam tilt position, and only one can be selected for the dark field imaging. Therefore, the number of loops measured must be multiplied by four to obtain the total number of loops for loop density measurements. This technique was capable of imaging faulted loops as small as 3 nm in diameter.

The dislocation loop images were taken at a magnification of 50 kX and analyzed using Scion Image® software (Scion Image® Beta 4.03) [173]. Since the loops were aligned edge-on, the length of the streak was regarded as the diameter of the loop. Each loop and its diameter was recorded and tabulated to determine the average loop diameter and loop density. In total, over 400 loops were counted to ensure statistically significant measurements. The loop density was calculated by multiplying the number of loops measured by four and dividing by the volume of the specimen analyzed.

3.8.2 Void imaging

The voids in the irradiated 316L specimens were examined by alternating between under- and over-focused conditions to see if the contrast of the specimen features changed to indicate the presence of a void. At times, it can be difficult to distinguish a void from a precipitate. It can be verified that the feature is a void if its contrast does not change significantly as the specimen is tilted. This occurs because the image of the void is formed by absorption contrast which is not sensitive to tilt, whereas the precipitate can be seen mainly due to diffraction contrast which is sensitive to tilt. The best images of the voids were obtained in a slightly underfocused condition.

Void images were taken at a magnification of 50kX and analyzed using the Scion Image® software. The diameters of the voids were measured from edge to edge. Each void and its diameter was recorded to determine the average void size and void density. The void density was calculated by dividing the number of voids by the volume of the specimen analyzed.

3.8.3 Radiation Induced Segregation (RIS) measurements

The elemental segregation at the grain boundaries was measured via STEM/EDS for both the unirradiated and irradiated TEM specimens. The specimens were loaded into the Gatan double-tilt holder. The degree of tilt was limited to 15-20 degrees due to the positioning of the microscope's pole piece. The criteria for selecting a grain boundary were (1) it must not be a coherent $\Sigma 3$ twin boundary, (2) it must be located in a thin area, and (3) boundaries that were already close to edge-on alignment were preferred.

RIS has been shown to be suppressed at Σ3 and Σ9 boundaries [128], and therefore measurements at such boundaries would not be representative of the specimen as a whole. Although the coherent Σ3 twin boundaries are easily identifiable and have the greatest contribution to the special boundary fraction, it is possible that other special boundaries may inadvertently be selected for analysis. Therefore, two grain boundaries were measured in the specimen to verify consistency.

Choosing boundaries in thin areas of the specimens limited the size of the excitation volume shown in Figure 3.22 due to the beam broadening as it passed through the specimen. Although a fine probe size of 0.5 nm was used, the actual sampling volume for each measurement was broader. In order to minimize the effects of this broadening on the composition measurements at the grain boundary, an additional 5 spots were measured at the exact boundary location. Boundaries aligned close to edge-on prior to tilting were preferred so that the degree of tilt required would not exceed the limitations of the specimen holder. Boundaries were aligned edge-on when the grain boundary, which appeared as a high contrast line between two grains, had a minimum width. Figure 3.23 illustrates an unaligned and a properly aligned grain boundary in a TEM specimen.

Once a boundary was selected and aligned, EDS line scans were performed perpendicular to the grain boundary. The line scans were 30 nm in length with a total of 50 measurements per line to yield 0.6 nm spacing between data points. These measurements were averaged over multiple measurements at 2 boundaries. Matrix composition measurements were also made in order to determine the k-factors for the composition calculations.

The x-ray intensity data for each of the elements of interest (Cr, Ni, and Fe) were integrated over the energy intervals for the respective elements to determine the number of counts detected from each element. The elements analyzed and the K x-ray energies for each element are given in Table 3.5. The ratio of the concentration (wt%) of an element A to element B in the alloy is proportional to the ratios of the integrated peak intensities as indicated by the Cliff-Lorimer equation [174],

$$\frac{C_A}{C_B} = k_{AB}\frac{I_A}{I_B} \tag{3.6}$$

where C_A and C_B are the concentrations of elements A and B, I_A and I_B are the measured intensities of elements A and B, and k_{AB} is the Cliff-Lorimer factor or k-factor. This k-factor is not a constant and must be calculated for each alloy composition measurement because it depends on the STEM/EDS system and beam energy. This relationship can be extended to a ternary alloy as shown in equations (3.7) and (3.8),

$$\frac{C_A}{C_C} = k_{AC}\frac{I_A}{I_C} \tag{3.7}$$

$$\frac{C_B}{C_C} = k_{BC}\frac{IB}{I_C}. \tag{3.8}$$

These equations can solved for the k factors by using the known matrix composition and the STEM/EDS matrix measurements. Once these k-factors are know, the concentrations of the various elements can be calculated from the x-ray peak intensities measured through the EDS line scan.

3.9 Constant Extension Rate Tensile (CERT) tests

CERT tests were performed on the irradiated tensile specimens in 400°C SCW at a pressure of 24 MPa to determine the cracking propensities of the grain boundaries in the specimens. Experiments were interrupted at plastic strains of 2%, 5%, and 10% to study the progression of the cracking behavior with strain. CERT tests on the unirradiated 316L and 316LGBE tensile specimens were performed in 500°C SCW at a pressure of 24 MPa, and were interrupted at roughly 15% and 25% nominal strain for cracking analysis. This section will describe the autoclave system, clevis design, and experimental procedures.

3.9.1 Supercritical water CERT system apparatus

The 400˚C CERT tests were performed on the IM1 multiple specimen CERT test system in the Irradiated Materials Testing Laboratory at the University of Michigan. A schematic of the closed water loop is shown in Figure 3.24. Water flows out of the primary water column, through a high pressure pump, through the preheater system, and into the inlet line of the autoclave assembly. The outlet line of the autoclave passes through a heat exchanger in the preheater system, and then through a chiller before the pressure is dropped as the water passes through the back pressure regulator before entering the primary column to complete the loop. The autoclave, head assembly, sealing gasket, and clevises were made from alloy 625 and the system was rated up to a pressure of 600°C and 4000 psi.

The autoclave apparatus can simultaneously strain four specimens, and was equipped with four independent pull rods and load cells. Each pull rod penetration was

sealed with a self-energizing graphite ball seal with an internal Inconel® spring that expanded under the system pressure. Each pull rod was attached to a Trandsducer Techniques load cell with a 1000 lb capacity. Each load cell was calibrated prior to performing the CERT test, and linearity in the voltage signal was verified up to a 200 lb load. Each load cell was fastened to the crosshead with segments of threaded rod.

The samples were strained using an Interactive Instruments™ servo-motor which displaced the system crosshead. A Solartron® linear variable differential transformer (LVDT) was affixed to the crosshead to measure the displacement, and was calibrated prior to the experiment and verified to have an error of <2%. The desired servo-motor displacement speed was entered in the digital controller, and it was verified to generate the target strain rate of 3×10^{-7} s^{-1} by the LVDT reading.

The water was first heated on the inlet line through a heat exchanger and then the rest of the preheater system that consisted of three 16" long Barnstead™ quartz heating cords wrapped around the system's inlet line in an insulating box. The vessel was also heated externally using three 1800 W Watlow® heating bands. The temperature of the vessel inlet line was maintained at approximately 385-395°C, as verified by a K-type thermocouple. A K-type thermocouple was also inserted through a penetration in the vessel to ensure that the internal temperature of the autoclave was maintained at 400 ± 1°C.

All critical sensor data including pressure, temperature, water conductivity, dissolved oxygen content, LVDT displacement, and load cell readings were recorded for the duration of the experiment using a LabView™ data acquisition program. The data was acquired at frequencies ranging from once every 5 seconds to once per minute. Due

to both experimental and safety considerations, it was necessary to ensure that the temperature and pressure were maintained within their set points. A drop in temperature or pressure due to pump or preheater failure would cause the water to enter the subcritical regime, and an increase in temperature or pressure could exceed the limitations of the system. Therefore a pager alert system was utilized to alert the researcher if the internal vessel temperature exceeded 400 ± 10°C, or if the outlet pressure exceeded 3500 ± 100 psi.

The 500˚C CERT tests were performed on the nearly identical multi-sample supercritical water (MSCW) system in the High Temperature Corrosion Laboratory (HTCL). Slight differences between the two systems include the absence of a second backup high pressure pump on the MSCW system, the presence of a second LVDT on the MSCW system to verify cross-head displacement measurements, and the use of city water rather than a chiller on the MSCW system. All temperature and pressure parameter controls and data collection settings, however, were identical between the two systems.

3.9.2 Sample loading

All specimens and clevis components were ultrasonically cleaned sequentially with acetone, methanol, and finally distilled water prior to loading into the system. The autoclave, head assembly, and gasket were all inspected for signs of damage from previous experiments. The Inconel® 625 clevises were designed with pin joints to ensure that no shear forces were imparted on the specimens during the tensile testing. The top clevis of the assembly was attached to the load frame using a threaded Inconel® 625 rod. The top and bottom clevises were joined with a connecting stud and two connecting pins.

The specimen was inserted into the lower clevis and threaded into the specimen nut that was seated on top of a transformation-toughened zirconia washer. The washer was used to prevent galvanic coupling between the gage section of the 316L stainless steel specimen and the Inconel® 625 clevis, and was supplied by CoorsTek™. A schematic of the clevis design is shown in Figure 3.25.

After the specimens were secured in the load frame, the autoclave shell was carefully lowered over the frame to sit flush on the head assembly. The deformable sealing gasket was located between the shell of the vessel and the head assembly. The IM1 system was sealed using a Pivicat ™ flange tensioner. The tensioner applied a pressure of 700-900 Torr to compress the sandwiched gasket, and reaction nuts were screwed down over the 12 Nitronic® 50 bolts on the system flange before releasing the pressure. This procedure ensured uniform compression of the gasket at high pressure, while requiring only a minimal amount of manually applied torque to the reaction nuts. This vessel sealing procedure had a 100% success rate. The MSCW system was sealed using a standard torque wrench to tighten the bolts securing the shell of the autoclave to the head assembly, thus compressing the sandwiched gasket. This vessel sealing procedure had a variable success rate.

3.9.3 Water chemistry and control

The irradiated 316L samples were strained in a 400°C, 24 MPa SCW environment to yield a density of approximately 0.14 g/cm^3. The unirradiated 316L and 316LGBE specimens were strained in a deaerated 500˚C, 24 MPa SCW environment. The

dissolved oxygen content was maintained in the deaerated condition of <10 ppb dissolved oxygen, and the conductivity of the water was <0.10 μS/cm.

The water used for the CERT tests was distilled using a Barnstead™ glass distillation unit and stored in a polyvinylidene fluoride tank. The water was then pumped through a PURA® ultraviolet purification system and finally a Barnstead™ EPure water purification system. The water was then pumped into the secondary column of the system. Argon was bubbled into the secondary column and the water was passed through a Barnstead™ mixed bed deionizing (DI) cartridge with a high flow recirculation pump for approximately half an hour to pretreat the water. The water was then used to fill the primary column of the system. The water in the primary column was also bubbled with argon and passed through another DI cartridge until the dissolved oxygen and conductivity reached the pre-test target of <50 ppb and <.07 μS/cm, respectively. The water was then circulated through the system piping, but bypassed the vessel until the inlet and outlet dissolved oxygen content and conductivity reached the target values. After the vessel was sealed, it was purged with argon at a pressure of 20 psi for 15 minutes to remove all of the oxygen containing air from the vessel. After increasing the pressure to 24 MPa, the water was circulated through the entire system until the pre-test target conditions were met at a flow rate of 30-90 ml/min. It was verified that no leaks were present around the gasket sealing area or pull rods, and then the vessel was covered with insulation in preparation for heating.

The water was slowly heated by increasing the target temperature of the preheater system and main heaters in 75°C increments. As the water approached the supercritical point (374°C, 22.1 MPa), the heating was slowed to minimize the rapid increase in flow

rate that occurred as the water underwent the phase transition. This precaution protected the dissolved oxygen and conductivity sensors, as a sudden increase in flow rate would have reduced the amount of cooling that occurred in the chiller, and the heated water could have damaged the sensors. The water was circulated through the system at temperature and pressure until the target test conditions of <10 ppb dissolved oxygen and <0.1 μS/cm were achieved and the straining commenced. This required between 16 hrs and 55 hrs.

The water chemistry for all experiments except for the final straining increment of the irradiated specimens (5% to 10% strain) was achieved with the specimens loaded in the vessel. The system was conditioned at 450°C and 3500 psi without the specimens loaded, however, prior to the final experiment on irradiated specimens. This conditioning was performed to minimize the specimen exposure time in the SCW environment and the resulting oxide layer thickness to create a favorable surface for post-experiment AFM analysis of the irradiated specimens.

3.9.4 Sample straining

Once the purified water chemistry had reached the target test conditions of <10 ppb dissolved oxygen and <0.1 μS/cm at the desired temperature (400°C) and pressure (3500 psi), the straining portion of the experiment was initiated. Each specimen was prestressed to 21-28 MPa to ensure that there was no slack in the load train, and that all specimen were evenly loaded. Displacement rates were entered in the digital controller of the servo motor, to generate target strain rates of 3×10^{-7} s^{-1} for the irradiated specimens at 400˚C and a rate of 1×10^{-7} s^{-1} for the unirradiated specimens at 500˚C.

These strain rates were verified using the LVDT displacement reading. The irradiated specimens were strained to 2%, 5%, and 10% plastic strain and removed between each straining increment to analyze the cracking propensity of the grain boundaries. All stress strain curves are shown in Appendix A. The strain in the irradiated region was measured by determining the initial and final spacing of the 6 microhardness indents on the gage surfaces of the specimens. After 2%, 5%, and 10% macroscopic plastic strain, the strain in the irradiated region of the specimens was approximately 0.9 ± 0.2%, 3.9 ± 0.3%, and 8.0 ± 0.4%, respectively as indicated in Table 3.6. One specimen was reserved for future analysis at each straining increment, and therefore all 4 specimens were strained to 2%, 3 specimens were strained to 5%, and 2 specimens were strained to 10%. The microhardness indents were only visible following oxide stripping, therefore, measurements of the strain in the irradiated region were only possible on 2 specimens following each straining increment.

The unirradiated specimens strained in 500˚C SCW were removed for analysis at approximately 5%, 15%, and 25% strain for SEM crack analysis. Cracks were not observed at 5% strain, but were observed at 15% and 25% strain. The 316LGBE specimen yielded plastically due to the internal autoclave pressure and pre-stressing which exerted a stress of approximately 132 MPa on the specimen, which resulted in a final plastic strain of 27% compared to 23% for the 316L specimen. The plastic strain accumulated in each specimen following each straining increment, as measured using a digital caliper is given in Table 3.7.

After the specimens had been pulled to the desire strain, the system crosshead was reversed to relieve the stress on the specimens. The system was then cooled by turning

off the main heaters and gradually reducing the preheater setpoint temperatures. The cooling was slowed and the high pressure pump speed was increased as the water approached the critical temperature (374°C) to maintain the system pressure of 3500 psi as the water condensed during to the phase transition. After the water reached room temperature, the insulation was removed and the water from inside of the vessel was purged into the primary column by flowing argon into the inlet line at a pressure of 20 psi. The autoclave shell was released using the Pivicat™ flange tensioner and lifted using a hoist, and the specimens were removed from the system.

The lengths of the specimens were measured to determine the macroscopic strain to correct for the compliance in the load train. The stress measured for each of the specimens was corrected to account for the additional stress exerted on the specimens from the internal system pressure. The stress was calculated by determining the difference in cross-sectional area of the pull rod and the specimens and multiplying that value by the system pressure. The system pressure typically exerted an additional 115-120 MPa of stress on the specimens. Stress-strain curves were then plotted for each of the specimens using the corrected stress values and the LVDT displacement measurements. Minor changes in the load cell calibrations in between experiments caused offsets in the stress-strain curves that were typically <10 MPa. The stress-strain curves were adjusted to account for these changes in calibration constants.

3.9.5 Argon CERT test

The IM1 system was also used to conduct a CERT test on irradiated 316L in an inert argon environment. A system was assembled to purify the 99.995% argon gas. The

gas was passed through a copper oxide tube at 170°C. The heat was provided by a Barnstead quartz heating cord and the voltage was manually adjusted to reach the target temperature. The copper oxide removed carbon monoxide, hydrogen and hydrocarbons, via chemical reaction. The gas then passed through a drier tube containing magnesium chlorate at ambient temperature to remove moisture and carbon dioxide by physical adsorption. Finally, the gas entered a titanium getter tube that was furnace heated to 850°C to remove oxygen and nitrogen by chemical reaction. The outlet line of the argon purification system was connected to the inlet line of IM1, and the purified argon flowed through the system at a rate of 50-100 ml/min. Previous experiment performed with this argon purification system demonstrated that the purified argon gas resulted in a factor of three reduction in the oxide thickness of T91 exposed for 10 days at 500°C, compared to non-purified (99.99% pure) argon [175].

The specimens were prepared and loaded according to the methods previously described for the CERT experiments in SCW. Heat was applied to the vessel with the main heater bands to reach a target temperature of 400°C. Straining commenced immediately after the temperature stabilized, and the specimens were strained at a rate of 3×10^{-7} s^{-1} to 5% plastic strain. Post experiment analysis of the specimen indicated that the specimen was strained to 4.8%.

3.10 Cracking analysis

The objective of this study was to determine the relative cracking susceptibilities of grain boundaries in 316L strained in SCW to gain insight into the mechanism of intergranular cracking in SCW. The parameters chosen for cracking analysis were the

character of the grain boundary, the Taylor factors of the adjacent grains, the Schmid factors of the adjacent grains, and the inclination of the grain boundary surface trace with respect to the tensile axis. Each of these parameters was recorded for each analyzed crack on the gage surfaces of the specimens.

Correct identification of the cracked grain boundaries was of critical importance in this study. Grain boundaries were unidentifiable in the pre-test electropolished condition as shown in Figure 3.26(a), but oxidation in SCW increased the grain contrast which assisted in grain boundary identification as shown in Figure 3.26(b). Half of each irradiated tensile specimen was scratched in the longitudinal direction with 1 μm diamond suspension solution to create surface scratches to aid later on in GBS analysis. Half of the specimen was masked with tape as shown in Figure 3.27(a), and stop-off lacquer was painted over the other half of the specimen. The tape was then removed and the stop-off lacquer was allowed to harden prior to gently running the specimen along a platen saturated with the 1 μm diamond suspension solution. This created fine surface scratches on half of the specimen as shown in Figure 3.27(b). The unirradiated specimens strained in 500˚C SCW were not scratched.

Following straining in SCW, the specimens were removed from the autoclave system and the cracks were analyzed using a JEOL^{TM} JSM-6480 SEM. Two different types of cracks were identified on the irradiated specimens strained in 400˚C SCW, (1) large IG cracks that preferentially occurred perpendicular to the tensile axis, and (2) small cracks that occurred in localized regions where dislocation channels intersected grain boundaries, and were limited to the distance between dislocation channels. These types of cracks will henceforth be referred to as normal stress (NS) cracks and grain boundary

channel (GBC) cracks, respectively. Examples of NS and GBC cracks are shown in Figure 3.28. The SEM images of the cracks were compared to the EBSD maps to determine the character of the boundary, and the Schmid and Taylor factors adjacent to the cracked boundaries. The angle between the surface trace of each cracked grain boundary plane and the tensile axis was also recorded. Several GBC cracks were often present along a single grain boundary. In such instances, the inclination of the grain boundary surface trace with respect to the tensile axis was recorded as a single occurrence regardless of the number of GBC cracks along the grain boundary. Dislocation channels did not form on the unirradiated specimens strained in 500˚C SCW. Therefore, no differentiation in the intergranular crack type was possible for the 500˚C SCW experiments.

3.11 Atomic Force Microscopy (AFM) analysis

AFM measurements were performed on replicas of the irradiated specimens using a NanoScope™ IIIa Phase Atomic Force Microscope in tapping mode. Due to space restrictions in the optical head of the AFM system, the specimen size was limited to 15 mm in length and 5 mm in height. As the tensile bars exceeded these dimensions, replicas of the gage surfaces of the specimens strained in SCW were generated following oxide stripping using Microset™ 101FF fluid. The use of these synthetic polymer replicas, which have a resolution of greater than 100 nm [176], made it possible to analyze the progression of localized deformation with strain within single grains at 2% and 5%. The replicas were carefully cut into three segments with a razor blade, and

measurements were performed on individual grains to determine the heights of the steps that developed as a consequence of dislocations passing through slip channels.

When performing AFM tapping mode measurements, the contour of a surface is measured with a cantilever that is oscillating near its resonance frequency. A laser beam is incident on the top of the cantilever and the reflected beam is deflected by a mirror onto a photodetector as shown in Figure 3.29. As the cantilever oscillates, it produces a laser strip on the photodetector, and the magnitude of the voltage generated depends on the deflection of the cantilever tip. As the tip approaches areas of the specimen at greater elevations, the cantilever oscillations dampen due to the Van der Waals forces acting between the atoms on the cantilever tip and the atoms on the surface of the specimen. This decreases the voltage from the photodector, and causes the piezoelectric ceramic in the scanner to shrink and lower the specimen to maintain a user defined voltage, and therefore a fixed height between the cantilever tip and the specimen. Similarly, if the oscillations increase in amplitude as the elevation of the surface decreases, the voltage from the photodetector increases which causes the piezoelectric ceramic to expand. In this way, as the cantilever is scanned across an area of a grain, a 3D representation of the sample surface is generated.

The specimen was mounted on a flat magnetic disk that sits on an AFMJV scanner which could scan a maximum area of 125 μm × 125 μm, with a height resolution of 0.05 nm [177]. Given this height resolution, it should be noted that the resolution for these measurements is limited by the resolution of the replica and not the AFM system. The portion of the scanner with the mounted specimen is inserted into the optical head of the AFM system, and the cantilever is positioned over the area of interest on the

specimen and lowered. The laser alignment screws in Figure 3.30 are used to position the laser over top of the cantilever. The laser alignment screws were then adjusted to maximize the laser beam intensity reflected off of the cantilever. Then the mirror was tilted to maximize the beam intensity on the photodiode. Finally, the photodetector adjustment screws were used to align the laser beam to the center of the photodiode.

After the laser beam was properly aligned, the sample translation screws were used to position the cantilever over the area of interest. Then the x and y dimensions of the scan area were defined into the AFM software program, and the amplitude setpoint voltage was defined as 0.8 V. Recall that this voltage defines the distance between the cantilever tip and specimen surface, with lower values bringing the tip closer to the specimen surface.

Grains on which multiple slip was observed were excluded from AFM measurements. Due to the significant variations in extent of slip on the various grains, multiple slip is defined here as visible slip on two different crystallographic slip planes, resulting in a minimum of 3 slip channels on each plane. Grains included in the analysis had a minimum of three slip channels active along the same crystallographic plane, and had a minimum length of 15 μm perpendicular to the slip channels. The scanning of the cantilever was aligned perpendicular to the slip channels, and an area with an 8:1 aspect ratio was scanned to measure the step height as shown in Figure 3.31. The number of steps, step height, and average step spacing were measured for each grain. The optical images of the replicas were compared to the OIM ^{TM} maps to identify the grain analyzed to determine the Schmid and Taylor factor of each grain.

3.12 Statistical analysis

In this study, insight into the mechanism of intergranular cracking in SCW is achieved by analyzing correlations between the cracking behavior of 316L and four crystallographic and microstructural parameters, (1) Taylor factor, (2) Schmid factor, (3) grain boundary character, and (4) grain boundary surface trace inclination to the tensile axis. To verify the integrity of the data, it was necessary to determine the uncertainties in the measurements. This section outlines the methods used to quantify the statistical and experimental uncertainties in the crack measurements in accordance with the method developed by Alexandreanu and Was [178].

The key to calculating the uncertainties in the crack measurements is to recognize that the cracking analysis can be modeled as a binomial distribution,

$$P(x) = \frac{n!}{(n-x)!x!} p^x (1-p)^{n-x}, \tag{3.9}$$

where, P(x) is the predicted probability distribution function, p is the probability of success, n is the number of trials, and x is the number of successes. In this study, successes are defined in several ways and examples include,

(1) A crack occurring at grain boundary of a specific character,

(2) A crack occurring adjacent to grains with specified Taylor factor values,

(3) A crack occurring adjacent to grains with specified Schmid factor values

(4) A crack occurring along a grain boundary with a specified inclination with respect to the tensile axis, etc.

The number of trials, n, is the total number of cracked boundaries analyzed and the number of successes, *x*, is the number of cracked boundaries characterized as "successes"

according to the chosen criterion. In this study, it is assumed that there is a fixed probability of a crack occurring at a particular site (boundary character, Taylor factor, etc.) for a specified amount of strain, and that this probability can be calculated as follows,

$$p = \frac{x}{n}, \tag{3.10}$$

where x is the number of tabulated successes.

For a binomial distribution, the standard deviation, σ, may be used to characterize the uncertainty in a measurement and is given as,

$$\sigma_x = \sqrt{x(1-p)}, \tag{3.11}$$

and because $\sigma_p = \sigma_x / n$, the fractional uncertainty in p is given by,

$$\frac{\sigma_p}{p} = \sqrt{\frac{1}{n}\frac{(1-p)}{p}}. \tag{3.12}$$

This equation can be solved for n to yield the required number of cracks that must be analyzed to define the probability of success with a given certainty,

$$n = \frac{1}{\left(\frac{\sigma_p}{p}\right)^2}\frac{(1-p)}{p}. \tag{3.13}$$

For example, if the probability of a crack occurring at a special boundary is 0.10, and the required fractional uncertainty is 0.15,

$$n = \frac{1}{(0.15)^2}\frac{(1-0.10)}{0.10} = 400,$$

it would be necessary to analyze 400 cracked boundaries.

In addition to the statistical uncertainties already discussed, experimental uncertainties in the data may arise from human error in identifying which grain boundary is cracked, and in determining the orientation of the grain following straining. Therefore, the fractional experimental uncertainty may be expressed as,

$$\left(\frac{\sigma_p}{p}\right)^2_{\text{exp}} = \left(\frac{\sigma_h}{h}\right)^2 + \left(\frac{\sigma_z}{z}\right)^2, \tag{3.14}$$

where, $\left(\frac{\sigma_h}{h}\right)$ is the fractional uncertainty due to human error in determining the boundary that cracked and $\left(\frac{\sigma_z}{z}\right)$ is the fractional uncertainty in the parameter of interest due to lattice rotation as the grain is strained. The experimental uncertainty may then be combined with the statistical uncertainty to yield a final equation for expressing the cumulative uncertainty,

$$\frac{\sigma_p}{p} = \sqrt{\frac{1}{n}\frac{(1-p)}{p} + \left(\frac{\sigma_h}{h}\right)^2 + \left(\frac{\sigma_z}{z}\right)^2}, \tag{3.15}$$

Figure 3.32(a) shows fractional uncertainties as a function of the number of analyzed cracks for various probabilities of success with a fixed experimental uncertainty of 0.05. It can be seen that the uncertainty decreases rapidly with higher probabilities of success, and that the total fractional uncertainty always approaches the experimental uncertainty as the number of cracked boundaries analyzed approaches infinity.

Table 3.1 Chemical composition of 316L plate received from Metal Short Incorporated (wt%).

Alloy	Fe	C	Mn	P	Si	Ni	Cr	Mo	Cu	Co
316L	Bal	0.00022	0.0186	0.0003	0.0051	0.1012	0.1662	0.0206	0.0024	0.0005

Table 3.2 Chemical composition of ferrite as measured by electron microprobe analysis (EMPA) (wt%).

Feature	Fe	Mn	P	Si	Ni	Cr	Mo	Cu	Co
ferrite	Bal	0.0092	0.0011	0.0061	0.0526	0.2263	0.0454	0.0015	0.0019

Table 3.3 Possible (p,n) reactions for 2 MeV and 3 MeV protons incident on 316L stainless steel and resulting isotopes.

Reaction				Cross section (mb)	
Parent isotope	(p,n) Energy threshold (MeV)	Daughter	Half-life	2 MeV	3 MeV
Ni-61	2.49	Cu-61	3.35 h	N/A	9.5
Ni-64	2.52	Cu-64	12.7 h	N/A	13.9
Cr-53	1.39	Mn-53	3.7×10^6 yr	5	42
Cr-54	2.21	Mn-54	312.1 d	N/A	30
Mn-55	1.03	Fe-55	2.73 yr	4.5	60.5
Fe-57	1.65	Co-57	271.8 d	0.9	12.4

Table 3.4 Post irradiation β counting measurements performed on 316L specimens irradiated to 7 dpa at 400°C with 2 and 3 MeV protons. Measurements were made 231.2 hours after irradiation ended.

Proton energy	Sample type	Stage position	b counts (/min)	Sample area (mm^2)	Normalized β counts (#/min/mm^2)	Deviation from average (%)
3 MeV	SCC	2	91,319	19.40	4707	3.1%
	TEM	7	88,036	19.90	4424	3.1%
2 MeV	SCC	2	3,242	20.1	161	0.3%
	TEM	3	3,175	19.6	162	0.1%
	SCC	4	3,255	20.1	162	0.1%

Table 3.5 X-ray emission energies for the elements analyzed via STEM/EDS.

	Cr	Ni	Fe
K_α energy (keV)	5.443	7.491	6.43

Table 3.6 Macroscopic strain and strain in analyzed irradiated area on 316L specimens strained in 400°C SCW.

	Specimen	Initial length (mm)	Final length (mm)	Macroscopic strain(%)	strain in irradiated area analyzed (%)
2% strain	316L-SCC-2	42.98	43.40	1.8%	0.9%
	316L-SCC-4	42.94	43.32	1.7%	---
	316L-SCC-6	42.97	43.49	2.2%	---
	316L-SCC-8	42.96	43.44	2.1%	0.9%
5% strain	316L-SCC-2	42.98	---	---	---
	316L-SCC-4	42.94	44.08	5.0%	3.7%
	316L-SCC-6	42.97	44.09	4.8%	---
	316L-SCC-8	42.96	44.10	5.0%	4.0%
10% strain	316L-SCC-2	42.98	---	---	---
	316L-SCC-4	42.94	---	---	---
	316L-SCC-6	42.97	45.21	9.7%	7.6%
	316L-SCC-8	42.96	45.20	9.8%	8.3%

Table 3.7 Plastic strain of each specimen following nominal straining to 5% 15% and 25%.

nominal strain	Plastic strain	
	316L	316LGBE*
5%	4%	7%
15%	13%	16%
25%	23%	27%

*316LGBE specimen plastically yielded due to the internal autoclave pressure.

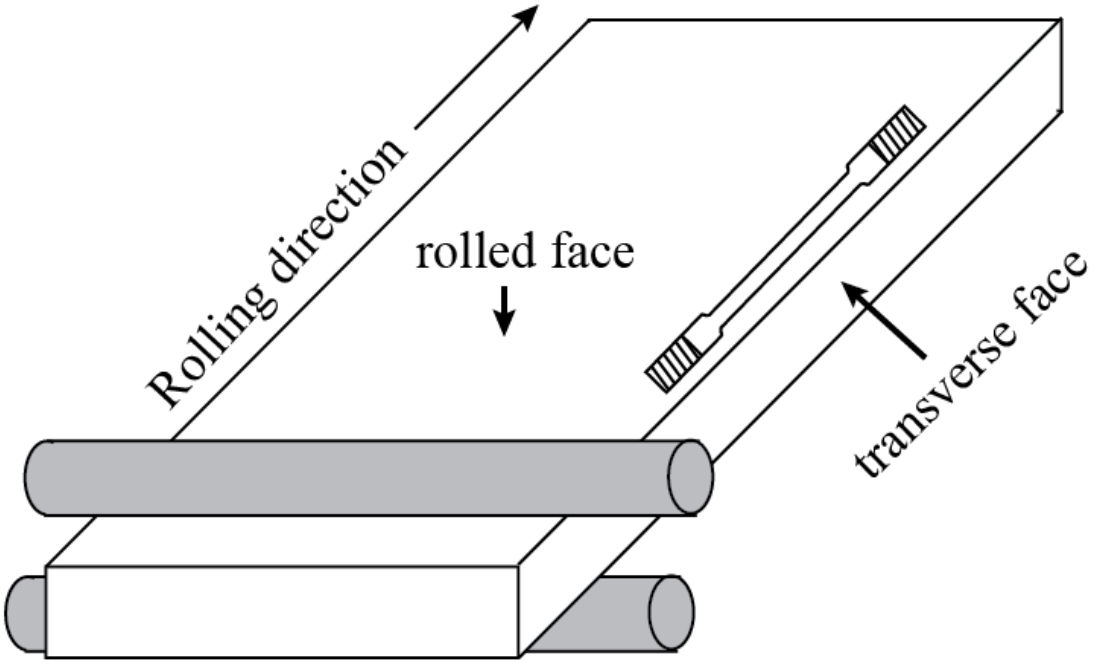

Figure 3.1 Diagram of 316L plate indicating rolled face and transverse face relative to the rolling direction.

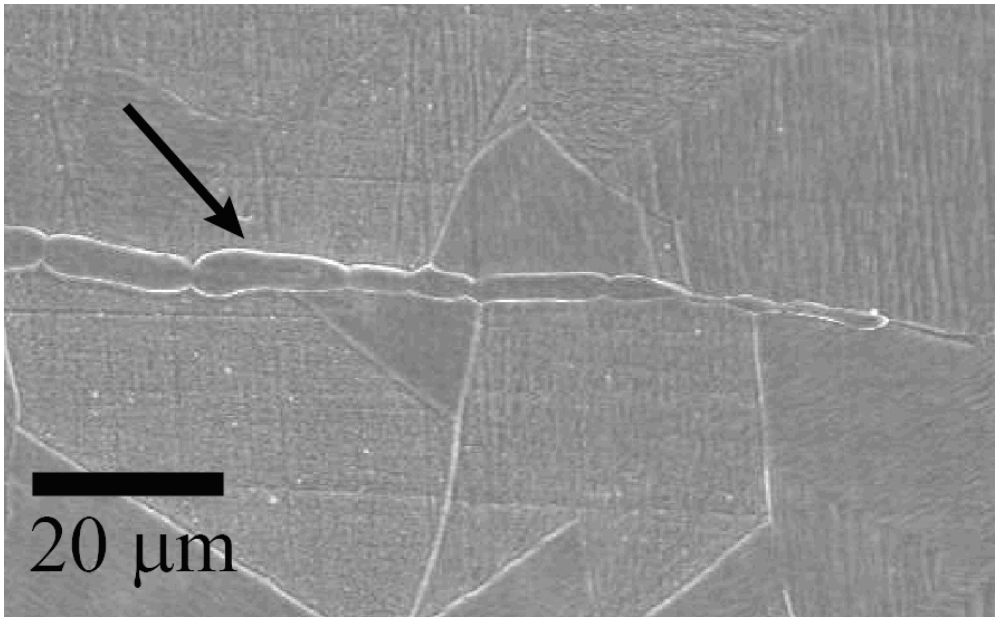

Figure 3.2 Ferrite banding in 316L stainless steel.

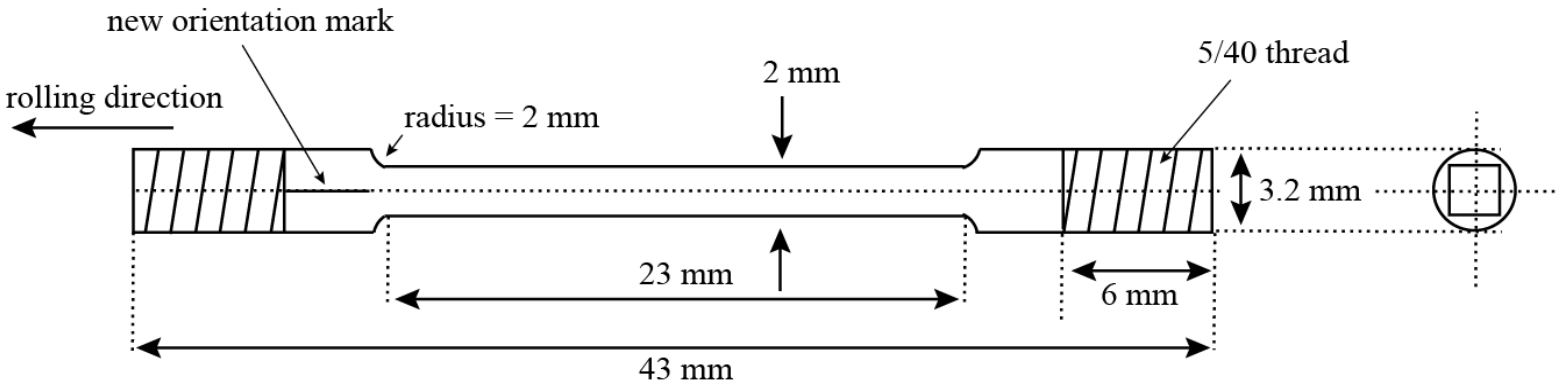

Figure 3.3 Tensile specimen.

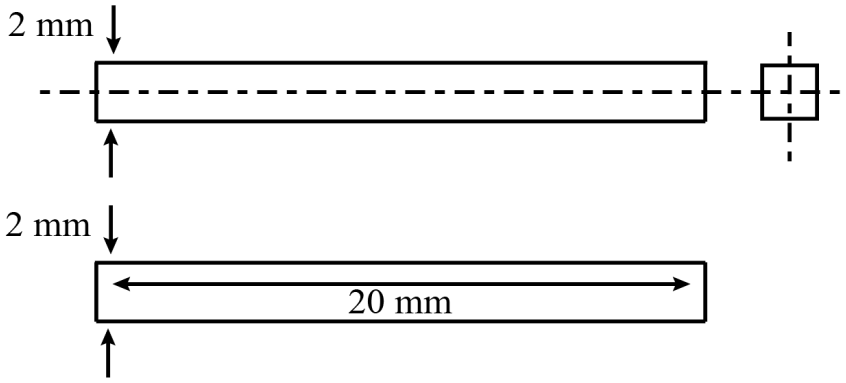

Figure 3.4 TEM specimen.

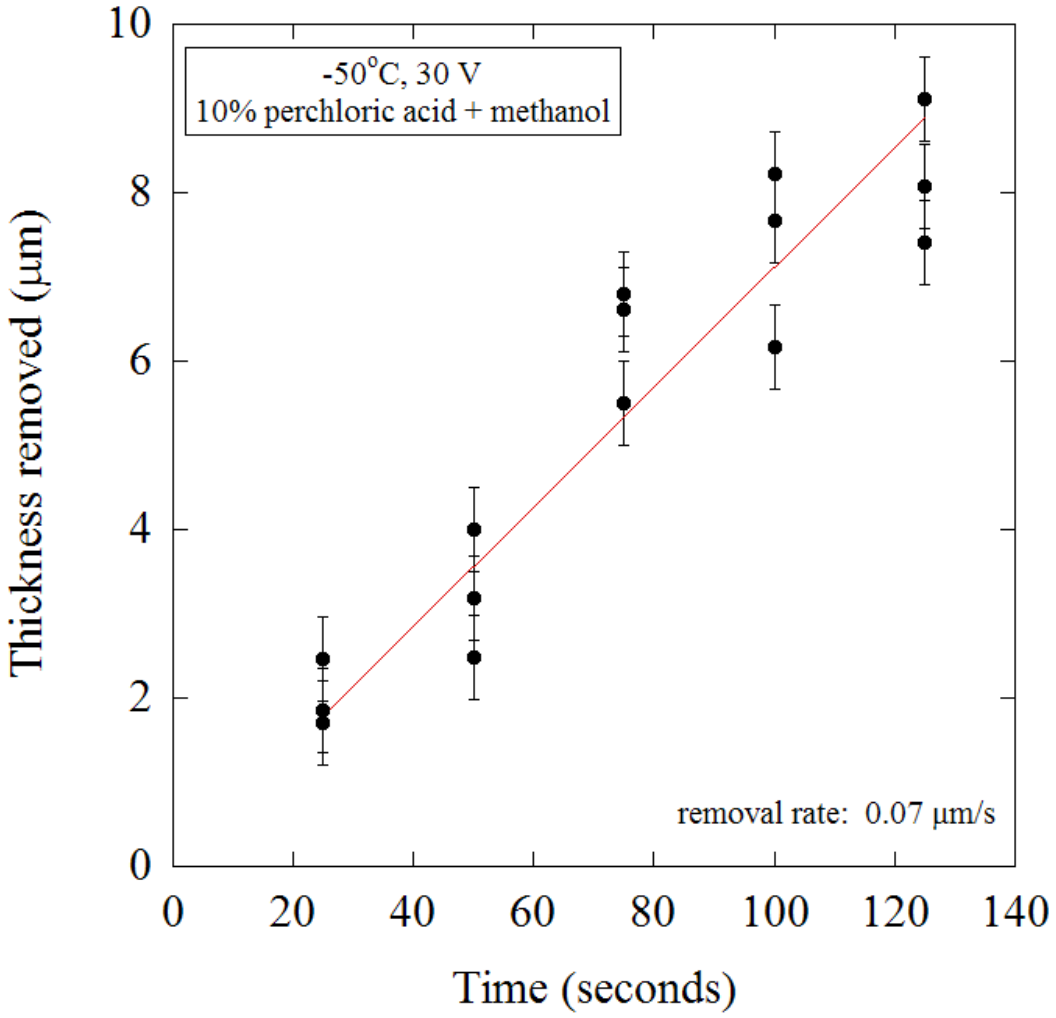

Figure 3.5 Electropolishing rate determination for 316L stainless steel electropolished in a 10% perchloric acid and methanol solution at -50˚C with an applied voltage of 30 V. Measurements were made with a Dektak3® precision profilometer.

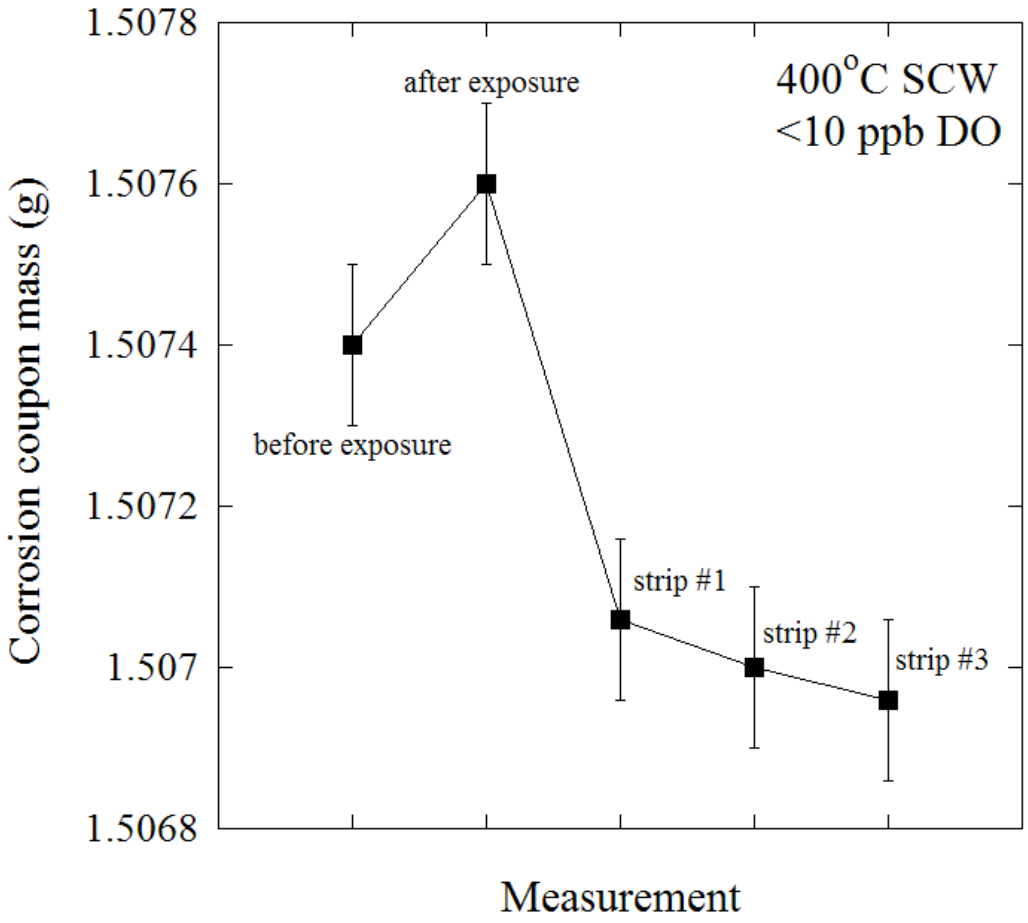

Figure 3.6 Mass of 316L corrosion coupon before exposure in 400˚C deaerated SCW, following exposure, and after three oxide stripping treatments.

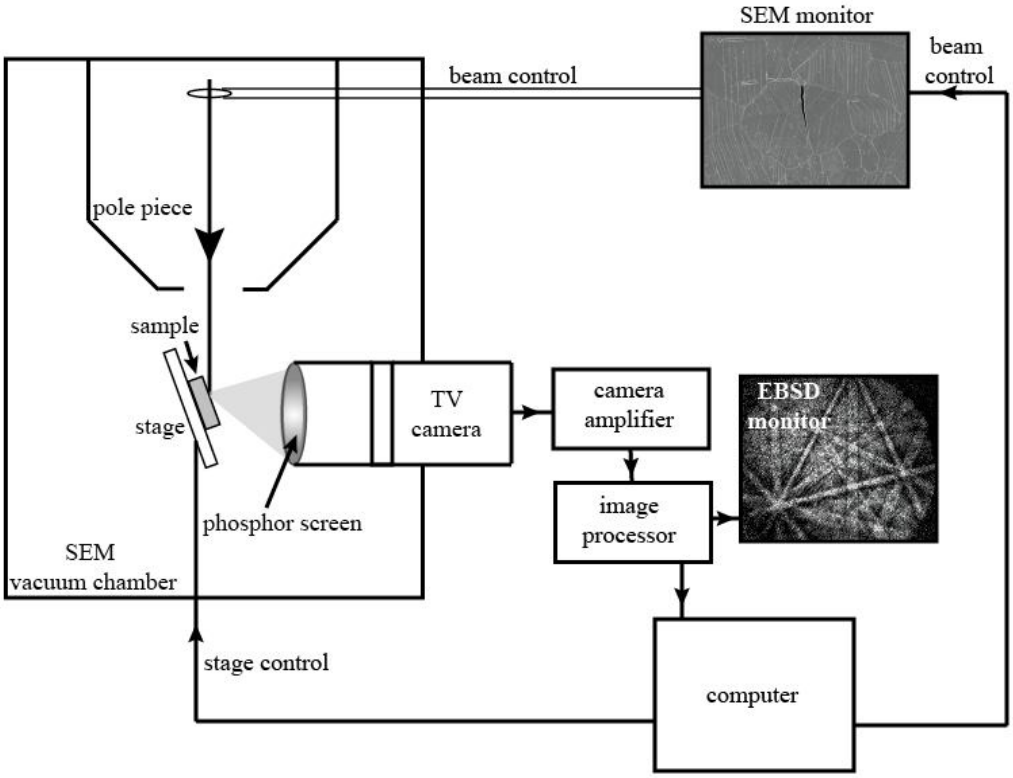

Figure 3.7 Schematic of OIM™ system on Philips® XL30FEG SEM.

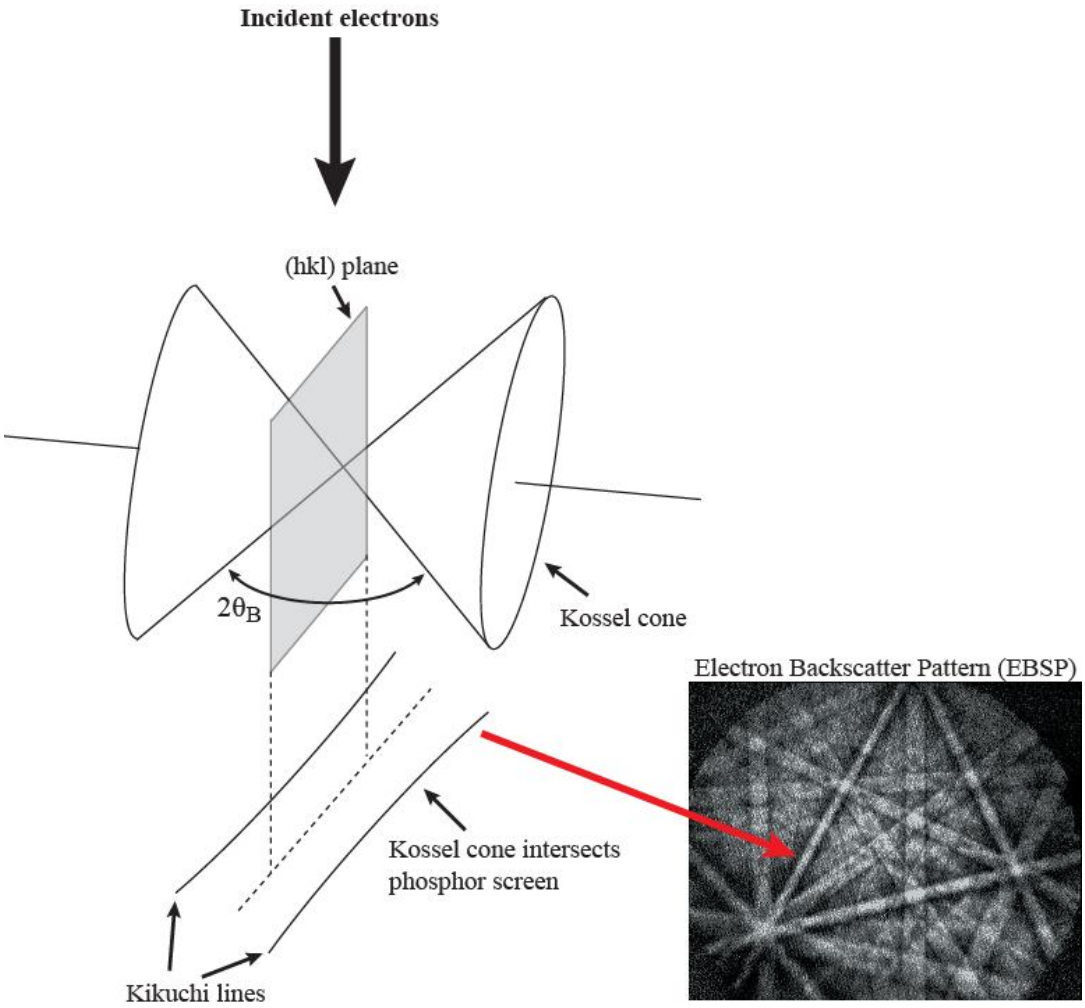

Figure 3.8 Illustration of the formation of Kikuchi lines by the Bragg scattering of electrons on crystallographic planes. EBSPs are formed by intersecting Kikuchi lines, and are representative of the orientation of the grain.

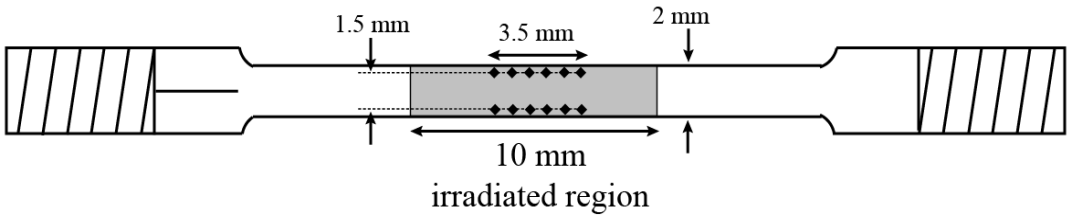

Figure 3.9 Microindentation placement on gage surface of tensile specimens. Twelve indentations were made on the specimens prior to the proton irradiation. These indentations were used as placemarkers during OIM ™ scans as well as for cracking analysis. Note that the indents in this figure are not drawn to scale.

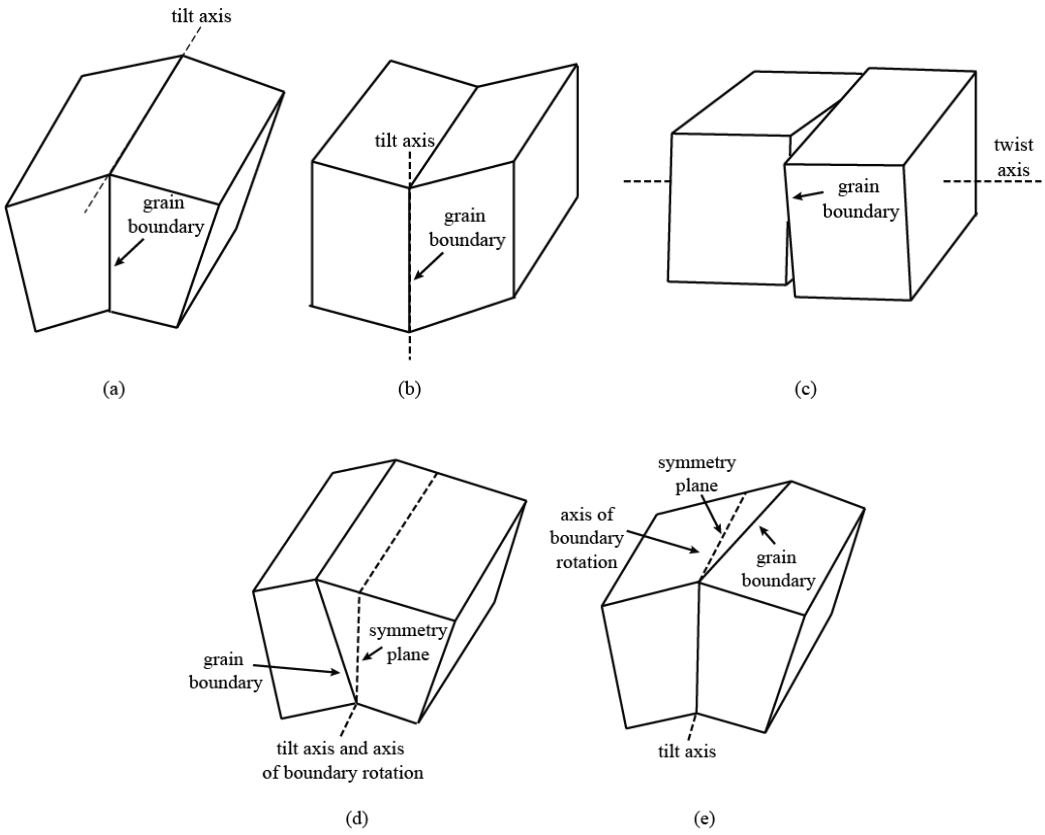

Figure 3.10 The five macroscopic degrees of freedom of a grain boundary. The degrees of freedom captured automatically by the OIM ^{TM} analysis are shown in (a), (b), and (c).

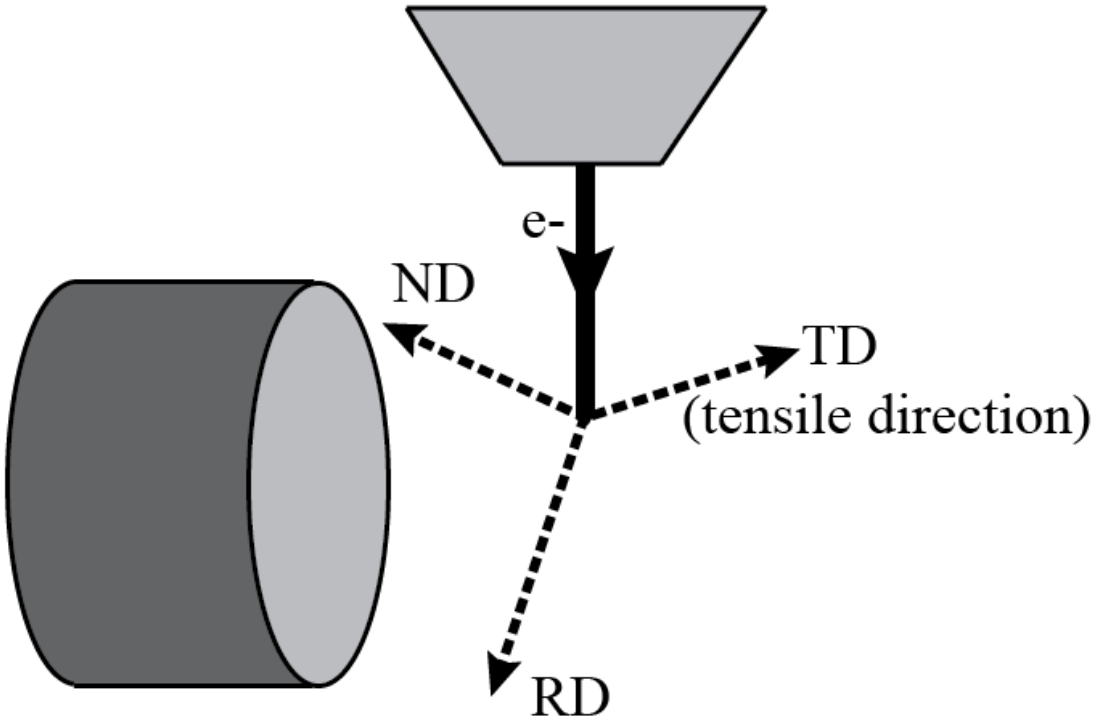

Figure 3.11 OIM ^{TM} coordinate system. The tensile directions of specimens were always oriented in the TD direction.

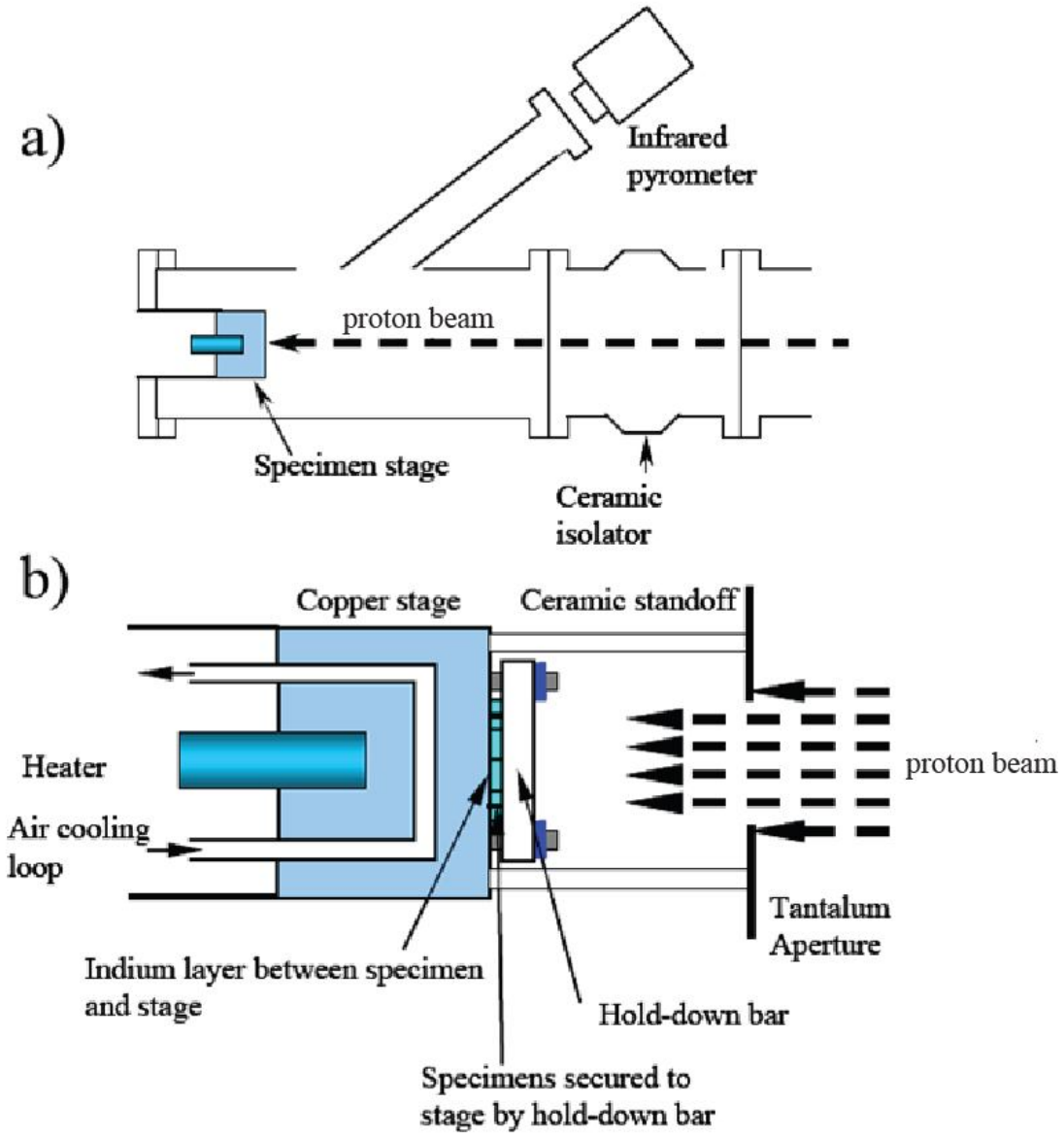

Figure 3.12 (a) Position of the infrared pyrometer while monitoring the infrared radiation emitted from the samples during the proton irradiation, and (b) schematic of the custom designed proton irradiation stage that was used to irradiate the 316L specimens [179].

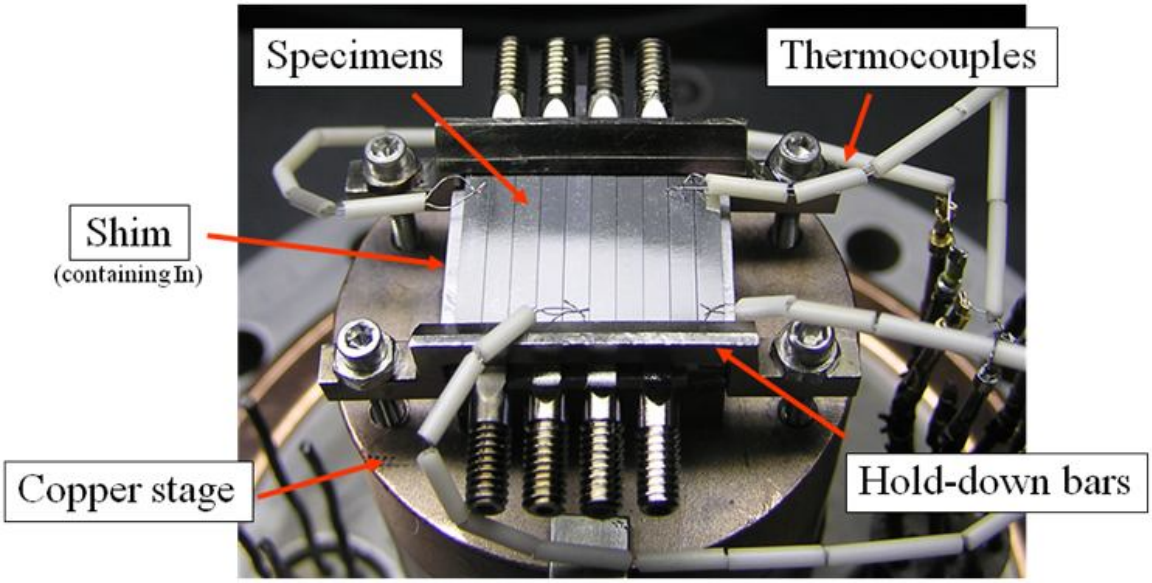

Figure 3.13 Image of a built proton irradiation stage with labeled components.

a)

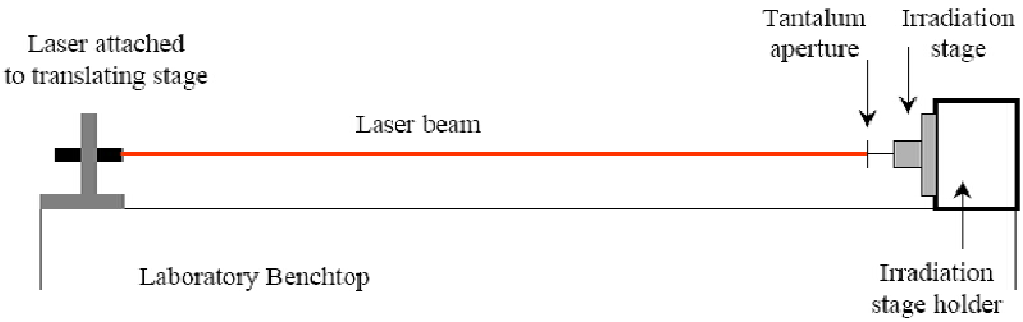

b)

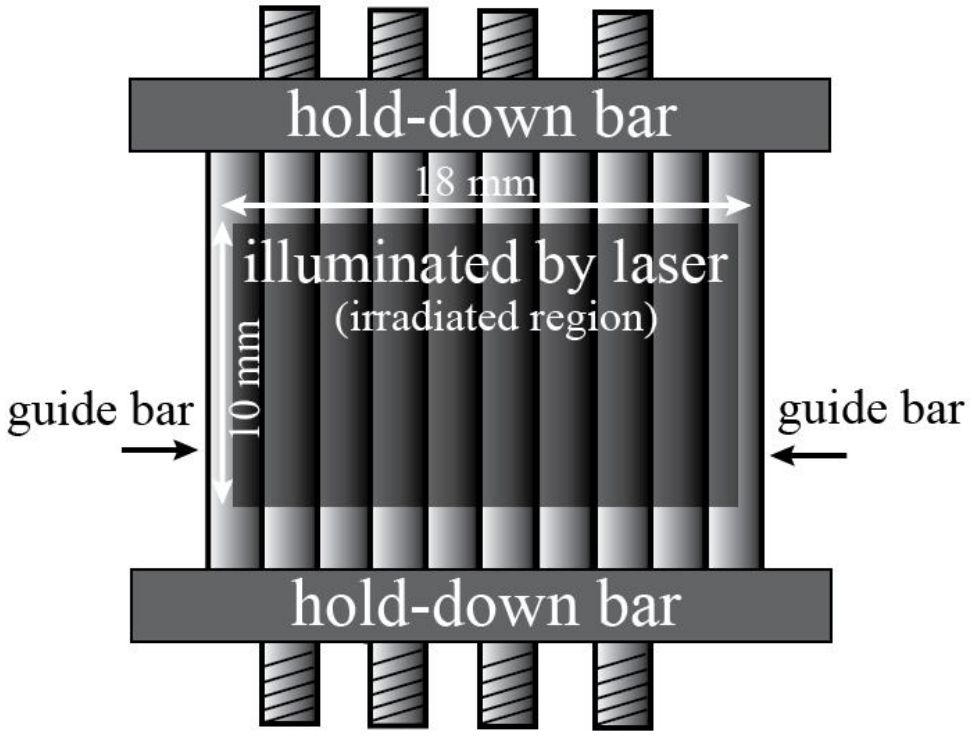

Figure 3.14 (a) Laser alignment system used to align apertures [171], (b) drawing of stage showing the irradiated region on the specimens for a perfectly aligned aperture. Note that areas of the specimen not illuminated are shielded by the apertures.

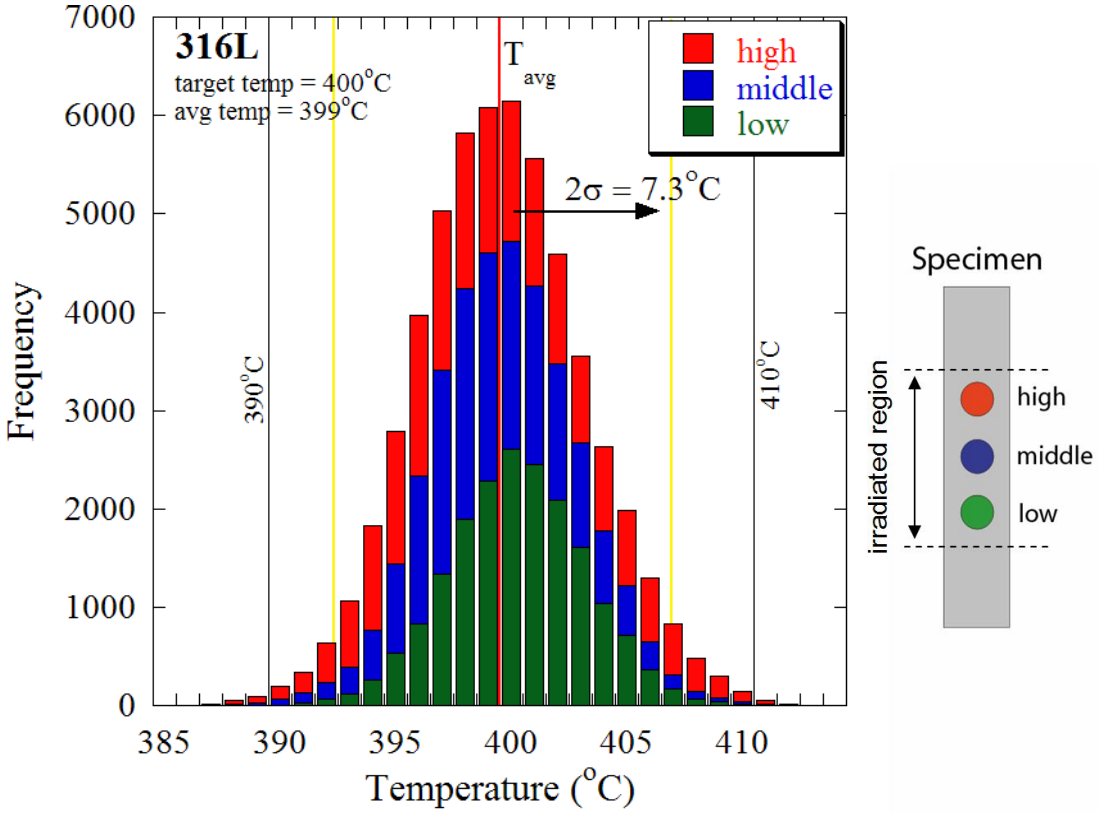

Figure 3.15 Example of a temperature profile from the 400°C, 7 dpa proton irradiation on 316L specimens.

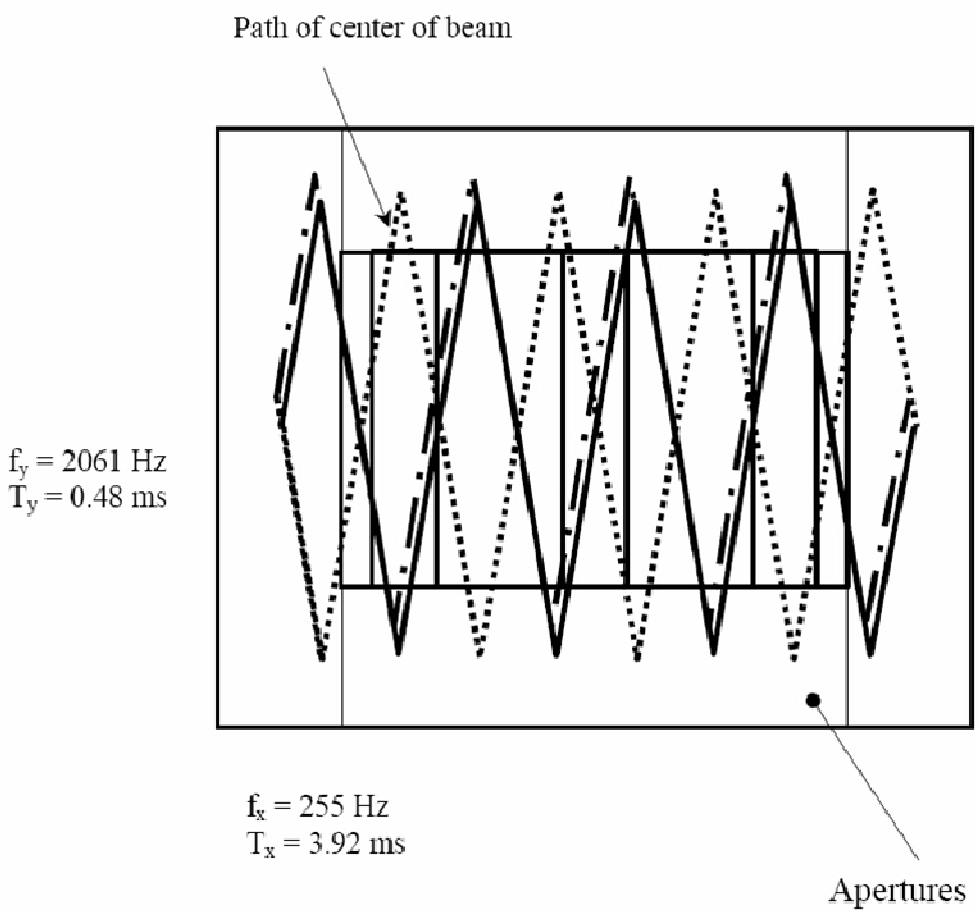

Figure 3.16 Pattern created by proton beam during raster-scanning over the proton irradiation stage and apertures [171].

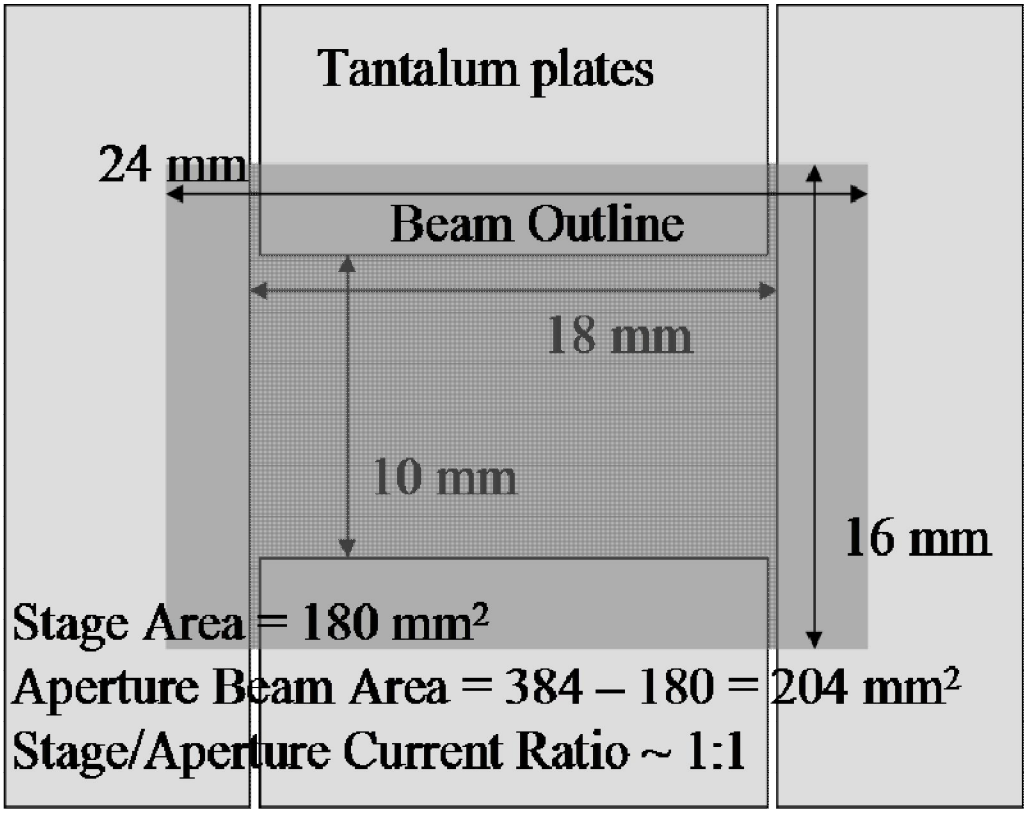

Figure 3.17 Diagram of the apertures and stage area scanned by the proton beam. In order to uniformly irradiate all specimens (including the guide bars) a 1:1 ratio between the stage and aperture current would be required for a 3 mm beam size [180].

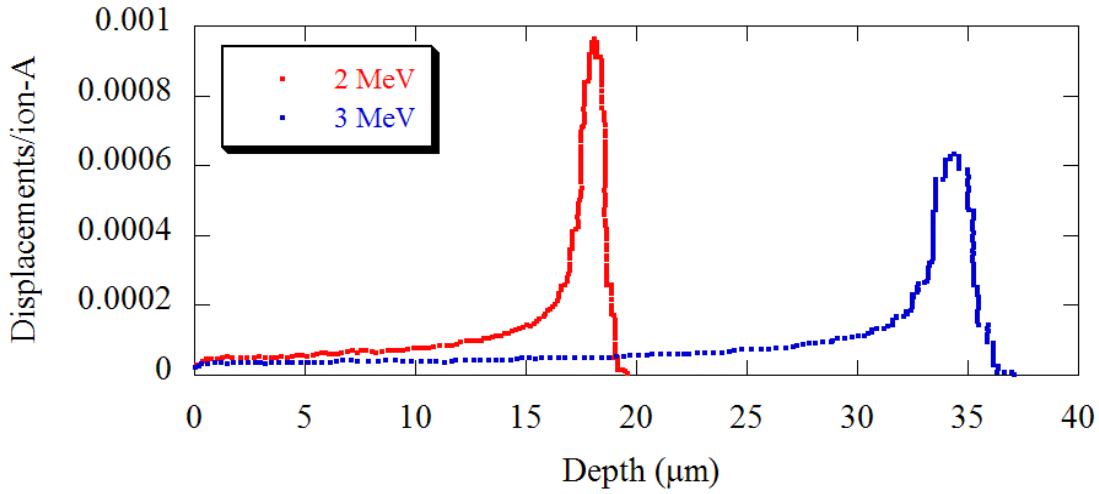

Figure 3.18 Displacement damage profiles for 2 and 3 MeV protons in 316L stainless steel as determined from SRIM ™ 2006 calculation [169].

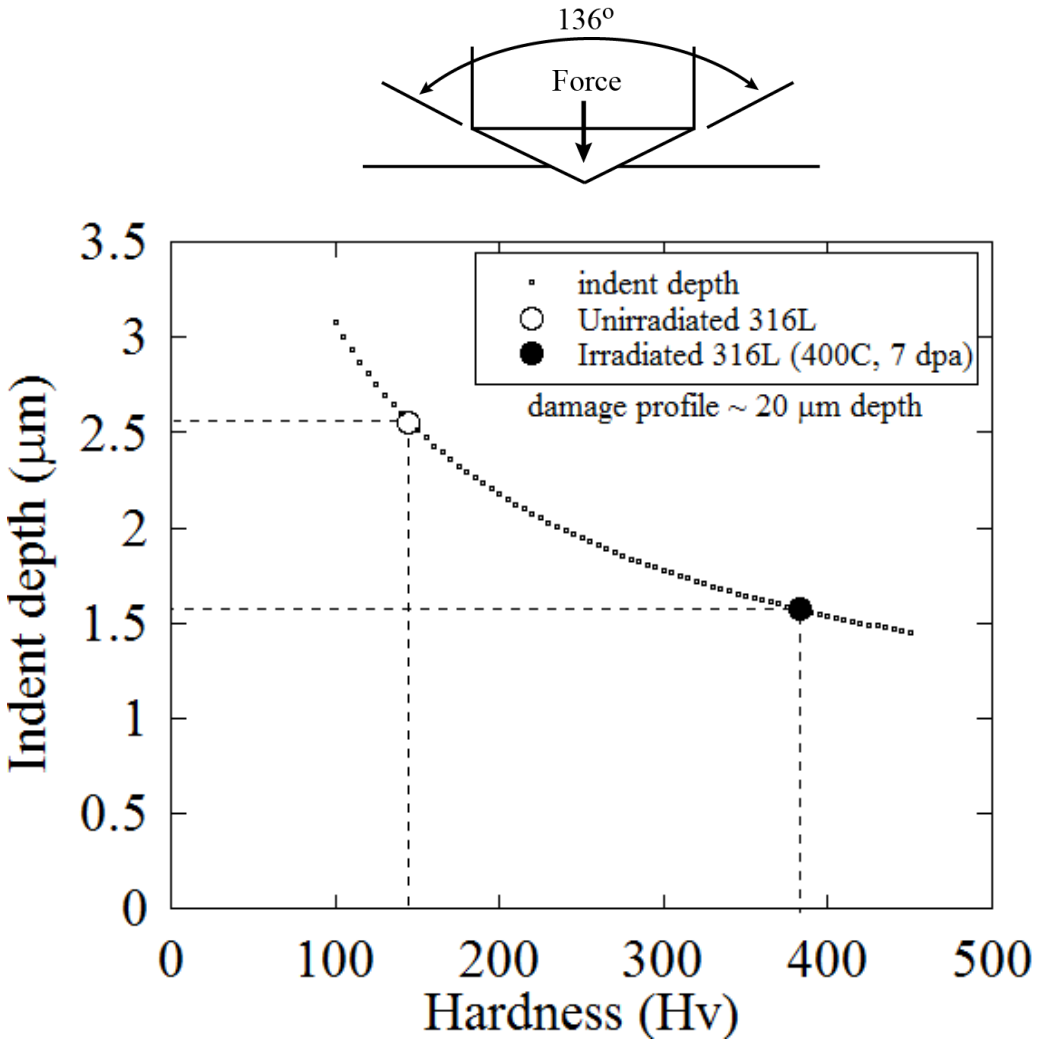

Figure 3.19 Indent penetration as a function of hardness for a 25 g load. The unirradiated and irradiated (400°C, 7 dpa) hardness values for the 316L specimens analyzed in this study are indicated.

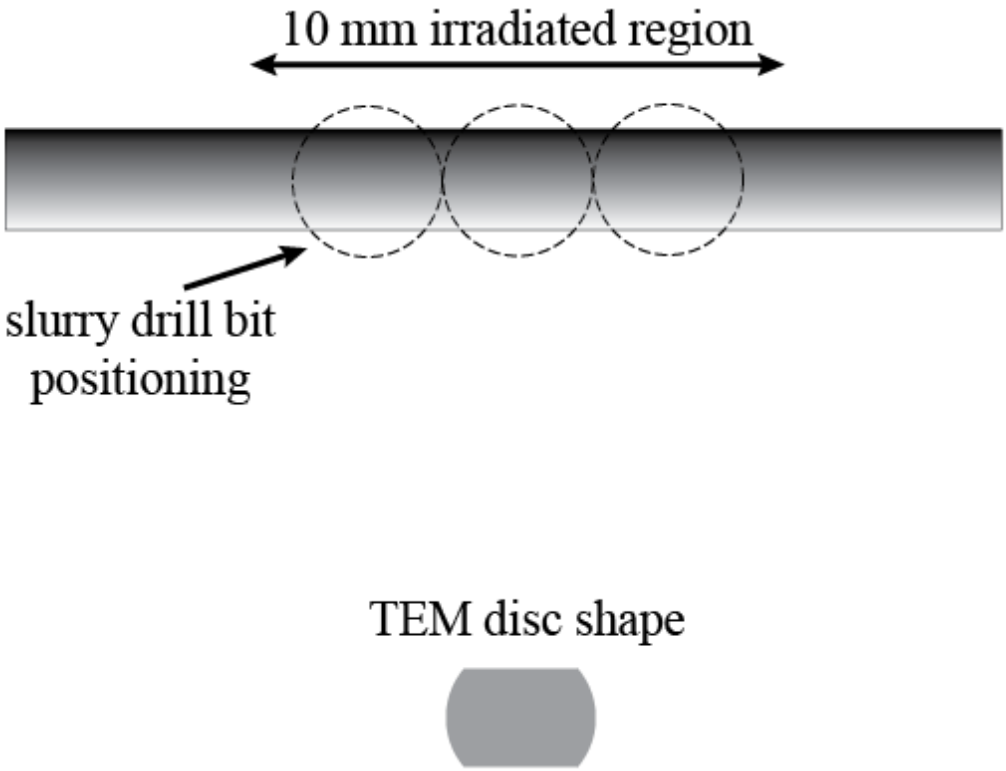

Figure 3.20 Illustration of the shapes of the TEM discs cut from an irradiated TEM bar.

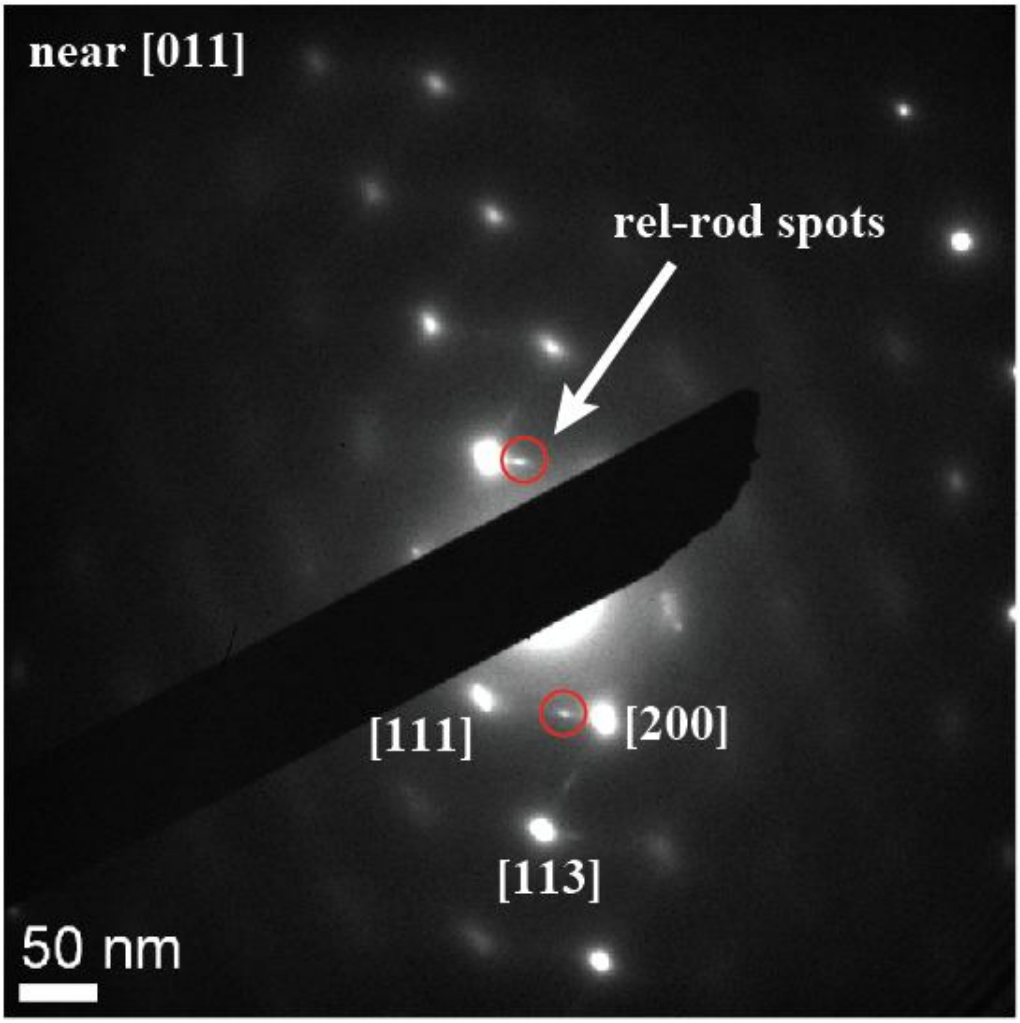

Figure 3.21 Diffraction pattern in 316L specimen irradiated to 7 dpa at 400^{o}C. The additional spots in the diffraction pattern arising from the intersection of the rel rod reflections with the reflecting sphere are circled in red.

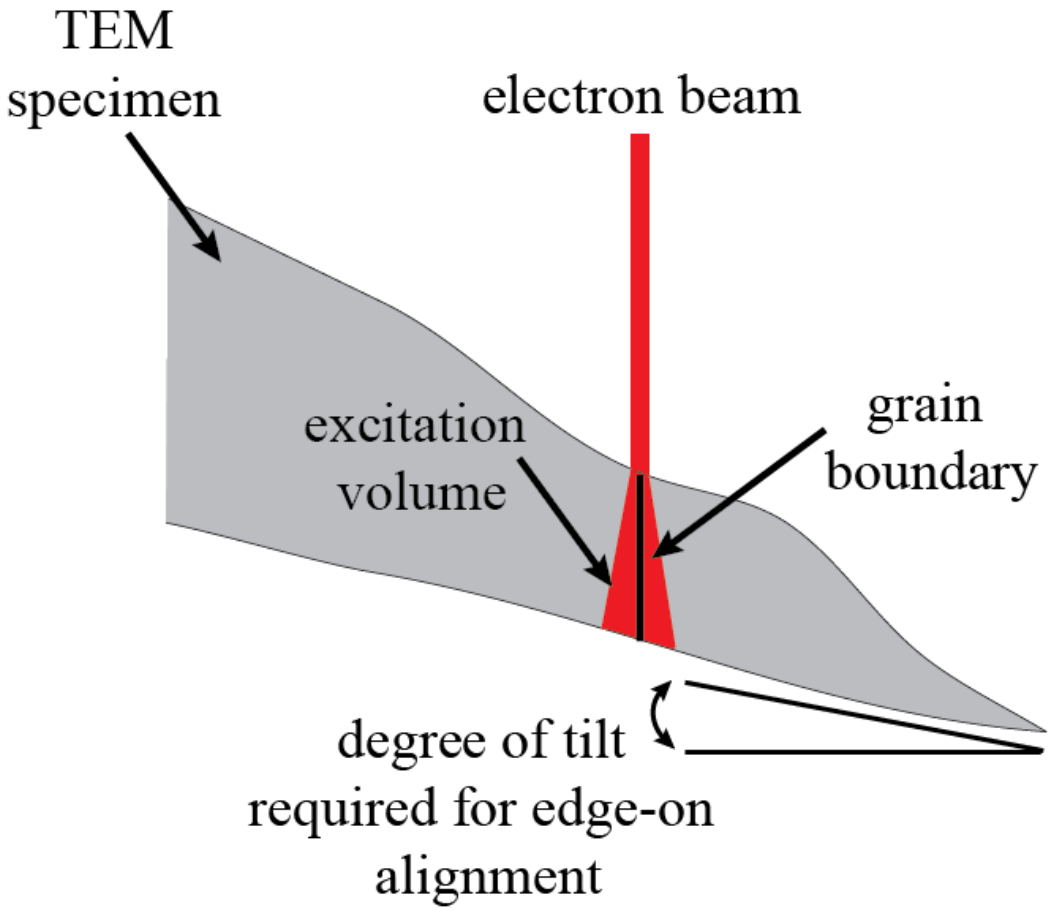

Figure 3.22 Tilted TEM specimen with grain boundary aligned edge-on. The excitation volume is shown as the electron beam broadens as it penetrates the specimen.

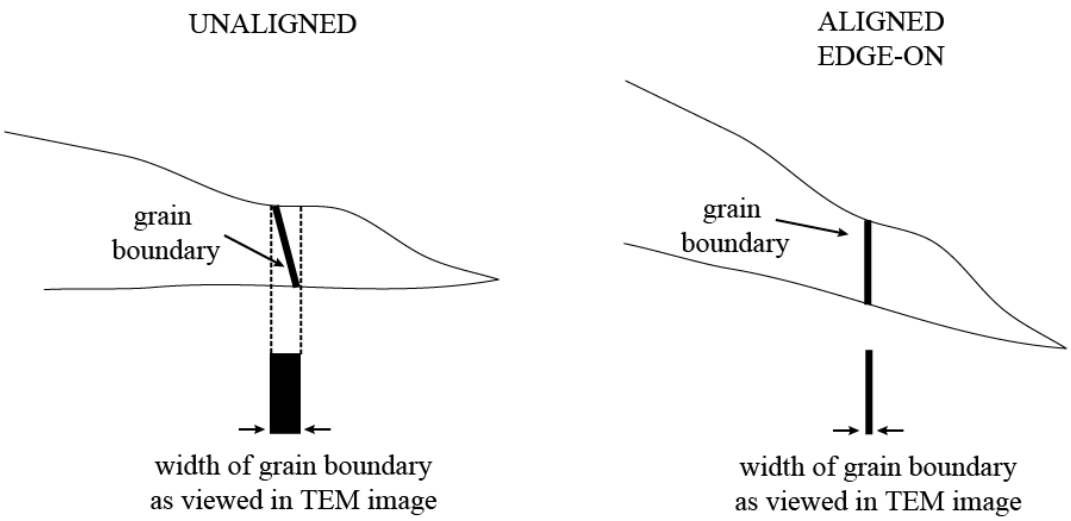

Figure 3.23 Illustrations of unaligned and properly aligned grain boundaries in TEM specimens. The width of the grain boundary as viewed in the TEM image is at a minimum when the specimen is properly tilted in the x and y directions to align the grain boundary edge-on.

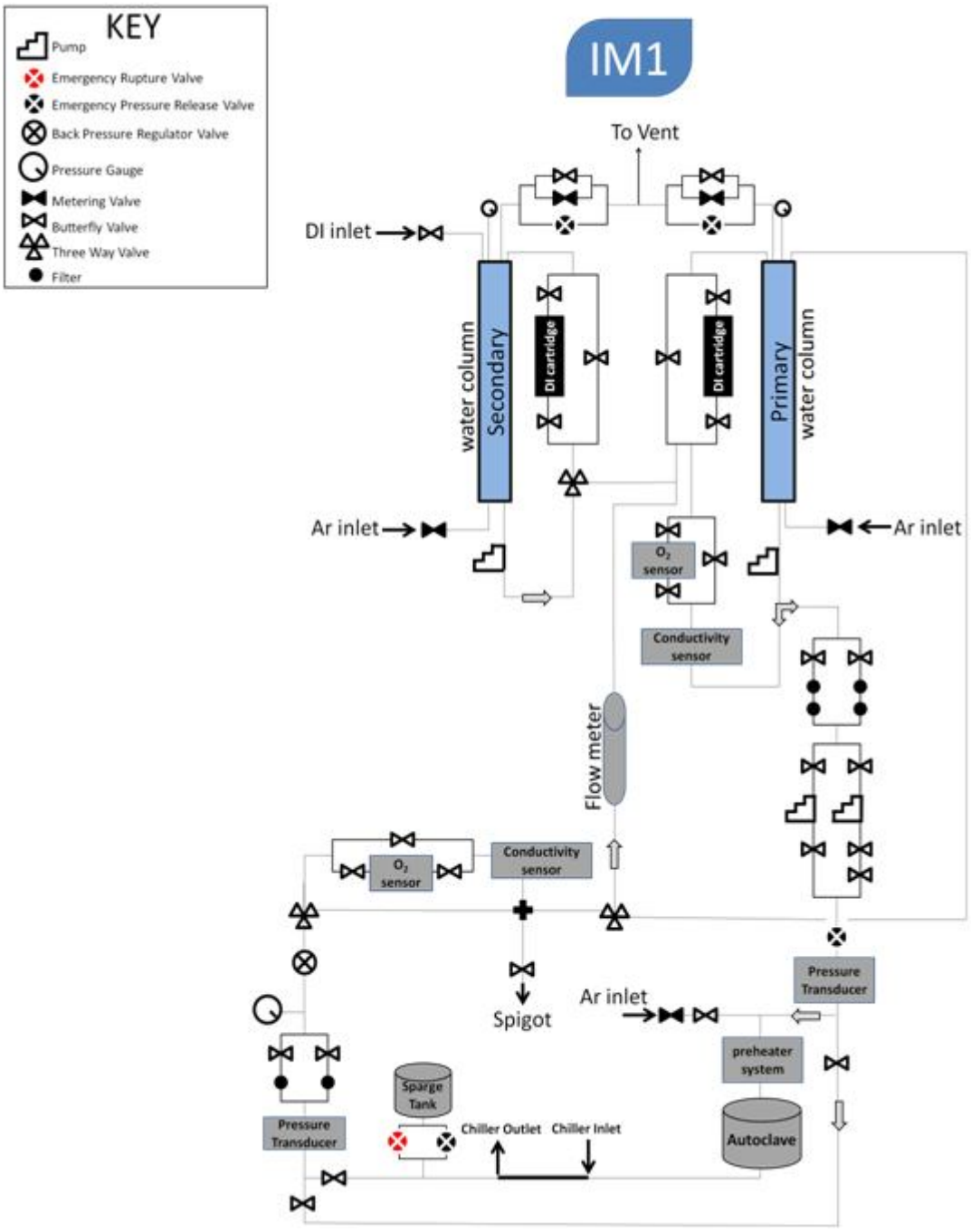

Figure 3.24 Schematic of IM1 supercritical water autoclave system in the irradiated materials testing laboratory at the University of Michigan [181].

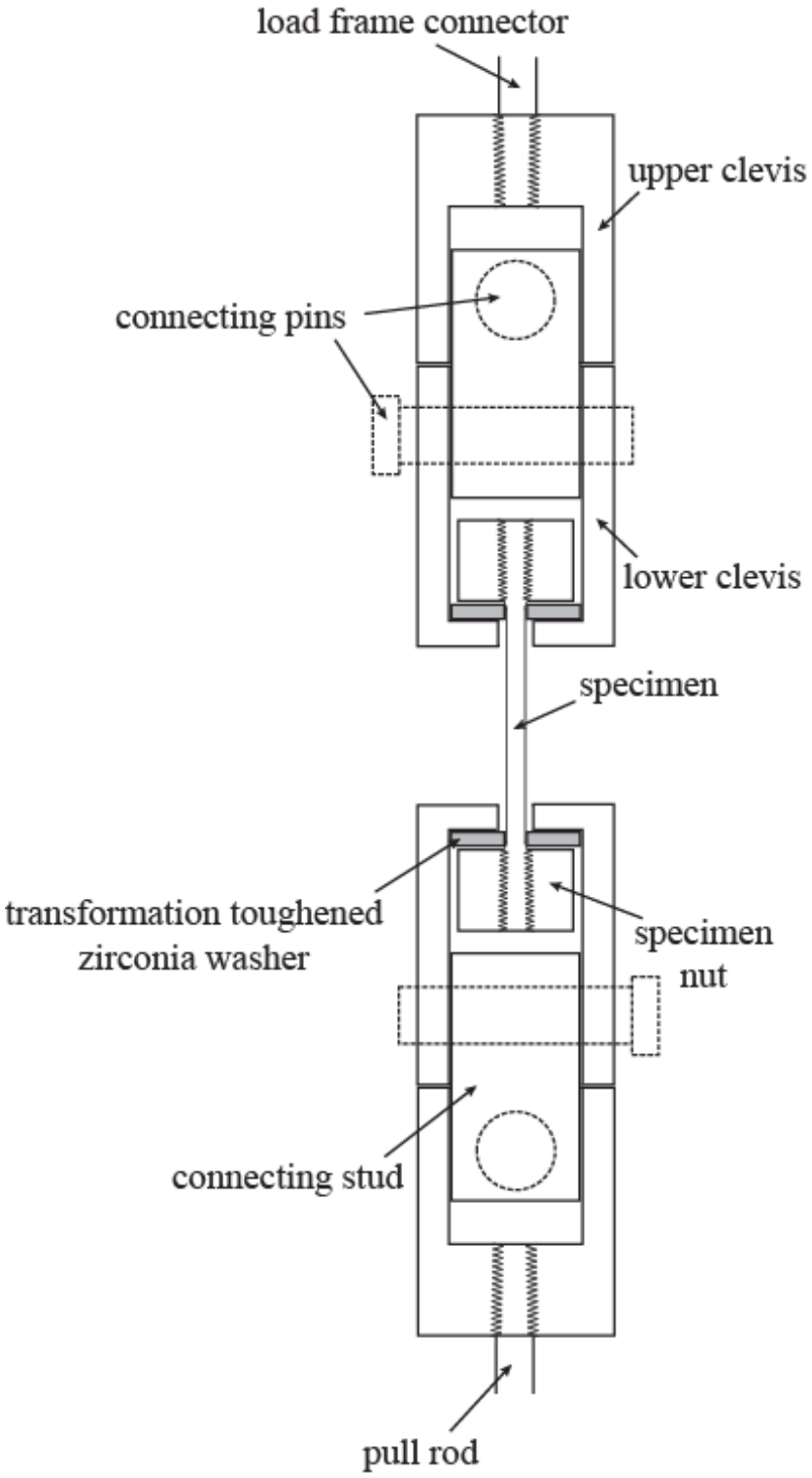

Figure 3.25 Schematic of the Inconel® 625 clevis and sample assembly in configuration during straining in IM1 SCW CERT system.

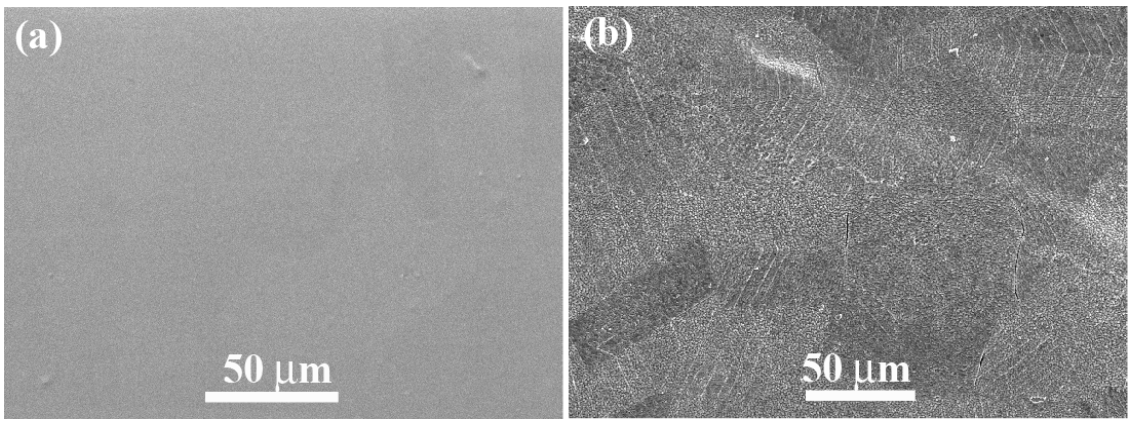

Figure 3.26 Gage surface of 316L specimens (a) prior to exposure in 400°C SCW, and (b) following exposure in 400°C SCW and straining to 5%. Note that these micrographs are not of the same area.

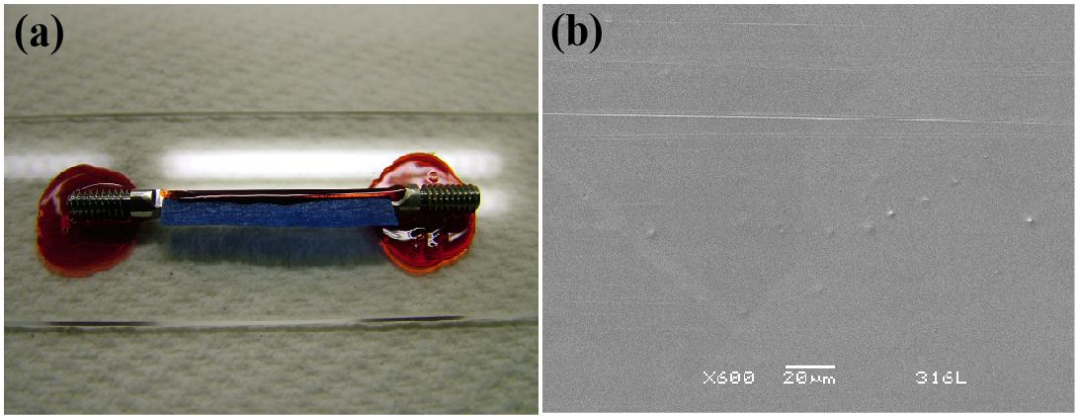

Figure 3.27 (a) Tensile specimen showing masking tape and stop-off lacquer that were used to mask the specimen from the diamond suspension solution. Prior to making scratches, tape was removed and half of the specimen was exposed to create the fine surface scratches shown in (b).

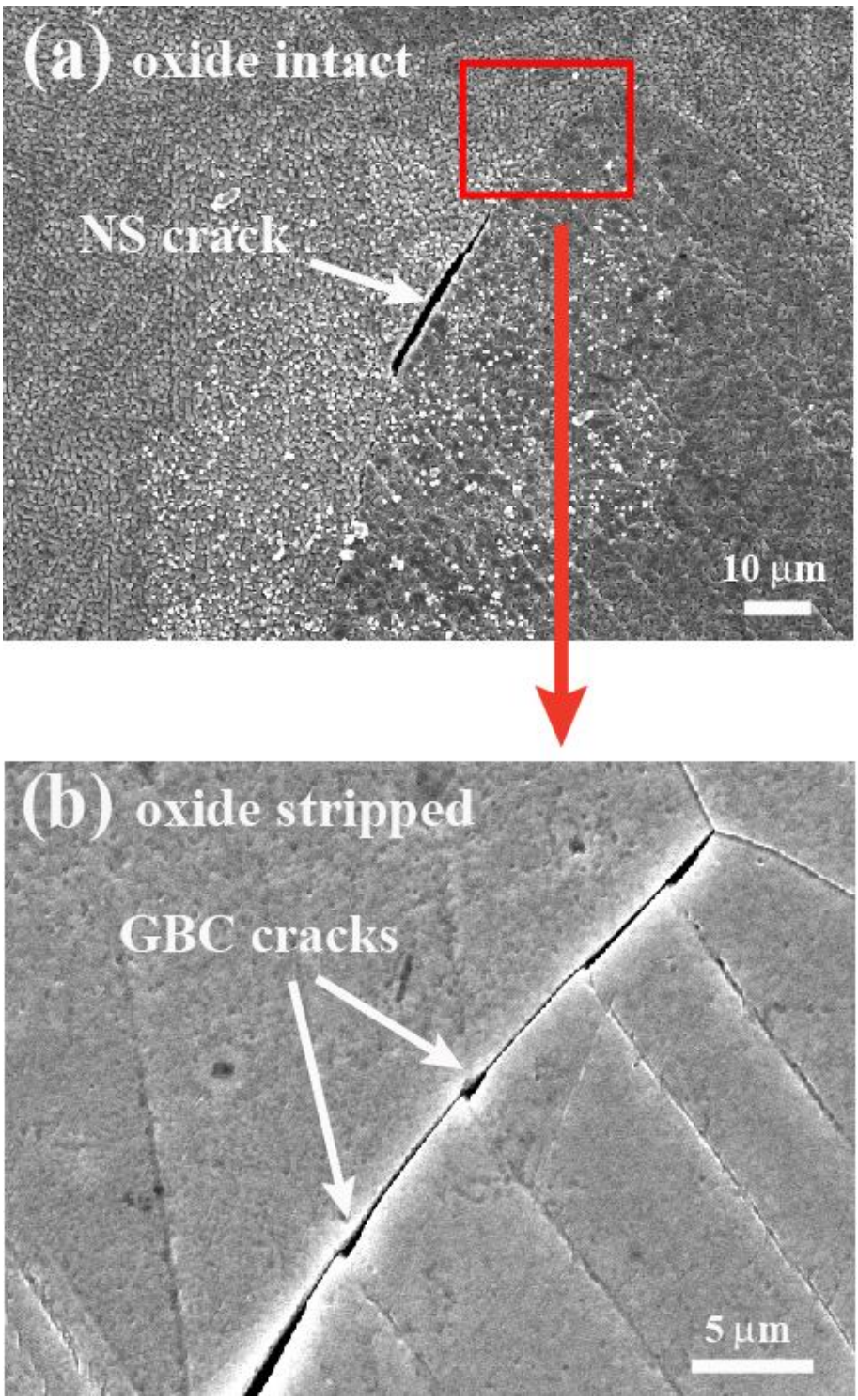

Figure 3.28 Micrographs of cracks on the gage surface of the 7 dpa proton irradiated 316L specimen strained to 5% in 400°C SCW (a) NS crack prior to oxide stripping, (b) GBC cracks that are visible following oxide stripping.

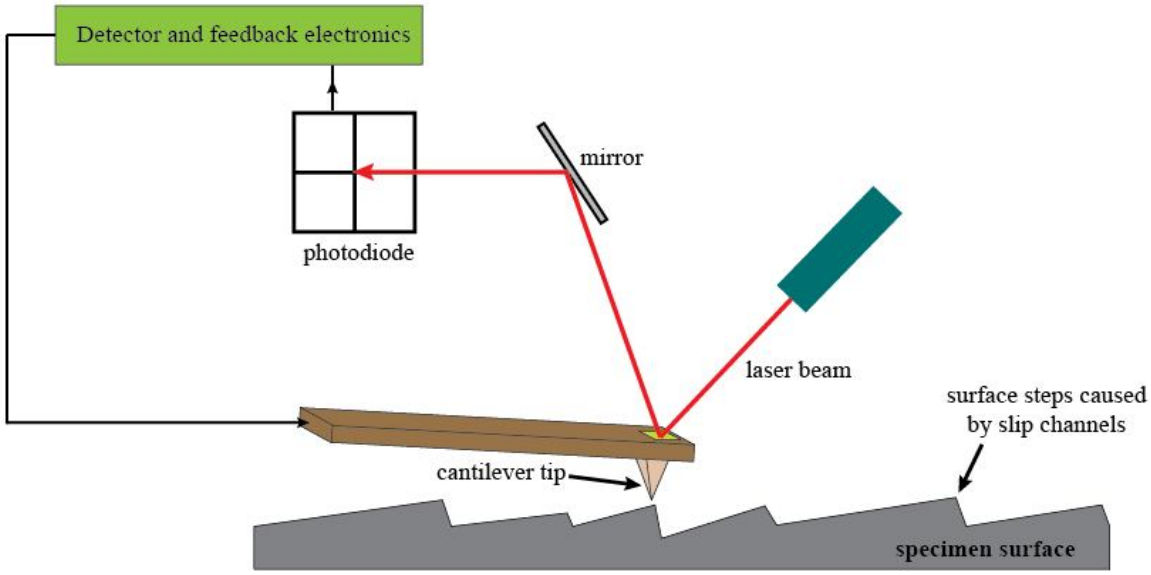

Figure 3.29 Schematic of AFM system that was used to measure the heights of the steps on the surface of the irradiated 316L specimens that were created as a consequence of the formation of slip channels.

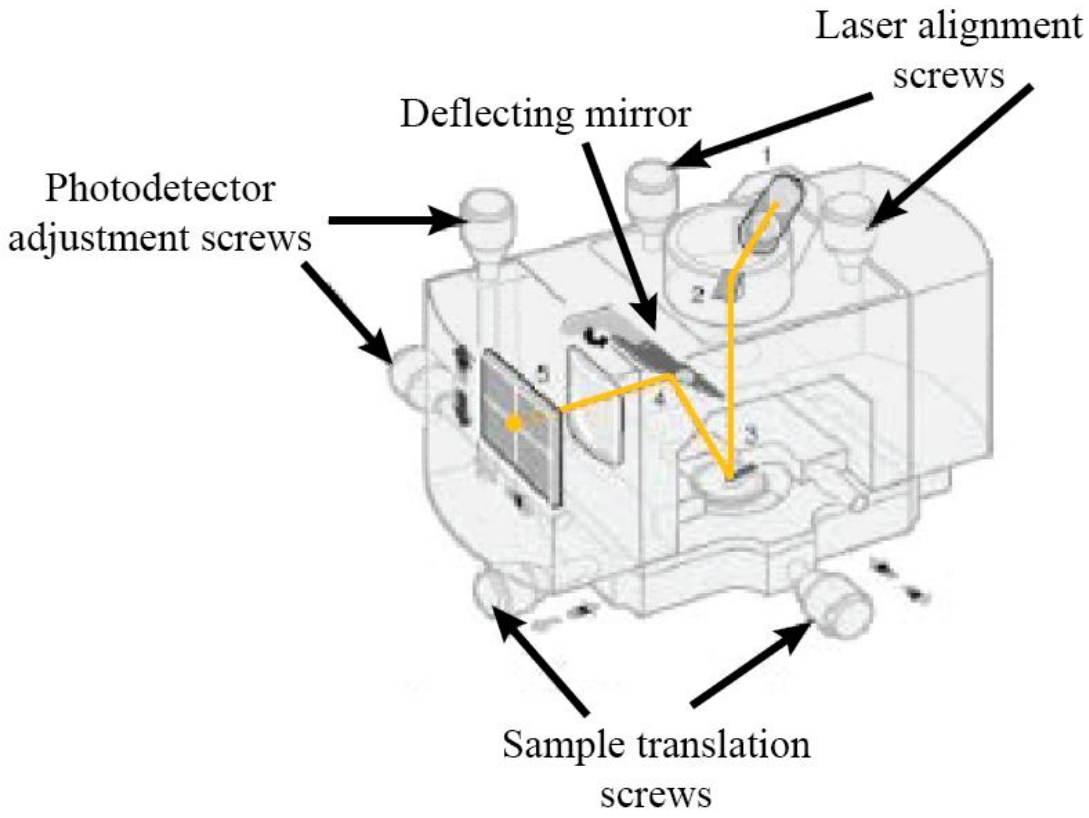

Figure 3.30 Optical head of AFM system apparatus.

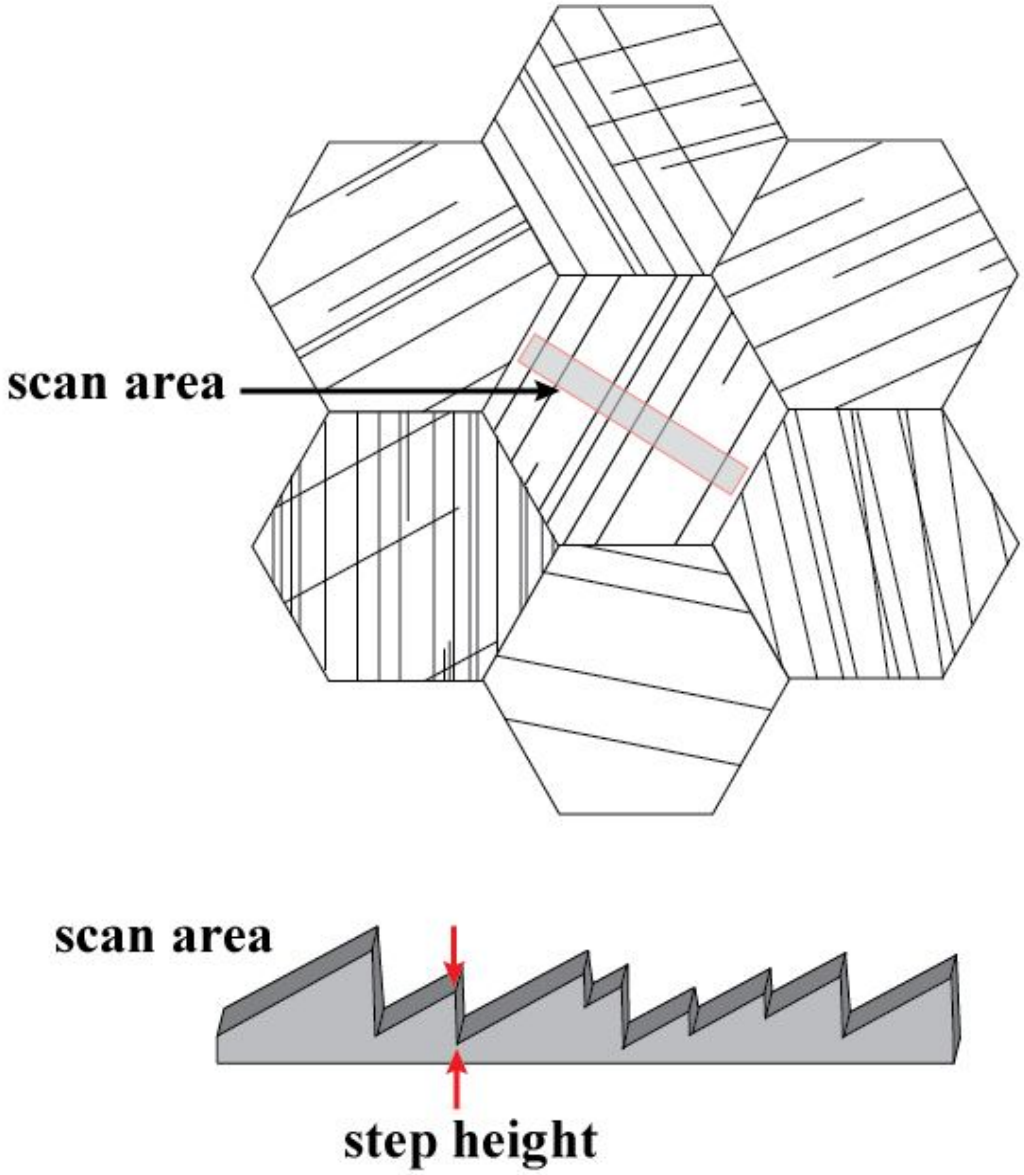

Figure 3.31 Illustration of grain selected for AFM measurement with evident slip channeling and the step height measurement performed on the resulting scan.

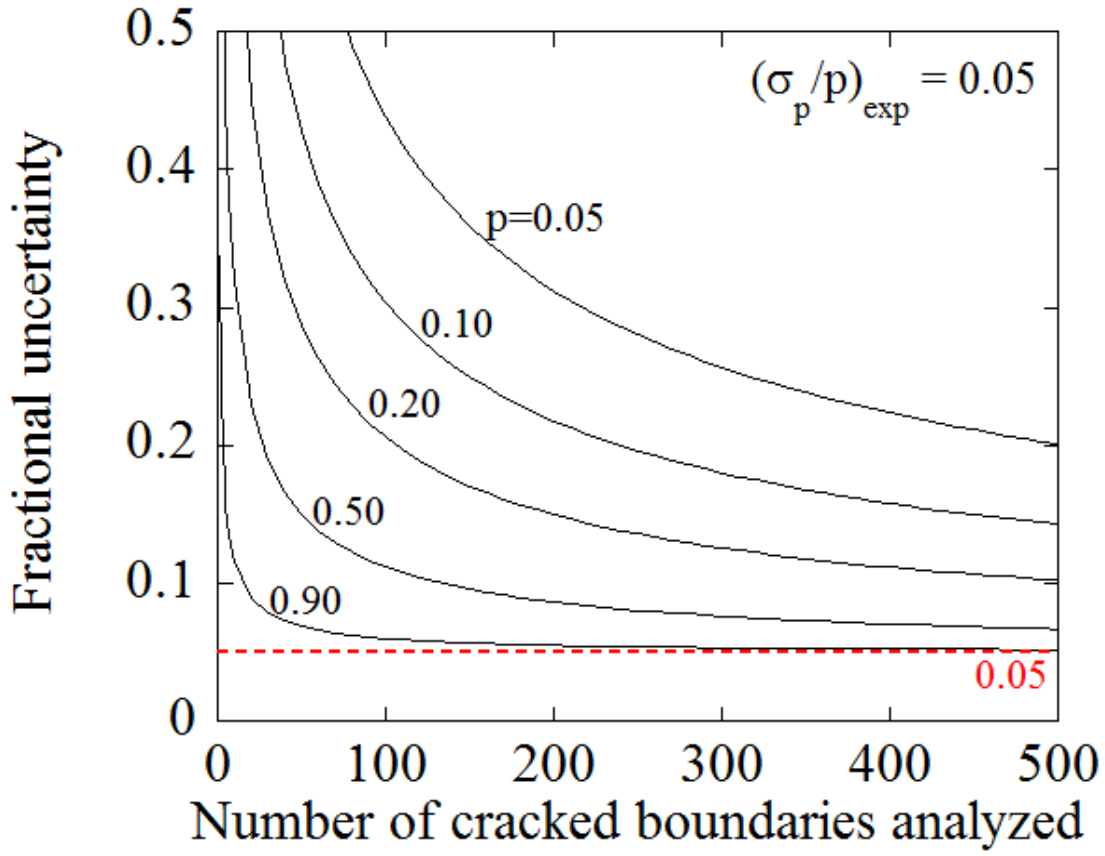

Figure 3.32 Fractional uncertainty in measurement versus the number of cracked boundaries analyzed. The total fractional uncertainty is limited by the experimental uncertainty as the number of cracked boundaries analyzed becomes large. The experimental uncertainty in the current study was approximately 0.05 as indicated by the dotted red line.

CHAPTER 4

RESULTS

This chapter presents the deformation and intergranular cracking analysis of 316L stainless steel. The first section characterizes the Schmid factor, Taylor factor, and GBCDs in the alloy. The analysis of the proton irradiation induced microstructural changes and radiation induced segregation are presented in the second section. The third section characterizes the deformation behavior of the proton irradiated steel by analyzing the correlations between the Schmid or Taylor factors of the grains and (1) the number of active slip planes, (2) the dislocation channeling behavior, (3) localized lattice rotation, and (4) slip continuity between adjacent grains. The intergranular cracking behavior of the steel in SCW is described in the fourth section. The dependence of the cracking propensity on Schmid factor, Taylor factor, grain boundary surface trace inclination, and grain boundary character is evaluated. The fifth section describes the intergranular cracking behavior of the irradiated steel in a purified argon environment. The deformation behavior at intergranular crack sites is described in the final section.

4.1 Alloy characterization

The grain boundary surface trace inclination to the tensile axis, Schmid factor, Taylor factor, and grain boundary character are four parameters of interest for analyzing grain boundary cracking propensity. It is therefore necessary to define and characterize these parameters prior to evaluating their influence on the cracking behavior. The

Schmid and Taylor factor distributions in the alloy were determined through manual analysis of OIM^{TM} grain maps of the gage surfaces of the specimens, and the grain boundary character measurements were performed through manual analysis of OIM^{TM} grain boundary maps. All OIM^{TM} maps are given in Appendix B. All measurements reported are number fractions and grain boundary character measurements include coherent twin boundaries.

4.1.1 Trace inclination

The grain boundary surface trace inclination, henceforth referred to as the "trace inclination", θ, is the angle between the surface trace of the grain boundary plane and the tensile axis. An illustration of the trace inclination is shown in Figure 4.1. A trace inclination of 90˚ is indicative of a grain boundary that is perpendicular to the tensile axis. The trace of each cracked grain boundary is measured from the line drawn between the triple junctions at either end of the cracked grain boundary. If the crack does not extend the entire length of the grain boundary, the trace inclination is measured from the line drawn between either ends of the crack tip.

4.1.2 Schmid and Taylor factor distributions

The Schmid and Taylor factors of the grains in the 316L stainless steel were analyzed to determine their bulk distributions. Descriptions of the Schmid and Taylor factors were provided in Section 2.5. The grinding and polishing procedures used to prepare the specimens were described in Section 3.3, and the procedures for conducting the OIM^{TM} analysis are described in Section 3.4. Examples of OIM^{TM} Schmid and Taylor factor maps of the sample gage surfaces of the 316L and 316LGBE tensile

specimens are shown in Figure 4.2 and Figure 4.3 respectively. All of the OIM^{TM} maps generated of the specimen surfaces are shown in Appendix B. The analysis of the 316L was performed using the TSL OIM^{TM} software by manually selecting each of the 6,000 grains used to generate the number fraction distributions. The distributions of Schmid and Taylor factors in the 316L are shown in Figure 4.4 (a) and (c), respectively. The distributions of the Schmid and Taylor factors in the 316LGBE specimen, which were measured from nearly 1,700 grains, are shown in Figure 4.4 (b) and (d), respectively. The similar distributions of Schmid and Taylor factors in the 316L and 316LGBE specimens, confirm that the distributions were not significantly altered by the thermomechanical processing treatment applied to the 316LGBE specimens.

Both the Schmid and Taylor factor distributions peak at values near the high end of their range, and this must be accounted for in later cracking analyses to ensure the data is unbiased. An observation that cracks preferentially occurred adjacent to grains with high Schmid factors, for example, may simply be the result of a random sampling of the bulk distribution. Consider, for example, that the Schmid factor distribution ranges from 0.27-0.50. If it were observed that 50% of the cracks occurred adjacent to grains with Schmid factors of greater than 0.45, it might be assumed that grains with high Schmid factors promoted cracking. 0.45, however, is the average Schmid factor in the current study, and such an observation would simply reflect a random sampling of the bulk distribution. Therefore, the Schmid and Taylor factor distributions were divided into ranges of low “L”, medium “M”, and high “H” values as indicated in Figure 4.4. Each of the ranges indicated contains one third of the total grain population. The sample to sample variations in Schmid and Taylor factor distributions were accounted for by

determining the limits of the low, medium, and high ranges that contained one-third of the grain population for each individual specimen analyzed. As shown in Table 4.1, the low Schmid factor range includes grains with Schmid factors up to 0.42-0.45 while the high range includes grains with Schmid factors as low as 0.47-0.49 depending on the specimen. Similarly, the low Taylor factor range includes grains with Taylor factors of up to 2.81-2.98 and the high range includes grains with Taylor factors as low as 3.28-3.41.

4.1.3 Grain boundary character distribution

The grain boundary character measurements of the 316L and 316LGBE were performed through manual analysis of the grain boundary character maps. Examples of grain boundary character maps are shown in Figure 4.5 and Figure 4.6. The characters of over 6,000 and 1,600 grain boundaries were tabulated in the 316L and 316LGBE specimens, respectively. The number fractions of each boundary type were then calculated by dividing the number of a specific type of boundary by the total number of boundaries analyzed. The results of these measurements and the associated uncertainties are given in Table 4.2. The uncertainties were calculated using equation (3.12).

The grain boundary number fractions of the 316L and 316LGBE are plotted in Figure 4.7. It can be seen that the 316LGBE has approximately 48% RHABs compared to 58% in the 316L. This difference is a result of the higher population of special boundaries in the 316LGBE of 52% compared to 42% in the 316L. Therefore, the special boundary population was increased by 24% through thermomechanical processing to achieve the 316LGBE condition. The increase in the special boundary

fraction is a result of to the increase in $\Sigma 3^n$ type boundaries, as the population of LABs is 2% in both the 316L and 316LGBE. In addition to having a higher fraction of special boundaries, the RHAB network in the 316LGBE is less continuous than that in the 316L, as can be seen by comparing Figure 4.5(b) and Figure 4.6(b).

4.2 Irradiation induced microstructure and chemistry

The proton irradiation induced changes in the microstructure and grain boundary composition of the 316L stainless steel, and the changes were analyzed via TEM analysis with a JEOL^{TM} 2010F TEM following the 7 dpa 400˚C irradiation. The formation of dislocation loops and a few voids caused irradiation induced hardening in the alloy which was evaluated through microhardness measurements. The size and density of the dislocation loops were measured from rel-rod dark field images, and the composition profiles in the unirradiated and irradiated condition were measured via scanning transmission electron microscopy (STEM)-EDS analysis.

4.2.1 Irradiation induced hardening

The hardness of the 316L specimens increased from approximately 150 Hv to 380 Hv as a result of the 7 dpa proton irradiation at 400˚C. The procedure for performing the microhardness measurements on the irradiated TEM bars was described in Section 3.6. The depths of the indents in the irradiated regions were approximately 1.6 μm, and so the sampling volume was confined to a region much less than the irradiated depths of approximately 20 and 37 μm for the 2 MeV and 3 MeV protons, respectively.

Hardness measurements were performed both prior to irradiating the specimens and following the proton irradiation. The irradiation induced hardening was calculated

by subtracting the hardness of the solution annealed 316L from the post-irradiation hardness. The proton irradiation induced hardening for each of the 7 dpa 400˚C irradiations performed in this study are given in Table 4.3, and the uncertainties given are the standard deviations of the measurements. Three separate irradiations were performed to generated three sets of specimens. One set was used for TEM analysis of the irradiation induced microstructure, another for the 400˚C SCW CERT experiments, and the final set for the 400˚C argon CERT experiments. The irradiation induced hardening is also plotted in Figure 4.8 for each irradiation, and it can be seen that the measurements are consistent for each irradiation and there was agreement between the 2 MeV and 3 MeV irradiations, indicating irradiation induced hardening of approximately 230 Hv.

4.2.2 Dislocation loops

The microstructure of the proton irradiated 316L contained a high density of faulted dislocation loops. The dislocation loops were analyzed using the rel-rod dark field technique described in Section 3.8. A representative image of the dislocation loops is shown in Figure 4.9 (a). The size and density of the loops were determined through manual measurements with Scion® Image software [173]. Recall that each image was collected from a rel-rod corresponding to a single $\{111\}$ plane, and therefore only one-fourth of the total number of loops was visible. The actual loop density is therefore a factor of 4 greater than is shown in the image, or 5.3×10^{22} m^{-3} as indicated in Table 4.4. The diameters of the dislocation loops vary substantially as shown in Figure 4.9(b) and were as large as 23 nm. The loop diameter distribution peaked at a value of

approximately 5 nm and decreased thereafter to yield an average diameter of 6.9 nm as indicated in Table 4.4.

4.2.3 Voids

Voids were present in the proton irradiated 316L specimens, although their size and density were too low to yield quantitative measurements of their population. The images of the voids were taken in a slightly underfocused condition as described in Section 3.8. A bright field image of a void is shown in Figure 4.10. From the few voids that were found, they appeared to have an average diameter of ~ 2 nm, and they were present at a density of less than 10^{20} m^{-3} as indicated in Table 4.4. Voids were not observed in the unirradiated 316L TEM specimens.

4.2.4 Radiation induced segregation

The extent of RIS of Cr, Fe, and Ni at the grain boundaries of 7 dpa proton irradiated 316L were measured using STEM-EDS analysis. EDS linescans were performed along boundaries that were aligned edge-on to the optical axis of the microscope as described in Section 3.8, and representative composition profiles at grain boundaries of unirradiated and 7 dpa proton irradiated 316L are shown in Figure 4.11 (a). Coherent Σ3 boundaries were excluded from the RIS analysis, and the measurements were performed on two boundaries to verify consistency in the composition profiles.

Spot measurements located directly on the grain boundaries of unirradiated 316L indicated Cr enrichment of 2.3 wt% over the bulk composition, Fe depletion of 5.9 wt%, and neither enrichment or depletion of Ni as shown in Figure 4.11 (b). Following proton irradiation to 7 dpa at 400˚C the chromium depleted by 2.4 wt% compared to the bulk

composition to reach a final level of 14.4 wt%. The change in the Fe composition at the grain boundary compared to the unirradiated condition was negligible, and the Ni composition enriched by 8.6 wt% compared to the bulk composition to reach a final level of 18.9 wt%. The RIS measurements are summarized in Table 4.5.

4.3 Deformation behavior

This section characterizes the deformation behavior of the proton irradiated 316L stainless steel strained in 400˚C SCW and examines the influence of the Schmid and Taylor factors of grains on their deformation propensities. The deformation behavior of the unirradiated 316L and 316LGBE specimens strained in 500˚C SCW were not characterized. Dislocation channels do not develop in unirradiated materials, and any slip lines formed as a result of deformation were not easily discernable as a result of the oxidation that occurred following the lengthy exposure in 500˚C SCW.

Measured correlations between deformation behavior and the Schmid and Taylor factors would support the use of these parameters as a platform for evaluating the relationship between deformation and cracking. In some instances, the influences of the grain boundary character and inclination on the deformation behaviors are also evaluated. The deformation behavior is quantified through various measures, (1) the number of activated slip planes in the grain, (2) AFM analysis of the step height and spacing created by the dislocation channeling, (3) SEM analysis of the slip continuity behavior at the grain boundary, and (4) OIM^{TM} analysis of the lattice rotation that occurs in individual grains.

4.3.1 Strain measurements

In this study, the strains reported for the irradiated specimens (2%, 5%, and 10%) are the macroscopic plastic strains of the tensile specimens. The plastic strains in the irradiated regions, however, were lower as a result of the higher yield strength of the material in such regions, which will be discussed extensively in Chapter 5. The plastic strains in the irradiated regions were measured from the spacing of the indents on the gage surfaces of the specimens as described in Section 3.9. As indicated in Table 3.6, the plastic strains in the irradiated regions following macroscopic plastic straining to 2%, 5%, and 10% were approximately 0.9 ± 0.2%, 3.9 ± 0.3%, and 8.0 ± 0.4%, respectively.

4.3.2 General dislocation channeling observations

The deformation in the proton irradiated regions of the 316L tensile specimens was heterogeneous in comparison to the unirradiated 316L. While the grains on the gage surface of the unirradiated 316L had fine, closely spaced slip lines, those on the gage surface of the irradiated 316L had coarser dislocation channels with varied spacing and height.

The locations along the gage surfaces at the border between the unirradiated and irradiated regions are interesting, as single grains are often partially irradiated and the accommodation of deformation can be analyzed in both conditions. In some grains, as shown in Figure 4.12(a), the dislocation channels simply fade as they enter the unirradiated region. In others, as shown in Figure 4.12(b), the dislocation channeling and slip line behavior are both visible along the same slip plane, but the spacing of the lines increases from the unirradiated to irradiated region. It was also observed that some

unirradiated regions of grains had multiple active slip planes, while the irradiated regions appeared to only have a single active slip plane as shown in (c). Some of the dislocation channels from one of the active slip planes appear continuous across the unirradiated to irradiated regions, while the slip lines from the second active slip plane are not visible in the irradiated region. The opposite was also observed, where multiple slip planes were active in the irradiated region, and a single slip plane appeared active in the unirradiated region as shown in (d).

4.3.3 Slip plane activation

The number of active slip planes in individual grains of the proton irradiated 316L specimens were determined through SEM analysis of the oxide stripped gage surfaces following straining to 5% in 400˚C SCW. The criterion used to make this determination was that more than two dislocation channels along a given plane must be discernable in a grain at a magnification of 150x for the slip plane to be considered active. One of the oxide stripped regions of the gage surface used to perform this analysis is shown in Figure 4.13.

SEM analysis revealed that only a single slip plane appeared to be active in 53% of grains, two slip planes were active in 37% of the grains, three were active in 3% of the grains, and none were active in 7% of the grains. These results are tabulated in Table 4.6 and plotted in Figure 4.13. The ability to activate two independent slip systems on a given $\{111\}$ slip plane indicates that a maximum of 2, 4, and 6 slip systems were active in grains where 1, 2, and 3 slip planes were observed to be active. It should be considered, however, that at specific crystallographic orientations where the surfaces traces of the

{111} planes are parallel, it may appear that only a single slip plane is active when two slip systems are truly active. As long as the surfaces traces deviate by more than 5˚, however, the slip planes can be visibly discerned.

The probability of activating a specified number of slip planes was also evaluated as a function of which Schmid and Taylor factor category the grain belonged to, i.e. low, medium, or high. As shown in Figure 4.14, the most striking trend is that the probability of the activation of multiple slip planes is greatest in grains with low Taylor factors, and to a lesser extent, in grains with high Schmid factors. The probabilities of activating two slip planes are similar in the low and medium Schmid factor categories and the medium and high Taylor factor categories and range from 0.23 to 0.31. The probability is substantially higher, however, for the low Taylor factor category, 0.61, and the high Schmid factor category, 0.50. Of the four grains that were found to have 3 active slip planes, all were included in the low Taylor factor category.

4.3.4 Dislocation channeling

The height and spacing of the steps that formed on the gage surfaces of the specimens as a result of the formation of dislocation channels were analyzed using NanoScope™ IIIa Phase Atomic Force Microscope in tapping mode as described in Section 3.11. The measurements were performed on polymer replicas of the oxide stripped gage surfaces of the proton irradiated specimens that had been strained in 400˚C SCW. Measurements were performed only on grains where a single slip plane was active, and where a minimum of three dislocation channels were discernable. The fact that these measurements were limited to grains with a single active slip plane makes these

measurements more applicable to Schmid analyses, which account for the activation of a single slip system.

The average step height in each of the 38 grains analyzed was determined by taking the average height of all steps measured in the grain. The heights were measured as the vertical distance from the peak of the step to the adjacent minimum as indicated in Figure 4.15. The average step height as a function of Schmid factor following straining to 2% and 5% are shown in Figure 4.15. There is substantial scatter in the data and no clear correlation between the average step height and the Schmid factor of the grain. The average step height data was divided into the low, medium, and high Schmid factor categories, and the average value for each category was determined. As shown in Figure 4.16, the averaged step height values in each category are similar.

The average step spacing, S_S, in each of the grains was calculated by dividing the distance between the peaks of the first and last steps, ℓ, by the number of steps analyzed, n_S, minus 1,

$$S_S = \frac{\ell}{n_S - 1}. \tag{4.1}$$

The average step spacing is plotted as a function of the Schmid factor following straining to 2% and 5% in SCW in Figure 4.17. The scatter in the data is again large, and no definitive correlation is observed. The average channel spacing was divided into the low, medium, and high Schmid factor categories, and an average value was calculated for each category. The results are plotted in Figure 4.18, where it can be seen that the average step spacing is similar in each category. The surface step measurements for all 38 grains

are summarized in Table 4.7. All of the raw AFM measurements are given in Appendix C.

Interpretation of the step height and spacing measurements requires additional consideration, as they were performed on the specimen surface, and the inclination of the dislocation channels with respect to the sample surface is unknown. Therefore, the actual displacement along the slip plane and minimum dislocation channel spacing are also unknown. These issues will be discussed in greater depth in Chapter 5.

4.3.5 Localized lattice rotation

The localized lattice rotation that occurred in the individual grains of the proton irradiated 316L was evaluated through OIM^{TM} analysis of the oxide stripped gage surface of the specimen following straining in SCW. Color coded maps were generated which indicated the misorientation of an individual point within the grain with respect to the average grain orientation as described in Section 3.4. As discussed in Section 3.9, the plastic strains in the irradiated regions of the specimens following macroscopic strains of 2%, 5%, and 10% were approximately 0.9%, 3.9%, and 8.0%, respectively. Therefore, minimal lattice rotation was detected following straining to 2%, but significant amounts were detected following straining to 5% and 10%, as can be seen in Figure 4.19.

The relationship between localized lattice rotation and the Schmid and Taylor factors of the grains was analyzed on a specimen following straining to 5%. A large area of approximately 0.7 mm x 1.4 mm was scanned with a step size of 2.5 μm. As can be seen from Figure 4.19, the localized lattice rotation occurred primarily along grain boundaries, and sometimes in multiple locations in a given grain. In some regions, the

lattice rotation was mirrored across the grain boundary into the adjacent grain, while in others it abruptly ended at the grain boundary. The regions with progressive local lattice rotations of >4˚ that were adjacent to grain boundaries were recorded and tabulated along with the Schmid and Taylor factors of the grains. Progressive localized lattice rotation here is defined as regions where the color gradient in the OIM^{TM} map builds up to a region with a >4˚ lattice rotation. Therefore potentially erroneously indexed isolated points and those on grain interiors are excluded. Using this method, multiple regions with lattice rotation of >4˚ may be recorded for each grain. Each region is defined as the area adjacent to a grain boundary segment. The regions with >4˚ rotation were binned according to their Schmid and Taylor factors, and the fraction of data points in each bin is plotted in Figure 4.20. This distribution is compared to the Schmid and Taylor factor in the specific area analyzed. It can be seen that the propensity for localized lattice rotation increases with the Taylor factor of the grain, but there does not appear to be a relationship between Schmid factor and localized lattice rotation.

4.3.6 Slip continuity

The dislocation channeling and deformation behavior in the grain matrix has been discussed in the previous sections; this section will focus on the propensity for slip continuity across a grain boundary in proton irradiated 316L stainless steel. When a dislocation channel intersects a grain boundary, it may immediately induce the formation of a dislocation channel in the adjacent grain (slip continuity), or it may arrest at the grain boundary (slip discontinuity) as illustrated in Figure 4.21. The dependence of slip continuity across the grain boundary on the trace inclination, grain boundary character,

and the Schmid and Taylor factors of the adjacent grains were analyzed for the oxide stripped specimens strained to 5% in 400˚C SCW. All slip continuity measurements performed are given in Appendix D.

The trace inclination was defined in Figure 4.1 as the inclination of the surface trace of the grain boundary plane to the tensile axis. The trace inclination was measured at each of the 502 locations in the area analyzed where a dislocation channel was observed to directly intersect a grain boundary, and the behavior at the grain boundary was characterized as either slip continuity or slip discontinuity at a magnification of 1000x. The behavior was characterized as slip continuity if the majority (>50%) of the slip channels that intersected the grain boundary followed continuous paths into the adjacent grain. Several examples of slip continuity and discontinuity are shown in Figure 4.22. By binning the data into 10˚ trace inclination increments, the fraction of boundaries in each inclination bin that exhibited slip continuity was determined and regarded as the probability of slip continuity for a given trace inclination. As shown in Figure 4.23(a), the probability of slip continuity is fairly constant from 0 to approximately 30˚ at 0.80, decreases sharply at trace inclinations between 30˚ and 50˚, and then levels off at a probability of approximately 0.30 for greater inclinations above 50°. The uncertainties in Figure 4.23 were calculated using equation (3.12).

The dependence of slip continuity on the character of the grain boundaries was also evaluated. The slip continuity and discontinuity behaviors were evaluated at the grain boundaries and grouped according to whether they were RHABs or some type of special boundary (LAB, Σ3, Σ9, or Σ27). The fractions of RHABs and special boundaries that underwent slip continuity were found to be 0.48 and 0.79, respectively, as shown in

Figure 4.23(b). It was shown in Figure 4.23(a) that slip continuity is strongly dependent on the trace inclination. Therefore, the probability of slip continuity at RHABs and special boundaries was also evaluated exclusively for the boundaries inclined greater than the threshold value of 50˚, which included 167 grain boundaries. Results of these measurements indicated that the probability for slip continuity was 0.24 at RHABs and 0.52 at special boundaries. Therefore, regardless of the inclination of the grain boundary, special boundaries were more likely to transmit slip than RHABs.

The Schmid and Taylor factors adjacent to the grain boundary of interest were also determined. Each grain boundary could be characterized according to the Schmid and Taylor factors of the adjacent grains. Adjacent grains with low Schmid factors would be characterized as LL type, a boundary adjacent to grains with low and medium Schmid factors would be characterized as LM, etc. Therefore, 6 different Schmid and Taylor factor pair types are possible (LL, LM, LH, MM, MH, HH). By categorizing the occurrences of slip continuity and discontinuity according to the Schmid and Taylor factor pair types of the adjacent grains, the probability of slip continuity as a function of pair type was determined. When all data were included in the analysis, no clear correlation was measured between Schmid and Taylor factor pair types and cracking, with the probability of slip continuity being 0.50 to 0.65 for all pair types as indicated in Table 4.8. As previously shown in Figure 4.23(a) and (b), the probability of slip continuity is strongly dependent on both the trace inclination and character. By including only boundaries above the threshold value of 50˚ and RHABs, which included 127 data points, correlations between Schmid and Taylor factor pair types and slip continuity were detected. As shown in Figure 4.23(c) and (d), slip continuity becomes increasingly

probable at boundaries with adjacent high Schmid factor and low Taylor factor pair types. The probability of slip continuity increases from 0 at LL Schmid factor pair types to 0.48 at HH pair types. Similarly the probability of slip continuity decreases from 0.57 at LL Taylor factor pair types to 0 at HH pair types.

In addition to evaluating the influence of the Schmid and Taylor factor pair types on the slip continuity at the grain boundary, the influence of the Schmid and Taylor factor mismatch of the adjacent grains on slip continuity was also analyzed. The mismatch was calculated by subtracting the Schmid/Taylor factor of the grain with the lower value from that of the adjacent grain with the higher value. Therefore, the Schmid and Taylor factor mismatch range measured extended from 0-0.22 and 0-1.4, respectively. The Schmid and Taylor factor mismatch ranges were divided into three bins, 0-0.01, 0.02-0.04, and 0.05-0.19 for Schmid factor mismatch, and 0-0.26, 0.27-0.56, and 0.57-1.28 for the Taylor factor mismatch. The probability of slip continuity in each bin was determined from the fraction of boundaries where slip continuity occurred. Again, no clear correlation was observed between Schmid or Taylor factor mismatch and cracking when all data were included. The probability of slip continuity ranged from 0.54 to 0.65 as indicated in Table 4.8. When the data from boundaries at inclinations of $\leq 50^{\circ}$ and special boundaries were excluded, however, a correlation between Schmid factor mismatch and continuity was revealed. As shown in Figure 4.23(e), the probability of slip continuity drops from 0.33 in the mismatch range of 0-0.1 to 0.14 at mismatches of 0.05-0.23. It should be noted, however, that large mismatch values require that one of the two adjacent grains have a low Schmid factor. No clear correlation was observed between Taylor factor

mismatch and cracking, however, and the probabilities of slip continuity in the three bins ranged from 0.21 to 0.26.

4.4 Intergranular cracking in supercritical water

This section describes the intergranular cracking behaviors of both the unirradiated 316L and 316LGBE specimens strained in 500˚C SCW and the 7 dpa proton irradiated 316L specimens strained in 400˚C SCW. The intergranular cracking behaviors on the gage surfaces of the specimens were analyzed through SEM analysis following incremental straining in SCW as described in Section 3.10. The unirradiated specimens were strained in deaerated 500˚C SCW to approximately 15% and 25% nominal strain, and the proton irradiated specimens were strained to approximately 2%, 5%, and 10% plastic strain. After each straining increment, the specimens were removed from the autoclave system for SEM analysis. Half of each of the four proton irradiated specimens was scratched prior to straining, and one of the four specimens was oxide stripped between each straining increment to perform AFM and OIM^{TM} analysis in addition to analyzing the cracking behavior. All of the cracked boundaries observed on the specimens were characterized according to the Schmid and Taylor factors of the adjacent grains, the trace inclination, and the grain boundary character. The measurements are summarized in Table 4.9 where it can be seen that intergranular NS cracks (defined in Section 3.10) occur preferentially adjacent to grains with low Schmid factors and high Taylor factors, large trace inclinations, and along RHABs. These relationships will be shown graphically in the subsequent sections. All crack measurements are given in Appendix E.

4.4.1 Crack morphology

The cracks on the gage surfaces of the 316L specimens following straining in SCW were primarily short and intergranular. Figure 4.24 through Figure 4.29 show low and high magnification images of the cracks on the gage surfaces of the specimens following straining. The cracks on the 316L and 316LGBE strained in 500˚C SCW to 15% and 25% strain were primarily intergranular in nature, but often arrest at triple junctions and continue to slowly grow as shallow transgranular cracks perpendicular to the tensile direction with subsequent straining as shown in Figure 4.25 and Figure 4.27. Some of the cracks propagate with strain as shown by the increase in the length of the cracks in the center of Figure 4.24 and Figure 4.26 following straining to 15% and 25%, but many do not.

IG cracks were also found on the proton irradiated specimens strained in 400˚C SCW as shown in Figure 4.28 and Figure 4.29 following straining to 2%, 5%, and 10% strain, but no transgranular cracks were observed. The high densities of dislocation channels are readily observed on the oxide stripped gage surfaces of the specimens following straining to 10% as shown in Figure 4.28. The channels were often aligned near 45˚ and greater with respect to the tensile axis, and their spacing decreased with strain. New cracks developed with subsequent straining, but the extent of crack propagation was relatively low as shown in Figure 4.29. The average number of cracked boundaries per crack was 1.1, 1.4, and 1.6 at 2%, 5%, and 10% strain, respectively. The existing cracks widened with subsequent straining and became easily discernable. Micrographs of each of the 409 cracks analyzed on the proton irradiated specimens at their final straining increment are shown in Appendix F.

In addition to the cracks shown in Figure 4.24 through Figure 4.29, cracks of a different morphology were also observed on the proton irradiated 316L specimens. The distinguishing feature of these cracks was that they occurred directly at the intersection of dislocation channels with grain boundaries and their lengths were limited to the distance between dislocation channels as seen in Figure 4.30. As described in Section 3.10, these cracks will be referred to as GBC cracks and the others will be referred to as NS cracks. Micrographs of each of the 102 GBC cracks analyzed on the proton irradiated specimens at 5% strain are shown in the Appendix F.

4.4.2 Schmid and Taylor factor dependence of NS cracks

The Schmid and Taylor factors of the grains adjacent to the NS cracked grain boundaries were determined by comparing OIM^{TM} Schmid and Taylor factor maps to the micrographs of the gage surfaces of the specimens following straining in SCW, as shown in Figure 4.31. Each of the cracked grain boundaries that comprised each crack were analyzed individually, and the Schmid and Taylor factor mismatch at each cracked boundary was determined by subtracting the lesser value from the greater value. In order to understand the influence of Schmid and Taylor factor mismatch on cracking propensity, the mismatch distribution in the alloy as a whole was considered. The distribution was calculated from the total Schmid and Taylor factor distributions shown in Figure 4.4. It was assumed that the grains were randomly distributed; that the probability of any two grains being adjacent to one another was equally likely. The total Schmid and Taylor factor mismatch distributions are shown in Figure 4.32(a) and (d). Both indicate that the probability of encountering adjacent grains with large mismatch is

unlikely. Consider that having a Schmid factor mismatch of 0.22 would require that the grain with the greatest Schmid factor (0.50) be adjacent to the grain with the lowest Schmid factor measured in the proton irradiated samples (0.28); as shown in Figure 4.32(a), the probability of this occurring is 0.003 or 1 out of every 370 grain boundaries.

The distributions of Schmid and Taylor factor mismatch adjacent to the cracked boundaries at 2%, 5%, and 10% strain are similar to the total mismatch distributions as shown in Figure 4.32(b) and (e). The crack data was normalized to the total mismatch distribution by dividing each Taylor/Schmid factor mismatch bin by that of the total distribution. The results are shown in Figure 4.32(c) and (f), and the error bars were calculated using equation (3.15). No obvious correlation between cracking and Taylor factor mismatch was observed, although a weak correlation between Schmid factor mismatch and cracking may exist at low strains. The Schmid and Taylor factor mismatch measurements at the cracked grain boundaries are summarized in Table 4.10 and Table 4.11, respectively.

In addition to the Schmid and Taylor factor mismatch, the Schmid and Taylor factor pair types of the grains adjacent to the cracked boundaries were determined and categorized as LL, LM, LH, MM, MH, or HH as described in Section 4.3. When a cracked grain boundary is analyzed, it is unknown whether the deformation behavior of one or both of the grains adjacent to the boundary may be responsible for crack formation. Therefore, the Taylor and Schmid factors of both adjacent grains are analyzed. It must be considered that the probabilities of encountering each pair type is not equal despite the fact that each bin, L, M, H, contains one-third of the total population of grains. The probability of encountering adjacent grains with LL, LM, LH, MM, MH,

and HH pair types are 1/9, 2/9, 2/9, 1/9, 2/9, and 1/9, respectively. Therefore, when the normalized cracked fractions are reported, they indicate the cracked fraction in the category specified divided by probability of encountering the pair type in the total population. The resulting normalized cracked fractions are shown in Figure 4.33 through Figure 4.36.

The Schmid factor pair type distributions all indicate that cracks preferentially occur adjacent to grains with low Schmid factors. This is observed for the unirradiated 316L and 316LGBE specimens strained to 15% and 25% strain in 500˚C SCW in Figure 4.33(a) through (d). The relationship is stronger at 15% than at 25% for both specimens, but it is observed at both levels of strain. The Schmid factor pair type data collected for the cracks in the proton irradiated specimens strained in 400˚C SCW indicates a strong preference for the cracks to occur adjacent to grains with low Schmid factors at 2% strain that gradually decreases with subsequent straining to 5% and 10% strain. At 2%, 5%, and 10% strain, 92%, 78%, and 67% of the cracked boundaries occurred adjacent to at least one low Schmid factor grain.

A similar, but inverse correlation between Taylor factor pair type and cracking was also observed. IG cracks preferentially occurred adjacent to grains with high Taylor factors as shown in Figure 4.35 and Figure 4.36. As shown in Figure 4.35, the IG cracks in the unirradiated 316L and 316LGBE following straining to 15% and 25% in 500˚C SCW preferentially occurred at boundaries adjacent to high Taylor factor grains, and the trend decreased with progressive straining. As shown in Figure 4.36, the same trend was observed in the proton irradiated 316L. The fraction of cracks occurring adjacent to at

least 1 high Taylor factor grain in the proton irradiated stainless steel were 84%, 71%, and 62% at 2%, 5%, and 10% strain, respectively.

These results illustrate that the intergranular NS cracking behavior of 316L in SCW correlates with both the Schmid factors and Taylor factors of the grains adjacent to the cracked boundary. The correlation between low Schmid factor and cracking, however, is consistently greater than that of high Taylor factor. The reasons and implications of these observations will be discussed in detail in Chapter 5.

4.4.3 Grain boundary trace inclination dependence of NS cracks

The propensity for NS cracks to occur along boundaries with trace inclinations perpendicular to the tensile axis can be seen from Figure 4.37 and Figure 4.38. Each of the cracked grain boundaries was analyzed and the trace inclination of the cracked grain boundary was measured by drawing a line from one end of the cracked grain boundary segment to the other end and determining the inclination of the line with respect to the tensile axis.

The NS cracks that formed on both the unirradiated and irradiated specimens that were strained in SCW demonstrated strong tendencies to form along grain boundaries which had trace inclinations perpendicular to the tensile axis. The inclination of the cracked grain boundary segments on the 316L and 316LGBE specimens following straining to 15% and 25% strain are shown in Figure 4.37. At 15% and 25% strain, 96% and 86% of the cracks on the 316L specimens strained in 500˚C SCW are inclined >60˚ with respect to the tensile axis. Similarly, 100% and 98% of the cracks on the 316LGBE specimen are inclined >60˚ to the tensile axis, respectively.

The NS cracks that formed on the proton irradiated specimens strained in 400˚C SCW also preferentially occurred along boundaries aligned perpendicular to the tensile axis. Figure 4.38 shows that at 2% strain, the cracked boundary inclination distribution is strongly peaked at 90˚. The distribution broadens substantially with subsequent straining to 5% and 10% strain, but the correlation is present for all three straining increments. At 2%, 5%, and 10% strain, 90%, 82%, and 76% of the cracked boundaries have trace inclinations >60˚.

4.4.4 Cross sectional analysis of NS crack penetration

The direction of penetration of the NS cracks into the substrate was analyzed from cross-sectional micrographs of the specimens. This analysis was performed on a 316L specimen from a previous study that had been irradiated under identical conditions (400˚C, 7 dpa, 2 MeV protons) and strained to failure in 400˚C SCW at the same strain rate, 3×10^{-7} s^{-1}. It can be seen from the cross-sectional micrographs in Figure 4.39 that the penetration of the cracks into the sample substrate along the grain boundaries preferentially occurred perpendicular to the tensile direction. The cracks generally penetrated through most of the irradiated regions of the specimen, but propagation generally did not continue into the unirradiated material. The direction of crack penetration, combined with the observation that the distributions of the cracked trace inclinations peaked at 90˚, confirmed that the NS cracks preferentially occurred along grain boundary *planes* aligned perpendicular to the tensile direction.

4.4.5 Grain boundary character dependence of NS cracks

The characters of the grain boundaries that cracked were determined by comparing grain boundary character maps to micrographs of the cracks on the specimen surfaces following straining in SCW as shown in Figure 4.31 and described in Section 3.10. The total fraction of RHABs and special boundaries (LAB, Σ3, Σ9, and Σ27) that cracked was determined. As shown in Figure 4.40, the RHABs in the unirradiated 316L and 316LGBE specimens strained in 500˚C SCW and the irradiated 316L specimens strained in 400˚C SCW had greater cracking propensities than the special boundaries.

The IG cracks on the 316L and 316LGBE strained in 500˚C SCW occurred primarily along RHABs, but the special boundaries did not exhibit immunity to cracking. Following straining to 15%, the percentage of special boundaries that cracked were 0.3 ± 0.2% and 0% for the 316L and 316LGBE, respectively. Following straining to 25%, the percentage increased to 1.2 ± 0.3% and 0.7 ± 0.2%, respectively. These percentages were all much less than that of the RHABs, which had cracked percentages of 10.5 ± 0.8% and 5.3 ± 0.5% for the 316L and 316LGBE, respectively, following straining to 25%.

The IG cracks on the proton irradiated 316L strained in 400˚C SCW also preferentially occurred at the RHABs. As the strain increased from 2% to 5% and 10%, the cracked fraction of special boundaries increased from 0% to 0.17 ± 0.04% to 1.2 ± 0.2%, respectively. The RHAB cracked fraction was much greater and increased from 0.24 ± 0.03% to 1.9 ± 0.1% and finally 11.7 ± 0.5%. Therefore, the results from both the 400˚C and 500˚C SCW experiments indicate that the RHABs are roughly an order of magnitude more likely to crack than the special boundaries. When special boundaries

were observed to crack, they were found to be 7-12 times less likely to crack than the RHABs.

4.4.6 Grain boundary channel (GBC) cracks

The GBC cracks were analyzed in a manner similar to that of the NS cracks. The gage surfaces of the specimens were scanned at a magnification of 1000x, and all observed GBC cracks were characterized. At 5% strain, the Schmid and Taylor factors adjacent to the GBC cracks, grain boundary characters, and trace inclinations were determined through visual inspection and comparisons of the SEM micrographs with the OIM^{TM} scans. At 2% and 10% strain, only the trace inclinations were determined. If multiple GBC cracks developed along a single grain boundary segment, as shown in Figure 4.30, the boundary was only counted a single crack occurrence.

The GBC cracks were the dominant form of intergranular cracking at 2% strain, but by 10% strain, the density of NS cracks was significantly higher as shown in Figure 4.41. The GBC cracks did not exhibit a strong tendency to form at grain boundaries adjacent to grains with high or low Schmid or Taylor as shown in Figure 4.42. The distributions of the trace inclinations of the GBC cracks were broader than those of the NS cracks. At 2% strain, the GBC cracks appeared to occur preferentially along boundaries with higher inclinations as shown in Figure 4.43, but the distribution was broader than that of the NS cracks. At 5% and 10% strain, fewer GBC cracks occurred along boundaries that were highly inclined to the tensile axis, and a peak developed between 30˚ and 50˚ as shown in Figure 4.43. GBC cracks were observed to occur along

boundaries with a broad range of trace inclinations, even a few boundaries nearly parallel to the tensile axis.

Some of the GBC cracks developed into NS cracks with subsequent straining, but the majority did not. Of the total 102 GBC cracks analyzed at 5% strain, 37 or 36% developed into NS cracks following straining to 10%. In a select 2 mm^2 region of the oxide stripped specimen at 5% strain, 86 GBC cracks were found. Of those, 31 (36%) developed into NS cracks at 10% strain. From 5% to 10% strain, the total cracked boundary density increased by a factor of 6 and the development of the GBC cracks into NS cracks only accounts for a factor of 2 the increase. The total grain boundary fraction cracked increased from 1% at 5% strain to 7% at 10% strain. Therefore, a randomly selected uncracked boundary at 5% strain had a 6% probability of developing into an NS crack at 10% strain. A GBC cracked boundary, however, had a 36% probability of developing into an NS crack at 10% strain.

4.4.7 NS cracking in scratched and oxide stripped regions

The effect of scratching and oxide stripping the proton irradiated specimens was evaluated by comparing the NS cracking behavior in these select regions to that in the unscratched and non-stripped regions. Half of each tensile specimen was scratched with 1 μm diamond suspension solution to create surface scratches for GBS analysis as described in Section 3.10. One of the four tensile specimens was oxide stripped with sodium hydroxide + potassium permanganate and ammonium oxalate solutions following each straining increment in SCW as described in Section 3.3 in order to perform AFM and OIM™ analysis on the specimen surface. Images of the scratched and oxide stripped

surfaces are shown in Figure 4.44. The scratches induced plastic deformation on the specimen surface, while the oxide stripping resulted in etching of the grain boundaries. It should be recalled, however, that all NS cracks were analyzed prior to oxide stripping the specimens. Therefore, any observed differences would not simply be due to the appearance of the oxide stripped surface, but would rather be the result of stripping treatments performed prior to straining the specimens in the SCW environment.

Intergranular cracking was observed to preferentially occur adjacent to grains with low Schmid factors and high Taylor factors regardless of whether the materials was scratched or oxide stripped. These Schmid and Taylor factor dependencies are shown in Figure 4.45 and Figure 4.46, respectively. The plots show (a) the relationship between the Schmid and Taylor factor pair types in the unscratched and non-stripped regions of the specimens, (b) data from the scratched regions of the specimens (excluding scratched and stripped regions), and (c) data from the oxide stripped specimen (excluding stripped and scratched regions). The Schmid and Taylor factor pair dependence of the intergranular NS cracking behaviors of the specimens may be slightly stronger in the scratched regions of the specimens, and slightly weaker in the oxide stripped regions. Regardless of the condition of the specimen, however, the IG cracks preferentially occur at grain boundaries adjacent to grains with low Schmid factors. The tendency of the cracks to occur adjacent to grains with high Taylor factors does not appear to be greatly affected in the by either scratching or oxide stripping the specimens.

The relationship between trace inclination and NS cracking propensity does not appear to be affected by scratching or oxide stripping the specimens. As shown in Figure 4.47, the distribution of the cracked grain boundary trace inclinations is peaked near 90˚

at 2%, 5%, and 10% strain regardless of whether the material was scratched or oxide stripped.

The propensity for the NS cracks to form along RHABs was observed regardless of whether the alloy was scratched or oxide stripped, but the strength of the correlation appears to depend on the condition of the material. The fraction of cracks that developed along RHAB and special boundaries as a function of strain for each of the three surface conditions is shown in Figure 4.48. It can be seen that the fraction of cracks at special boundaries was much lower than the fraction of special boundaries in the alloy as a whole, indicating their resistance to cracking. If the cracking susceptibilities of the special boundaries and RHABs were equal, the fraction of cracks at each type of boundary would be equal to its bulk population in the alloy, regardless of the crack density. In the unscratched and non-stripped regions as well as the scratched regions, the fraction of cracks at each type of boundary approached its bulk population in the alloy, indicating the decreasing resistance of special boundaries to IG cracking with progressive straining. In the oxide stripped regions at 10% strain, the fraction of special boundaries that cracked is only 3% compared to 12% in the unscratched and non-stripped material.

In summary, scratching and oxide stripping the specimens does not change the fact that IG cracks preferentially occur adjacent to grains with low Schmid factors and high Taylor factors, along boundaries with trace inclinations perpendicular to the tensile axis, or at RHABs. It may slightly alter the strengths of these correlations, but it is also possible that such variations are simply the result of sample to sample variations in cracking propensity. Therefore, these sets of data will be considered legitimate, and henceforth all data will be included as a single data set.

4.5 Intergranular cracking in argon

The intergranular cracking behavior of proton irradiated 316L was evaluated in a 400˚C purified argon environment as described in Section 3.9. The gage surface of the specimen was scanned at a magnification of 1000x to identify cracked boundaries. Both NS and GBC crack morphologies were observed on the gage surfaces of the specimens following straining to 5% as shown in Figure 4.49. Images of all 5 NS cracks and 25 GBC cracks are shown in Appendix F.

4.5.1 Crack density

The GBC and NS cracking morphologies were both observed on the gage surfaces of the proton irradiated specimen strained in the purified argon environment, but at lower densities than observed in the SCW environment. As indicated in Table 4.13, the densities of NS and GBC cracks in argon were 1.0 and 11.9 mm^{-2}, respectively, while in the 400˚C SCW, the densities were 17.4 and 41.0 mm^{-2}, respectively. These values are plotted in Figure 4.50, where the lower densities of cracks in the argon environment can be readily observed.

4.5.2 Grain boundary trace inclination dependence

The trace inclination distribution for all GBC and NS cracked boundaries does not exhibit a peak near 40-50˚ as was observed for the proton irradiated samples in the 400˚C SCW environment at 5% strain. As shown in Figure 4.51, the distribution is strongly peaked towards boundaries nearly perpendicular to the tensile axis for both the GBC and NS cracked boundaries. All of the NS cracked boundaries analyzed had trace inclinations

of >60˚ to the tensile axis, while 23 out of the 25 GBC cracks were along boundaries with inclinations of >60˚.

4.5.3 Schmid and Taylor factor dependence

The influence of the Schmid and Taylor factors of grains on the GBC cracking propensity of adjacent grain boundaries was evaluated over a 1 mm^2 region of the specimen surface. This region contained 11 GBC cracks and 0 NS cracks. While the number of cracks analyzed was too limited to yield statistically significant measurements of the cracking propensity at each of the Schmid and Taylor factor pair types as shown in Figure 4.52(a) and (b), it can be definitively stated from (c) and (d) that GBC cracks in 400˚C argon preferentially formed adjacent to grains with at least one low Schmid factor grain or at least 1 high Taylor factor grain.

4.6 Deformation surrounding cracks

The deformation surrounding the NS cracked boundaries was analyzed through AFM analysis of the step height and spacing in the grains adjacent to the cracked boundaries and OIM^{TM} analysis of the localized lattice rotation around the cracked boundaries. The correlations that exist between Taylor and Schmid factor and deformation behavior were discussed in Section 4.3, and the objective of this section is to determine if the observed correlations extend to the intergranular cracking behaviors of the proton irradiated 316L.

4.6.1 Dislocation channeling at cracks

The dislocation channeling behavior in grains adjacent to uncracked grain boundaries was discussed in Section 4.3, and this section will compare the measurements with those adjacent to cracked grain boundaries in the proton irradiated specimens strained in SCW. The cracked grain boundaries selected for this analysis had two adjacent grains where a single slip plane was active, as described in Section 4.3. The dislocation channeling behavior in terms of the step spacing and height were determined in both of the two grains for a total of 18 measurements at 9 cracked boundaries.

It was observed that the propensity for the formation of new slip channels declined when NS cracks formed at the adjacent boundary. As shown in Figure 4.53, dislocation channel formation continued in the grain adjacent to GBC cracked grain boundary where full grain boundary separation had not occurred, but new dislocation channels did not develop in the grains adjacent to the NS cracked boundary. This behavior is important because it indicates that knowledge of the dislocation channeling behavior at the precise time of crack nucleation (while desired) is nearly impossible to obtain. Consider for example the NS crack in Figure 4.53. If the crack was first detected at 5% strain, AFM measurements may indicate greater than average channel spacing, even though when the crack actually nucleated at 2% strain, the channel spacing appears to be smaller than average in the grain on the left hand side. Therefore, although the cracked boundaries reported here are those that were detected at 5% strain and were not present at 2% strain, AFM measurements following straining to 2% and 5% strain will be reported. Therefore, these measurements will describe the deformation behavior in the

grains both prior to and following crack nucleation as the cracks must have developed sometime between 2% and 5% strain.

Step height measurements performed following straining to 2% and 5% strain on grains adjacent to boundaries that cracked at 5% strain showed a weak correlation at best with crack formation. The average step height distribution is shown in Figure 4.54 for grains adjacent to uncracked (a), (d) and boundaries that cracked by 5% strain (b), (e). The cracked distribution appears similar to the uncracked distribution, but it peaks at slightly lower values at 2% strain. It should be considered that both of the grains adjacent to the cracked boundary are plotted in Figure 4.54 (b) and (e) and that it is possible that one of the two grains contributed more to the cracking propensity of the adjacent grain boundary than the other. It may be assumed that the grain with the greater average step height would contribute more to the cracking propensity than the other grain. Therefore, instead of plotting the step height data for two grains for each cracked grain boundary, the grain with the greater average step height may be selected and plotted as shown in Figure 4.54 (c) and (f). From the AFM data at 5% strain, it can be seen that at least one of the two grains adjacent to each NS cracked boundary has an average step height of >200 nm following crack formation.

The step spacing measurements in the grains adjacent to the cracked boundaries also showed a weak correlation at best with cracking. As shown in Figure 4.55, the average step spacing distribution for grains adjacent to boundaries that cracked at 5% strain (performed at 2% and 5% strain), appears similar to the uncracked distributions. It may be assumed that the grain with the closer average channel spacing contributes more to crack development than the other grain. By plotting only the grain with the smaller

channel spacing, it can be seen from Figure 4.55(f) that at least one of the two grains adjacent to each NS cracked boundary has an average channel spacing of <6 μm.

4.6.2 Localized lattice rotation at cracks

The lattice rotation around the NS cracked boundaries was analyzed by performing high resolution OIM™ scans on the metal surrounding the crack. The scans were performed at magnifications as high as 4000x and step sizes as low as 0.1 μm.

It was observed that localized lattice rotation initially developed around triple junctions at either end of the crack and then extended over more extensive regions of the metal. The localized lattice rotation measurements were performed on the specimens after unloading them from the autoclave system. Because of the absence of an applied load, the localized lattice rotation measurements reflect plastic rather than elastic deformation in the specimens. Localized lattice rotation maps are shown in Figure 4.56 at 2%, 5%, and 10% strain. When the cracks first developed, the lattice rotation was primarily visible around the triple junctions. As the straining progressed, the lattice rotation either spread along the extent of the cracked boundary or along adjoining boundaries. The development of localized lattice rotation as a continuous gradient rather than as an abrupt change in the grain orientation indicates that new grain boundaries (as defined in this study as having misorientations of >10˚) have not formed.

Table 4.1 Low, medium, and high ranges for Schmid (m) and Taylor (M) factors of grains in 316L stainless steel.

Tensile specimen	Category	m	M
400˚C, SCW 316L, 7 dpa Specimen #1	Low	0.27 - 0.44	2.27 - 2.90
	Medium	0.45 - 0.47	2.91 - 3.30
	High	0.48 - 0.50	3.31-3.67
400˚C, SCW 316L, 7 dpa Specimen #2	Low	0.27-0.45	2.27-2.90
	Medium	0.46-0.47	2.91-3.34
	High	0.48-0.50	3.35-3.67
400˚C, SCW 316L, 7 dpa Specimen #3	Low	0.27-0.42	2.27-2.89
	Medium	0.43-0.46	2.90-3.31
	High	0.47-0.50	3.32-3.67
400˚C, SCW 316L, 7 dpa Specimen #4	Low	0.27-0.45	2.27-2.98
	Medium	0.46-0.48	2.99-3.40
	High	0.49-0.50	3.41-3.67
400˚C, Argon 316L, 7 dpa	Low	0.27-0.44	2.27-2.85
	Medium	0.45-0.47	2.86-3.27
	High	0.48-0.50	3.28-3.67
500˚C, SCW 316L, 0 dpa	Low	0.27-0.42	2.27-2.81
	Medium	0.43-0.46	2.82-3.27
	High	0.47-0.50	3.28-3.67
500˚C, SCW 316LGBE, 0 dpa	Low	0.27-0.44	2.27-2.93
	Medium	0.45-0.47	2.94-3.35
	High	0.48-0.50	3.36-3.67

Table 4.2 Grain boundary number fractions of RHAB, LAB, Σ3, Σ9, and Σ27 boundaries in 316L and 316LGBE. Uncertainties were calculated using equation (3.12)

Grain boundary character	Number fraction 316L	Number fraction 316LGBE
RHAB	0.579 ± 0.005	0.484 ± 0.009
LAB	0.023 ± 0.002	0.019 ± 0.002
Σ3	0.334 ± 0.005	0.385 ± 0.009
Σ9	0.048 ± 0.002	0.077 ± 0.005
Σ27	0.015 ± 0.001	0.035 ± 0.003

Table 4.3 Proton irradiation induced hardening following 400˚C, 7 dpa irradiations with 2 and 3 MeV protons. A total of three irradiations were performed to generated sets of specimens for each of the experiments listed. Uncertainties indicated are the standard deviations of the hardness measurements.

Experiment	Proton energy (MeV)	Unirradiated hardness (Hv)	Irradiated hardness (Hv)	Irradiation induced hardening (Hv)
TEM analysis	3	149 ± 8	386 ± 12	237 ± 14
SCW CERT	2	145 ± 8	382 ± 17	237 ± 19
Argon CERT	2	150 ± 10	376 ± 13	226 ± 16

Table 4.4 Dislocation loop and void density measurements for 316L proton irradiated to 7 dpa at 400˚C.

Feature	# Measured	Avg. diameter (nm)	Density (#/m^3)
Dislocation loops	492	6.9	5.3×10^{22}
Voids	NA	~2	$<10^{20}$

Table 4.5 Compositions of Cr, Fe, and Ni in the bulk of 316L and at unirradiated and proton irradiated grain boundaries.

Element	Bulk composition (wt%)	Unirradiated composition (wt%)	7 dpa, 400C composition (wt%)
Cr	16.8	19.1±1.1	14.4±0.5
Fe	69.7	63.8±2.9	63.2±0.6
Ni	10.3	9.5±0.5	18.9±0.6

Table 4.6 Number and probability of active slip systems in grains with low, medium, and high Schmid and Taylor factors in proton irradiated 316L strained to 5% in 400˚C SCW. Uncertainties were calculated using equation (3.15).

		Number of active slip planes				Probability of number of active slip planes			
	Category	0	1	2	3	0	1	2	3
Schmid factor	Low	3	27	11	1	0.07 ± 0.04	0.64 ± 0.07	0.26 ± 0.07	0.02 ± 0.03
	Medium	3	19	11	2	0.09 ± 0.05	0.54 ± 0.08	0.31 ± 0.08	0.06 ± 0.04
	High	2	21	24	1	0.04 ± 0.03	0.44 ± 0.07	0.50 ± 0.07	0.02 ± 0.02
Taylor factor	Low	3	10	27	4	0.07 ± 0.04	0.23 ± 0.06	0.61 ± 0.07	0.09 ± 0.04
	Medium	1	30	9	0	0.03 ± 0.02	0.75 ± 0.07	0.23 ± 0.07	0
	High	4	27	10	0	0.10 ± 0.05	0.66 ± 0.07	0.24 ± 0.07	0
Total	---	8	67	46	4	0.06 ± 0.02	0.54 ± 0.04	0.37 ± 0.04	0.03 ± 0.02

Table 4.7 Slip step measurements for proton irradiated 316L strained to 2% and 5% strain in 400˚C SCW.

		Avg. step height (nm)		Max. step height (nm)		Avg. step spacing (μm)	
m	M	2%	5%	2%	5%	2%	5%
0.46	3.54	382	240	659	496	9.50	3.50
0.45	3.57	215	170	306	350	11.67	4.93
0.43	3.61	409	271	849	497	12.00	4.69
0.44	3.63	311	308	669	680	6.47	3.78
0.39	3.47	211	182	528	631	6.00	2.65
0.48	3.41	393	383	828	659	7.00	4.57
0.46	3.54	262	269	467	525	5.56	4.00
0.48	3.42	219	277	358	513	6.50	3.92
0.48	2.42	135	320	191	447	10.75	7.90
0.47	2.41	199	319	311	457	7.60	5.71
0.43	2.34	114	155	177	300	7.50	4.29
0.48	2.42	339	541	461	1064	13.67	13.00
0.46	2.59	302	239	366	369	13.50	6.14
0.50	2.78	98	225	209	428	5.80	5.63
0.49	2.55	309	277	354	506	10.50	4.36
0.50	2.71	405	284	495	531	10.00	3.73
0.45	2.34	309	171	392	543	11.50	5.83
0.49	2.80	84	117	168	273	3.22	2.83
0.47	2.40	406	339	607	451	8.50	5.29
0.47	2.72	42	81	86	159	6.13	3.26
0.47	2.89	223	243	417	374	10.67	5.62
0.46	2.83	204	307	399	459	9.75	8.14
0.49	2.80	206	235	362	329	15.00	6.63
0.48	3.30	296	303	563	508	15.60	6.92
0.44	3.14	76	131	146	311	6.50	3.70
0.49	3.30	240	253	342	559	6.20	3.50
0.50	2.93	347	338	536	438	13.75	6.29
0.49	3.11	288	313	504	673	10.00	5.00
0.47	3.48	277	223	508	457	9.30	3.79
0.49	3.21	204	260	369	460	6.14	4.50
0.44	3.23	254	193	316	317	9.80	4.29
0.50	3.12	234	221	304	400	7.20	3.93
0.49	3.33	198	235	341	365	5.55	3.83
0.49	3.20	445	426	583	768	13.50	6.38
0.49	3.23	248	225	389	463	8.25	6.20
0.50	3.07	363	199	412	408	14.33	4.92
0.46	3.27	215	258	413	738	7.00	4.47
0.48	2.94	320	386	421	636	16.67	7.75
Averages		257	261	416	488	9	5

Table 4.8 Slip continuity dependence on boundary type, Schmid and Taylor factor, and trace inclination. Uncertainties were calculated using equation (3.15).

		All data		**>50˚ only**		**>50˚, RHABs only**	
		Prob. slip cont.	Prob. slip discont.	Prob. slip cont.	Prob. slip discont.	Prob. slip cont.	Prob. slip discont.
Bdy type	RHABs	0.48 ± 0.03	0.52 ± 0.03	0.24 ± 0.04	0.76 ± 0.04	---	---
	Special	0.79 ± 0.03	0.21 ± 0.03	0.52 ± 0.08	0.48 ± 0.08	---	---
Schmid factor	LL	0.55 ± 0.09	0.45 ± 0.09	---	---	0	1
	LM	0.57 ± 0.05	0.43 ± 0.05	---	---	0.14 ± 0.07	0.86 ± 0.07
	LH	0.62 ± 0.04	0.38 ± 0.04	---	---	0.10 ± 0.06	0.90 ± 0.10
	MM	0.65 ± 0.06	0.35 ± 0.06	---	---	0.18 ± 0.12	0.82 ± 0.12
	MH	0.54 ± 0.04	0.46 ± 0.04	---	---	0.32 ± 0.08	0.68 ± 0.08
	HH	0.61 ± 0.05	0.39 ± 0.05	---	---	0.48 ± 0.11	0.52 ± 0.11
Schmid factor mismatch	0-0.01	0.61 ± 0.04	0.39 ± 0.04	---	---	0.33 ± 0.08	0.67 ± 0.08
	0.02-0.04	0.56 ± 0.04	0.44 ± 0.04	---	---	0.24 ± 0.06	0.76 ± 0.06
	0.05-0.19	0.59 ± 0.04	0.41 ± 0.04	---	---	0.14 ± 0.05	0.86 ± 0.05
Taylor factor	LL	0.65 ± 0.07	0.35 ± 0.07	---	---	0.57 ± 0.13	0.43 ± 0.13
	LM	0.63 ± 0.05	0.37 ± 0.05	---	---	0.31 ± 0.08	0.69 ± 0.13
	MM	0.55 ± 0.05	0.45 ± 0.05	---	---	0.17 ± 0.09	0.83 ± 0.14
	LH	0.65 ± 0.06	0.35 ± 0.06	---	---	0.21 ± 0.08	0.79 ± 0.15
	MH	0.50 ± 0.05	0.50 ± 0.05	---	---	0.14 ± 0.07	0.86 ± 0.14
	HH	0.60 ± 0.07	0.40 ± 0.07	---	---	0	1
Taylor factor mismatch	0-0.26	0.65 ± 0.03	0.35 ± 0.03	---	---	0.26 ± 0.07	0.74 ± 0.07
	0.27-0.56	0.54 ± 0.04	0.46 ± 0.04	---	---	0.24 ± 0.07	0.76 ± 0.07
	0.57-1.28	0.55 ± 0.04	0.45 ± 0.04	---	---	0.21 ± 0.06	0.79 ± 0.06
Bdy inclination	0-10˚	0.77 ± 0.04	0.23 ± 0.04	---	---	---	---
	10-20˚	0.80 ± 0.04	0.20 ± 0.04	---	---	---	---
	20-30˚	0.80 ± 0.05	0.20 ± 0.05	---	---	---	---
	30-40˚	0.62 ± 0.08	0.38 ± 0.08	---	---	---	---
	40-50˚	0.45 ± 0.08	0.55 ± 0.08	---	---	---	---
	50-60˚	0.32 ± 0.08	0.68 ± 0.08	---	---	---	---
	60-70˚	0.29 ± 0.06	0.71 ± 0.06	---	---	---	---
	70-80˚	0.31 ± 0.08	0.69 ± 0.08	---	---	---	---
	80-90˚	0.30 ± 0.07	0.70 ± 0.07	---	---	---	---

Table 4.9 Intergranular crack data summary indicating fraction of cracks that occurred at each boundary type, Schmid factor pair type, Taylor factor pair type, and trace inclination. Uncertainties were calculated using equations (3.12) and (3.15).

		316L, 500°C SCW		316LGBE 500°C SCW		316L 7 dpa 400°C SCW NS cracks			316L 7 dpa 400°C SCW GBC cracks	316L 7 dpa 400°C argon NS cracks	316L 7 dpa 400°C argon GBC cracks
		15%	25%	15%	25%	2%	5%	10%	5%	5%	5%
Bdy type	RHABs	0.94 ± 0.04	0.92 ± 0.03	1.00 ± 0.02	0.87 ± 0.03	1.00 ± 0.02	0.94 ± 0.02	0.93 ± 0.02	0.94 ± 0.03	---	---
	LABs	0.02 ± 0.02	0.02 ± 0.01	0	0	0	0	0.01 ± 0.005	0	---	---
	Σ3	0.02 ± 0.02	0.03 ± 0.01	0	0.06 ± 0.02	0	0.02 ± 0.01	0.03 ± 0.01	0.03 ± 0.02	---	---
	Σ9	0.02 ± 0.02	0.02 ± 0.01	0	0.04 ± 0.02	0	0.03 ± 0.01	0.02 ± 0.01	0.02 ± 0.01	---	---
	Σ27	0	0.01 ± 0.01	0	0.04 ± 0.02	0	0.01 ± 0.01	0	0.01 ± 0.01	---	---
Schmid factor	LL	0.42 ± 0.13	0.30 ± 0.08	0.40 ± 0.21	0.29 ± 0.08	0.48 ± 0.10	0.43 ± 0.08	0.25 ± 0.05	0.15 ± 0.05	---	0.29 ± 0.19
	LM	0.24 ± 0.07	0.23 ± 0.05	0.13 ± 0.09	0.18 ± 0.04	0.23 ± 0.05	0.17 ± 0.03	0.17 ± 0.03	0.18 ± 0.04	---	0.36 ± 0.13
	LH	0.16 ± 0.05	0.17 ± 0.04	0.27 ± 0.12	0.17 ± 0.04	0.20 ± 0.05	0.17 ± 0.03	0.20 ± 0.04	0.23 ± 0.05	---	0.14 ± 0.09
	MM	0.06 ± 0.04	0.09 ± 0.03	0.13 ± 0.13	0.14 ± 0.05	0.08 ± 0.05	0.10 ± 0.03	0.17 ± 0.04	0.17 ± 0.05	---	0.14 ± 0.14
	MH	0.03 ± 0.02	0.10 ± 0.03	0.07 ± 0.06	0.10 ± 0.03	0.01 ± 0.01	0.08 ± 0.02	0.11 ± 0.02	0.15 ± 0.04	---	0.07 ± 0.07
	HH	0.09 ± 0.05	0.11 ± 0.04	0	0.11 ± 0.04	0	0.05 ± 0.02	0.10 ± 0.03	0.11 ± 0.04	---	0
Taylor factor	LL	0.03 ± 0.03	0.07 ± 0.03	0	0.08 ± 0.03	0.03 ± 0.03	0.04 ± 0.02	0.10 ± 0.03	0.19 ± 0.06	---	0
	LM	0.08 ± 0.04	0.11 ± 0.03	0	0.13 ± 0.03	0.01 ± 0.01	0.13 ± 0.03	0.17 ± 0.03	0.15 ± 0.04	---	0
	MM	0.18 ± 0.06	0.17 ± 0.04	0.14 ± 0.10	0.16 ± 0.04	0.16 ± 0.04	0.14 ± 0.03	0.18 ± 0.04	0.13 ± 0.03	---	0.13 ± 0.09
	LH	0.06 ± 0.04	0.10 ± 0.03	0.14 ± 0.14	0.21 ± 0.06	0.17 ± 0.07	0.13 ± 0.03	0.14 ± 0.03	0.20 ± 0.06	---	0.13 ± 0.13
	MH	0.22 ± 0.06	0.21 ± 0.05	0.43 ± 0.15	0.20 ± 0.05	0.29 ± 0.06	0.25 ± 0.04	0.17 ± 0.03	0.20 ± 0.05	---	0.33 ± 0.12
	HH	0.43 ± 0.13	0.34 ± 0.08	0.29 ± 0.19	0.22 ± 0.06	0.34 ± 0.09	0.30 ± 0.06	0.24 ± 0.05	0.12 ± 0.04	---	0.40 ± 0.21
Trace inclination	0-10°	0	0	0	0	0	0	0	0.03 ± 0.02	0	0
	10-20°	0	0	0	0	0	0	0	0.03 ± 0.02	0	0
	20-30°	0	0.01 ± 0.01	0	0	0	0.01 ± 0.01	0.02 ± 0.01	0.05 ± 0.02	0	0
	30-40°	0	0.01 ± 0.01	0	0	0	0.01 ± 0.01	0.02 ± 0.01	0.15 ± 0.04	0	0
	40-50°	0	0.04 ± 0.02	0	0	0	0.05 ± 0.01	0.07 ± 0.01	0.23 ± 0.05	0	0.04 ± 0.04
	50-60°	0.04 ± 0.03	0.08 ± 0.02	0	0.02 ± 0.01	0.10 ± 0.04	0.11 ± 0.02	0.13 ± 0.02	0.17 ± 0.05	0	0.04 ± 0.04
	60-70°	0.08 ± 0.01	0.14 ± 0.03	0.18 ± 0.12	0.06 ± 0.02	0.14 ± 0.05	0.18± 0.02	0.22 ± 0.02	0.12 ± 0.05	0.20 ± 0.18	0.12 ± 0.06
	70-80°	0.27 ± 0.06	0.29 ± 0.03	0.27 ± 0.13	0.32 ± 0.04	0.25 ± 0.06	0.33 ± 0.03	0.29 ± 0.02	0.11 ± 0.06	0	0.36 ± 0.10
	80-90°	0.60 ± 0.07	0.43 ± 0.04	0.55 ± 0.15	0.59 ± 0.04	0.51 ± 0.07	0.31 ± 0.03	0.25 ± 0.02	0.13 ± 0.09	0.80 ± 0.18	0.44 ± 0.10

Table 4.10 Schmid factor mismatch in 316L, and fraction of cracks that fall into each Schmid factor mismatch category. Uncertainties were calculated using equation (3.15).

Schmid factor mismatch	Total fraction	2% strain cracked fraction	5% strain cracked fraction	10% strain cracked fraction
0-0.03	0.48	0.31 ± 0.07	0.45 ± 0.08	0.48 ± 0.05
0.04-0.06	0.28	0.29 ± 0.07	0.25 ± 0.04	0.25 ± 0.03
0.07-0.09	0.11	0.14 ± 0.05	0.14 ± 0.03	0.13 ± 0.02
0.09-0.12	0.07	0.10 ± 0.04	0.08 ± 0.02	0.09 ± 0.02
0.12-0.15	0.04	0.14 ± 0.05	0.05 ± 0.02	0.04 ± 0.01
0.16-0.18	0.01	0.02 ± 0.02	0.02 ± 0.01	0.01 ± 0.01
0.18-0.22	0.00	0	0.01 ± 0.01	0

Table 4.11 Taylor factor mismatch in 316L, and fraction of cracks that fall into each Taylor factor mismatch category. Uncertainties were calculated using equation (3.15).

Taylor factor mismatch	Total fraction	2% strain cracked fraction	5% strain cracked fraction	10% strain cracked fraction
0-0.20	0.28	0.33 ± 0.07	0.35 ± 0.07	0.30 ± 0.04
0.21-0.40	0.22	0.16 ± 0.05	0.21 ± 0.03	0.20 ± 0.03
0.41-0.60	0.19	0.22 ± 0.06	0.14 ± 0.03	0.18 ± 0.02
0.61-0.80	0.14	0.18 ± 0.06	0.13 ± 0.02	0.17 ± 0.02
0.81-1.00	0.10	0.10 ± 0.04	0.09 ± 0.02	0.08 ± 0.01
1.01-1.20	0.07	0.02 ± 0.02	0.06 ± 0.02	0.05 ± 0.01
1.21-1.40	0.02	0	0.01 ± 0.01	0.03 ± 0.01

Table 4.12 Fraction of boundaries cracked in 316L and 316LGBE following straining in 400˚C and 500˚C SCW.

	Strain	Area analyzed (mm^2)	#special bdy	#RHABs	Total # bdy	special fraction cracked	RHAB fraction cracked	total fraction cracked
316L 400C 7 dpa	2%	25.2	0	51	51	0	0.0024 ± 0.0003	0.0014 ± 0.0002
	5%	13.65	14	224	238	0.0017 ± 0.0004	0.019 ± 0.001	0.0120 ± 0.0008
	10%	4.20	32	416	448	0.012 ± 0.002	0.117 ± 0.005	0.0734 ± 0.003
316L 500C	15%	1.89	3	45	48	0.003 ± 0.002	0.028 ± 0.004	0.017 ± 0.002
	25%	1.89	14	168	182	0.012 ± 0.003	0.105 ± 0.008	0.066 ± 0.005
316LGBE 500C	15%	9.45	0	11	11	0	0.005 ± 0.001	0.0023 ± 0.0007
	25%	9.45	18	124	142	0.007 ± 0.002	0.053 ± 0.005	0.0293 ± 0.0024

Table 4.13 Densities of NS and GBC cracks in select regions of 7 dpa proton irradiated 316L strained to 5% in 400˚C purified argon and SCW.

Environment	Crack type	Area analyzed (mm^2)	# cracked boundaries	crack density ($\#/mm^2$)
Argon	NS	5.2	5	1.0 ± 0.4
	GBC	2.1	25	11.9 ± 2.4
SCW	NS	2.1	31	14.8 ± 2.7
	GBC	2.1	86	41.0 ± 4.4

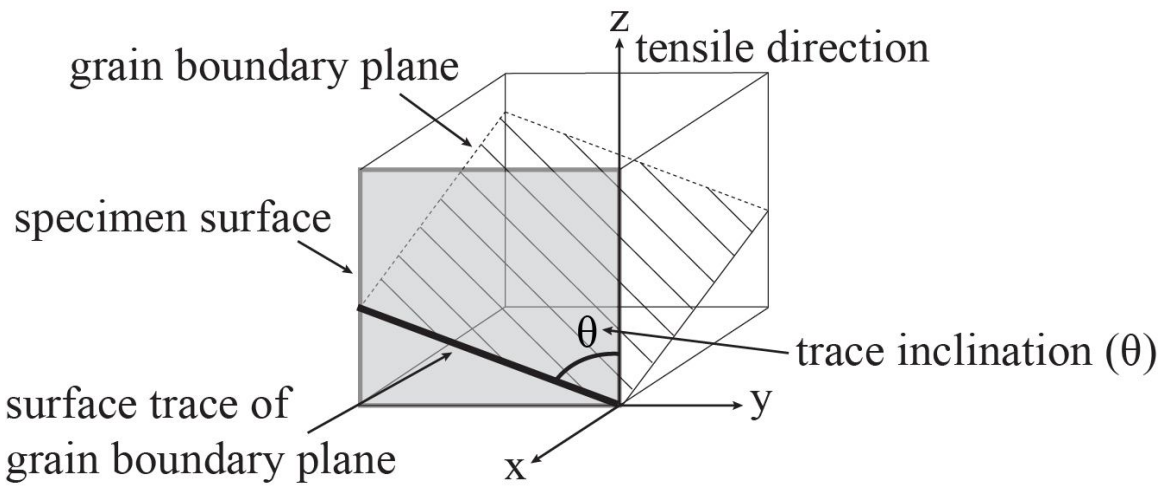

Figure 4.1 Illustration of trace inclination, θ, which is the angle between the surface trace of the grain boundary plane and the tensile direction.

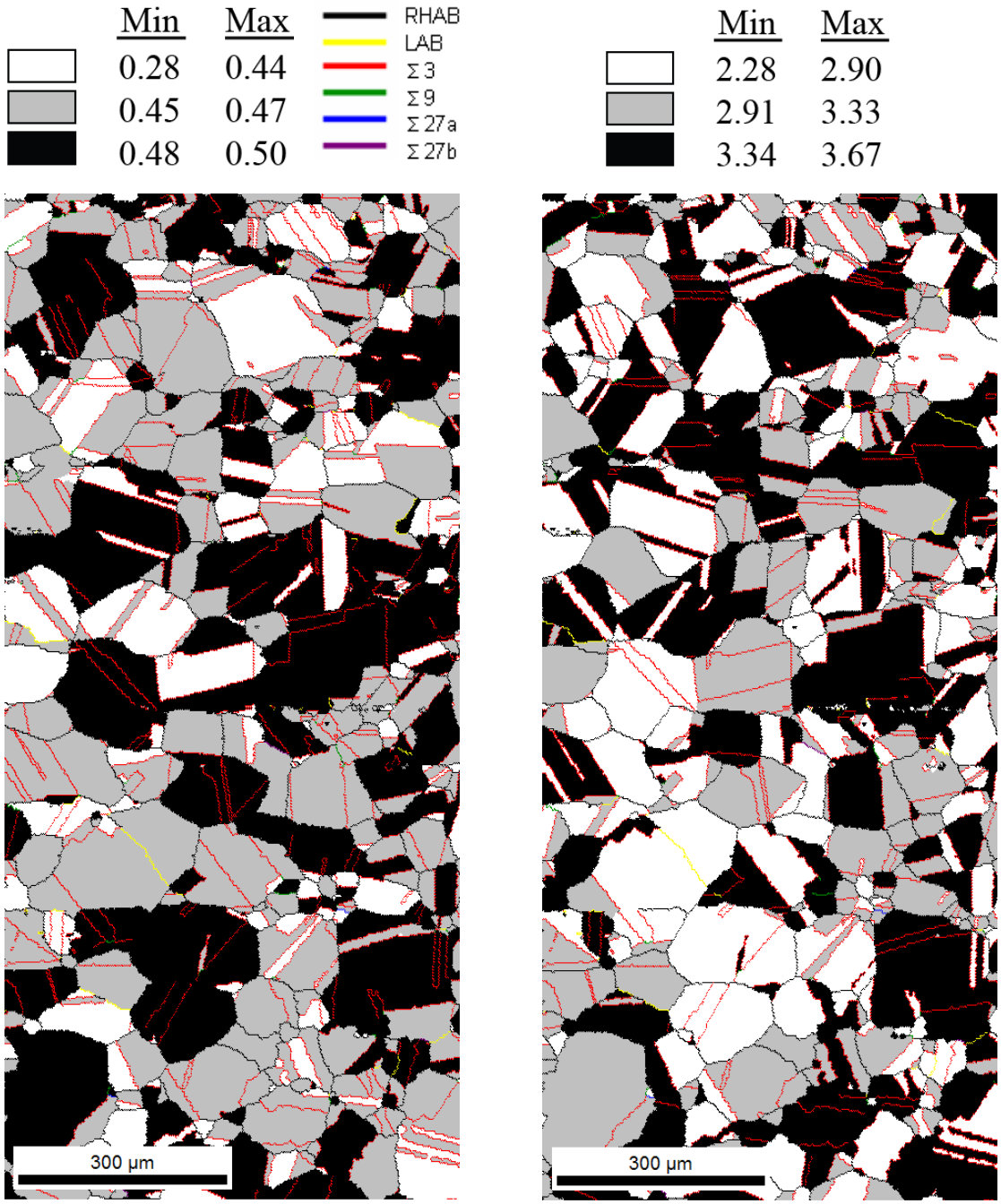

(a) (b)

Figure 4.2 Grain maps of 316L (a) Schmid factor map and (b) Taylor factor map.

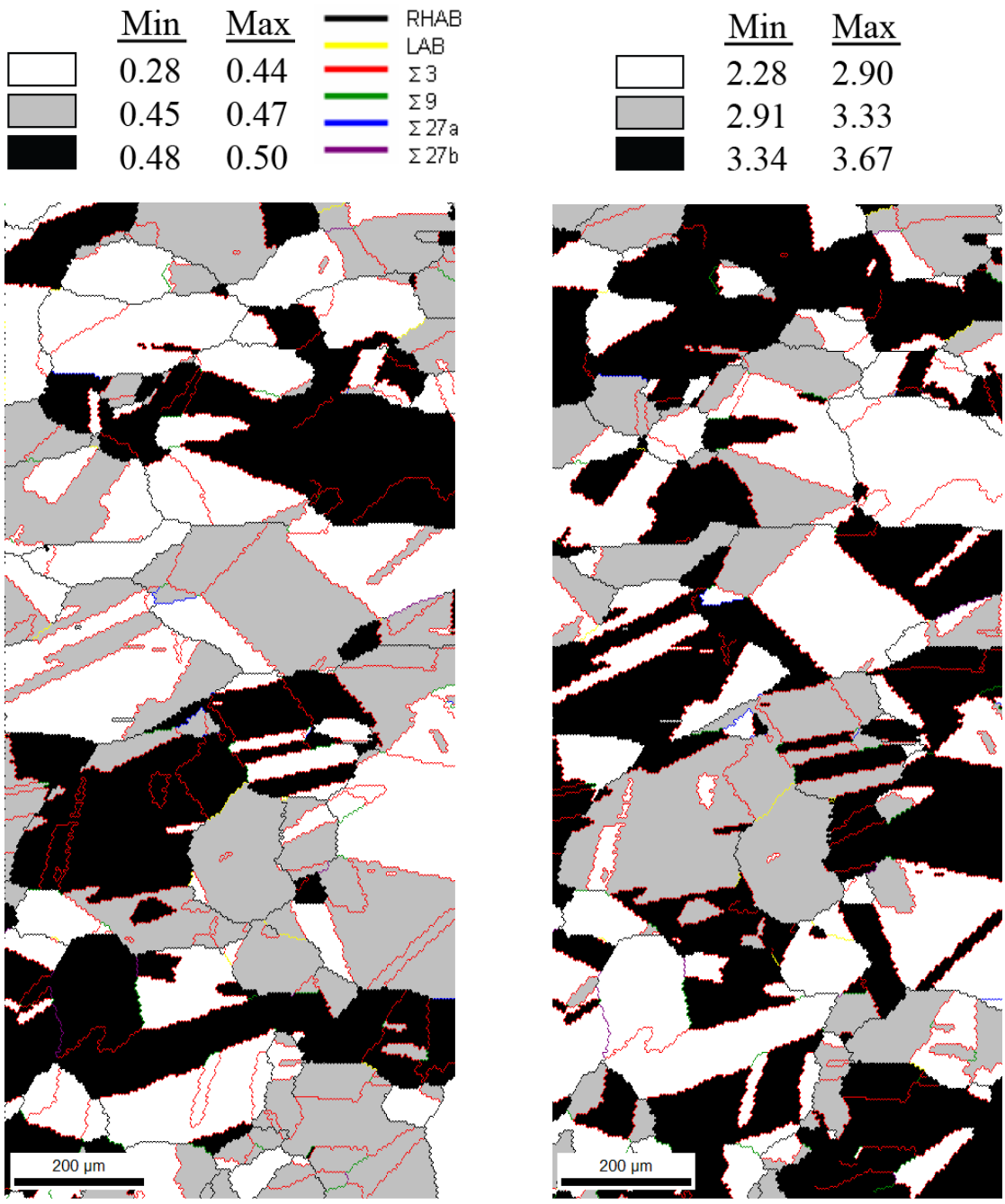

(a) (b)

Figure 4.3 Grain maps of 316LGBE (a) Schmid factor map and (b) Taylor factor map.

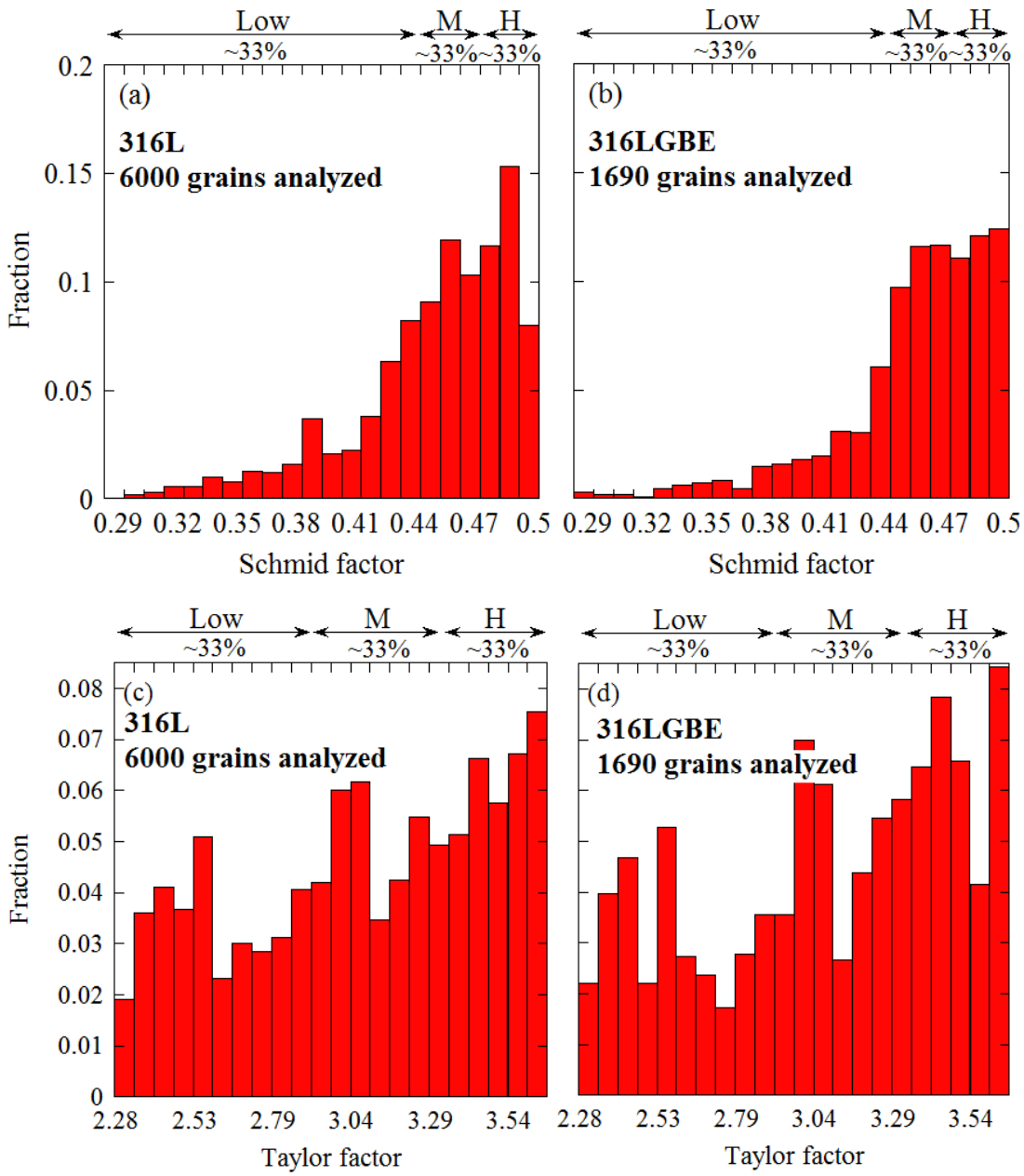

Figure 4.4 (a) Schmid and (b) Taylor factor distributions of grains in 316L. The low, medium, and high categories each contain one third of the total grain population.

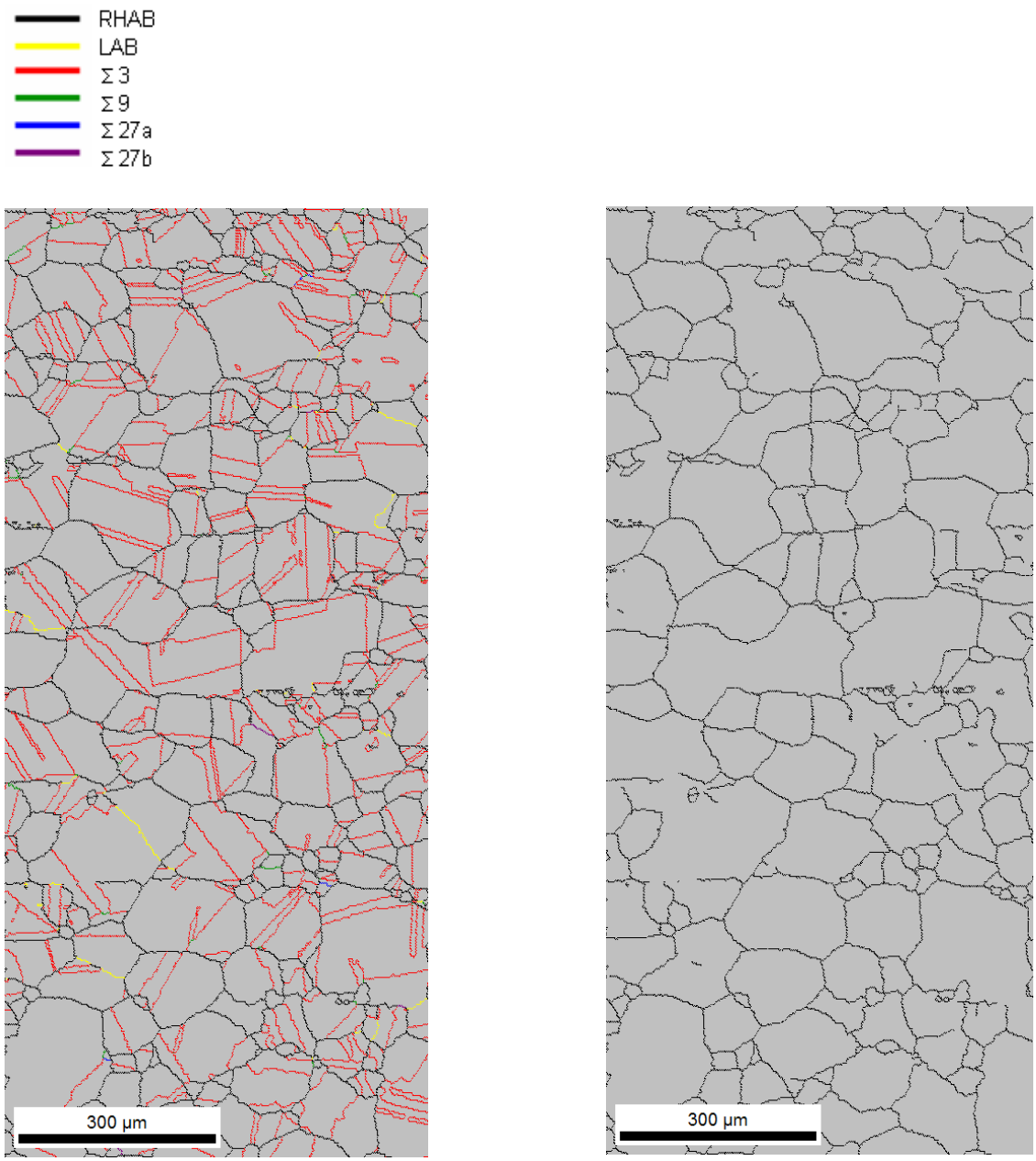

(a) (b)

Figure 4.5 Grain boundary character maps of 316L (a) all boundaries and (b) RHABs only.

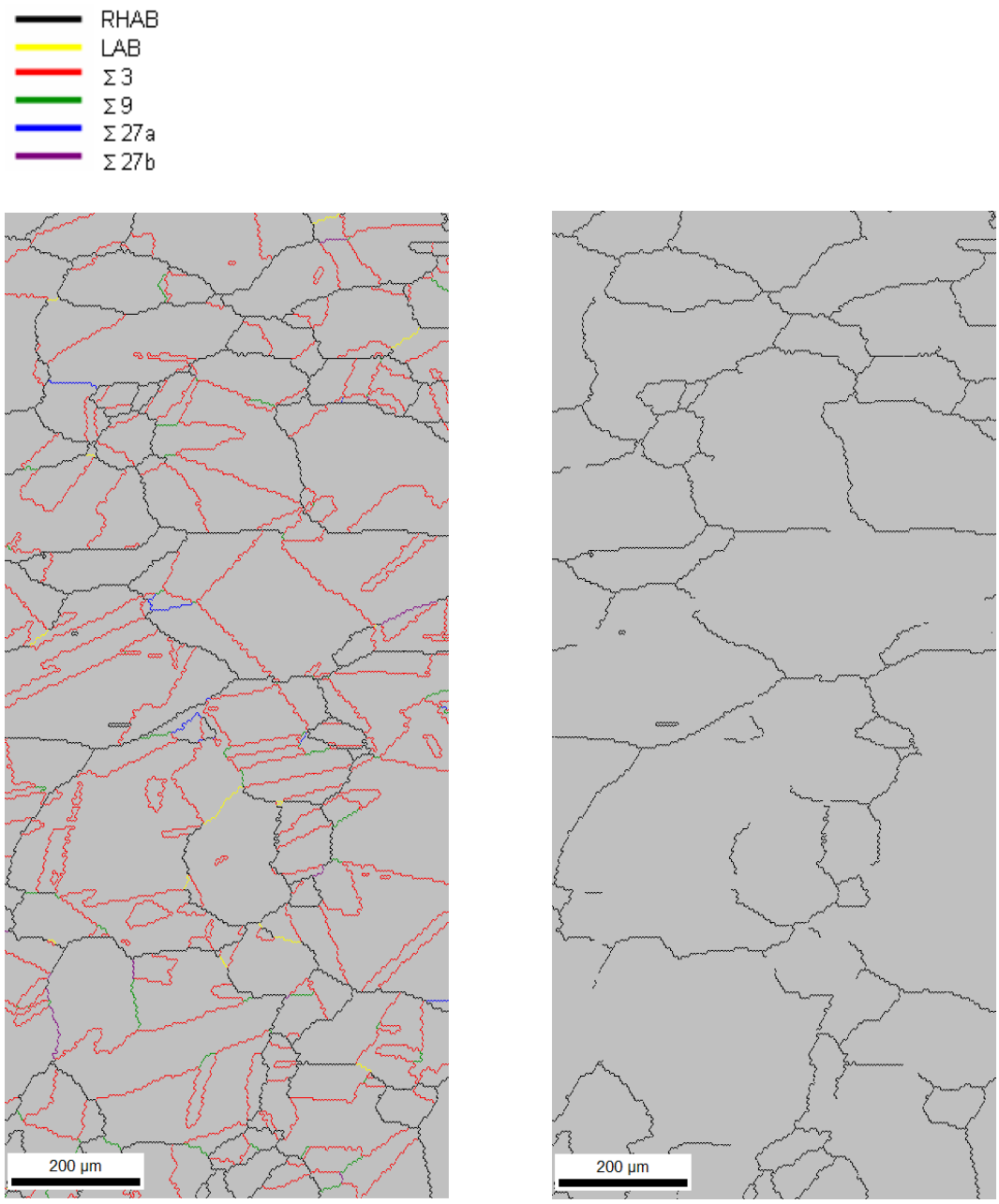

(a) (b)

Figure 4.6 Grain boundary character maps of 316LGBE (a) all boundaries and (b) RHABs only.

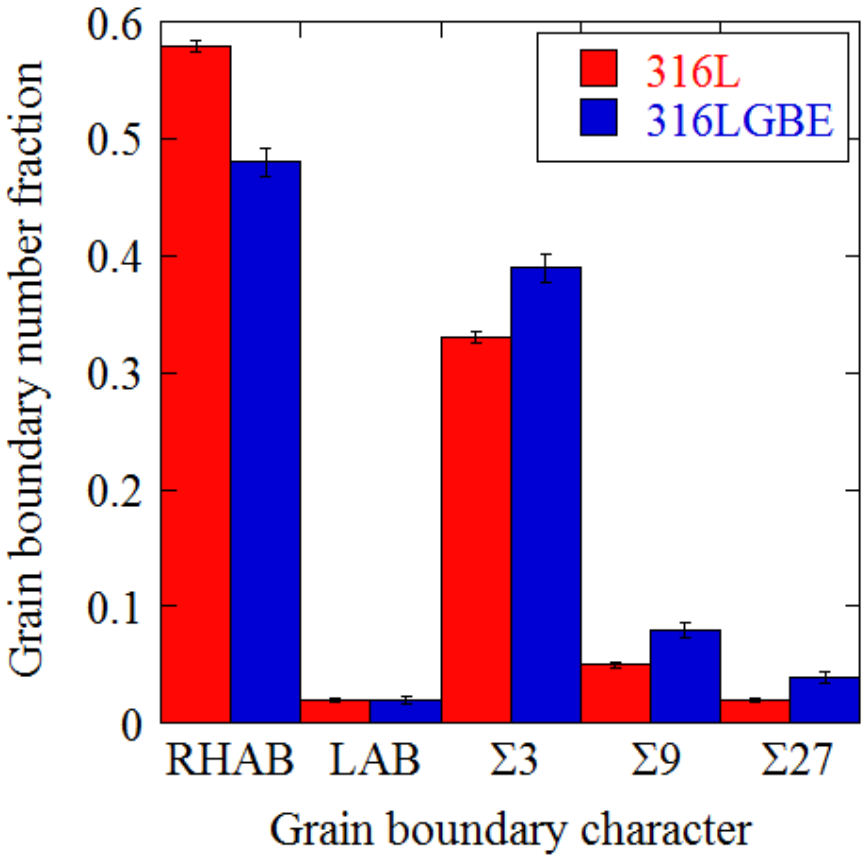

Figure 4.7 Grain boundary number fractions of RHAB, LAB, Σ3, Σ9, and Σ27 boundaries in 316L and 316LGBE.

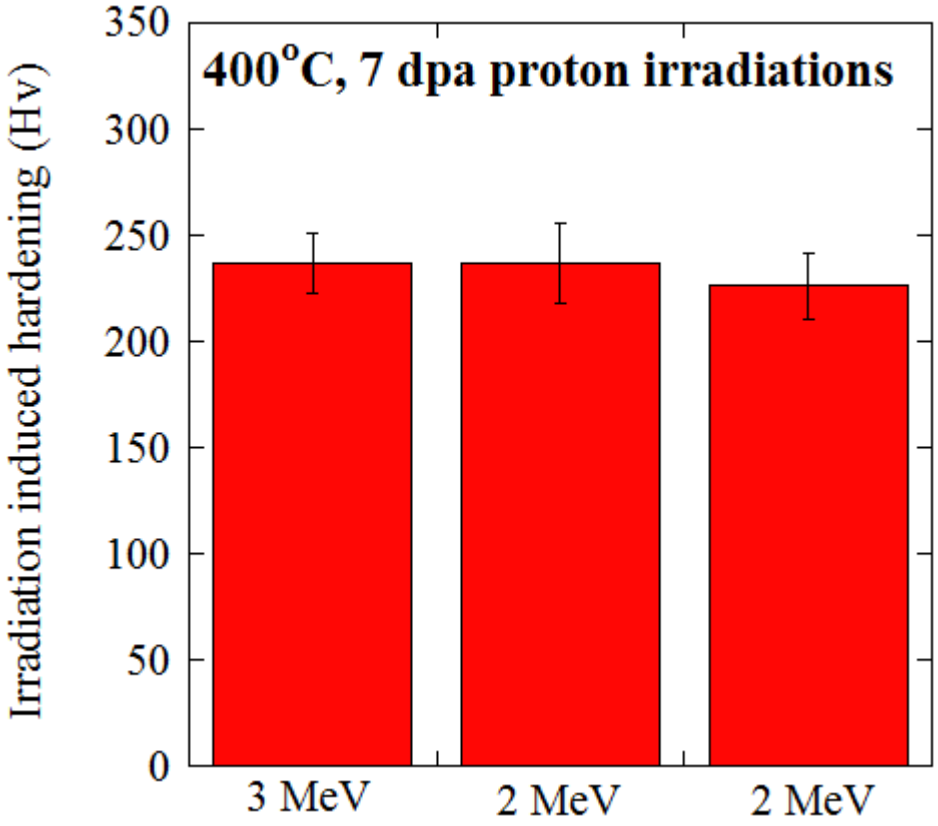

Figure 4.8 Proton irradiation induced hardening in 316L specimens irradiated to 7 dpa at 400˚C with 2 and 3 MeV protons.

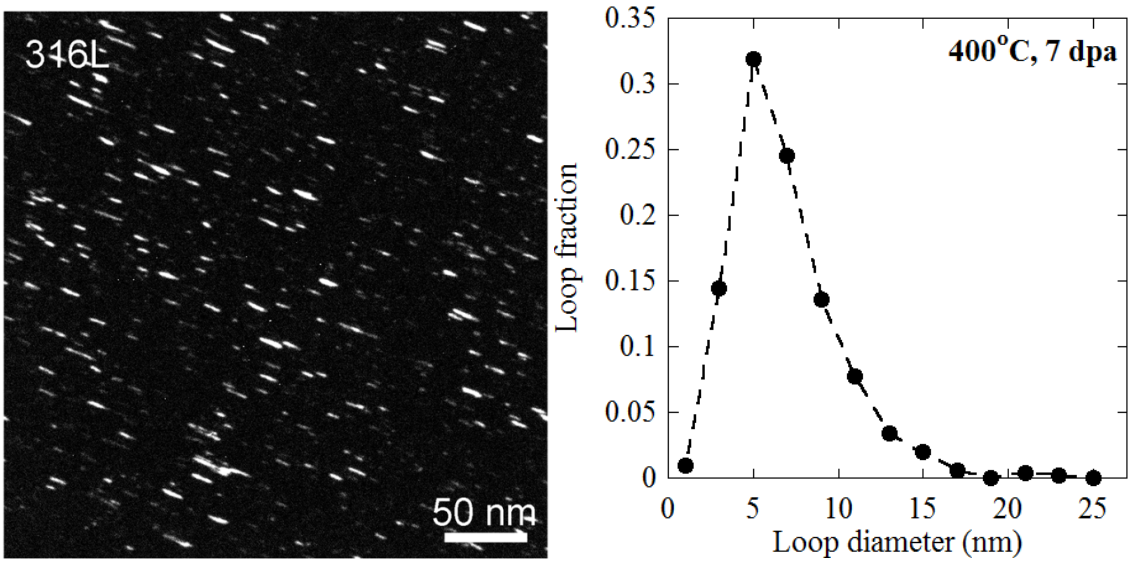

(a) (b)

Figure 4.9 (a) Rel-rod dark field image of dislocation loops in 316L stainless steel proton irradiated to 7 dpa at 400˚C, (b) loop diameter distribution.

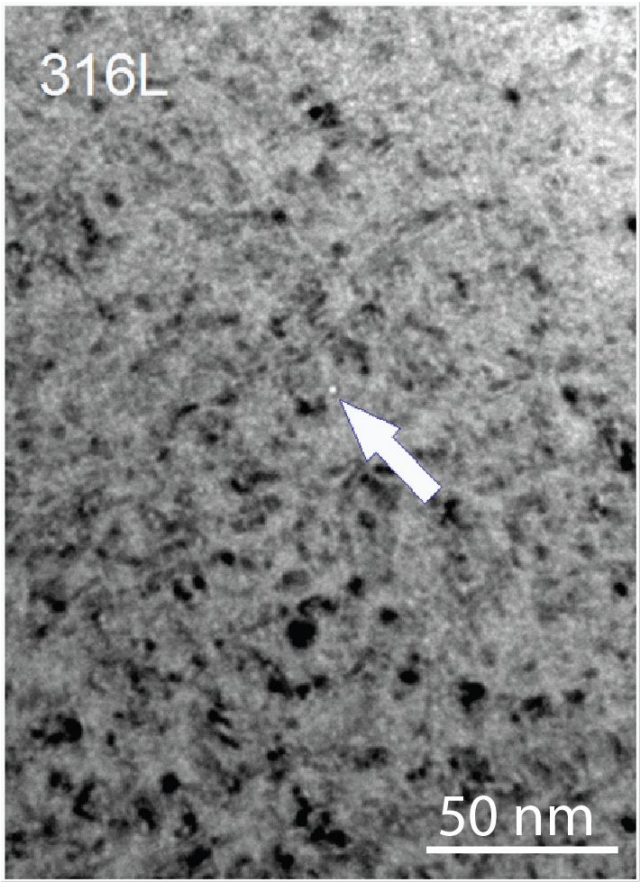

Figure 4.10 Bright field image of void in 316L stainless steel proton irradiated to 7 dpa at 400˚C.

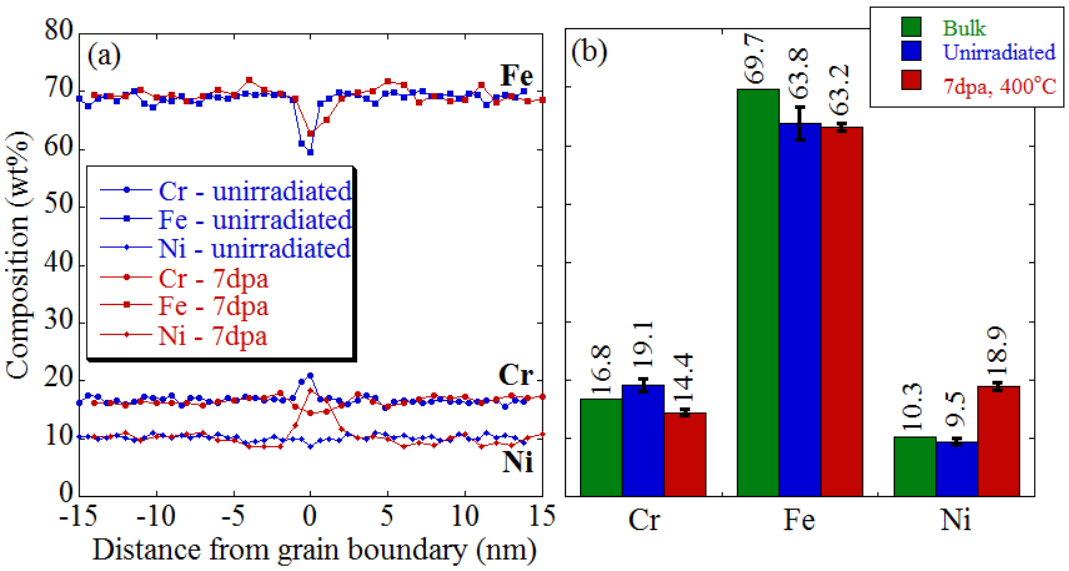

Figure 4.11 Grain boundary composition profiles for unirradiated and 7 dpa proton irradiated 316L stainless steel.

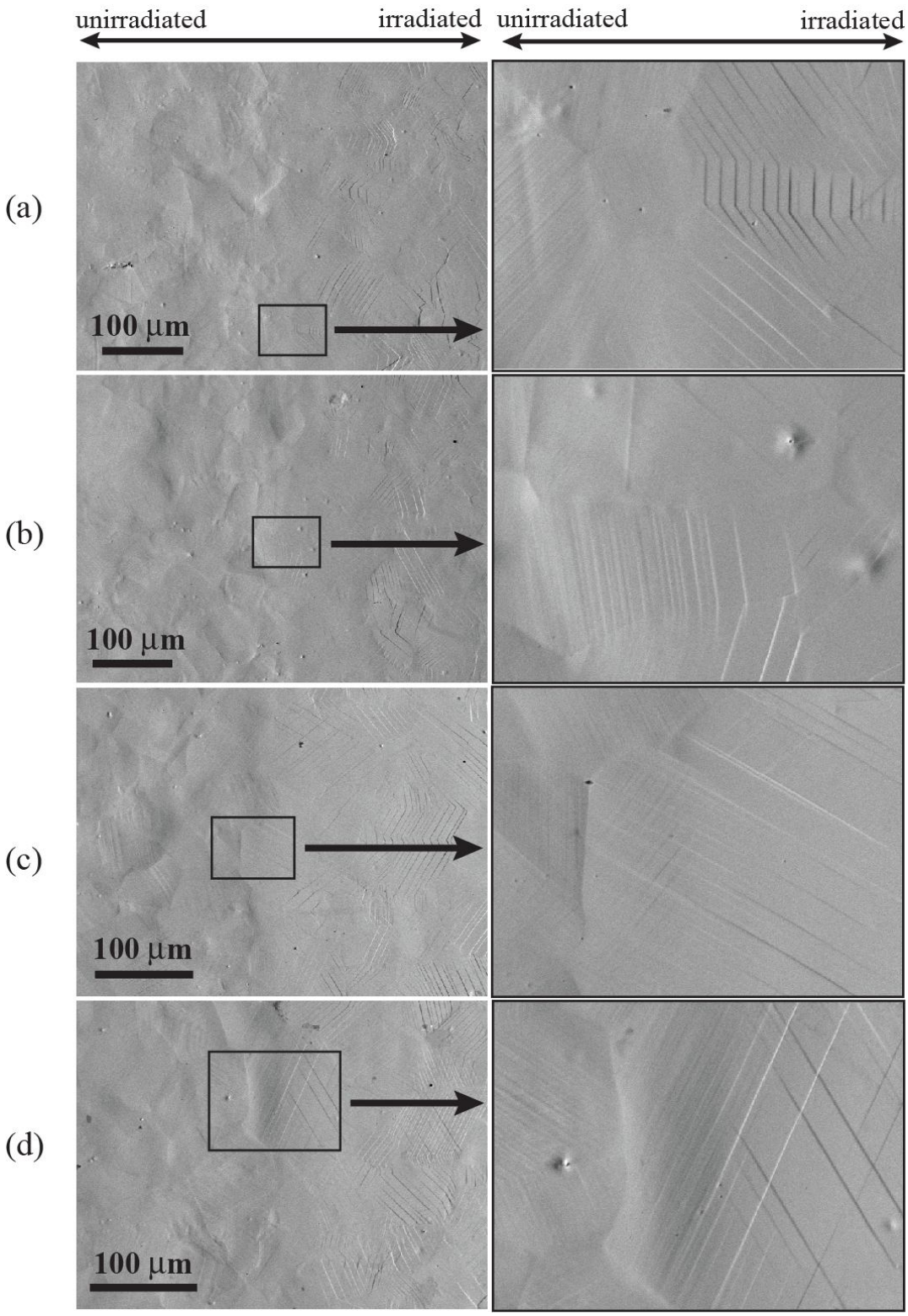

Figure 4.12 Backscattered electron SEM images of dislocation channeling behavior on gage surface of tensile specimen at interface between irradiated and unirradiated regions of 7 dpa proton irradiated 316L following straining to 5% in 400˚C argon environment.

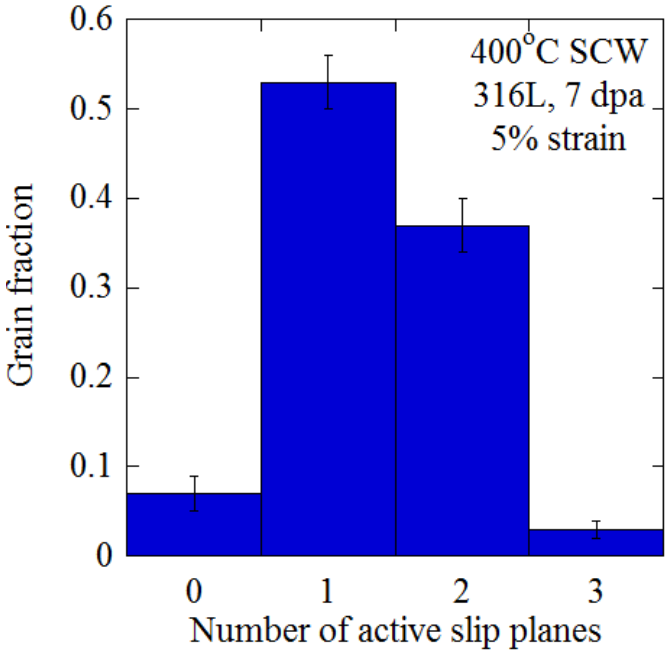

(a)

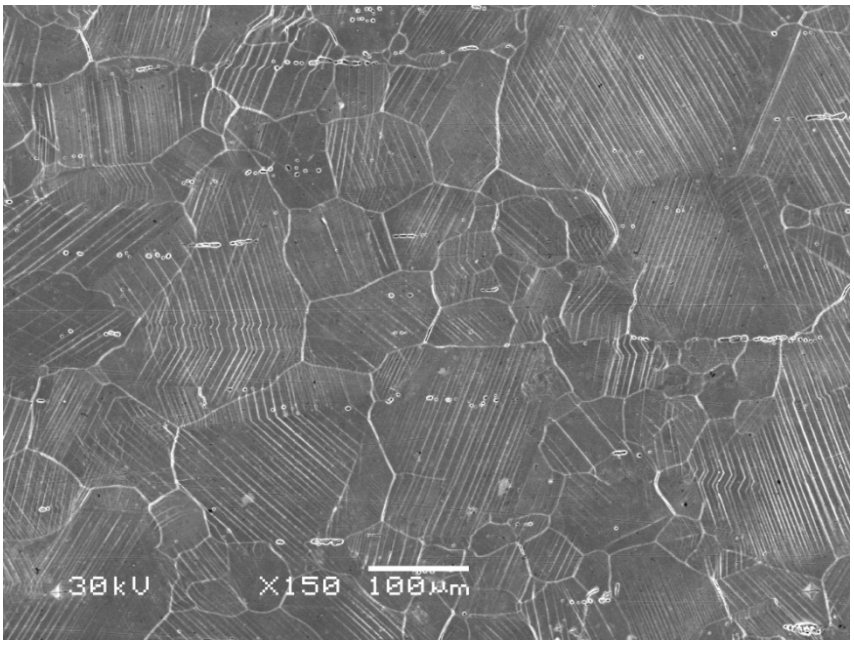

←tensile direction→

(b)

Figure 4.13 (a) Number of active slip planes in individual grains of proton irradiated 316L strained to 5% in 400˚C SCW, and (b) representative area over which the measurements were taken at a magnification of 150x. The activation of a single slip plane indicates that a maximum of 2 independent slip systems were activated.

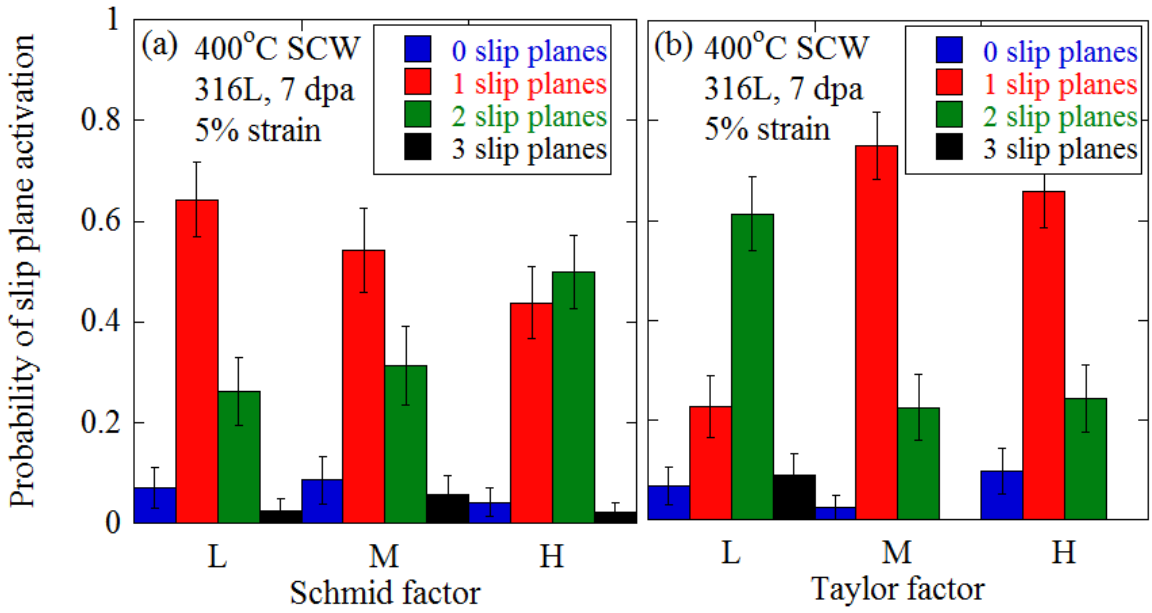

Figure 4.14 Probability of activation of 0, 1, 2, or 3 slip planes as a function of (a) Schmid factor and (b) Taylor factor.

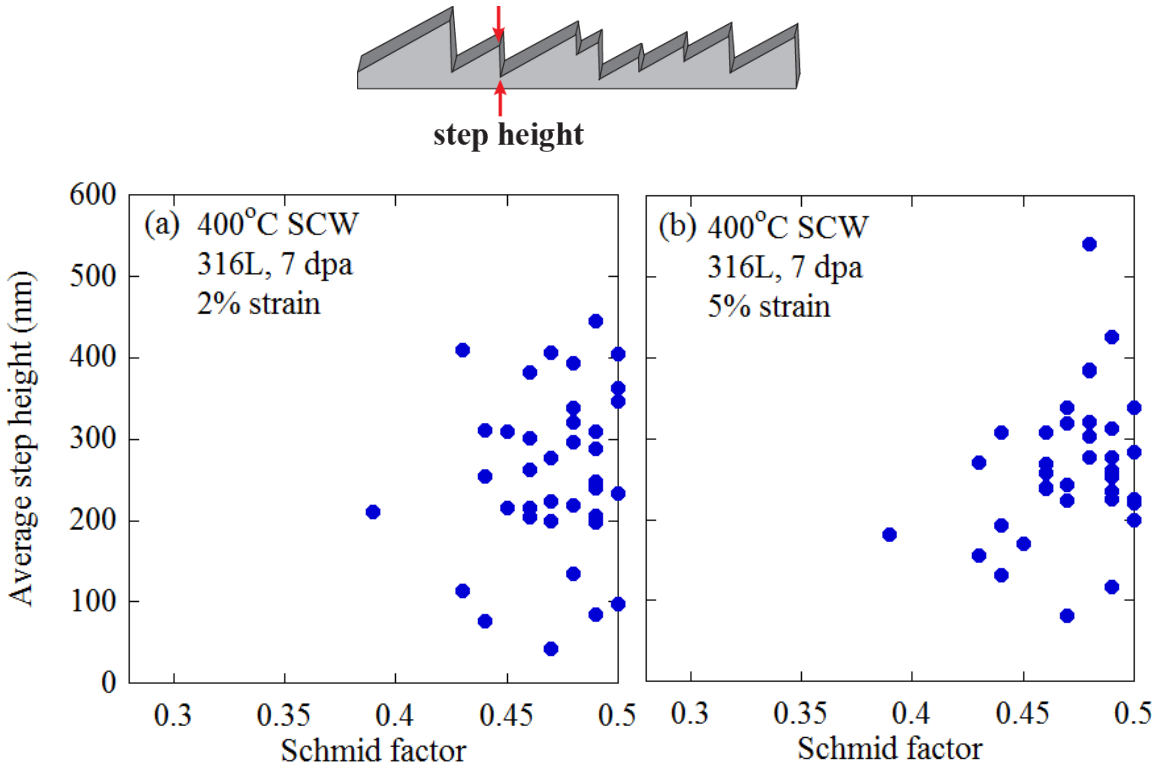

Figure 4.15 Average step height as a function of Schmid factor for proton irradiated 316L specimen strained to (a) 2% and (b) 5% in 400˚C SCW.

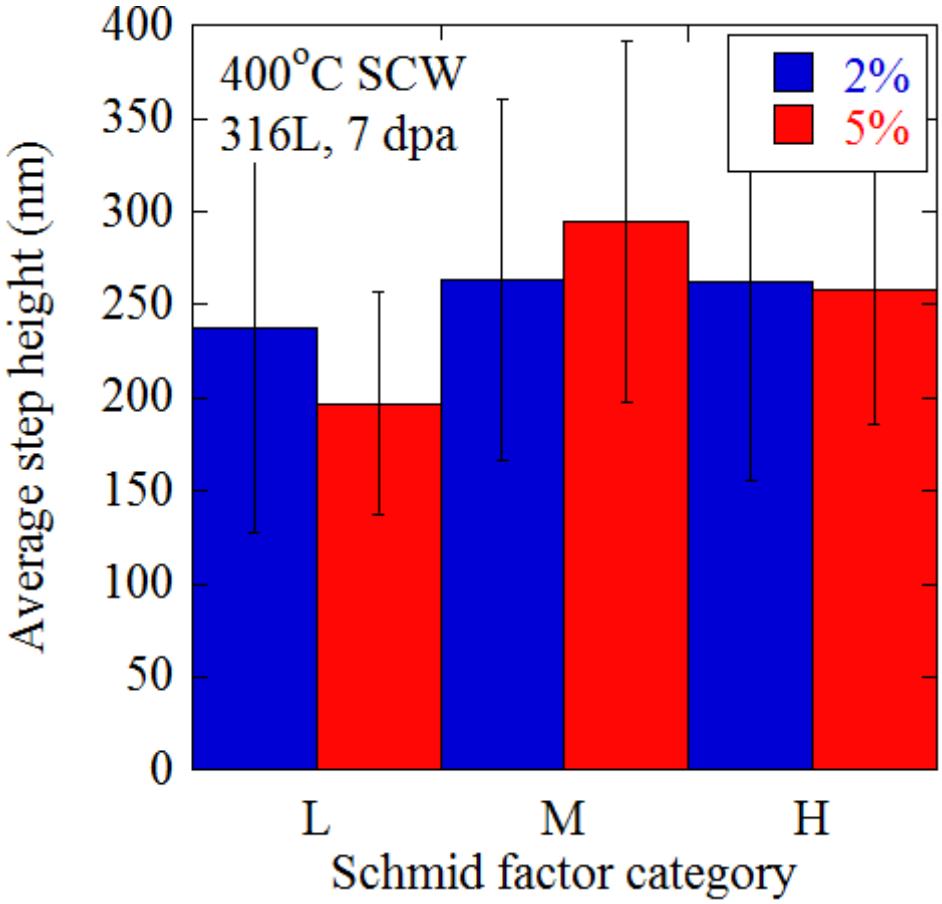

Figure 4.16 Average step height for low, medium, and high Schmid factor categories for proton irradiated 316L specimen strained to 2% and 5% in 400˚C SCW.

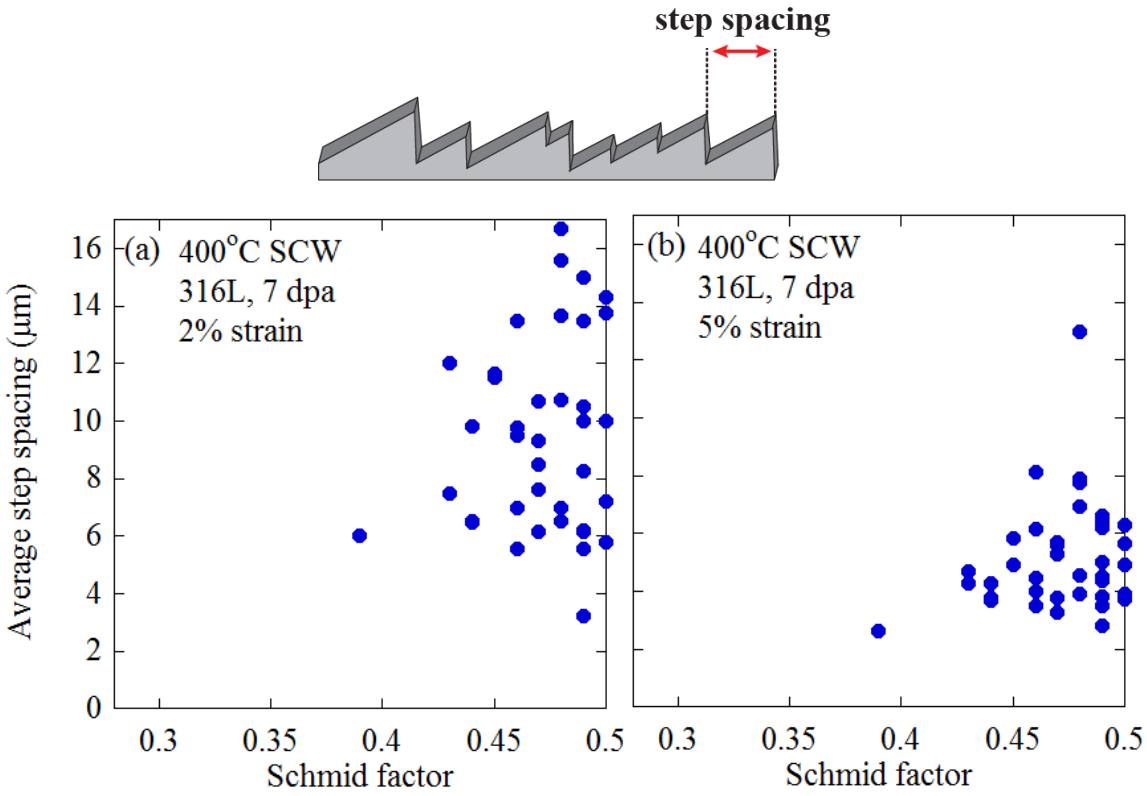

Figure 4.17 Average step spacing as a function of Schmid factor for proton irradiated 316L specimen strained to (a) 2% and (b) 5% in 400˚C SCW.

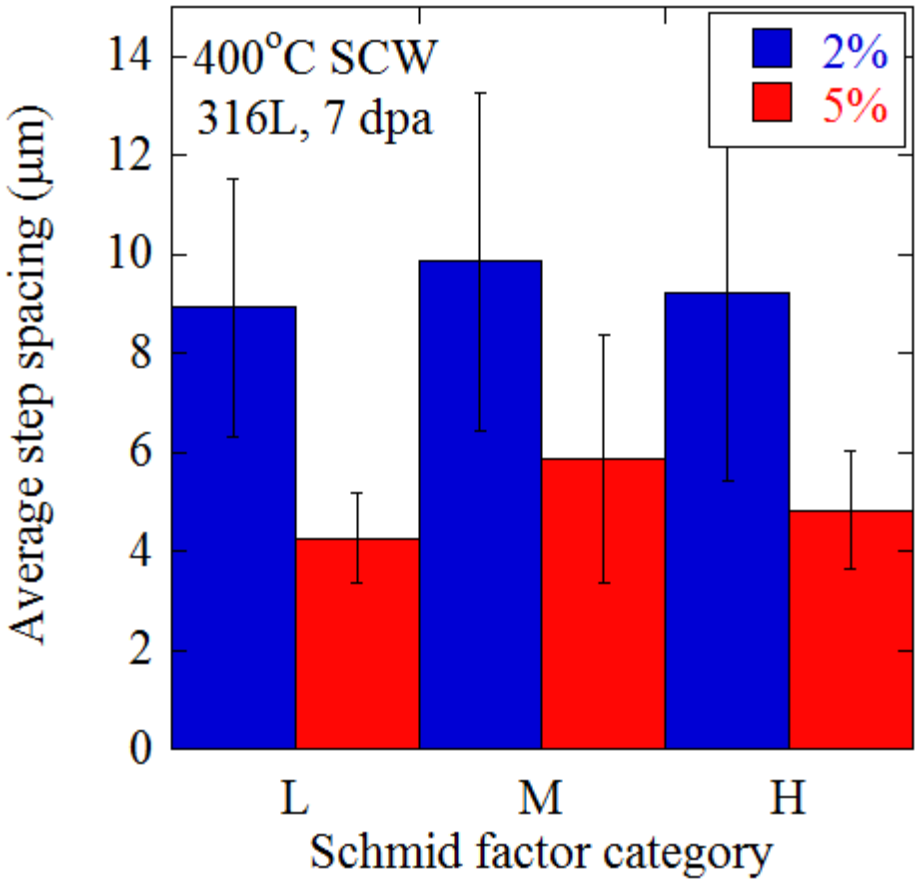

Figure 4.18 Average step spacing for low, medium, and high Schmid factor categories for proton irradiated 316L specimen strained to 2% and 5% in 400˚C SCW.

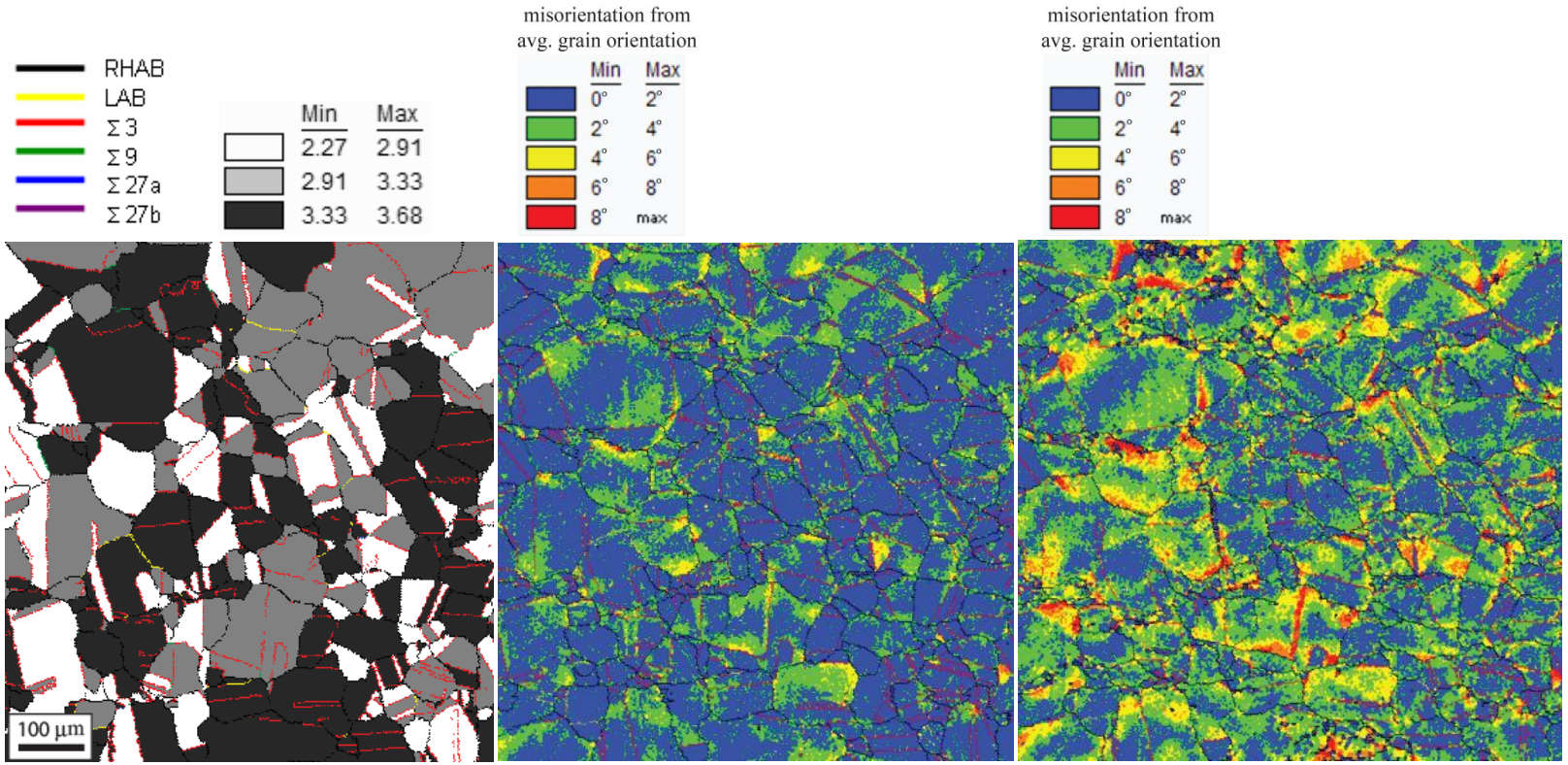

Taylor factor map | 5% strain | 10% strain

←tensile direction→

Figure 4.19 Taylor factor and localized lattice rotation maps of proton irradiated 316L specimen strained to 5% and 10% in 400˚C SCW.

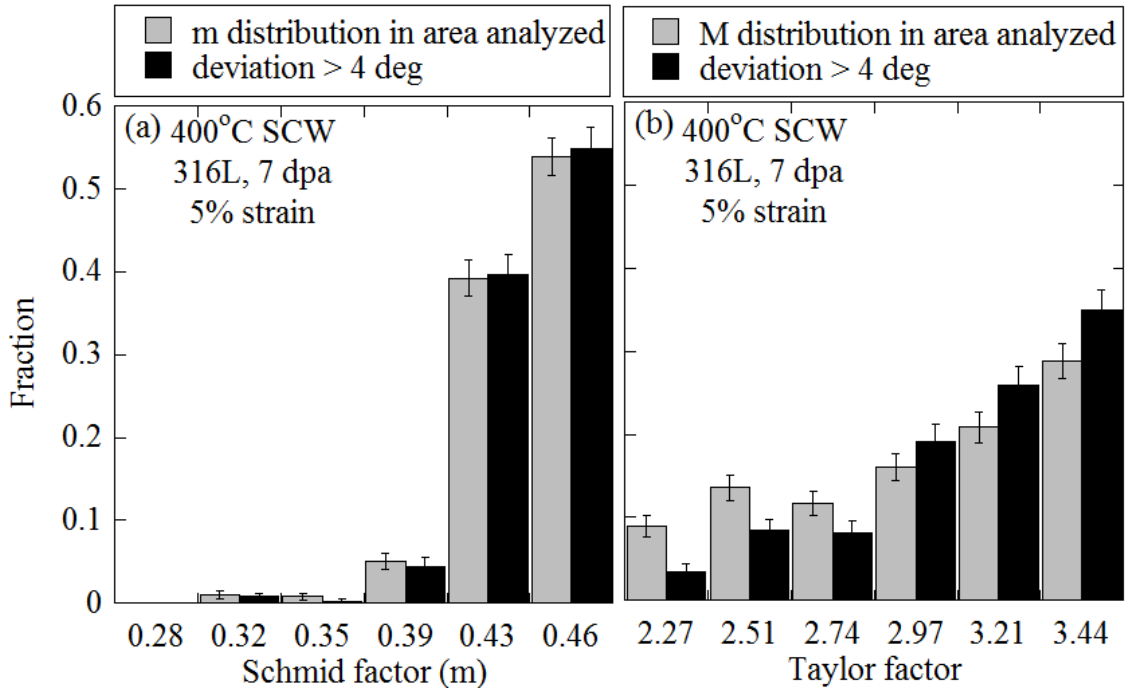

Figure 4.20 Fraction of regions in grains of proton irradiated 316L with orientation deviations of greater than 4˚ from the average orientation of the grain following straining to 5% in 400˚C SCW. These fractions are compared to the Schmid and Taylor factor distributions in the specific region analyzed and plotted as a function of (a) the Schmid factor, and (b) Taylor factor.

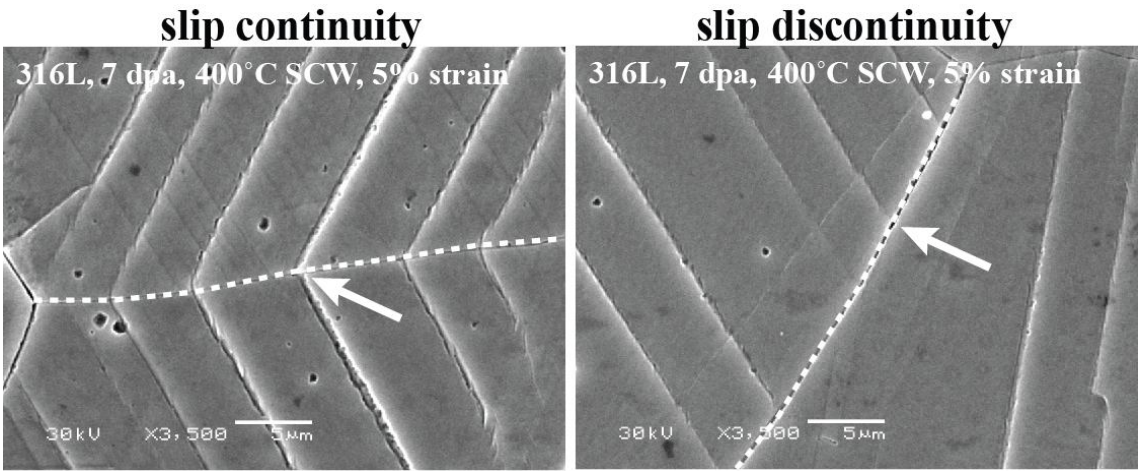

(a) (b)

←Tensile direction→

Figure 4.21 Intersection of dislocation channels with grain boundaries resulting in (a) slip continuity and (b) slip discontinuity. The dotted white lines indicate the location of the grain boundary, and the arrows indicate the intersection of a dislocation channel with the grain boundary.

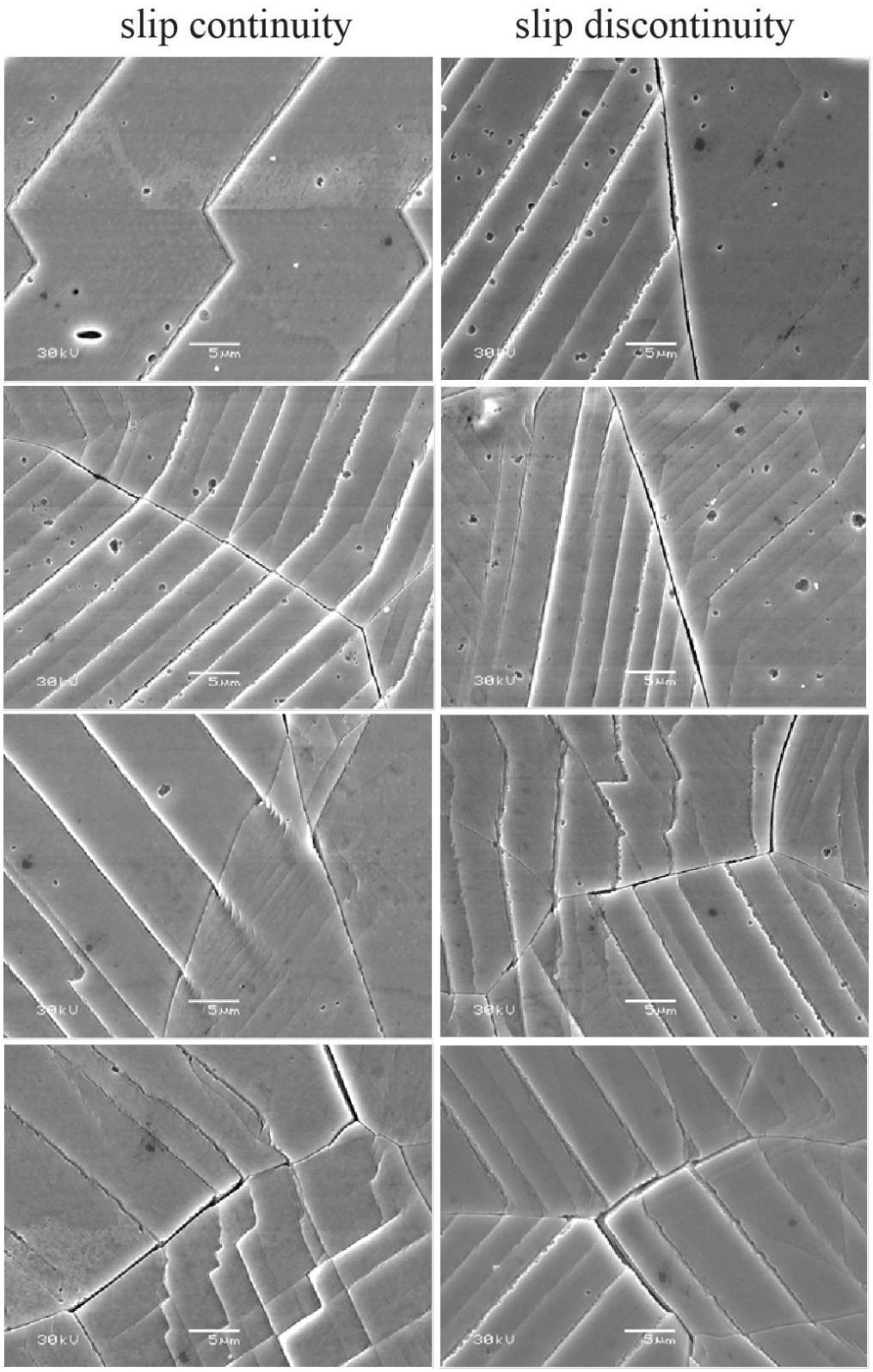

Figure 4.22 Examples of slip continuity and slip discontinuity at grain boundaries of proton irradiated 316L specimens following straining to 5% in 400˚C SCW.

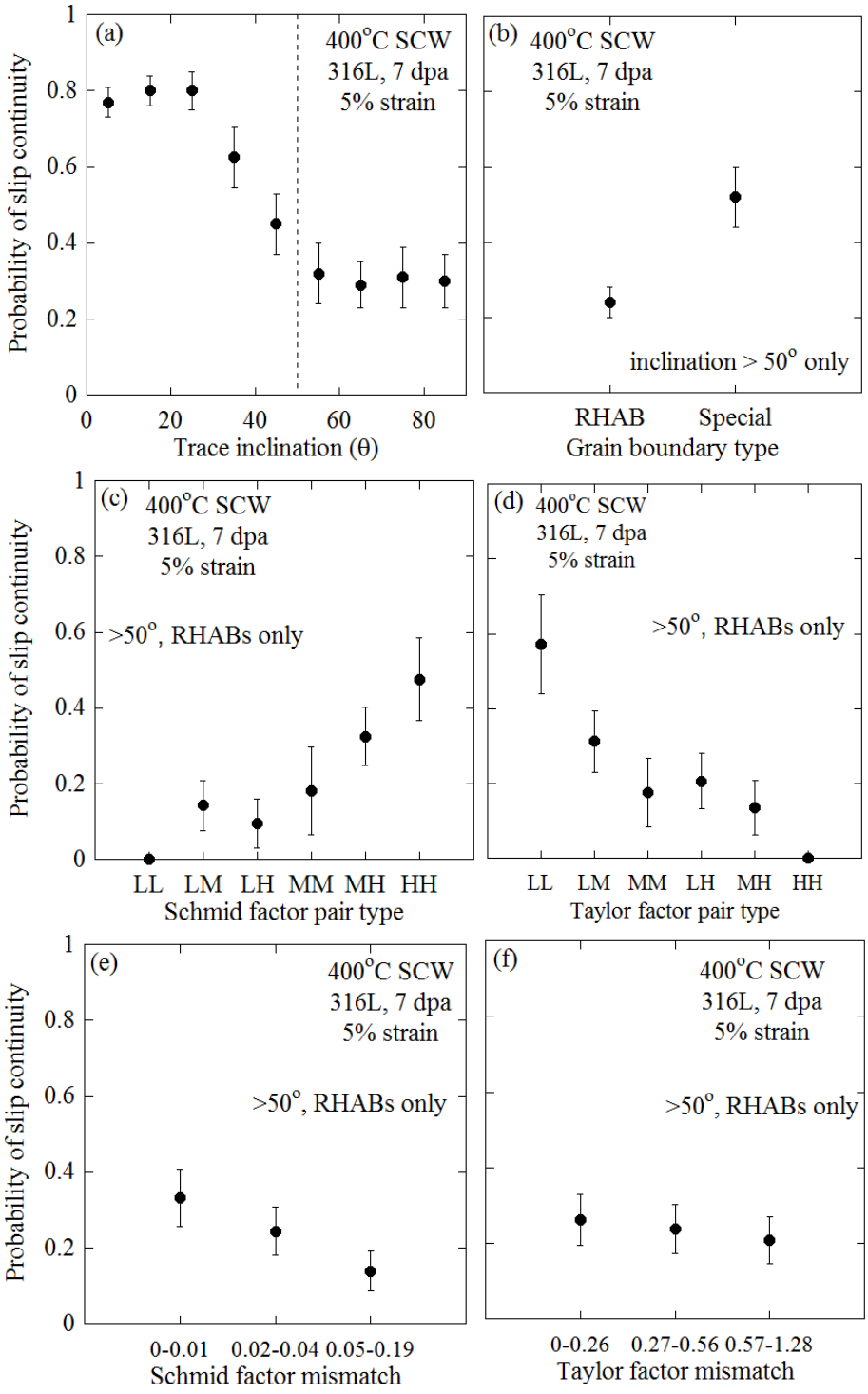

Figure 4.23 Probability of slip continuity across grain boundaries as a function of (a) trace inclination, (b) grain boundary type, (c) Schmid factor pair type, and (d) Taylor factor pair type, (e) Schmid factor mismatch, (f) Taylor factor mismatch.

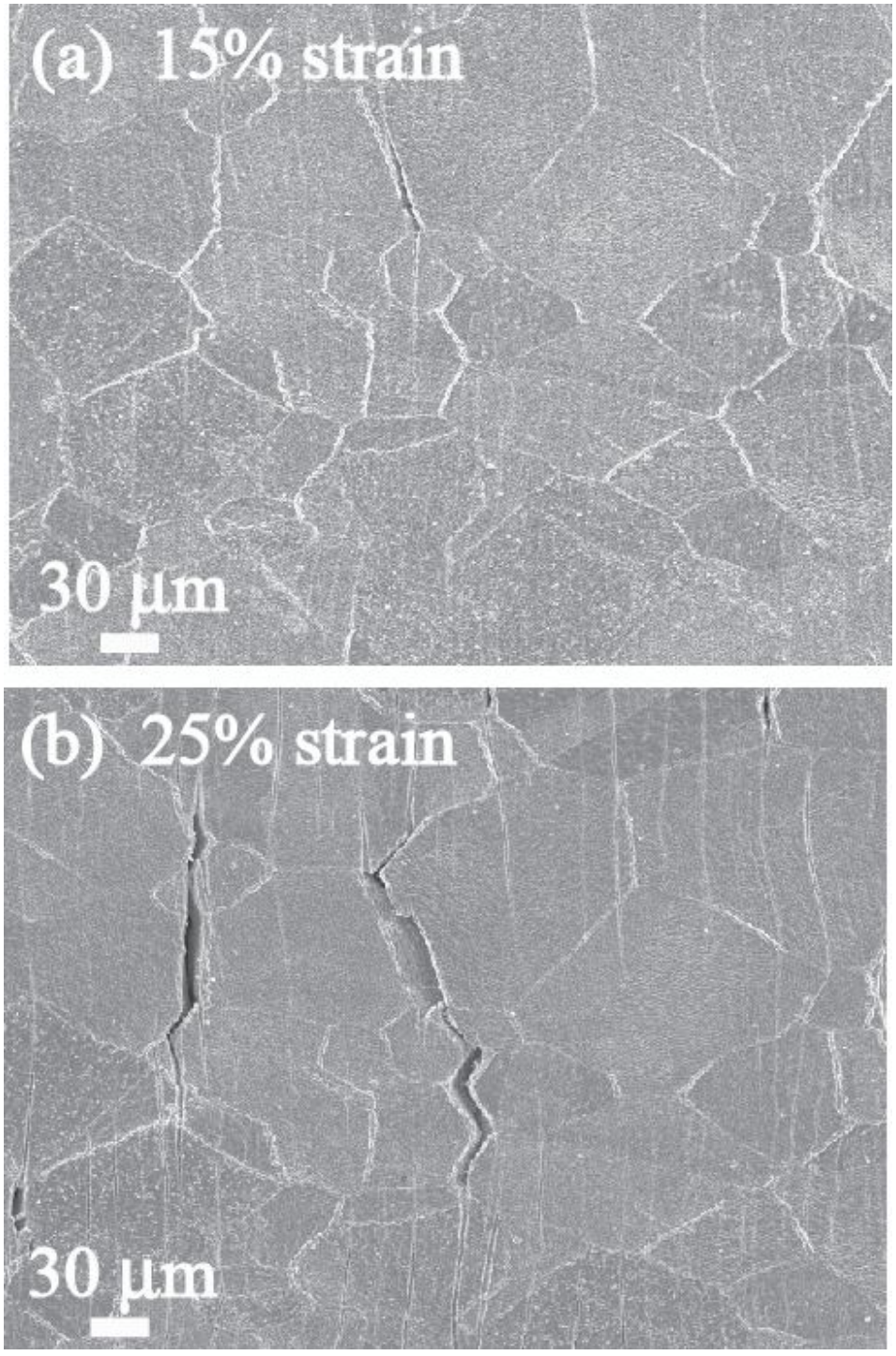

Figure 4.24 Crack micrographs of unirradiated 316L following straining to (a) 15% and (b) 25% strain in 500˚C SCW.

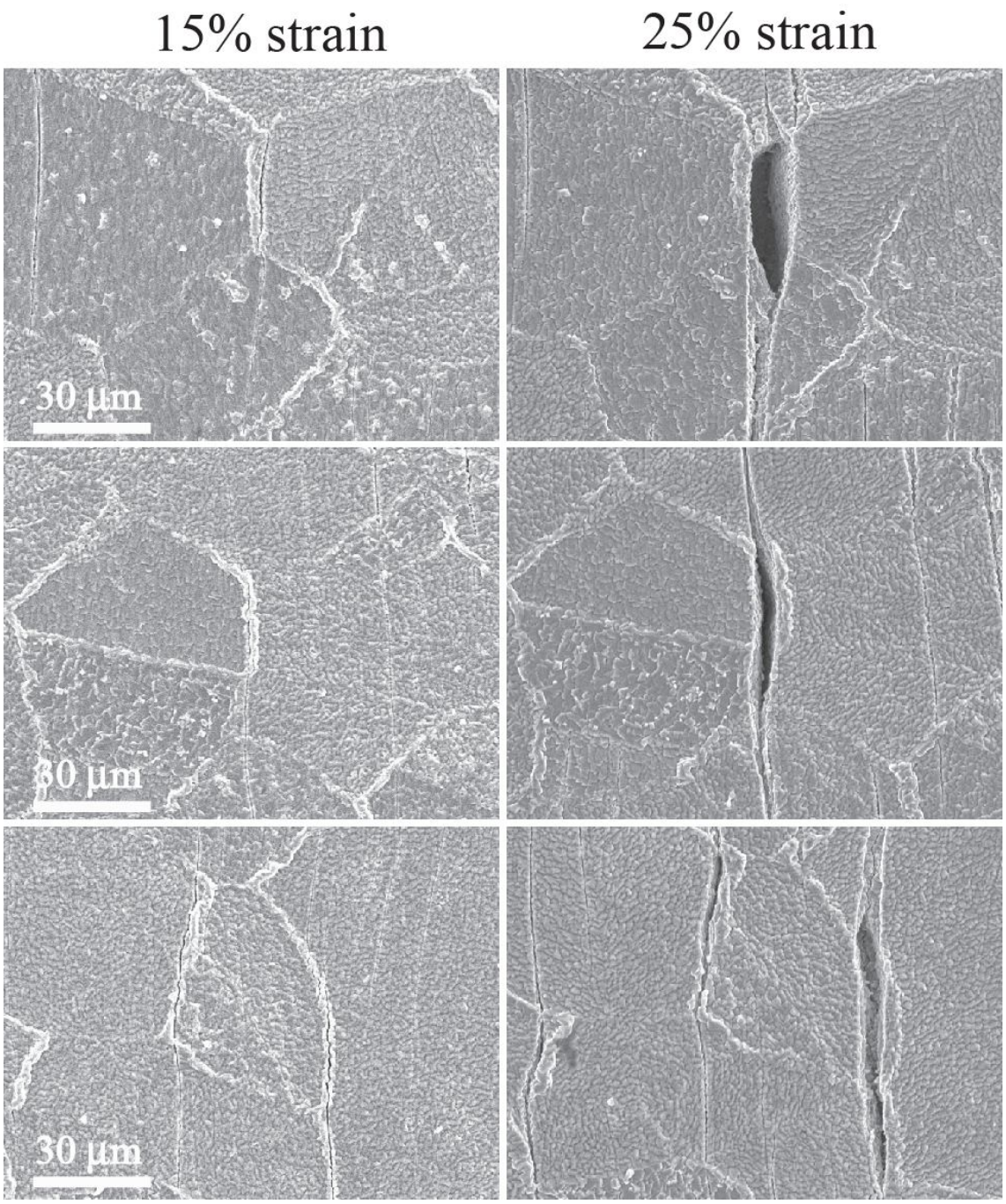

Figure 4.25 Crack micrographs of unirradiated 316L following straining to 15% and 25% strain in 500˚C SCW.

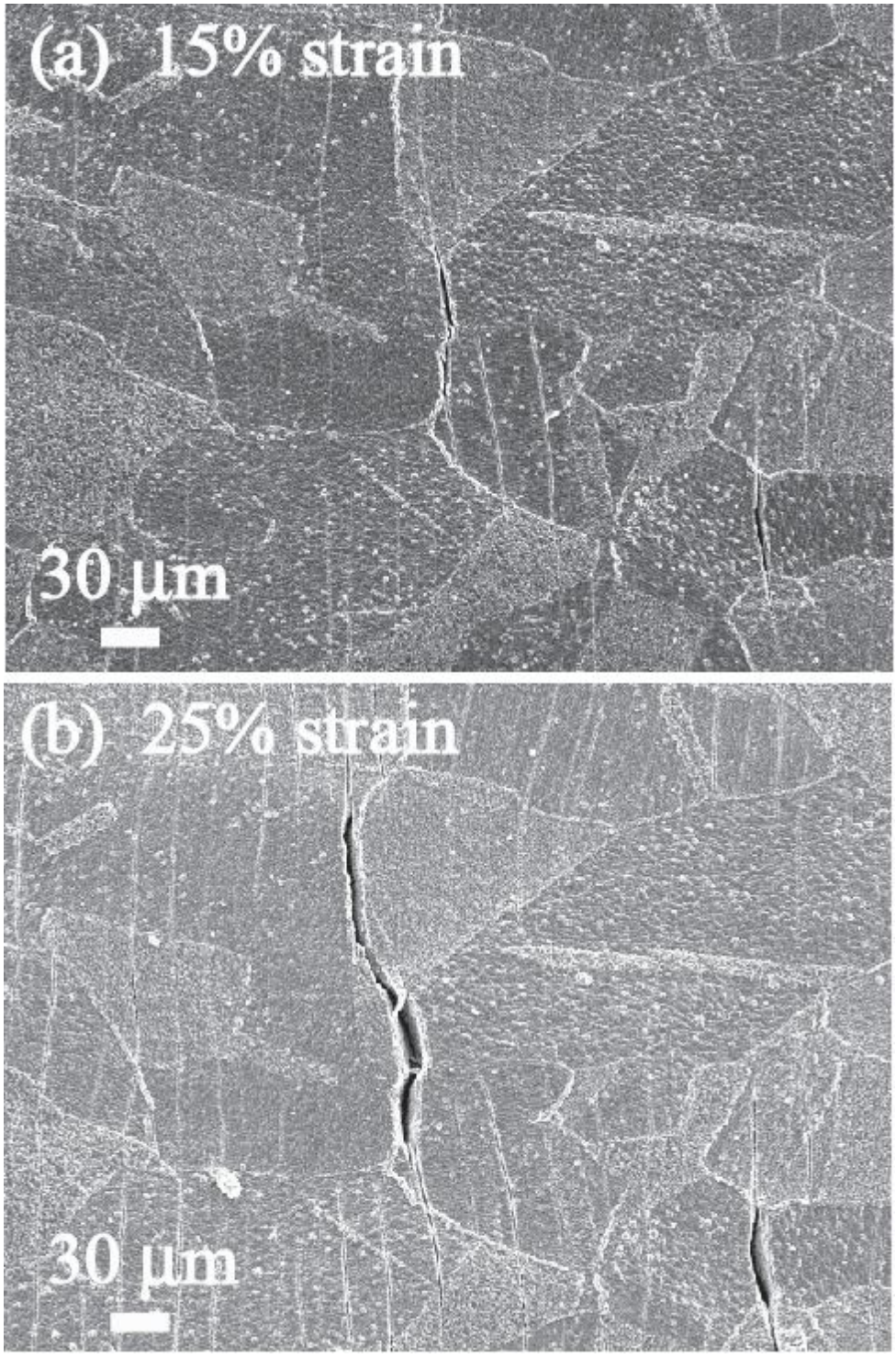

Figure 4.26 Crack micrographs of unirradiated 316LGBE following straining to 15% and 25% strain in 500˚C SCW.

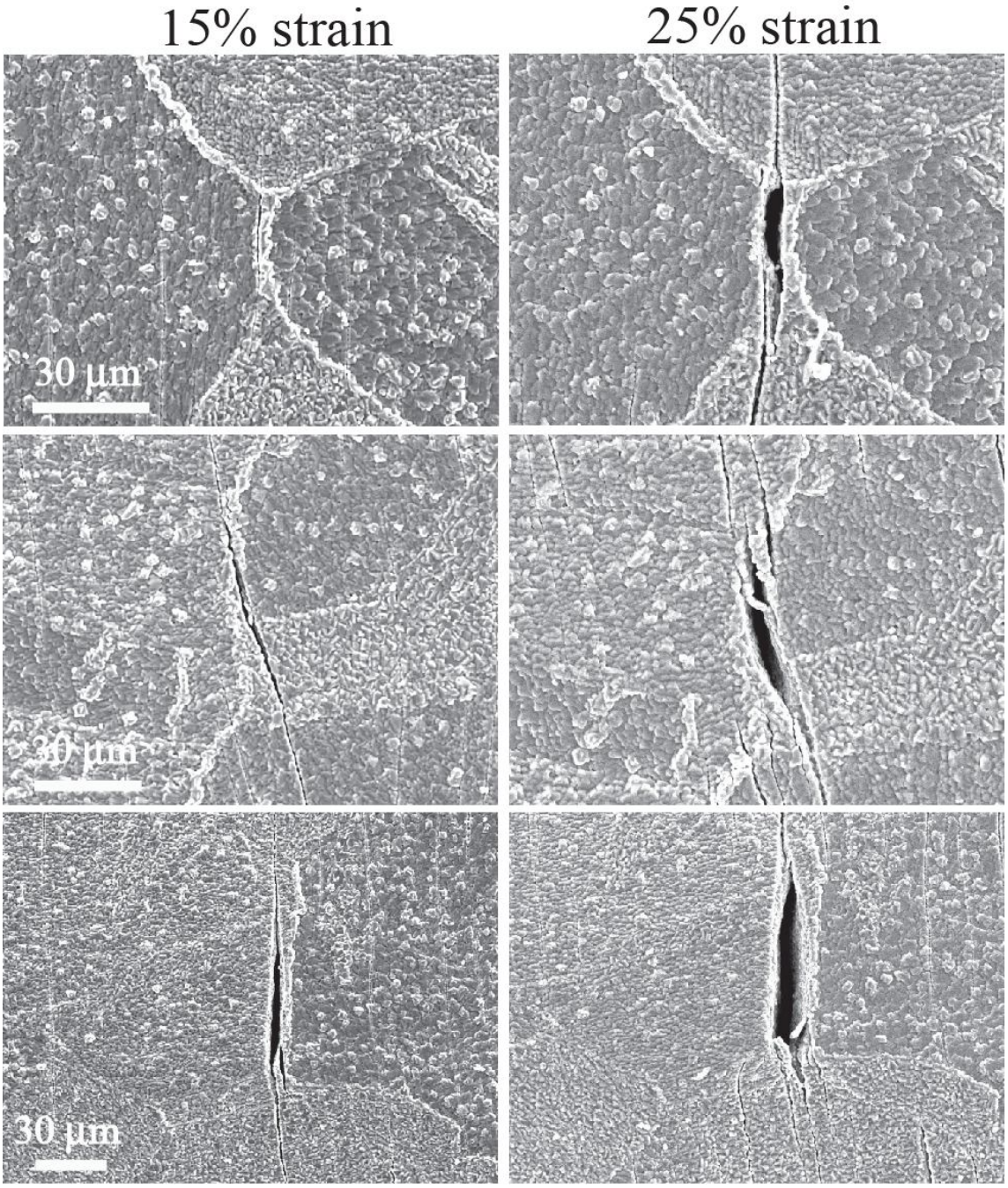

Figure 4.27 Crack micrographs of unirradiated 316LGBE following straining to 15% and 25% strain in 500˚C SCW.

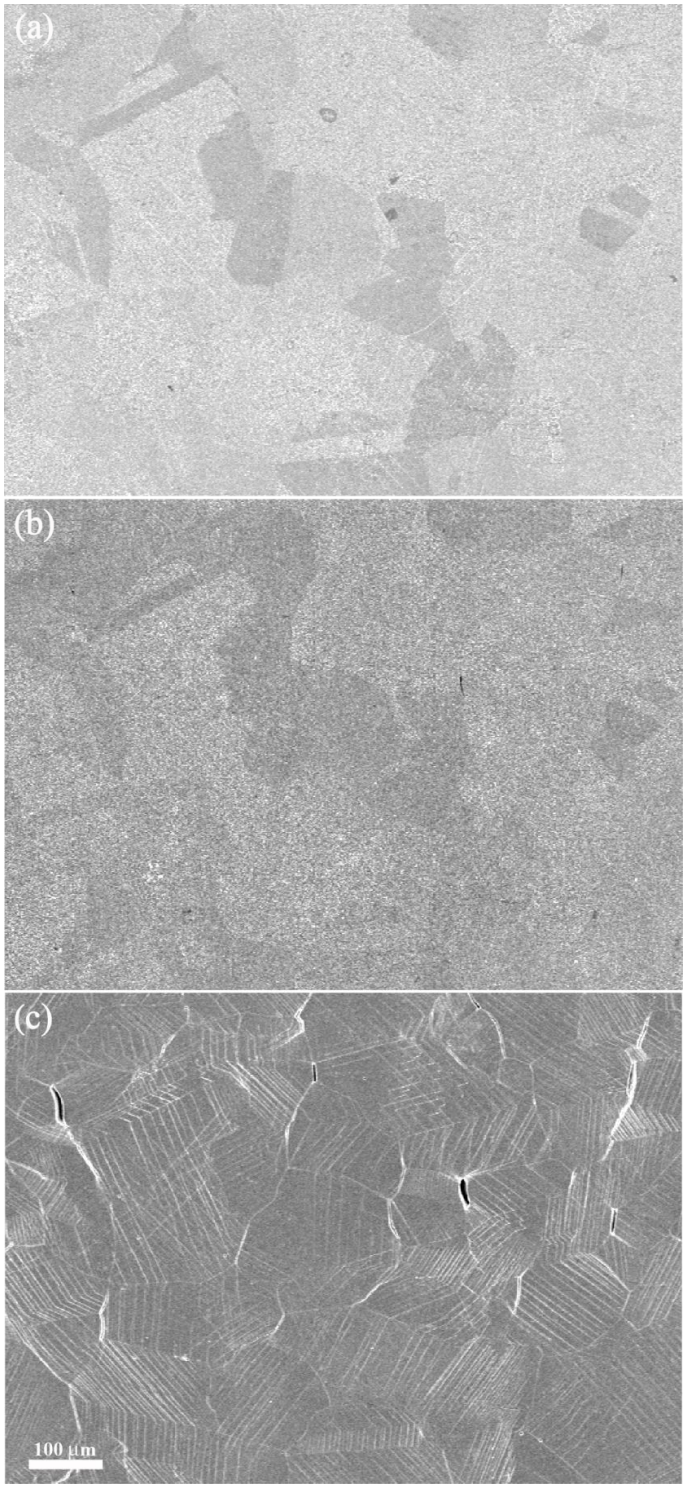

Figure 4.28 Crack images of 7 dpa proton irradiated 316L following straining to (a) 2%, (b) 5%, and (c) 10% strain in 400˚C SCW. The oxide layer is intact in (a) and (b) and stripped in (c).

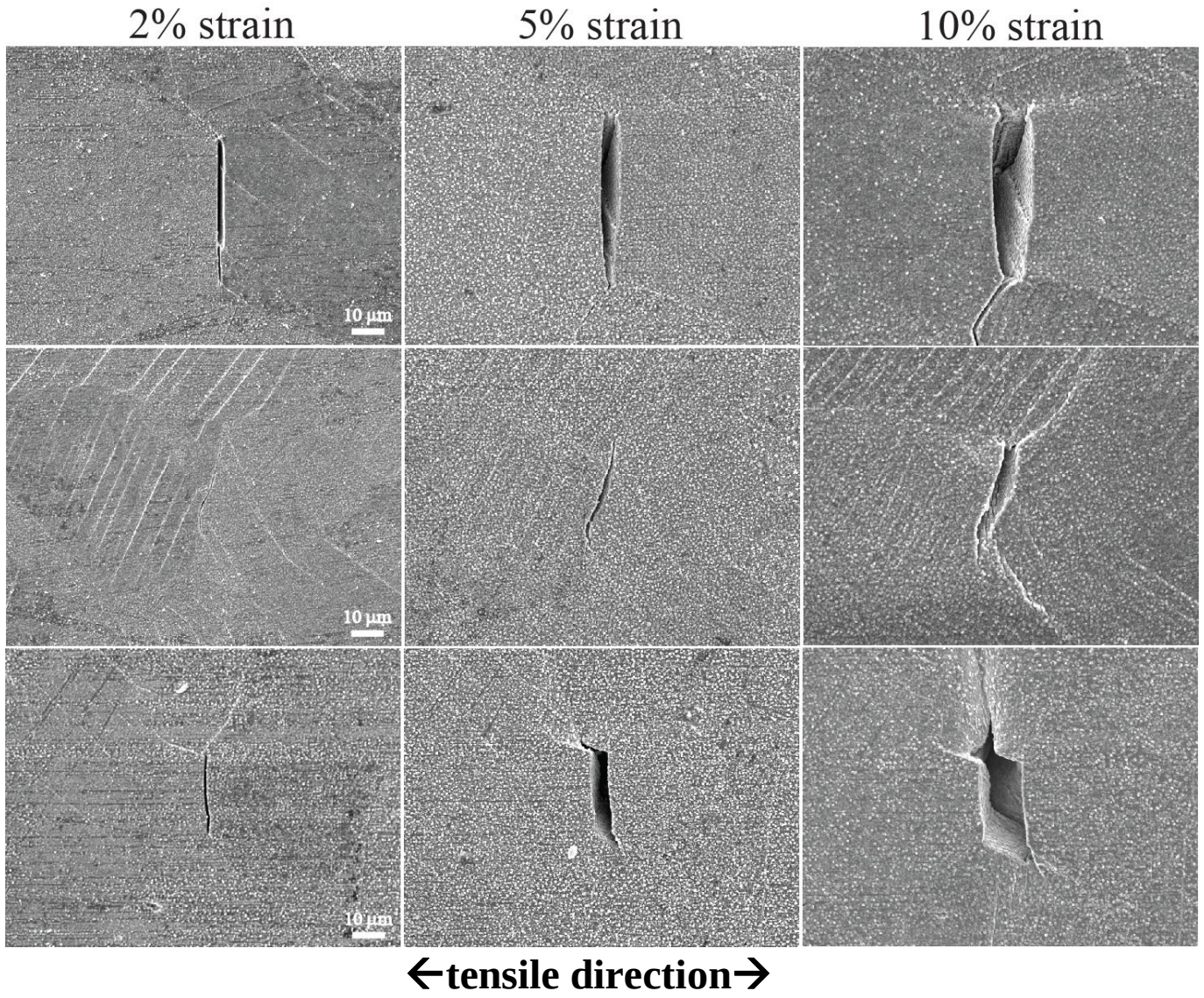

Figure 4.29 Crack micrographs of 7 dpa proton irradiated 316L following straining to 2%, 5%, and 10% strain in 400˚C SCW.

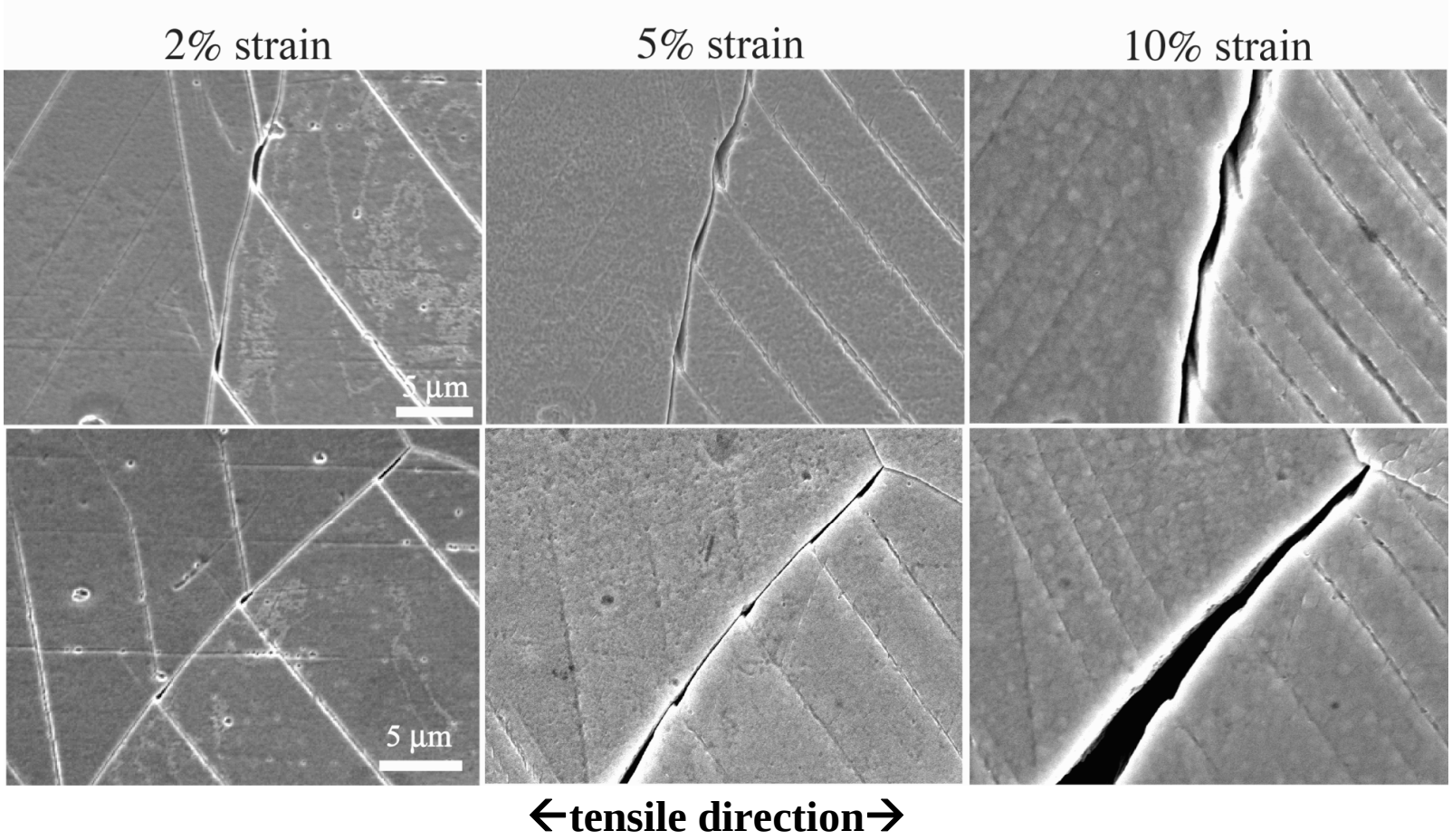

Figure 4.30 Development of GBC cracks into NS cracks with increasing strain in 7 dpa proton irradiated 316L strained to 2%, 5%, and 10% strain in 400˚C SCW.

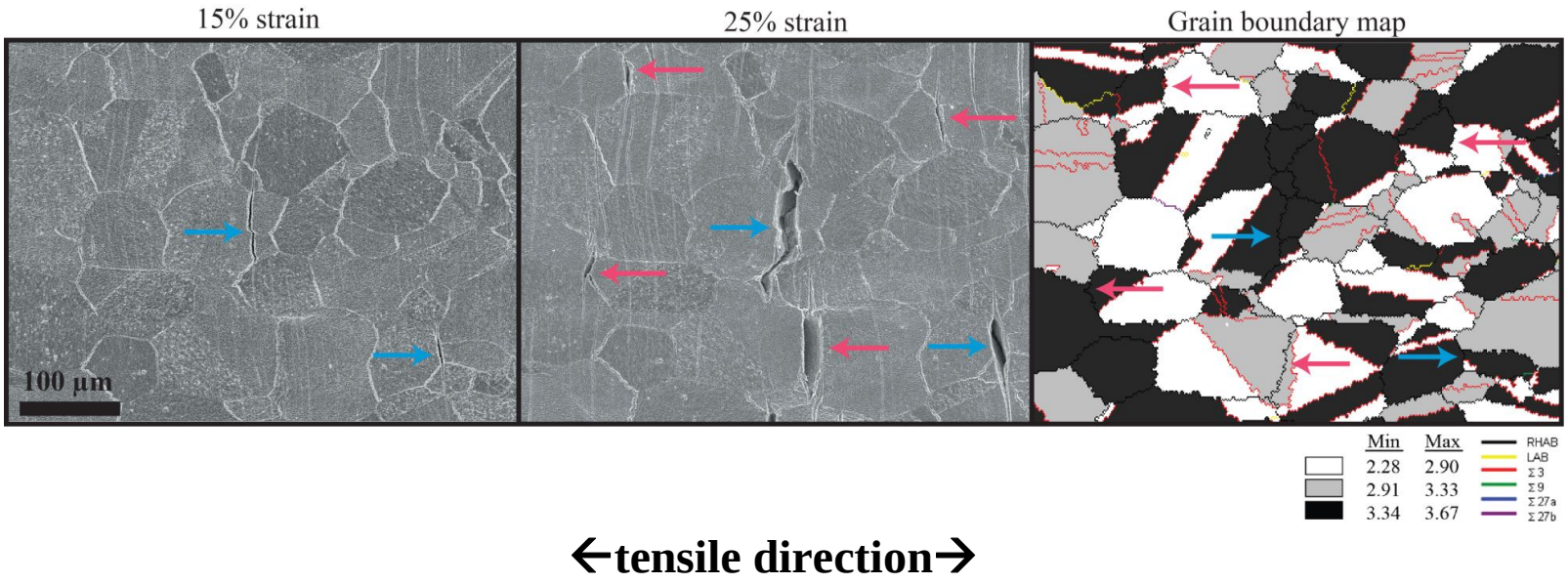

Figure 4.31 Intergranular cracking of 316L specimen strained to 15% and 25% strain in 500˚C SCW and corresponding grain boundary character and Taylor factor map. Blue arrows indicate IG cracks that developed following straining to 15% and pink arrows indicate cracks that developed following straining to 25%.

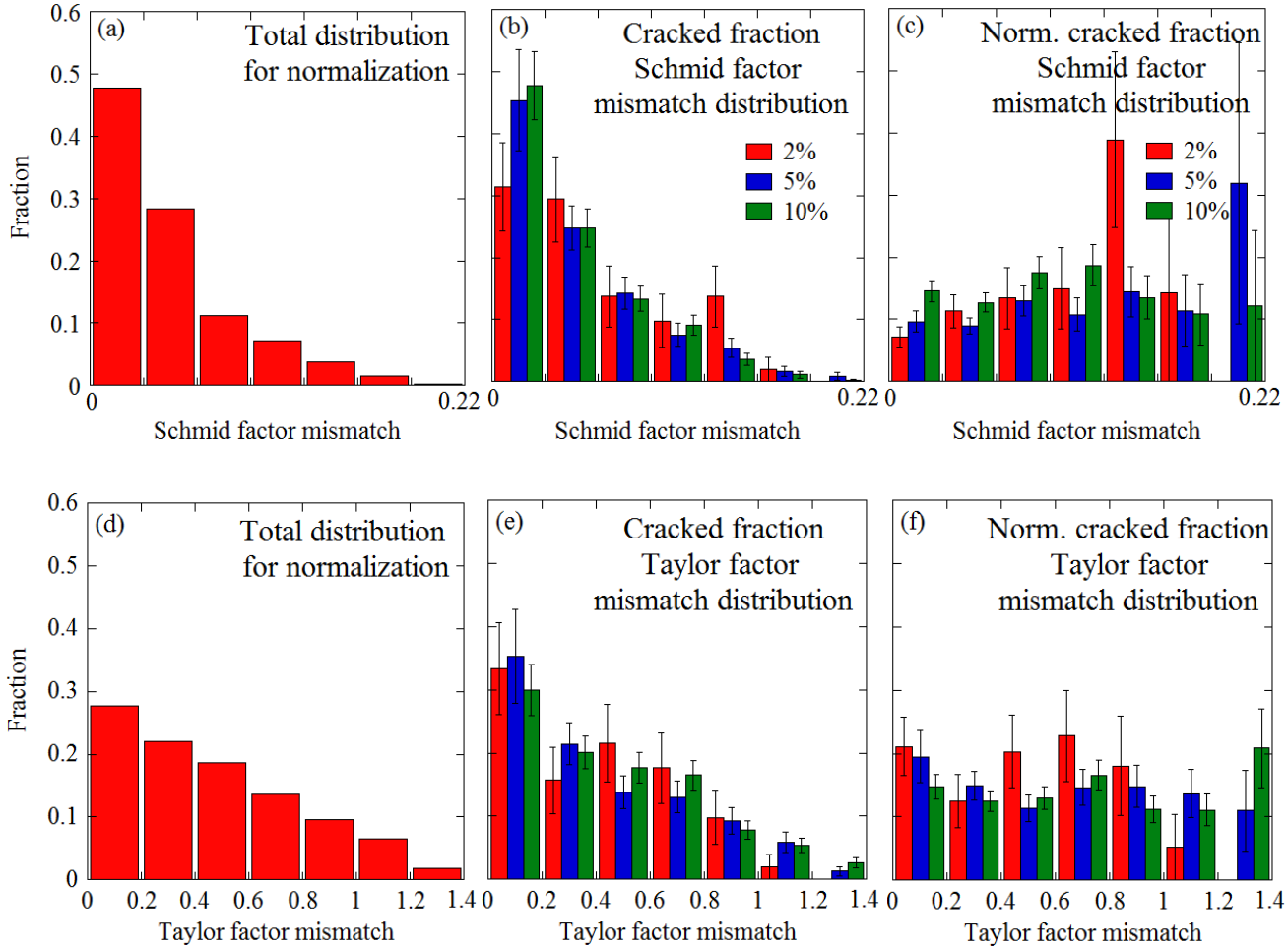

Figure 4.32 Schmid and Taylor factor mismatch distributions (a), (d) in bulk 316L, (b), (e) of grains adjacent to cracked boundaries, (c), (f) of grains adjacent to cracked boundaries normalized to mismatch distribution in bulk 316L.

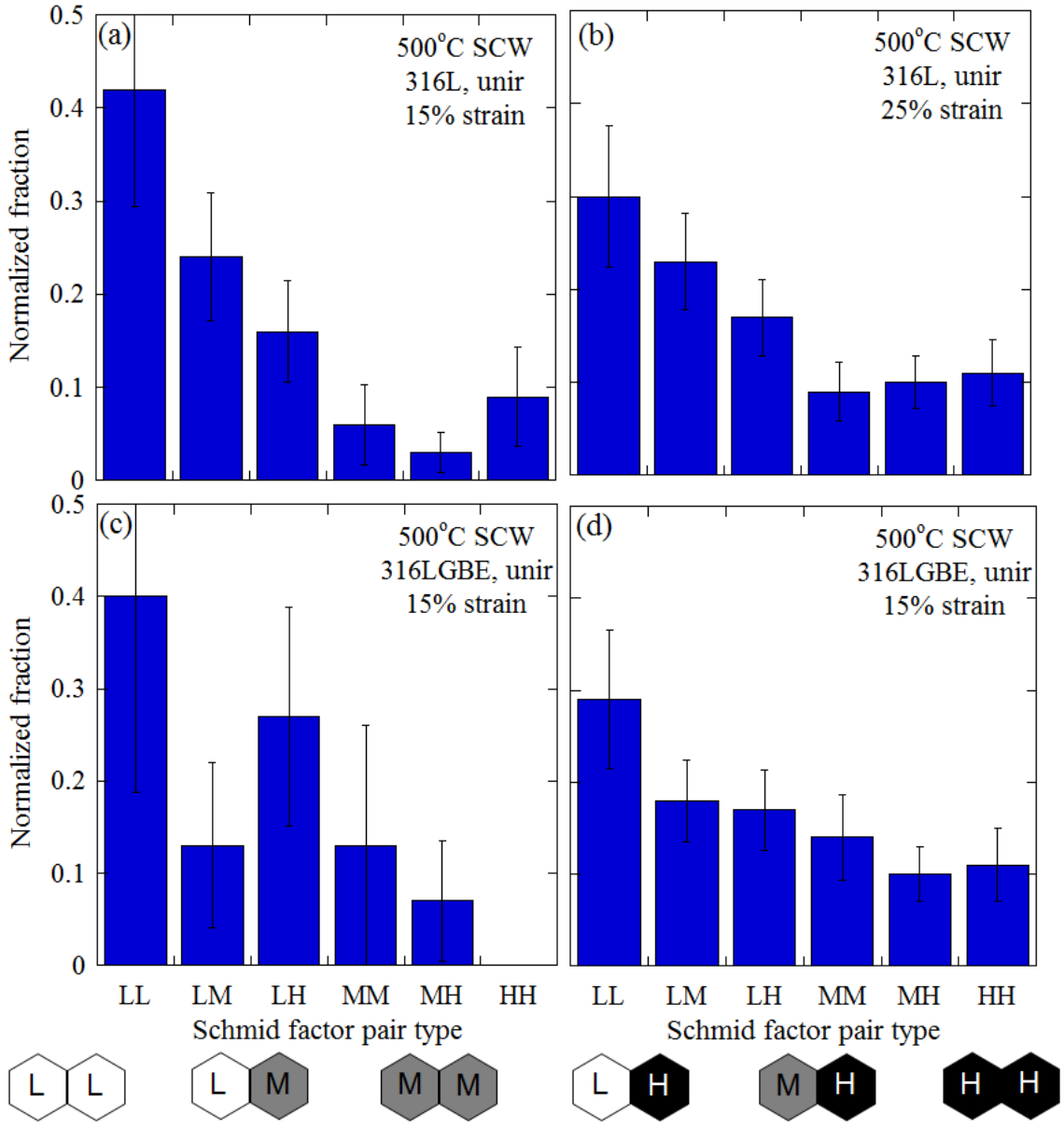

Figure 4.33 Normalized fraction of cracked grain boundaries with specified Schmid factor pair types for unirradiated 316L and 316LGBE strained to (a), (c) 15% strain and (b), (d) 25% strain in 500˚C SCW.

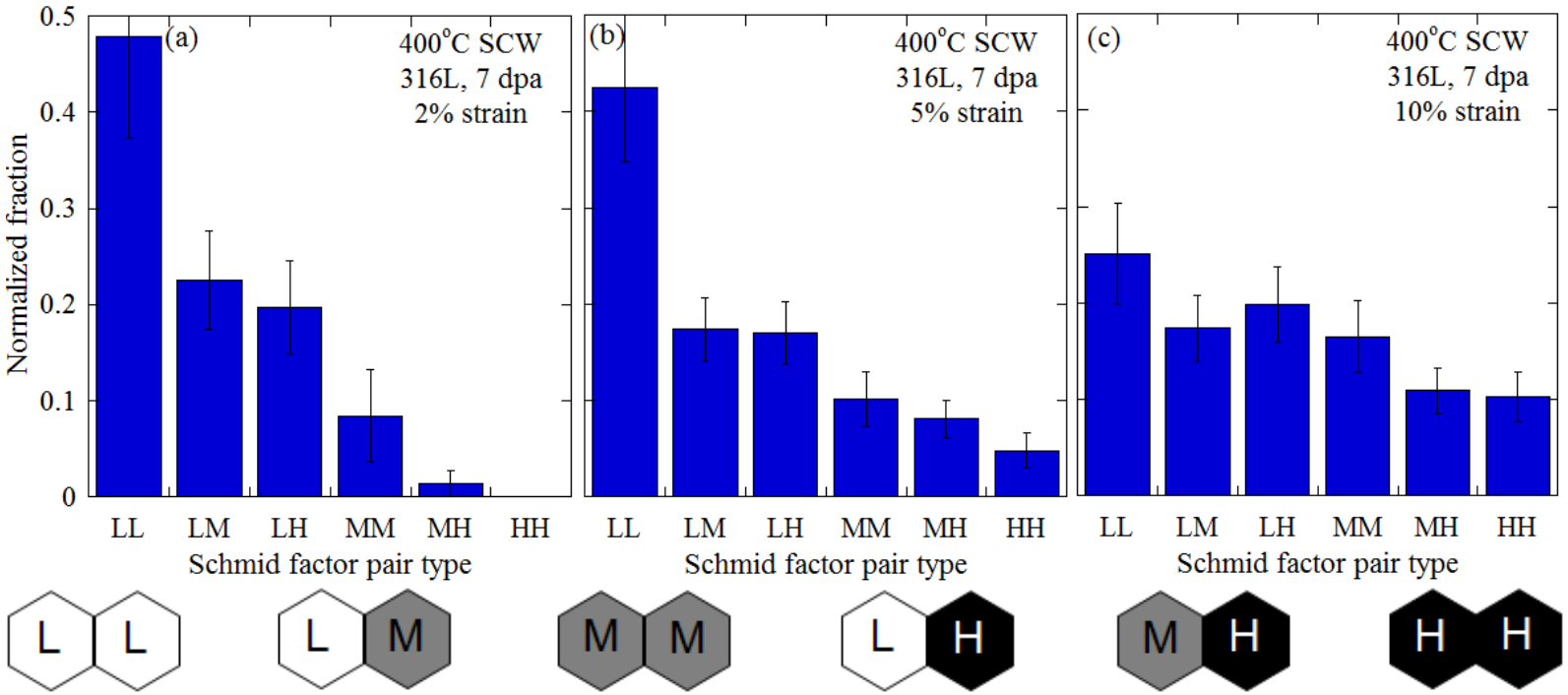

Figure 4.34 Normalized fraction of cracked grain boundaries with specified Schmid factor pair types for 7 dpa proton irradiated 316L strained to (a) 2%, (b) 5%, and (c) 10% strain in 400˚C SCW.

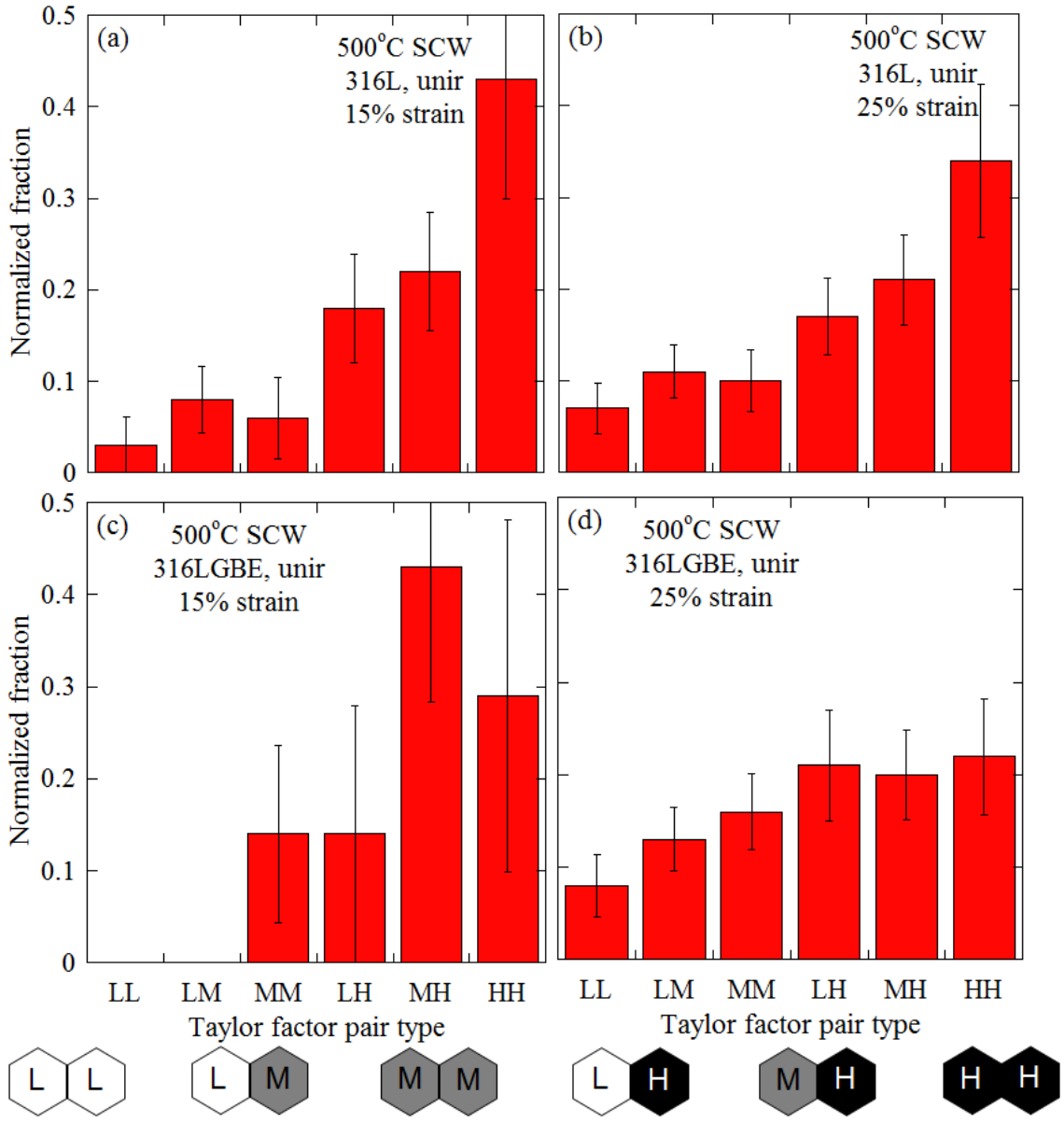

Figure 4.35 Normalized fraction of cracked grain boundaries with specified Taylor factor pair types for unirradiated 316L and 316LGBE strained to (a), (c) 15% strain and (b), (d) 25% strain in 500˚C SCW.

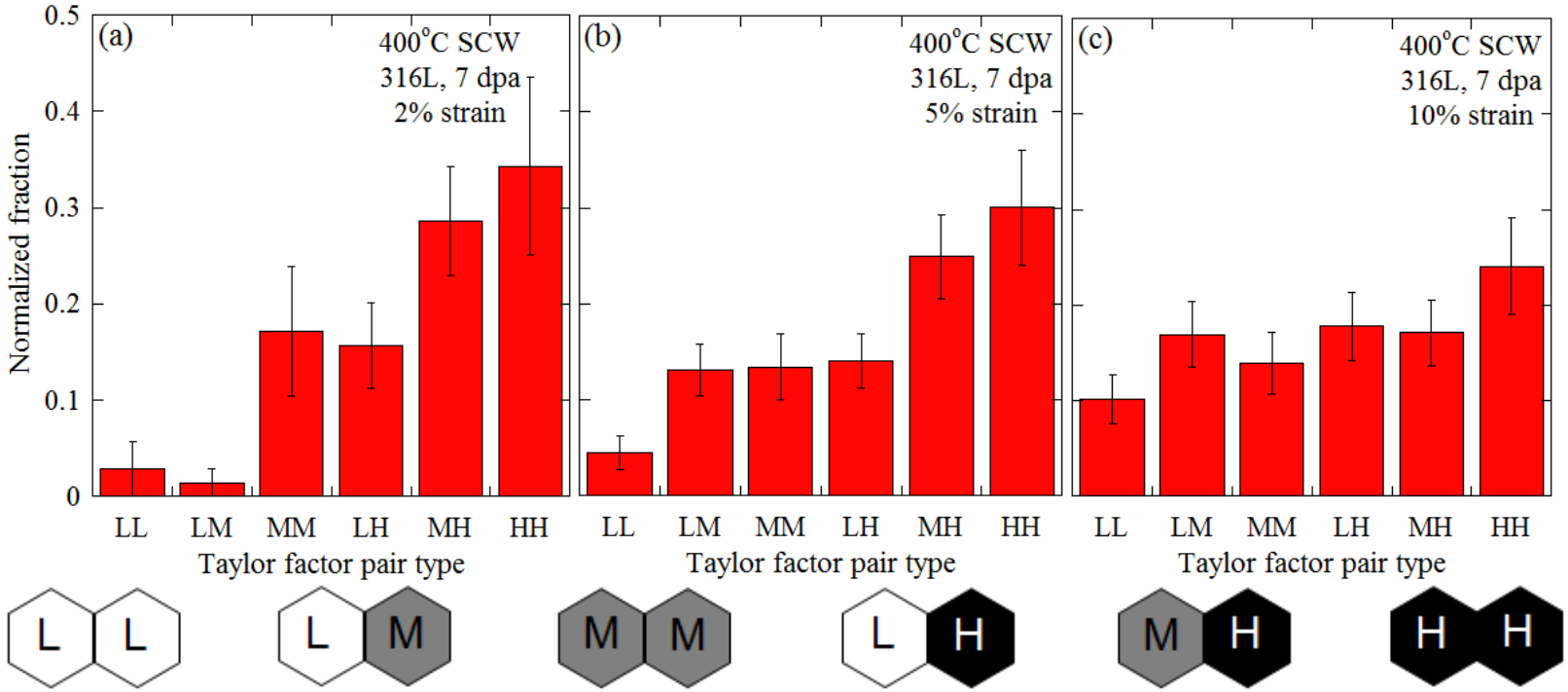

Figure 4.36 Normalized fraction of cracked grain boundaries with specified Taylor factor pair types for 7 dpa proton irradiated 316L strained to (a) 2%, (b) 5%, and (c) 10% strain in 400˚C SCW.

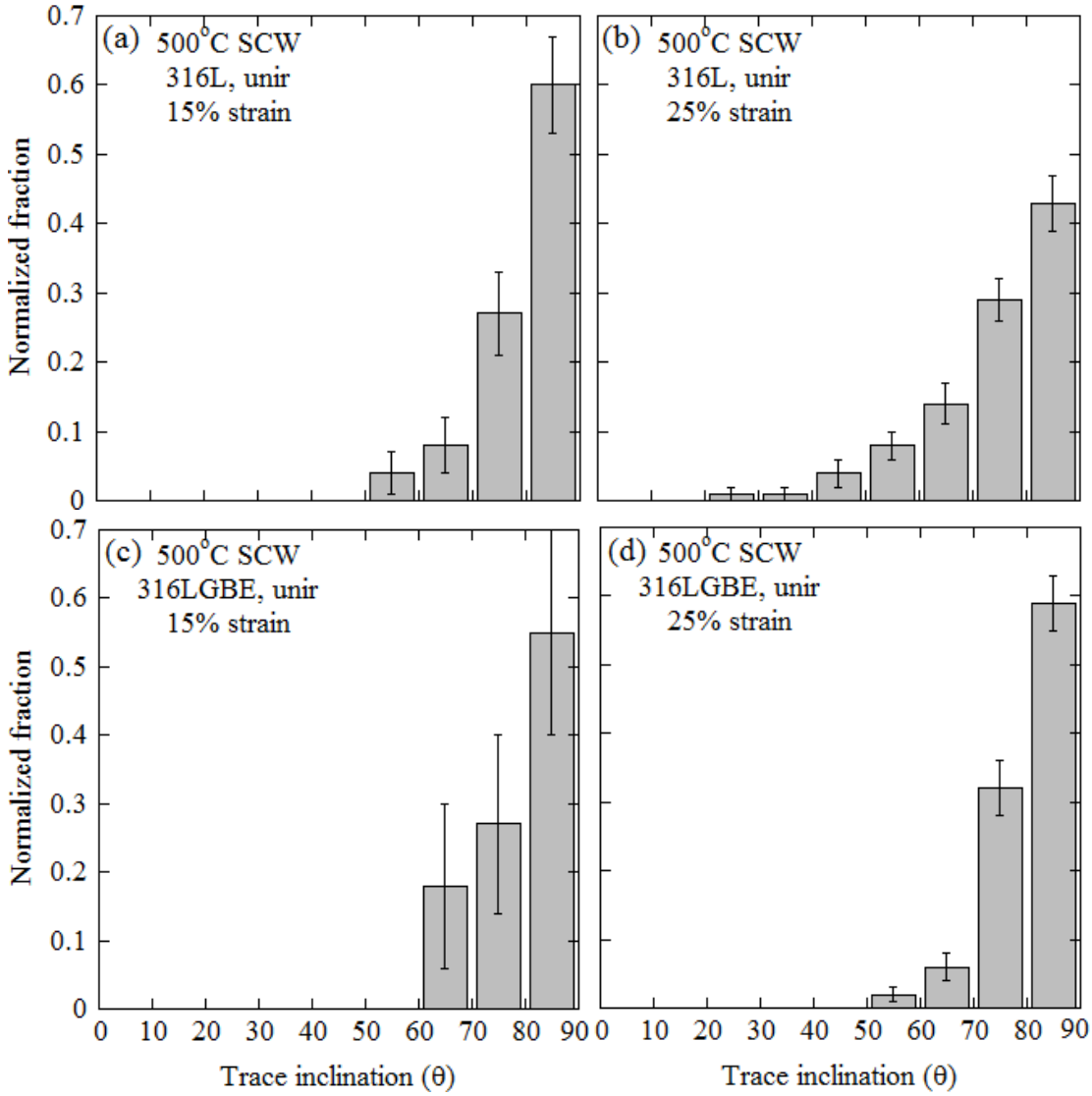

Figure 4.37 Fraction of cracked grain boundaries with specified trace inclinations for unirradiated 316L and 316LGBE at (a), (c) 15% strain and (b), (d) 25% strain in 500˚C SCW.

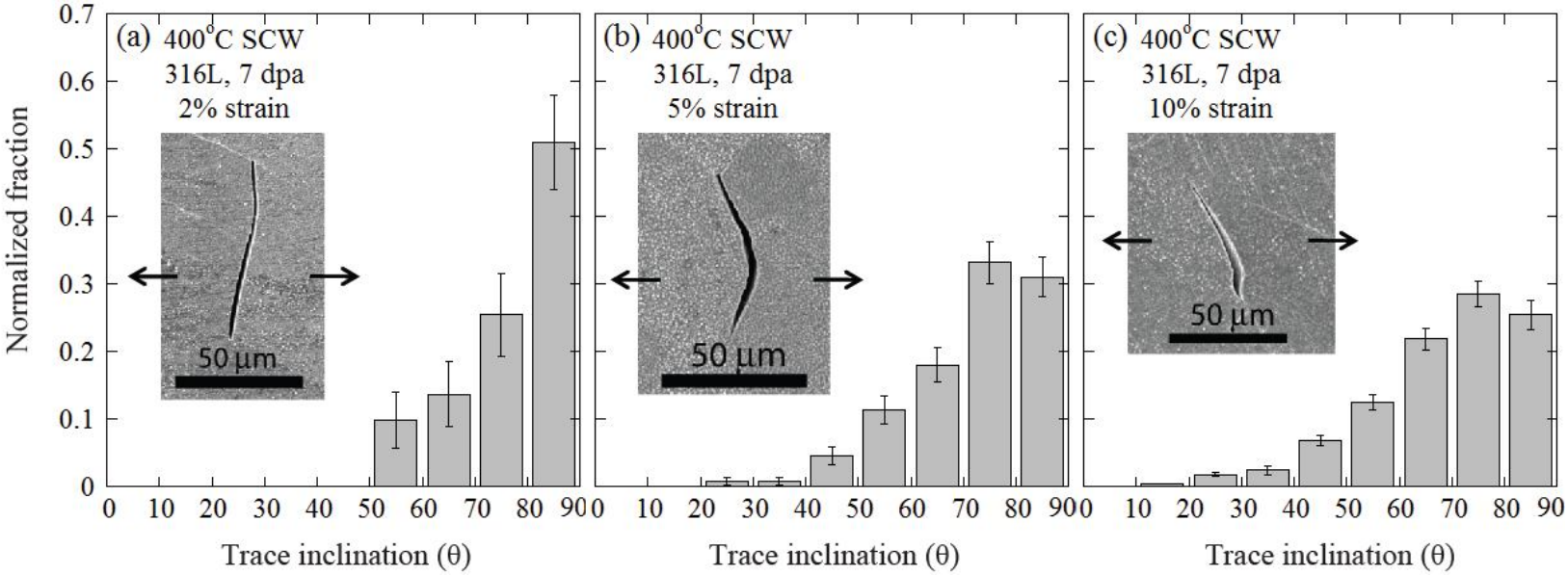

Figure 4.38 Fraction of cracked grain boundaries with specified trace inclinations for 7 dpa proton irradiated 316L strained to (a) 2%, (b) 5%, and (c) 10% strain in 400˚C SCW.

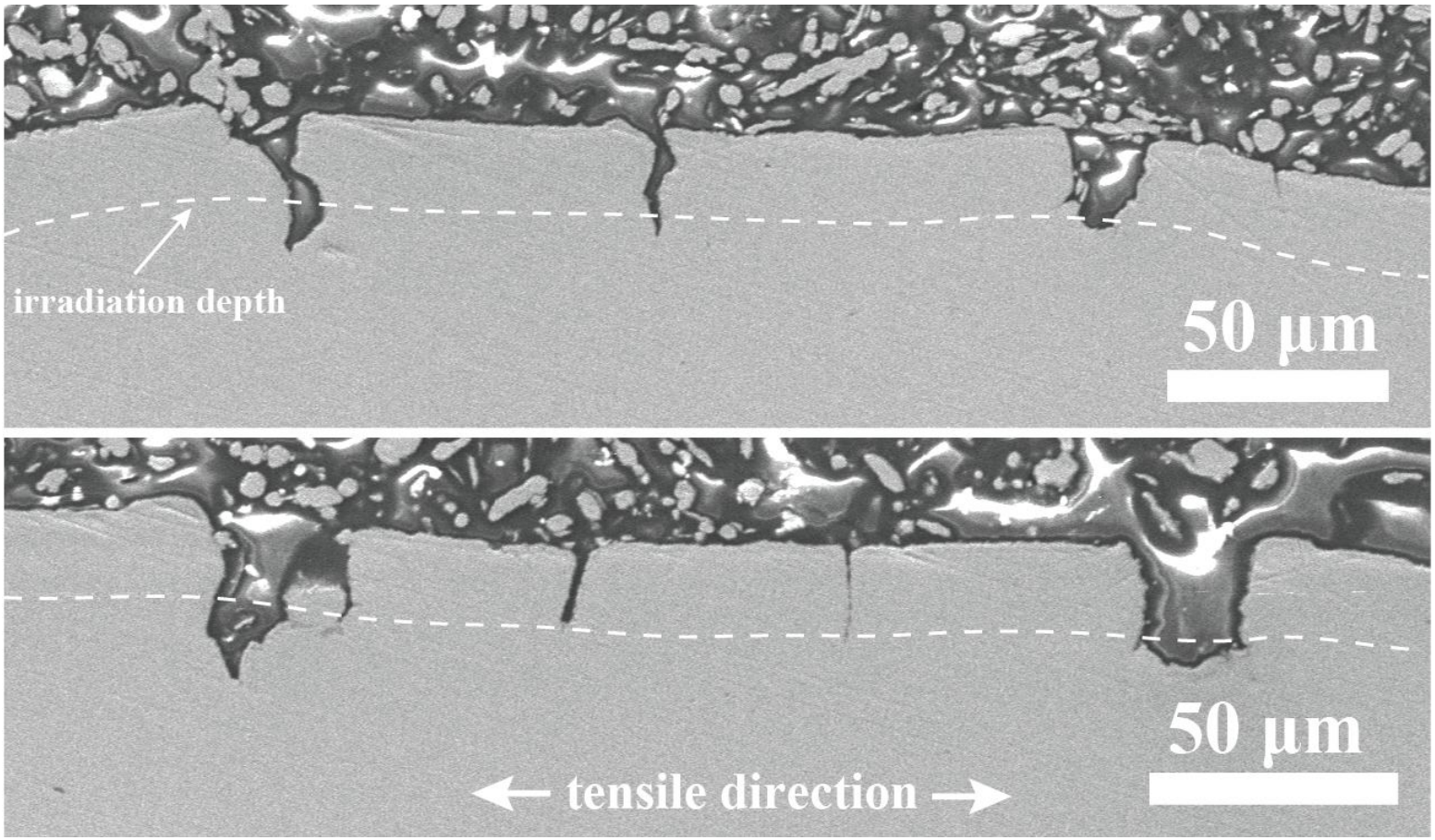

Figure 4.39 Cross sectional view of cracked grain boundaries in 316L 7 dpa irradiated tensile specimens following straining to failure in 400˚C SCW. White dotted lines indicate the depth of proton penetration into the sample.

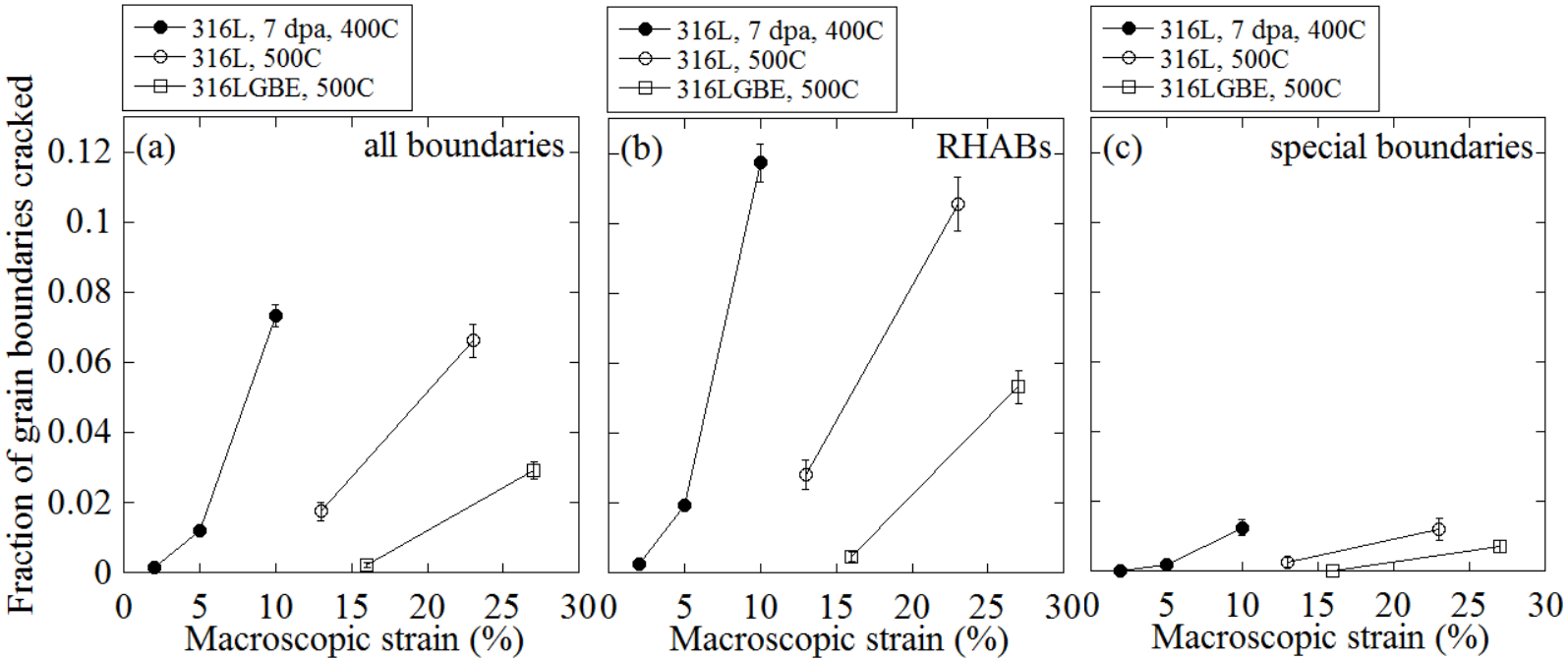

Figure 4.40 Fraction of (a) all boundaries, (b) RHABs, and (c) special boundaries that cracked in 316L and 316LGBE specimens following straining in 400˚C and 500˚C SCW.

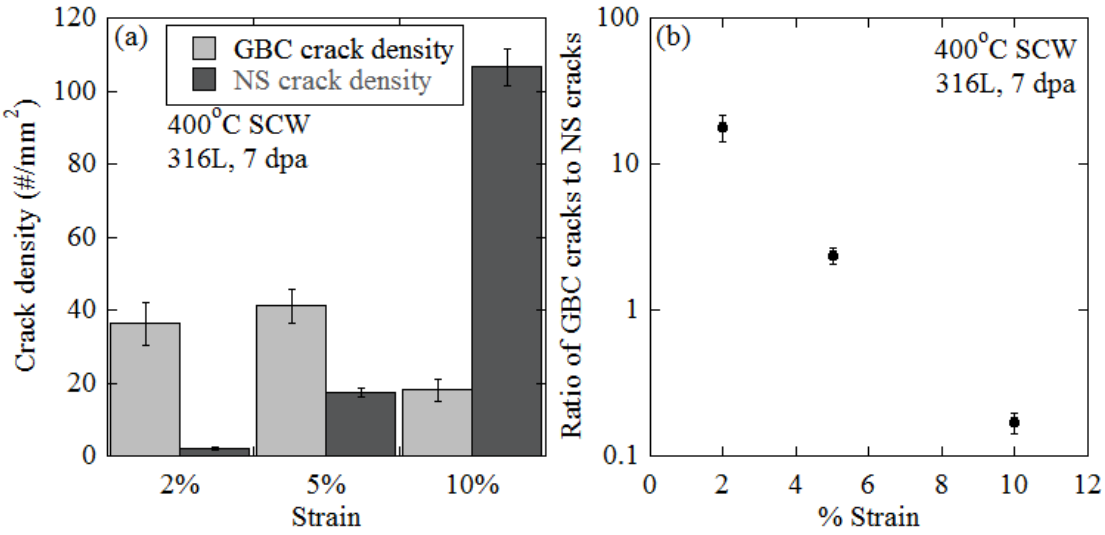

Figure 4.41 (a) Densities of GBC and NS crack in proton irradiated 316L strained in 400˚C SCW, and (b) ratio of GBC cracks to NS cracks on gage surface of irradiated 316L strained in 400˚C SCW.

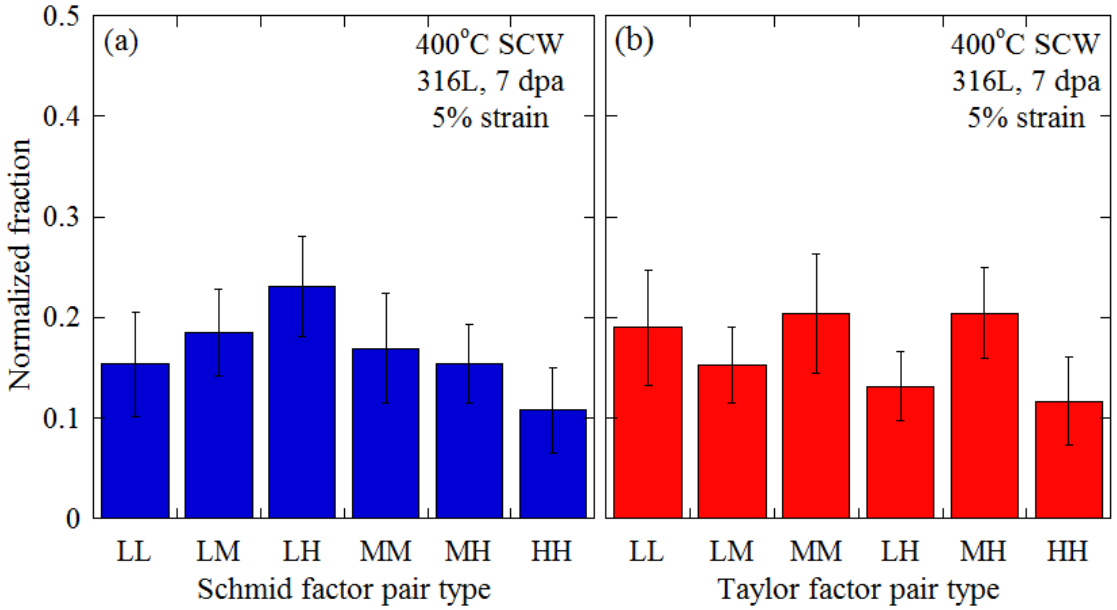

Figure 4.42 Normalized fraction of GBC cracked grain boundaries with specified (a) Schmid factor and (b) Taylor factor pair types for 7 dpa proton irradiated 316L strained to 5% in 400˚C SCW.

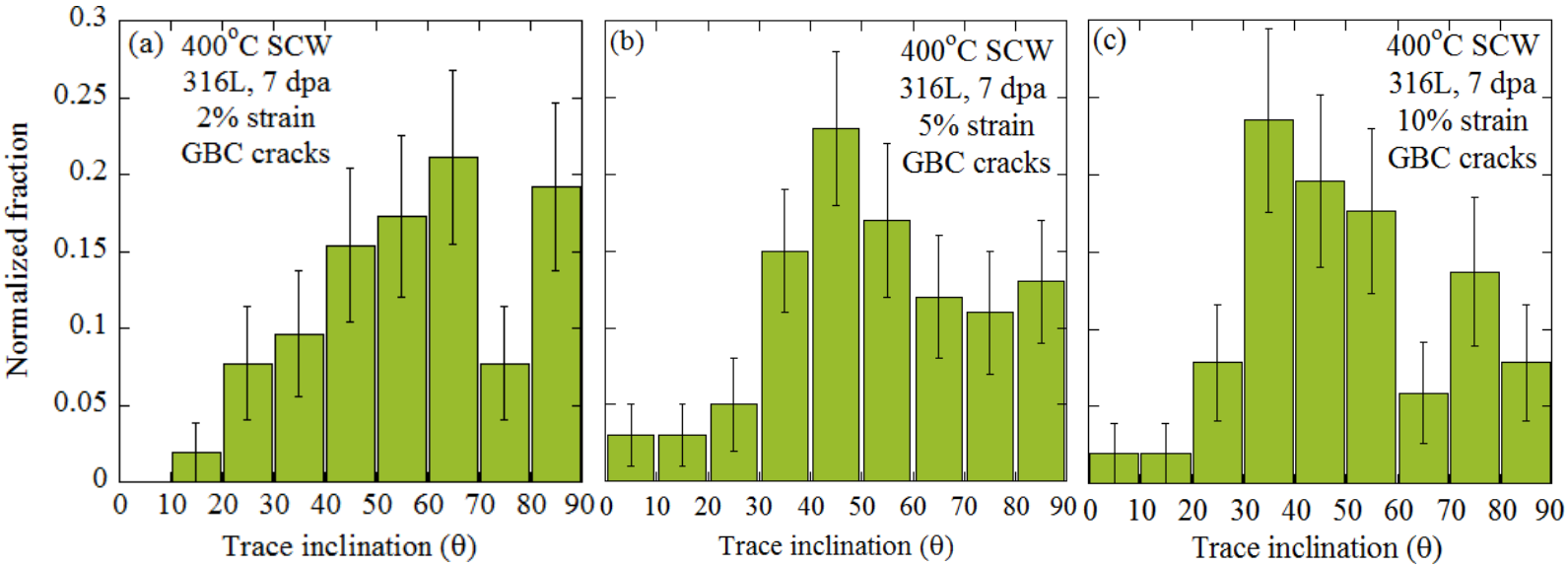

Figure 4.43 Fraction of GBC cracks that occur along boundaries with specified trace inclinations for 7 dpa proton irradiated 316L strained to (a) 2%, (b) 5% and (c) 10% in 400˚C SCW.

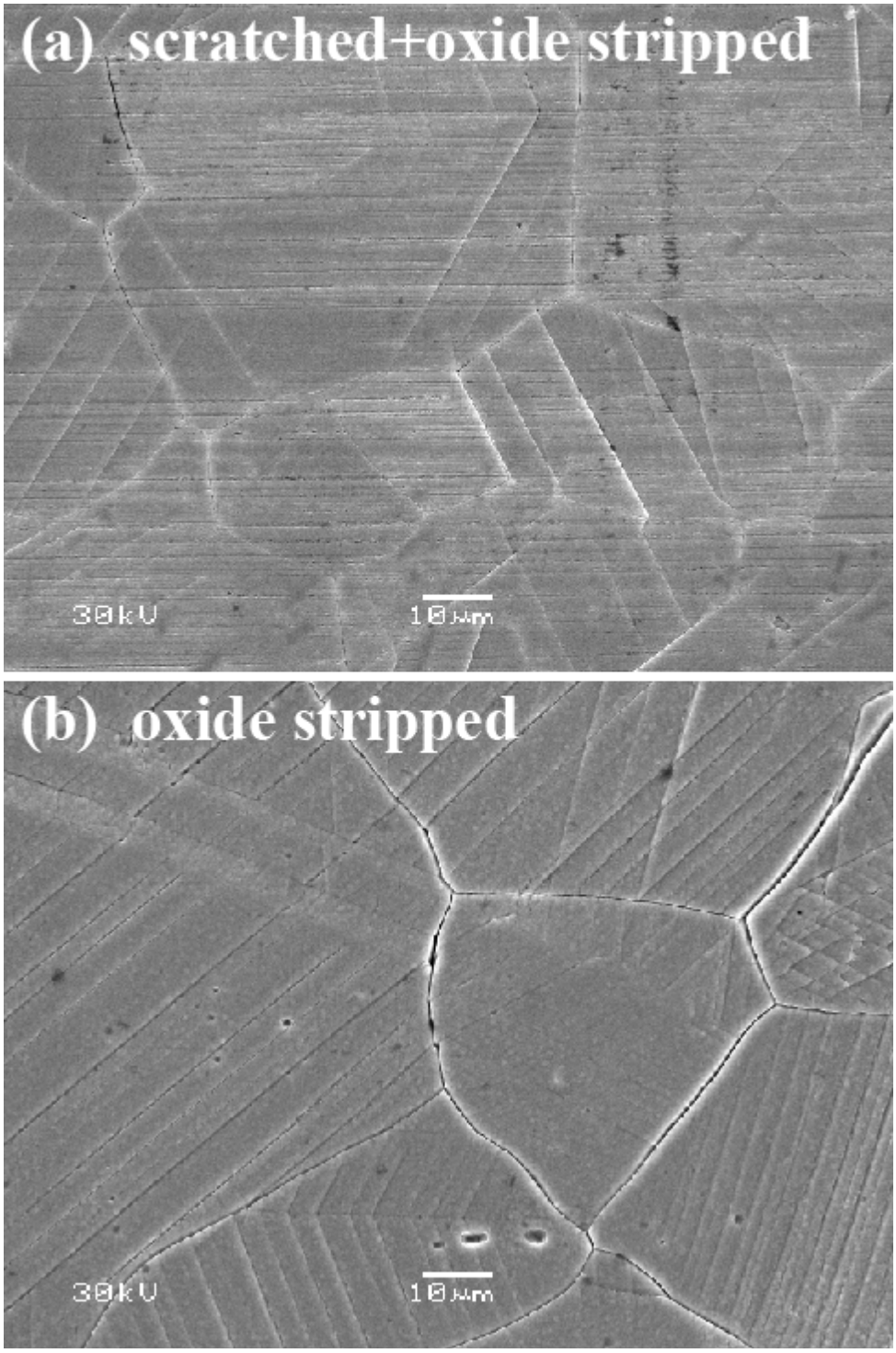

Figure 4.44 Gage surface of proton irradiated 316L stainless steel following straining in 400˚C SCW. (a) Micrograph of scratched specimen surface following straining to 2% and oxide stripping, (b) micrograph of oxide stripped region of specimen surface following straining to 10%.

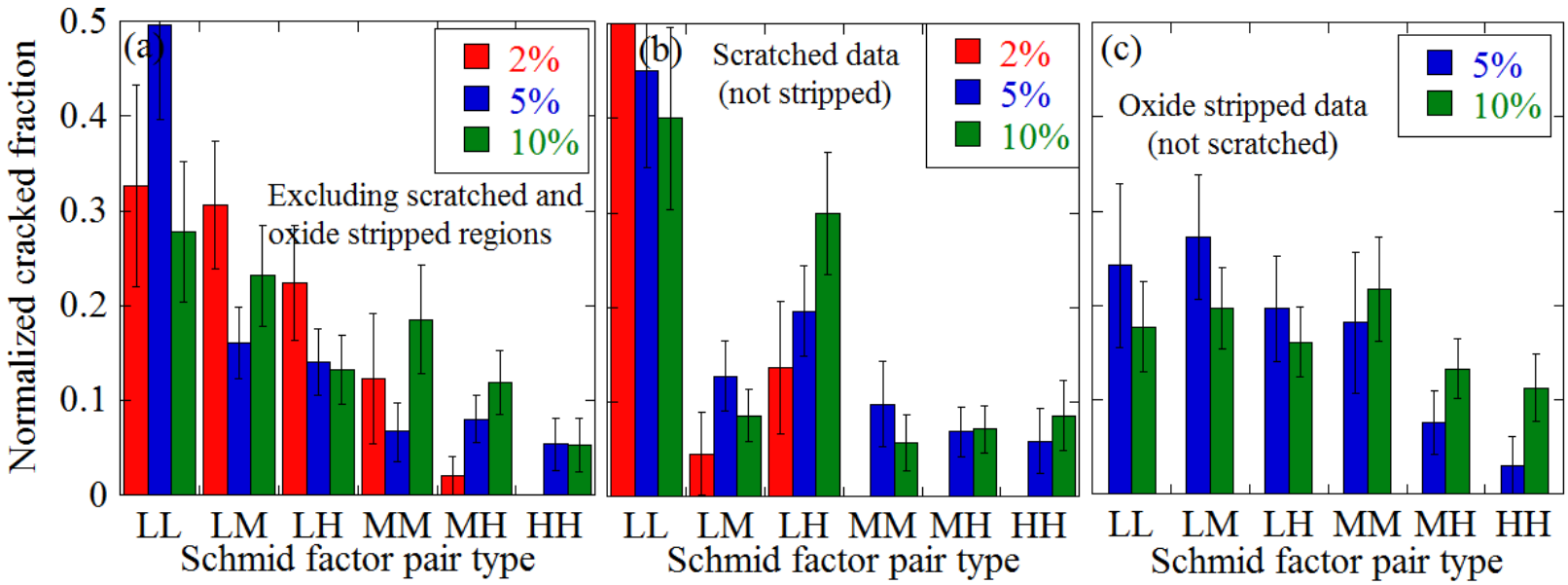

Figure 4.45 Normalized fraction of cracks as a function of Schmid factor pair type for proton irradiated 316L specimens strained to 2%, 5%, and 10% strain in 400˚C SCW, (a) cracks occurring in non-scratched and non-oxide stripped regions, (b) cracks occurring in scratched regions, (c) cracks occurring in oxide stripped regions.

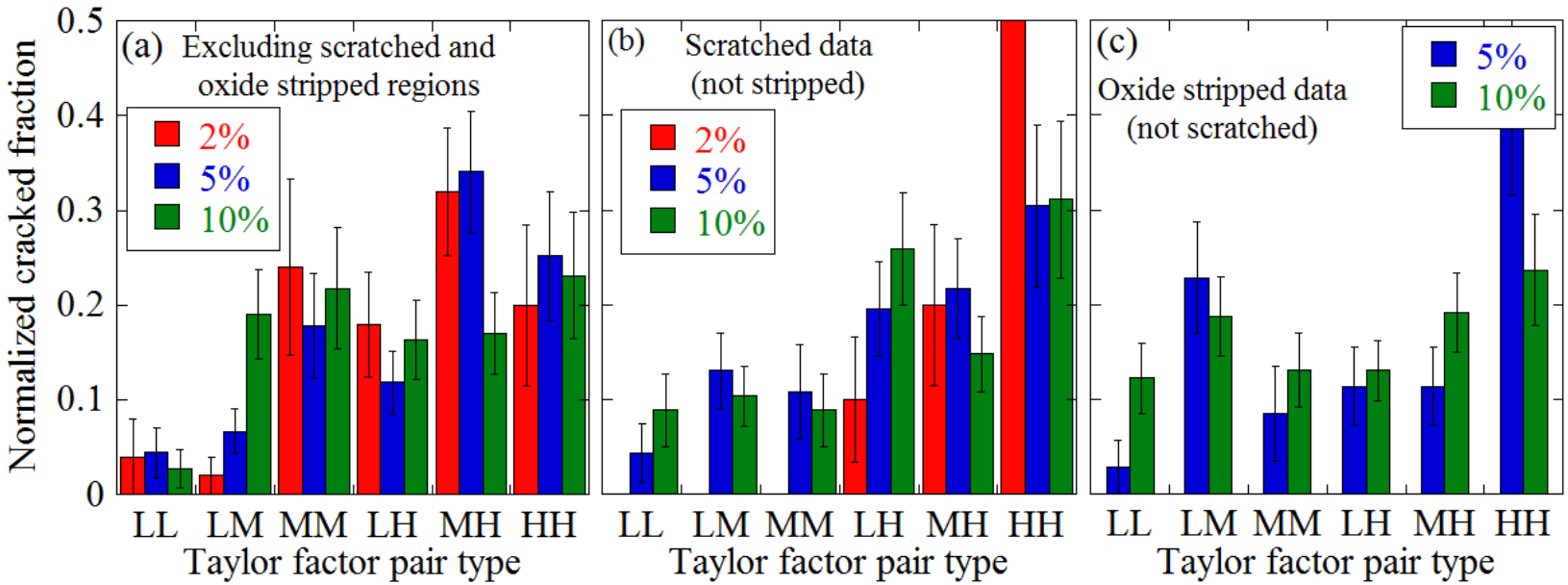

Figure 4.46 Normalized fraction of cracks as a function of Taylor factor pair type for proton irradiated 316L specimens strained to 2%, 5%, and 10% strain in 400˚C SCW, (a) cracks occurring in non-scratched and non-oxide stripped regions, (b) cracks occurring in scratched regions, (c) cracks occurring in oxide stripped regions.

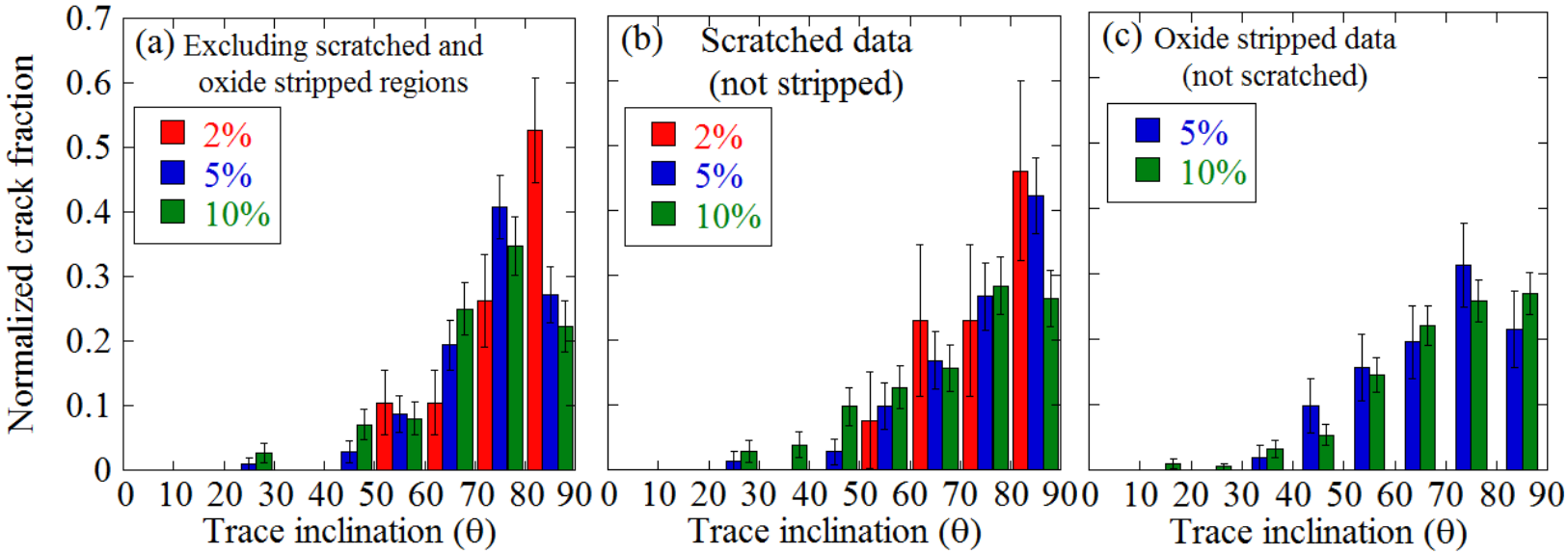

Figure 4.47 Fraction of cracks as a function of trace inclination for proton irradiated 316L specimens strained to 2%, 5%, and 10% strain in 400˚C SCW, (a) cracks occurring in non-scratched and non-oxide stripped regions, (b) cracks occurring in scratched regions, (c) cracks occurring in oxide stripped regions.

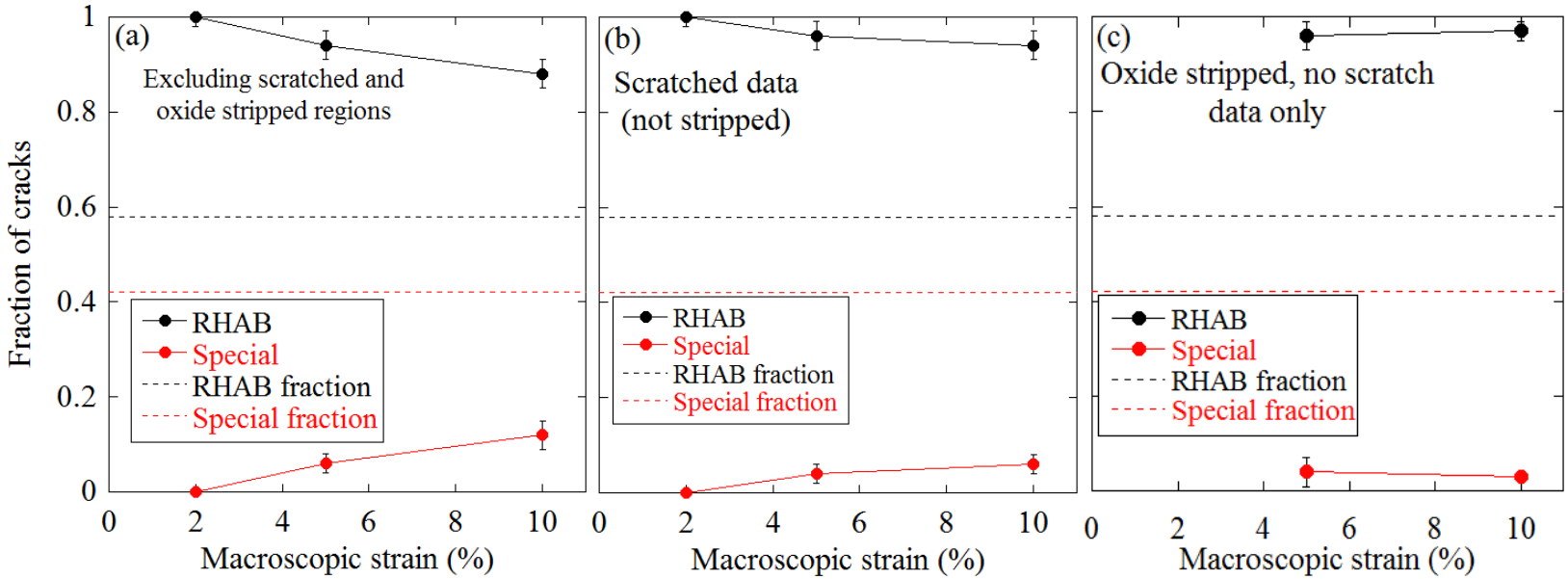

Figure 4.48 Fraction of cracks at RHABs and special boundaries as a function of strain for proton irradiated 316L specimens strained to 2%, 5%, and 10% strain in 400˚C SCW, (a) cracks occurring in non-scratched and non-oxide stripped regions, (b) cracks occurring in scratched regions, (c) cracks occurring in oxide stripped regions.

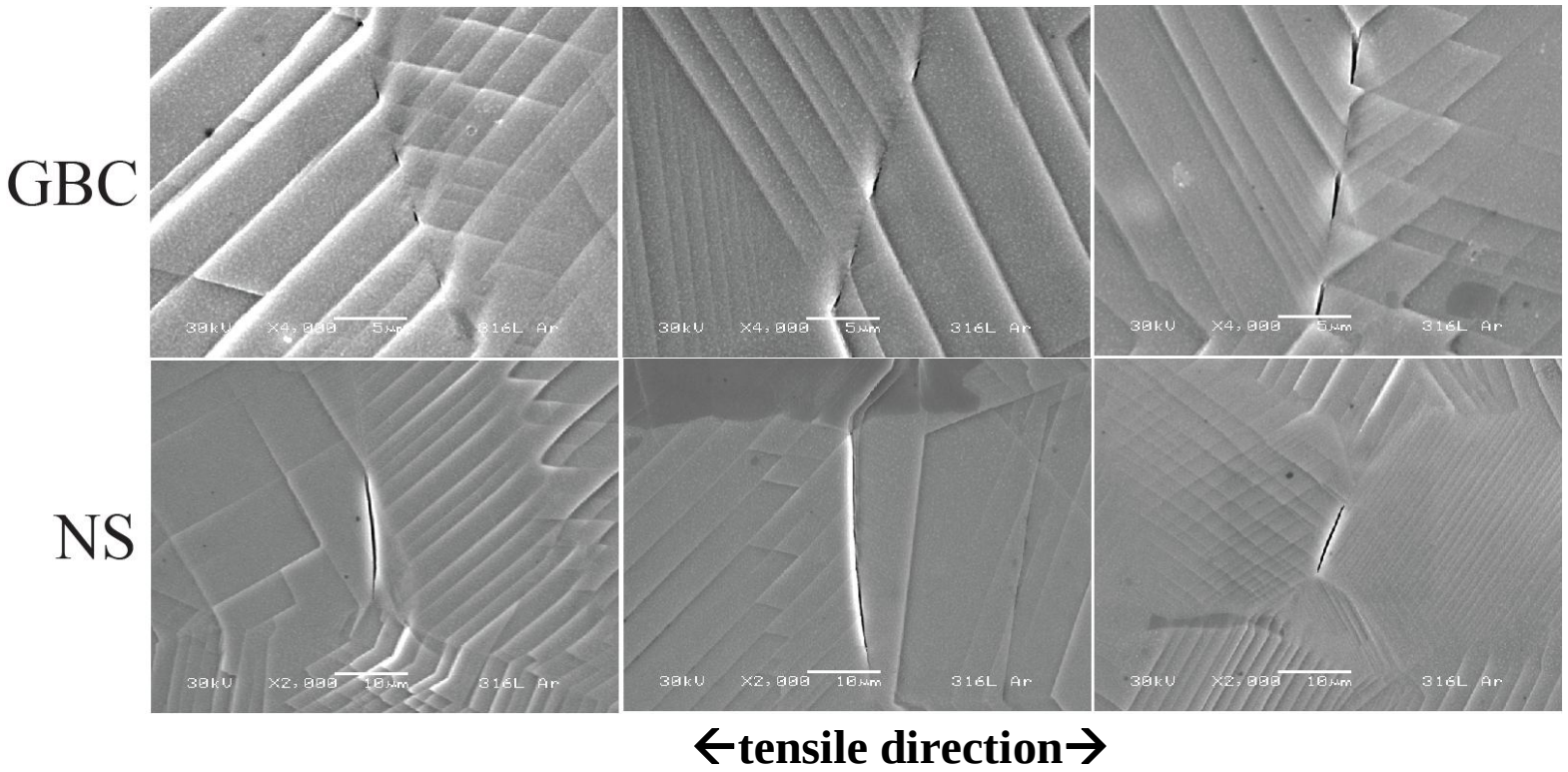

Figure 4.49 GBC and NS cracks on the gage surface of 7 dpa proton irradiated 316L strained to 5% in 400˚C purified argon.

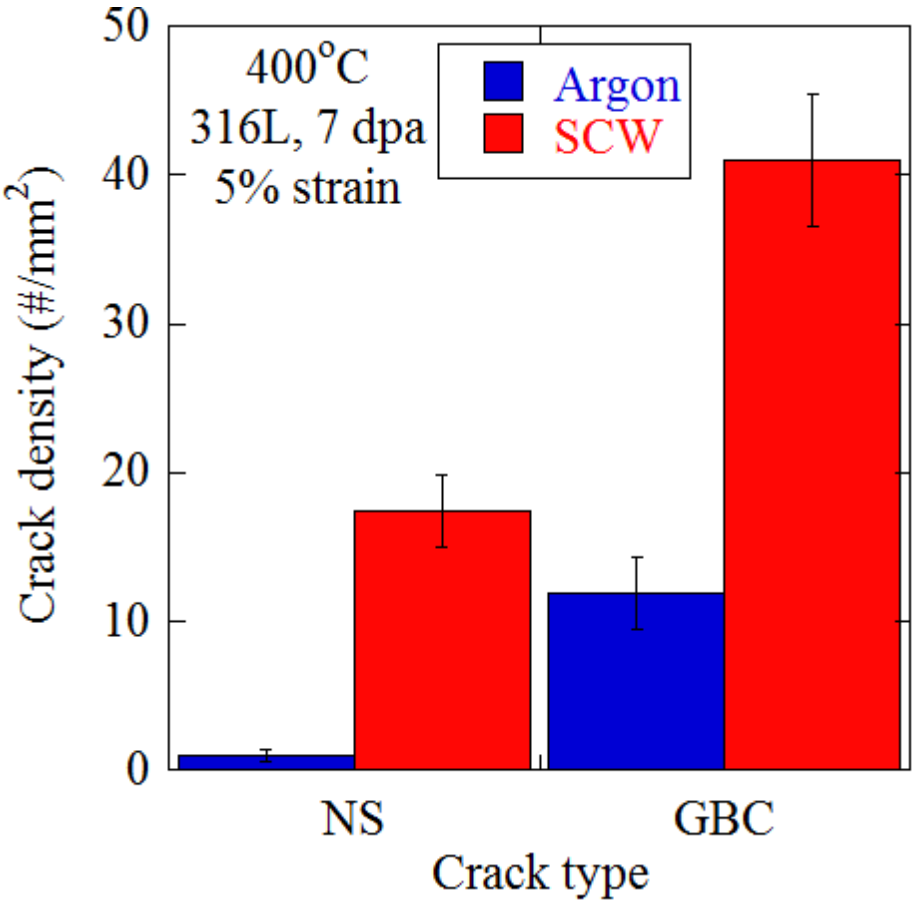

Figure 4.50 Density comparison of NS and GBC cracks in 7 dpa proton irradiated 316L strained to 5% in 400˚C argon and SCW.

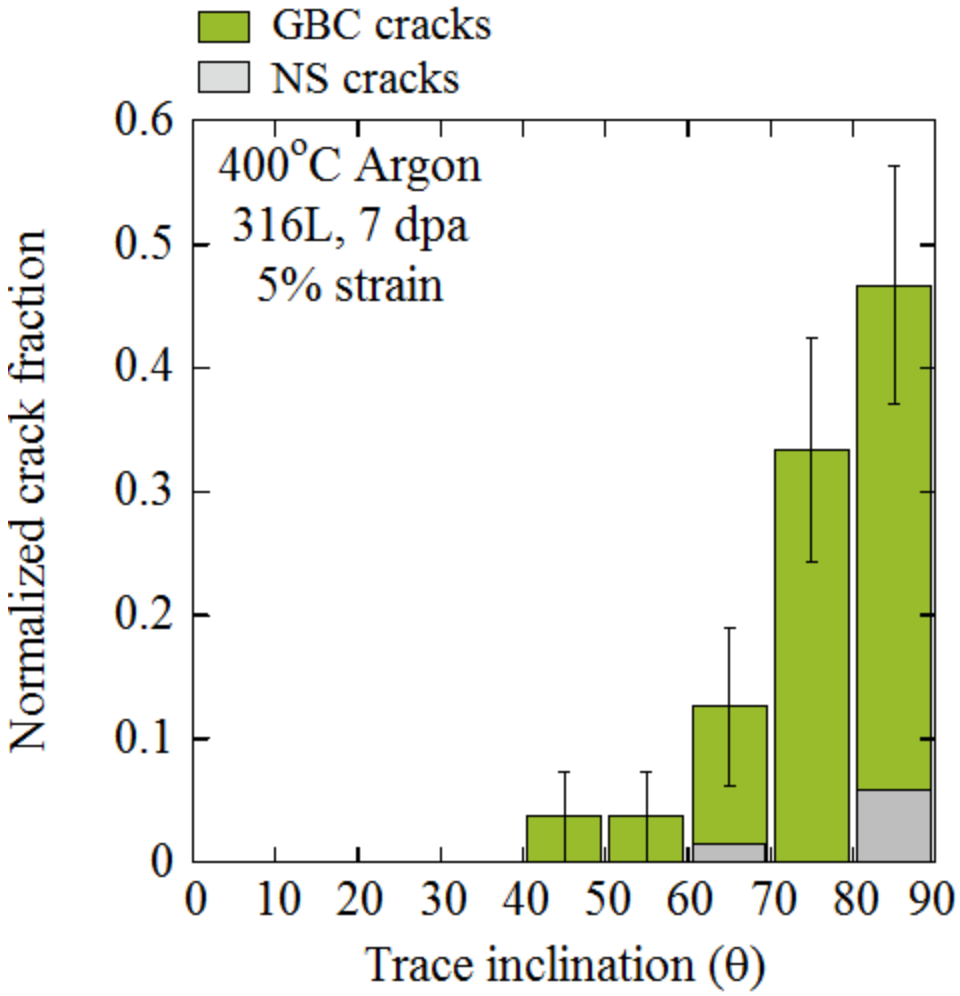

Figure 4.51 Fraction of cracked grain boundaries with specified trace inclinations for 7 dpa proton irradiated 316L strained to 5% in 400˚C purified argon.

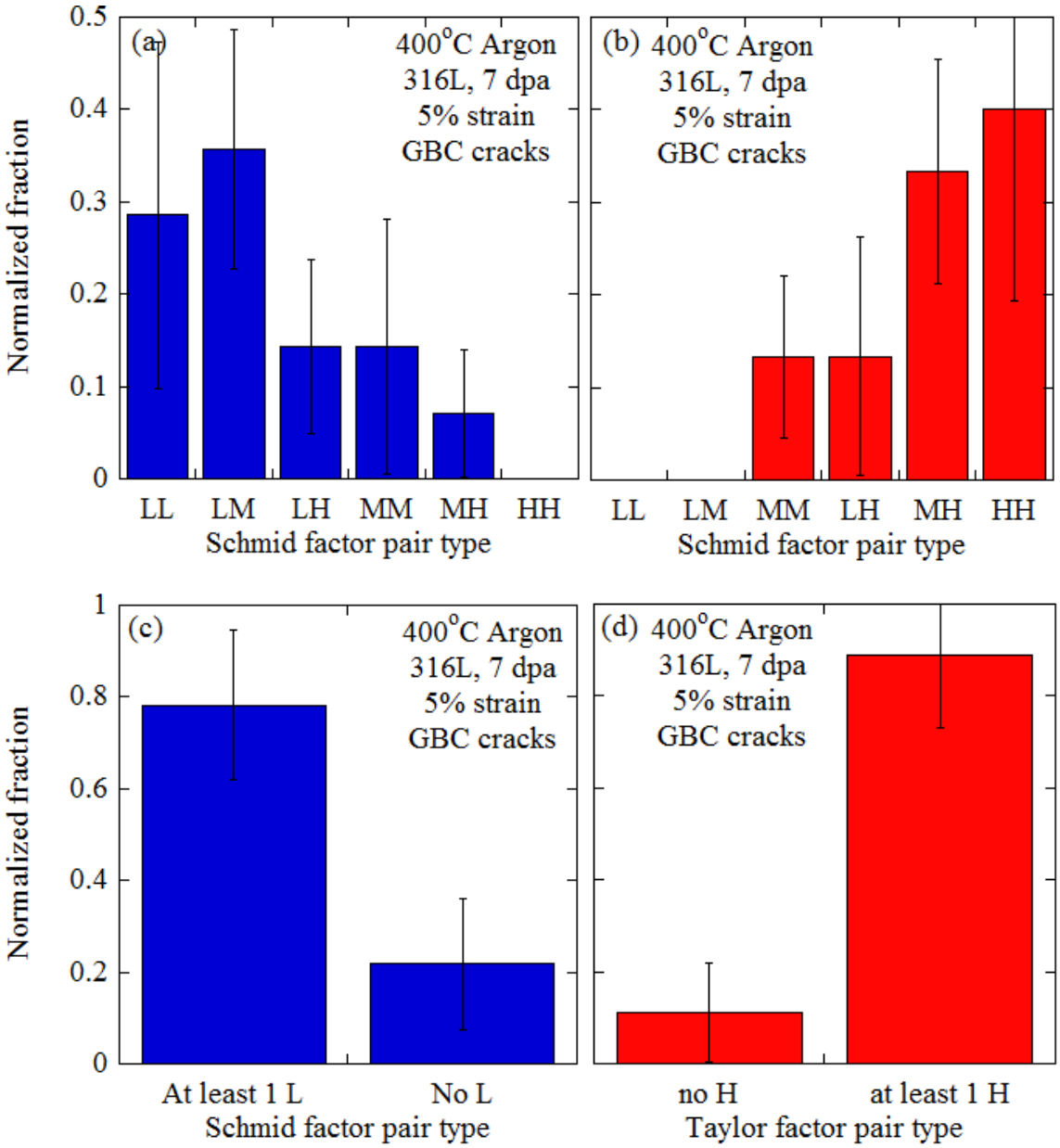

Figure 4.52 Schmid and Taylor factor pair types at GBC cracks on irradiated 316L specimens strained to 5% in 400˚C argon.

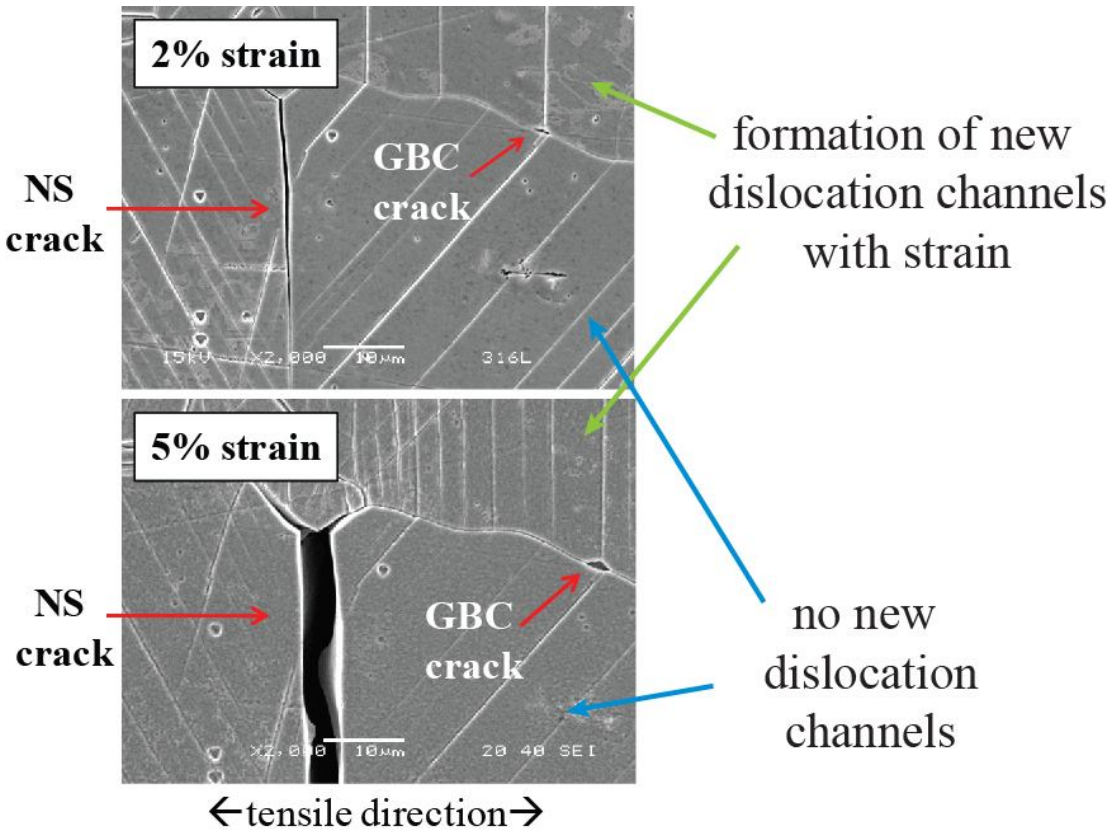

Figure 4.53 Micrographs of GBC and NS cracks following straining to 2% and 5% strain in 400˚C SCW. Additional slip channels form in the grain adjacent to the GBC crack, but no new slip channels form in the grain adjacent to the NS crack from 2% to 5% strain.

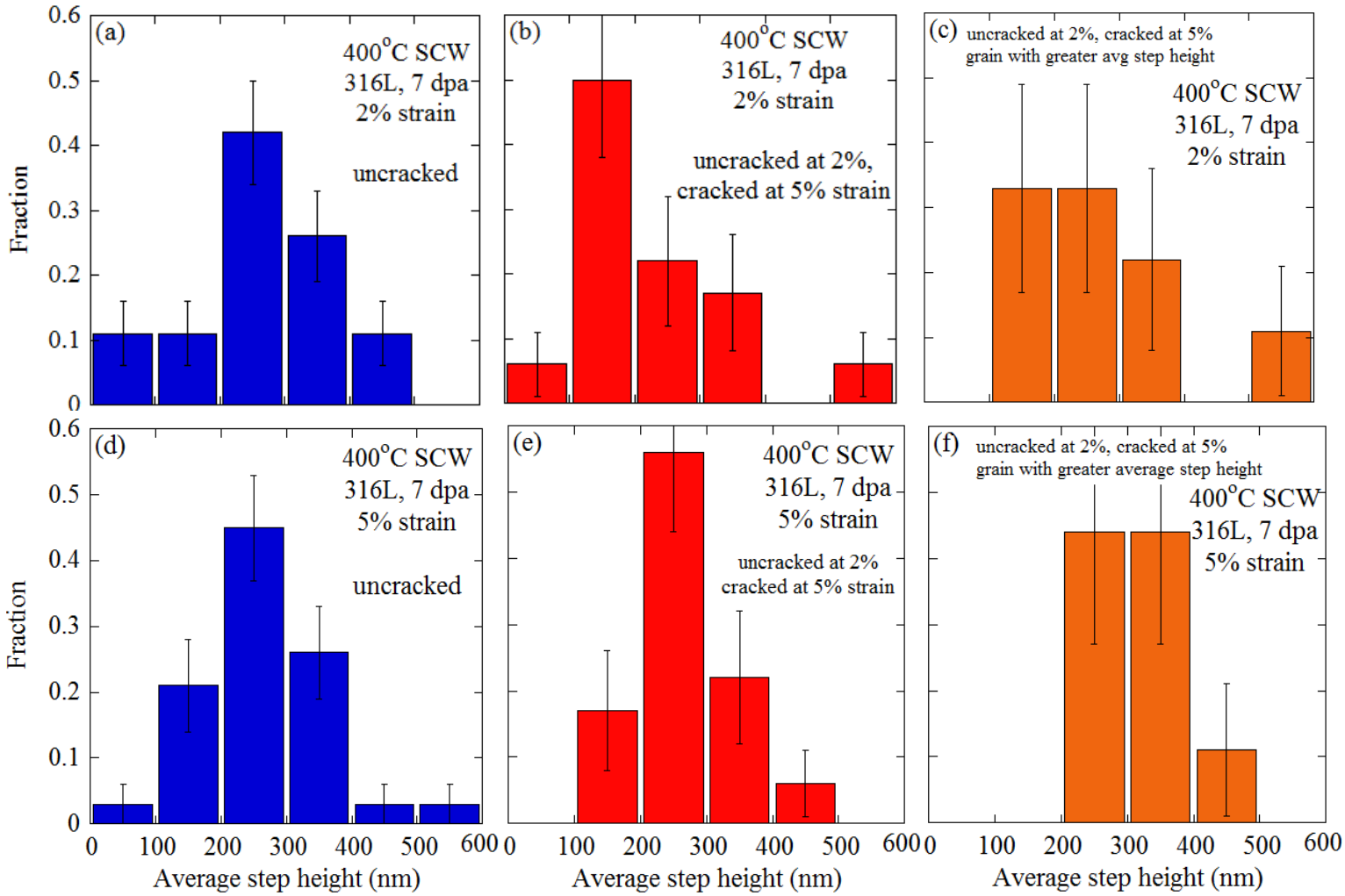

Figure 4.54 Average step height distributions in proton irradiated 316L specimens strained to 2% and 5% in 400˚C SCW. (a), (d) indicate measurements adjacent to uncracked boundaries at 2% and 5% strain, (b) and (e) indicate measurements from both grains adjacent to the cracked boundary, and (c), (f) indicate measurements from the grain adjacent to the cracked boundary with the greater average step height.

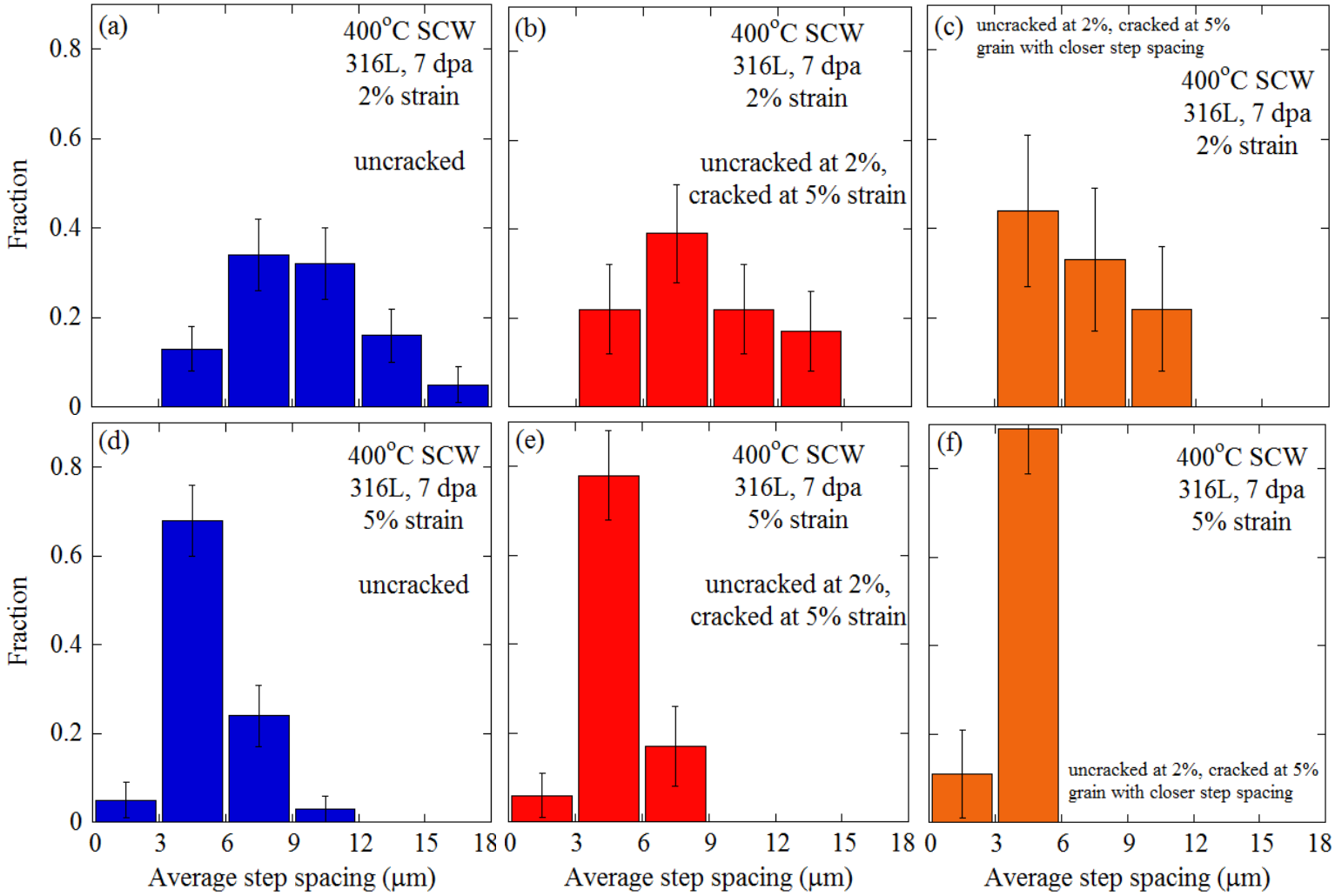

Figure 4.55. Average step spacing distributions in proton irradiated 316L specimens strained to 2% and 5% in 400˚C SCW. (a), (d) indicate measurements adjacent to uncracked boundaries at 2% and 5% strain, (b) and (e) indicate measurements from both grains adjacent to the cracked boundary, and (c), (f) indicate measurements from the grain adjacent to the cracked boundary with the closer average step spacing.

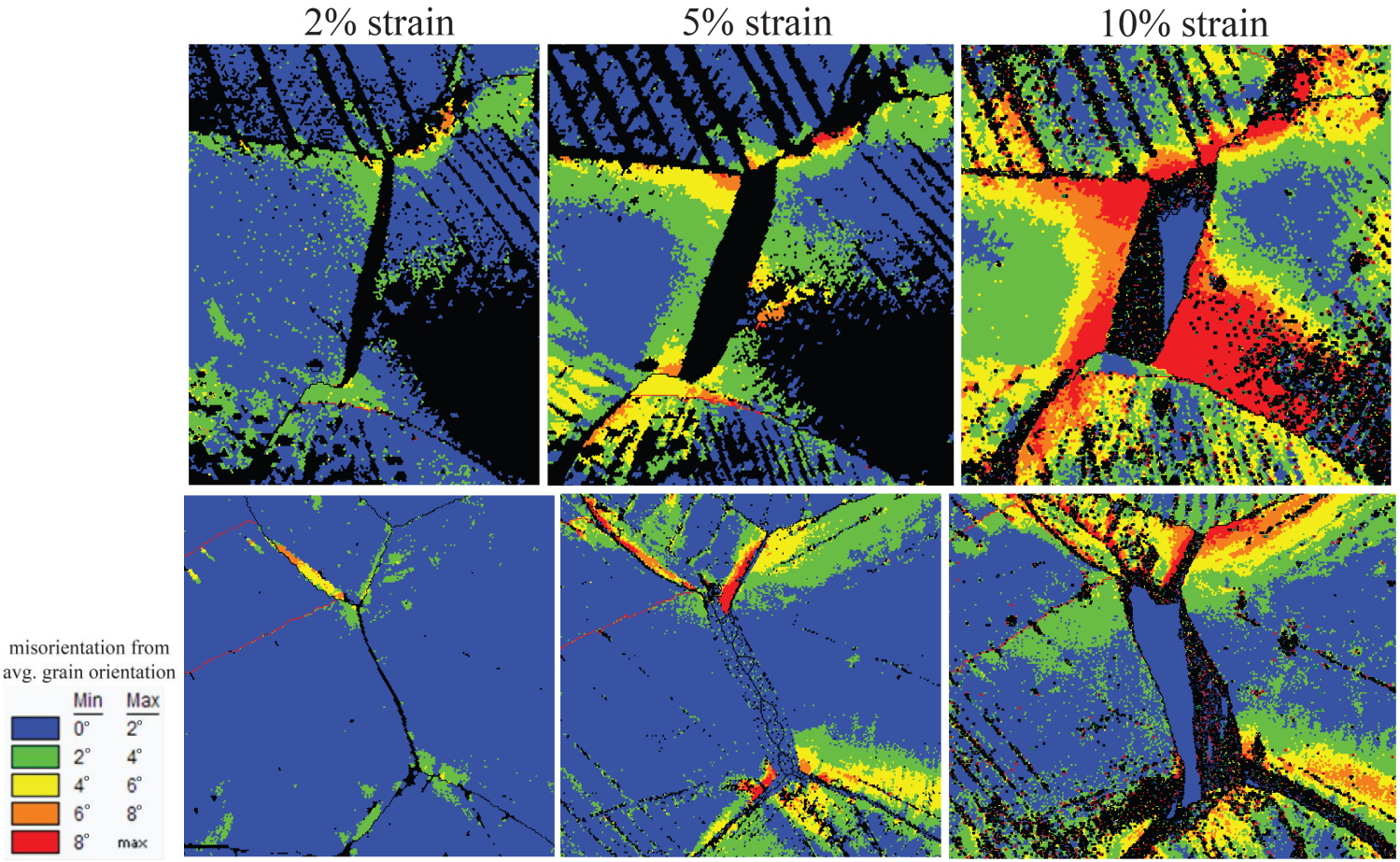

Figure 4.56 Localized lattice rotation around cracked boundaries in proton irradiated 316L specimens following straining in SCW and oxide stripping.

CHAPTER 5

DISCUSSION

In this chapter, the influence of both local strain and stress on the intergranular cracking behavior of 316L in SCW will be evaluated. It was shown in Chapter 4 that the intergranular NS cracking propensity is influenced by the Schmid and Taylor factors of the grains adjacent to the cracked boundary, the trace inclination, and the grain boundary character. It was also shown that these parameters influence the propensity for slip continuity across the grain boundary. This chapter will also discuss the influence of the Schmid factor and trace inclination on the stress acting on the grain boundary.

The first section of this chapter will focus on the deformation behavior of the proton irradiated 316L in regards to the layered irradiated/unirradiated structure of the specimens. The relationship between the Schmid and Taylor factors will be described in the second section, as well as the implications of the interdependence of these factors on the observed cracking correlations. The third section will determine the role of localized deformation in the cracking behavior of the irradiated 316L. The fourth section will investigate how the orientations of slip systems may influence slip continuity behavior. The stress dependencies of the intergranular cracking behavior and slip continuity behavior will be discussed in the fifth section by applying a simple model which utilizes an isostrain assumption to explore the influence of both Schmid factor and grain

boundary plane orientation on the stress acting on a grain boundary during plastic deformation. The influence of grain boundary engineering on the cracking behavior of 316L in SCW will be evaluated in the final section.

5.1 Deformation behavior of proton irradiated 316L

5.1.1 Increase in yield strength

The increase in yield strength of alloy 316L due to proton irradiation damage was calculated from measurements of the irradiation induced hardening and compared to measurements of the irradiation induced microstructure. The yield strengths of proton irradiated specimens cannot be determined directly from stress strain curves because the vast majority of the sample volume is unirradiated. With an approximately 2 mm × 2 mm specimen gage section and a 20 μm irradiated depth, only 1% of the specimen cross section was irradiated. Therefore, the stress-strain behavior is more indicative of the behavior of the unirradiated 316L. The increase in yield strength, therefore, will be estimated from hardness measurements and from the irradiated microstructure using the dispersed barrier hardening model.

The relationship between hardness and yield strength in neutron irradiated and CW austenitic stainless steels was evaluated by Busby et al. [182]. The study combined data from seven separate studies on 304, 316, and 347 stainless steels that had been neutron irradiated to doses ranging from 0.2 to 30 dpa or CW to various levels. They plotted the change in yield stress, $\Delta\sigma_y$, as a function of change in hardness, ΔH_v, for all data sets and applied a linear least squares fit with the added condition that the line passed through the origin, with the following result,

$$\Delta\sigma_y = 3.03\Delta H_v. \quad (5.1)$$

In the current study, the proton irradiation damage increased the hardness of the specimens from approximately 150 Hv to 380 Hv as described in Section 4.2. A change in hardness of 230 Hv would yield an increase in yield strength of approximately 700 ± 90 Hv as illustrated in Figure 5.1, where the dotted black lines indicate the region that contains the true hardness-yield stress relation with 95% confidence. As the yield strength in the unirradiated 316L is approximately 150 MPa, the yield strength in the irradiated region is expected to be approximately 850 MPa.

The increase in yield strength can also be estimated from the measurements of the irradiation induced microstructure using a dispersed barrier hardening model [183],

$$\Delta\sigma_y = M\rho\mu b\sqrt{Nd}, \quad (5.2)$$

where $\overline{M}$ is the average Taylor factor (3.06), ρ is the obstacle strength, μ is the shear modulus (76 GPa), b is the Burgers vector of the moving dislocation (2.5×10^{-10} m), N is the obstacle density, and d is the obstacle size. In this study, the void population was negligible and the dislocation loop density and size were given in Section 4.2 as 5.3×10^{22} m^{-3} and 6.9×10^{-9} m, respectively. An obstacle strength of $\rho = 0.6$ would result in an increase in yield strength of 667 MPa, comparable to that calculated from the irradiation induced hardening measurements. This value of ρ, however, is substantially larger than the values of 0.33-0.45 reported for Frank loops in other irradiated austenitic steels [184-186]. This indicates that other components of the irradiation induced microstructure,

such as small defect clusters that cannot be quantified through TEM analysis may yield significant contributions to the irradiation induced hardening.

5.1.2 Strain and stress inhomogeneities in irradiated region

The higher yield strength of the irradiated 316L has important implications regarding the homogeneity of stress and strain in the tensile specimens. The embrittled irradiated layer is comparable to a thin film adherent to a softer substrate. While the unirradiated 316L is expected to plastically deform at an applied stress of approximately 150 MPa, the magnitude of applied stress or macroscopic strain required to reach the yield stress in the irradiated layer is not immediately known.

Plastic strain measurements on the tensile specimens indicated that the strain in the irradiated regions was consistently less than the macroscopic strain as described in Section 3.9. At macroscopic strains of 2% and 10%, the strains in the irradiated regions were 1% and 8%, respectively. These results are consistent with the FEM modeling results of 2 dpa proton irradiated Zircaloy-4 conducted by Fournier et al. [187]. They modeled the unirradiated and 30 μm irradiated layers of Zircaloy-4 as homogenous material (neglecting grain to grain inhomogeneities in stress and strain) and evaluated the volumetric stress and strain distributions in the layers at 0.5% and 1.1% macroscopic plastic strain. They found that the irradiated layer was still in the elastic regime at 0.5% macroscopic plastic strain (although experimental results indicated dislocation channeling occurred), and reached plasticity at 1.1% macroscopic strain. Although the anisotropy assumptions used for modeling Zircaloy-4 complicates a direct comparison with irradiated 316L stainless steel, it is noteworthy that linear extrapolation of the irradiated

316L strain data to 0% would yield a macroscopic strain of 0.9% which is comparable to that of the 1.1% for the irradiated Zircaloy-4 as shown in Figure 5.2.

The methodology of the current study did not allow for determination of the stress distribution in the irradiated region and so it is instructive to further discuss the findings of Fournier et al. for Zircaloy-4 [187]. As expected, they observed highly elevated stresses in the harder irradiated region compared to the unirradiated region, and a sharp gradient developed at the interface between the unirradiated and irradiated regions. They also found that a lateral compressive stress developed in the irradiated layer as a result of the plastic deformation in the unirradiated layer. This compressive stress was greater in the middle of the specimens than at the edge of the specimen.

As similar stress and strain gradients likely exist in the tensile specimens in the current study, the impact of these inhomogeneities on the cracking behavior of the irradiated 316L in the current study deserves consideration. The crack measurements on the tensile specimens were confined to regions far from either end of the 10 mm irradiated length of the surface interface between the unirradiated and irradiated regions as indicated in Figure 3.9, and did not extend to either edge of the specimen. Therefore, the sharp surface stress gradient at either end of the 10 mm irradiated length should not influence the cracking behavior, and the variation in the lateral compressive stress in the region analyzed would be less than if the entire 2 mm width of the specimen were analyzed. The lateral compressive stresses in proton irradiated tensile specimens could potentially influence the cracking behavior of the irradiated surface layer, however, it is noteworthy that Busby [171] witnessed similar dose dependence of cracking behavior (%IG on irradiated fracture surface) of neutron irradiated and 3.2 MeV proton irradiated

304 and 316 stainless steels following straining in normal water chemistry (NWC). Therefore, the stress and strain inhomogeneities that develop in the tensile specimens due to their dual layered (irradiated and unirradiated) structures do not appear to have a dominating influence on the cracking propensities of the stainless steel.

In addition to the free surface interfaces between the unirradiated and irradiated regions of the specimens, the internal interface at the 20 μm depth beneath the surface also deserves consideration. The dislocation channeling behavior in the region near the damage peak at the interface between ion irradiated and unirradiated material has been investigated by other researchers through cross sectional TEM analysis of specimens fabricated from tensile bars [95]. To evaluate whether the dislocation channeling behavior in the current study may be consistent with previous findings, the free surface interface between the unirradiated and irradiated regions was analyzed as shown in Figure 4.12. Although this region is a free surface and therefore not necessarily representative of the subsurface interface between the irradiated and unirradiated 316L, it may lend insight into the continuity of the slip behavior between the more ductile unirradiated layer and the embrittled irradiated layer of the 316L. It is unknown whether the slip lines in the unirradiated region developed before the dislocation channels. In general, the unirradiated metal plastically deformed before the irradiated region, but it will be argued in a later section, that dislocation channels may nucleate on the irradiated surface as well. It was shown in Figure 4.12 that the continuity in slip across the unirradiated/irradiated interface varied. In some grains, slip lines continued in the irradiated region as dislocation channels (albeit at lower densities), while in others the slip lines faded into obscurity in the irradiated region. In the large majority of grains,

however, these transitions appear gradual, with no abrupt arrest of dislocation channels at the free surface interface between the unirradiated and irradiated regions.

The lower densities of dislocation channels in the irradiated regions compared to slip lines in the unirradiated regions indicated that not all of the slip lines that formed in the unirradiated substrate penetrated through the 20 μm irradiated layer. The gradual transition in slip behavior at the interface between the unirradiated and irradiated regions, however, indicates that the slip lines may not terminate directly at the damage peak. These observations appear consistent with the slip line and dislocation channeling behavior observed by Miura et al. at 200keV He+ ion damage peaks in irradiated 304 and 316 stainless steel [95]. They analyzed the slip line and dislocation channeling behavior through cross sectional TEM analysis following plastic straining to 2%, and observed that slip lines from the matrix penetrated the damage region in the form of dislocation channels at doses higher than 0.5 dpa at the damage peak. Some of the dislocation channels did not extend the entire length of the irradiated region, while others extended to the surface and resulted in the formation of steps.

These results indicate that it is possible that the dislocation channeling behavior observed in the grains on the surface of the irradiated 316L specimens may sometimes originate from the slip activity in the underlying unirradiated material. The same slip plane or sets of slip planes, however, may not always be active in both the unirradiated and irradiated regions of the grain, indicating that dislocation channels can also nucleate independently in the irradiated region.

5.2 Relationship between Schmid and Taylor factors

The influence of both the Schmid and Taylor factors on the cracking propensity and slip continuity at the grain boundary were presented in Chapter 4, but it is important to consider that the Schmid and Taylor factors are not independent variables. It was shown in Section 2.5 that both factors are determined from the orientations of the slip systems, and therefore are also determined by the grain orientation. Therefore, relationships between slip continuity and cracking and Schmid factor may also result in a measured correlation between Taylor factor and the phenomena, or vice versa. This section will discuss the potential influence of the interdependences of Schmid and Taylor factors on their measured correlations with cracking.

It is noteworthy that the Schmid and Taylor factors can be expressed in terms of similar variables,

$$m = \frac{\tau_{CRSS}}{\sigma_{y_g}} = \cos\lambda \cos\phi, \tag{5.3}$$

and,

$$M = \frac{\sigma_{f_g}}{\tau_{CRSS}}, \tag{5.4}$$

where σ_{y_g} is the yield strength of an isolated grain (or single crystal) and σ_{f_g} is the flow stress applied to the grain in the tensile direction. These expressions indicate that the Schmid factor of a grain is proportional to τ_{CRSS} while the Taylor factor is a proportional to $\frac{1}{\tau_{CRSS}}$, which says that the Schmid and Taylor factors are inversely related. As shown

in Figure 5.3, the Schmid and Taylor factors are inversely related, but the relationship $M = 1/m$ exists only for the $\{100\}$ and $\{111\}$ orientations.

As discussed in Section 2.5, the expression for the Schmid factor applies to a single crystal that deforms via slip along the most favorably oriented slip system, and the Taylor factor calculation assumes that 5 independent slip systems are activated as the grain deforms. Therefore, the expression for the Taylor factor will reduce to that of the inverse Schmid factor only if the applied stress results in equivalent resolved shear stresses on at least 5 slip systems. In uniaxial loading, this condition is only achieved for the $\{100\}$ and $\{111\}$ orientations [62], which results in equal resolved shear stresses on 8 and 6 slip systems, respectively. At these orientations, the Taylor factor reduces to $1/m$ as indicated in Figure 5.3. At all other orientations, the Taylor factor is greater than the inverse Schmid factor, indicating that the required stress for slip along 5 slip systems exceeds that required to activate the most favorably oriented slip system. The Taylor factor calculation, however, does not actually account for whether or not the stress state of the grain can physically activate five slip systems. Rather, it is assumed that even when a uniaxial load is applied, the stress field in the polycrystal is multiaxial due to the deformation restrictions of the surrounding grains such that five slip systems activate.

Although it is excluded from the assumptions of the Taylor factor calculation, variations in strain hardening along the slip systems may also result in the activation of additional slip systems. It is interesting to note that in irradiated materials, where strain hardening is reduced, the number of slip systems activated may be reduced. It has been reported that the deformation of irradiated 316LN resulted in the activation of fewer slip systems than in the unirradiated condition [12]. It was suggested that this behavior may

be the result of the strain hardening that occurred in the unirradiated specimens and the softening effect of the removal of defects, as a result of deformation, in the dislocation channels of the irradiated materials. In the current study, it was shown that in the majority of grains, only a single active slip plane was detected. While it will be shown in a later section that it is possible that 2 slip planes are active in some of these grains, these results confirm that the activation of 5 independent slip systems rarely occurs in the irradiated grains analyzed in this study. This may be the result of softening in the dislocation channels, the lack of strain hardening described by Byun et al. [12], the fewer restrictions to deformation on the free surface of the specimen described by Kocks [188] and Hosford [74], or a combination thereof. This finding, therefore, violates a critical assumption of the Taylor factor calculation that 5 independent slip systems are active in each grain.

The Schmid factor calculation only accounts for the stress required to activate a single slip system, and does not account for the restrictions to deformation imposed by surrounding grains. It will be shown in a later section that the slip plane that contains the most favorably oriented slip system nearly always activates, although additional slip planes may also activate. This indicates that any multiaxial loading that may be occurring is generally not great enough in the current study to overpower the influence of Schmid's law on predicting the slip system activated on the basis of the resolved shear stress acting on each slip system. The observation of multiple slip in many grains, however, does indicate that the effects of multiaxial loading and/or strain hardening are not negligible. The Schmid factor, however, still appears to be a consistent predictor of whether or not the most favorably oriented slip system activates, and therefore will be used as an indicator of the flow strengths of the individual grains in a later section.

The crack measurements shown in Figure 4.34 and Figure 4.36 indicate that the correlations observed between Schmid factor and cracking may be slightly greater than that between Taylor factor and cracking. Therefore, it is possible that the measured correlation between Taylor factor and cracking may simply be because the Schmid and Taylor factor are not independent variables and are inversely related. To address this question, the Taylor factor pair type distribution at the cracked boundaries will be predicted based on the Schmid factor pair type distribution at the grain boundaries.

If the total grain population is divided into the three equally populated bins on the basis of Schmid and Taylor factor (low, medium, high), there is a certain probability that a grain with a low Schmid factor will have a low, medium, or high Taylor factor. These probabilities are listed in the table to the right of Figure 5.3. Based on these probabilities, the probability of having a certain Taylor factor pair type can be determined if the Schmid factor pair type is known. For example, given that a boundary has an LL Schmid factor pair type, the probability that the boundary is also an LL Taylor factor pair type is approximately $0.06 \times 0.06 = 0.004$, and the probability of having an LM pair type is $0.06 \times 0.35 \times 2 = 0.04$, where the factor of 2 is included to account for the possibilities of having either LM or ML. Such calculations can be performed for each pair type. Using these probabilities, a predicted Taylor factor pair type distribution can be generated from that of the Schmid factor. The probability of having an LL Taylor factor pair type, for example, can be calculated by multiplying the fraction of cracks in each Schmid factor pair type category by the probability that each Schmid factor pair type would yield the LL Taylor factor pair type. Using this method, the Taylor factor pair type distributions were predicted from the Schmid factor pair type distributions at the cracked boundaries

of the irradiated 316L specimens strained in SCW to 2%, 5%, and 10% strain and are shown in Figure 5.4. It can be seen that, for the most part, the Taylor factor pair type distributions can be accurately predicted by the Schmid factor pair distributions, indicating that the correlation between Taylor factor and cracking could simply be the result of the correlation between Schmid factor and Taylor factor.

5.3 Role of localized deformation

The formation of IG cracks at the intersection of dislocation channels with grain boundaries observed in the current study is consistent with the findings of several other researchers [8, 9, 11, 14, 15, 97]. Following straining of the irradiated 316L specimens to 5% strain, 100% of the GBC and NS cracks on the gage surface of the specimens strained in argon were intersected by a dislocation channel, and in SCW the amounts were 100% for the GBC cracks and 87% for the NS cracks. It is likely that the remaining 13% of the NS cracks in SCW originally had fine dislocation channels intersecting them that were no longer visible following oxidation and oxide stripping. It can be seen from Figure 4.30 that many of the original dislocation channels after 2% strain are obscured after 5% strain due to subsequent oxidation and oxide stripping.

Before further discussing the step height measurements, the influence of the oxide growth and subsequent stripping will be addressed. It was shown by Was et al. [36] that the weight gain of 316L stainless steel in 400˚C deaerated SCW following an exposure time of 575 hours was approximately 0.188 mg/dm^2-day, and the oxide was identified as Fe_3O_4. It is likely that an undetectable thin inner layer of spinel is also present, as the dual structured oxide is often reported at higher temperatures [28, 36, 37]. The spinel is

generally richer in Ni and Cr, but if the stoichiometries of the spinel and magnetite are considered, both have a 3:4 metal to oxygen ratio which results in a similar mass ratio as the magnetite. Therefore, although the presence of the spinel layer is likely, it can be neglected for this analysis. The measured weight gain is due to oxygen, and in Fe_3O_4, the Fe to O mass ratio is approximately 2.6:1. Therefore, for every 1 g of oxygen gained, 2.6 g of Fe is incorporated into the oxide which amounts to 0.489 mg/dm^2-day. The density of 316L is 8.02 g/cm^3, and therefore the approximate removal rate of the substrate due to incorporation of Fe into the oxide is 0.006 μm/day. In Section 3.3 and Figure 3.6, it was reported that, following exposure for 326 hours and subsequent oxide stripping the total amount of weight loss corresponded to the removal of 0.07-0.17 μm of the metal substrate. This amount of measurement uncertainty makes it difficult to determine the extent to which subsequent oxidation and oxide stripping treatments influence the step height measurements. The calculations presented here indicate that approximately 0.08 μm of metal would be lost from oxidation alone. Therefore, it is possible that up to an additional 0.09 μm (0.17 μm – 0.08 μm) of metal was lost during the oxide stripping treatment. If the removal of metal was uniform across the surface, the step height measurements would be unaffected. The loss of definition in some dislocation channels at progressive straining increments as seen in Figure 4.30, however, indicates that iterations of oxidation and oxide stripping may cause some loss in measured step height. Therefore, uncertainties will be applied to the data to indicate the potential influence of the oxidation and oxide stripping on the step height measured. At 2% strain, the specimens had been exposed for 45 hours leading to a metal loss of 10 nm due to oxidation and up to 90 nm from oxide stripping, and at 5% strain following exposure for

93 hours, 24 nm of metal would be lost due to oxidation and up to 90 nm from oxide stripping. Although it is unlikely that the removal of metal from the specimen surface as a result of oxidation and oxide stripping would be irregular enough to cause such errors in step height measurements, these values will be used to generate conservative error bars on the measured step heights.

The dislocation channel strain has been shown to range from roughly 20% to nearly 100% for proton irradiated stainless steels at strains ranging from 3% to 12% [189]. Thus, the region of the material undergoing dislocation channeling is subject to strains that are up to an order of magnitude greater than the bulk strain. It is also important to consider, that the step height and spacing measured via AFM indicate the apparent, but not true, step height and dislocation channels spacing. As shown in Figure 5.5, because the dislocation channels are inclined to the sample surface, the step height and spacing measurements indicated in the current study yield lower and upper bound measurements, respectively. The true step height and spacing would only be equal to the apparent height and spacing if the steps were perpendicular to the specimen surface, which is unlikely because the resolved shear stress acting on the slip system in such a condition would be equal to zero.

The possibility that the intergranular cracking of irradiated 316L stainless steel is driven by a slip oxidation type mechanism, and the film rupture is induced by the localized deformation will now be considered. Following straining to 5% in SCW, an average step height of approximately 260 nm was measured on the specimens, or up to 374 nm if loss of metal is considered. At this point, the samples had been exposed to

SCW for approximately 5.75 days. Assuming a density of 5.18 g/cm^3 for the Fe_3O_4 [190], the oxide thickness should be approximately,

$$\frac{1.88\times10^{-6}\,g}{cm^2-day}\times 5.75 days\times\frac{g(Fe_3O_4)}{0.277g(O)}\times\frac{cm^3}{5.18g}\times\frac{10^7\,nm}{cm}=75nm,$$

indicating that the average step height exceeds the oxide thickness. Porosity in the oxide is also likely, but as long as the porosity is less than 70%, the average step height will exceed the oxide thickness. Therefore, regardless of the true step height, it can be stated that the majority of the dislocation channels formed that directly intersect grain boundaries rupture the oxide film at the grain boundary and expose bare metal. The fact that IG cracks are not observed at all sites of dislocation channel intersections with grain boundaries, however, indicates that factors other than the rupturing of the oxide film are influencing the cracking propensity of the boundary. Furthermore, IG cracks were also observed on the irradiated specimens following straining in an inert purified argon environment, indicating that, while the SCW environment may enhance intergranular cracking, corrosion is not the root cause of the intergranular cracking.

The ability of IG cracks to form as a result of dislocation pileup and subsequent coalescence at an obstacle via the Zener-Stroh mechanism was discussed in Section 2.5. This was argued to be possible if (1) the stress normal to the plane of the crack approached the fracture stress of the material and (2) the formation of the crack would decrease the energy of the system [102]. The second criterion was shown to be achieved when equation (2.22) was satisfied,

$$\sigma_n^{\,2} r_\ell > \frac{16\gamma G}{\pi(1-\nu)},,$$

recalling that σ_n is the normal stress, r_ℓ is the crack length, γ is the surface energy per unit area, and G is the rigidity modulus. The expression for the normal stress acting on the obstacle plane as a result of dislocation pileup was given as (equation (2.23)),

$$\sigma_n = \frac{3}{2}(L_0 / r_\ell)^{1/2}\sigma_0 \sin\theta \cos\frac{1}{2}\theta ,$$

recalling that L_0 is the length of the slip plane occupied by the pileup, σ_0 is the stress holding the dislocations in equilibrium, and θ is the angle between the obstacle plane and the slip plane. As shown in Section 2.5, equation (2.22) and equation (2.23) can be combined and reduced to equation (2.26) when the value of θ that maximizes the normal stress on the obstacle, 70.5˚, is selected,

$$n > \frac{12\gamma}{b\sigma_0},$$

recalling that n is the number of dislocations in the pileup at the obstacle. It is noteworthy that the substitution of equation (2.23) into equation (2.22) results in the cancellation of the r_ℓ values. This indicates that, if the aforementioned criteria for crack formation are met, a decrease in energy will occur through the formation of a crack at all stages of development. To determine the number of dislocations required for crack formation, σ_0 will be taken as the observed fracture stress in accordance with the first criterion and Stroh's calculations [102, 191]. The surface energy of 316L is approximately 2.2 J/m^2 [192], the Burgers vector is approximately 0.258 nm [193]. The fracture stress will be approximated as the calculated yield strength, 850 MPa, of the irradiated stainless steel, as the strain hardening is expected to be low in the 7 dpa irradiated condition. Using these values, the minimum number of dislocations required for crack formation was determined to be 120 dislocations. With a burgers vector of

0.258 nm, this number of dislocations corresponds to a displacement of 31 nm. Given that the average apparent step height is 260 nm, and the average true step height must be greater, it is likely that stable crack formation is possible at the intersections of many dislocation channels with the grain boundary. Furthermore, in a later paper, Stroh showed that the number of dislocations required for crack formation could be substantially reduced if dislocation pileups exist on parallel slip planes [191]. It is important to consider, however, that although the number of dislocations is sufficient for crack formation, this does not necessarily mean that a crack will nucleate and grow to detectability. It is possible, for example, that the adjacent grain may deform to accommodate the strain, which will be discussed in a subsequent section.

The previous discussion suggests that a critical step height may be required for the formation of an intergranular crack. This theory is supported by the findings of Jiao and Was [150], who evaluated the intergranular cracking susceptibility of several austenitic stainless steels irradiated to doses of 1 and 5 dpa and strained to 1% and 3% strain in a simulated BWR environment. They reasoned that larger steps are more likely to cause intergranular cracking and gave larger steps greater weight by calculating a weighted average channel height as,

$$\bar{h}' = \frac{\Sigma_{i=1}^{n} h_i'^2}{\Sigma_{i=1}^{n} h_i'}, \tag{5.5}$$

where, h' is the apparent step height as measured via AFM. They found that a critical weighted average channel height range existed spanning from 290-360 nm, above which the alloys were susceptible to intergranular cracking and below which they were not. The data from the current study are plotted with alongside their data in Figure 5.6. It can be

seen that the data from the SCW experiments appear to fall into the “mixed” region encompassing both cracked and uncracked data in the simulated BWR environment. Considering the amount of metal removed during oxidation and oxide stripping, however, these data may be located in the “cracked” region. It can be seen from Figure 5.6 that the weighted average channel heights measured in the current study exceed the values required for intergranular cracking of some of the austenitic alloys in the BWR environment, which makes the current findings consistent with the available literature data.

These findings indicate that the threshold step height for crack nucleation in SCW is comparable or lower than that for a BWR environment. It was shown in Figure 4.54 that there is not a significant difference in the distributions of step heights in the grains adjacent to cracked and uncracked boundaries. Therefore, the threshold average step height must be substantially lower than the measured average step height of 260 nm, or 374 nm if oxidation and oxide stripping are considered. Each of the grain pairs analyzed adjacent to a cracked boundary contained a step height of at least 330 - 444 nm. It was also determined that, by 5% strain, dislocation channels were observed in 93% of the grains in the irradiated specimens. Therefore, although there may be a critical step height, it is possible that the population of grains with critical step heights is so great, that this is not the limiting factor in crack formation.

In summary, these findings indicate that dislocation channeling in 7 dpa irradiated 316L is capable of inducing strains high enough to create stable crack nuclei following straining in 400˚C SCW to 2% and 5% strain. The grain to grain variations in step height, however, do not appear to influence the propensity for NS cracks to form, at a

specific boundary. This may indicate that the threshold step height required for crack formation is substantially lower than the average step height of 260-374 nm. As cracks are not detected at the majority of intersections of dislocation channels with grain boundaries, factors in addition to the step height must be limiting the propensity of the grain boundary to crack.

5.4 Relationship between slip continuity and cracking

Intergranular crack formation at the intersections of slip lines or dislocation channels with grain boundaries has been observed by many researchers [8, 9, 11, 14, 15, 97] and indicates that the compatibility in slip between adjacent grains may influence the cracking propensity of the grain boundary. The influence of the trace inclination, grain boundary character, and Schmid and Taylor factors on slip continuity at the grain boundary were evaluated and shown in Figure 4.23. From this figure, it can be seen that slip *discontinuity* increased with increasing trace inclination, decreased at special boundaries, decreased across boundaries with adjacent high Schmid factor or low Taylor factors, and increased with increasing Schmid factor mismatch. Therefore, all of the observed relationships between these parameters and cracking suggest that for intergranular NS cracks in the SCW environment, slip discontinuity across the grain boundary promotes cracking. In this section, the method applied to determine the active slip planes will be described, followed by a discussion on why the propensity for multiple slip varies between grains. Later sections will discuss the propensity for slip continuity and the influence of slip continuity on intergranular cracking. This section will focus primarily on boundaries that are highly inclined to the tensile axis (generally >50˚),

where the Schmid and Taylor dependence is observed. The trace inclination dependence of the slip continuity behavior will be discussed in a later section. It is important to note that this section will discuss two different types of Schmid factor analyses, (1) the Schmid factors of *grains*, which is most widely used in this study, and (2) the Schmid factors of specific *slip systems* within the grain. It may be recalled from Section 2.5, that the Schmid factor of a grain is determined by calculating the Schmid factors for each of the 12 systems within the grain and selecting the greatest value.

5.4.1 Slip plane and Schmid factor identification

The upcoming analysis regarding the propensities for multiple slip and slip continuity will require knowledge of the surface traces of each of the four $\{111\}$ planes as well the Schmid factors of each of the 12 slip systems. This section will describe how the active slip plane can be identified on the basis of the inclination of its surface trace to the tensile axis, and how the Schmid factors of each of the 12 slip systems can be determined. Such measurements are not provided by the OIM^{TM} software, but they can be deduced. All variables used to determine the surface traces of the slip planes and the Schmid factors of the slip systems are shown in Figure 5.7. The expected surface traces were determined by calculating the common vector of intersection, v_{int}, between the sample surface and each of the four $\{111\}$planes by taking the cross product of each $\{111\}$ plane normal, $(h_1 k_1 l_1)$, with the normal to the crystallographic plane parallel to the sample surface, $(h_2 k_2 l_2)$:

$$v_{\text{int}} = (h_1 k_1 l_1) \times (h_2 k_2 l_2). \tag{5.6}$$

The angle of the expected surface trace with respect to the tensile direction was then calculated by taking the arc cosine of the dot product of the normalized vector of intersection with the normalized vector of the crystal direction aligned with the tensile direction, v_{td},

$$\xi = \arccos\left(\frac{\vec{v}_{td} \cdot \vec{v}_{\text{int}}}{|v_{td}||v_{\text{int}}|}\right). \tag{5.7}$$

The Schmid factor of each slip system was calculated as:

$$m = |\cos\lambda \cos\phi|, \tag{5.8}$$

recalling from Figure 5.7 that λ is the angle between the slip direction and the tensile axis and ϕ is the angle between the slip plane normal, v_{sn}, and the tensile axis. λ was calculated as the arc cosine of the normalized dot products of the slip direction, v_{sd}, and v_{td},

$$\lambda = \arccos\left(\frac{\vec{v}_{sd} \cdot \vec{v}_{td}}{|v_{sd}||v_{td}|}\right), \tag{5.9}$$

and ϕ was calculated from the arc cosine of the normalized dot products of the slip plane normal, v_{sn}, and v_{td},

$$\phi = \arccos\left(\frac{\vec{v}_{sn} \cdot \vec{v}_{td}}{|v_{sn}||v_{td}|}\right). \tag{5.10}$$

For each grain of interest in the following sections, the inclination of the surface trace of the active slip plane to the tensile axis was measured and compared to the calculated ξ values of for each of the grain's four $\{111\}$ planes. The Schmid factors for each of the three slip directions on the activated plane were calculated using equation (5.8).

5.4.2 Propensity for multiple slip

Dislocation channeling in irradiated 316L occurred primarily along the close-packed {111}planes with the greatest resolved shear stress. The propensity for the activation of multiple slip systems should depend on the inclination of the slip systems to the tensile axis which is defined by the grain orientation. Therefore, the orientation dependencies of the Schmid and Taylor factors shown in Figure 2.20 and Figure 2.23 are likely responsible for the observed correlation between the Schmid and Taylor factors and the propensity for the activation of multiple slip planes. For example, the [100] orientation results in identical resolved shear stresses acting on 8 slip systems, while the [111] orientation results in identical resolved shear stresses acting on 6 slip systems. If nearly identical resolved shear stresses are acting on each of the planes that are favorably oriented, it is more likely that multiple slip planes would activate. As discussed in Section 5.4, the occurrence of multiple slip at orientations where multiple slip systems are not expected to experience equivalent shear stresses may be the result of either the restrictions to deformation imposed by surrounding grains or some degree of strain hardening.

While it would perhaps be most logical to analyze the probability for the activation of multiple slip planes as a function of orientation, a final aim of this study is to determine the reason for the Schmid and Taylor factor dependence of the NS cracking. Therefore, the propensity for the activation of multiple slip systems will be analyzed in terms of the Schmid and Taylor factors of the grains. It will be emphasized here again that in the following discussions, the Schmid factors of the *slip systems* will often be mentioned. The Schmid factor of an *individual grain*, which is the value most often

reported in this study, is the Schmid factor of the most favorably oriented slip system and therefore is not indicative of the Schmid factors of the remaining 11 slip systems.

It was shown in Figure 4.13 and Figure 4.14 that the majority of grains appear to undergo slip along a single plane, and that the propensity for the activation of multiple slip planes is greater for grains with high Schmid factors and low Taylor factors. The weaker correlation between the Schmid factor and the activation of multiple slip planes may indicate that such a correlation only exists because of the inverse correlation between the Schmid and Taylor factors. Individual grains were chosen from this data set to evaluate the conditions leading to multiple slip. Three of the grains that appeared to have only a single active slip plane are shown in Figure 5.8. The slip direction was assumed to be whichever $\langle 110 \rangle$ direction on the $\{111\}$ plane experienced the greatest resolved shear stress, and is indicated with the corresponding Schmid factor of the slip system in Figure 5.8. This assumption is not expected to be correct with a 100% accuracy, as it is possible that the stress state may be altered by neighboring grains, but it is an assumption that is applied in practice when the specific slip system cannot be determined [194]. It can be seen from Figure 5.8(a) that some of the slip planes have nearly identical surface traces. In such cases, the greatest Schmid factors for both planes are listed. It is noteworthy that this observation of two slip planes having nearly identical surface traces indicates that some of the grains which appear to have only a single active slip plane may actually have two active slip planes, or a maximum of 4 independent slip systems. All indicated surface traces matched the calculated values to an accuracy of 4˚. The surface traces of the $\{111\}$ planes are shown in the OIM scans above the SEM images to illustrate the agreement. In a few instances, which are not shown here, the deviation

was slightly greater than 4˚. This may be the result of lattice rotation that occurred as the grain deformed, which is not accounted for in the OIM scans which were performed prior to straining. It can be seen from Figure 5.8 that the Schmid factors of the grains, which indicate the slip system with the greatest resolved shear stress, generally agree with the Schmid factors of the activated slip planes (and assumed slip systems). This indicates that the slip systems with the greatest resolved shear stress are activating and supports the use of the Schmid factor in the current study.

Three of the grains where slip was visible on three slip planes are shown in Figure 5.9. It can be seen that all three grains have low Taylor factors and each of these grains had at least three {111}planes with relatively high Schmid factor slip systems. The Schmid factors of the grains, however, were not high compared to the Schmid factor distribution of the metal as a whole. In fact, only 1 of the three grains analyzed here with triple slip is classified in the high Schmid factor category. The greatest Schmid factors for each of the four {111}planes of these three grains are compared to those of the three grains undergoing slip on a single slip system in Table 5.1. It can be seen that the grains with three active slip planes had maximum Schmid factors on three planes greater than 0.40, while none of the grains with a single active slip plane meet such criteria. It should be noted, however, that the three active slip planes were not necessarily the ones with the maximum Schmid factors. Furthermore, the greatest spread in the maximum Schmid factors on the three most favorably oriented {111}planes was 0.07 for the grains with three active slip planes and 0.32 for the grains with a single active slip plane. This indicates that grains oriented such that multiple slip planes experience magnitudes of resolved shear stress comparable to that of the slip system with the highest Schmid factor were more likely to have

multiple active slip planes. The greater propensity for the activation of 2 or 3 slip planes in grains with low Taylor factors indicates that these grains often have multiple slip systems with relatively high Schmid factors.

5.4.3 Description of slip continuity and discontinuity

It is helpful to review the definition and implications of the slip continuity observed in the current study before discussing why certain parameters may influence the propensity for this behavior. When dislocations impinge on grain boundaries, they are usually initially incorporated into the boundary regardless of the grain boundary character or the ultimate stress relief mechanism [147, 195, 196]. As subsequent dislocations are incorporated, however, the grain boundary will eventually respond. The mode by which the grain boundary responds to stress concentrations is critical and five possibilities will be considered,

(1) The dislocations may be transmitted directly across the grain boundary [197].

(2) Dislocation sources may be activated in the adjacent grain [196].

(3) A grain boundary crack may develop [196].

(4) Dislocations may become mobile in the grain boundary plane to relieve stress concentration [195].

Although it is possible for dislocations to be transmitted directly across grain boundaries, such an event requires that the slip planes have a common line of intersection along the their grain boundary plane [197]. While a common line of intersection may occur at coherent twin boundaries or simple tilt boundaries, it has been established that this type of direct transfer cannot occur across general grain boundaries

[196, 198-200]. As shown in Figure 5.10, any two slip planes in adjacent grains are unlikely to have a common line of intersection along the grain boundary plane. Therefore, in the current study, direct transmission is impossible for the majority of grain boundaries. The observed slip continuity at most boundaries is, therefore, indicative of the activation of dislocation sources in the adjacent grain due to the stress concentration induced by impinging dislocations. It can be seen from Figure 5.10, however, that any two slip planes in adjacent grains will only be coincident at a single point along the grain boundary plane. Therefore, the frequent occurrence of slip continuity observed at RHABs suggests that a substantial fraction of the dislocation channels are nucleating near the surface of the specimen. This behavior may occur because the tensile stress required to cause deformation is lower at a free surface than on the interior of the specimen [74]. As shown in Figure 5.11, the orange peel effect [74] is evident on the surface of the specimens, indicating that the constraints on deformation are indeed relaxed on the free surface.

As for slip *discontinuity*, if slip is not continuous across the grain boundary, it indicates that the impingement of dislocations on the grain boundary at the specimen surface was not great enough to initiate dislocation sources in the adjacent grain. It is recognized that the operative stress relief mechanism at the grain boundary is the one that requires the lowest activation stress [196]. Therefore, if the cohesive strength of the grain boundary is sufficiently low that it requires less stress to fracture the boundary than to activate slip in the adjacent grain, the boundary will crack. Alternatively, the stress may become redistributed along the grain boundary through mechanisms such as the glide or climb of dislocations along the grain boundary to reduce the stress concentration at the

head of the pileup. This could also result in cross-slip and the activation of a dislocation source in an adjacent grain, albeit at a different location than the initial impinging dislocation pileup. It may also lead to GBS which is a process that is known to require the absorption of lattice dislocations into the grain boundary and movement of dislocations along the grain boundary plane [142, 201, 202]. In summary, in the current study, slip continuity and discontinuity are indicative of the following,

(1) Slip continuity is indicative of the activation of new dislocation sources in a grain as a result of the stresses imposed by a dislocation pileup in the adjacent grain. The possibility of direct transmission of dislocations does exist, however, if the slip planes have a common line of intersection along the grain boundary.

(2) Slip discontinuity indicates that the stress induced by dislocation pileup at the grain boundary at the surface of the specimen is not high enough to nucleate new dislocation sources in the adjacent grain at the site of impingement. This may be a result of redistribution of stress along the grain boundary as a result of dislocation mobility in the grain boundary which may cause sliding, cross-slip or grain boundary fracture.

5.4.4 Analysis of slip continuity and discontinuity

Several sets of criteria have been proposed for predicting which slip system would activate in a grain following dislocation pile-up at a grain boundary [198, 203-206]. Such criteria require knowledge of the grain boundary plane orientation which is unknown in the current study. Less focus has been placed on the circumstances leading to slip

discontinuity [195]. Having established the definitions of slip continuity and discontinuity, the parameters influencing these behaviors will now be discussed.

The propensity for slip continuity at the grain boundary was shown to be relatively low at boundaries highly inclined to the tensile axis, and dependent on the Schmid and especially the Taylor factors of the adjacent grains. Examples of the slip behavior at grain boundaries are shown in Figure 5.12 through Figure 5.15. Three examples of continuous slip across the boundaries along $\{111\}$ planes are shown in Figure 5.12. The trace inclinations of two of the boundaries are oriented nearly perpendicular to the tensile axis and it can be seen that the surface traces of the slip planes are nearly parallel across all three grain pairs. In all three examples, at least one of the two grains falls into the low Taylor factor and high Schmid factor categories.

The slip behaviors at grain boundaries that exhibited slip continuity, but not directly along close-packed $\{111\}$ planes, are shown in Figure 5.13. In each of these examples, the slip in a second grain appears to be induced by slip in the first, as suggested by the degree of alignment between the dislocation channels in the adjacent grains. The dislocation channels in the second grain either trail off or change direction to follow a $\{111\}$plane. None of these examples, however, indicates that the dislocations in the second grain are initially mobile along $\{111\}$planes. It was also verified that none of the $\{100\}$ plane traces coincided with the surface traces. Therefore, with the information available, it is not possible to identify the planes on which the dislocation motion occurred. It can also be seen that the primary dislocation channels in the adjacent grains are highly inclined to one another in each example.

Examples of slip discontinuity at eight grain boundaries are shown in Figure 5.14 and Figure 5.15. It can be seen that, in all examples, the surface traces of the active slip planes in the adjacent grain are inclined to one another or only one of the two grains has an active slip plane. In the majority of the examples, at least one of the two grains has a high Taylor factor and low Schmid factor.

These findings suggest that the propensity for slip continuity across grain boundaries depends on the availability of favorably oriented slip systems in adjacent grains. It has been shown, through Figure 4.14 and Figure 5.9, that adjacent grains with high Schmid factors, and especially ones with low Taylor factors tend to have a higher probability of having multiple favorably oriented slip systems. This is likely the reason for the observed increase in slip continuity across adjacent grains with low Taylor factors shown in Figure 4.23. The availability of several favorably oriented slip systems increases the probability that at least one will have an orientation similar to that of the adjacent grain and allow easy slip activation at a similar level of stress. It was also shown in Figure 4.23 that although there is no correlation between Taylor factor mismatch and slip continuity propensity, there is a higher propensity for slip discontinuity across grains with high Schmid factor mismatch. The existence of high Schmid factor mismatch (0.05-0.19), however, requires the presence of at least one grain with a relatively low Schmid factor. Therefore, the low propensity for slip continuity when Schmid factor mismatch is high may be the result of (1) the lack of availability of favorably oriented slip systems, (2) the difference in the amount of stress required to activate slip in the two grains, or (3) a lack of alignment between the most favorably oriented slip planes at the grain boundary.

The dependence of slip continuity on Taylor factor and Schmid factor at high grain boundary inclinations is likely the result of the availability of slip systems that satisfy the LRB criteria for slip transfer [198-200]. These criteria indicate that the slip system that activates in a grain as a result of a dislocation pileup in an adjacent grain is the one that (1) minimizes the angle between the lines of intersection along the grain boundary of the incoming and outgoing slip planes, (2) maximizes the resolved shear stress on the outgoing system, and (3) minimizes the magnitude of the Burgers vector of the residual dislocations left at the grain boundary. While, in the current study the application of such criteria is not possible due to the unknown orientation of the grain boundary plane, the degree of alignment between the surface traces of the active slip systems shown in Figure 5.12 and the fact that most slip planes activated contain the highest Schmid factor slip system suggests that the LRB criteria may be governing dislocation interactions at the more highly inclined grain boundaries (>50˚). The higher degree of slip continuity at grain boundaries with lower inclinations to the tensile axis indicates that the amount of stress acting on the grain boundary may influence the propensity for slip continuity, and this observation will be addressed in a later section.

5.4.5 Temperature dependence of slip continuity

A final consideration is that the majority of the in-situ TEM analyses of dislocation interactions with grain boundaries have been conducted at low temperatures. In the current study, the dislocation interaction occurred at the grain boundaries in a high temperature, water environment. Therefore, understanding the potential influence of temperature on the grain boundary dislocation interactions is critical. TEM studies on

deformed FCC materials, have indicated that dislocation mobility is sometimes observed [147, 195], while other times it is not, regardless of whether the ultimate relief mechanism was through the activation of new dislocation sources or fracture [196]. Dislocations may migrate in the grain boundary through glide or by climb. While their glide behavior is insensitive to temperature, climb is only possible at temperatures where the vacancy population is sufficiently high. It may be considered that while glide is caused only by shear stresses, compressive and tensile stresses are capable of inducing positive and negative climb, respectively. Lim and Raj [197] evaluated the slip continuity behavior at symmetrical tilt boundaries in pure nickel bicrystals at temperatures ranging from 78K to 623K (homologous temperatures of approximately 0.05 to 0.36), and showed that the degree of slip continuity decreased slightly with increasing temperature. This could be an indication that the mobility of dislocations in grain boundaries increases with temperature to decrease slip continuity at grain boundaries. The slip continuity observed in the current experiment (at a homologous temperature of 0.41), therefore, is likely less than would be observed at lower temperatures.

5.4.6 Influence of slip continuity on intergranular cracking propensity

Several studies have been conducted to investigate the relationship between the orientations of slip systems and both intergranular and transgranular fracture [19, 20, 86-89, 207]. Crack formation has been attributed to the interaction of a dominant slip system with the grain boundary to form a step [20, 90], and to the discontinuity in slip across grain boundaries [21]. Intergranular cracking has also been attributed to strain

incompatibilities caused by the mismatch in the Schmid [21] or Taylor factors of grains at grain boundaries [19, 87]. Therefore, the strain incompatibilities in the current study, which were quantified in terms of the slip discontinuity at grain boundaries, are expected and may be influencing the cracking propensities of grain boundaries.

Slip discontinuity is indicative of the resistance of a grain to deform in response to the stresses created on the free surface by the impinging dislocations, which may result in intergranular cracking. Robertson et al. [195] observed that materials that were susceptible to transgranular and intergranular failure responded differently to local stress concentrations associated with dislocation pileup at grain boundaries. They observed that the ultimate stress relief mechanism operating in materials that cracked intergranularly was the nucleation and propagation of an intergranular crack, as opposed to the transfer of slip that occurred in materials that cracked transgranularly. They discussed the role of the boundary cohesive energy and argued that the operative stress relief mechanism (crack formation or slip transfer) would be the one that required the lower critical stress. The irradiation induced defects in the current study, including dislocation loops present along the $\{111\}$ planes, were shown to increase the yield strength of the material to approximately 850 MPa. Therefore, while grain boundary dislocations may nucleate in the grain boundary, higher stresses would be required to cause dislocation channeling than for slip in an unirradiated material. Furthermore, the intergranular cracking observed in the argon environment indicates that the equicohesive temperature has been exceeded at 400˚C, and the grain boundaries are weaker than the matrix. Therefore, it is possible that, unless the slip systems are oriented favorably as shown in Figure 5.12, it

may require less stress to nucleate a crack than to create a dislocation channel in the adjacent grain.

Slip discontinuity and cracking are both more prevalent at grain boundaries with trace inclinations close to perpendicular to the tensile axis and adjacent to grains with pair types that include high Taylor factors and low Schmid factors, as shown in Figure 5.16. If only the NS cracks along RHABs inclined >50˚ to the tensile axis are considered, a direct comparison can be made between the slip discontinuity data and NS cracking data as shown in Figure 5.16. It can be seen that the propensity for NS crack formation increases dramatically as the probability of slip discontinuity approaches 1. These results suggest slip discontinuity promotes intergranular cracking, and indicate that the propensity for NS cracking is not simply proportional to the propensity for slip discontinuity.

The NS cracking propensity is a stronger function of the Schmid and Taylor factor pair types at the boundary than the slip discontinuity behavior. The significance of the asymptotic behavior of the curves in Figure 5.16(d) - (f) is that the NS cracks are primarily occurring at the grain boundaries that are *most highly* prone to slip discontinuity. It is noteworthy, for example, that the slip discontinuity percentage reaches 100% at LL Schmid factor and HH Taylor factor pair type grain boundaries as shown in Figure 4.23, and the cracking propensity at such grain boundaries is disproportionately high. The NS cracks do not form at all grain boundaries that experience slip discontinuity, rather it was observed that the density of slip discontinuity sites on the gage surface of the specimen at 5% strain is a factor of 21 greater than the density of NS cracks. These findings indicate that the asymptotic behavior of the NS

cracking propensity with the slip discontinuity propensity is the result of the NS cracks forming at the subset of the slip discontinuity sites that are *most highly* prone to slip discontinuity.

The propensity for slip discontinuity also appears to increase with increasing Schmid factor mismatch, however, it was shown in Figure 4.32 that there is not a strong correlation between Schmid factor mismatch and cracking. If the data in Figure 4.32 are scrutinized further, however, it can be seen that there may be a weak correlation between Schmid factor mismatch and cracking. While 24% of the total grain boundary population has a mismatch greater than 0.063, 39±12%, 30±7%, and 27±6% of the NS cracks occur at locations exceeding this mismatch at 2%, 5%, and 10% strain, respectively. The influence of Schmid factor mismatch on cracking, however, appears weaker than the influence of having a low Schmid factor or high Taylor factor pair type grains at the boundary as can be seen by from Figure 4.34 and Figure 4.36. If the relationship between Taylor or Schmid factor mismatch and NS cracking were greater than that of having a high Taylor factor or low Schmid factor grain, then the LH Schmid factor and Taylor factor categories should be greater than that of the LL and HH, respectively.

In summary, the propensity for slip continuity at the grain boundary is influenced by the availability of similarly oriented slip systems in adjacent grains with relatively high Schmid factors. Grains with low Taylor factors are observed to undergo multiple slip more frequently than grains with high Taylor factors, which indicates that such grains generally have multiple slip systems that are favorably oriented. This explains the observation that the degree of slip continuity at grain boundaries with trace inclinations >50˚ to the tensile axis is higher at grain boundaries adjacent to grains with low Taylor

factors. Slip discontinuity at the grain boundary appears to contribute to the propensity of the grain boundary to crack, as the NS cracks occur primarily along the types of grain boundaries that are most highly prone to slip discontinuity. The inclination of the grain boundary with respect to the tensile axis also appears to be a key parameter influencing the propensity of the grain boundary to crack. Therefore, the influence of the stress acting on the grain boundary, which depends on the grain boundary plane inclination to the tensile axis, will be addressed in the next section.

5.5 Stress dependence

The shear and normal forces acting on grain boundaries are known to influence the propensity for intergranular cracking. While shear forces may induce GBS and subsequent fracture [62-64], normal stresses may reduce the critical stable cavity radius [69, 70] or increase crack growth [64]. In this study, the tendency of the NS cracks to form along grain boundaries with trace inclinations and cross sectional penetrations perpendicular to the tensile axis suggests a potential normal stress dependence of the cracking behavior. This section will investigate the relationship between the stress acting on grain boundaries and cracking propensity by applying a simple model henceforth referred to as the Schmid-Modified Grain Boundary Stress (SMGBS) model. The SMGBS model is not intended to yield quantitative results and is only applicable to the grain boundary stresses during plastic deformation. It will be used to qualitatively describe the relationship between the stress acting on grain boundaries and the propensity for intergranular cracking and slip continuity across grain boundaries. The influence of the inclination of the grain boundary plane to the tensile axis as well as the propensity of

the grain to deform on the basis of its Schmid factor will be considered when evaluating the stress acting on the grain boundary.

5.5.1 Schmid-Modified Grain Boundary Stress model for determining stress on grain boundaries

As discussed in Section 2.5, the deformation behavior in polycrystalline materials is often discussed through (1) upper-bound or (2) lower-bound analyses, which assume either (1) geometrically self-consistent deformation fields while stress is averaged over all grains, or (2) self-consistent internal stress fields and strain is averaged over all grains [74]. Neither approach is entirely accurate, however, as they violate equilibrium of stress and strain, respectively. Instead, the restricted deformation of individual grains within a polycrystalline material results in deformation behavior that is a compromise between isostress and isostrain conditions [208]. While techniques are available to directly measure the plastic strain fields [209], techniques are not currently available to directly measure stress fields in polycrystalline materials. Indirect stress measurements may become more widely used, however, by analyzing the elastic strain field through submicron X-ray diffraction [210] or neutron diffraction techniques [211]. Characterizing the true stress field at the grain boundary interface, therefore, is beyond the scope of the current study. This study will instead use an isostrain assumption to evaluate the stress acting on grain boundaries in polycrystalline 316L.

First, the yielding behavior of a single crystal will be considered. The strain that occurs in a crystal lattice is influenced by both its elastic and plastic anisotropies [208]. An isolated crystal will strain elastically until the applied stress reaches the yield stress, at

which point it will plastically deform. In the elastic regime, the stress-strain behavior of the crystal will be dictated by the elastic stiffness of the grain. The plastic regime will be reached when the magnitude of the applied stress is such that the τ_{CRSS} is reached on the most favorably oriented slip system. Therefore, the stress required for the onset of plastic deformation will be inversely proportional to the Schmid factor of the crystal. The strain at which deformation occurs, therefore, depends on both the elastic stiffness of the crystal as well as the slip system orientation.

Consider crystals with two different orientations that undergo the same nominal strain, similar to the isostrain structural analog described by Wong and Dawson [208]. The first and second crystals have elastic stiffness values and Schmid factors of E_1 and m_1, and E_2 and m_2, respectively. As shown in Figure 5.17, despite the fact that crystal 1 has a higher yield stress, it reaches its yield stress first because it has a stiffer orientation. Crystal 2 reaches its yield stress after additional straining. Once plastic deformation commences, however, it is the flow stress (approximated here as inversely proportional to the Schmid factor) rather than the elastic stiffness, which determines the strength of the crystal if the effects of strain hardening are neglected. Fully developed plasticity is generally defined as macroscopic strains exceeding 2% [208], which therefore encompasses the majority of the data collected in the current study. Clausen et al. [211] applied a self-consistent polycrystal deformation model to predict the development of lattice strains in stainless steel during uniaxial tensile loading, and their model predictions of elastic strains in the tensile direction generally agreed with their strain measurements obtained via neutron diffraction. Their modeling results indicated that the ratio of the single crystal elastic stiffness in the $\langle 111 \rangle$ crystal direction to that in the $\langle 100 \rangle$ direction,

r_E, was 3.2, indicating a high degree of elastic anistropy. Finite element simulations by Wong and Dawson [208] on fcc crystal structures showed that the propensity for the $\{111\}$ crystal orientation to yield plastically before the $\{100\}$ orientations increased with increasing r_E. Therefore, Figure 5.17 may be applicable to the yielding behavior of individual grains in 316L in the current study, but this has not been confirmed experimentally. While the plastic deformation that occurs in actual polycrystalline materials is complex, these discussions have established that stress gradients are expected in polycrystalline materials as a result of the variations in the slip system orientations. Therefore, the macroscopic applied stress is not expected to be indicative of the localized stress experienced by each grain in the polycrystal as it plastically deforms.

The stress heterogeneity in polycrystalline materials will now be extended to the stresses acting on the grain boundaries in the polycrystal. The resolved shear, τ_{RSS}, and normal, σ_N, stresses acting on a grain boundary plane can be expressed as a function of the flow stress of the specific grain as it plastically deforms, σ_{f_g}, and the angle between the normal to the grain boundary plane and the tensile axis, α (indicated in Figure 5.18), as:

$$\tau_{RSS} = \sigma_{f_g} \sin\alpha \cos\alpha, \tag{5.11}$$

and,

$$\sigma_N = \sigma_{f_g} (\cos\alpha)^2, \tag{5.12}$$

respectively. Therefore, the shear stress is maximum when $\alpha = 45^\circ$ and the normal stress is a maximum when $\alpha = 0^\circ$. It has already been established, however, that the flow stress of the polycrystal, σ_f, is not necessarily equal to the flow stress of each individual grain as

it deforms, σ_{f_g}, because σ_{f_g} depends on the grain orientation. In this study, the Schmid factor will be used as a measure of the grain to grain variations in σ_{f_g} for the irradiated specimens where strain hardening is low.

To qualitatively explore the influence of the grain orientation on the magnitude of the applied stress acting on the grain boundary, the simple assumption will be made that σ_{f_g} is inversely proportional to its Schmid factor and σ_f, as the material deforms plastically, is inversely proportional to the average Schmid factor,

$$\sigma_{f_g} = \sigma_f \frac{m_{avg}}{m_g}, \tag{5.13}$$

where m_{avg} is the average Schmid factor of 0.45, and m_g is the Schmid factor of the grain of interest. The assumption that the strength of the grain is inversely proportional to its Schmid factor is analogous to the directional strength measure for a single crystal used by Wong and Dawson [208]. Therefore, if the constraints on deformation imposed by neighboring grains are neglected, deformation of a grain with the minimum Schmid factor of 0.27 would require $\frac{0.45}{0.27} \times 100 = 167\%$ of the flow stress of a polycrystal with an average Schmid factor of 0.45. Equations (5.11) and (5.12) may then be rewritten to illustrate the influence of the grain-to-grain stress variations to yield expressions for the Schmid-modified resolved shear and effective normal stresses:

$$\tau_{RSS} = \sigma_f \frac{0.45}{m} \sin\alpha \cos\alpha, \tag{5.14}$$

and,

$$\sigma_N = \sigma_f \frac{0.45}{m} (\cos\alpha)^2. \tag{5.15}$$

Again, it will be emphasized here that the true stress distributions in polycrystalline materials are likely very complex, and the actual stress acting on a particular grain boundary would likely depend on the orientations of *both* of the grains adjacent to the boundary as well as surrounding grains in the microstructure. These equations are simply intended as a rough indicator of the influence of the deformation propensity of a grain on the stress acting on adjacent boundaries. As shown in Figure 5.19, if two neighboring grains have the same propensity to deform, the stress acting on the grain boundary between them will simply depend on the grain boundary plane inclination to the tensile axis. If the grain boundary plane inclinations are identical, however, and the grains have different propensities to deform, the grain that requires a higher level of stress to deform will have more stress acting on the grain boundary. Note that the maximum and minimum resolved shear and normal stresses in equations (5.14) and (5.15) are achieved adjacent to grains with Schmid factors of 0.27 and 0.50, respectively. In the SMGBS model, the effects of strain hardening are neglected, and the stress acting on the grain as it deforms is assumed to continue to be inversely proportional to its Schmid factor. While the strain hardening is not likely to be completely absent, the magnitude of work hardening that occurs in irradiated material decreases significantly with dose [92, 212], and so this assumption is more reasonable for irradiated 316L.

5.5.2 Applicability of SMGBS model assumptions to unirradiated materials

One of the primary assumptions of the SMGBS model is that strain hardening is negligible, which permits the assumption that the flow stress is equal to the yield stress.

While this assumption is generally applicable to highly irradiated stainless steels where the strain hardening is often on the order of only 10% of the true fracture stress, this assumption is unjustifiable for unirradiated stainless steels where the strain hardening may be on the order of 70-80% of the true fracture stress [212].

If power-law hardening is assumed, the Taylor factors of grains may be used to evaluate their flow stresses since the Taylor factor is a measure of the crystallographic shear strain required to achieve the uniaxial strain. Therefore, a grain with a higher Taylor factor would undergo more crystallographic slip and strain harden more readily. As shown by Hosford [74], the ratio of the flow stresses of wires with 2 different textures, σ_{f_1} and σ_{f_2}, can be expressed as a function of their Taylor factors, M_1 and M_2,

$$\frac{\sigma_{f_1}}{\sigma_{f_2}} = \left(\frac{M_1}{M_2} \right)^{1+n} \tag{5.16}$$

where n is the strain hardening exponent. If M_2 is taken as the average Taylor factor of a random polycrystal (3.06), the right-hand side of this expression can be substituted into equations (5.14) and (5.15) to yield,

$$\tau_{RSS} = \sigma_f \left(\frac{M_1}{3.06} \right)^{1+n} \sin\alpha \cos\alpha, \tag{5.17}$$

and,

$$\sigma_N = \sigma_f \left(\frac{M_1}{3.06} \right)^{1+n} (\cos\alpha)^2. \tag{5.18}$$

These expressions are applicable to unirradiated materials which strain harden, but in practice it should be considered that the Schmid and Taylor factor predictions of local stresses in polycrystalline materials may be more accurate at low strains. As plastic

straining progresses, lattice rotation occurs and the local stresses that develop as a result of the specific grain boundary geometries will influence the stress and strain gradients that develop in the alloy. Such deformation behaviors are not considered in the SMGBS model and therefore deviation from the model predictions of stress development would likely result at high levels of strain.

5.5.3 Accounting for stress on grain boundaries in with the SMGBS model when the boundary plane orientation is unknown

This section will illustrate how equations (5.14) and (5.15) can be applied in the current study where the value of α is unknown. The results of this study indicate that the trace inclination has a strong influence on the slip continuity at the grain boundary as well as the cracking propensity of the grain boundary. In reality, the correlations should depend on the inclination of the grain boundary *plane* to the tensile axis. This was confirmed by viewing the samples in cross-section and observing that the penetrations of the cracks into the sample substrate also developed along grain boundaries perpendicular to the sample surface.

While the orientations of the specific grain boundary planes will remain unknown, methodologies will be applied to account for the possible plane inclinations based on the known trace inclination of the grain boundary. Alexandreanu [142] evaluated the relationship between the trace inclination, θ, and the grain boundary plane inclination to the tensile axis, α. He defined a third angle, φ, as the angle between the tensile direction and the trace of the grain boundary plane on the side surface perpendicular to the sample surface. With the coordinate system illustrated in Figure 5.18, the sample surface is in

the yz plane, the specimen side surface is in the xz plane, and the tensile direction is in the z direction. The grain boundary plane surface trace can be represented by a vector, v_1, and the trace of the grain boundary plane on the side surface can be represented by a vector, v_2. Therefore, θ and φ can be expressed as,

$$\theta = \arccos\left(\frac{\vec{v}_1 \cdot \vec{z}}{|v_1||z|}\right) \tag{5.19}$$

and,

$$\varphi = \arccos\left(\frac{\vec{v}_2 \cdot \vec{z}}{|v_2||z|}\right) \tag{5.20}$$

respectively. Recall that while the surface trace of the grain boundary, θ, is known, the value of φ may vary from 0˚ to 90˚. Not all values of φ are equally likely, however. Rather, all rotations around the trace inclination vector, v_1, are equally likely. This angle of rotation, β, is illustrated in Figure 5.18. The reference orientation for β (β=0) occurs when the grain boundary plane and specimen surface are coincident. The equal likelihood of having any value of β results in a bias for low values of φ for all values of θ other than θ=90˚, and the bias increases with decreasing values of θ. The expressions for α and β in terms of φ and θ are (derivations for α and β and illustrations of the φ bias are given in Appendix G),

$$\alpha = \arccos\left(\sqrt{\frac{1}{\tan^2\varphi} + \frac{1}{\tan^2\theta} + 1}\right)^{-1} \tag{5.21}$$

and,

$$\beta = \arccos\left(\frac{\frac{1}{\tan\varphi}}{\sqrt{\frac{1}{\tan^2\varphi}+\frac{1}{\tan^2\theta}+1}}\right) \tag{5.22}$$

The Schmid-modified normalized resolved shear, $^*\tau_{NRSS}$, and normal, $^*\sigma_{NNS}$, forces acting on a grain boundary plane during plastic deformation can next be calculated by setting $\sigma_f = 1$ and substituting the expression for α, equation (5.21), into equations (5.14) and (5.15) to yield final expressions of,

$$^*\tau_{NRSS} = \frac{0.45}{m}\sin\left[\arccos\left(\sqrt{\frac{1}{\tan^2\varphi}+\frac{1}{\tan^2\theta}+1}\right)^{-1}\right]\cos\left[\arccos\left(\sqrt{\frac{1}{\tan^2\varphi}+\frac{1}{\tan^2\theta}+1}\right)^{-1}\right] \tag{5.23}$$

and,

$$^*\sigma_{NNS} = \frac{0.45}{m}\cos\left[\arccos\left(\sqrt{\frac{1}{\tan^2\varphi}+\frac{1}{\tan^2\theta}+1}\right)^{-1}\right]^2, \tag{5.24}$$

where,

$$\varphi = \arctan\sqrt{\frac{\frac{1}{\cos^2\beta}-1}{\frac{1}{\tan^2\theta}+1}} \tag{5.25}$$

respectively. In this way, the resolved shear and normal forces can be calculated as a function of three independent variables, θ, β, and m. The stresses will often be plotted as a function of θ or m, which are the experimentally measured parameters. Normalized stress curves can be generated for each possible value of β (0-90˚) and m (0.27-0.50) as a function of θ. As shown in Figure 5.20, the highest normalized resolved shear stress will be achieved when m=0.27, and β and θ are such that α=45˚. When m=0.50 and α=45˚, the normalized resolved shear stress is reduced by 46%. The highest normalized normal

stress will be achieved when $\beta=\theta=90^{\circ}$ and m=0.27. When $\beta=\theta=90^{\circ}$ and m=0.50, the normalized normal stress is reduced by 46% as shown in Figure 5.21.

A final consideration is the bulk distributions of the three independent variables used to calculate the grain boundary stresses, θ, β, and m. A random sampling of over 330 trace inclinations, θ, indicated some variations in different regions, but no statistically significant deviation from a random distribution. As previously discussed, the grain boundary plane is expected to be equally likely to occur at any angle β around the surface trace vector, v_1. The distribution of m, however, *is not random* as was shown in Figure 4.4(a). Even in an untextured polycrystalline material, the distribution of Schmid factors is not randomly distributed between its minimum and maximum values (0.27-0.50) due to the high probability that at least one of the 12 slip systems will be favorably oriented. Therefore, the curves in Figure 5.20 and Figure 5.21 were weighted by the probability of sampling a grain with each Schmid factor. The weighting for the Schmid factor was performed by considering the Schmid factor distribution in the bulk alloy. As was shown in Figure 4.4, none of the 6,000 grains measured in the irradiated samples had Schmid factors of 0.27, and the probability of encountering a grain with a Schmid factor of 0.28 was only ~0.2%, whereas the probability of encountering a grain with a Schmid factor of 0.49 was ~15.3%. Therefore, grains with higher Schmid factors were given more weight. For example, grains with Schmid factors of 0.49 were given a weight of 0.153, while grains with Schmid factors of 0.28 were given a weight of 0.002.

It is proposed here that the propensity for intergranular cracking or slip continuity across a grain boundary is not necessarily linearly proportional to the stress acting on the grain boundary, but rather that either phenomena requires a critical threshold stress. The

assumed existence of a threshold stress is based on the results of Alexandreanu [18, 142], where it was observed that the intergranular cracking propensity, as well as the grain boundary deformation propensity of Ni-16Cr-9Fe in 360˚C water, appeared to require a threshold shear stress. The likelihood that the stress acting on a grain boundary is above a critical resolved shear (CSS) or normal stress (CNS), for a given value of θ can be determined from the number of SMGBS model points above the threshold stress. Consider the weighted number of points above a CNS value for a given trace inclination, WN_θ. The WN_θ values are calculated by summing all of the weighted modeling points which exceed a specified critical stress value for each value of θ. The SMGBS model curve generation procedure is illustrated in Figure 5.22, and the summation is described with the following equations,

$$WN_\theta = \sum_{\beta=0}^{\beta=90} \sum_{m=0.27}^{m=0.50} N_{>CNS}(\theta, \beta, m) \tag{5.26}$$

where,

$$N_{>CNS} = \begin{cases} 0 \text{ if } {}^*\sigma_{NNS}(\theta, \beta, m) \le CNS \\ f_\beta f_m \text{ if } {}^*\sigma_{NNS}(\theta, \beta, m) > CNS \end{cases} \tag{5.27}$$

f_β is the fraction of boundaries with the specified degree of rotation about v_1 (with all angles being equally likely), and f_m the fraction of grains with the specified Schmid factor, i.e. 0.2% of the grains have Schmid factors of 0.28 so $f_{0.28}$ = 0.002. The WN_θ value can be calculated for each value of θ (0˚ - 90˚) to generate a smooth WN_θ vs θ curve. In order to compare the SMGBS model dependence of θ to the crack dependence of θ (which is always normalized to 1), this model curve is also normalized. Thus,

regardless of the number of SMGBS model points above the critical stress, the area under the SMGBS model curve is always constant. This is analogous to the crack normalization treatment in that, regardless of the total number of cracks, the sum of the normalized crack fraction is always 1. Depending on the number of angle divisions used for the SMGBS model, it may be necessary to multiply the SMGBS model curve by a constant to compare it to the cracking data. In this study, the cracking results were binned in 10˚ intervals, while the SMGBS model curves were generated using 5˚ intervals. Thus, it was necessary to normalize the SMGBS model curve to a value of approximately 2 (rather than 1) to yield a proper comparison the crack distribution.

SMGBS model curves for various CSS and CNS values are shown in Figure 5.23. As CSS is increased, the peak in the distribution near 45˚ strengthens and the probability of exceeding the CSS at lower inclinations, θ, decreases. As the CNS increases, the peak in the distribution develops near θ=90˚ and strengthens. This same procedure can be used to generate SMGBS model curves for any one of the three independent variables (θ, β, or m). The normalized fraction of SMGBS model points exceeding a CSS or CNS on the grain boundary is plotted as a function of the Schmid factor, m, in Figure 5.24. The SMGBS model predicts that the shear and normal stresses acting on the grain boundary will decrease with Schmid factor. It also indicates that the relative influence of the Schmid factor, or the slope of the SMGBS model curve, on the stress acting on the grain boundary increases with increasing CSS or CNS.

5.5.4 Applying SMGBS model to grain boundary inclination dependence of cracking behavior

Using these Schmid-modified resolved shear and normal stress expressions, the shear and normal stress dependencies of the intergranular cracking behavior of irradiated 316L can be evaluated. The tendency of the NS cracks to occur along grain boundaries with trace inclinations perpendicular to the tensile axis indicates that the normal stress acting on the grain boundary may be influencing the NS cracking propensity. As the CNS is varied, the strength of the SMGBS model peak at $\theta = 90°$ also varies, as shown in Figure 5.23. In this section the CNS values that result in best fits to the cracked trace inclination distributions will be reported. For each crack distribution analyzed the CNS value was selected that provided the best fit to the crack distribution by maximizing the portion of the SMGBS model curve that fit the NS crack distribution data. The strain dependence of the CNS for NS cracks is shown in Figure 5.25. As the strain increases from 2% to 5% to 10% strain, the CNS decreases from 0.92 to 0.67 and finally 0.57, respectively. Indicating that the relative amount of normal stress required for crack development decreases as plastic strain accumulates in the specimens. This could be indicative of a decrease in the cohesive strength of the grain boundary with progressive straining. Data collected in a previous study [56], on a 7 dpa proton irradiated tensile specimen strained to failure in 400˚C SCW, may also be considered, as shown in Figure 5.25 (d). It can be seen that a reasonable model fit to the cracking data is achieved with a CNS of 0.30. The fit between the model and the cracking data confirm that NS cracking is driven by the normal stress acting on the grain boundary and that the cracks are opening via mode I cracking as indicated in Figure 5.26.

The intergranular GBC cracking results in SCW are more challenging to interpret. The observation that some GBC cracks develop into NS cracks prompts the question of whether NS cracks are simply a subset of GBC cracks that offer more favorable conditions for crack propagation. It was shown in Figure 4.41 that the GBC cracks dominate the crack population at 2% strain, but by 10% strain the NS crack population dominates. It was also reported that only 36% of the GBC cracks at 5% strain developed into NS cracks at 10% strain. These findings indicate that the GBC crack population does contribute to the NS crack population. It is unlikely, however, that the NS cracks are a subset of the GBC crack population. If the NS cracks were simply GBC cracks that occurred along grain boundaries that were more prone to crack propagation, the densities of GBC and NS cracks would increase together. It was shown in Figure 4.41, however, that the NS crack density increased with progressive straining, while the GBC crack density did not change significantly from 2% to 5% strain and then decreased from 5% to 10% strain. Furthermore, while some of the NS cracks appear to be forming via coalescence of GBC cracks as shown in Figure 5.27(c) and (d), the majority of the NS cracks did not have a higher than average frequency of dislocation channel intersections with the grain boundary (as viewed from the gage surface), as was shown in Figure 4.55. As indicated in Figure 5.27(b), it is possible that some NS cracks formed as a result of coalescence of GBC cracks. The absence of serrations at the cracked boundary shown in Figure 5.27(a), however, is more typical of the NS crack population.

In Figure 5.28, the distribution of GBC cracks at 5% strain is broken down into two data sets, (1) those that remain GBC cracks at 10% strain and (2) those that develop into NS cracks at 10% strain. It can be seen that the GBC cracks that developed into NS

cracks were those with higher inclinations. With more NS cracks developing with subsequent straining than GBC cracks, the net influence of GBC cracks developing into NS cracks may be responsible for the lesser number of GBC cracked grain boundaries at higher inclinations shown in Figure 4.43. It is also possible, however, that the peak in the inclination distributions near 45˚ at 5% and 10% strain is indicative of a shear stress dependence of the GBC crack formation. Intergranular crack nucleation in high temperature environments is widely believed to be driven by the inability to accommodate GBS driven by shear stresses [62-64]. For example, Alexandreanu found that grain boundary deformation driven by shear stress was a precursor to intergranular cracking of Ni-16Cr-9Fe in 360˚C primary water [142]. While GBS was not detected in the surface plane of the specimens by offsets in the scratches, localized GBS was consistently observed perpendicular to the surface at the intersections of dislocation channels with grain boundaries in both the SCW and argon environments as shown in Figure 5.29. This indicates that the GBC cracks are primarily opening via mode III cracking described in Figure 5.26 [62].

The stress dependencies of NS and GBC cracking data in the 400˚C purified argon environment are different than those observed in SCW. It was shown in Figure 4.51 that the total cracked boundary inclination distribution is strongly peaked towards 90˚, and it is dominated by what appear to be GBC cracks. It is noteworthy, however, that their strong tendency to form along boundaries with trace inclinations perpendicular to the tensile axis is more consistent with the NS crack trace inclination distribution in SCW than the GBC distribution. The application of a CNS of 0.84 results in excellent agreement between the crack distribution and the model, as shown in Figure 5.30. This

confirms that intergranular cracking in argon is driven by the normal stress acting on the grain boundary. Furthermore, the total crack density in argon (GBC+NS) is similar to that of the NS crack density in SCW at 5% strain. The total crack density in argon is 13 mm^{-2}, while the NS crack density in SCW is 17 mm^{-2}. These observations, combined with the fact that the "GBC" cracks observed in argon formed adjacent to grains with low Schmid factors and high Taylor factors (Figure 4.52) suggests that the boundaries susceptible to GBC cracking in the argon environment may be the same boundaries that would be susceptible to NS cracking in the 400˚C SCW environment.

In summary, the analysis of the stress dependence of the cracking behavior indicates that the NS cracks are strongly dependent on the normal stress acting on the grain boundary and are opening via mode I cracking. The GBC cracks develop primarily through mode III cracking. Although the development of GBC cracks into NS cracks does occur along boundaries that are oriented favorably to the tensile axis, the total NS crack population is not simply a subset of the GBC crack population where conditions are more favorable for crack propagation.

5.5.5 Implications of normal stress dependence of cracking

The finding that intergranular cracking of irradiated 316L can occur in an inert purified argon environment indicates that corrosion is not required for intergranular fracture. Therefore, the cracking observed in the argon environment cannot be classified as stress corrosion cracking. The extent of intergranular cracking observed in SCW was, however, shown to be much greater than that observed in argon as was shown in Figure 4.50. It is noteworthy that other researchers have observed apparent creep cracking of

stainless steels in argon and high temperature air environments [4, 60]. The similarities in the cracking morphologies of creep cracks observed by Arioka et al. on 316 stainless steel following straining in air at 525˚C [60] and the intergranular fracture of 7 dpa proton irradiated 316L following straining in 400˚C SCW is shown in Figure 5.31. It is noteworthy that, in both cases, the cracks tend to be short and preferentially occur along boundaries with trace inclinations perpendicular to the tensile axis. As discussed in Section 2.3, the activation energies of ~100 kJ/mol measured by Arioka et al. for creep crack growth rate of 316 in high temperature air [59, 60] are similar to the activation energies for crack growth of 105 kJ/mol and 85 kJ/mol for 304 and 316L measured by Teysseyre and Was [4]. These results offer qualitative and quantitative support for the existence of a creep based mechanism for intergranular cracking in SCW.

As discussed in Section 2.4, creep fracture can occur via two modes, wedge-type or r-type cracks. Wedge cracks generally occur at high stresses and intermediate temperatures and are believed to occur as a result of the shear stresses that develop at triple junctions [66]. At lower stresses and higher temperatures, cracking occurs through the nucleation and growth of grain boundary cavities, which are characterized as r-type cracks. While wedge cracks are generally stated to occur preferentially along boundaries aligned for maximum shear [62], the frequent observations of apparent wedge and r-type cracks along boundaries perpendicular to the tensile axis has been attributed to several factors including (1) an increased ability of the cracks to grow along boundaries oriented perpendicular to the tensile axis [64], (2) a smaller critical cavity radius along boundaries perpendicular to the tensile axis as a result of the normal stress acting on the grain

boundary [69, 70], (3) the thermal nucleation of cavities through condensation of vacancies on stressed surfaces [63].

The tendency of the NS cracks to occur along boundaries perpendicular to the tensile axis in the current study is consistent with the cracked boundary inclination distributions of stainless steels from other experiments in high temperature aqueous environments. It is shown in Figure 5.32 that the cracked boundary trace inclination distribution is dependent on temperature, irradiation damage, and alloy. By comparing Figure 5.32 (a) and (b), it can be seen that the inclination distribution of cracked boundaries in irradiated 316L strained in SCW broadens with decreasing temperature. It can also be seen from (c) and (d) that the inclination distribution of 316L broadens with irradiation damage. It is interesting to note that by comparing (c) – (f), it can be seen that the inclination distribution may be more alloy dependent in the irradiated condition than in the unirradiated condition in 500˚C SCW. It can be seen that the IG cracks on unirradiated 316L stainless steel and nickel-base alloy 690 both preferentially occur along boundaries with trace inclinations oriented nearly perpendicular to the tensile axis. In the irradiated condition, the 316L distribution simply broadens, while the 690 distribution appears to be developing a peak near 45˚, indicating a potential shear stress dependence of cracking. Although the correlations are less pronounced in (g) and (h), it can be seen that the inclination distribution of the IG cracks on unirradiated 316L strained in subcritical water peak close to 90˚, while that of nickel-base alloy 625 peaks near 45˚.

This alloy dependence of the cracked trace inclination distribution may explain the differences observed in the NS crack distribution of irradiated 316L stainless steel at 10% strain in the current study and the cracking results of Alexandreanu [142] for Ni-

16Cr-9Fe in 360˚C water, as shown in Figure 5.33. While Alexandreanu successfully demonstrated that grain boundary deformation induced by shear stresses caused the IG cracks on the Ni-16Cr-9Fe, the NS crack distribution in the current study exhibits a normal stress dependence which is more consistent with the crack inclination distributions of 316L in high temperature aqueous environments.

In summary, the observations of intergranular cracking of irradiated 316L in a purified argon environment indicate that the SCW environment is not required for the formation of IG cracks, thus this type of cracking cannot be referred to as stress corrosion cracking; environmentally assisted cracking may be more appropriate given that SCW was shown to increase the crack density (Figure 4.50). The crack morphology in the SCW environment is similar to that of creep cracks observed on 316L in air, and the activation energy for creep crack growth rate of stainless steels is similar to that measured for intergranular cracking of 316L in SCW. These findings suggest that a creep cracking mechanism is operating on irradiated 316L in the SCW environment, and that either the crack nucleation or growth mechanism is influenced by the normal stress acting on the grain boundary.

5.5.6 Application of the SMGBS model to Schmid factor dependence of cracking

The SMGBS model predictions for the NS crack dependence on the Schmid factor will now be considered. As previously shown, the SMGBS model predicts that the normal stress acting on the grain boundary increases with trace inclination, θ, and decreases with Schmid factor, m, of the grain adjacent to the boundary. It was also previously determined that imposing CNS of 0.92, 0.67, and 0.57 provided reasonable

fits to the NS crack data in SCW at 2%, 5%, and 10% strain, respectively. By imposing these same CNS values, the SMGBS model prediction of the Schmid factor dependence of being above the CNS can be evaluated.

The SMGBS model predicted dependence is plotted as a function of the Schmid factor distribution of both grains adjacent to cracked boundaries following straining to 2%, 5%, and 10% strain in Figure 5.34. It can be seen that, as strain increases, the Schmid factor dependence of the cracking behavior decreases. This is also predicted by the model, in that, as the CNS decreases, the Schmid factor dependence of the SMGBS model curve also decreases. It can be seen, however, that the negative slope of the SMGBS model curve is less than the slope of the cracking data, indicating that the correlation between cracking and Schmid factor is slightly greater than that predicted by the model.

The implications of these observations will now be considered. One of the assumptions of the SMGBS model is that the stress acting on a grain boundary for a given value of φ is always proportional to 0.45/m. Therefore, the influence of the Schmid factor of the grain on the stress on the adjacent grain boundary will always be greater when the normal stress acting on the grain boundary is higher, i.e. for smaller values of α (larger values of β and θ). Therefore, as the CNS decreases, the relative influence of the Schmid factor on the normal stress decreases, as was shown in Figure 5.24. The fact that the cracking data also exhibits the same relationship, thus supports the modeling assumptions. This relationship between Schmid factor and cracking supports the contention that it is not the Schmid factor mismatch at the grain boundary that necessarily causes cracking, but rather the presence of grains with low Schmid factors.

As previously discussed, if the Schmid factor mismatch were responsible for cracking, more cracks would be observed at LH Schmid factor pair types than LL, and as shown in Figure 4.34, clearly this is not the case.

The model indicates that the boundaries adjacent to grains with low Schmid factors will experience greater stresses. Alternatively, if an isostress assumption were to be applied, it could be argued that the deformation rate would be lower in grains with lower Schmid factors. Modeling results have demonstrated that the deformation rates of grains with $\{111\}$orientations, which correspond to grains with high Taylor factors and low Schmid factors, have reduced plastic deformation rates compared to other crystallographic orientations [208]. Since the restricted deformation behavior of individual grains within a polycrystalline material is a compromise between isostress and isostrain conditions [208], it could also be argued that the correlations observed between Schmid factor and cracking are the result of the higher stresses required to deform grains with low Schmid factors and the lower plastic deformation rates of such grains.

It can be seen from Figure 5.34, that the cracking data appears to exhibit a slightly stronger Schmid factor dependence than the model predicts. At first glance, it suggests that this may be a result of the model neglecting to account for the Schmid factors of both grains adjacent to the boundary. If, for example, it were assumed that the applied stress acting on the grain boundary would be the sum of the applied stresses to each of the two adjacent grains, equation (5.24), might be modified to yield,

$$*\sigma_{NNS} = \frac{1}{2}\left(\frac{0.45}{m_1}+\frac{0.45}{m_2}\right)\cos\left[\arccos\left(\sqrt{\frac{1}{\tan^2\varphi}+\frac{1}{\tan^2\theta}+1}\right)^{-1}\right]^2, \qquad (5.28)$$

where m_1 and m_2 are the Schmid factors of both grains adjacent to the boundary. The normal stress acting on the grain boundary would then be a maximum when $m_1=m_2=0.27$, and a minimum when $m_1=m_2=0.50$. While the maximum and minimum normalized stresses will remain the same, the cumulative result would be a *reduction* in the influence of the Schmid factor on the normalized stress due to the low probability of having two adjacent grains with low Schmid factors. Therefore, neglecting the influence of the adjacent grain does not appear to be responsible for the strength of the Schmid factor correlation. Other possible reasons for this strong correlation between cracking and Schmid factor include,

(1) Modeling results [208] indicate that grains with $\{111\}$orientations, which correspond to grains with high Taylor factors and low Schmid factors, have lower plastic deformation rates, which are not accounted for by the current isostrain assumptions.
(2) The correlation between Schmid factor and cracking may not be due to the stress acting on the grain boundary alone, but enhanced by another factor such as slip continuity across the boundary.
(3) The elastic stiffness of the grain, which is also orientation dependent [208], could be influencing the cracking propensity.

The finding that the GBC cracking propensity does not appear to correlate with either the Schmid or Taylor factors of the adjacent grains further suggests that the formation of this type of crack may be weakly dependent on the magnitude of the applied tensile stress acting on the grain boundary and more strongly dependent on the localized

stresses at the site of dislocation impingement on the grain boundary. If the propensity for GBC cracks to form was influenced by the dislocation pileup stress acting on the grain boundary, however, it might be predicted that a grain with a high Schmid factor with slip systems oriented for maximum shear stress might be more likely to supply the necessary dislocations and shear stress for crack formation. No such relationship appears to exist, however, and the step height measurements at grains with high Schmid factors shown in Figure 4.15 and Figure 4.16 are not necessarily greater than those with low Schmid factors.

In summary, the analysis of the stress dependence of the cracking data indicate that the likelihood of a crack developing is dependent on the normalized normal stress on the grain boundary exceeding a critical value. The normal stress is argued to be dependent on both the inclination of the grain boundary plane with respect to the tensile axis and the strength of the grain which is taken to be inversely proportional to the Schmid factor. The normal stress dependence of the cracking behavior confirms that the cracks are opening via mode I cracking. The normal stress dependence of the cracking may be the result of a reduced critical cavity size along boundaries with high normal stress, a greater crack growth rate along such boundaries, or the thermal nucleation of cavities through the condensation of vacancies on such highly stressed surfaces. The tendency of the NS cracks to form along grain boundaries perpendicular to the tensile axis is consistent with the results of previous studies. The similarities in the activation energies for creep crack growth rate of 316 stainless steel in air and in SCW and similarities in the cracking morphologies indicate that creep may plays a key role in the mechanism of intergranular cracking in SCW.

5.5.7 Applying SMGBS model to grain boundary inclination dependence of slip continuity

In this section the applicability of the proposed SMGBS model to the slip continuity data will be evaluated. The SMGBS model may apply not only to cracking data, but to any phenomena which depends on the critical shear or normal stress on the grain boundary. It may be considered, that if the mobility of dislocations in the grain boundary decreases the continuity in slip across the grain boundary, any normal and shear stresses acting on the grain boundary may cause movement of the dislocations through climb and glide, respectively, for properly aligned Burgers vectors. Only grain boundaries inclined parallel to the tensile axis would experience neither shear nor normal stress. The correlation between the slip continuity at the grain boundary, and the inclination of the grain boundary trace with respect to the tensile axis is sigmoidal. Furthermore, the plateau at low and high θ values shown in Figure 4.23 indicates that it is the normal, rather than the shear stress on the grain boundary that is limiting slip continuity. The propensity for slip continuity decreases at boundaries that are highly inclined to the tensile axis. Therefore, while slip *discontinuity* may become more likely *above* a CNS, the propensity for slip *continuity* is likely greater *below* a CNS. Therefore, the SMGBS model will be used to determine the probability of being below a CNS for a given trace inclination. By applying various CNS values, it can be seen that the model can be fit to the normalized data by applying a CNS value of 0.28 as shown in Figure 5.35. This indicates that a CNS of approximately 0.28 exists, above which the probability of slip continuity abruptly decreases.

The grain boundary character dependence of the slip continuity was established in Section 4.3, where it was shown that special boundaries are more likely to exhibit slip continuity than RHABs. Therefore, it is interesting analyze the individual slip continuity propensities of the RHABs and special boundaries as a function of θ. As shown in Figure 5.36(a), the probability of slip transmission at RHABs for inclinations of 0-30˚ is roughly 68% and drops to 23% at inclinations greater than 50˚. The probabilities of slip continuity at special boundaries are consistently greater, although the inflection point in the data still occurs around a critical grain boundary trace angle of approximately θ=30˚. At inclinations of 0-30˚, roughly 94% of the boundaries intersected by dislocation channels exhibit slip transmission, while this drops to roughly 63% at inclinations above 30˚ (with the exception of the data point at 65˚). The influence of grain boundary character on IG cracking as a function of trace inclination is shown in Figure 5.36(b). Although the probability of RHABs cracking is approximately an order of magnitude greater than that of special boundaries at 5% strain, the inflection points in the curves are located at approximately the same value of θ, as indicated with the dotted black line. These observations indicate that the structure of special boundaries promotes slip continuity and reduces cracking propensity.

The increased propensity for slip continuity at special boundaries is likely the result of the increased structural order at CSLBs which decreases the propensity for absorption, mobility, and dissociation of dislocations in the grain boundary [122]. When lattice dislocations enter grain boundaries, they may dissociate into smaller grain boundary dislocations to reduce their strain energy [197]. These dislocations are often stated to have Burgers vectors of the DSC lattice of the particular grain boundary [213].

As shown in Figure 5.37[214], the DSC lattice is the set of all displacement vectors by which a lattice can be translated while still preserving the CSL structure of the grain boundary. The red grid shown in Figure 5.37(b) is the DSC lattice for a Σ5 grain boundary. Indeed, Dingley and Pond observed linear structures in both CSLBs and RHABs and in some instances were able to confirm the presence of perfect dislocations in the grain boundary with Burgers vectors of the DSC lattice [147]. They suggested that the ability of the trapped lattice dislocations to dissociate into smaller grain boundary dislocations and the mobility of these resulting dislocations varies between grain boundaries of different structures. This is supported by the TEM analysis of Was et al. [119] on UHP Ni-16Cr-9Fe, where it was shown that the densities of the EGBDs generated through lattice dislocation interactions with grain boundaries were three times higher at CSLBs than RHABs. From these results, it was suggested that the reduced mobility of dislocations in the grain boundary would oppose the absorption of subsequent dislocations. This indicates that the stress concentration at CSLBs by impinging dislocations would be greater than that at RHABs where the dislocations are not as highly localized in the boundary.

Lim and Raj [197] also pointed out that, as the Σ value of boundary decreases, or the coincidence between the adjacent lattices increases, the magnitude of the primitive DSC vector increases [105] which increases the energy of the dissociated lattice dislocations in the boundary. In order for slip to be induced in the adjacent grain, the dissociated dislocations need to recombine in the boundary to form a crystal slip vector, and the energy required for this to occur is expected to be greater at RHABs where the dissociation products are smaller [197].

The continuity of slip across CSLBs in the current study supports the contention that the reduced absorption, dissociation, and mobilities of dislocations at such boundaries is responsible for the propensity for slip continuity. The current results are similar to the behaviors of screw dislocations at grain boundaries nickel bicrystals analyzed by Lim and Raj [197]. Lim and Raj observed that the degree of slip continuity of screw dislocations, as quantified by the percentage of slip traces that were continuous across a single grain boundary, decreased with increasing Σ value. Their measurements of slip continuity are compared to those of the current study in Figure 5.38. Although the methods used to quantify the slip continuity at the grain boundaries are not the same, this comparison indicates the similar finding that the propensity for slip continuity is greater at special boundaries. It should be considered, however, that Lim and Raj found a consistently low degree of slip continuity regardless of the Σ value of the boundary when the dislocations had an edge component [197].

It is recognized that not all special boundaries, as characterized solely by their misorientation, exhibit the same degree of resistance to intergranular degradation. The degree of resistance likely depends on the true degree of alignment between the interfaces of the lattice planes at the grain boundary. This grain boundary geometry is not fully characterized by the misorientation which only accounts for 3 of the 5 degrees of freedom described in Figure 3.10. The susceptibility of boundaries to intergranular degradation has been found to be dependent on the Σ value of the boundary [108, 111], the angular deviation from exact coincidence [106], and the orientation of the grain boundary plane [215]. As a result, the definition of a "special boundary" has been the subject of much debate. It has been observed for example, that under certain conditions, Σ9 and Σ27

boundaries can be as prone to cracking as other non-Σ3 boundaries [111], that the often applied Brandon criterion for misorientation tolerance is too lenient [106], and that the boundary should only be classified as special if at least one low-index plane exists along the grain boundary plane [215]. In this study, the overall propensity for slip continuity and crack resistance at special boundaries is greater than that at RHABs. The boundaries that are found to be susceptible to slip discontinuity and cracking, however, exhibit the same normal stress dependence (same inflection point) as RHABs as shown in Figure 5.36. This behavior is analogous to the propensity for grain boundary deformation at special boundaries witnessed by Alexandreanu [142]. It was found that the total deformed fraction of the CSLBs was significantly lower than that of the RHABs, but when deformation was observed at the CSLBs, it was nearly equal in magnitude to that observed at the RHABs. Therefore, there is likely a fraction of the boundaries included in the "special" category are not non-special in terms of their resistance to intergranular degradation. The normal stress dependence of the slip continuity and intergranular cracking observed at special boundaries is likely a result of the contribution of this non-special fraction.

The observation that the normalized slip continuity data agrees with the SMGBS model with an imposed critical minimum normalized normal stress of 0.28 at 5% strain indicates that slip continuity is controlled by a different critical stress than that required for NS crack formation, which was observed to be approximately 0.67 for NS cracks at 5% strain in SCW. Therefore, a higher critical minimum normal stress is required for NS crack formation than is required for slip discontinuity at 5% strain. It is possible, however, that the boundaries with the highest normalized normal stress crack first, but

that the slip continuity at the grain boundary ultimately influences whether or not the grain boundary will crack at higher levels of strain.

In summary, the slip continuity behavior at grain boundaries is influenced by both the normal stress acting on the grain boundary and the structure of the grain boundary. Grain boundaries oriented nearly parallel to the tensile axis were observed to experience higher degrees of slip continuity than more highly inclined grain boundaries which may be the result of limited grain boundary dislocation mobility. Such boundaries experience low shear and normal stresses which are required for grain boundary dislocations to move via glide and climb. The reduced absorption, mobility, and dissociation of dislocations at CSLBs is likely responsible for their high propensities for slip continuity. When high stresses build up at the sites of dislocation impingement at the grain boundary and are not easily relieved through prompt absorption and subsequent dissociation of the dislocations, the dislocations will not mobilize. This suggests that the localization of stress at CSLBs is greater than at RHABs which is likely responsible for their higher degree of slip continuity.

5.6 Grain Boundary Engineering

The objectives of the GBE study conducted on the unirradiated specimens strained in 500˚C SCW were to (1) determine if GBE reduced cracking propensity in SCW, and (2) determine if special boundaries are resistant to intergranular cracking in SCW. The data from the irradiated specimens strained to 10% in 400˚C SCW will also be included in a portion of this discussion, as the observed cracking propensities of special boundaries under these conditions contribute towards the second objective.

The influence of the thermomechanical processing treatment performed on the 316L specimens to achieve the GBE condition is illustrated in Figure 5.39. It can be seen that at both 15% and 25% strain, the fraction of grain boundaries cracked in the 316LGBE specimens is 13% and 44% of that observed on the 316L specimens, respectively. It was shown in Figure 4.40 that special boundaries are consistently less likely to crack than the RHABs. Therefore, the higher fraction of special boundaries in GBE material must contribute to the reduction in the total cracked grain boundary fraction.

Although it is widely accepted that grain boundaries with certain structures are resistant to various forms of intergranular degradation, a universal definition of the criteria required for a boundary to be considered "special" has not been established. In this study, the boundaries included in the "special" category include LABs, Σ3, Σ9, and Σ27 boundaries. While the resistance of the special boundary population as a whole has been confirmed, the cracking resistance of each boundary type has not. It is confirmed in Figure 5.40 that RHABs in 316L are consistently more likely to crack in SCW than LABs, Σ3, Σ9, and Σ27 boundaries regardless of whether the material is GBE or irradiated. The Σ3 boundaries in the unirradiated and irradiated 316L specimens are consistently more resistant to cracking than the LABs and Σ9 boundaries. This is likely to due, at least in part, to the contribution of the coherent twin boundaries to the total Σ3 boundary population. Under some experimental conditions, the coherent twin population is so resistant to intergranular cracking that it is regarded as immune to cracking and excluded from grain boundary measurements [142]. Their inclusion in the current study is based on the findings that some Σ3 boundaries were observed to crack (15 in irradiated

316L at 10% strain), and the uncertainty in differentiating coherent Σ3 twin boundaries from other Σ3 boundaries without knowledge of the grain boundary plane orientation. While LABs, Σ9, and Σ27 grain boundaries all have lower cracking propensities than RHABs, there is limited data to analyze the relative propensities of these special boundaries to crack intergranularly in SCW.

It can be seen from Figure 5.40 that the Σ9 grain boundaries in the irradiated 316L specimens appear more susceptible to IG cracking than the Σ27 boundaries. It has been shown that the effective energies of special twist grain boundaries increase monotonically for increasing Σ value [216], and therefore this observation was unexpected. Not all grain boundaries with the same Σ value, however, have the same energy which is also a strong function of the grain boundary plane orientation [217]. Thus, the apparently greater cracking susceptibility of the Σ9 grain boundaries in the irradiated 316L specimen is not necessarily incorrect and may be a result of the unknown grain boundary plane orientation. The increasing cracking propensity with increasing Σ value observed for the 316LGBE specimen, however, was more consistent with the anticipated results.

Although special boundaries are less likely to crack in SCW than are RHABs, the relative susceptibilities of the RHABs and special boundaries to intergranular cracking as a function of strain are not necessarily constant. As shown in Figure 5.41, the fraction of cracks at special boundaries appears to increase with strain. The results of this study, therefore, are consistent with the findings of others [108, 116, 143] which suggest that, as damage accumulates under strain, even boundaries that are resistant to intergranular cracking can ultimately fail.

It should also be considered that the GBE treatment increased the grain size of the material in addition to the special boundary population. This is likely responsible for the decrease in the yield strength of the GBE alloy and the change in work hardening behavior as shown in the stress-strain curves in Appendix A. While the influence of such parameters on the cracking propensity of the alloy could not be quantified in the current study, the comparison of the fraction of grain boundaries cracked rather than simply the crack density does account for the fact that larger grained materials have fewer potential sites per unit area for intergranular crack initiation.

In summary, the findings of this study indicate that (1) GBE treatments may be applied to 316L to decrease the total fraction of grain boundaries cracked in 500˚C SCW, (2) LABs, Σ3, Σ9, and Σ27 boundaries in 316L are all less likely to crack in 400˚C and 500˚C SCW than RHABs and may therefore be regarded as "special" and (3) the cracking resistance of special boundaries decreases with strain. The reasons for their resistance to intergranular cracking may be due, at least in part, to the increased propensity for slip continuity across such boundaries as discussed in earlier sections.

Table 5.1 The greatest Schmid factors for each of the four {111} planes in the grains that underwent apparent slip on one and three slip planes as shown in Figure 5.8 and Figure 5.9, respectively.

Grain	(111)	(1-11)	(11-1)	(-111)
1 slip plane, Figure 5.8(a)	0.26	0.48	0.34	0.5
1 slip plane, Figure 5.8(b)	0.44	0.08	0.15	0.47
1 slip plane, Figure 5.8(c)	0.46	0.28	0.34	0.02
3 slip planes, Figure 5.9(a)	0.45	0.35	0.42	0.46
3 slip planes, Figure 5.9(b)	0.31	0.44	0.44	0.46
3 slip planes, Figure 5.9(c)	0.42	0.19	0.41	0.48

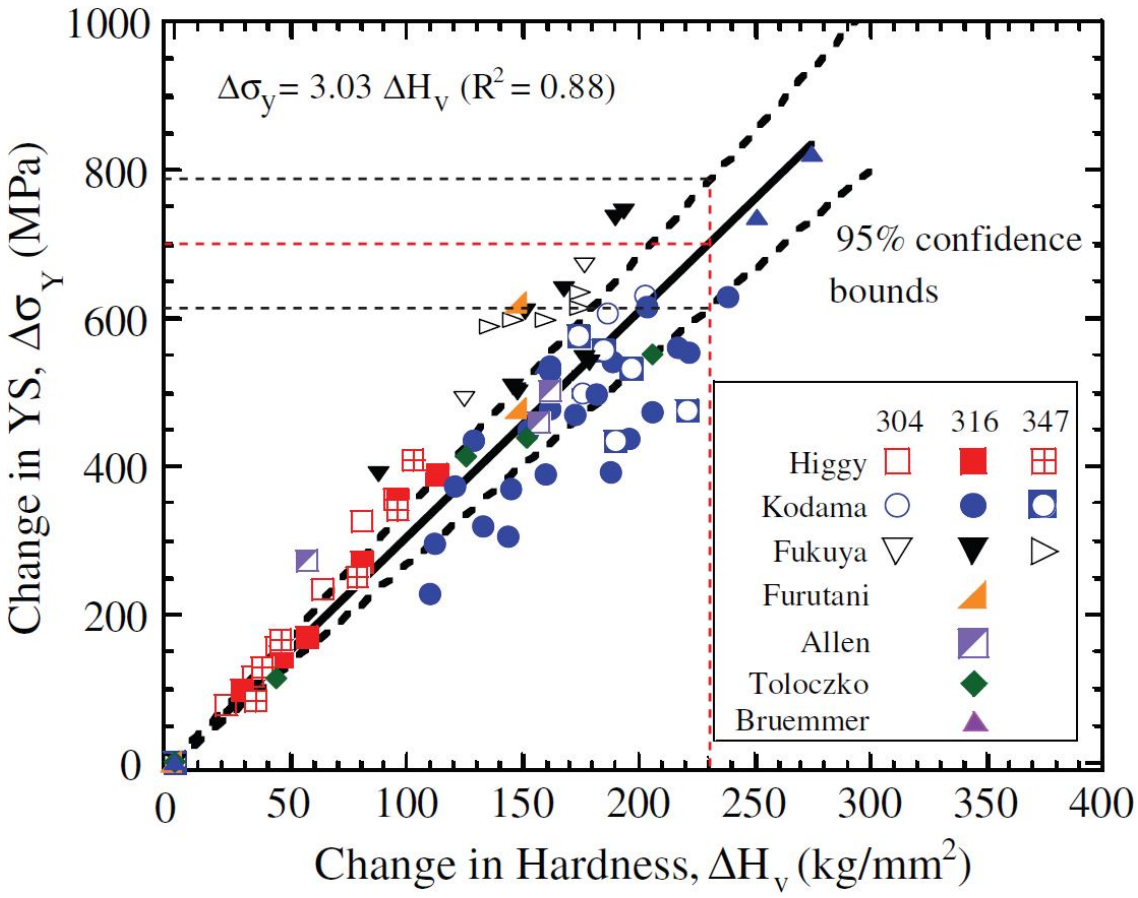

Figure 5.1 Correlation between irradiation induced hardening and change in yield strength of austenitic stainless steels. The vertical dotted red line indicates the irradiation induced hardening in the current study [182].

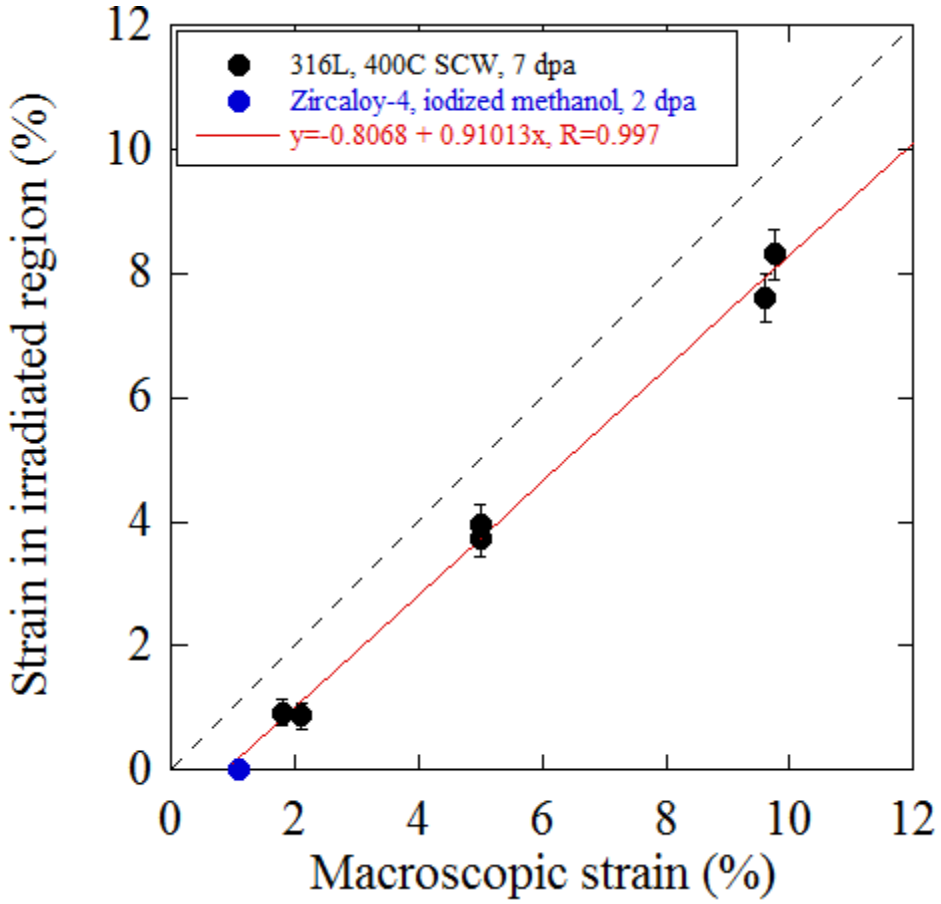

Figure 5.2 Plastic strain in irradiated region of 316L specimens versus macroscopic tensile strain. Zircaloy-4 data is taken from Fournier et al. [187].

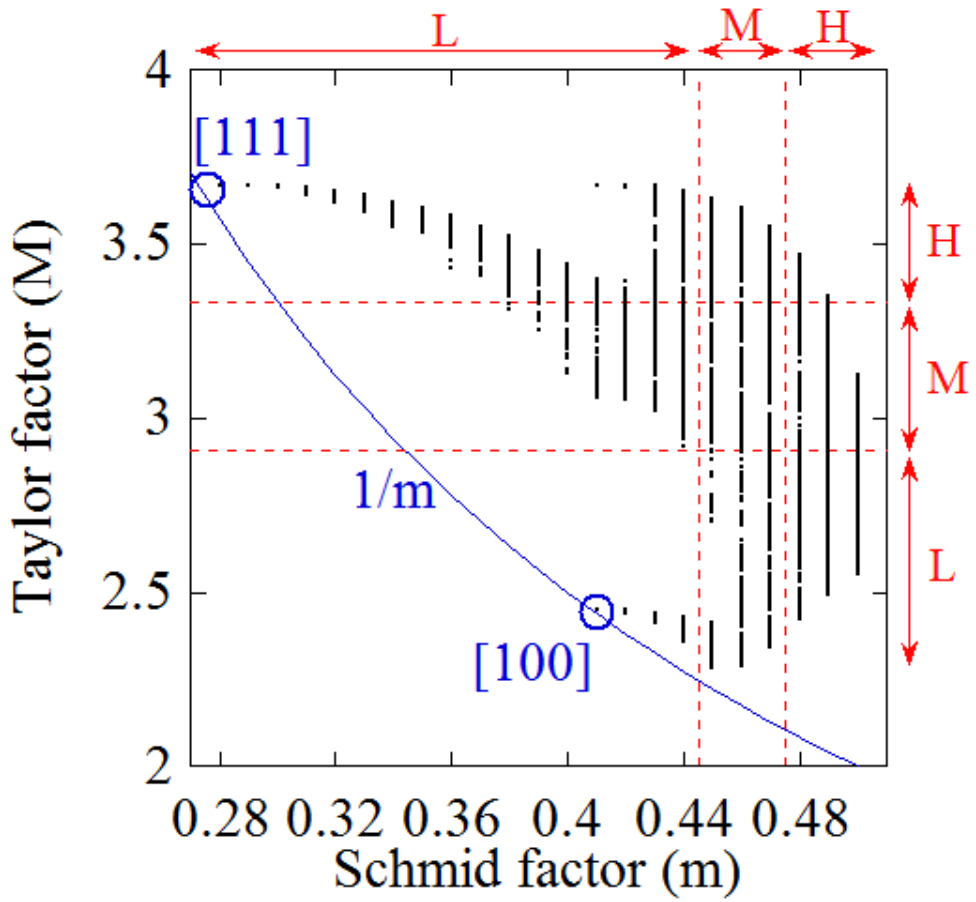

		Taylor factor		
		Low	Medium	High
Schmid factor	Low	0.06	0.35	0.60
	Medium	0.33	0.31	0.35
	High	0.57	0.34	0.08

Figure 5.3 Correlation between Taylor factor and Schmid factor. The limits that bound one-third of the grain population for the low (L), medium (M), and high (H) Schmid and Taylor factor categories are indicated with the dotted red lines. The resulting probability that the grain is binned into a certain m category given that it falls into a given M category is indicated in the table at the right.

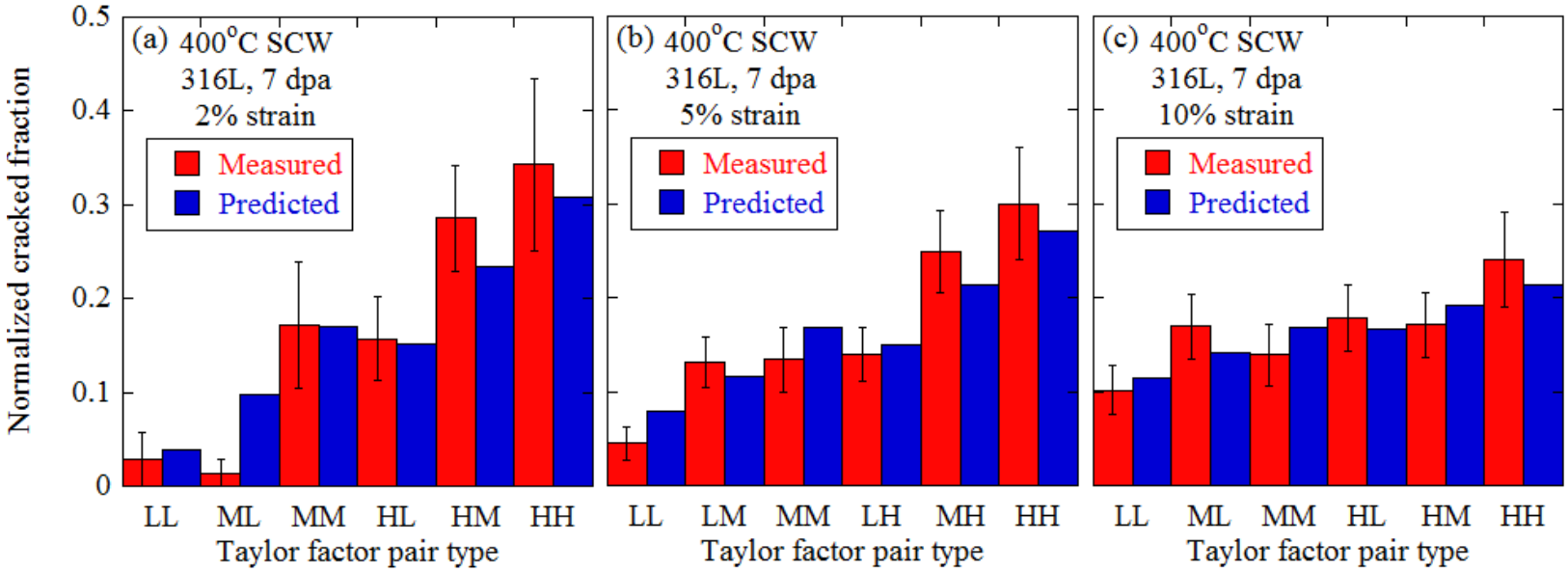

Figure 5.4 Measured Taylor factor pair type distributions at cracked grain boundaries following straining in 400˚C SCW compared to the Taylor factor pair type distributions predicted from the measured Schmid factor pair type distributions at (a) 2%, (b) 5%, and (c) 10% strain.

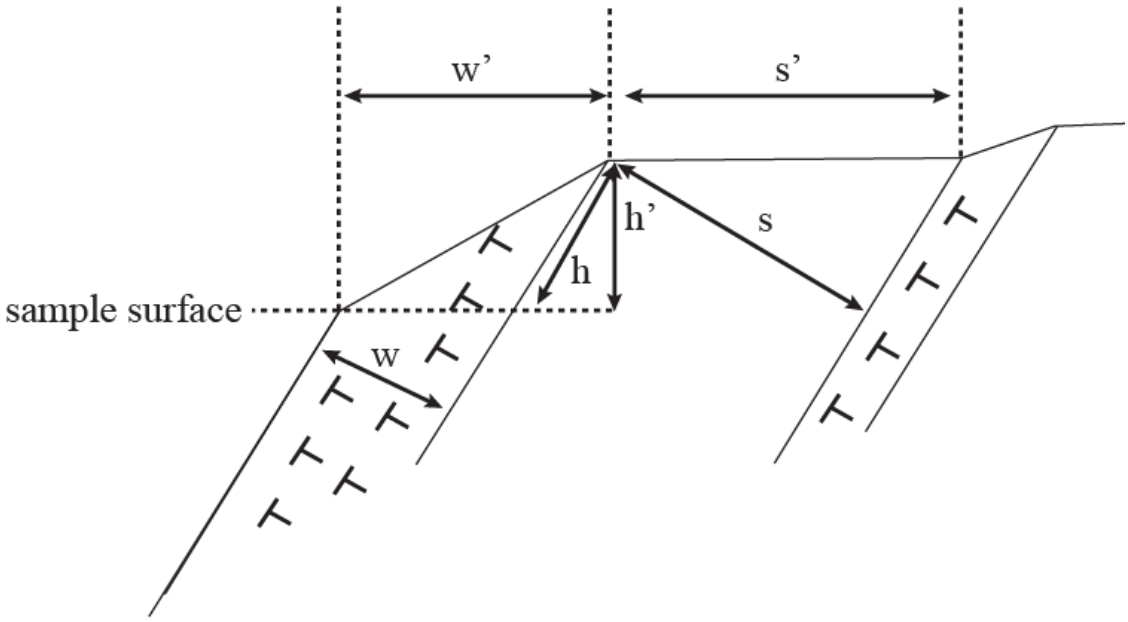

h = true step height
h' = apparent step height

s = true dislocation channel spacing
s' = apparent dislocation channel spacing

w = true dislocation channel width
w' = apparent dislocation channel width

Figure 5.5 Distinction between the true and apparent height, spacing, and width of steps created when dislocation channels intersect a free surface. (reproduced from [92])

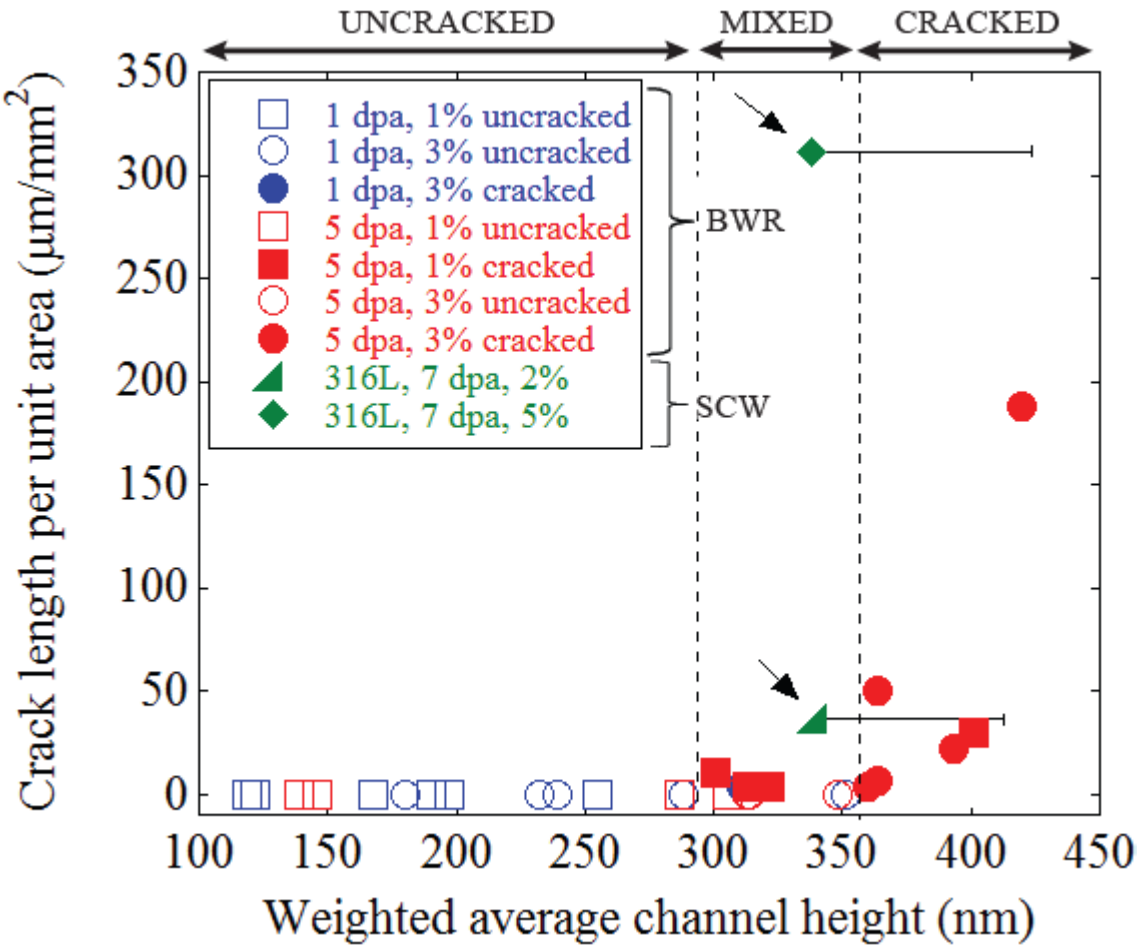

Figure 5.6 Crack length per unit area on gage surface of irradiated tensile specimen as a function of the weighted average channel height measured via AFM. The data from the simulated BWR environment was borrowed from [150], and the green SCW data indicated with arrows are from the current study. The error bars indicate the maximum amount of metal that may have been removed as a result of oxidation and oxide stripping.

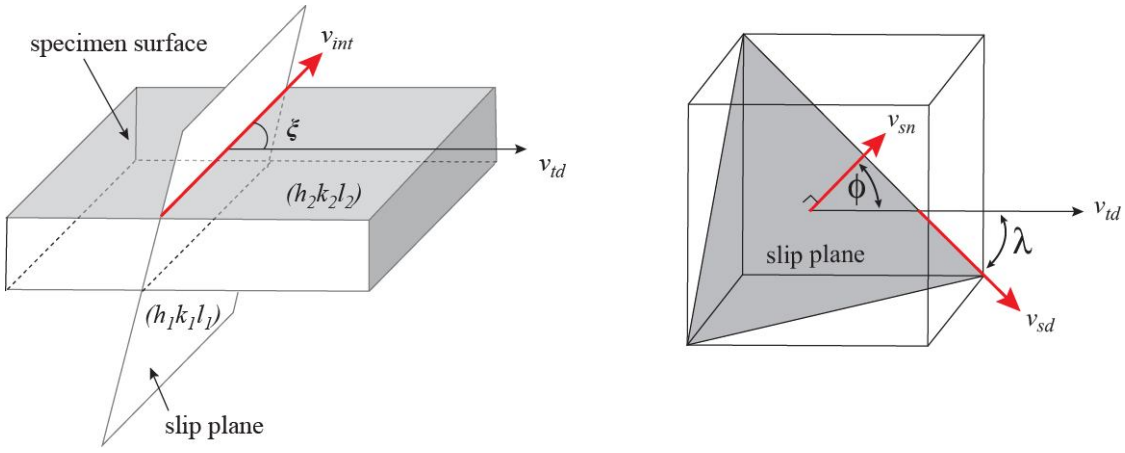

(a) (b)

Figure 5.7 Illustration of variables for determining (a) the inclination of surface trace of slip plane to tensile direction, and (b) the Schmid factor of the slip system.

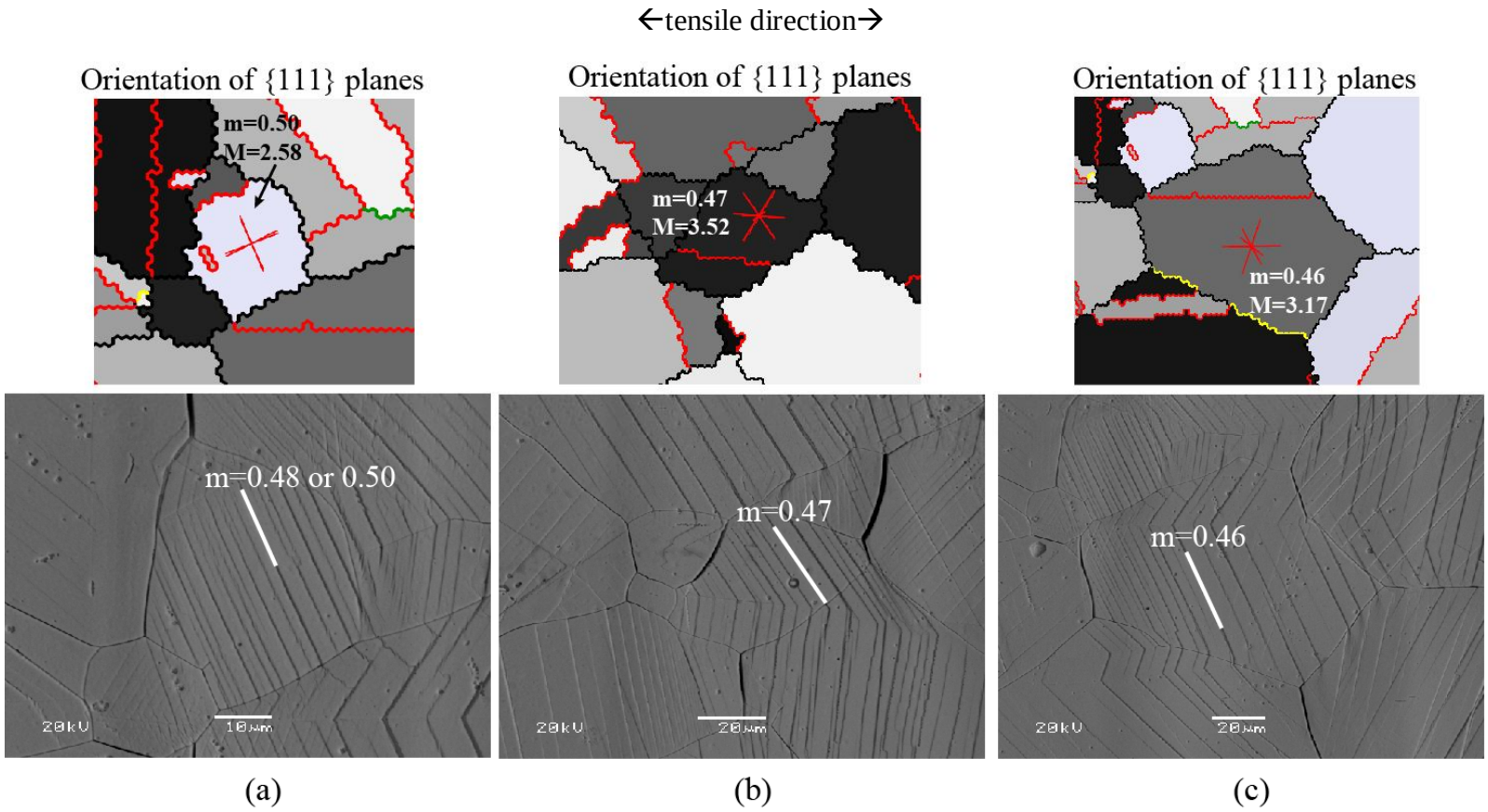

Figure 5.8 Grains with activation of a single slip plane in proton irradiated 316L strained to 5% in 400˚C SCW. The Schmid factor of the slip system expected to experience the greatest resolved shear stress for the activated slip plane is indicated. The Schmid and Taylor factors of the grains are given, and the surface traces of the four {111} planes are shown with the red lines.

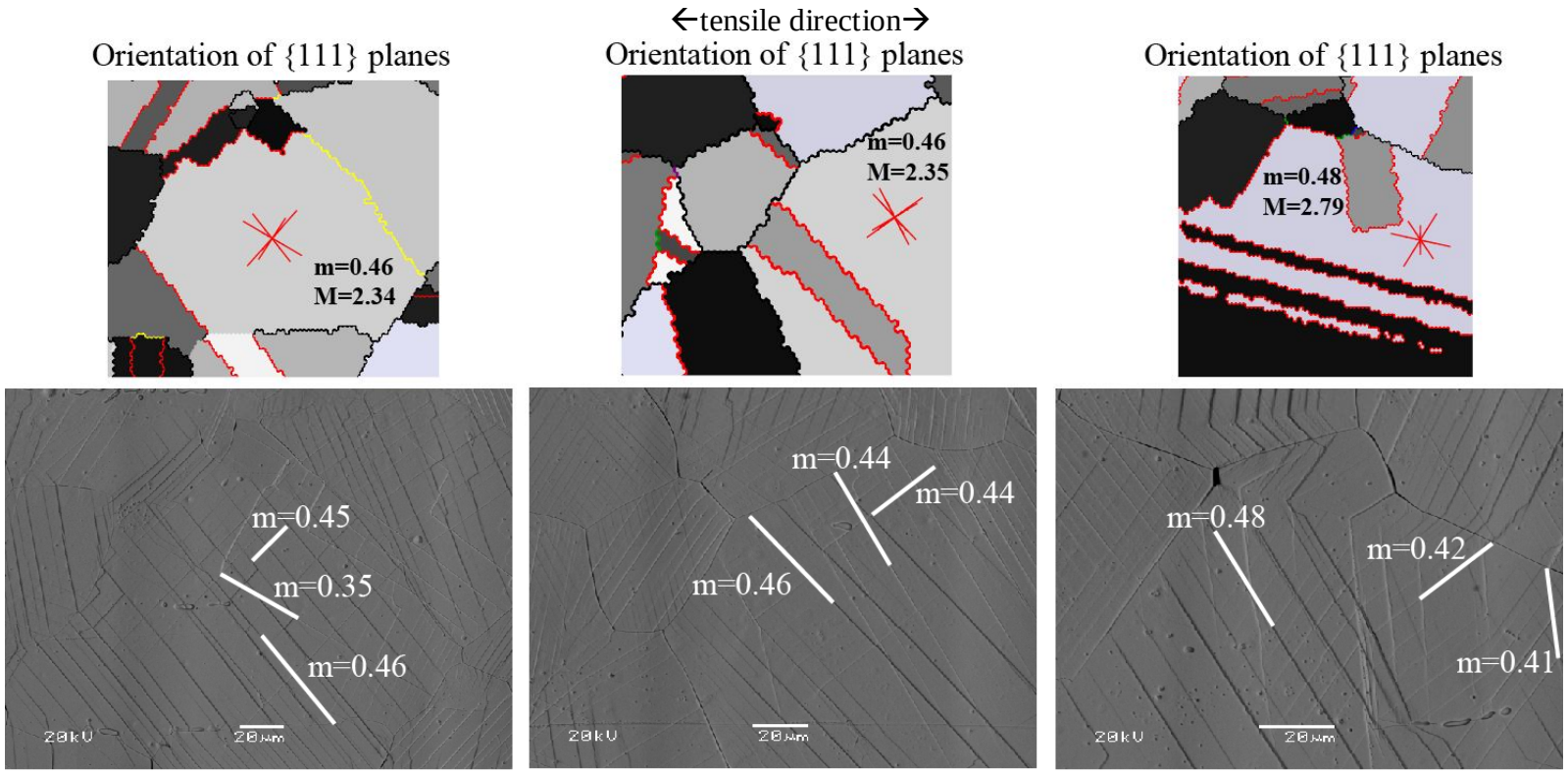

Figure 5.9 Grains with apparent activation of three slip planes in proton irradiated 316L strained to 5% in 400˚C SCW. The Schmid factors of the slip systems expected to experience the greatest resolved shear stresses for the activated slip planes are indicated. The Schmid and Taylor factors of the grains are also given, and the surface traces of the four {111} planes are shown with red lines.

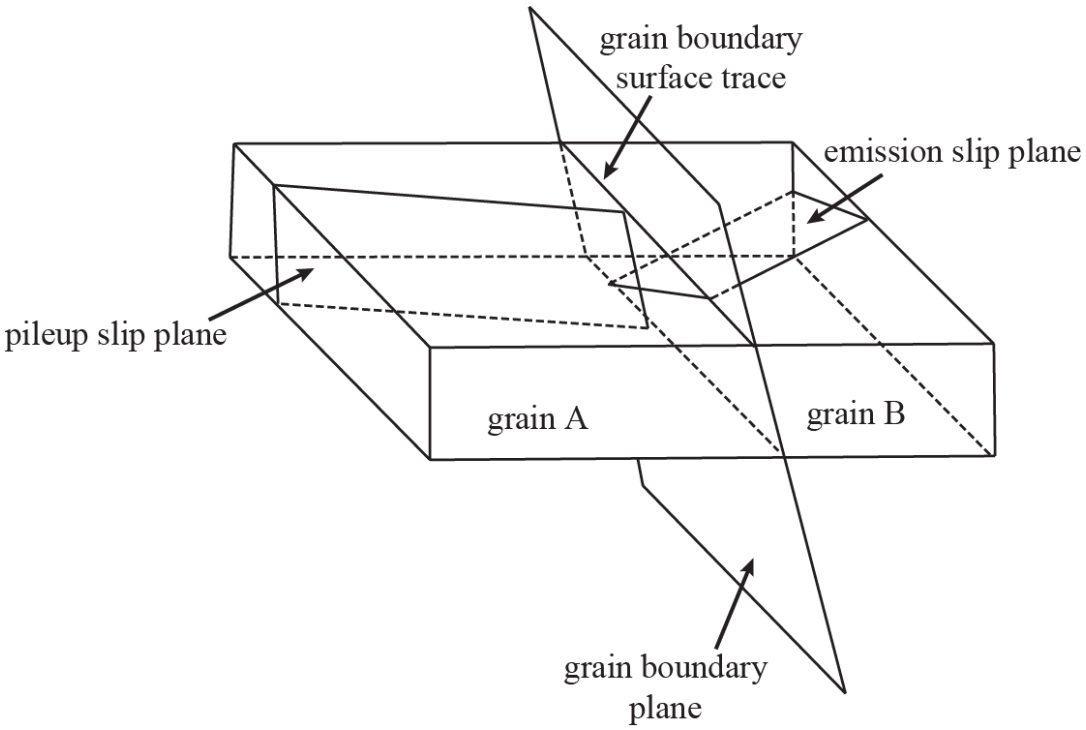

Figure 5.10 Intersection of slip planes with a grain boundary plane (reproduced from [203]).

←tensile direction→

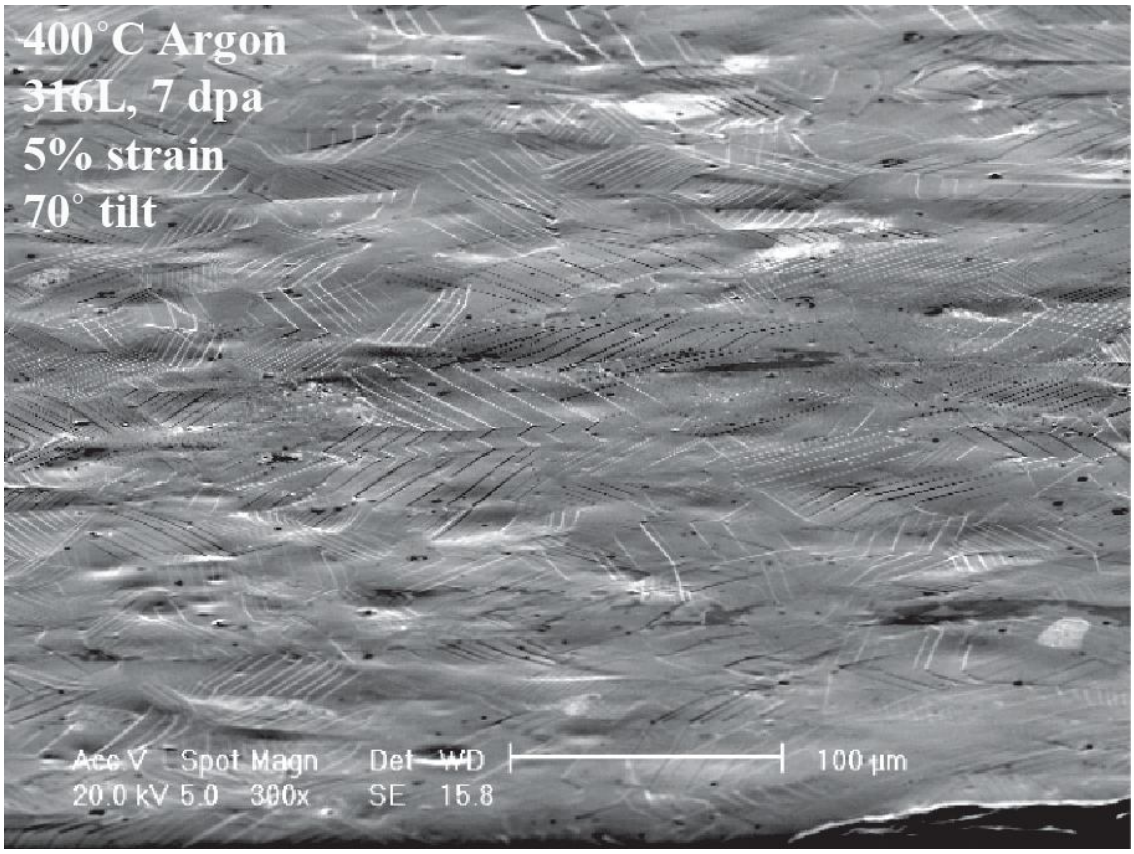

Figure 5.11 Faceted surface appearance of 7 dpa proton irradiated 316L specimen strained to 5% in 400˚C argon environment. The specimen was tilted to 70˚ to view facets.

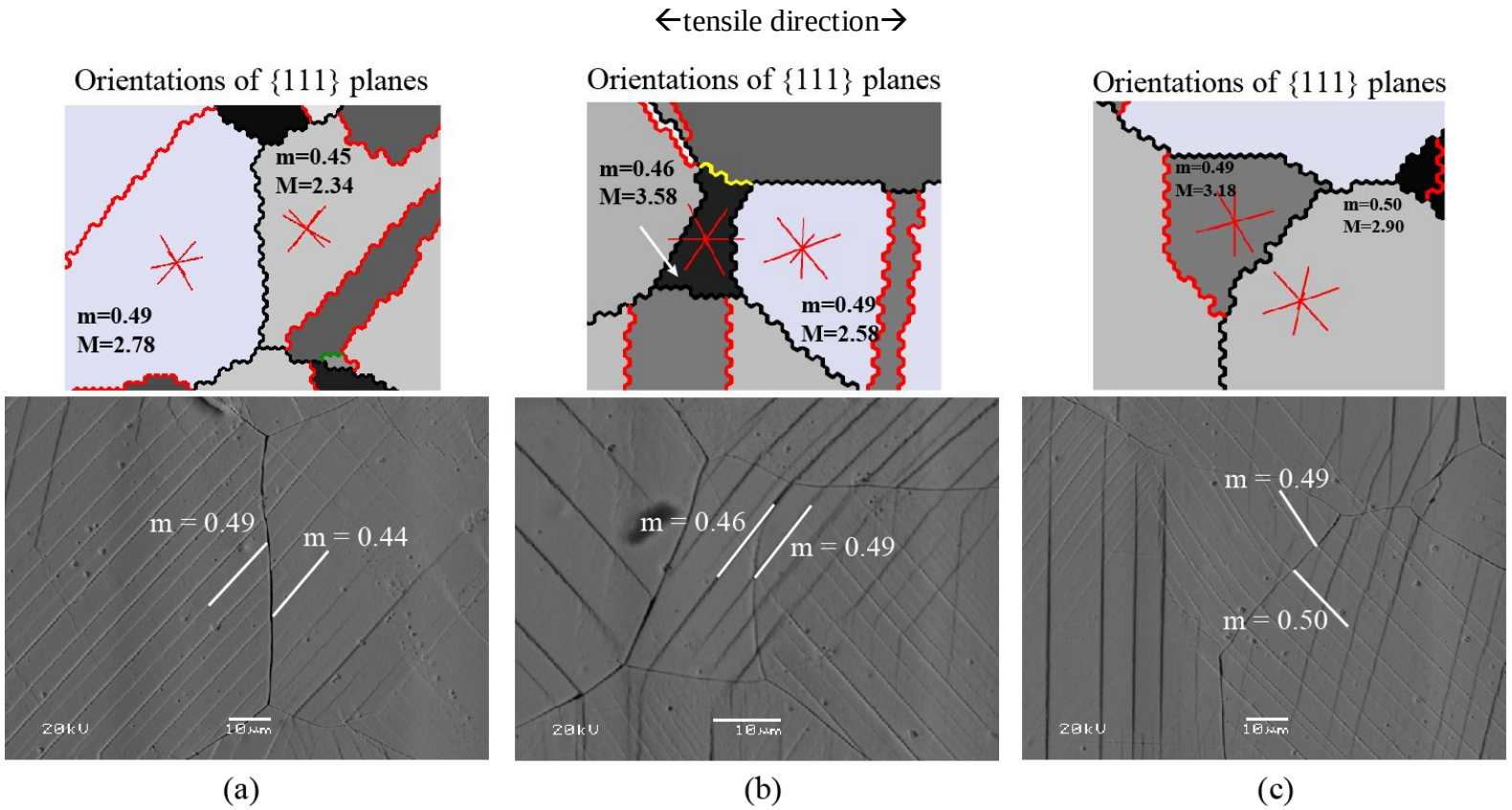

Figure 5.12 Slip continuity at grain boundaries of proton irradiated 316L strained to 5% in 400˚C SCW. The Schmid factors of the slip systems expected to experience the greatest resolved shear stresses for the activated slip planes are indicated. The Schmid and Taylor factors of the grains are given, and the surface traces of the four {111} planes are shown with red lines.

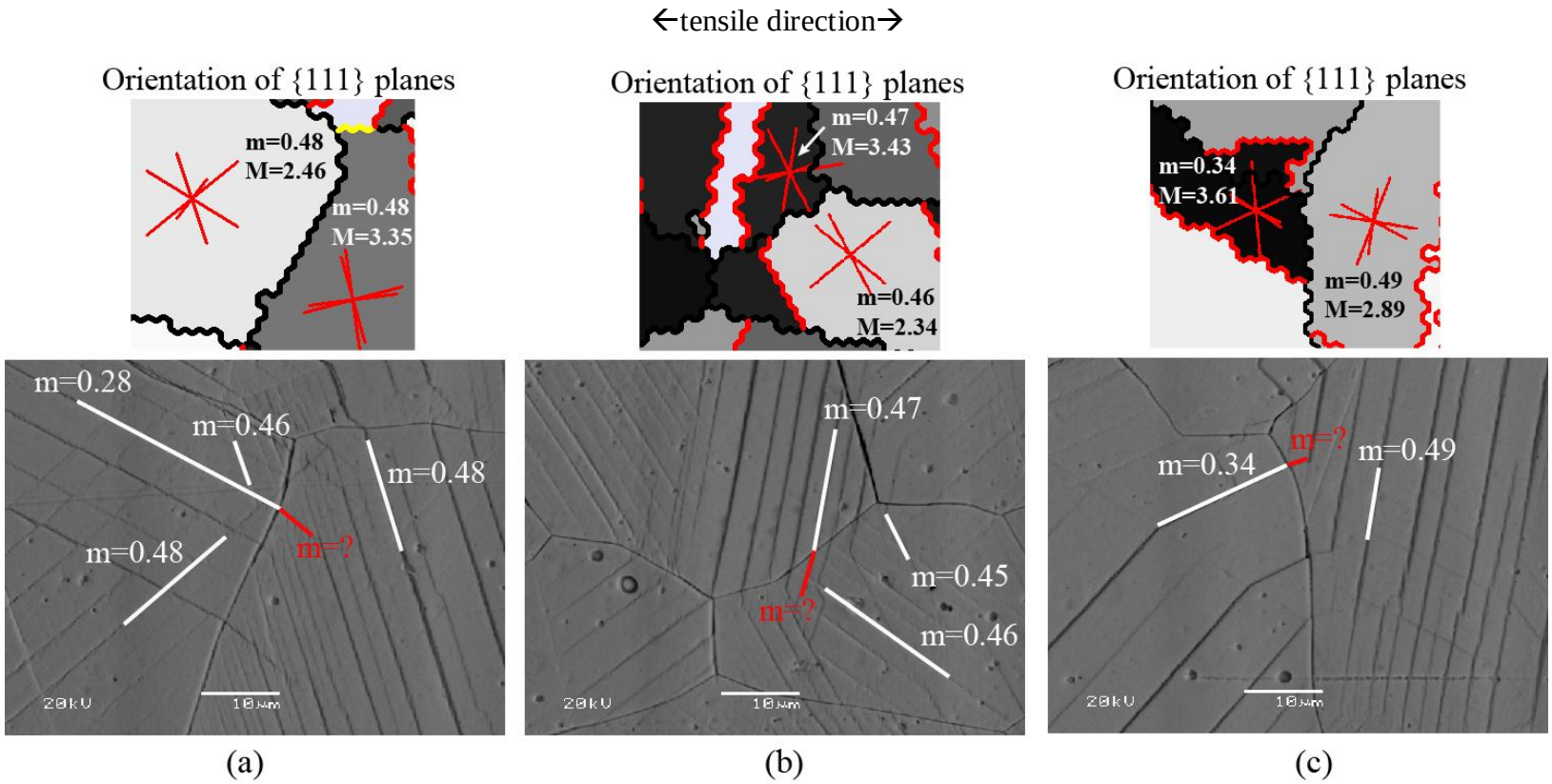

Figure 5.13 Difficult slip continuity at grain boundaries of proton irradiated 316L strained to 5% in 400˚C SCW. The Schmid factors of the slip systems expected to experience the greatest resolved shear stresses for the activated slip planes are indicated. The Schmid and Taylor factors of the grains are given, and the surface traces of the four {111} planes are shown with the red lines.

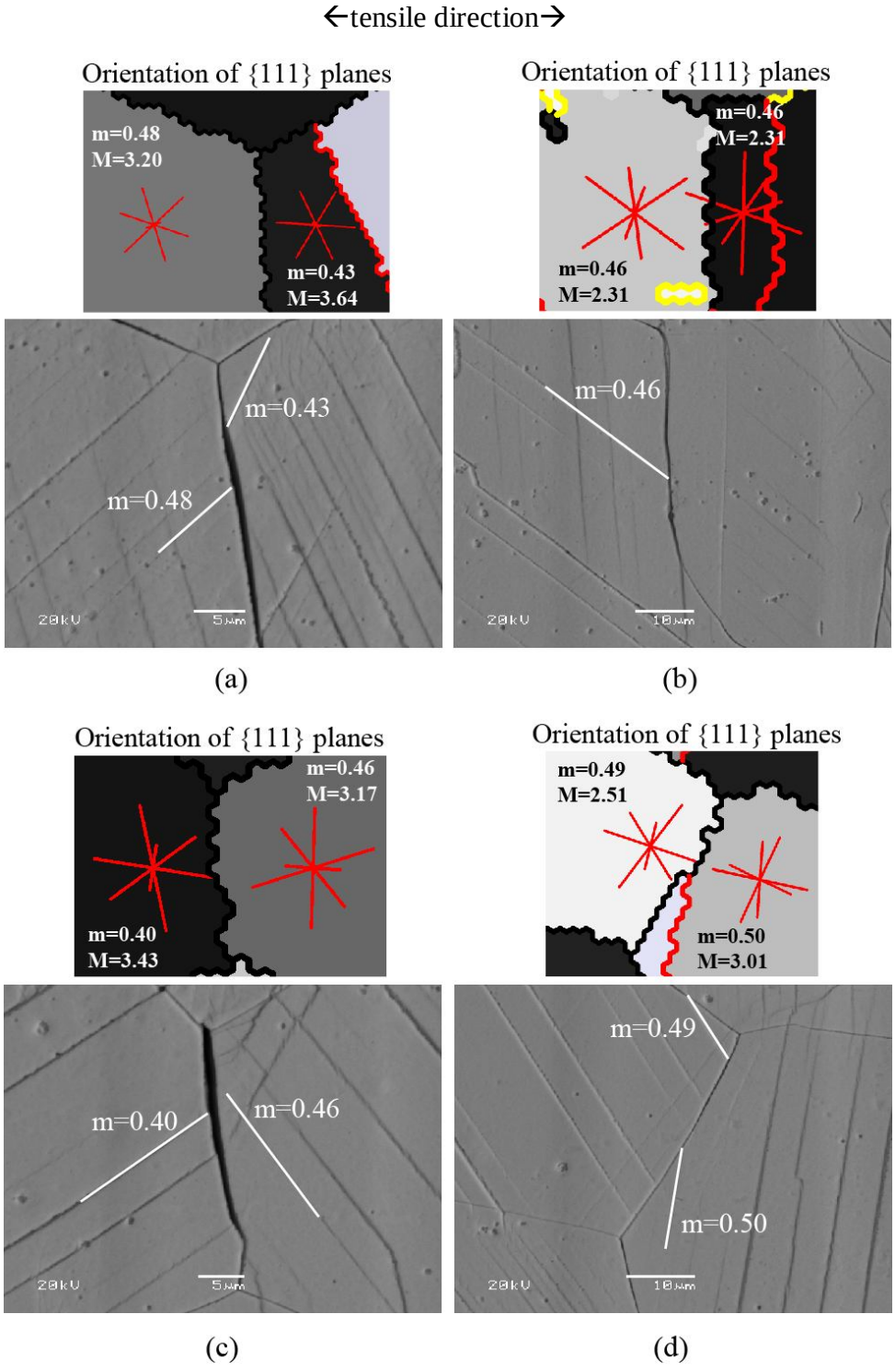

Figure 5.14 Slip discontinuity at grain boundaries of proton irradiated 316L strained to 5% in 400˚C SCW. The Schmid factors of the slip system expected to experience the greatest resolved shear stresses for the activated slip plane are indicated. The Schmid and Taylor factors of the grains are given, and the surface traces of the four {111} planes are shown with red lines.

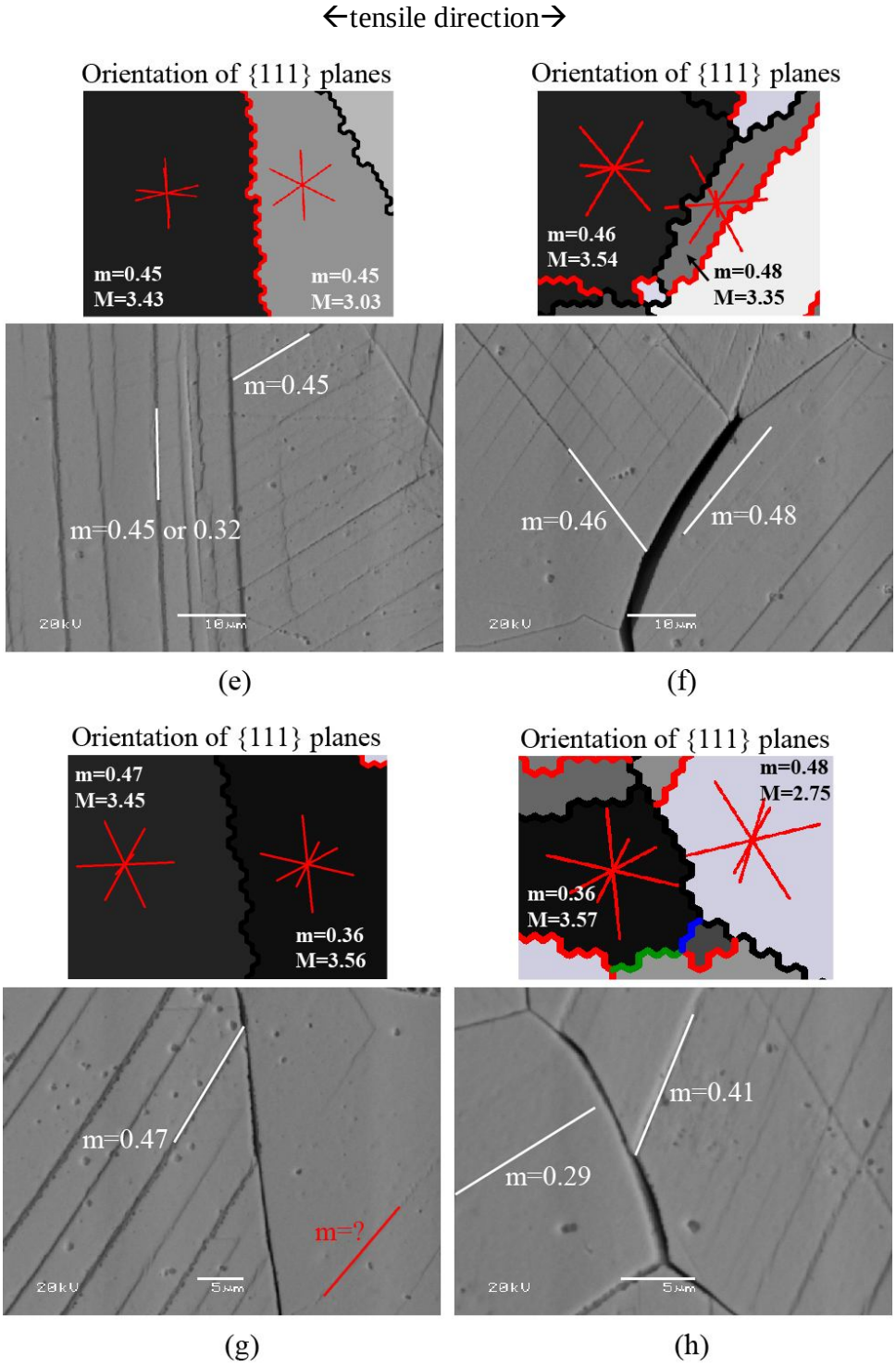

Figure 5.15 Slip discontinuity at grain boundaries of proton irradiated 316L strained to 5% in 400˚C SCW. The Schmid factors of the slip systems expected to experience the greatest resolved shear stresses for the activated slip plane are indicated. The Schmid and Taylor factors of the grains are given, and the surface traces of the four {111} planes are shown with the red lines.

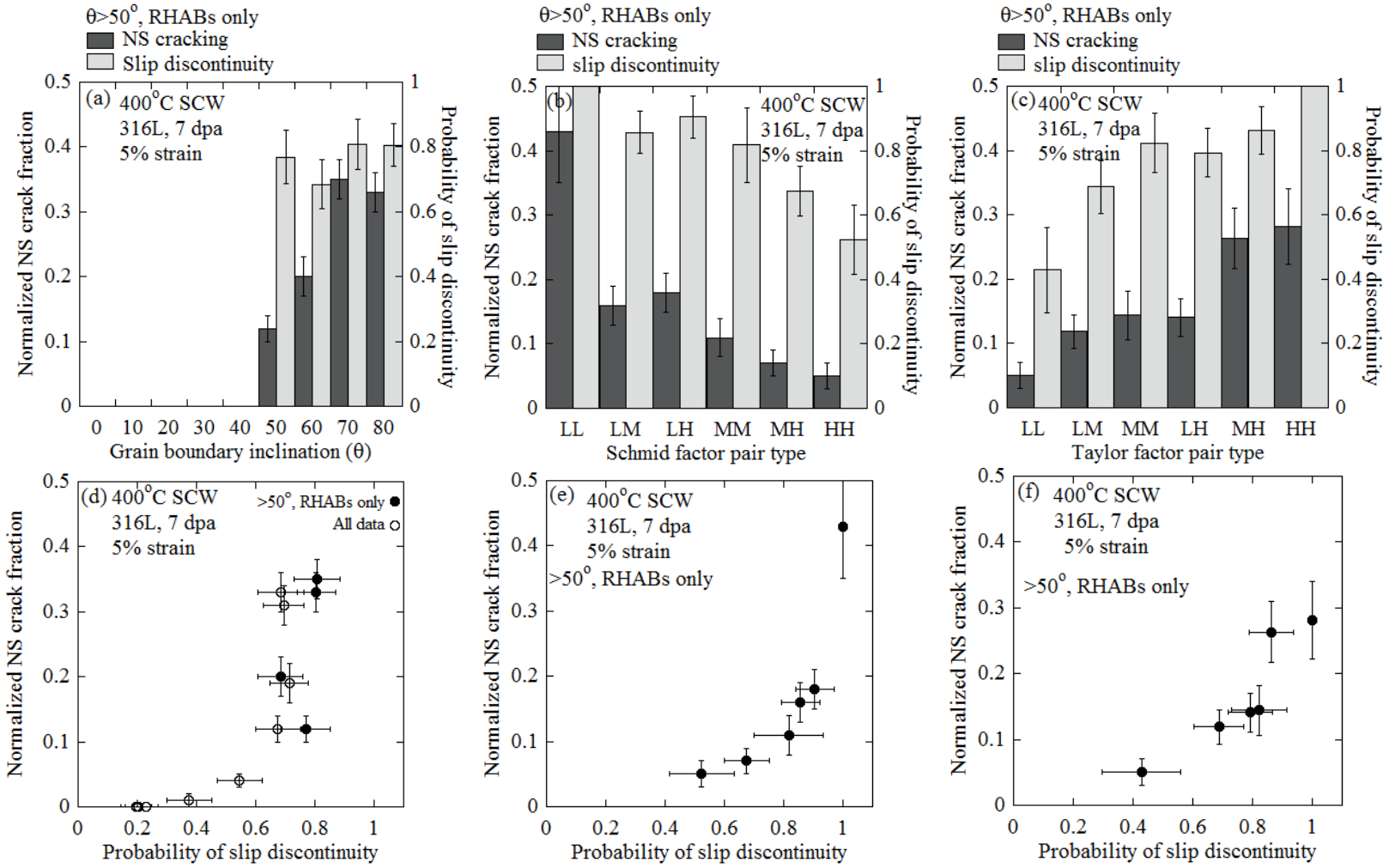

Figure 5.16 Plots of the co-dependence of NS cracking propensity and slip discontinuity on (a) trace inclination, (b) Schmid factor pair type and (c) Taylor factor pair type. The direct NS crack dependence on slip discontinuity is shown in (d)-(f). Each solid data point in (d) corresponds to a trace inclination bin given in (a), each data point in (e) corresponds to a Schmid factor pair type bin given in (b), and each data point in (f) corresponds to a Taylor factor pair type bin in (c).

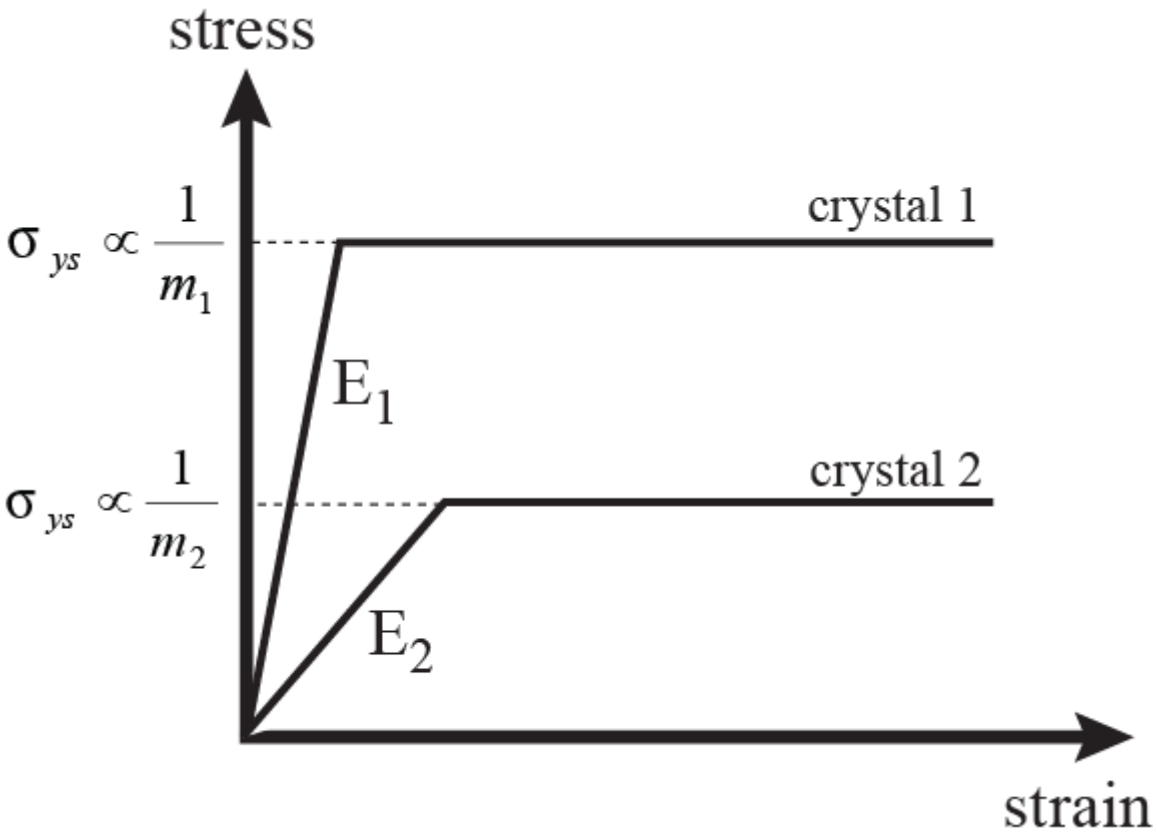

Figure 5.17 The individual stress-strain response of two single crystals with different orientations. (modified from [208])

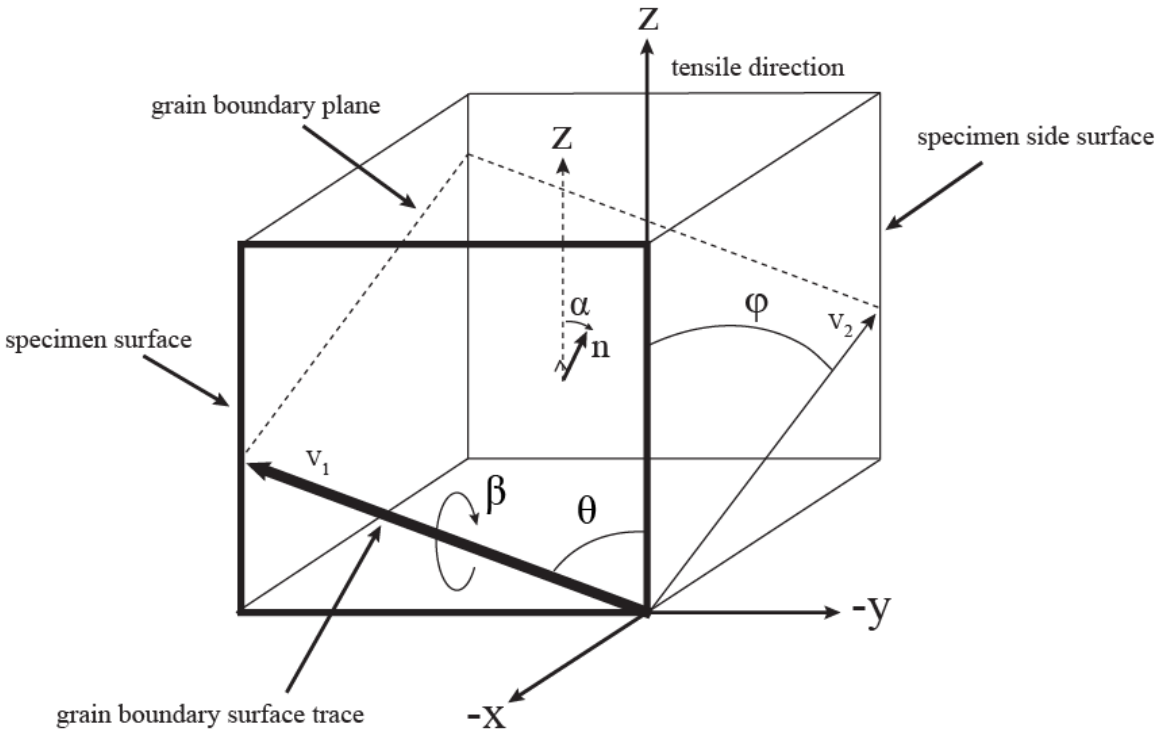

Figure 5.18 Illustration of grain boundary geometry, and definition of variables used in this study: n is the normal to the grain boundary plane, α is the angle between the normal to the grain boundary plane and the tensile direction, φ is the angle between the tensile direction and the trace of the grain boundary on the side surface of the specimen, θ is the trace inclination, and β is the angle of rotation about the grain boundary surface trace vector.

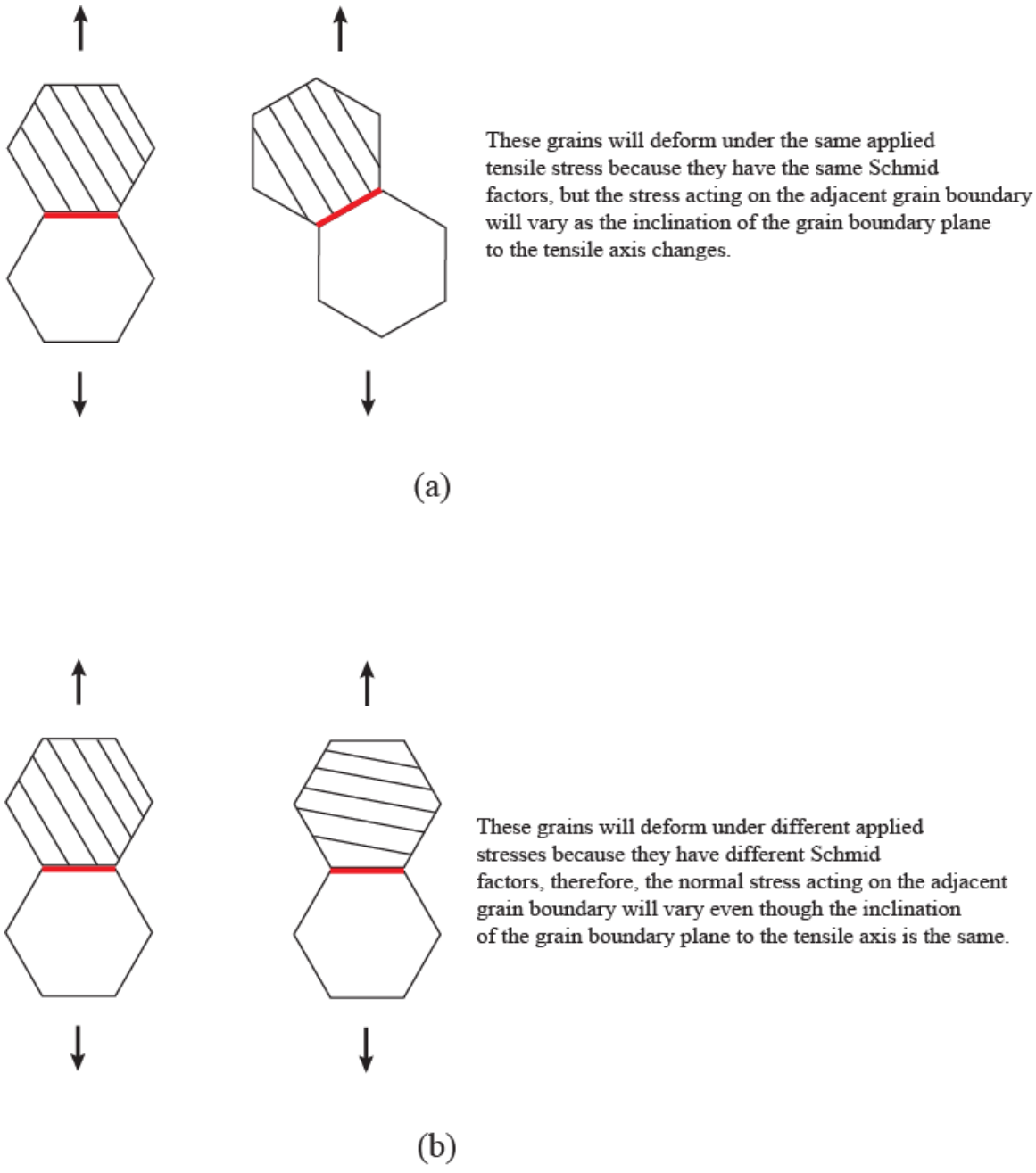

Figure 5.19 Illustration of influence of both Schmid factor and grain boundary inclination with respect to tensile axis on the stress acting on the grain boundary.

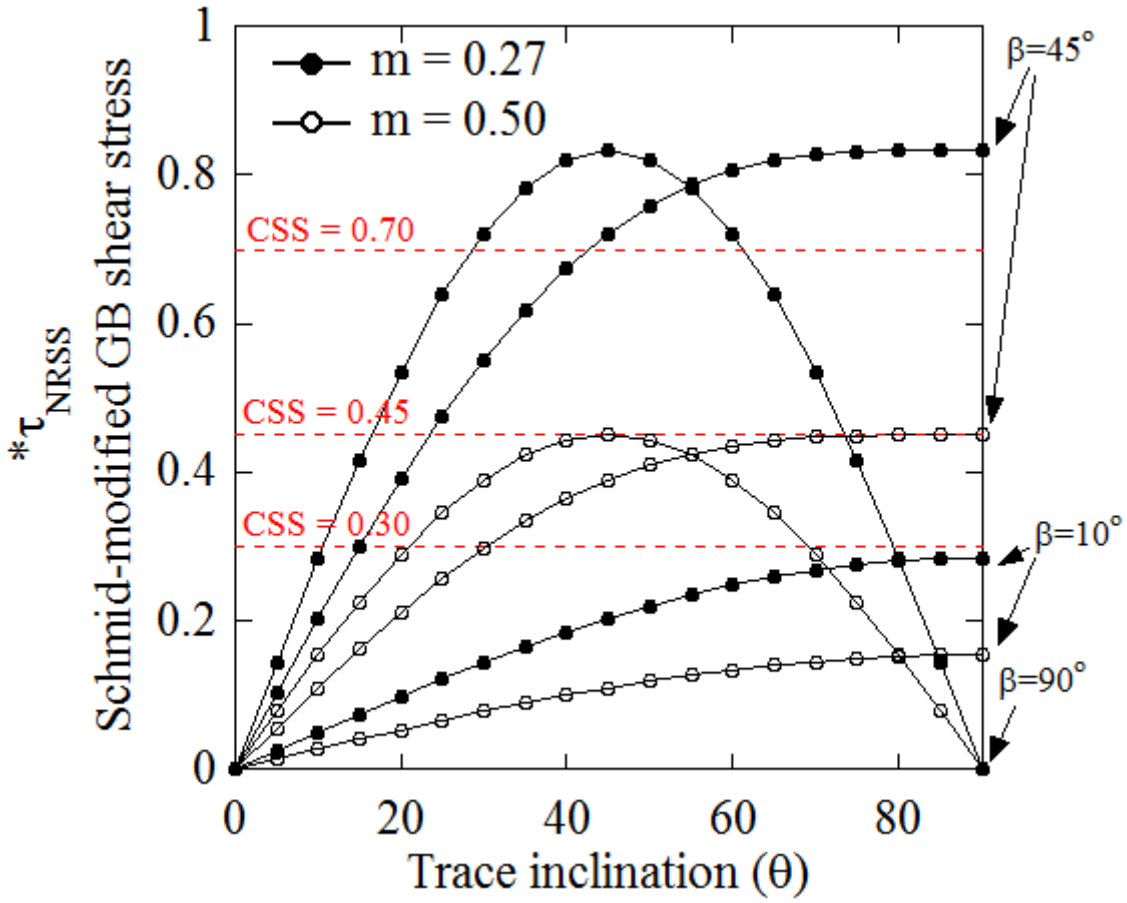

Figure 5.20 Normalized resolved shear stress as a function of trace inclination to the tensile axis, θ. Various critical shear stress (CSS) values are indicated with dotted red lines.

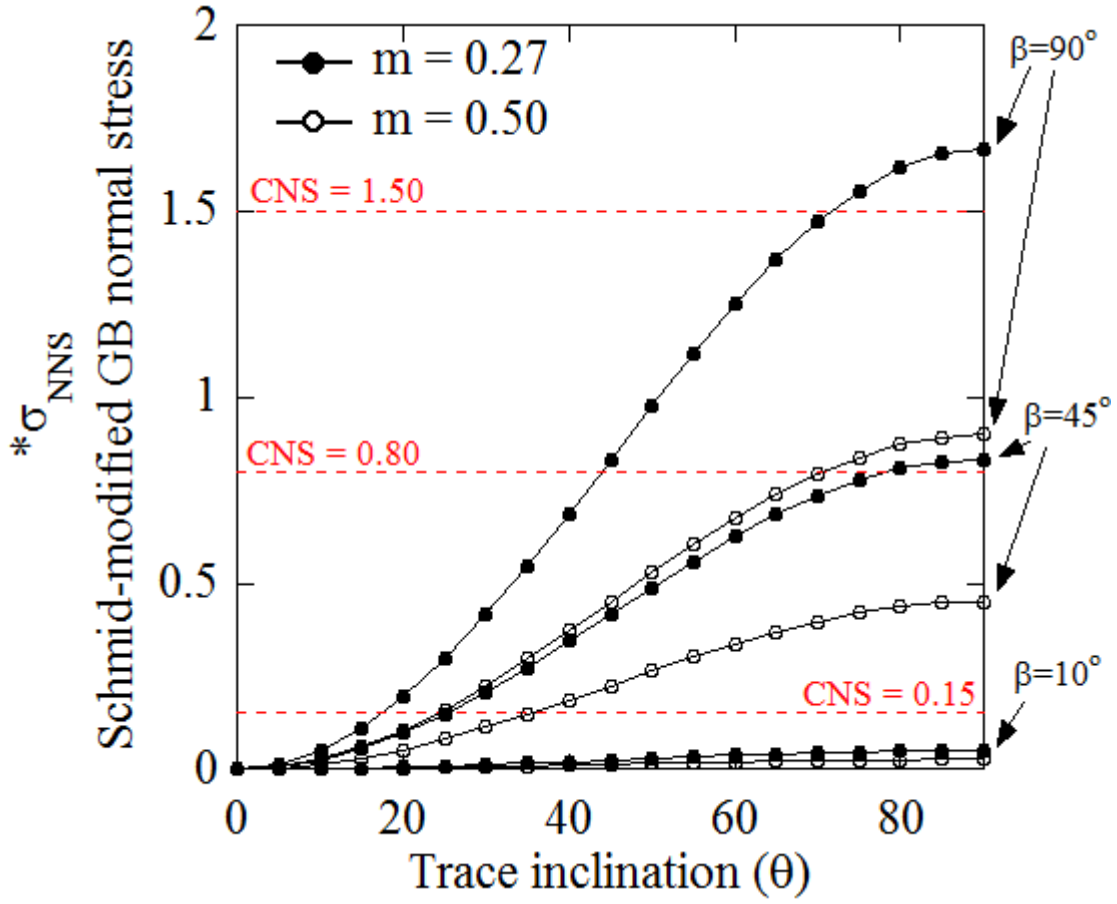

Figure 5.21 Normalized normal stress as a function of trace inclination to the tensile axis, θ. Various critical normal stress (CNS) values are indicated with dotted red lines.

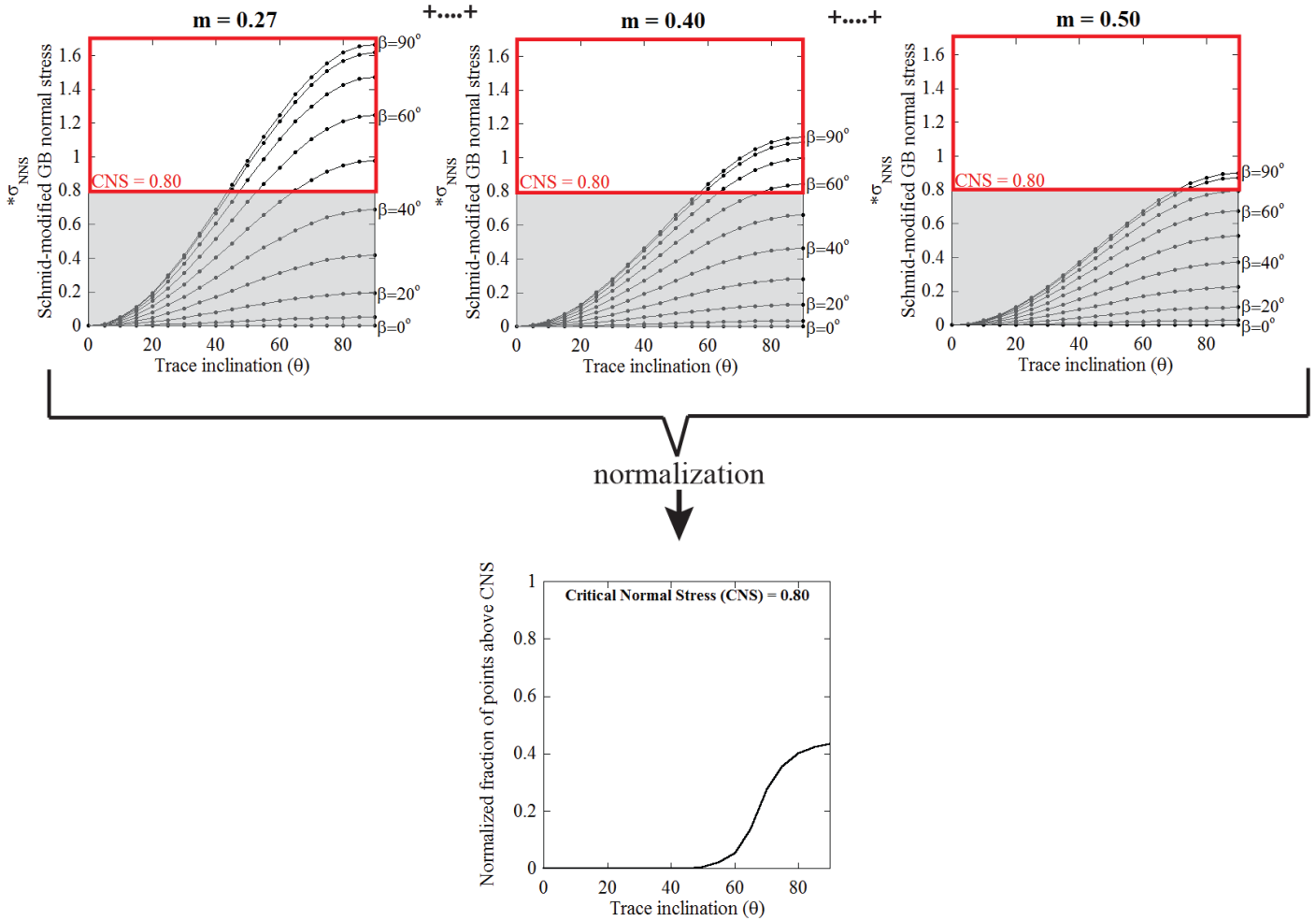

Figure 5.22 Illustration of the procedure used to generate the SMGBS model curves. The modeling points with $*\sigma_{NNS}(\theta,\beta,m) > CNS$ are weighted according to the m and β populations, summed, and then the distribution is normalized to generate the final SMGBS model curve.

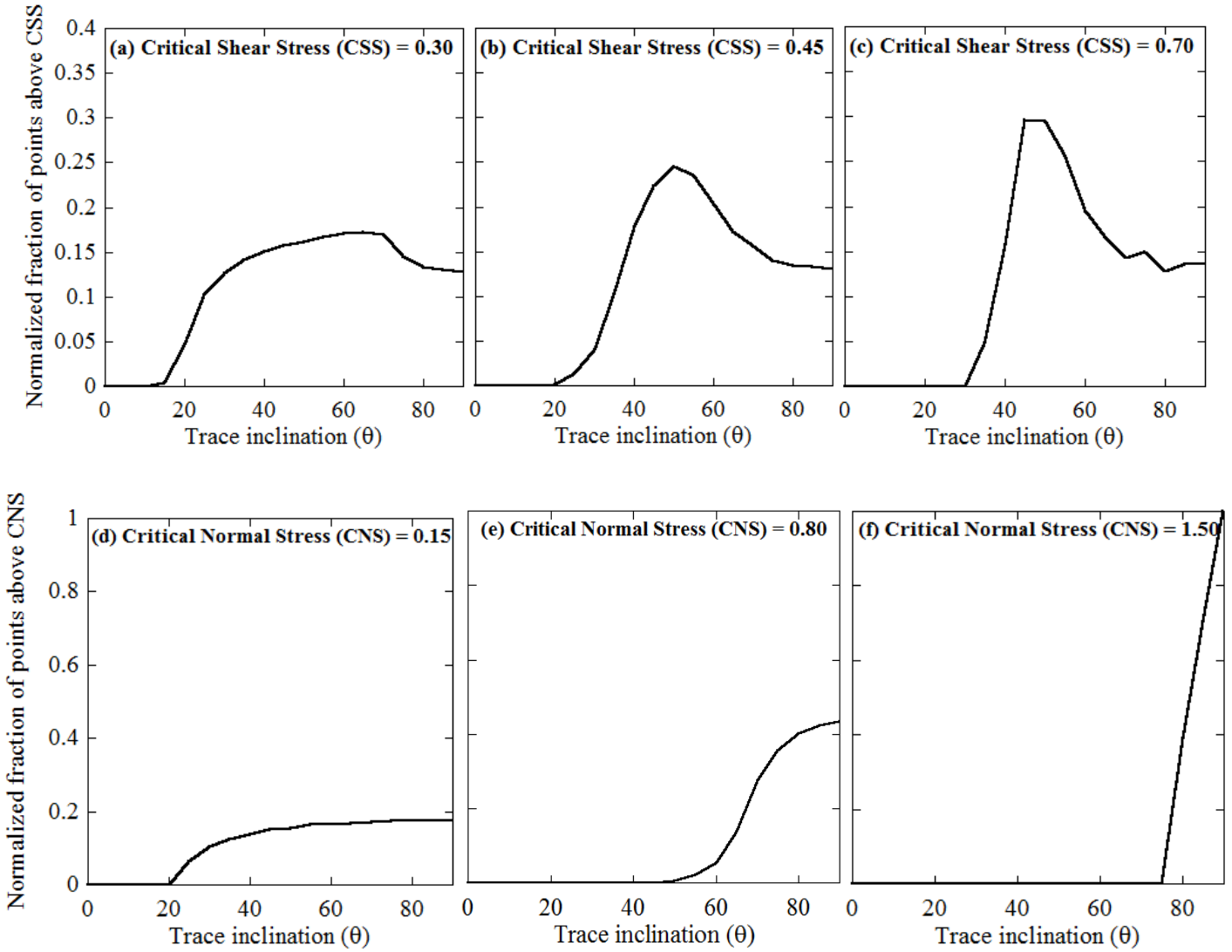

Figure 5.23 The fractions of data points at each inclination above the critical resolved shear (a)-(c) and normal (d)-(f) stresses given in Figure 5.20 and Figure 5.21 are determined and used to generate the normalized SMGBS model curves shown above.

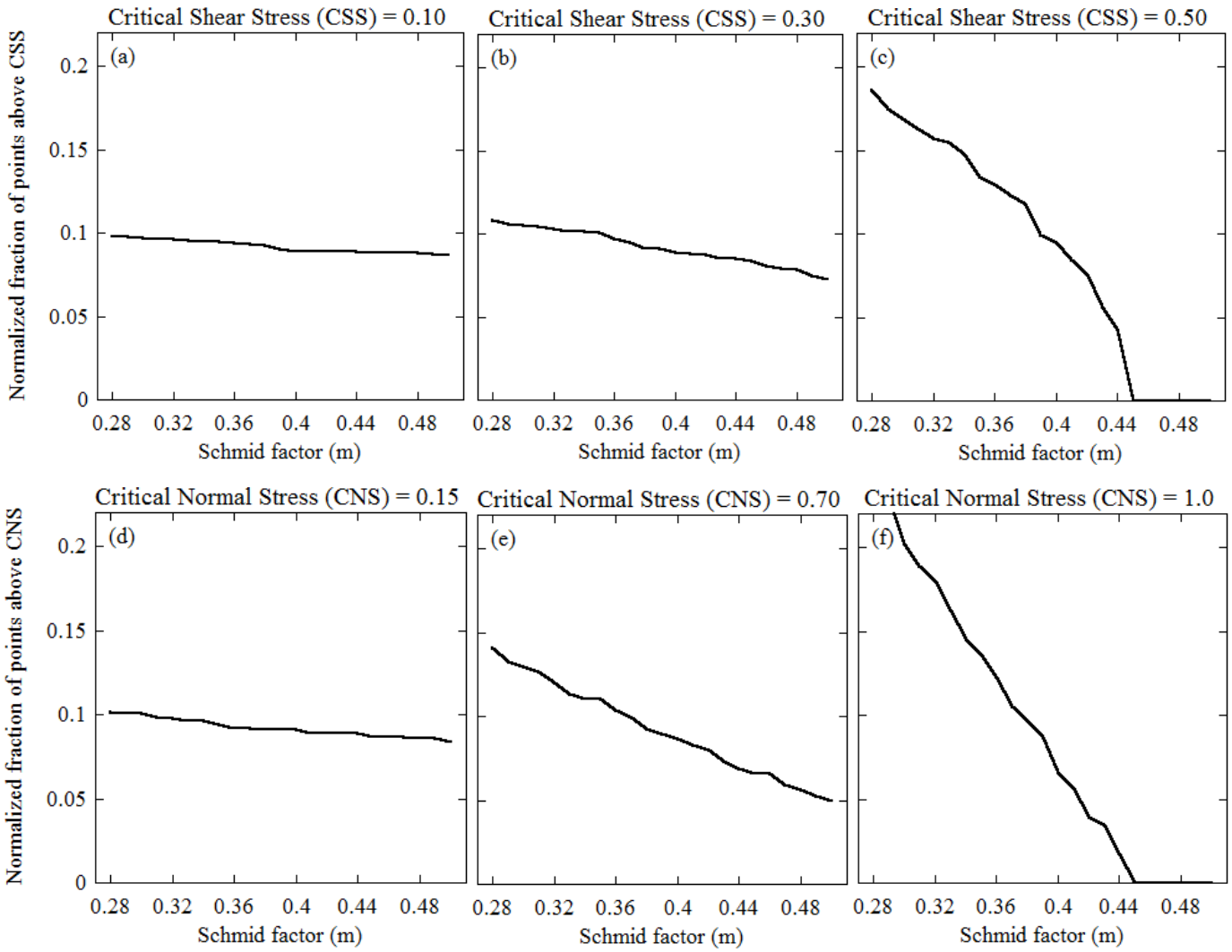

Figure 5.24 Normalized fraction of SMGBS modeling points above indicated critical shear (a), (b), (c) and normal (d), (e), (f) stresses. The influence of the Schmid factor on the stress acting on the grain boundary increases with increasing critical shear or normal stress.

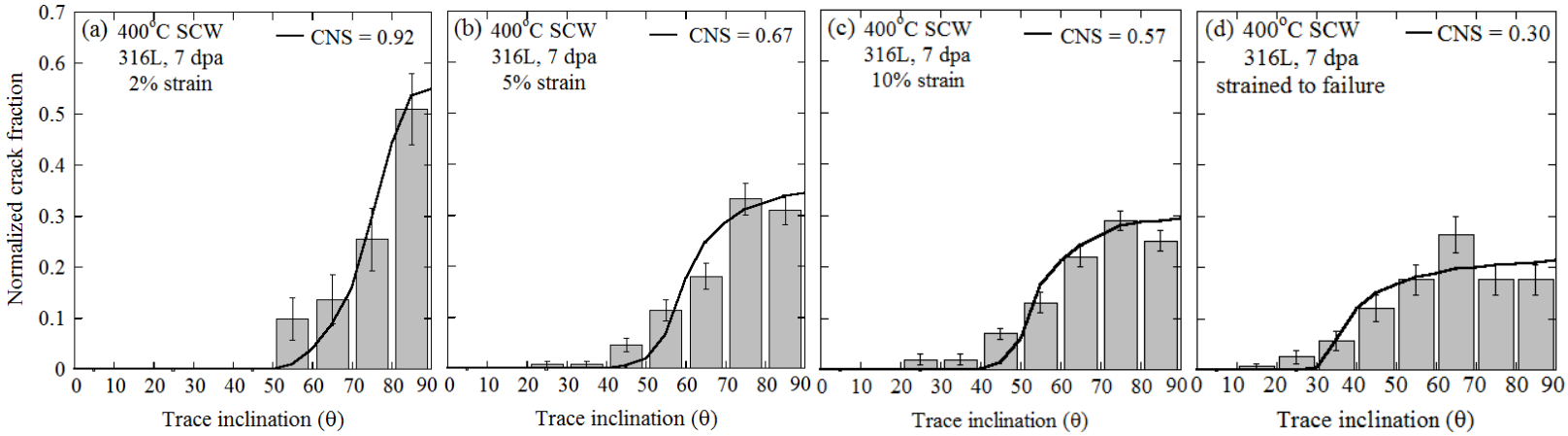

Figure 5.25 Distributions of trace inclinations for NS cracks on 7 dpa irradiated 316L following straining in 400˚C SCW to (a) 2%, (b) 5%, (c) 10%, and (d) 30% strain (data for (d) taken from [218]). The SMGBS model curves for the CNS values indicated are shown with solid black lines.

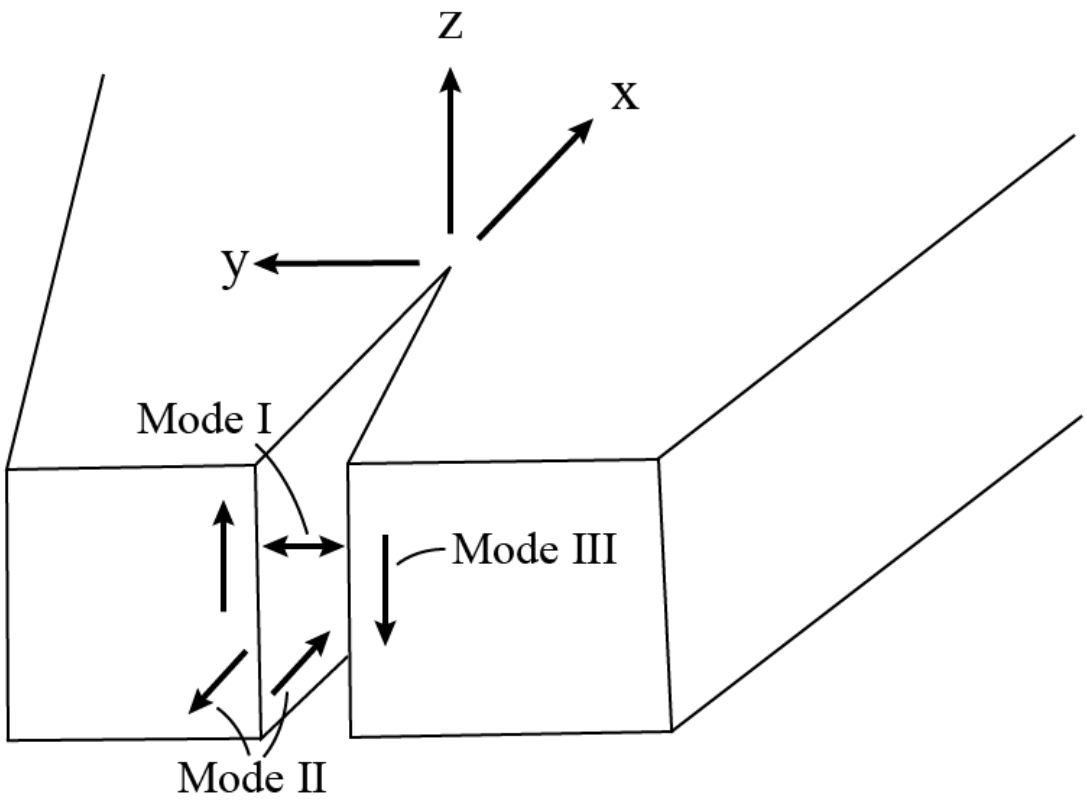

Figure 5.26 Crack opening modes. GBC cracks are opening via Mode III and NS cracks are opening via Mode I. (reproduced from [62])

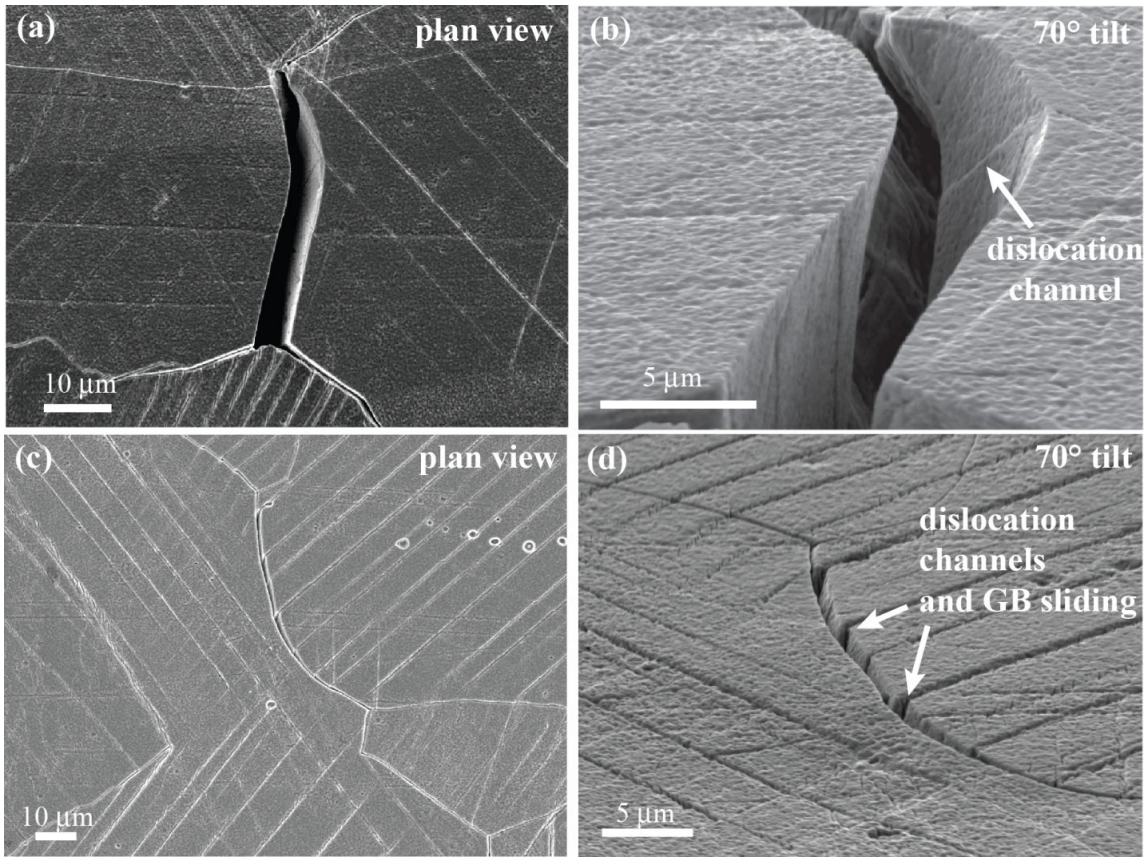

Figure 5.27 Images of IG cracks on irradiated 316L specimens following straining in 400˚C SCW. Images on the left show plan views of the cracks, while images on the right show the same cracks following tilting to 70˚.

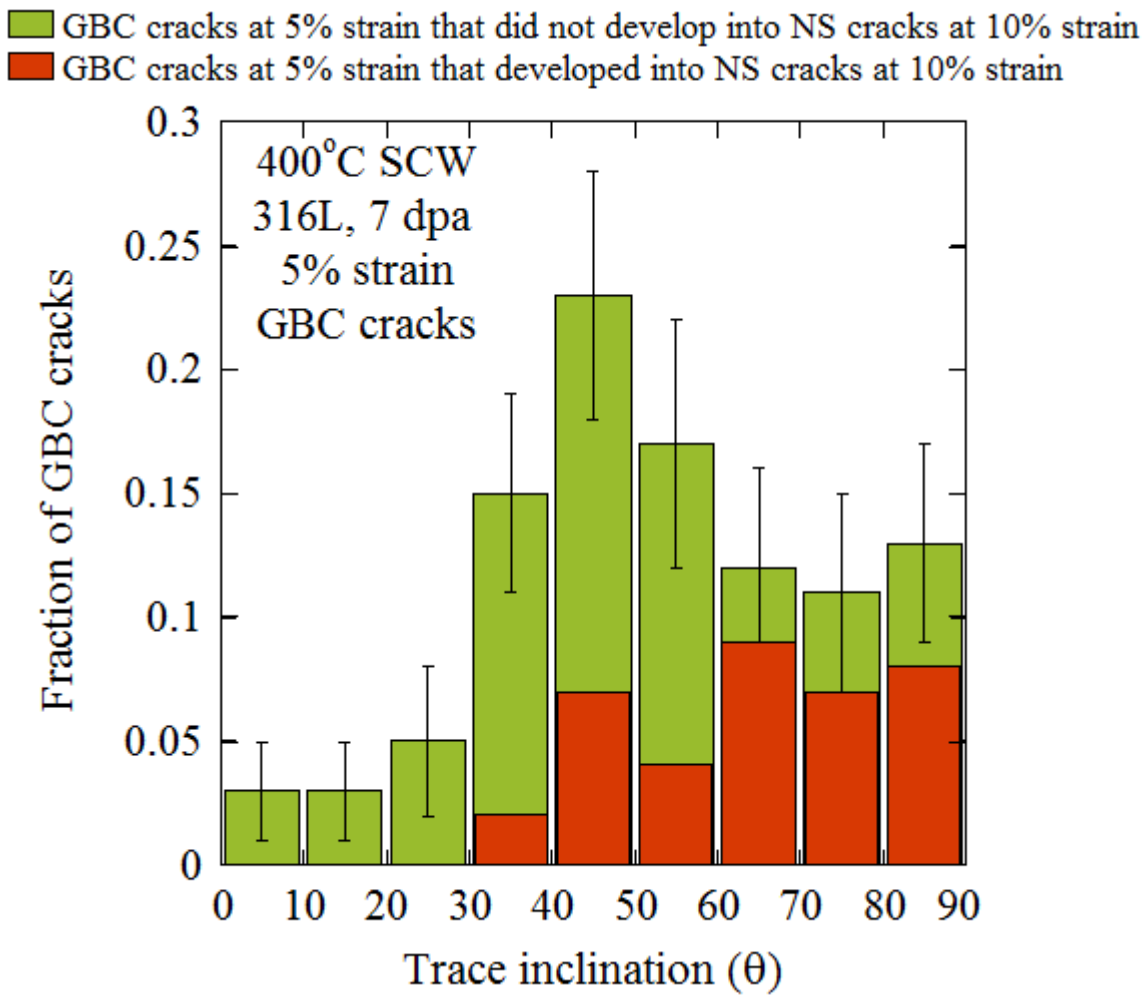

Figure 5.28 Trace inclination dependence of GBC cracks following straining to 5% in 400˚C SCW. Data shown in green indicate GBC cracks that remained GBC cracks at 10% strain, while those in orange indicate GBC cracks that developed into NS following further straining to 10%.

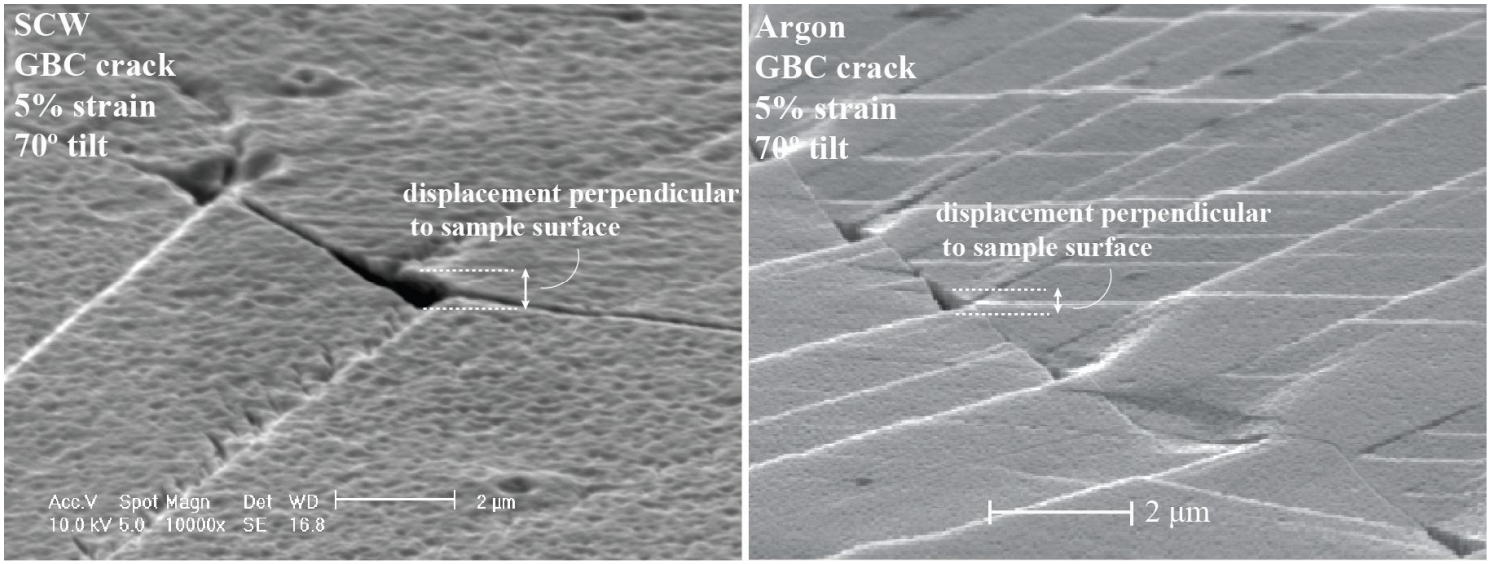

Figure 5.29 Displacement perpendicular to the surface of the specimen at the location of a GBC crack in irradiated 316L specimen following straining to 5% in 400˚C SCW.

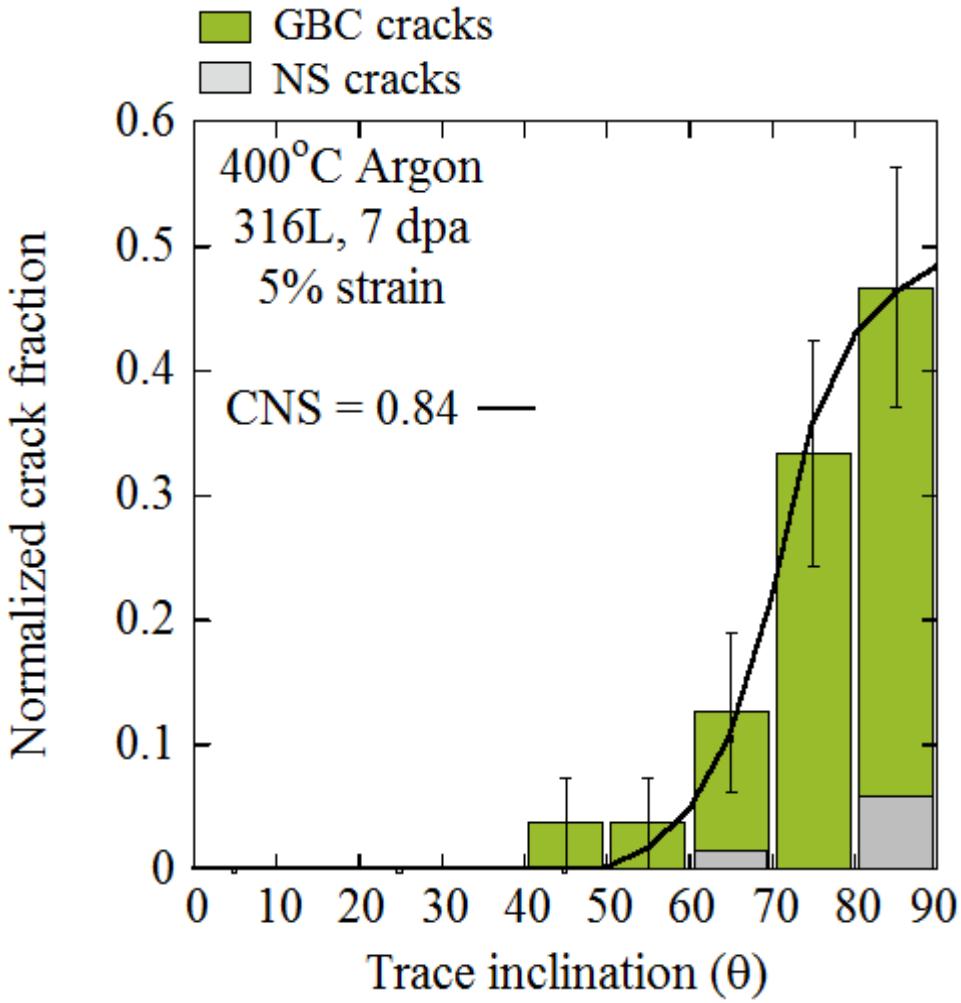

Figure 5.30 Distribution of trace inclinations with respect to tensile axis for IG cracks on 7 dpa proton irradiated 316L following straining to 5% in 400˚C purified argon.

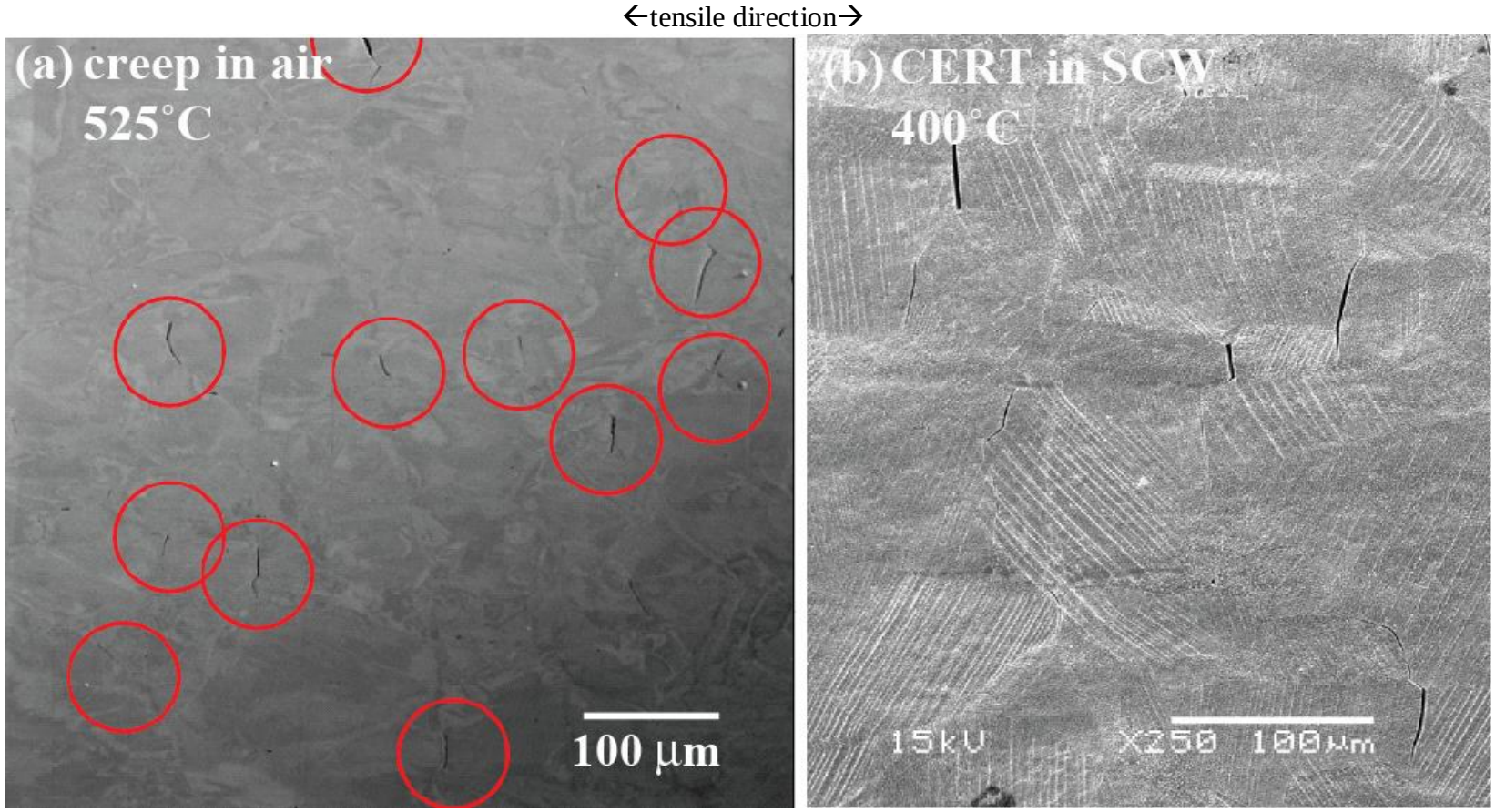

Figure 5.31 (a) Intergranular fracture observed on 316 stainless steel following creep test in air [58, 60], (b) IG cracks on gage surface of 7 dpa proton irradiated tensile specimen strained in 400˚C SCW.

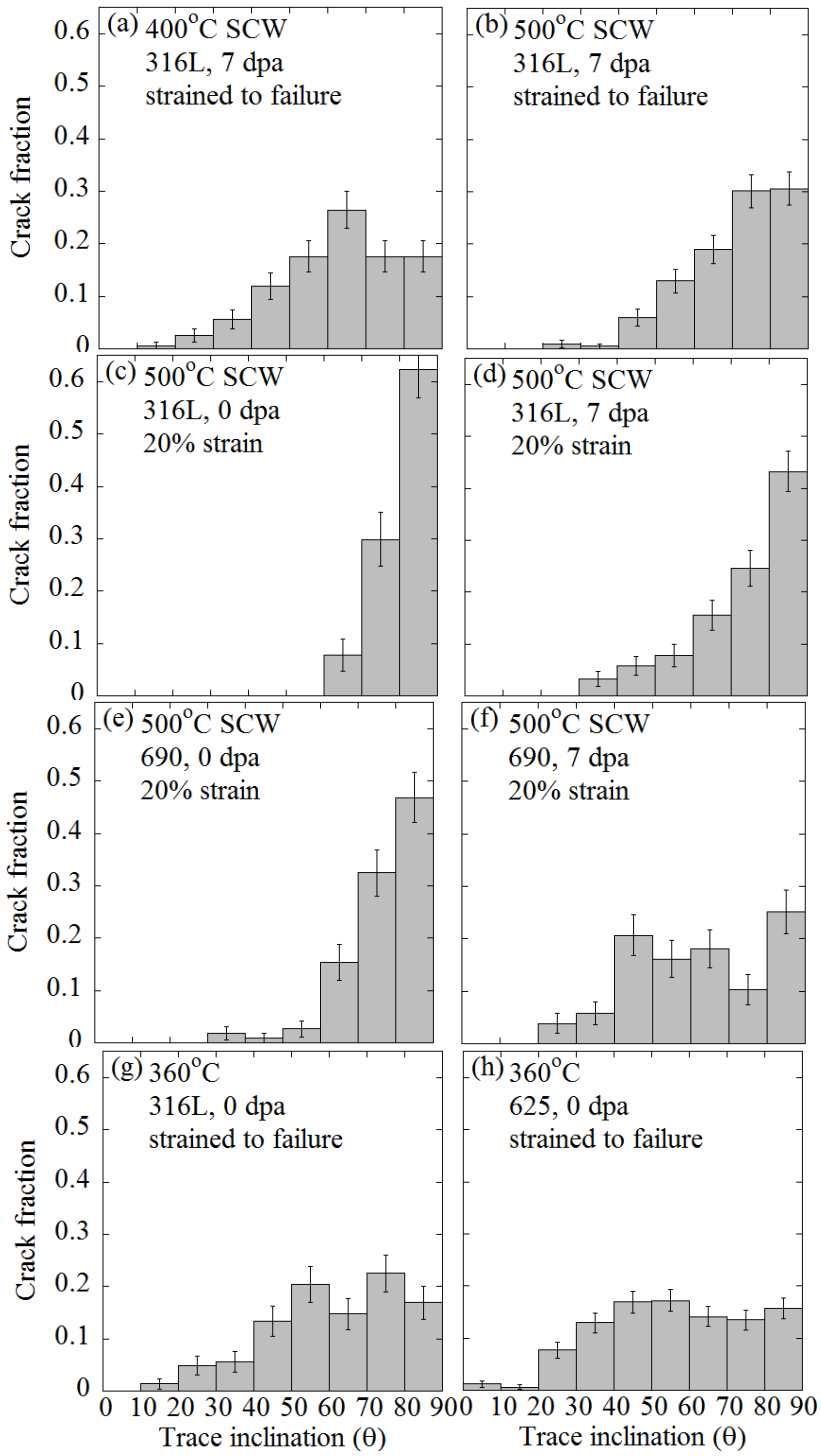

Figure 5.32 Influence of (a) & (b) temperature, (c) – (f) irradiation, and (e) – (h) alloy on trace inclination dependence of intergranular cracking of austenitic alloys in high temperature aqueous environments. These measurements were collected from micrographs borrowed from other researchers from previous experiments [53, 219], but this analysis was performed independently.

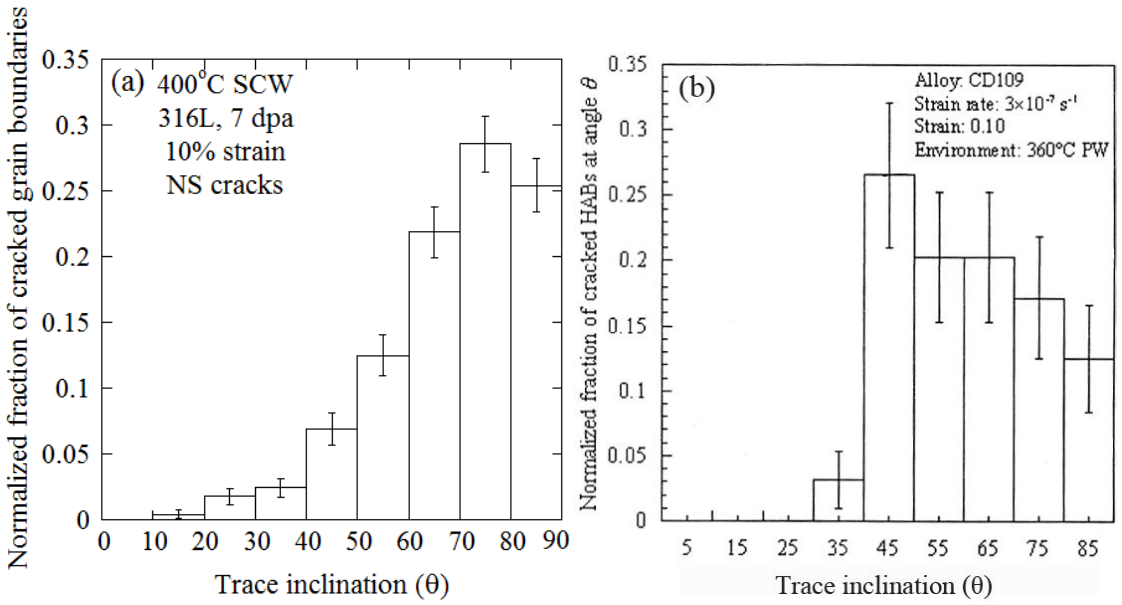

Figure 5.33 (a) Distribution of NS cracks on irradiated 316L specimens strained to 10% in 400˚C SCW, (b) distribution of IG cracks at HABs of Ni-16Cr-9Fe following straining to 10% in 360˚C primary water [142].

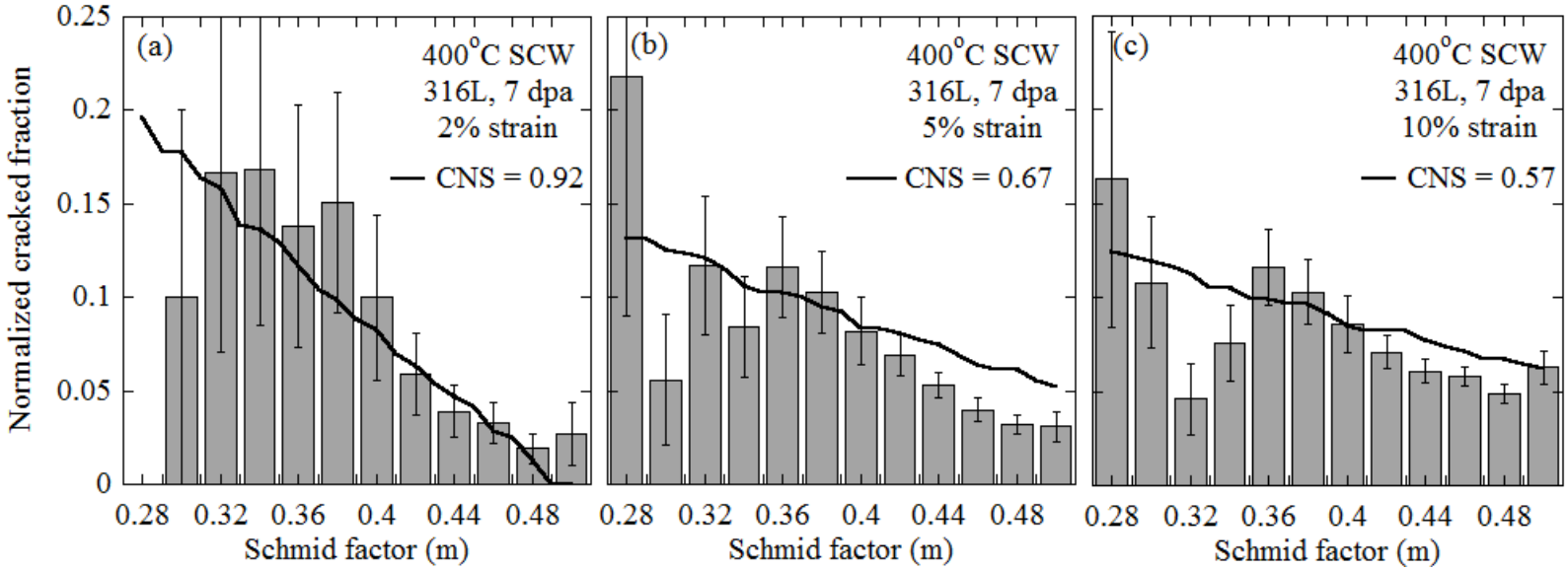

Figure 5.34 Cracked boundary fraction as a function of Schmid factor of grains adjacent to boundary. The solid black curves are the SMGBS model curves generated using the CNS values used to fit the model to the trace inclination distribution at (a) 2%, (b) 5%, and (c) 10% strain.

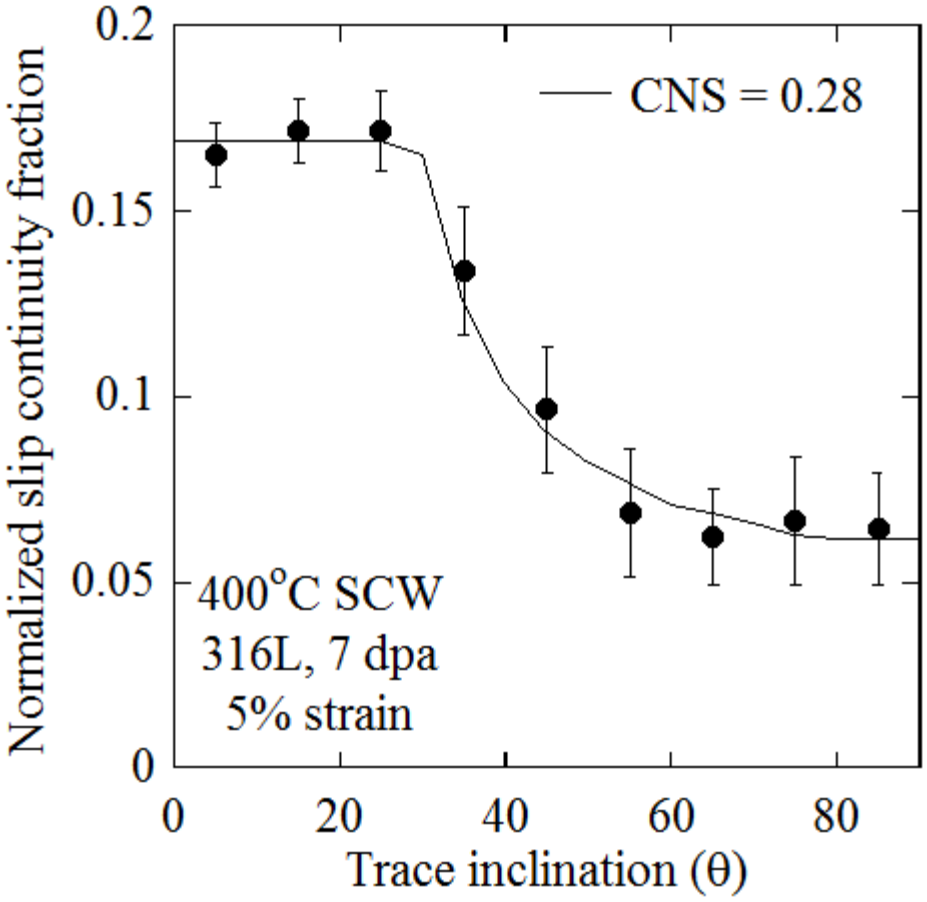

Figure 5.35 Normalized slip continuity fraction as a function of trace inclination with respect to the tensile axis. The solid black line indicates the curve generated by the SMGBS model with a critical normal stress of 0.28. Note that this SMGBS model curve indicates the normalized fraction of data points for each trace inclination bin that fall *below* the CNS.

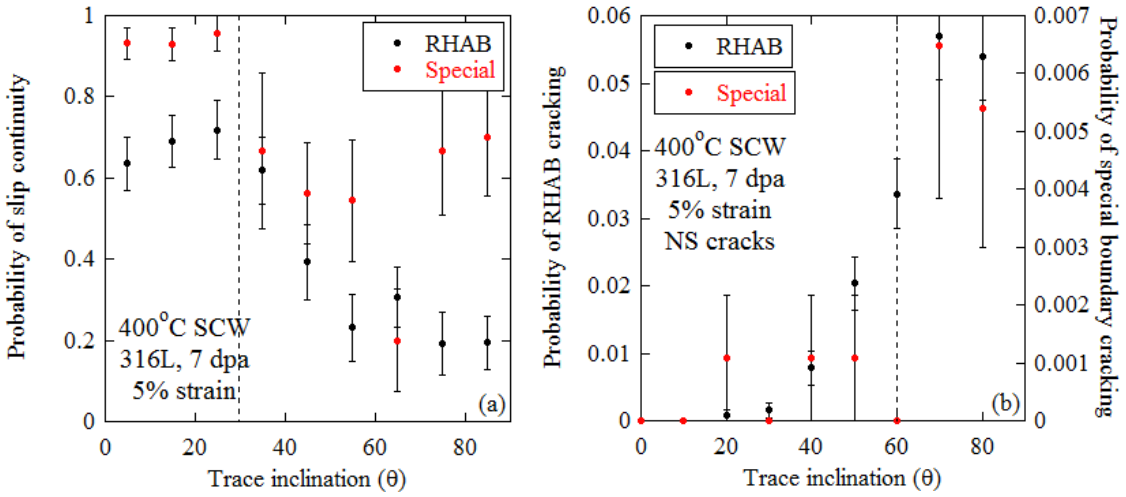

Figure 5.36 Influence of grain boundary character on (a) slip continuity and (b) cracking propensity as a function of trace inclination.

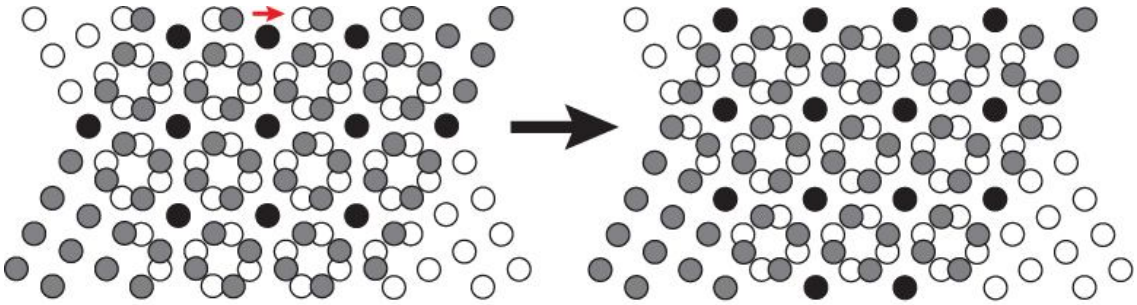

(a)

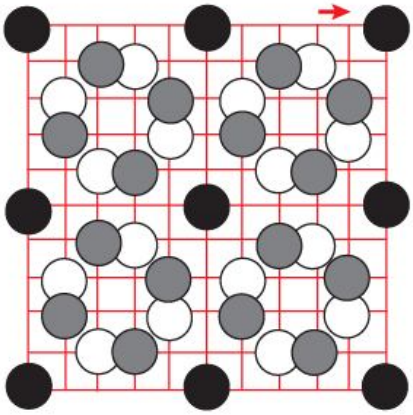

(b)

Figure 5.37 Illustration of the DSC lattice (a) demonstration of how a small displacement vector (red arrow) of the DSC lattice can preserve the CSL structure of the grain boundary, (b) the red lines indicate the DSC lattice. (reproduced from [214])

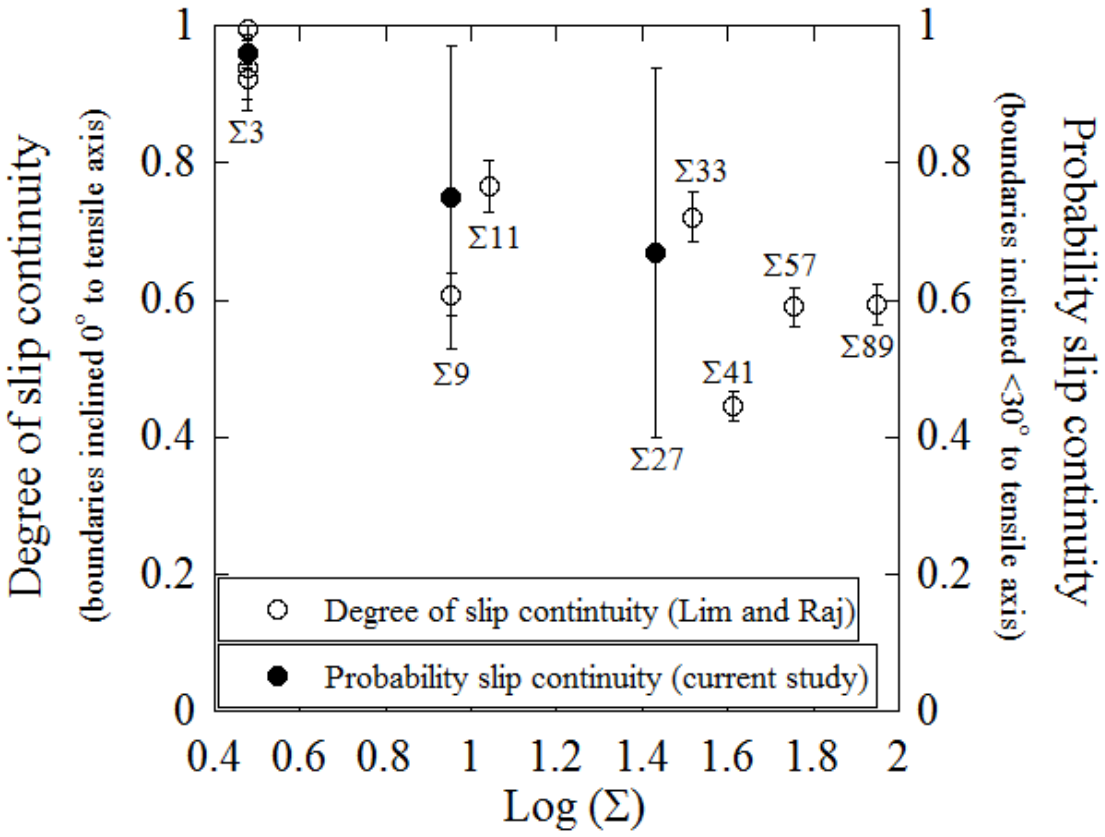

Figure 5.38 Current results of slip continuity behavior compared to the results of Lim and Raj [197]. The "probability of slip continuity" in the current study was calculated by dividing *the number of grain boundaries* where slip continuity was observed by the total number of grain boundaries intersected by dislocation channels. Lim and Raj determined the "degree of slip continuity" by counting the *number of slip traces* which were continuous across the boundary and dividing by the total number of slip traces impinging at the interface from either crystal.

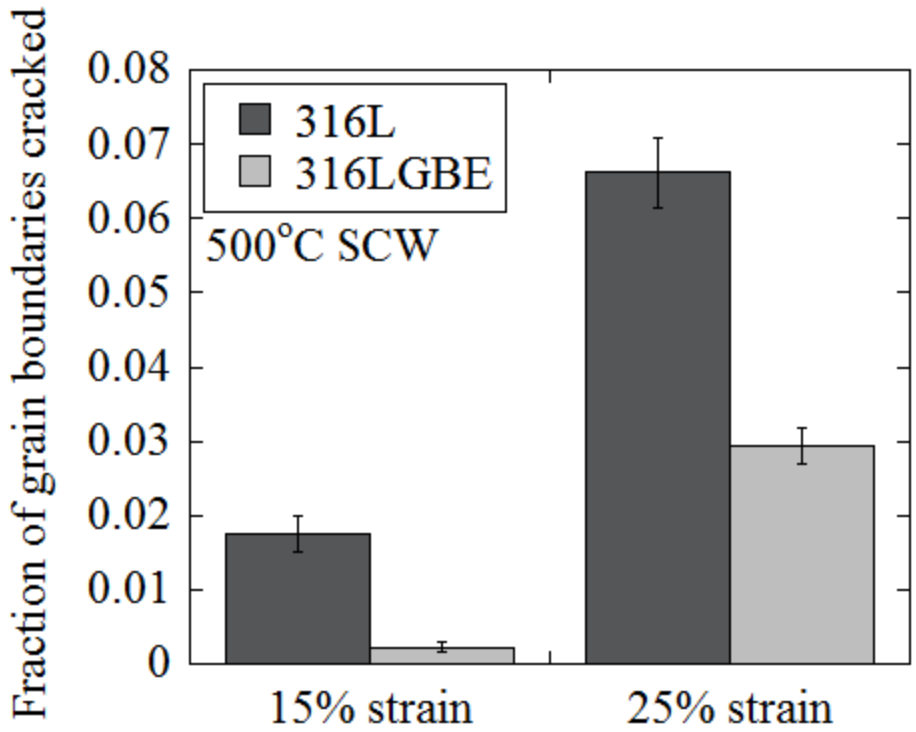

Figure 5.39 Fraction of grain boundaries cracked in 316L and 316LGBE specimens following straining in 500˚C SCW.

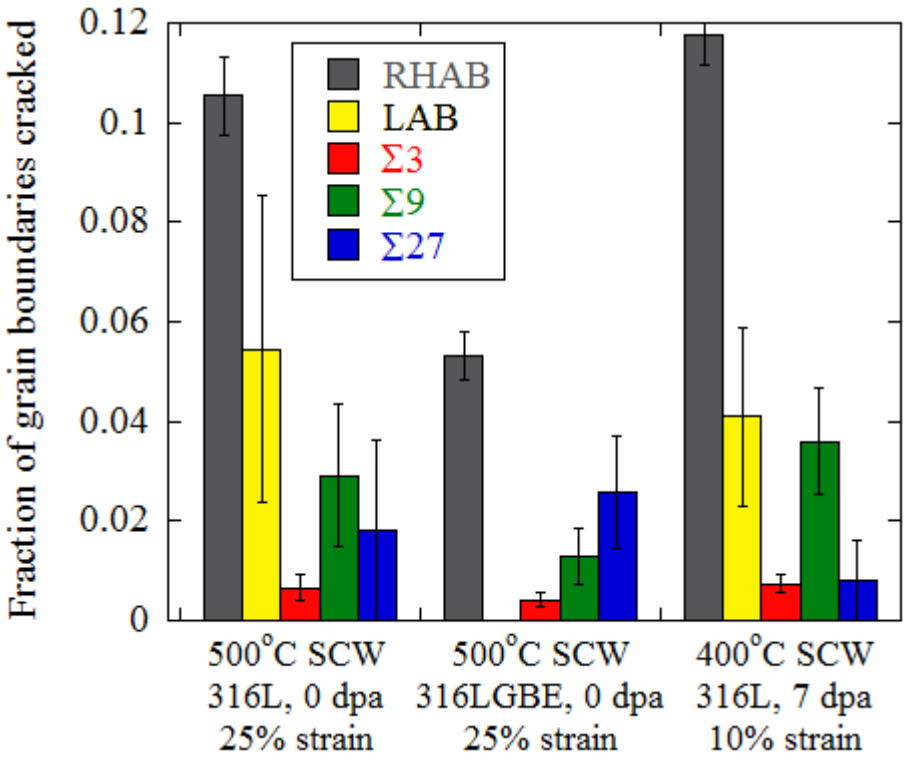

Figure 5.40 Fraction of grain boundaries of each character that cracked following straining in deaerated SCW environments.

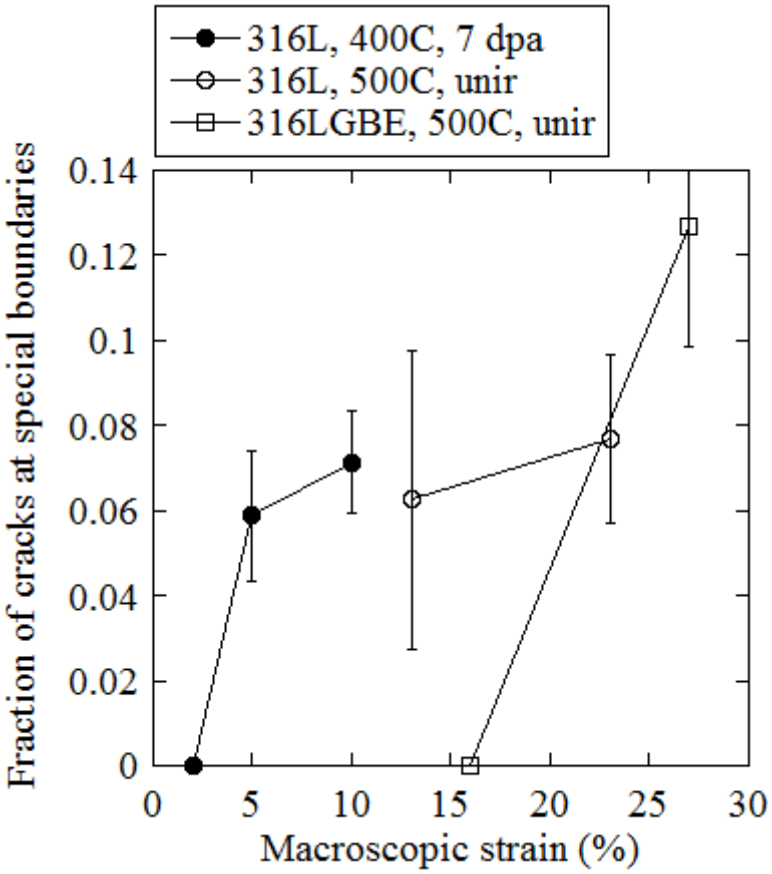

Figure 5.41 Fraction of total number of cracks on gage surface of specimen that occur at special grain boundaries following straining in deaerated SCW.

CHAPTER 6

CONCLUSIONS

The conclusions of this thesis are:

1. Intergranular NS cracks in supercritical water preferentially occurred adjacent to grains with low Schmid factors and along grain boundaries perpendicular to the tensile axis.
2. A model (SMGBS) was developed to evaluate the relative magnitudes of stress experienced by individual grain boundaries in irradiated metals as a function of the Schmid factor of the adjacent grain and the inclination of the grain boundary plane to the tensile axis. The model was validated by showing that it could predict the Schmid factor dependence of the NS cracking from the distribution of cracked trace inclinations to the tensile axis.
3. The NS cracking of 316L stainless steel in the current study was driven by the normal stresses acting on the grain boundaries rather than shear stresses. Furthermore, the stress dependence of intergranular cracking in high temperature aqueous environments was shown to depend on the temperature, irradiation damage, and alloy.
4. Two different crack morphologies were observed in irradiated 316L stainless steel in 400˚C SCW and purified argon environments; NS cracks and GBC cracks. The lack of influence of Schmid and Taylor factor on the GBC cracking propensity in

SCW and the occurrence of GBC cracks along grain boundaries with a broad range of inclinations to the tensile axis indicate that the driving forces for the NS and GBC cracks in SCW was different. In the purified argon environment, however, the driving forces were similar.

5. The 400˚C SCW environment increased the cracking propensity of irradiated 316L stainless steel to levels far above that experienced in a purified 400˚C argon environment. The NS and GBC crack densities were increased by factors of 18 and 3, respectively. Although the SCW environment enhanced cracking, it was not essential to the development of either NS or GBC cracks on irradiated 316L at 400˚C.
6. Grains with low Taylor factors and high Schmid factors enhanced the propensity for slip continuity at boundaries highly inclined (θ>50˚) to the tensile axis because they provided multiple, favorably oriented slip systems on which deformation can occur.
7. Grain boundary engineering of 316L stainless steel resulted in reduced intergranular cracking propensity, as measured by the fraction of grain boundaries cracked following straining in 500˚C SCW. Σ3, Σ9, Σ27, and LABs were all confirmed to have superior resistance than RHABs as measured by the amount of intergranular cracking in 400˚C SCW (irradiated 316L) and 500˚C SCW (unirradiated 316L and 316LGBE).
8. The finding that special grain boundaries facilitated slip continuity at the grain boundaries of irradiated 316L in 400˚C SCW suggests that their resistance to strain incompatibilities contributes to their reduced propensity for cracking.

9. The findings of this study indicate that the intergranular cracking propensity of 316L stainless steel in SCW would be lowest in a material with the following microstructural characteristics; (1) a large population of grains with high Schmid factors (for a specified tensile direction), (2) a high frequency of grain boundaries oriented nearly parallel to the tensile axis, and (3) a large fraction of special grain boundaries.

FUTURE WORK

The results of this study indicated that the intergranular cracking propensity of 316L stainless steel in SCW is greater (1) at grain boundaries highly inclined to the tensile axis, (2) at random, high angle grain boundaries, and (3) at grain boundaries adjacent to grains with low Schmid factors (and high Taylor factors). While the first two findings have been observed in a variety of environments, the third finding is new and is likely applicable to high temperature environments other than SCW and purified argon. Grain boundary engineering has been shown to improve the intergranular degradation of materials, and is often attributed to the special properties of the enhanced special boundary population. It is proposed here that superior materials may be produced through a broader type of "microstructural engineering". It may be possible to produce materials with textures of high Schmid factor and low Taylor factor grains (for a specified loading direction) in addition to enhanced special boundary fractions. Such microstructures may prove useful in a variety of high temperature applications where materials are prone to creep cracking.

The slip continuity behavior observed in the current study was grouped into two categories, continuous or discontinuous. The classification depended on whether or not the majority of the dislocation channels that intersected the grain boundary were continuous at the grain boundary at the precise location of intersection. Further analysis of the slip planes that activated, however, indicated that it was not uncommon for the

continuity across the grain boundary to be achieved through the activation of slip along planes not included in the family of close packed {111} planes. In such instances, it is therefore questionable whether the availability of favorably oriented slip systems on {111} planes would promote continuity of slip across the grain boundary, as was observed at boundaries highly inclined to the tensile axis in the current study. It is suggested here that dividing the slip *continuity* into subcategories of continuity along (1) {111} and (2) non-{111} planes might yield further insights into the observed dependencies of slip continuity on grain boundary inclination and Taylor factor. It is also possible that there are different categories of slip *discontinuity*. In some instances, it was observed that the frequency of slip lines intersecting the grain boundaries on either sides of the grain boundary were similar, but they did not directly intersect at the grain boundaries. This suggests that the dislocation channeling in one grain may be inducing channeling in the adjacent grain beneath the surface of the specimen. Consideration of the different types of slip discontinuity may lend further insight into the mechanisms of NS and GBC cracking in SCW.

The GBC cracks observed in the current study are of less concern than the NS cracks from a materials performance perspective as the majority do not propagate and their densities do not increase substantially with progressive straining. Their formation at the intersection of dislocation channels with grain boundaries, however, and their absence in the unirradiated condition indicates that their development requires localized deformation. While these cracks are primarily dormant in SCW, their behavior in other aggressive environments is questionable. The localized GBS that was observed at the GBC cracks indicated that oxide film must have ruptured at these locations. Experiments

in more aggressive environments or at different strain rates could be conducted to determine if such localized crack sites are capable of developing into more detrimental cracks.

It was determined that the SCW environment was not vital to the development of IG cracks and evidence was presented in support of the operation of a creep-based cracking mechanism in SCW. The higher densities of NS and GBC cracks in the SCW environment compared to the purified argon environment indicates that the SCW environment does, however, significantly enhance intergranular cracking of irradiated 316L stainless steel. It has been reported that the creep rates of metals can be enhanced by oxidation in the passive state through the injection of vacancies into the metal which subsequently diffuse into the stressed metal and interact with dislocations to increase their mobility [220, 221]. Parallel creep experiments could be performed in SCW and inert environments to determine if the creep rate of the stainless steel is enhanced by the environment. If IG cracks are developing via a creep based mechanism that requires the coalescence of vacancies on grain boundaries to form stable crack nuclei, the injection of vacancies during oxidation in the SCW environment could promote intergranular cracking.

APPENDICES

APPENDIX A

Stress Strain Curves

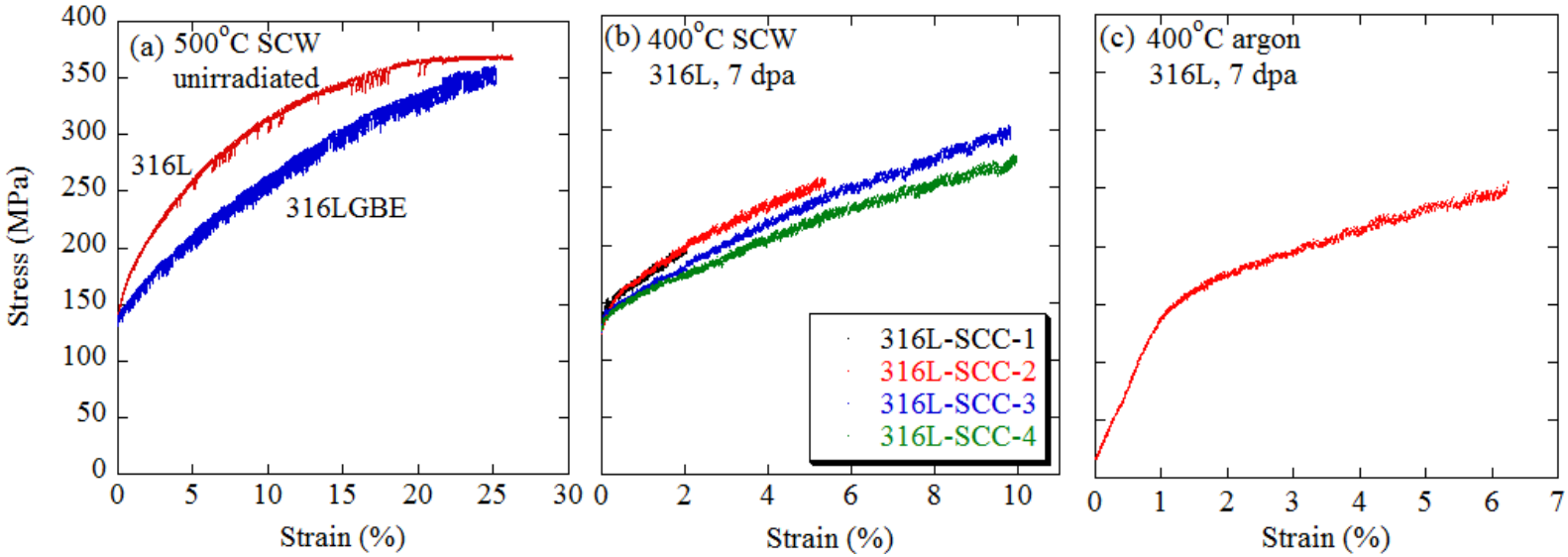

Figure A.1 Stress strain curves for specimens strained in (a) 500˚C and (b) 400˚C deaerated SCW, and (c) 400˚C argon environments.

APPENDIX B

OIM™ Maps of Specimen Gage Surfaces

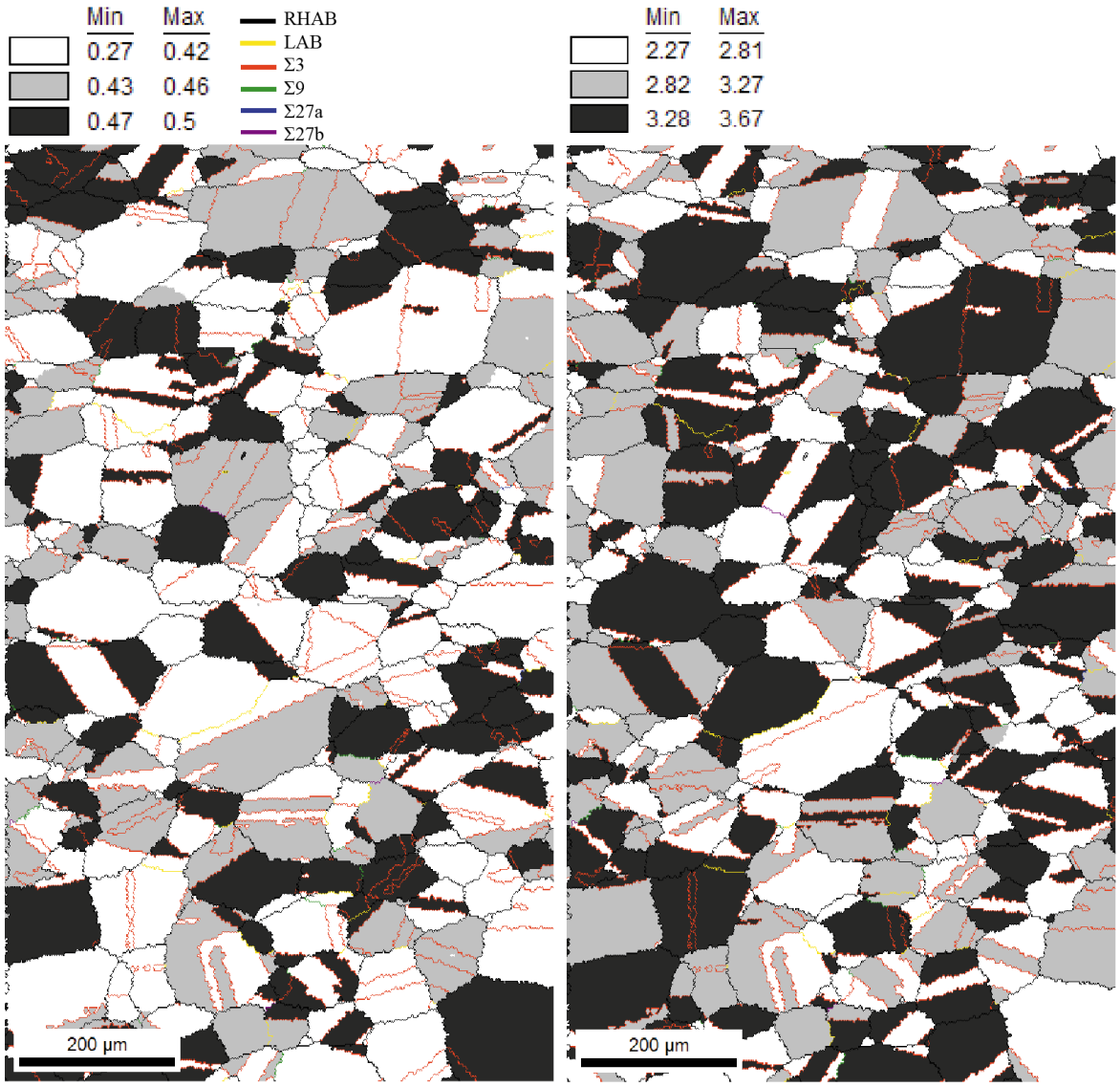

(a) (b)

Figure B.1 OIM™ maps of grain boundary characters and (a) Schmid factors and (b) Taylor factors from 316L specimens strained in 500˚C SCW.

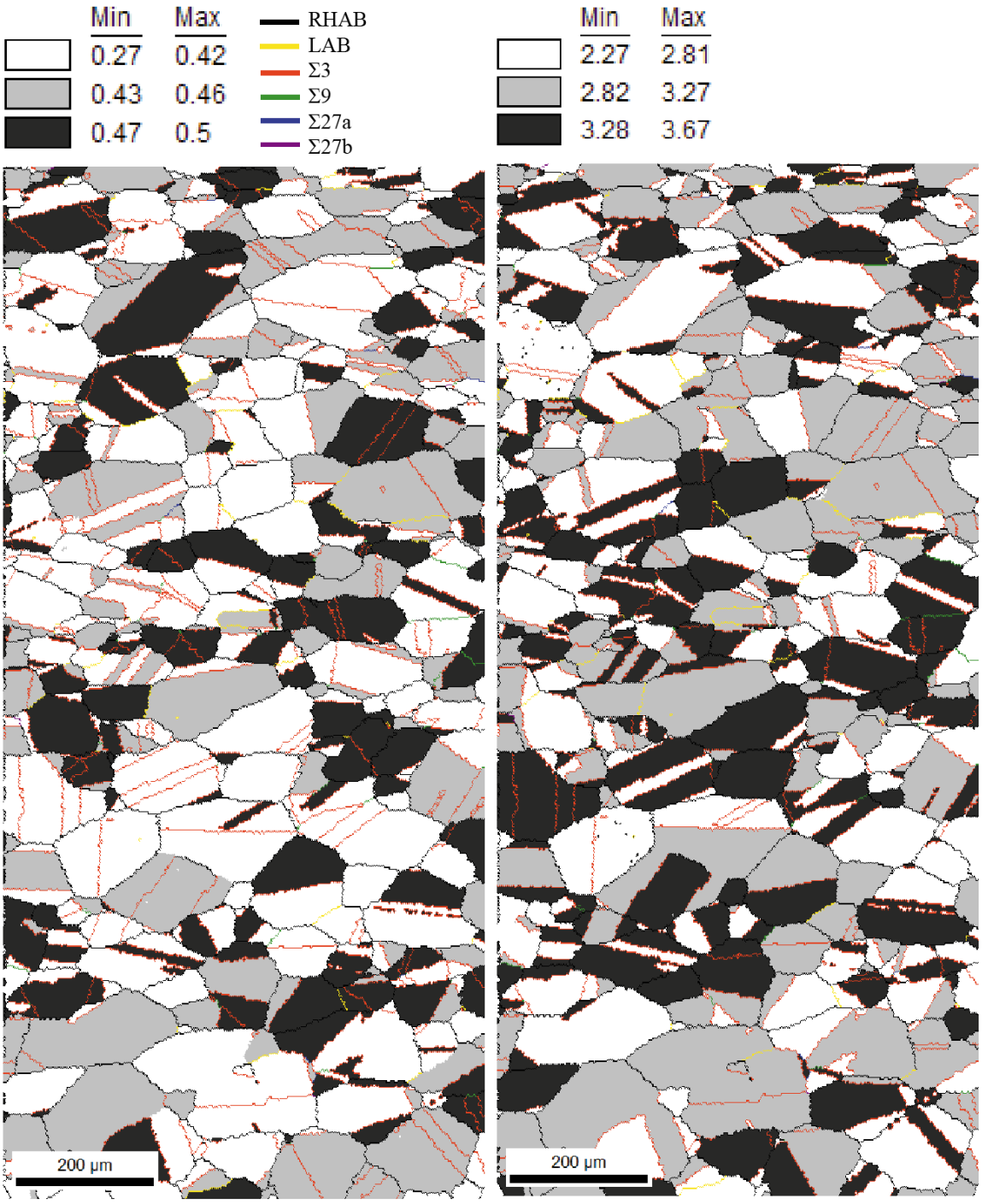

(a) (b)

Figure B.2 OIM™ maps of grain boundary characters and (a) Schmid factors and (b) Taylor factors from 316L specimens strained in 500˚C SCW.

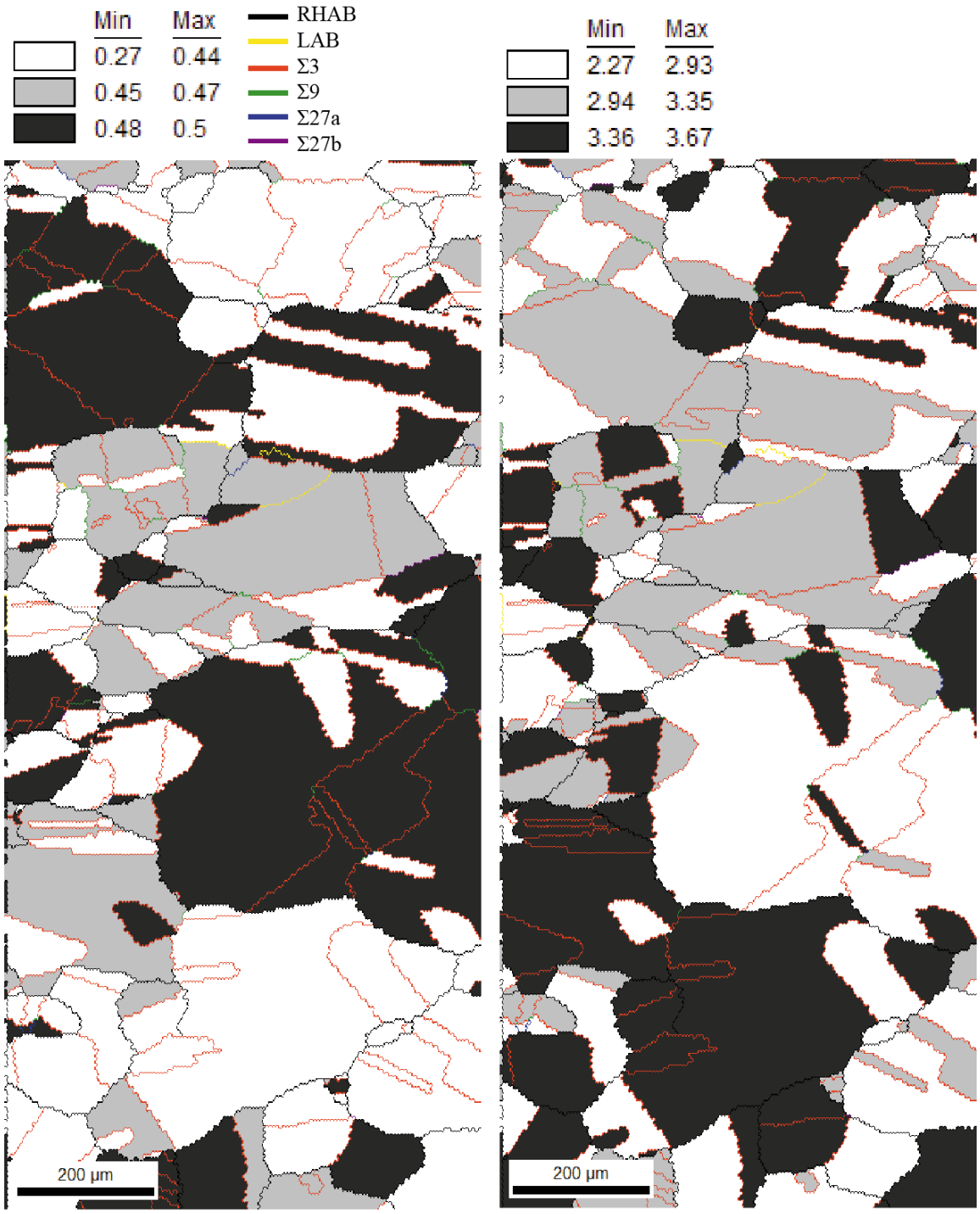

(a) (b)

Figure B.3 OIM™ maps of grain boundary characters and (a) Schmid factors and (b) Taylor factors from 316LGBE specimens strained in 500˚C SCW.

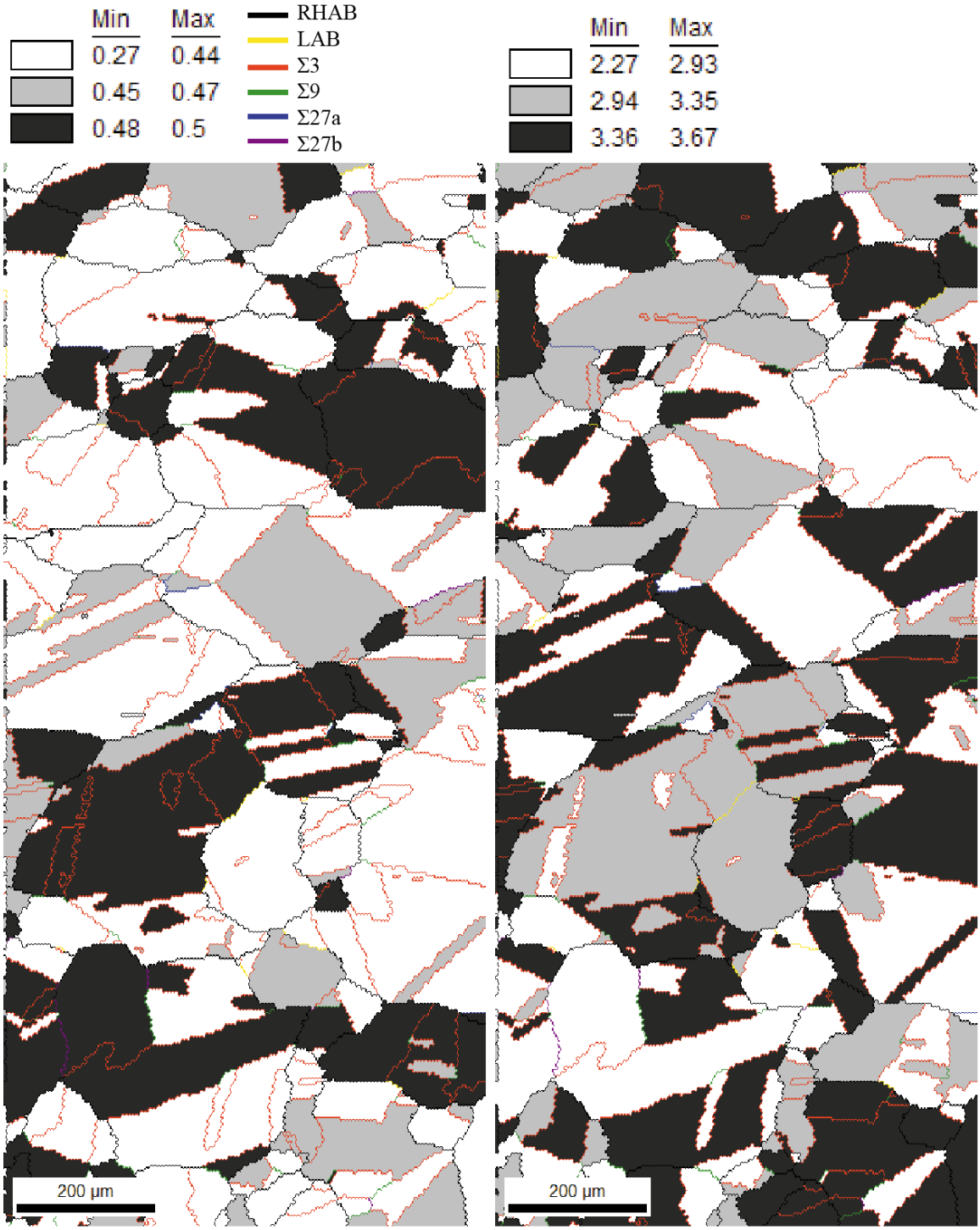

(a) (b)

Figure B.4 OIM™ maps of grain boundary characters and (a) Schmid factors and (b) Taylor factors from 316LGBE specimens strained in 500˚C SCW.

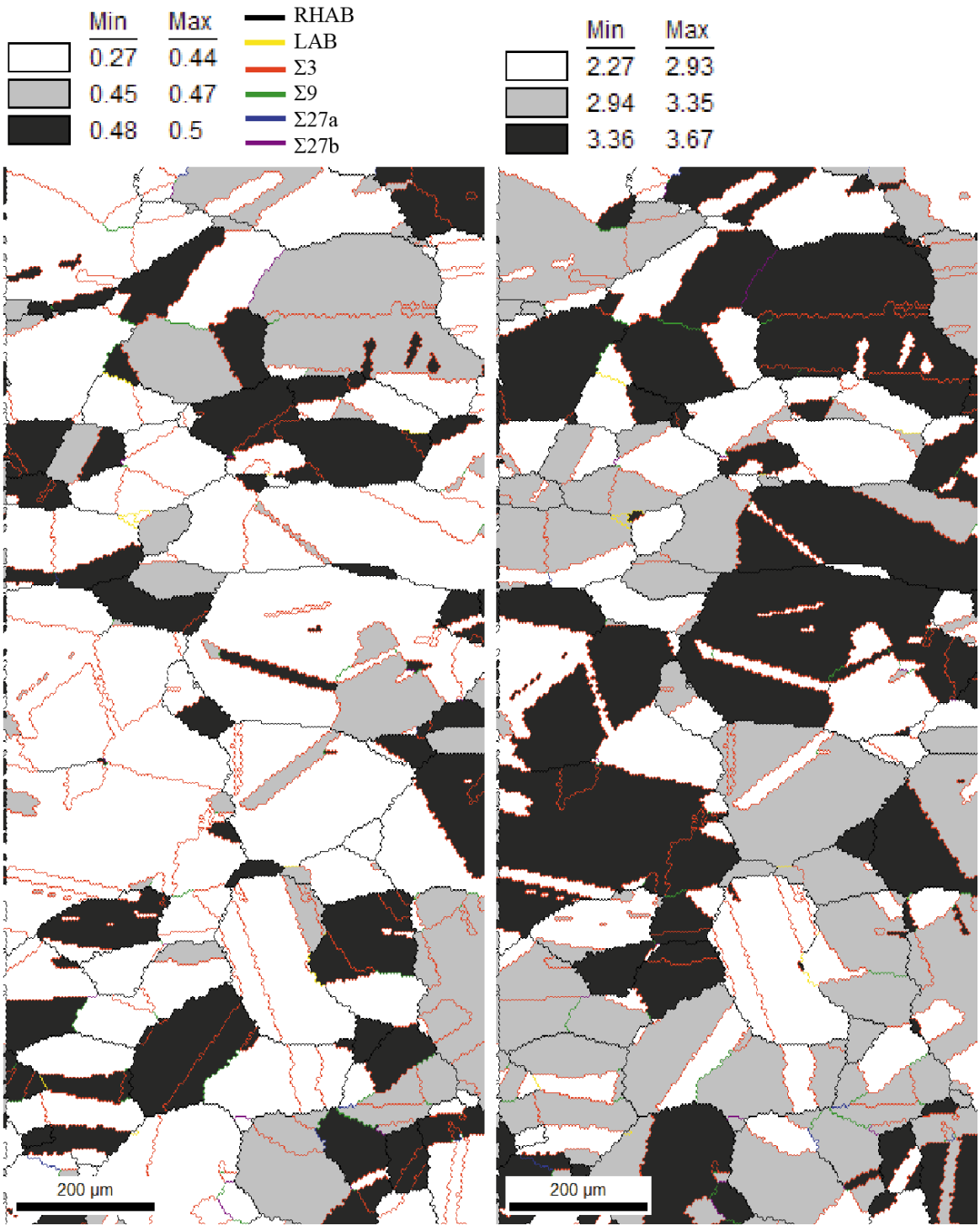

(a) (b)

Figure B.5 OIM™ maps of grain boundary characters and (a) Schmid factors and (b) Taylor factors from 316LGBE specimens strained in 500˚C SCW.

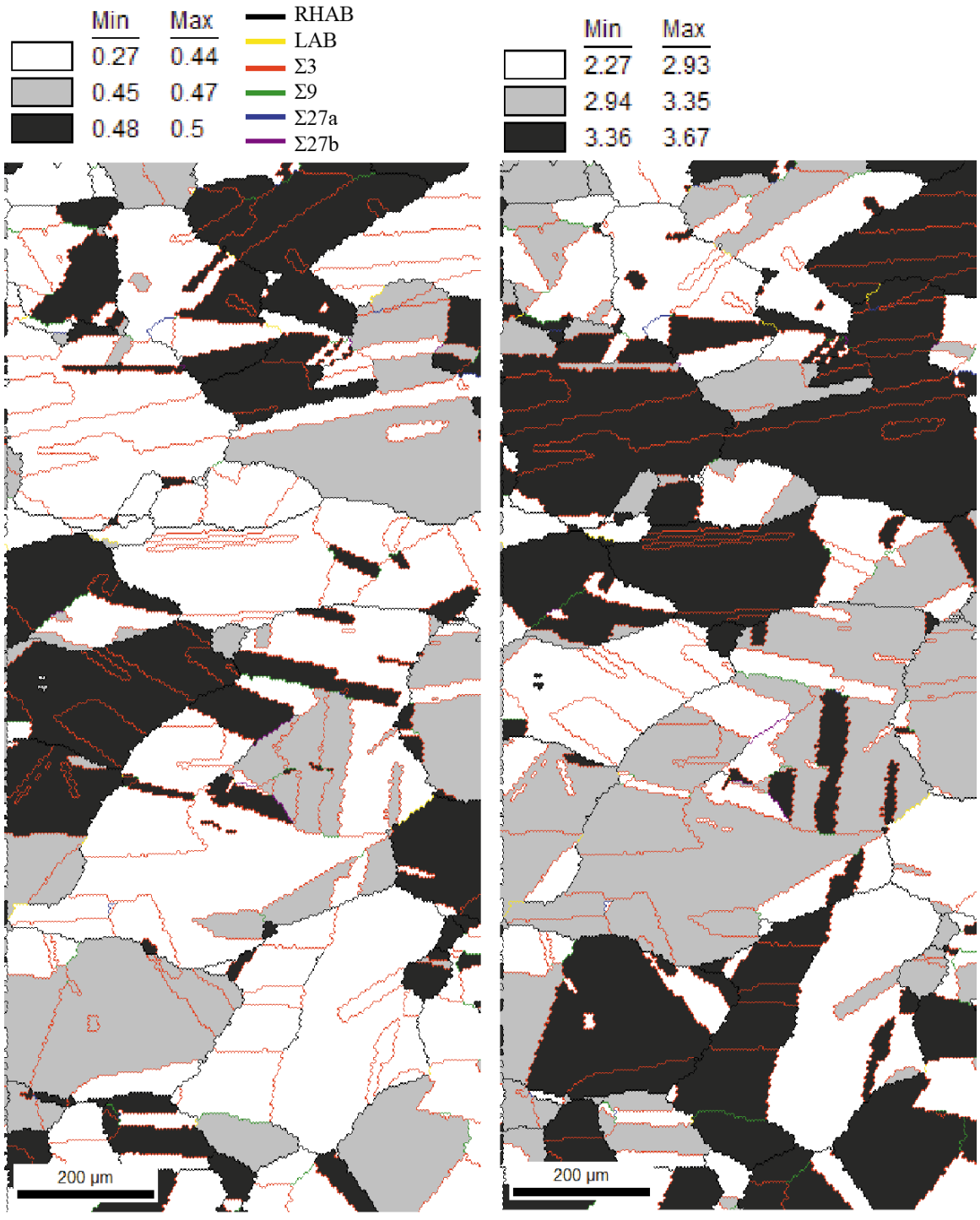

(a) (b)

Figure B.6 OIM™ maps of grain boundary characters and (a) Schmid factors and (b) Taylor factors from 316LGBE specimens strained in 500˚C SCW.

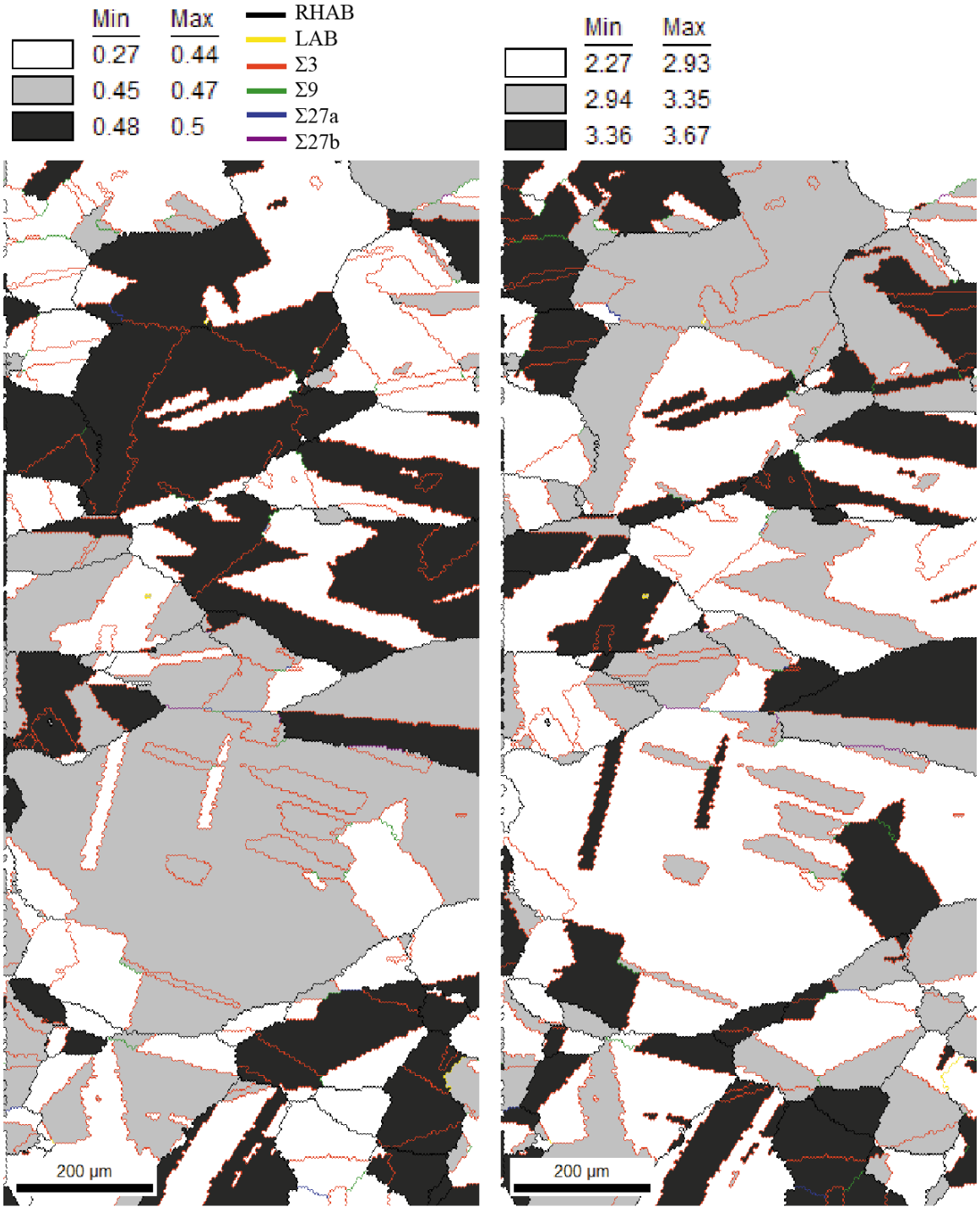

(a) (b)

Figure B.7 OIM™ maps of grain boundary characters and (a) Schmid factors and (b) Taylor factors from 316LGBE specimens strained in 500˚C SCW.

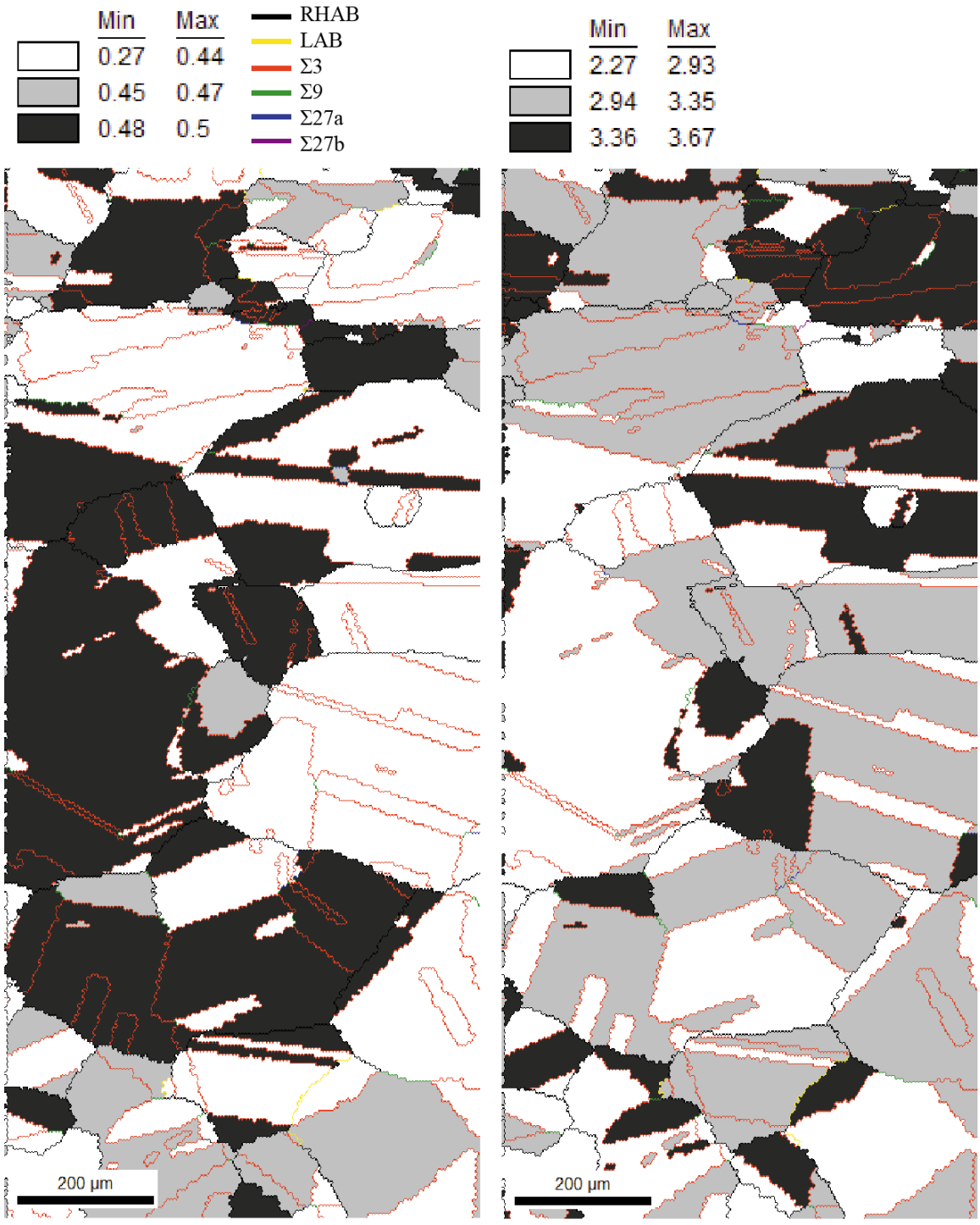

(a) (b)

Figure B.8 OIM™ maps of grain boundary characters and (a) Schmid factors and (b) Taylor factors from 316LGBE specimens strained in 500˚C SCW.

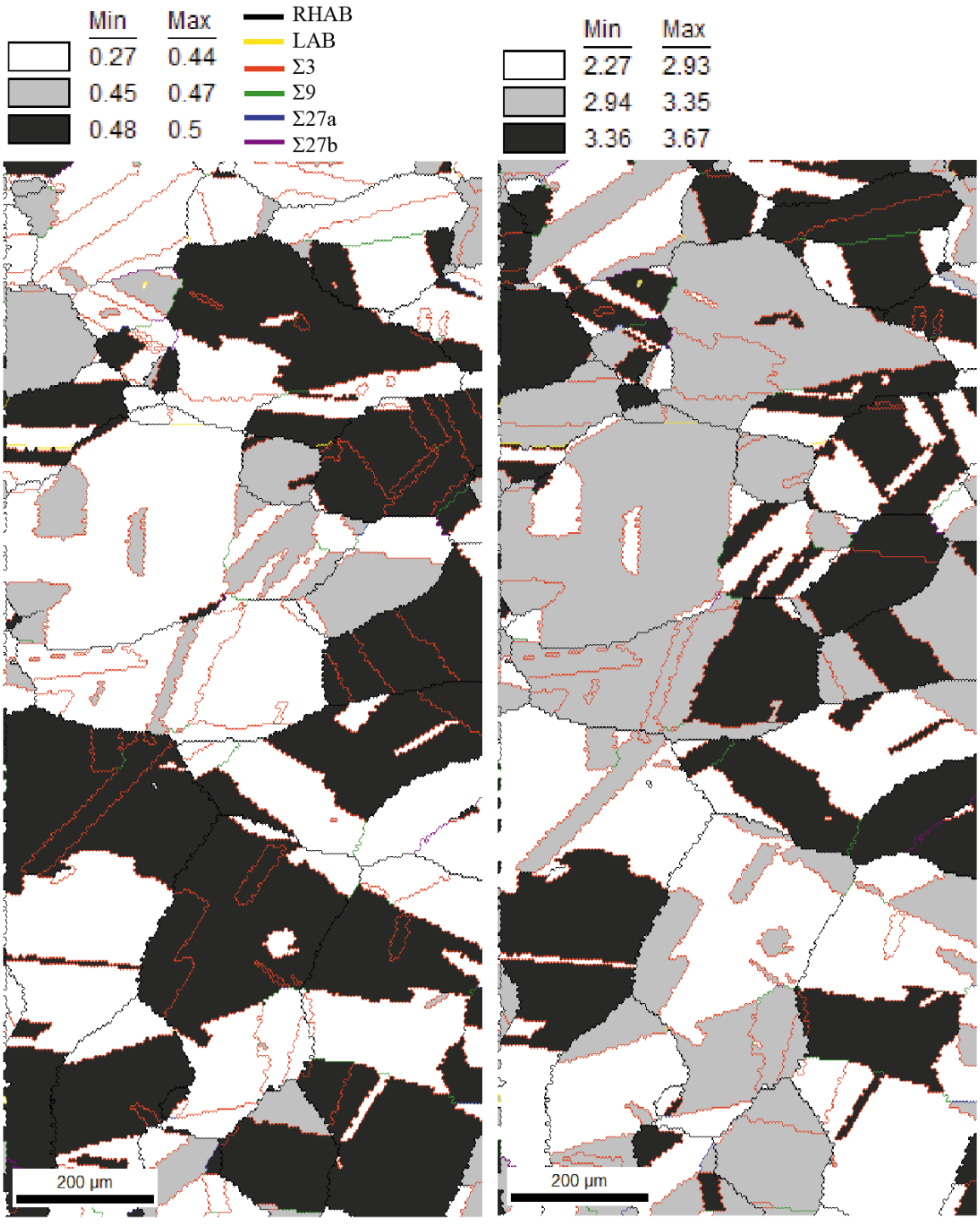

(a) (b)

Figure B.9 OIM™ maps of grain boundary characters and (a) Schmid factors and (b) Taylor factors from 316LGBE specimens strained in 500˚C SCW.

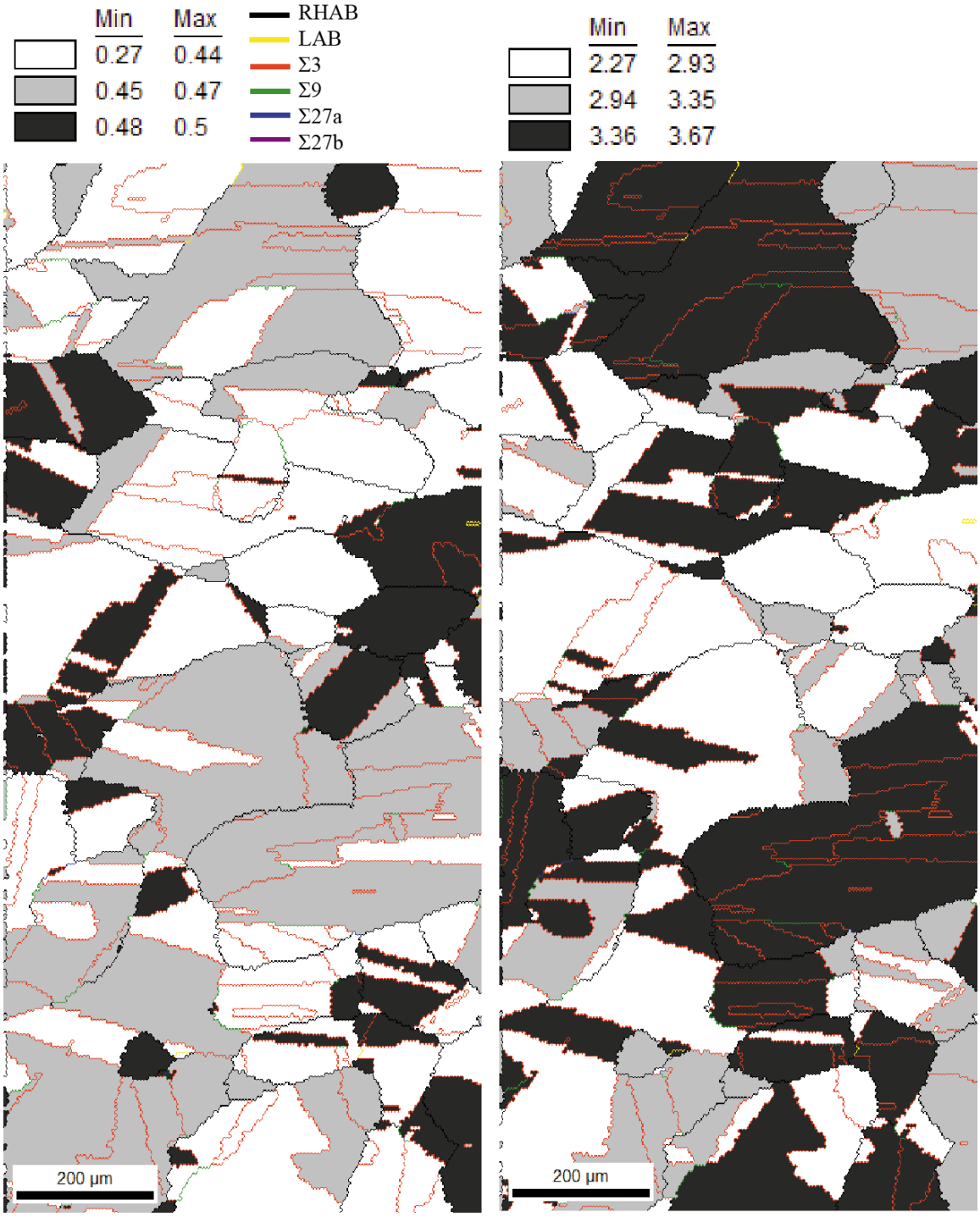

(a) (b)

Figure B.10 OIM™ maps of grain boundary characters and (a) Schmid factors and (b) Taylor factors from 316LGBE specimens strained in 500˚C SCW.

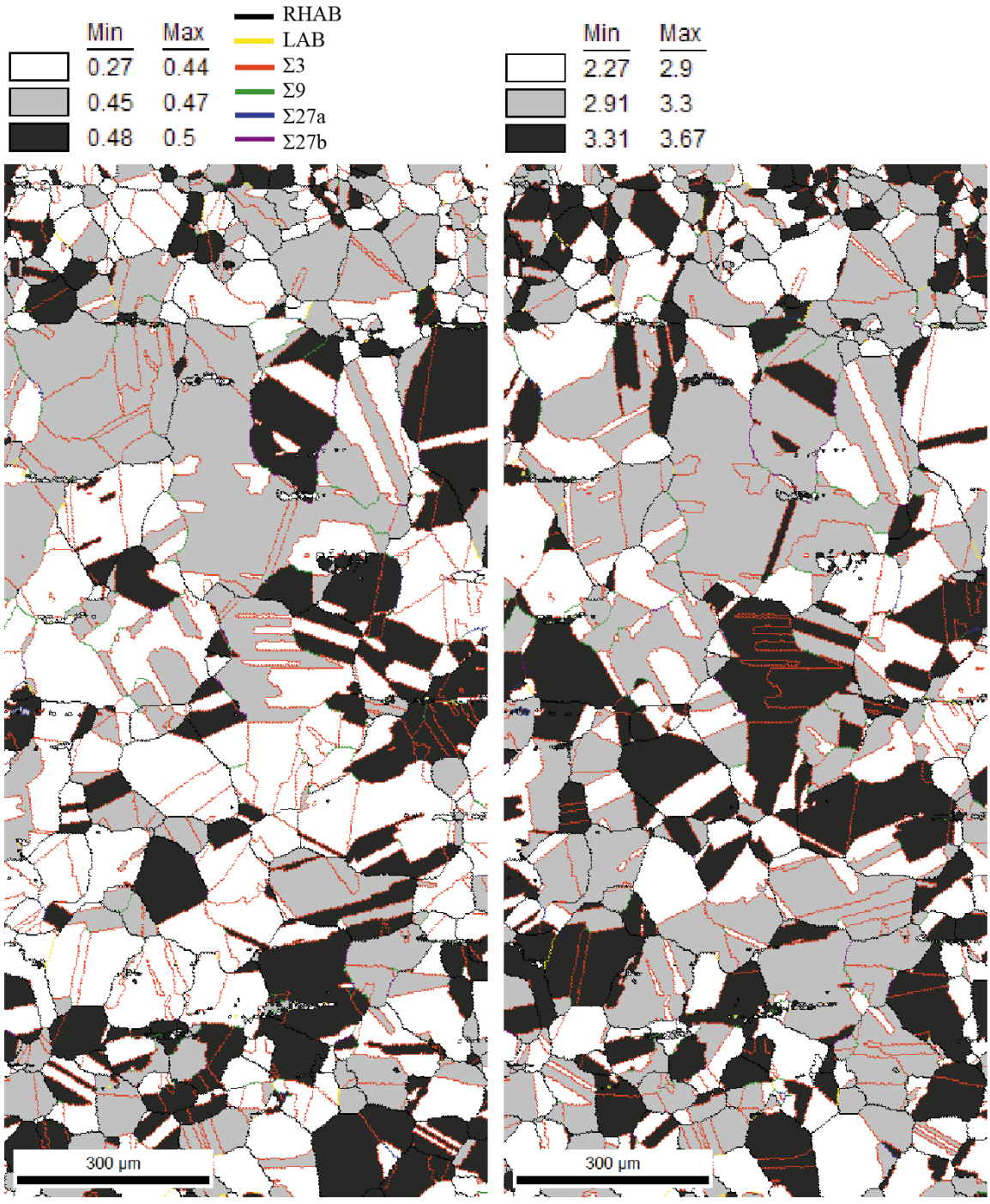

(a) (b)

Figure B.11 OIM™ maps of grain boundary characters and (a) Schmid factors and (b) Taylor factors from 7 dpa proton irradiated 316L specimens strained in 400˚C SCW (Specimen #1).

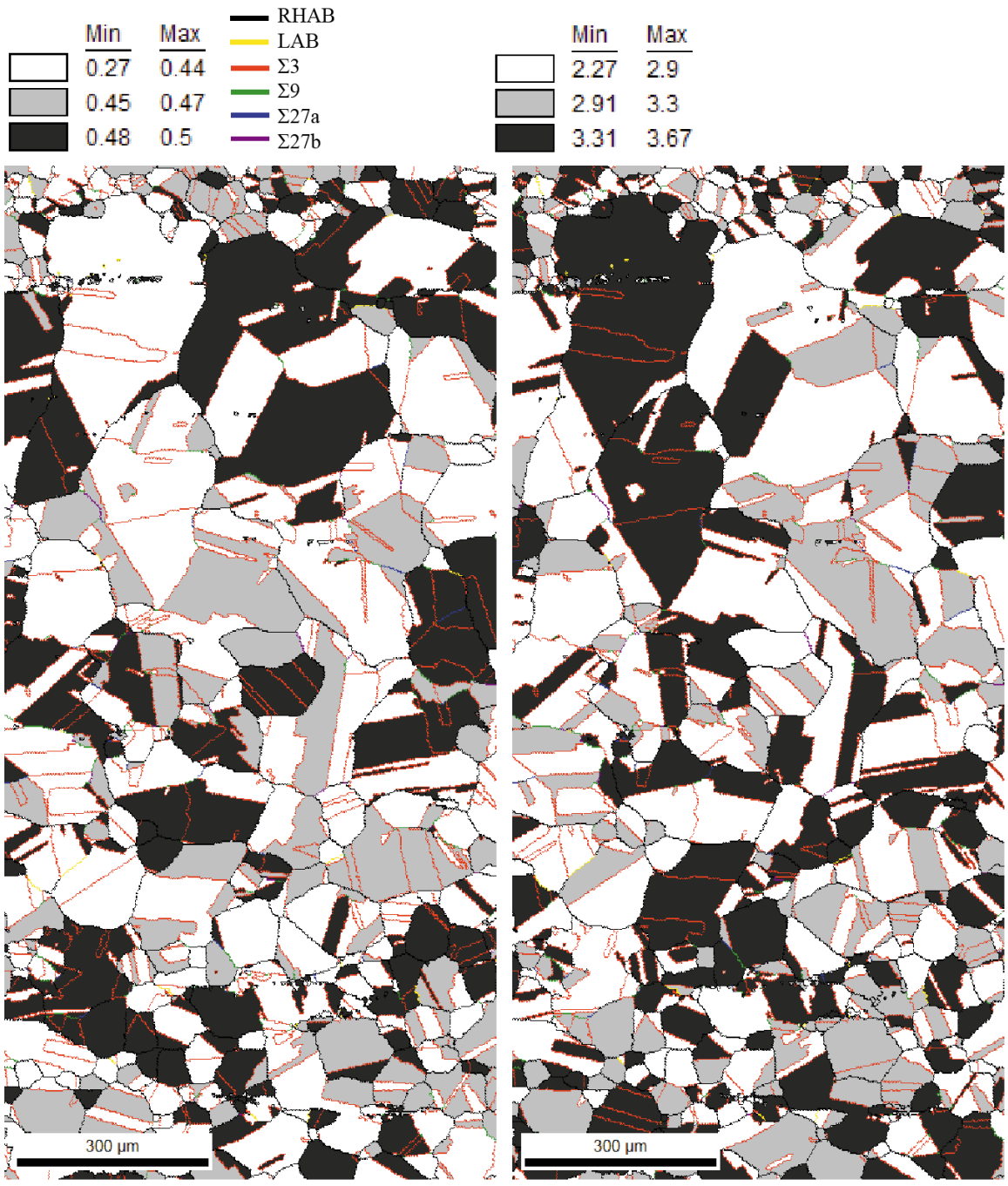

(a) (b)

Figure B.12 OIM™ maps of grain boundary characters and (a) Schmid factors and (b) Taylor factors from 7 dpa proton irradiated 316L specimens strained in 400˚C SCW (Specimen #1).

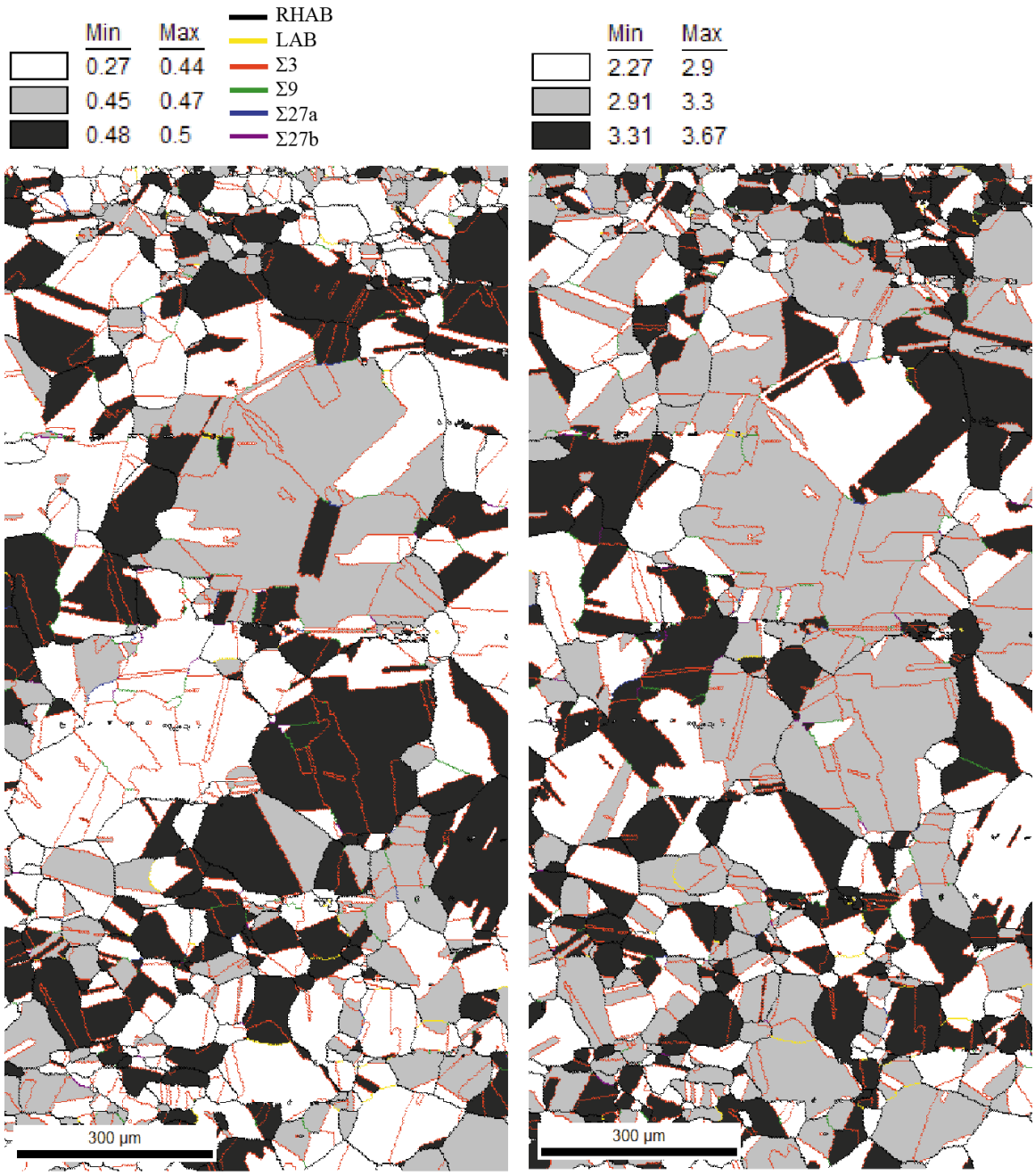

(a) (b)

Figure B.14 OIM™ maps of grain boundary characters and (a) Schmid factors and (b) Taylor factors from 7 dpa proton irradiated 316L specimens strained in 400˚C SCW (Specimen #1).

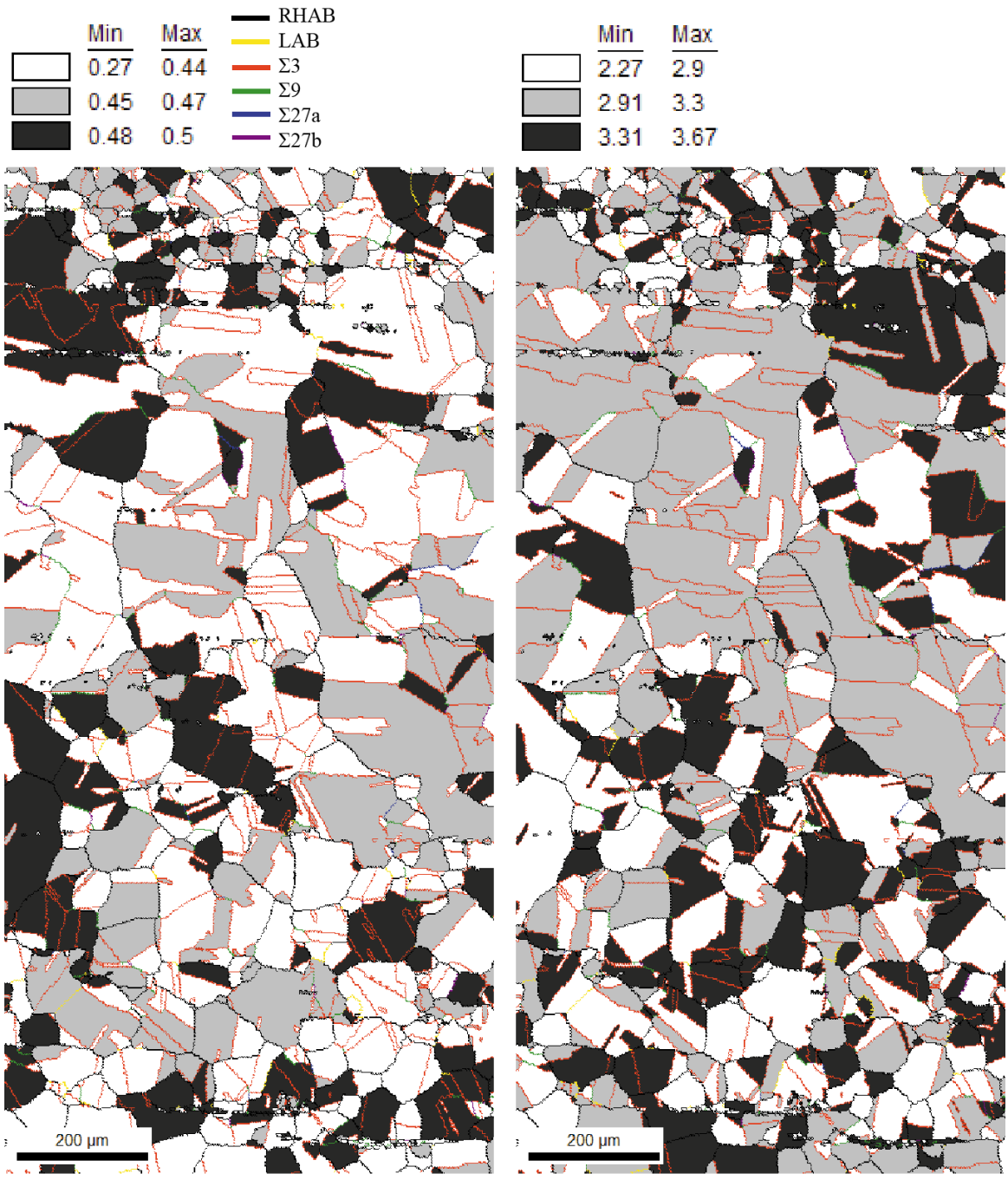

(a) (b)

Figure B.15 OIM™ maps of grain boundary characters and (a) Schmid factors and (b) Taylor factors from 7 dpa proton irradiated 316L specimens strained in 400˚C SCW (Specimen #1).

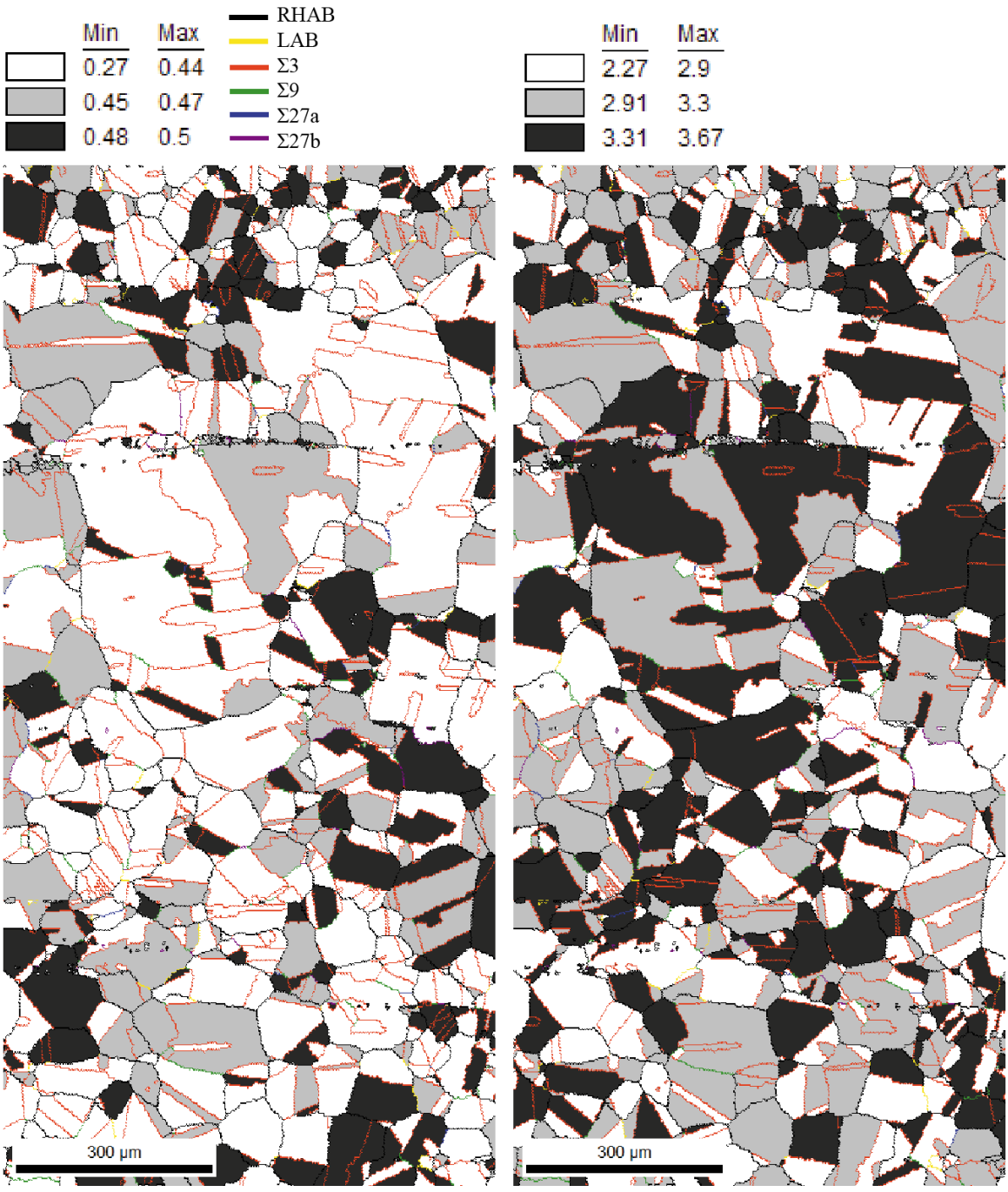

(a) (b)

Figure B.16 OIM™ maps of grain boundary characters and (a) Schmid factors and (b) Taylor factors from 7 dpa proton irradiated 316L specimens strained in 400˚C SCW (Specimen #1).

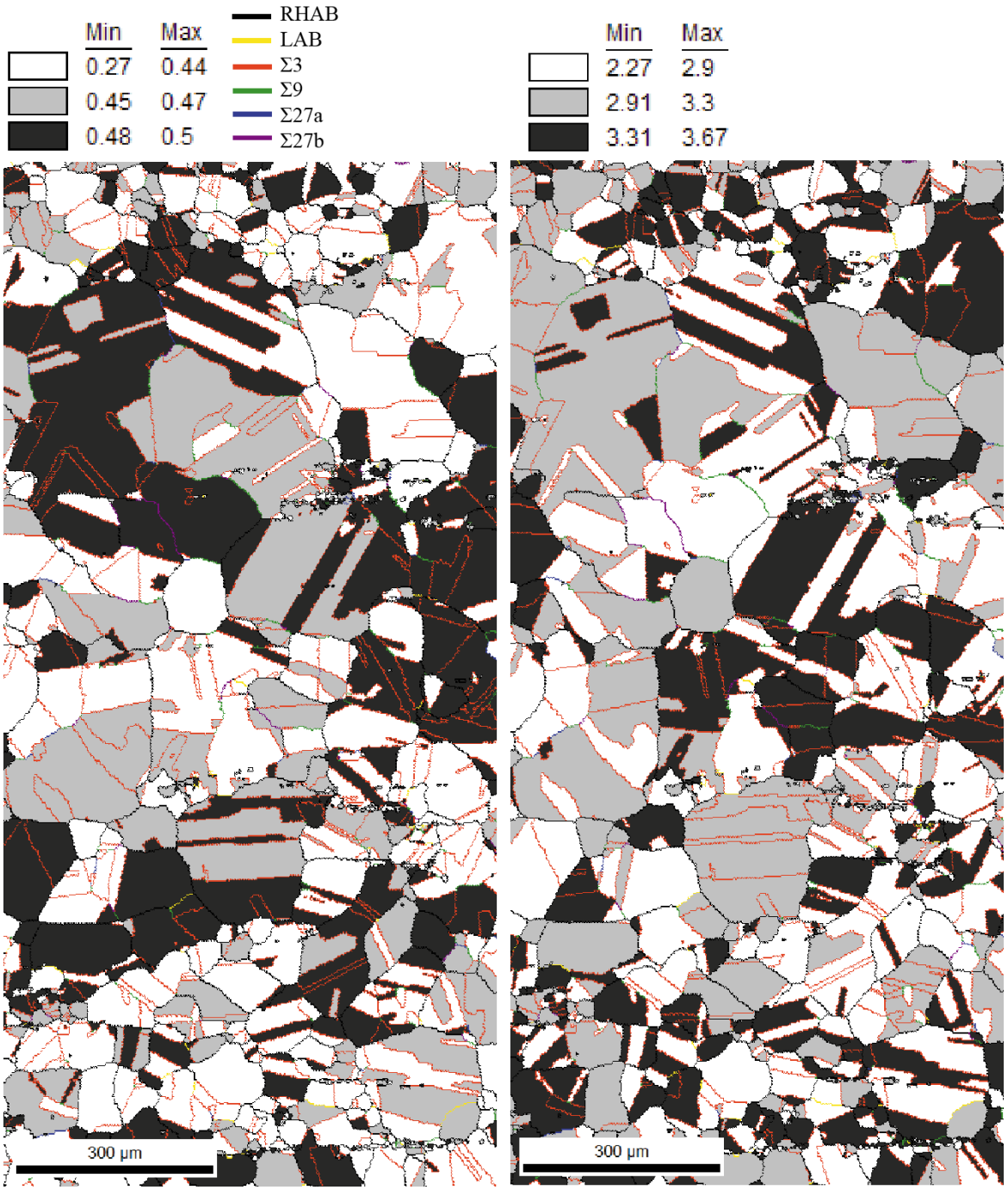

(a) (b)

Figure B.17 OIM™ maps of grain boundary characters and (a) Schmid factors and (b) Taylor factors from 7 dpa proton irradiated 316L specimens strained in 400˚C SCW (Specimen #1).

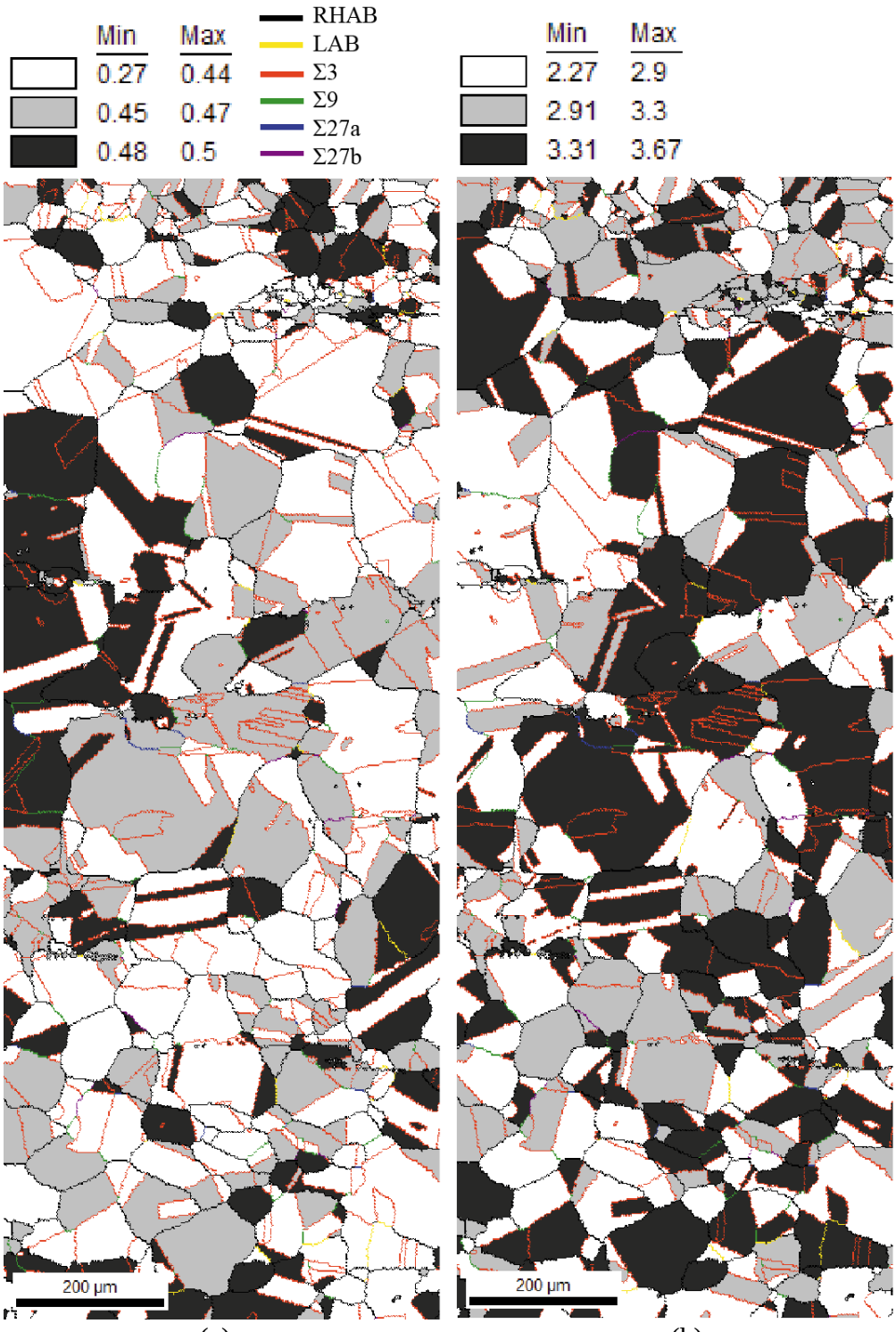

(a) (b)

Figure B.18 OIM™ maps of grain boundary characters and (a) Schmid factors and (b) Taylor factors from 7 dpa proton irradiated 316L specimens strained in 400˚C SCW (Specimen #1).

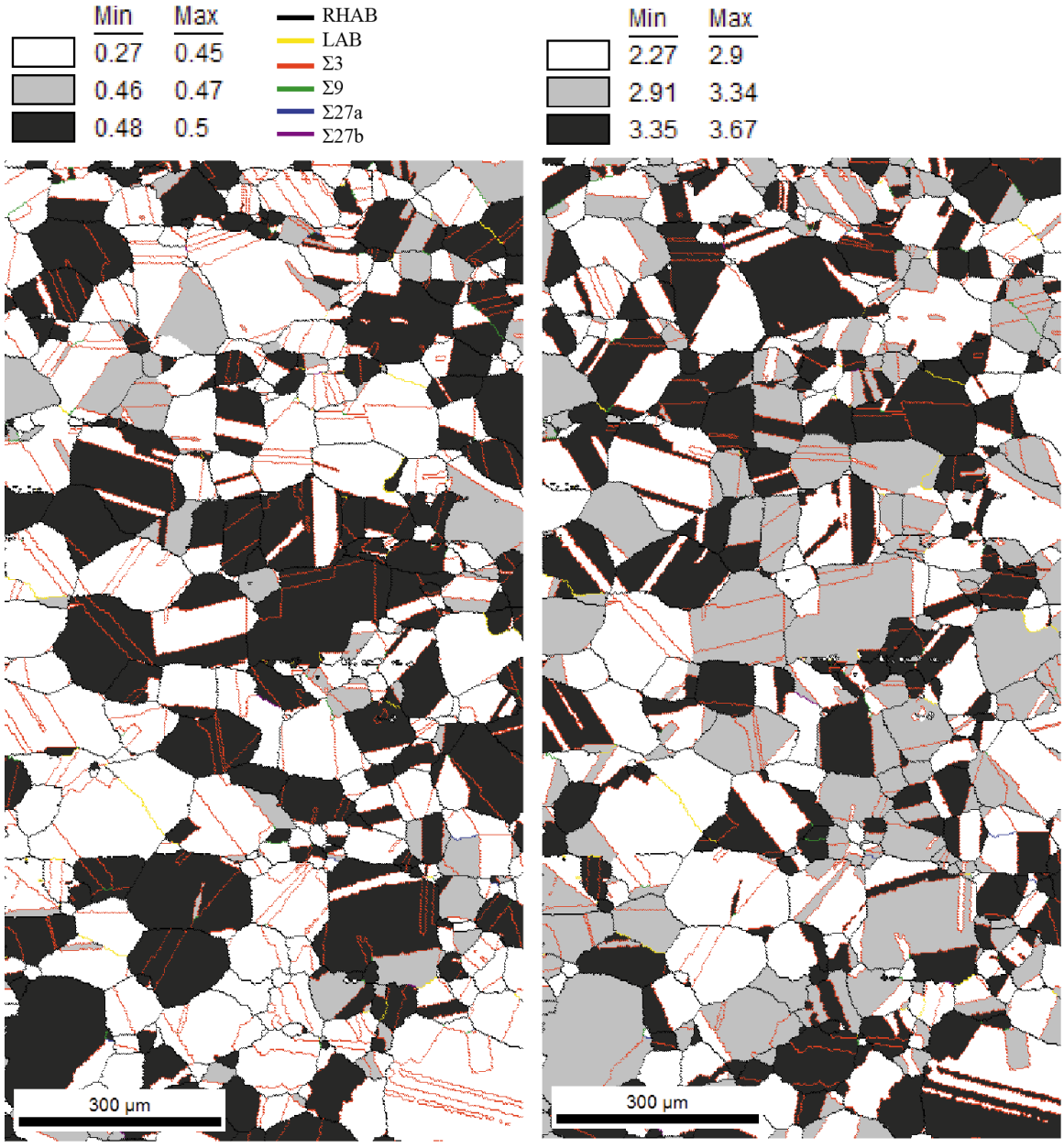

(a) (b)

Figure B.19 OIM™ maps of grain boundary characters and (a) Schmid factors and (b) Taylor factors from 7 dpa proton irradiated 316L specimens strained in 400˚C SCW (Specimen #2).

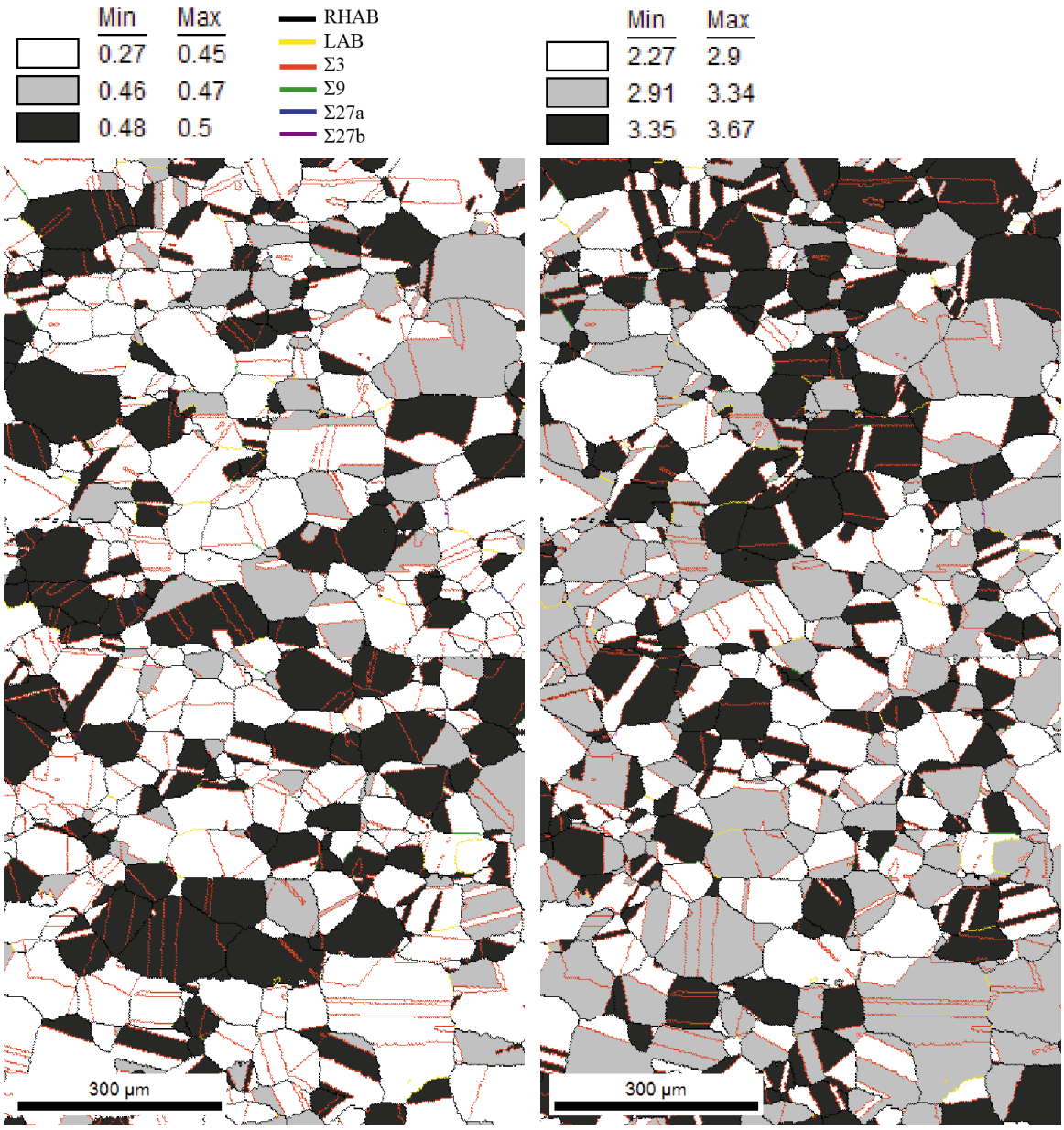

(a) (b)

Figure B.20 OIM™ maps of grain boundary characters and (a) Schmid factors and (b) Taylor factors from 7 dpa proton irradiated 316L specimens strained in 400˚C SCW (Specimen #2).

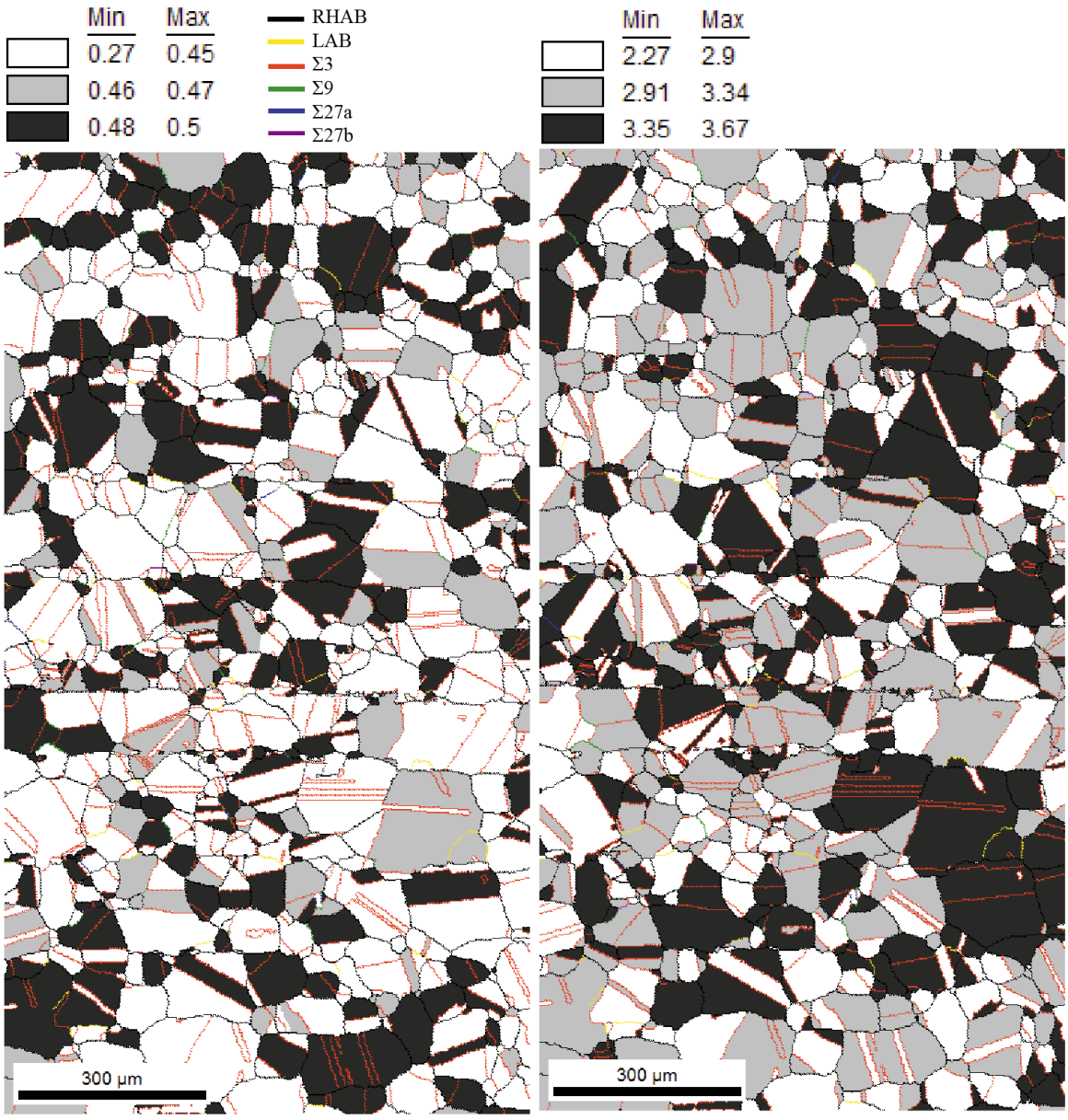

(a) (b)

Figure B.21 OIM™ maps of grain boundary characters and (a) Schmid factors and (b) Taylor factors from 7 dpa proton irradiated 316L specimens strained in 400˚C SCW (Specimen #2).

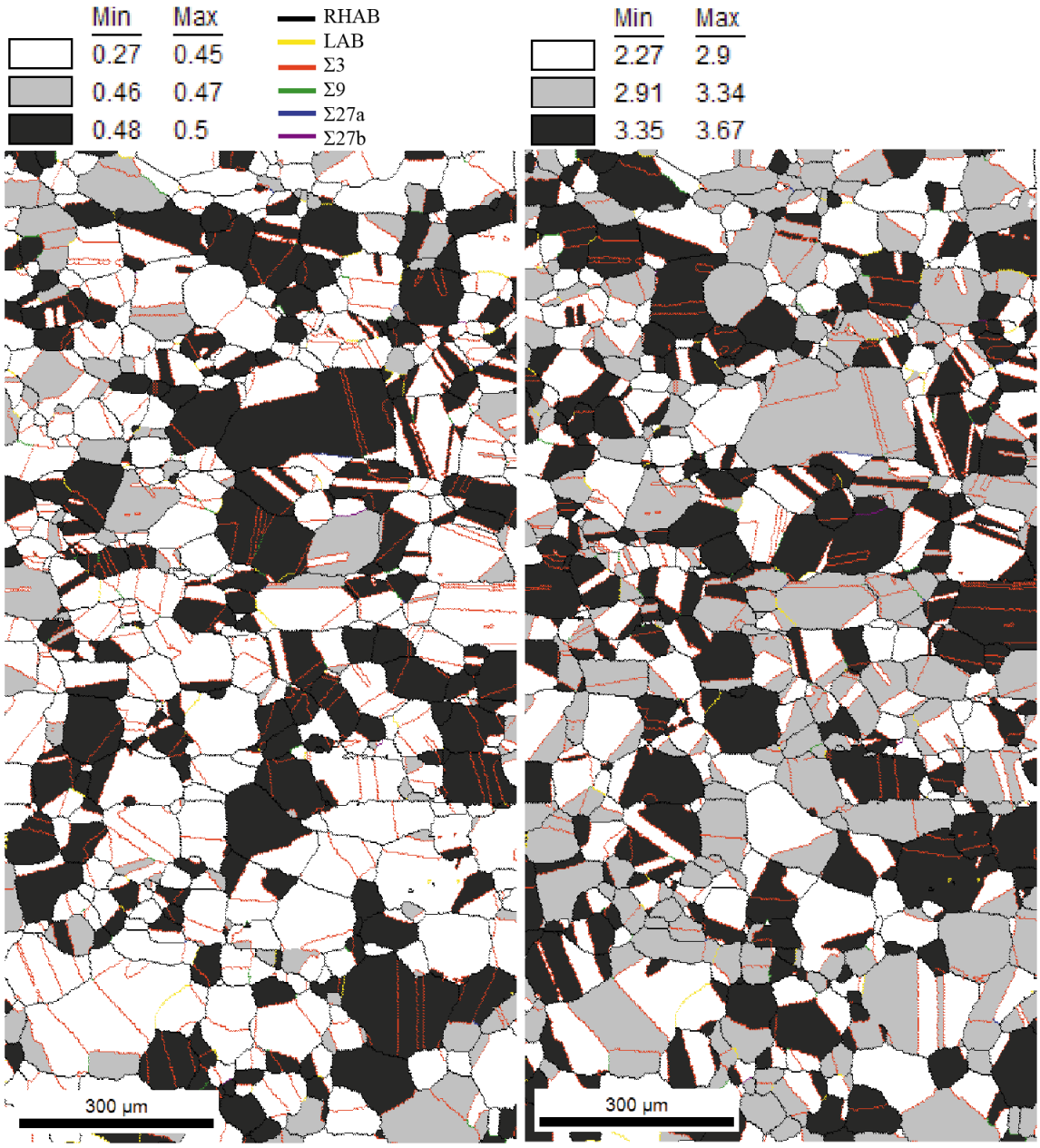

(a) (b)

Figure B.22 OIM™ maps of grain boundary characters and (a) Schmid factors and (b) Taylor factors from 7 dpa proton irradiated 316L specimens strained in 400˚C SCW (Specimen #2).

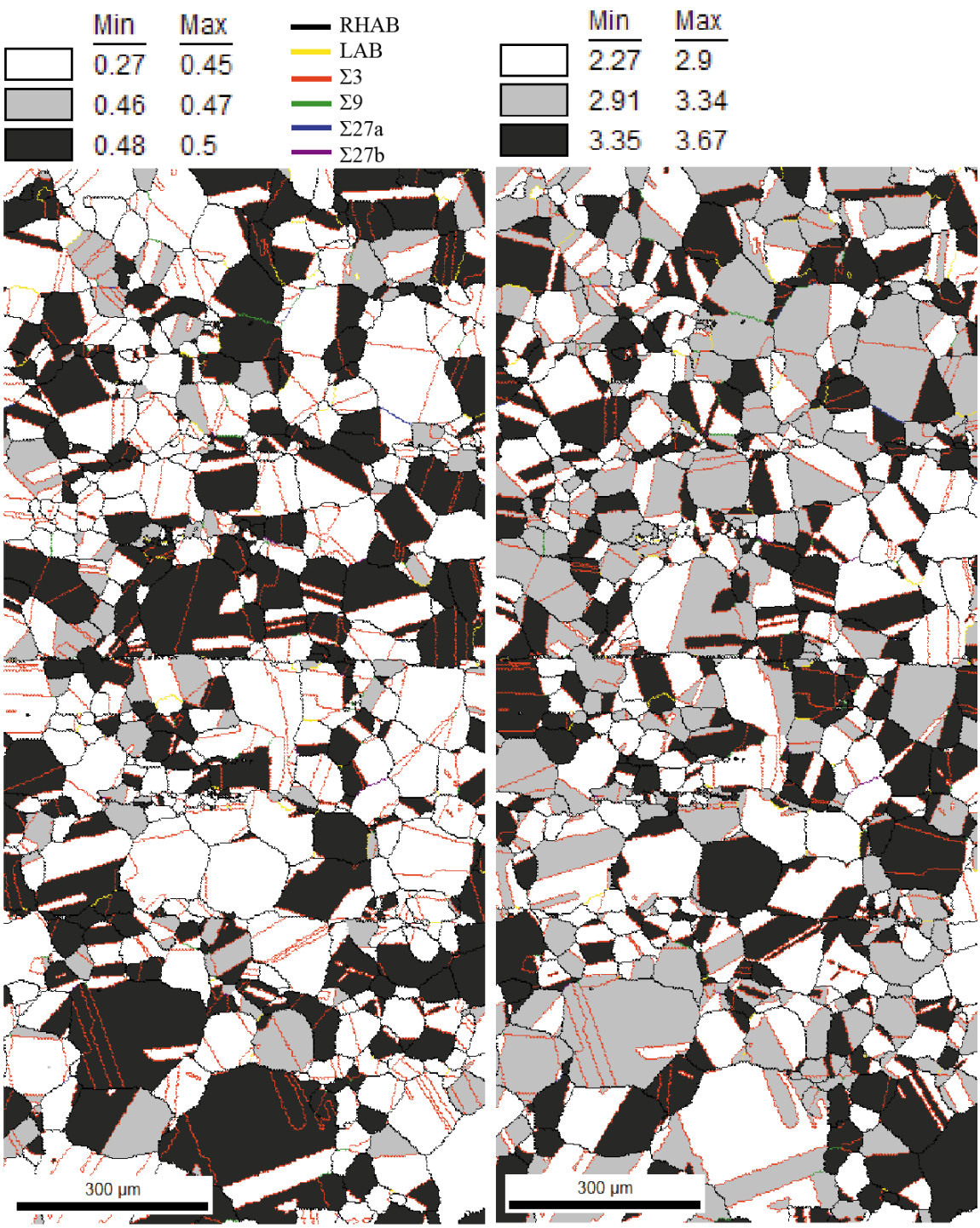

(a) (b)

Figure B.23 OIM™ maps of grain boundary characters and (a) Schmid factors and (b) Taylor factors from 7 dpa proton irradiated 316L specimens strained in 400˚C SCW (Specimen #2).

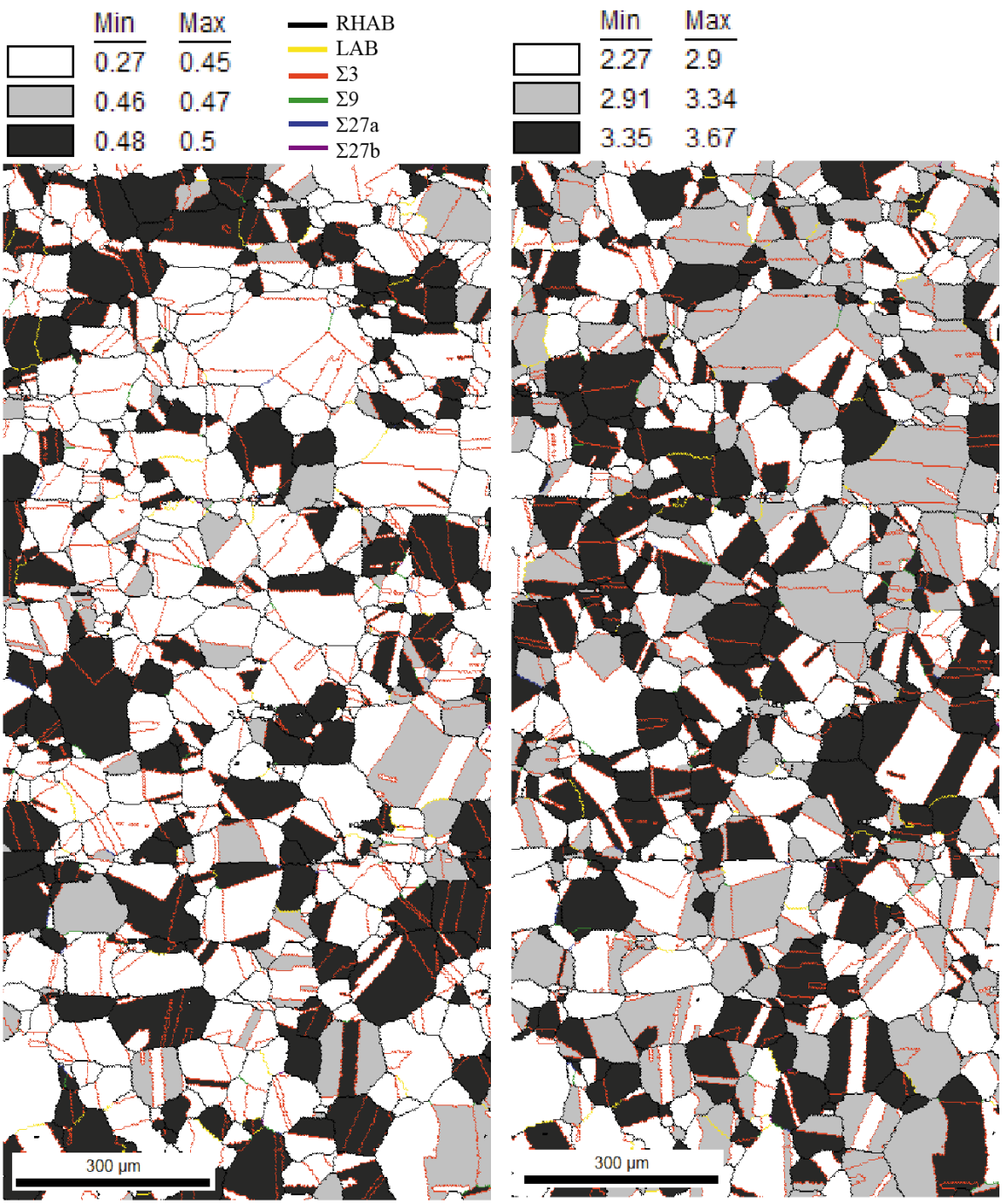

(a) (b)

Figure B.24 OIM™ maps of grain boundary characters and (a) Schmid factors and (b) Taylor factors from 7 dpa proton irradiated 316L specimens strained in 400˚C SCW (Specimen #2).

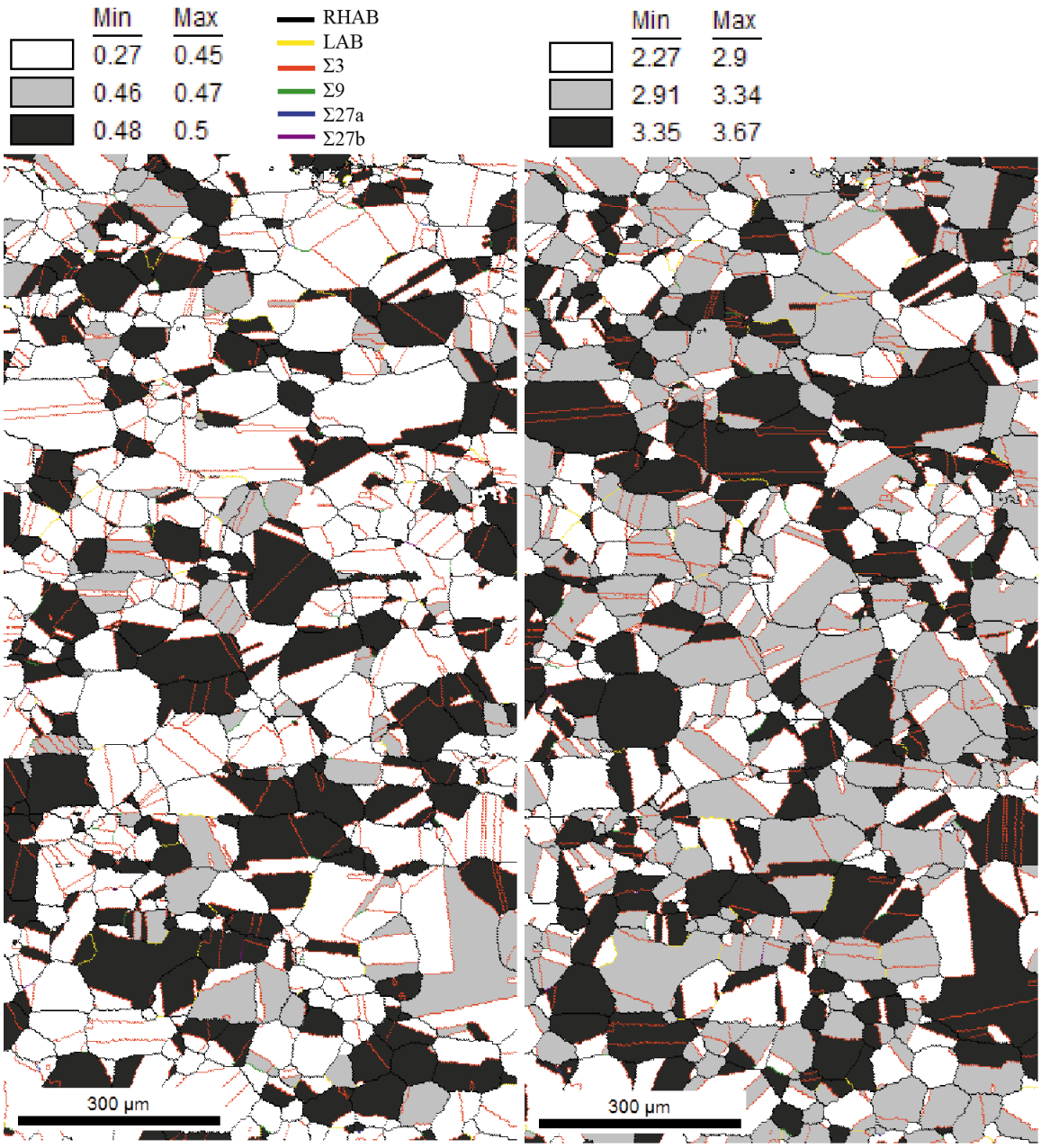

(a) (b)

Figure B.25 OIM™ maps of grain boundary characters and (a) Schmid factors and (b) Taylor factors from 7 dpa proton irradiated 316L specimens strained in 400˚C SCW (Specimen #2).

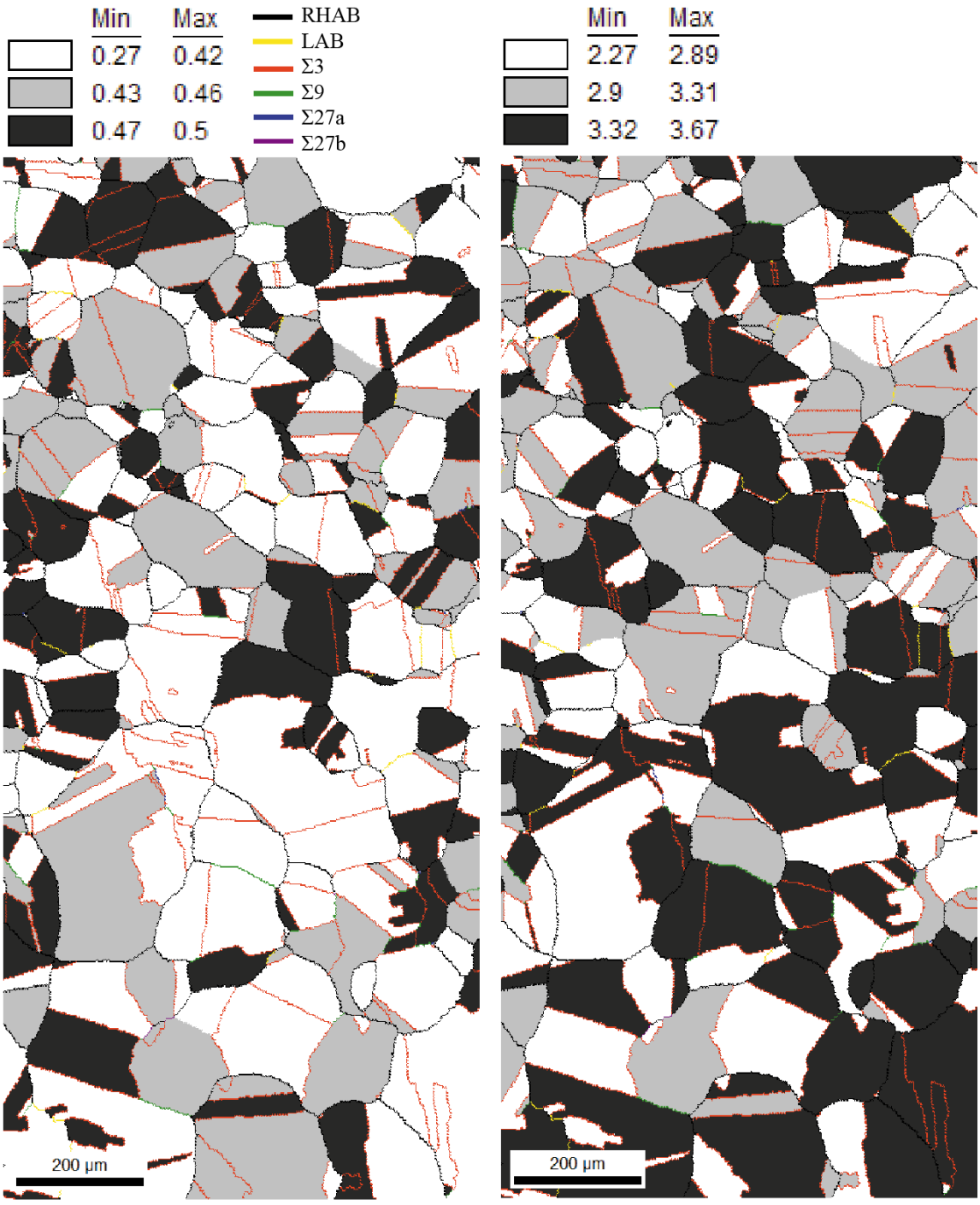

(a) (b)

Figure B.26 OIM™ maps of grain boundary characters and (a) Schmid factors and (b) Taylor factors from 7 dpa proton irradiated 316L specimens strained in 400˚C SCW (Specimen #3).

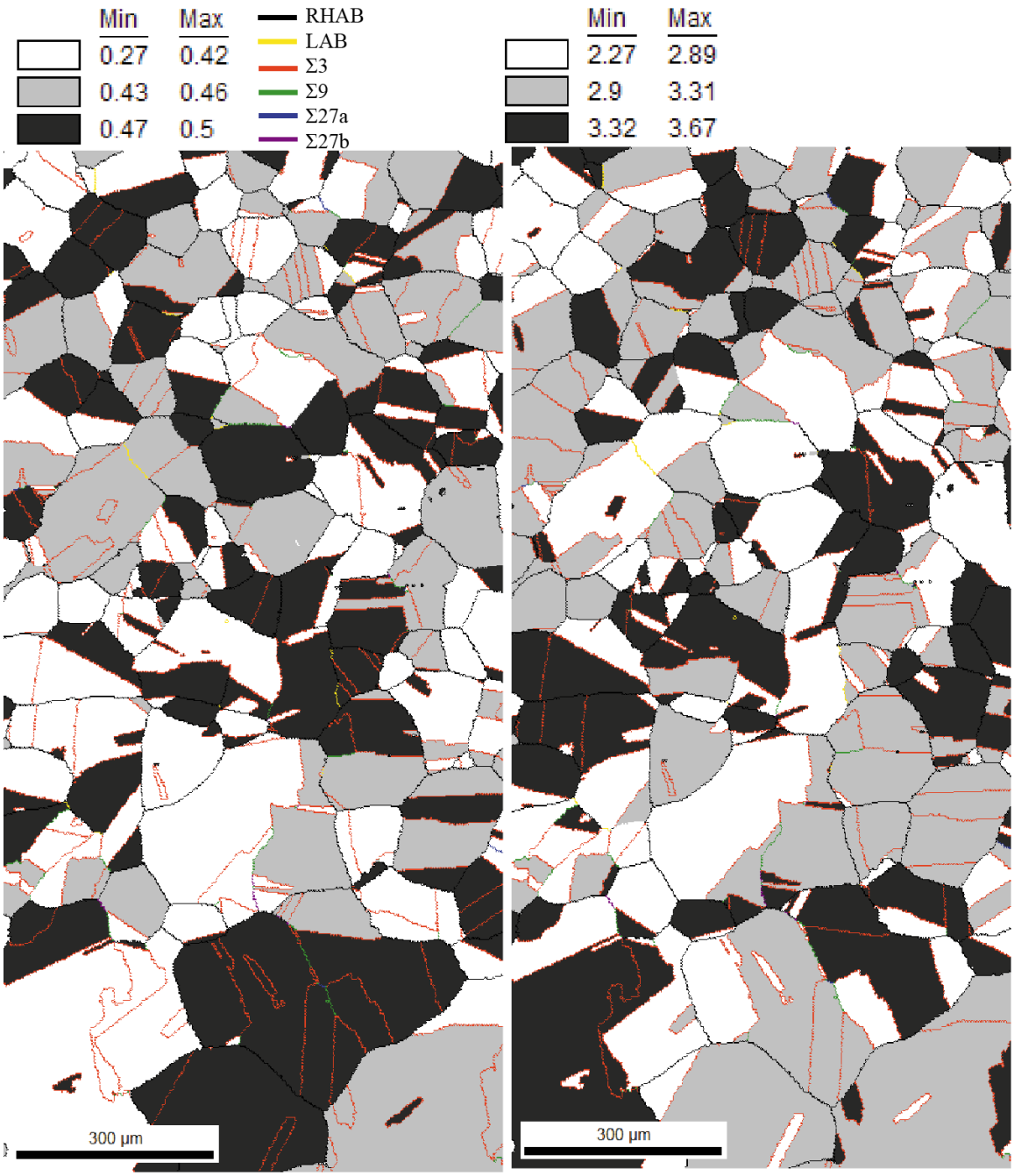

(a) (b)

Figure B.27 OIM™ maps of grain boundary characters and (a) Schmid factors and (b) Taylor factors from 7 dpa proton irradiated 316L specimens strained in 400˚C SCW (Specimen #3).

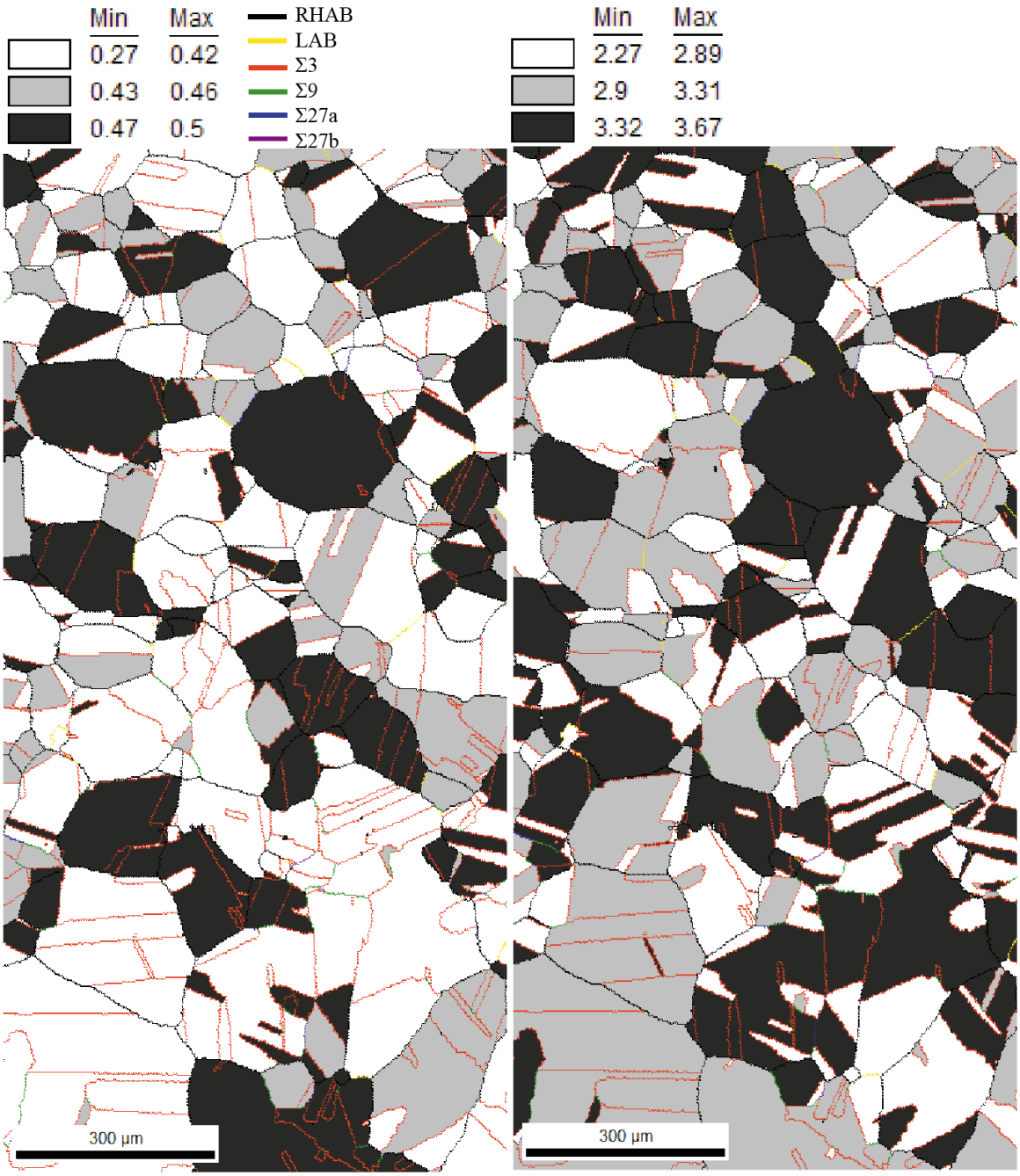

(a) (b)

Figure B.28 OIM™ maps of grain boundary characters and (a) Schmid factors and (b) Taylor factors from 7 dpa proton irradiated 316L specimens strained in 400˚C SCW (Specimen #3).

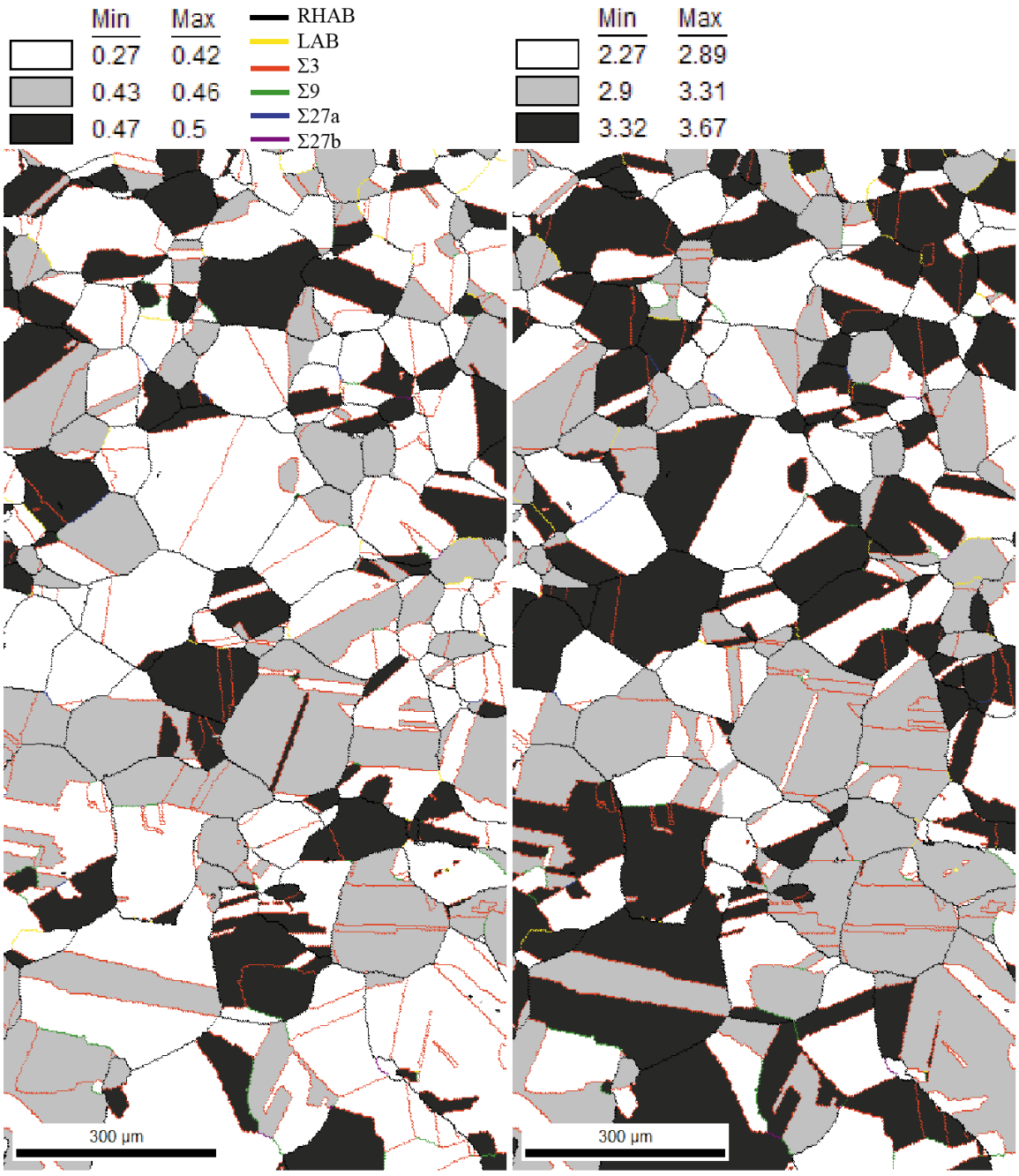

(a) (b)

Figure B.29 OIM™ maps of grain boundary characters and (a) Schmid factors and (b) Taylor factors from 7 dpa proton irradiated 316L specimens strained in 400˚C SCW (Specimen #3).

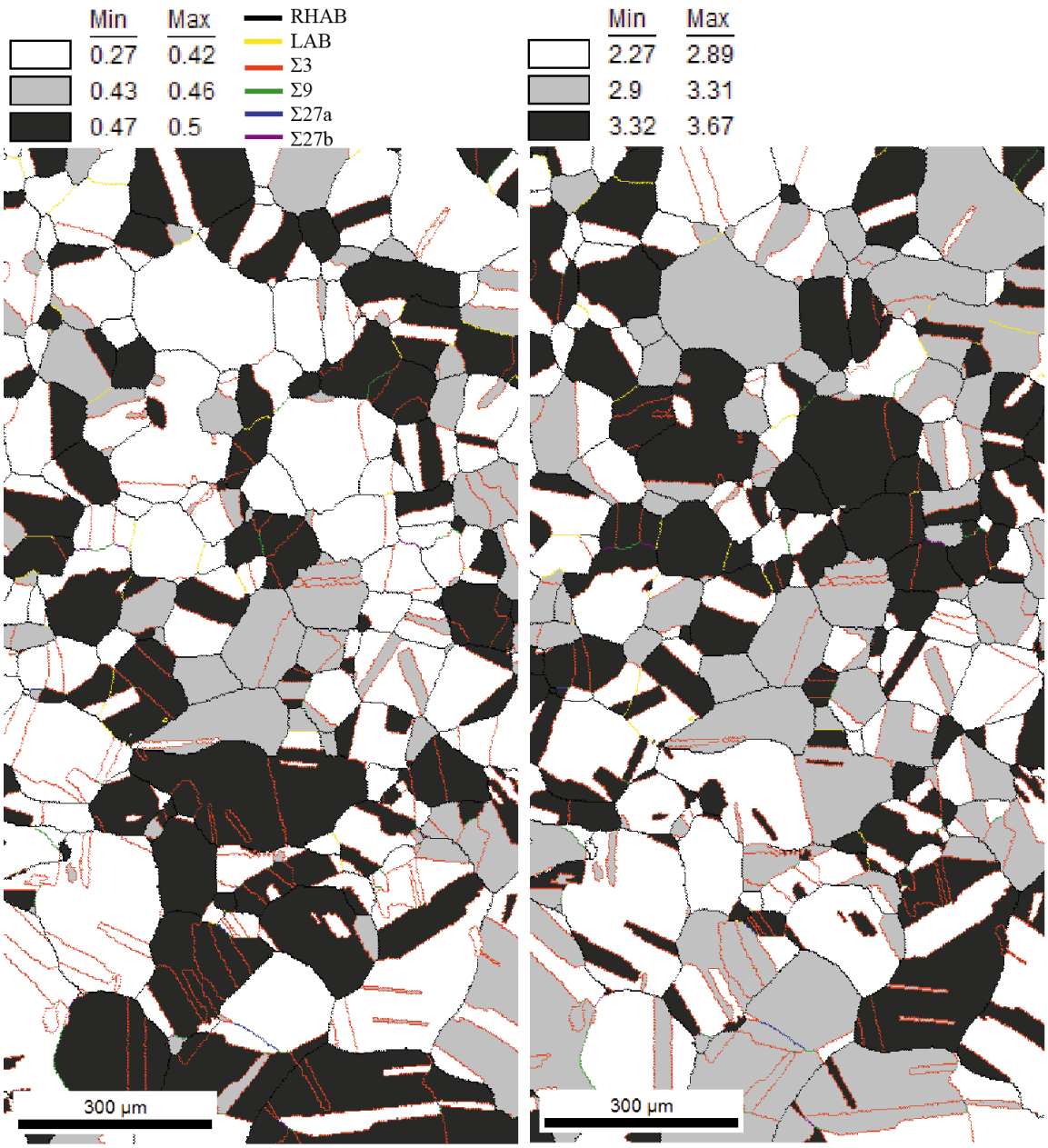

(a) (b)

Figure B.30 OIM™ maps of grain boundary characters and (a) Schmid factors and (b) Taylor factors from 7 dpa proton irradiated 316L specimens strained in 400˚C SCW (Specimen #3).

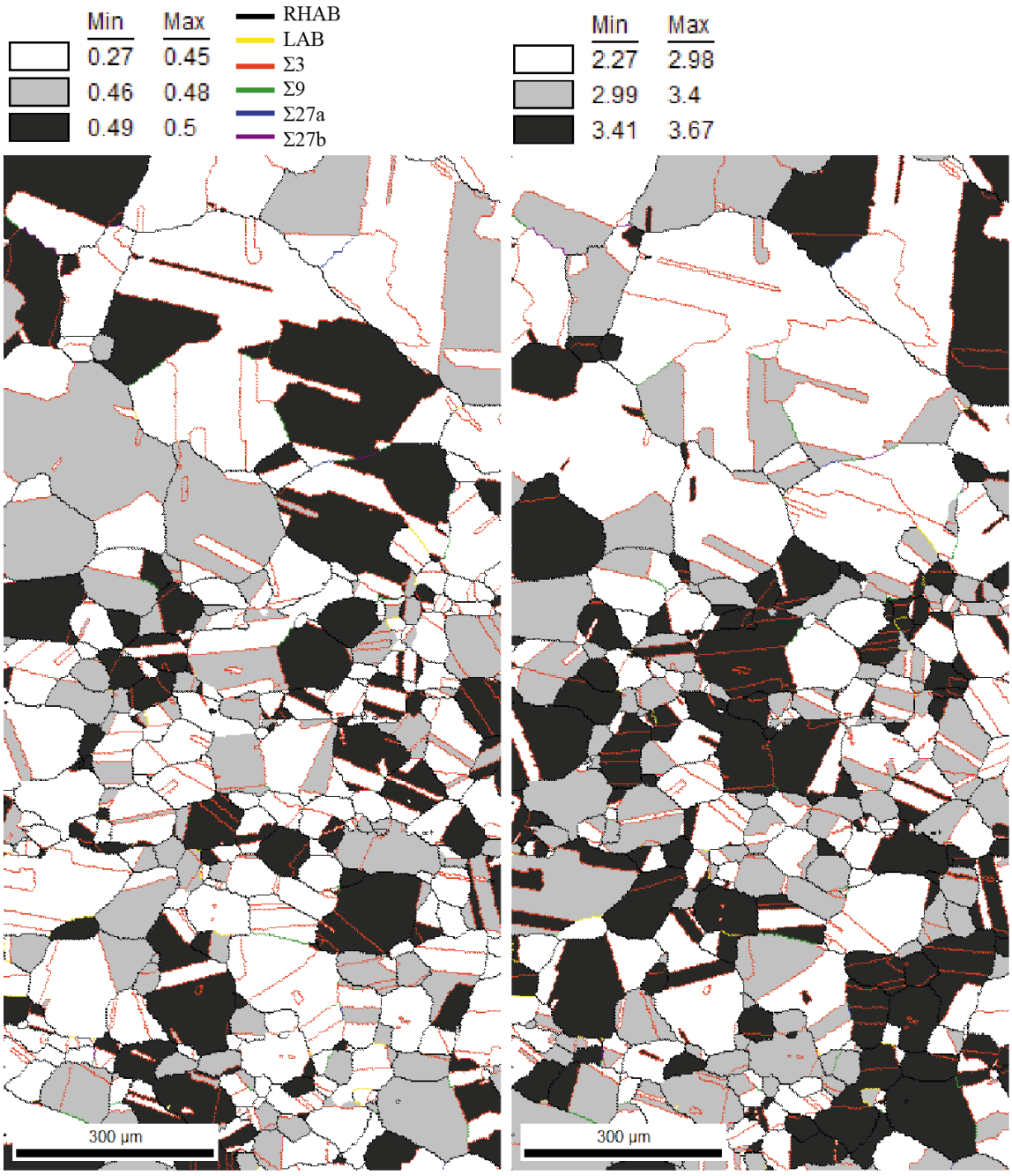

(a) (b)

Figure B.31 OIM™ maps of grain boundary characters and (a) Schmid factors and (b) Taylor factors from 7 dpa proton irradiated 316L specimens strained in 400˚C SCW (Specimen #4).

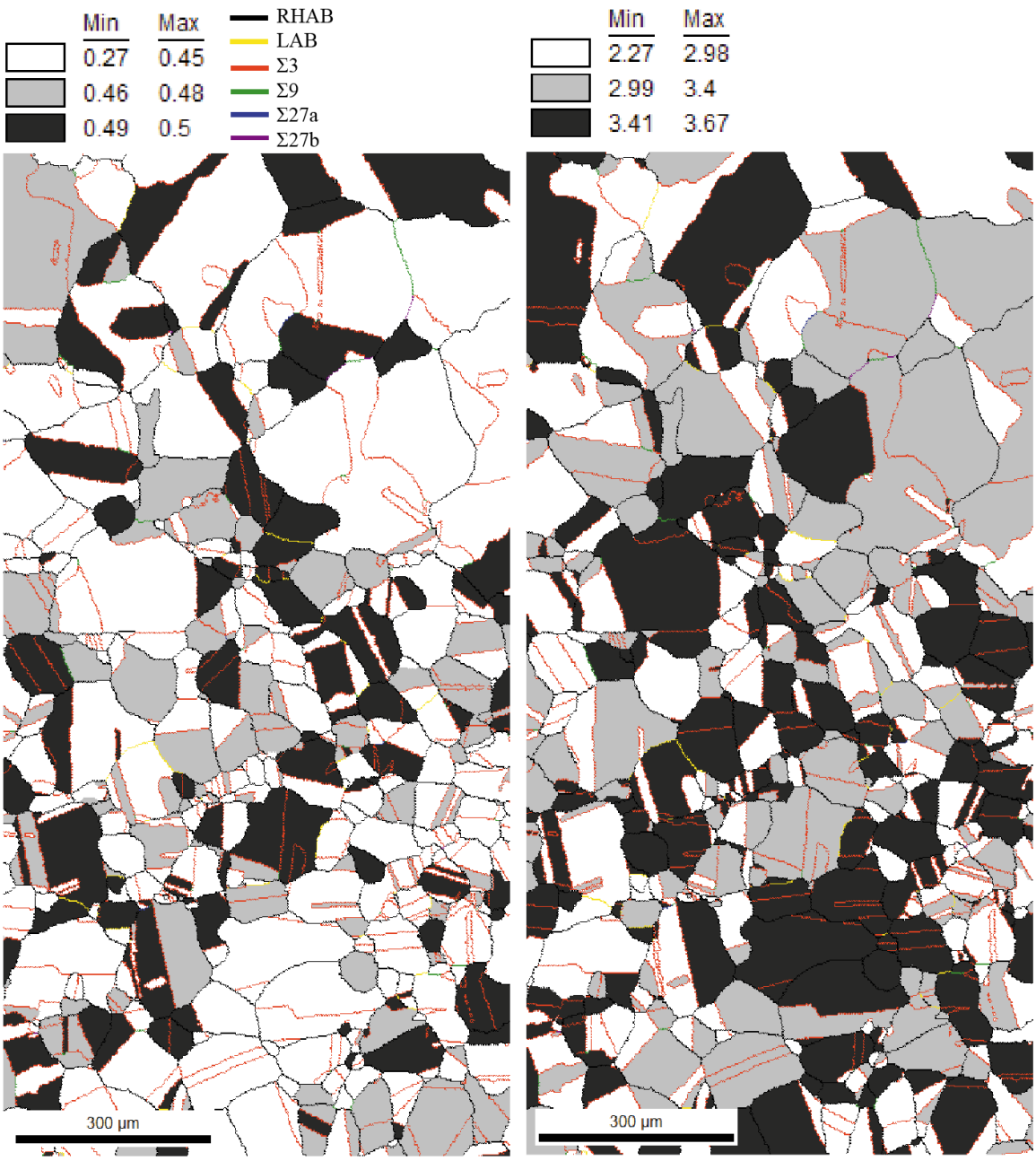

(a) (b)

Figure B.32 OIM™ maps of grain boundary characters and (a) Schmid factors and (b) Taylor factors from 7 dpa proton irradiated 316L specimens strained in 400˚C SCW (Specimen #4).

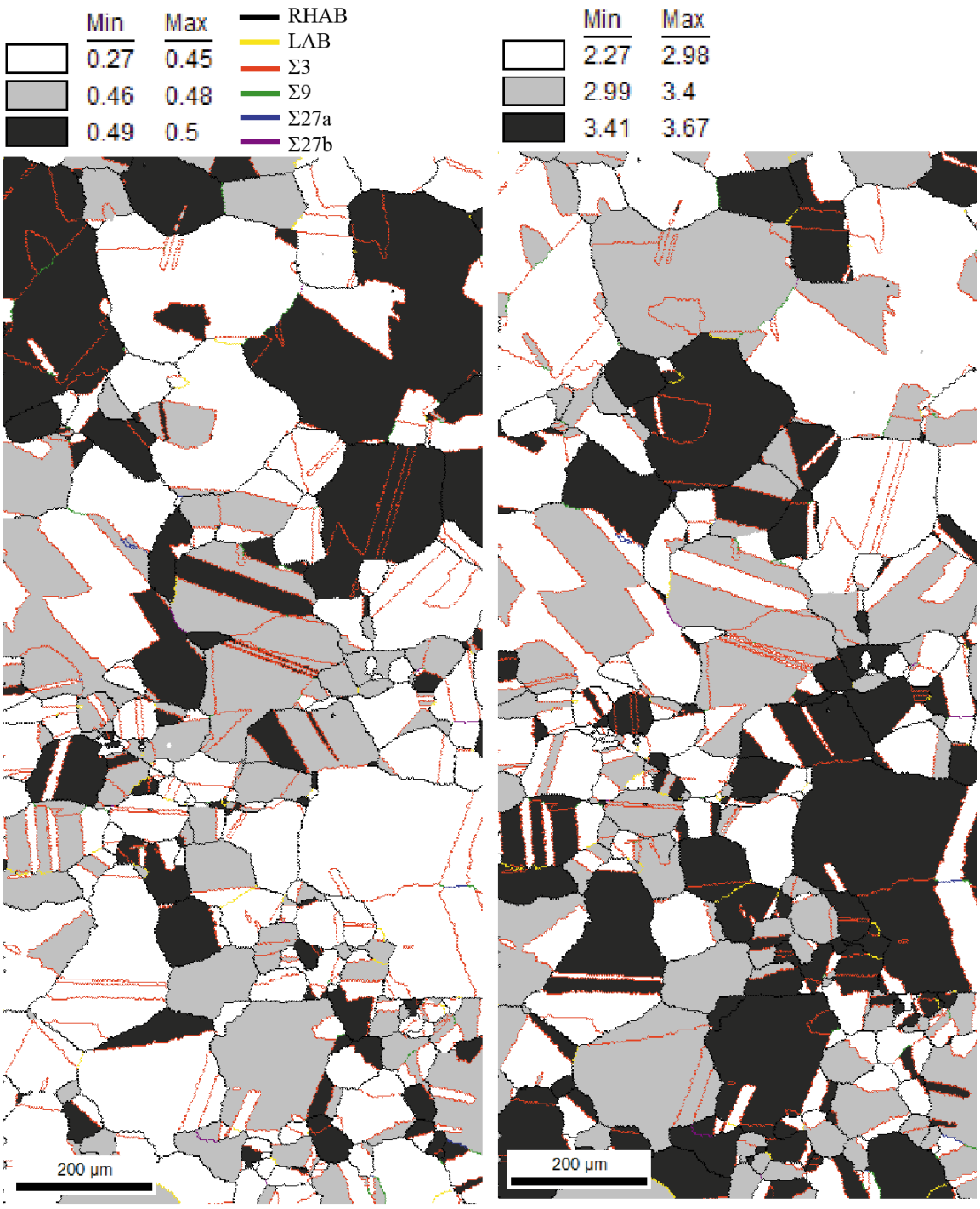

(a) (b)

Figure B.33 OIM™ maps of grain boundary characters and (a) Schmid factors and (b) Taylor factors from 7 dpa proton irradiated 316L specimens strained in 400˚C SCW (Specimen #4).

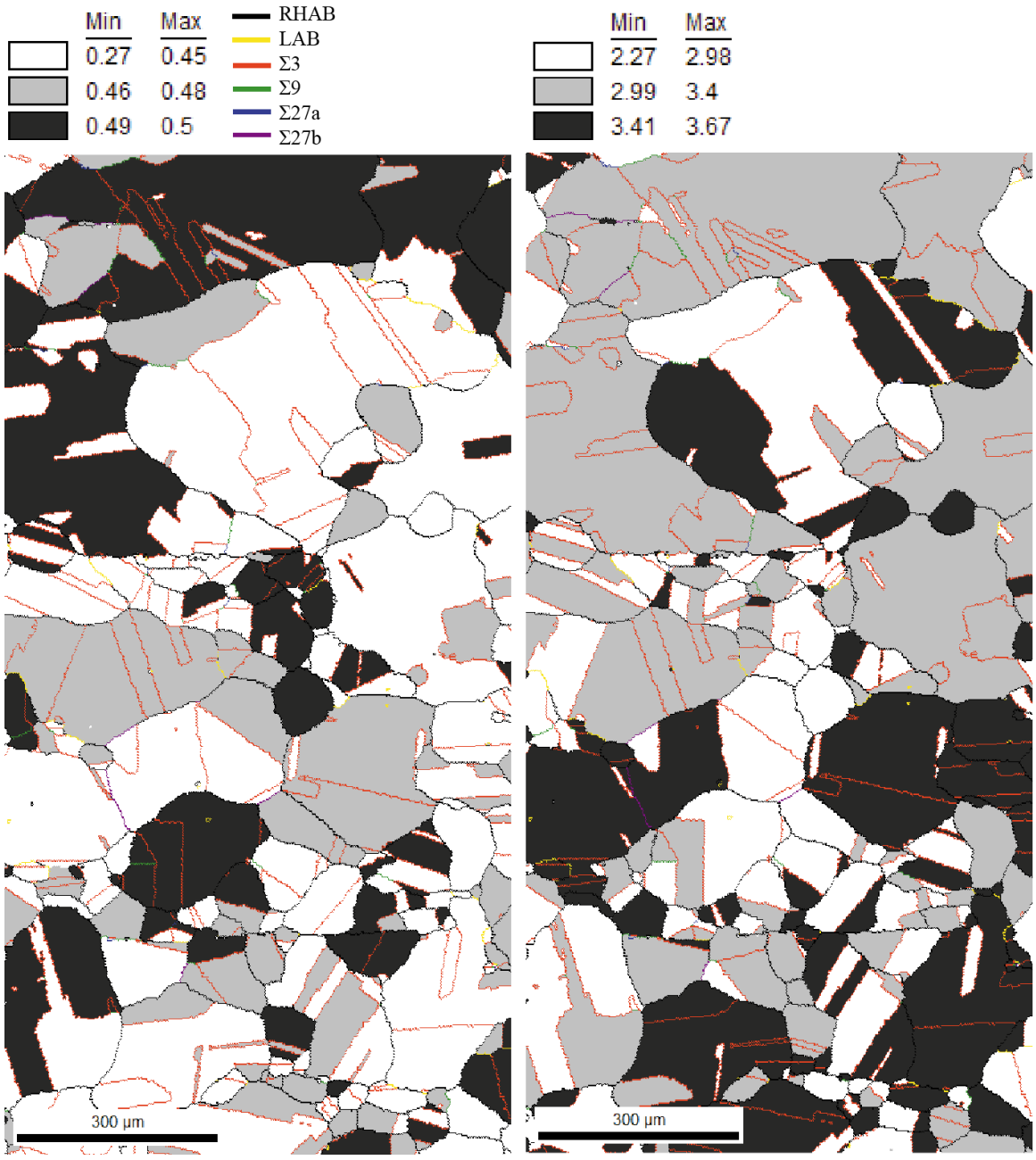

(a) (b)

Figure B.34 OIM™ maps of grain boundary characters and (a) Schmid factors and (b) Taylor factors from 7 dpa proton irradiated 316L specimens strained in 400˚C SCW (Specimen #4).

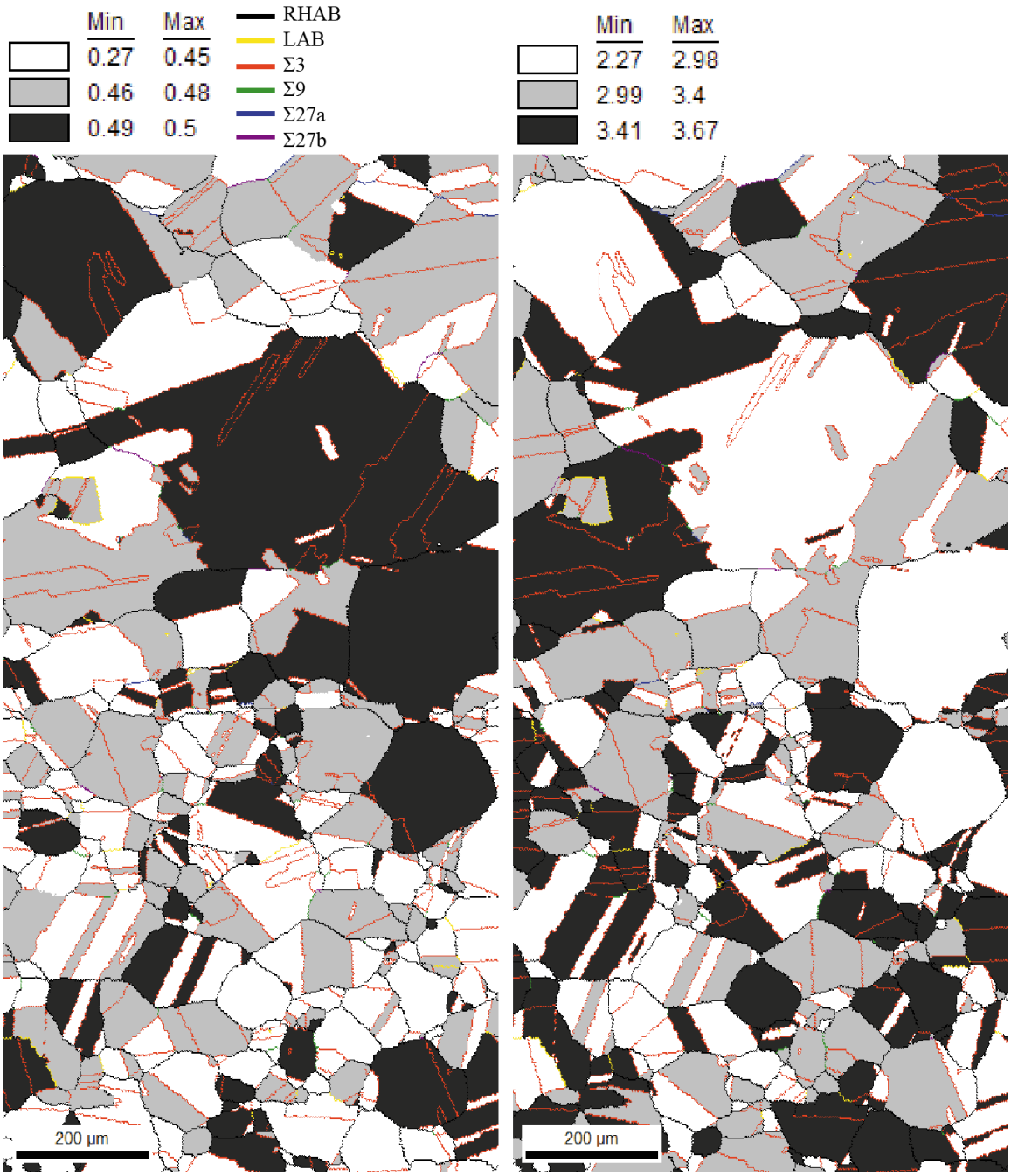

(a) (b)

Figure B.35 OIM™ maps of grain boundary characters and (a) Schmid factors and (b) Taylor factors from 7 dpa proton irradiated 316L specimens strained in 400˚C SCW (Specimen #4).

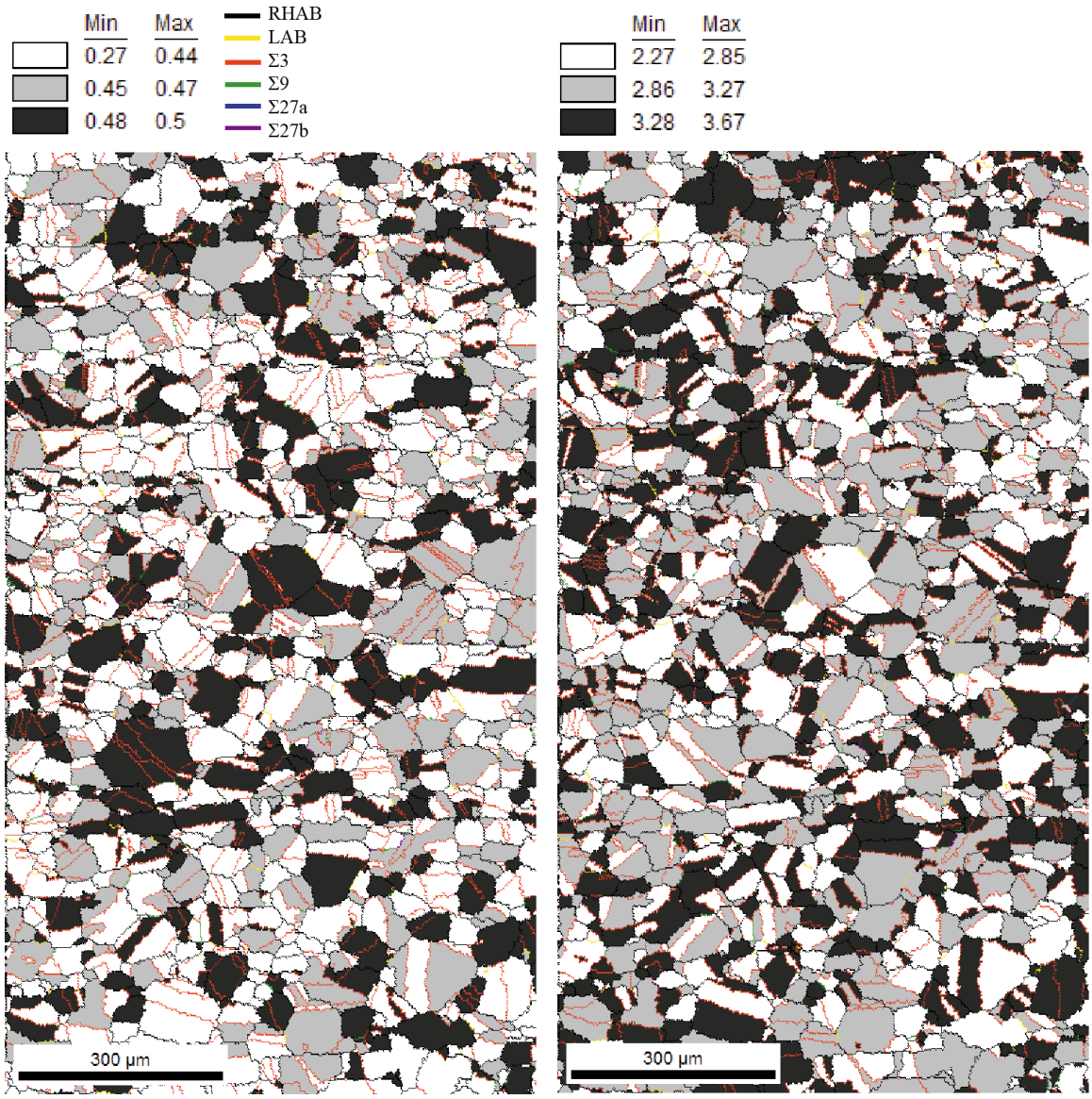

(a) (b)

Figure B.35 OIM™ maps of grain boundary characters and (a) Schmid factors and (b) Taylor factors from 7 dpa proton irradiated 316L specimens strained in 400˚C argon.

APPENDIX C

AFM Measurements

Table C.1 AFM measurements on grains of proton irradiated 316L stainless steel following straining to 2% and 5% in 400˚C SCW.

% Strain	m	M	Individual step height measurements (nm)
2	0.46	3.54	659,203,374,243,404,292,496
2	0.45	3.57	306,186,243,202,272,197,101
2	0.43	3.61	361,622,227,201,849,192
2	0.44	3.63	628,175,495,141,69,477,154,669,452,91,499,90,387,324,125,204
2	0.39	3.47	277,367,38,91,528,67,119,284,56,198
2	0.48	3.41	337,139,266,828
2	0.46	3.54	314,124,467,177,388,172,279,402,67,228
2	0.48	3.42	214,214,160,246,193,63,303,358,147,338,305,132,262,149,247,154,244
2	0.48	2.42	147,112,191,128,99
2	0.47	2.41	259,225,108,204,311,89
2	0.43	2.34	177,100,140,143,9
2	0.48	2.42	275,324,461,296
2	0.46	2.59	291,333,356,366,164
2	0.5	2.78	75,48,117,209,52,84
2	0.49	2.55	304,354,269
2	0.5	2.71	495,460,391,275
2	0.45	2.34	392,231,303
2	0.49	2.8	112,48,61,21,122,86,28,118,78,168
2	0.47	2.4	407,182,543,293,607
2	0.47	2.72	86,25,39,42,37,62,24,33,34
2	0.47	2.89	109,258,417,108
2	0.46	2.83	399,364,170,75,13

% Strain	m	M	Individual step height measurements (nm)
2	0.49	2.8	204,203,54,362
2	0.48	3.3	93,563,226,489,197,207
2	0.44	3.14	47,52,69,85,63,71,146
2	0.49	3.3	199,257,342,294,118,237,318,203,195,258,223
2	0.5	2.93	168,295,453,536,281
2	0.49	3.11	388,504,361,248,52,146,317
2	0.47	3.48	275,183,501,237,71,508,137,286,484,142,221
2	0.49	3.21	369,154,236,266,118,69,157,259
2	0.44	3.23	165,316,262,205,270,303
2	0.5	3.12	304,250,303,183,140,221
2	0.49	3.33	108,309,50,313,313,114,341,262,196,111,150,107
2	0.49	3.2	583,479,437,495,178,512,433
2	0.49	3.23	175,191,253,233,389
2	0.5	3.07	412,410,333,296
2	0.46	3.27	124,308,290,31,413,38,335,177
2	0.48	2.94	299,227,334,421
5	0.46	3.54	282,65,249,35,331,86,287,279,284,496,143,277,241,70,335,183,252,105,336,227,247,160,446,267,323
5	0.45	3.57	159,350,337,166,54,73,74,22,278,180,77,278,210,116,170
5	0.43	3.61	419,139,249,353,348,497,73,443,202,270,266,93,214,134,159,303,437
5	0.44	3.63	594,557,177,584,134,360,477,110,544,377,680,376,71,395,348,291,420,192,168,323,75,276,125,253,105,254,271,91
5	0.39	3.47	413,43,71,108,43,48,33,631,12,387,49,225,20,211,207,322,166,287
5	0.48	3.41	433,461,659,146,373,170,393,429
5	0.46	3.54	231,95,40,160,479,316,116,301,309,126,443,240,242,234,525,287,373,211,392
5	0.48	3.42	356,151,475,405,111,506,455,298,100,33,193,243
5	0.48	2.42	186,275,447,294,357,257,440,408,438,288,126

% Strain	m	M	Individual step height measurements (nm)
5	0.47	2.41	243,266,457,368,378,285,166,385
5	0.43	2.34	143,300,64,254,140,93,164,78
5	0.48	2.42	419,1064,249,431
5	0.46	2.59	103,132,240,252,327,239,369,250
5	0.5	2.78	56,428,348,75,68,206,307,253,288
5	0.49	2.55	356,151,475,405,111,506,455,298,100,33,193,243
5	0.5	2.71	148,273,411,531,145,246,428,197,217,521,29,260
5	0.45	2.34	247,93,141,71,104,212,135,180,128,192,48,543,204
5	0.49	2.8	96,37,129,63,20,109,170,118,112,63,196,132,273
5	0.47	2.4	428,377,294,402,123,427,451,208
5	0.47	2.72	115,31,23,49,110,159,133,59,56,93,132,65,29,92,90,69,73,130,55,55
5	0.47	2.89	256,374,331,231,131,317,313,185,186,265,221,274,87,228
5	0.46	2.83	89,72,430,344,363,459,313,388
5	0.49	2.8	329,317,212,162,281,207,220,110,280
5	0.48	3.3	344,291,227,442,312,120,392,153,332,439,196,189,508
5	0.44	3.14	163,57,111,51,134,54,124,121,182,138,311
5	0.49	3.3	166,211,282,245,326,105,62,77,559,304,264,186,552,307,388,134,459,289,282,263,67,351,230,37,332,135,208
5	0.5	2.93	230,402,438,284,425,323,344,254
5	0.49	3.11	572,664,631,673,306,300,150,153,168,192,175,150,229,107,228
5	0.47	3.48	20,109,283,100,210,146,165,172,139,430,447,19,280,367,457
5	0.49	3.21	187,369,382,278,261,333,460,220,148,102,299,115,225
5	0.44	3.23	154,290,208,106,266,217,317,151,223,93,117,93,288,74,292,68,214,300
5	0.5	3.12	141,89,179,206,400,325,318,126,243,206,380,291,241,49,108,238
5	0.49	3.33	365,200,315,138,298,248,192,285,292,29,361,296,36,101,361,61,322,315,249
5	0.49	3.2	361,348,588,400,624,451,196,405,374,426,482,104,768,435

% Strain	m	M	Individual step height measurements (nm)
5	0.49	3.23	272,463,242,388,112,70,180,90,316,194,147
5	0.5	3.07	216,200,65,258,157,350,152,408,55,275,92,281,190,80
5	0.46	3.27	283,19,205,408,78,325,361,333,111,201,738,286,383,57,363,97,193,197
5	0.48	2.94	383,636,477,85,371,283,307,413,520

APPENDIX D

Slip Continuity Measurements

Table D.1 Slip continuity parameters measured for grain boundary intersection by a dislocation channel for 7 dpa proton irradiated 316L stainless steel following straining to 5% in 400˚C SCW.

%Strain	m_1	m_2	M_1	M_2	GB type	Trace incl. (deg)	Slip continuity
5	0.49	0.28	3.11	3.67	RHAB	14	no
5	0.46	0.49	2.34	2.86	RHAB	1	yes
5	0.47	0.50	3.54	2.56	Σ27	61	no
5	0.36	0.50	3.51	2.63	RHAB	7	yes
5	0.36	0.44	3.51	3.65	RHAB	87	no
5	0.49	0.50	2.85	2.58	RHAB	49	yes
5	0.38	0.47	3.38	3.52	RHAB	65	no
5	0.44	0.44	3.64	3.65	Σ9	6	yes
5	0.49	0.46	2.65	2.38	RHAB	83	yes
5	0.48	0.45	3.23	3.38	Σ3	12	no
5	0.46	0.47	3.53	3.52	Σ3	4	yes
5	0.48	0.44	3.06	3.64	RHAB	6	yes
5	0.44	0.48	3.19	3.34	RHAB	7	no
5	0.50	0.41	2.78	3.36	Σ3	5	yes
5	0.48	0.44	3.06	3.65	RHAB	27	yes
5	0.44	0.42	3.16	3.32	RHAB	61	no
5	0.44	0.46	3.65	2.38	Σ3	63	no
5	0.47	0.48	2.67	3.06	RHAB	72	no
5	0.47	0.45	2.67	3.02	RHAB	47	no
5	0.46	0.49	2.80	3.19	RHAB	55	no
5	0.45	0.50	3.02	2.88	RHAB	10	no
5	0.44	0.50	3.51	2.88	RHAB	4	no
5	0.44	0.50	3.52	2.88	RHAB	35	yes
5	0.50	0.48	2.88	3.06	Σ3	19	yes
5	0.46	0.44	2.98	3.63	RHAB	12	yes
5	0.44	0.48	3.64	3.06	RHAB	32	no
5	0.48	0.48	3.06	3.06	LAB	45	yes
5	0.47	0.43	2.70	3.30	RHAB	31	no
5	0.48	0.49	3.06	3.24	Σ3	29	no
5	0.49	0.44	2.98	3.16	RHAB	79	no
5	0.49	0.49	3.24	3.19	Σ3	21	yes
5	0.47	0.48	3.54	3.35	RHAB	58	no
5	0.49	0.44	3.19	3.40	Σ3	28	yes
5	0.44	0.44	3.52	3.03	Σ3	78	no
5	0.50	0.49	3.00	2.51	RHAB	62	no
5	0.44	0.44	3.03	3.64	RHAB	11	yes
5	0.40	0.45	3.29	3.02	Σ3	13	yes
5	0.45	0.40	3.02	3.29	RHAB	83	no
5	0.49	0.43	3.10	3.37	RHAB	10	no
5	0.40	0.50	3.29	2.65	RHAB	56	no
5	0.41	0.43	3.22	3.05	Σ3	0	yes
5	0.44	0.44	2.98	3.63	RHAB	82	no
5	0.46	0.43	2.38	3.03	RHAB	59	no

%Strain	m_1	m_2	M_1	M_2	GB type	Trace incl. (deg)	Slip continuity
5	0.48	0.41	2.53	3.22	RHAB	62	yes
5	0.48	0.44	2.53	3.04	RHAB	23	yes
5	0.40	0.47	3.40	2.70	RHAB	30	yes
5	0.48	0.48	3.30	2.53	RHAB	1	no
5	0.48	0.49	3.30	3.22	Σ3	74	yes
5	0.48	0.46	3.36	2.58	RHAB	5	no
5	0.48	0.44	2.47	3.65	RHAB	37	yes
5	0.46	0.47	3.36	3.53	RHAB	10	no
5	0.46	0.47	2.35	3.54	RHAB	14	yes
5	0.47	0.43	3.47	3.64	RHAB	23	no
5	0.47	0.48	3.53	2.53	Σ3	48	no
5	0.49	0.44	3.15	3.32	RHAB	11	no
5	0.47	0.39	3.53	3.30	RHAB	19	yes
5	0.49	0.46	2.53	3.57	Σ3	83	no
5	0.48	0.47	3.30	3.47	RHAB	75	no
5	0.48	0.48	2.53	2.53	LAB	27	yes
5	0.50	0.38	2.65	3.46	Σ3	12	yes
5	0.38	0.50	3.46	2.65	Σ3	11	yes
5	0.46	0.47	2.72	3.54	RHAB	11	yes
5	0.46	0.46	3.36	3.01	Σ3	89	no
5	0.44	0.45	3.16	2.34	Σ3	51	yes
5	0.50	0.46	2.65	3.58	RHAB	61	no
5	0.38	0.49	3.39	2.57	RHAB	24	yes
5	0.44	0.47	3.64	2.70	Σ3	66	no
5	0.46	0.48	3.58	2.49	Σ3	52	no
5	0.46	0.46	2.34	3.17	Σ3	51	yes
5	0.45	0.49	3.57	2.65	Σ3	58	no
5	0.45	0.42	2.73	3.67	Σ3	57	no
5	0.45	0.45	2.34	3.44	RHAB	36	no
5	0.49	0.45	3.19	2.36	RHAB	34	yes
5	0.48	0.48	3.45	2.49	Σ3	48	no
5	0.39	0.45	3.43	2.31	RHAB	5	no
5	0.44	0.49	3.36	2.65	RHAB	24	yes
5	0.46	0.45	3.17	2.31	RHAB	24	yes
5	0.49	0.48	3.08	2.92	RHAB	17	no
5	0.49	0.47	2.51	3.47	RHAB	17	no
5	0.41	0.49	3.36	2.65	RHAB	18	yes
5	0.47	0.49	3.46	2.59	RHAB	9	yes
5	0.47	0.44	3.25	3.36	Σ27	19	yes
5	0.50	0.42	2.61	3.32	Σ3	20	yes
5	0.49	0.44	3.17	3.36	RHAB	22	no
5	0.49	0.47	2.81	3.54	Σ3	55	yes
5	0.46	0.49	3.01	3.17	RHAB	67	no
5	0.49	0.48	3.26	3.45	RHAB	42	no
5	0.50	0.44	3.01	3.17	RHAB	11	no
5	0.40	0.49	3.40	3.20	RHAB	13	no

%Strain	m_1	m_2	M_1	M_2	GB type	Trace incl. (deg)	Slip continuity
5	0.50	0.46	2.78	3.01	RHAB	0	no
5	0.49	0.45	3.15	3.38	Σ3	14	no
5	0.46	0.49	3.35	3.14	Σ3	17	yes
5	0.49	0.46	3.14	3.36	Σ3	16	yes
5	0.46	0.36	3.35	3.57	RHAB	16	yes
5	0.47	0.32	2.58	3.65	Σ3	17	yes
5	0.46	0.49	3.35	3.13	Σ3	11	yes
5	0.45	0.49	3.61	2.53	RHAB	36	yes
5	0.32	0.47	3.65	2.38	RHAB	2	yes
5	0.49	0.46	3.13	3.35	Σ3	11	yes
5	0.50	0.50	3.08	2.60	Σ3	46	no
5	0.49	0.50	3.08	3.08	RHAB	27	yes
5	0.45	0.47	3.54	3.54	RHAB	4	yes
5	0.49	0.44	3.08	3.36	Σ3	13	yes
5	0.50	0.46	3.01	3.01	RHAB	70	yes
5	0.47	0.50	3.51	2.58	RHAB	5	yes
5	0.50	0.37	2.58	3.49	RHAB	67	no
5	0.48	0.36	2.49	3.43	Σ3	30	yes
5	0.50	0.46	2.58	3.14	RHAB	20	no
5	0.32	0.46	3.64	2.69	Σ3	16	yes
5	0.43	0.44	3.05	3.46	Σ3	82	yes
5	0.44	0.44	2.41	3.40	Σ3	48	yes
5	0.44	0.45	3.46	2.33	RHAB	36	no
5	0.46	0.45	2.34	2.33	LAB	36	yes
5	0.44	0.48	3.63	2.50	RHAB	28	no
5	0.42	0.48	3.33	3.34	RHAB	44	yes
5	0.44	0.48	3.63	2.49	RHAB	32	no
5	0.45	0.43	2.33	3.40	RHAB	17	yes
5	0.44	0.45	3.64	3.63	RHAB	4	yes
5	0.42	0.45	3.32	2.33	RHAB	16	no
5	0.45	0.39	2.31	3.48	RHAB	82	no
5	0.42	0.35	3.34	3.57	RHAB	71	no
5	0.29	0.48	3.67	2.50	RHAB	86	no
5	0.42	0.49	3.34	3.17	Σ3	18	yes
5	0.50	0.35	3.11	3.57	RHAB	78	no
5	0.47	0.50	3.47	3.01	RHAB	46	no
5	0.47	0.49	2.37	2.90	RHAB	11	yes
5	0.28	0.49	3.67	3.20	RHAB	23	no
5	0.49	0.49	2.90	2.50	Σ3	46	yes
5	0.45	0.45	3.54	3.01	Σ3	73	yes
5	0.49	0.50	2.90	2.99	RHAB	22	yes
5	0.50	0.47	3.00	2.60	RHAB	36	yes
5	0.49	0.48	3.04	2.50	RHAB	49	yes
5	0.35	0.49	3.57	2.90	Σ9	0	no
5	0.49	0.49	2.49	3.20	RHAB	53	no
5	0.48	0.49	2.92	3.20	RHAB	47	yes

%Strain	m_1	m_2	M_1	M_2	GB type	Trace incl. (deg)	Slip continuity
5	0.50	0.35	2.87	3.60	RHAB	75	no
5	0.48	0.50	2.92	2.70	RHAB	61	yes
5	0.48	0.45	2.88	3.62	RHAB	38	no
5	0.50	0.48	2.70	2.75	RHAB	37	yes
5	0.45	0.49	3.03	2.98	RHAB	65	yes
5	0.49	0.48	3.20	2.75	RHAB	23	no
5	0.49	0.42	3.19	3.67	RHAB	21	yes
5	0.42	0.43	3.67	3.66	Σ3	0	yes
5	0.43	0.42	3.66	3.67	Σ3	0	yes
5	0.42	0.43	3.67	3.66	Σ3	4	yes
5	0.44	0.42	3.03	3.67	RHAB	85	no
5	0.49	0.48	3.06	3.06	Σ3	15	yes
5	0.45	0.46	2.73	2.72	Σ27	4	yes
5	0.48	0.47	3.06	2.59	RHAB	14	yes
5	0.47	0.48	2.59	2.51	RHAB	27	yes
5	0.48	0.46	3.41	3.50	Σ9	1	yes
5	0.41	0.47	3.06	2.96	RHAB	24	yes
5	0.46	0.46	3.46	3.35	LAB	28	yes
5	0.47	0.49	2.96	2.56	RHAB	42	no
5	0.45	0.45	3.43	3.03	Σ3	86	no
5	0.48	0.39	3.06	3.40	RHAB	27	yes
5	0.49	0.50	3.06	2.89	RHAB	66	yes
5	0.50	0.50	2.99	2.58	Σ3	47	no
5	0.48	0.50	2.44	2.61	RHAB	16	yes
5	0.50	0.50	3.00	2.59	Σ3	48	no
5	0.48	0.50	3.28	2.89	RHAB	0	yes
5	0.50	0.50	2.56	2.97	RHAB	75	no
5	0.49	0.46	2.73	3.30	RHAB	23	yes
5	0.47	0.49	3.47	3.06	RHAB	25	no
5	0.49	0.48	2.73	3.28	RHAB	64	yes
5	0.37	0.48	3.50	3.28	RHAB	46	no
5	0.45	0.40	3.00	3.42	RHAB	67	no
5	0.50	0.47	2.58	3.13	RHAB	26	yes
5	0.50	0.49	2.99	2.60	RHAB	27	yes
5	0.50	0.48	3.01	2.44	RHAB	16	no
5	0.50	0.37	2.90	3.50	RHAB	19	no
5	0.45	0.45	3.00	3.61	RHAB	37	no
5	0.37	0.47	3.50	2.41	RHAB	11	yes
5	0.44	0.44	3.59	2.98	Σ3	66	no
5	0.47	0.42	2.41	3.20	Σ3	29	yes
5	0.45	0.45	3.37	3.03	Σ3	71	no
5	0.44	0.44	2.98	3.59	Σ3	70	no
5	0.47	0.45	3.43	3.37	RHAB	77	no
5	0.43	0.43	3.38	3.03	RHAB	41	no
5	0.46	0.45	3.00	3.62	RHAB	73	no
5	0.47	0.37	3.45	3.48	RHAB	26	yes

%Strain	m_1	m_2	M_1	M_2	GB type	Trace incl. (deg)	Slip continuity
5	0.47	0.46	2.70	3.33	RHAB	52	no
5	0.37	0.45	3.48	3.61	RHAB	86	no
5	0.45	0.46	3.61	2.34	Σ3	66	no
5	0.47	0.46	3.43	2.34	RHAB	31	yes
5	0.43	0.46	3.52	3.51	RHAB	24	yes
5	0.45	0.47	2.36	3.46	RHAB	80	yes
5	0.43	0.40	3.52	3.42	RHAB	21	no
5	0.44	0.44	3.63	3.65	Σ3	1	yes
5	0.47	0.44	3.54	3.64	RHAB	68	no
5	0.44	0.44	3.65	3.63	Σ3	3	yes
5	0.45	0.40	2.39	3.42	Σ3	27	yes
5	0.45	0.45	3.61	3.63	Σ3	9	yes
5	0.43	0.49	3.51	3.08	RHAB	86	no
5	0.45	0.46	2.36	2.34	LAB	51	yes
5	0.48	0.49	3.23	2.80	RHAB	70	no
5	0.45	0.47	2.39	2.97	RHAB	89	no
5	0.49	0.44	3.20	3.64	RHAB	83	no
5	0.45	0.50	3.37	2.69	RHAB	77	yes
5	0.49	0.45	3.19	3.37	RHAB	32	yes
5	0.49	0.50	2.59	2.78	Σ3	50	yes
5	0.45	0.49	3.40	3.19	Σ3	13	yes
5	0.49	0.43	3.19	3.05	RHAB	63	no
5	0.45	0.44	3.38	3.19	RHAB	18	yes
5	0.43	0.45	3.05	3.40	RHAB	85	no
5	0.44	0.47	3.19	3.54	RHAB	70	no
5	0.37	0.43	3.50	3.05	RHAB	89	no
5	0.48	0.45	3.27	3.63	RHAB	78	no
5	0.44	0.50	3.02	2.56	RHAB	81	no
5	0.49	0.49	2.58	3.18	RHAB	11	yes
5	0.50	0.43	3.01	3.37	RHAB	16	no
5	0.49	0.50	3.18	2.90	RHAB	51	yes
5	0.43	0.50	3.18	2.58	Σ3	29	yes
5	0.46	0.48	2.38	2.75	RHAB	55	no
5	0.49	0.50	2.58	2.90	RHAB	6	yes
5	0.49	0.44	2.98	3.30	Σ3	12	yes
5	0.33	0.50	3.63	2.90	RHAB	32	yes
5	0.32	0.50	3.64	2.90	RHAB	20	no
5	0.49	0.48	3.19	2.43	RHAB	13	yes
5	0.47	0.32	3.41	3.64	RHAB	35	no
5	0.48	0.40	2.44	3.19	RHAB	41	no
5	0.48	0.49	2.49	3.26	RHAB	13	yes
5	0.45	0.48	3.10	3.34	RHAB	86	no
5	0.49	0.47	2.58	2.99	RHAB	82	yes
5	0.49	0.49	2.53	3.29	RHAB	1	no
5	0.48	0.46	2.49	3.26	RHAB	50	yes
5	0.49	0.49	2.59	2.85	RHAB	7	no

%Strain	m_1	m_2	M_1	M_2	GB type	Trace incl. (deg)	Slip continuity
5	0.45	0.49	2.30	2.58	RHAB	6	yes
5	0.49	0.49	2.78	3.20	RHAB	61	yes
5	0.48	0.36	2.79	3.56	Σ3	15	yes
5	0.39	0.46	3.43	3.17	RHAB	82	no
5	0.50	0.50	2.87	2.58	RHAB	43	yes
5	0.45	0.50	3.43	3.01	RHAB	5	yes
5	0.46	0.49	3.25	2.58	RHAB	4	yes
5	0.48	0.36	2.79	3.56	Σ3	15	yes
5	0.46	0.41	3.01	3.30	Σ3	11	yes
5	0.46	0.46	3.25	3.58	LAB	29	yes
5	0.50	0.48	2.66	3.34	Σ3	86	yes
5	0.36	0.48	3.56	2.79	Σ3	15	yes
5	0.44	0.49	3.32	3.02	Σ3	13	yes
5	0.49	0.50	2.53	2.86	RHAB	36	yes
5	0.50	0.42	2.99	3.67	RHAB	18	yes
5	0.46	0.49	3.58	2.58	RHAB	87	yes
5	0.45	0.46	3.04	3.25	Σ3	69	no
5	0.42	0.50	3.31	3.01	Σ3	5	yes
5	0.46	0.44	2.69	3.02	Σ3	85	yes
5	0.49	0.46	2.65	3.33	RHAB	9	yes
5	0.45	0.44	3.44	2.41	RHAB	79	yes
5	0.45	0.49	3.62	2.59	RHAB	1	yes
5	0.35	0.46	3.57	3.25	RHAB	69	no
5	0.45	0.45	3.31	3.00	Σ3	62	yes
5	0.46	0.44	3.50	3.17	RHAB	12	yes
5	0.43	0.46	3.27	3.25	LAB	15	yes
5	0.47	0.46	2.70	2.38	RHAB	57	no
5	0.45	0.46	3.48	3.17	RHAB	30	yes
5	0.46	0.47	3.53	3.50	Σ3	4	yes
5	0.45	0.29	3.33	3.67	RHAB	62	no
5	0.47	0.43	2.36	3.27	RHAB	63	no
5	0.49	0.43	2.83	3.27	RHAB	21	yes
5	0.46	0.40	2.96	3.40	Σ3	5	yes
5	0.49	0.47	2.53	3.51	RHAB	49	no
5	0.46	0.45	2.99	3.04	Σ3	20	yes
5	0.39	0.46	3.40	2.96	Σ3	4	yes
5	0.45	0.49	3.04	3.04	RHAB	47	no
5	0.42	0.42	3.32	3.33	RHAB	76	no
5	0.49	0.49	3.04	2.84	RHAB	56	no
5	0.48	0.47	2.84	3.04	RHAB	72	no
5	0.45	0.49	2.30	2.84	RHAB	72	no
5	0.47	0.49	2.42	3.04	RHAB	21	yes
5	0.49	0.43	2.88	3.27	Σ3	8	yes
5	0.44	0.45	2.98	3.61	RHAB	13	yes
5	0.49	0.49	2.83	2.88	LAB	57	yes
5	0.46	0.47	2.88	2.42	Σ9	25	yes

%Strain	m_1	m_2	M_1	M_2	GB type	Trace incl. (deg)	Slip continuity
5	0.43	0.50	2.41	2.87	RHAB	20	yes
5	0.43	0.49	3.67	2.84	RHAB	43	no
5	0.48	0.49	3.28	2.84	RHAB	10	yes
5	0.50	0.47	2.99	3.46	RHAB	25	yes
5	0.42	0.48	2.45	3.28	RHAB	50	no
5	0.47	0.46	3.52	2.69	RHAB	74	no
5	0.36	0.47	3.53	2.42	Σ3	23	yes
5	0.45	0.48	3.62	2.79	Σ3	57	no
5	0.43	0.45	2.41	3.54	Σ3	39	yes
5	0.46	0.36	2.33	3.53	Σ3	28	yes
5	0.49	0.40	2.84	3.43	Σ3	9	yes
5	0.45	0.46	3.48	2.34	RHAB	68	yes
5	0.46	0.45	2.34	3.61	RHAB	27	yes
5	0.40	0.49	3.43	2.83	Σ3	10	yes
5	0.42	0.49	3.67	2.53	RHAB	27	yes
5	0.39	0.49	3.48	2.84	RHAB	74	no
5	0.44	0.44	2.98	3.59	Σ3	75	yes
5	0.45	0.44	2.34	3.50	RHAB	79	yes
5	0.50	0.45	2.57	3.62	RHAB	58	no
5	0.40	0.45	3.35	3.62	RHAB	70	no
5	0.46	0.48	2.38	3.44	RHAB	53	no
5	0.41	0.46	3.37	2.31	RHAB	14	no
5	0.45	0.49	3.62	2.84	RHAB	3	yes
5	0.45	0.47	3.62	3.37	RHAB	3	yes
5	0.48	0.46	2.43	3.50	RHAB	87	no
5	0.48	0.44	2.84	3.63	RHAB	0	yes
5	0.48	0.45	2.75	3.00	RHAB	23	yes
5	0.49	0.48	2.84	2.47	RHAB	62	yes
5	0.47	0.44	2.76	3.01	Σ3	42	yes
5	0.48	0.48	2.47	2.87	RHAB	68	no
5	0.47	0.48	2.97	3.34	RHAB	20	yes
5	0.46	0.49	3.00	2.75	Σ3	71	yes
5	0.47	0.48	3.37	2.87	RHAB	37	no
5	0.45	0.35	3.62	3.58	RHAB	62	no
5	0.49	0.50	2.51	3.01	RHAB	64	no
5	0.48	0.50	2.74	2.79	RHAB	46	no
5	0.45	0.49	3.62	2.54	RHAB	64	no
5	0.47	0.49	2.70	2.65	RHAB	57	no
5	0.45	0.49	2.39	2.54	RHAB	16	yes
5	0.49	0.49	2.59	2.65	RHAB	5	no
5	0.49	0.35	2.54	3.58	Σ3	15	yes
5	0.35	0.49	3.58	2.54	Σ3	16	yes
5	0.35	0.45	3.58	2.30	RHAB	58	no
5	0.45	0.48	2.39	2.55	RHAB	19	yes
5	0.33	0.48	3.63	2.55	Σ3	14	yes
5	0.48	0.49	2.55	3.18	RHAB	77	no

%Strain	m_1	m_2	M_1	M_2	GB type	Trace incl. (deg)	Slip continuity
5	0.48	0.42	2.55	2.45	RHAB	39	yes
5	0.45	0.44	3.09	3.19	RHAB	67	yes
5	0.48	0.33	2.55	3.63	Σ3	16	yes
5	0.46	0.48	3.36	3.26	Σ3	0	yes
5	0.49	0.42	2.84	3.31	Σ3	18	yes
5	0.42	0.47	3.31	3.41	RHAB	4	no
5	0.42	0.44	3.31	3.04	RHAB	56	no
5	0.47	0.44	3.41	3.04	RHAB	71	no
5	0.47	0.44	2.98	3.04	RHAB	86	no
5	0.47	0.50	2.98	3.08	RHAB	36	no
5	0.48	0.44	3.34	3.44	RHAB	76	no
5	0.41	0.48	3.27	2.44	RHAB	63	no
5	0.48	0.42	2.44	3.09	Σ3	9	yes
5	0.50	0.48	2.57	2.44	RHAB	9	no
5	0.45	0.48	3.01	2.88	RHAB	9	no
5	0.42	0.43	3.09	3.05	Σ3	4	yes
5	0.43	0.42	3.05	3.10	Σ3	5	yes
5	0.42	0.43	3.10	3.05	Σ3	4	yes
5	0.46	0.50	3.00	2.69	Σ3	25	yes
5	0.50	0.47	2.69	2.97	Σ3	23	yes
5	0.43	0.42	3.05	3.08	Σ3	1	yes
5	0.46	0.45	3.28	3.31	RHAB	33	yes
5	0.50	0.42	2.69	3.08	RHAB	81	no
5	0.47	0.42	2.97	3.08	RHAB	83	no
5	0.43	0.45	3.64	3.61	Σ3	6	yes
5	0.48	0.36	3.45	3.56	RHAB	87	no
5	0.44	0.48	3.39	3.36	RHAB	19	yes
5	0.42	0.49	3.08	2.86	LAB	30	yes
5	0.48	0.46	3.34	3.46	Σ3	8	no
5	0.49	0.50	2.78	3.01	RHAB	15	yes
5	0.49	0.40	2.86	3.40	Σ3	7	yes
5	0.44	0.48	3.02	2.79	RHAB	17	yes
5	0.42	0.33	3.08	3.61	RHAB	63	no
5	0.47	0.47	3.14	2.97	RHAB	6	yes
5	0.45	0.49	3.38	3.15	Σ3	14	yes
5	0.49	0.44	2.96	3.19	Σ3	7	yes
5	0.47	0.47	2.97	3.38	Σ3	70	yes
5	0.48	0.47	3.26	3.14	RHAB	15	yes
5	0.46	0.39	3.17	3.40	LAB	26	yes
5	0.38	0.50	3.38	2.97	RHAB	20	yes
5	0.49	0.45	3.20	3.33	Σ3	52	yes
5	0.47	0.47	3.14	3.38	RHAB	5	yes
5	0.50	0.50	2.58	2.99	Σ3	49	yes
5	0.46	0.48	3.28	3.22	Σ3	3	yes
5	0.42	0.47	3.67	3.54	RHAB	2	yes
5	0.49	0.49	3.02	2.78	RHAB	33	yes

%Strain	m_1	m_2	M_1	M_2	GB type	Trace incl. (deg)	Slip continuity
5	0.50	0.49	2.86	3.27	RHAB	84	yes
5	0.48	0.48	3.22	3.26	Σ3	1	yes
5	0.47	0.48	3.47	3.41	RHAB	8	yes
5	0.49	0.49	3.22	3.09	Σ3	74	yes
5	0.43	0.49	3.37	3.13	Σ3	6	yes
5	0.49	0.48	2.53	2.49	RHAB	50	yes
5	0.49	0.48	2.85	2.91	Σ3	26	yes
5	0.47	0.45	3.47	3.61	RHAB	40	yes
5	0.42	0.46	3.09	3.28	LAB	71	yes
5	0.42	0.49	3.09	3.05	RHAB	41	yes
5	0.50	0.49	3.03	2.96	RHAB	42	yes
5	0.46	0.48	2.98	2.84	Σ3	47	yes
5	0.49	0.50	2.78	2.58	RHAB	58	yes
5	0.43	0.42	3.06	3.09	Σ3	4	yes
5	0.45	0.46	3.06	2.99	Σ3	2	yes
5	0.50	0.49	2.70	2.85	RHAB	39	yes
5	0.32	0.29	3.64	3.67	RHAB	46	yes
5	0.47	0.44	3.52	3.59	Σ3	8	yes
5	0.48	0.44	3.44	3.59	RHAB	24	yes
5	0.45	0.43	3.63	3.06	RHAB	22	no
5	0.45	0.45	3.62	3.63	Σ3	5	yes
5	0.44	0.48	3.30	3.23	RHAB	1	yes
5	0.46	0.48	3.46	2.88	Σ27	15	no
5	0.45	0.38	3.31	3.38	RHAB	7	yes
5	0.47	0.45	3.46	3.62	LAB	10	yes
5	0.45	0.48	2.36	2.43	RHAB	82	yes
5	0.50	0.47	2.57	3.46	RHAB	59	no
5	0.39	0.50	3.48	2.58	RHAB	86	no
5	0.48	0.47	2.47	3.46	RHAB	7	yes
5	0.49	0.48	2.55	2.47	RHAB	16	yes
5	0.47	0.49	3.52	2.53	RHAB	31	yes
5	0.44	0.47	3.04	2.54	Σ3	28	yes
5	0.47	0.44	2.54	3.04	Σ3	29	yes
5	0.49	0.44	2.84	3.04	RHAB	0	yes
5	0.49	0.46	2.75	3.25	RHAB	11	yes
5	0.46	0.46	3.17	2.96	RHAB	25	yes
5	0.44	0.50	3.04	2.78	RHAB	40	yes
5	0.49	0.50	2.84	2.76	RHAB	82	no
5	0.48	0.45	2.79	3.00	Σ3	80	yes
5	0.46	0.45	3.35	3.62	RHAB	24	no
5	0.47	0.48	3.46	3.37	Σ3	43	no
5	0.46	0.50	3.55	2.76	Σ9	52	no
5	0.45	0.50	3.09	2.76	Σ3	21	yes
5	0.38	0.50	3.38	2.56	RHAB	18	no
5	0.50	0.42	2.76	3.06	RHAB	46	no
5	0.44	0.49	3.59	3.25	RHAB	16	yes

%Strain	m_1	m_2	M_1	M_2	GB type	Trace incl. (deg)	Slip continuity
5	0.36	0.48	3.57	2.75	RHAB	63	no
5	0.43	0.47	3.03	2.72	Σ3	35	no
5	0.50	0.47	2.97	3.48	RHAB	72	yes
5	0.47	0.48	3.48	2.80	RHAB	57	no
5	0.50	0.47	2.97	3.48	RHAB	85	no
5	0.41	0.47	3.30	3.45	RHAB	68	yes
5	0.47	0.47	3.45	2.90	RHAB	86	no
5	0.44	0.44	3.56	3.01	Σ3	74	no
5	0.45	0.49	3.63	2.78	RHAB	68	no
5	0.49	0.46	2.78	3.28	RHAB	23	yes
5	0.50	0.47	2.68	3.54	RHAB	85	no
5	0.49	0.48	2.97	3.26	RHAB	35	no
5	0.44	0.49	3.56	3.27	RHAB	29	no
5	0.44	0.49	3.29	2.97	Σ3	16	yes
5	0.47	0.49	2.60	2.78	RHAB	8	no
5	0.49	0.40	3.11	3.40	RHAB	45	no
5	0.45	0.50	2.34	2.66	RHAB	57	yes
5	0.45	0.48	3.63	3.45	RHAB	86	no
5	0.47	0.49	3.54	3.24	RHAB	37	no
5	0.49	0.46	3.20	3.53	RHAB	15	yes
5	0.47	0.46	3.46	2.61	RHAB	81	no
5	0.49	0.46	2.61	3.46	RHAB	84	no
5	0.46	0.31	2.61	3.66	Σ3	15	yes
5	0.44	0.49	3.59	2.53	RHAB	32	yes
5	0.31	0.47	3.66	2.60	Σ3	15	yes
5	0.46	0.31	2.61	3.65	Σ3	18	yes
5	0.31	0.46	3.65	2.61	Σ3	16	yes
5	0.46	0.49	3.00	3.23	LAB	7	no
5	0.48	0.46	2.89	3.00	LAB	89	yes
5	0.48	0.46	2.89	3.00	LAB	9	yes
5	0.37	0.48	3.53	2.89	RHAB	2	yes
5	0.49	0.48	2.61	2.89	RHAB	15	no
5	0.46	0.44	3.12	3.56	RHAB	2	yes
5	0.46	0.49	2.58	3.02	RHAB	48	yes
5	0.47	0.45	2.41	3.30	RHAB	36	yes
5	0.45	0.49	3.30	3.15	Σ3	10	yes
5	0.50	0.45	2.78	2.34	RHAB	90	yes
5	0.46	0.46	2.38	3.28	RHAB	14	yes
5	0.49	0.42	3.15	3.06	RHAB	18	yes
5	0.44	0.49	3.01	2.57	RHAB	26	yes
5	0.48	0.38	2.49	3.39	Σ3	32	yes
5	0.49	0.48	3.15	2.89	LAB	85	yes
5	0.42	0.45	3.28	2.36	RHAB	16	yes
5	0.49	0.45	3.22	3.48	RHAB	52	yes
5	0.48	0.48	2.89	2.52	RHAB	40	yes
5	0.42	0.46	3.06	3.12	RHAB	66	no

%Strain	m_1	m_2	M_1	M_2	GB type	Trace incl. (deg)	Slip continuity
5	0.43	0.49	3.30	3.04	Σ3	8	yes
5	0.45	0.45	3.03	3.41	Σ3	84	yes
5	0.49	0.44	3.13	3.19	RHAB	62	no
5	0.46	0.50	2.35	2.92	RHAB	3	yes
5	0.41	0.46	3.27	2.35	RHAB	62	no
5	0.50	0.47	2.87	3.45	RHAB	10	yes
5	0.37	0.46	3.53	2.35	RHAB	64	no
5	0.48	0.46	2.78	2.35	RHAB	26	no
5	0.46	0.47	2.31	3.53	RHAB	76	no
5	0.49	0.46	3.08	2.99	RHAB	59	no
5	0.45	0.44	2.34	3.57	Σ3	49	no
5	0.47	0.49	2.60	2.51	RHAB	10	no
5	0.49	0.37	3.08	3.53	RHAB	5	no
5	0.46	0.49	2.99	3.09	RHAB	19	no
5	0.49	0.49	2.55	3.08	RHAB	73	no
5	0.49	0.50	2.51	2.61	RHAB	50	no
5	0.46	0.48	2.95	2.78	Σ3	42	yes
5	0.50	0.48	2.94	2.78	RHAB	19	yes
5	0.44	0.46	2.97	2.80	Σ3	47	yes
5	0.48	0.48	2.76	2.83	Σ3	65	no
5	0.44	0.48	3.50	3.34	Σ3	17	yes
5	0.48	0.44	3.34	3.50	Σ3	18	yes
5	0.30	0.48	3.66	2.76	RHAB	37	no
5	0.49	0.48	2.54	2.76	RHAB	90	yes
5	0.46	0.42	2.37	3.28	RHAB	40	no
5	0.48	0.47	2.91	3.13	RHAB	16	yes
5	0.49	0.48	3.18	2.76	RHAB	82	no
5	0.48	0.44	2.76	3.35	RHAB	10	yes
5	0.44	0.49	3.35	3.13	Σ3	8	yes
5	0.45	0.48	3.60	2.80	RHAB	6	yes
5	0.41	0.50	3.30	2.97	RHAB	3	yes
5	0.49	0.43	3.22	2.41	RHAB	65	yes
5	0.48	0.36	2.80	3.57	Σ3	20	yes
5	0.36	0.48	3.57	2.80	Σ3	21	yes
5	0.49	0.49	3.08	2.56	Σ3	40	no
5	0.36	0.48	3.57	2.79	Σ3	14	yes
5	0.46	0.49	3.17	2.65	RHAB	59	no
5	0.49	0.47	2.56	2.97	RHAB	43	yes
5	0.36	0.46	3.54	2.88	Σ3	32	yes
5	0.44	0.46	2.98	2.98	RHAB	71	no
5	0.47	0.50	2.70	2.70	RHAB	49	no
5	0.39	0.48	3.40	3.41	RHAB	50	no
5	0.45	0.44	3.00	2.98	RHAB	56	no
5	0.47	0.48	2.72	2.75	RHAB	8	no
5	0.42	0.42	3.67	3.67	Σ3	0	yes

APPENDIX E

IG Crack Measurements

Table E.1 Parameters measured for each cracked grain boundary of unirradiated 316L stainless steel following straining to 15% and 25% strain in 500˚C SCW.

%Strain	m_1	m_2	M_1	M_2	GB type	Trace incl. (deg)
15	0.43	0.41	3.09	3.39	RHAB	88
15	0.34	0.42	3.61	3.31	RHAB	51
15	0.48	0.42	2.61	3.31	RHAB	61
15	0.34	0.40	3.61	3.18	RHAB	80
15	0.38	0.28	3.39	3.67	RHAB	72
15	0.44	0.28	2.99	3.67	RHAB	74
15	0.37	0.45	3.53	3.02	RHAB	82
15	0.45	0.41	2.34	3.26	RHAB	83
15	0.45	0.46	2.34	2.97	RHAB	76
15	0.41	0.28	3.39	3.67	RHAB	87
15	0.41	0.46	3.39	2.46	RHAB	86
15	0.33	0.45	3.63	2.40	RHAB	82
15	0.33	0.44	3.63	3.21	RHAB	75
15	0.46	0.35	3.13	3.60	RHAB	90
15	0.37	0.35	3.46	3.60	Σ3	86
15	0.49	0.50	3.18	2.74	RHAB	61
15	0.49	0.46	3.18	3.04	RHAB	59
15	0.41	0.46	3.30	3.55	RHAB	72
15	0.50	0.46	2.89	3.55	RHAB	84
15	0.37	0.41	3.55	3.26	RHAB	75
15	0.37	0.46	3.55	3.02	RHAB	85
15	0.48	0.37	2.81	3.48	RHAB	81
15	0.48	0.47	2.81	2.90	RHAB	90
15	0.32	0.35	3.64	3.58	RHAB	81
15	0.48	0.35	2.44	3.58	RHAB	77
15	0.47	0.48	2.50	2.67	RHAB	90
15	0.40	0.41	3.41	3.34	RHAB	86
15	0.40	0.35	3.41	3.56	RHAB	88
15	0.40	0.44	3.41	2.42	RHAB	82
15	0.36	0.49	3.56	2.78	RHAB	77
15	0.32	0.39	3.63	3.44	RHAB	67
15	0.44	0.39	3.17	3.44	RHAB	67
15	0.47	0.32	2.42	3.63	RHAB	80
15	0.41	0.34	3.35	3.56	RHAB	82
15	0.41	0.41	3.35	3.30	RHAB	84
15	0.41	0.48	3.35	2.42	RHAB	82
15	0.43	0.46	3.04	3.27	RHAB	88
15	0.33	0.27	3.60	3.67	LAB	72
15	0.47	0.37	2.38	3.44	RHAB	78
15	0.40	0.39	3.36	3.45	RHAB	84
15	0.36	0.50	3.57	2.59	RHAB	87
15	0.36	0.43	3.57	3.21	RHAB	88
15	0.35	0.47	3.53	2.91	RHAB	89

%Strain	m_1	m_2	M_1	M_2	GB type	Trace incl. (deg)
15	0.45	0.41	2.37	3.23	RHAB	86
15	0.39	0.48	3.40	2.82	RHAB	77
15	0.45	0.37	3.35	3.50	RHAB	80
15	0.49	0.37	3.18	3.50	RHAB	87
15	0.45	0.34	2.79	3.56	Σ9	88
25	0.43	0.41	3.09	3.39	RHAB	88
25	0.43	0.49	3.33	2.53	Σ27	85
25	0.42	0.49	3.14	2.53	Σ3	88
25	0.43	0.40	3.33	3.27	Σ3	55
25	0.38	0.39	3.51	3.33	RHAB	83
25	0.37	0.45	3.53	3.02	RHAB	86
25	0.45	0.41	2.34	3.26	RHAB	58
25	0.45	0.46	2.34	2.97	RHAB	65
25	0.34	0.46	3.61	2.97	RHAB	83
25	0.41	0.28	3.39	3.67	RHAB	81
25	0.50	0.28	2.59	3.67	RHAB	84
25	0.41	0.46	3.39	2.46	RHAB	90
25	0.33	0.45	3.63	2.40	RHAB	82
25	0.33	0.44	3.63	3.21	RHAB	80
25	0.37	0.49	3.46	3.33	RHAB	49
25	0.37	0.35	3.46	3.60	RHAB	85
25	0.46	0.35	3.13	3.60	RHAB	87
25	0.49	0.50	3.18	2.74	RHAB	50
25	0.49	0.50	3.18	2.73	RHAB	66
25	0.49	0.46	3.18	3.04	RHAB	56
25	0.43	0.41	3.26	3.26	LAB	64
25	0.37	0.41	3.55	3.26	RHAB	67
25	0.37	0.46	3.55	3.02	RHAB	81
25	0.32	0.35	3.64	3.58	RHAB	81
25	0.32	0.49	3.64	2.67	RHAB	71
25	0.48	0.35	2.44	3.58	RHAB	75
25	0.47	0.48	2.50	2.67	RHAB	87
25	0.40	0.48	3.41	3.46	RHAB	46
25	0.38	0.35	3.42	3.56	RHAB	55
25	0.38	0.38	3.42	3.49	RHAB	72
25	0.40	0.41	3.41	3.34	RHAB	85
25	0.40	0.35	3.41	3.56	RHAB	86
25	0.40	0.44	3.41	2.42	RHAB	76
25	0.36	0.49	3.56	2.78	RHAB	79
25	0.32	0.39	3.63	3.44	RHAB	58
25	0.44	0.39	3.17	3.44	RHAB	69
25	0.47	0.32	2.42	3.63	RHAB	77
25	0.41	0.41	3.35	3.30	RHAB	77
25	0.41	0.34	3.35	3.56	RHAB	78
25	0.41	0.48	3.35	2.42	RHAB	75
25	0.49	0.41	2.83	3.30	RHAB	82

%Strain	m_1	m_2	M_1	M_2	GB type	Trace incl. (deg)
25	0.43	0.46	3.04	3.27	RHAB	89
25	0.33	0.27	3.60	3.67	LAB	79
25	0.32	0.37	3.64	3.44	LAB	78
25	0.32	0.37	3.64	3.44	RHAB	78
25	0.47	0.37	2.38	3.44	RHAB	78
25	0.40	0.39	3.36	3.45	RHAB	78
25	0.49	0.39	3.17	3.45	RHAB	50
25	0.49	0.39	3.14	3.45	RHAB	61
25	0.36	0.50	3.57	2.59	RHAB	86
25	0.36	0.43	3.57	3.21	RHAB	89
25	0.35	0.47	3.53	2.91	RHAB	87
25	0.35	0.43	3.53	3.05	RHAB	61
25	0.45	0.37	3.35	3.50	RHAB	80
25	0.45	0.46	3.35	2.41	RHAB	61
25	0.49	0.37	3.18	3.50	RHAB	87
25	0.45	0.34	2.79	3.56	Σ9	88
25	0.44	0.47	2.41	3.48	RHAB	87
25	0.45	0.39	3.34	3.41	RHAB	90
25	0.49	0.39	3.17	3.41	RHAB	86
25	0.40	0.47	3.40	2.85	RHAB	77
25	0.47	0.49	2.98	2.68	RHAB	88
25	0.47	0.45	2.41	3.03	RHAB	80
25	0.46	0.49	2.35	2.77	RHAB	57
25	0.47	0.46	2.37	2.31	RHAB	82
25	0.41	0.42	3.31	2.44	Σ3	90
25	0.43	0.30	3.05	3.67	RHAB	87
25	0.47	0.47	3.18	2.43	RHAB	82
25	0.47	0.29	3.18	3.67	RHAB	74
25	0.47	0.34	2.41	3.61	RHAB	86
25	0.34	0.34	3.61	3.61	Σ3	78
25	0.39	0.43	3.46	3.26	RHAB	81
25	0.27	0.34	3.67	3.59	RHAB	84
25	0.27	0.48	3.67	3.12	RHAB	68
25	0.27	0.46	3.67	3.01	RHAB	87
25	0.40	0.46	3.36	3.01	RHAB	78
25	0.47	0.46	2.36	2.98	RHAB	81
25	0.47	0.45	2.98	2.38	RHAB	80
25	0.47	0.44	2.98	3.63	RHAB	82
25	0.45	0.41	3.03	3.25	RHAB	79
25	0.45	0.44	3.03	3.03	RHAB	90
25	0.46	0.47	3.01	2.86	RHAB	79
25	0.38	0.44	3.50	3.05	RHAB	74
25	0.48	0.35	2.47	3.54	RHAB	82
25	0.34	0.38	3.62	3.41	RHAB	66
25	0.45	0.38	2.33	3.41	RHAB	72
25	0.46	0.38	2.82	3.41	RHAB	60

%Strain	m_1	m_2	M_1	M_2	GB type	Trace incl. (deg)
25	0.46	0.34	2.93	3.59	RHAB	76
25	0.39	0.41	3.45	3.34	RHAB	88
25	0.39	0.50	3.45	2.83	RHAB	86
25	0.39	0.40	3.41	3.36	RHAB	86
25	0.40	0.41	3.36	3.36	RHAB	72
25	0.40	0.46	3.39	2.31	RHAB	67
25	0.40	0.46	3.36	2.31	RHAB	86
25	0.40	0.46	3.36	2.99	RHAB	58
25	0.40	0.46	3.39	3.01	RHAB	74
25	0.46	0.41	3.51	3.20	Σ9	77
25	0.45	0.45	3.02	2.41	RHAB	78
25	0.49	0.46	2.54	2.91	RHAB	80
25	0.35	0.35	3.59	3.60	RHAB	84
25	0.48	0.35	2.75	3.60	RHAB	84
25	0.48	0.47	2.74	2.75	RHAB	86
25	0.46	0.35	3.56	3.60	RHAB	76
25	0.46	0.45	3.56	2.35	RHAB	83
25	0.49	0.43	2.69	3.08	RHAB	68
25	0.45	0.32	3.04	3.63	RHAB	75
25	0.46	0.31	3.08	3.63	RHAB	85
25	0.47	0.31	2.41	3.65	RHAB	60
25	0.50	0.46	2.83	3.26	RHAB	90
25	0.50	0.44	2.72	2.99	RHAB	66
25	0.50	0.44	2.55	2.99	RHAB	87
25	0.33	0.44	3.63	2.99	RHAB	78
25	0.37	0.44	3.55	2.99	RHAB	85
25	0.46	0.44	3.02	2.99	RHAB	58
25	0.40	0.50	3.36	2.55	RHAB	86
25	0.43	0.49	3.05	2.59	RHAB	76
25	0.48	0.48	3.38	2.74	RHAB	83
25	0.38	0.47	3.36	2.95	RHAB	76
25	0.39	0.48	3.40	2.49	RHAB	83
25	0.50	0.45	2.68	3.02	RHAB	84
25	0.39	0.45	3.40	3.02	RHAB	76
25	0.35	0.40	3.57	3.43	RHAB	85
25	0.43	0.42	2.43	3.28	RHAB	89
25	0.42	0.42	3.27	3.30	RHAB	82
25	0.42	0.42	3.27	3.28	RHAB	88
25	0.42	0.46	3.27	3.53	RHAB	58
25	0.42	0.49	3.27	2.93	RHAB	90
25	0.47	0.46	2.38	3.53	Σ3	86
25	0.40	0.48	3.39	2.66	RHAB	85
25	0.49	0.48	2.58	2.66	RHAB	83
25	0.48	0.49	2.46	3.33	RHAB	65
25	0.46	0.47	2.51	2.39	RHAB	86
25	0.45	0.35	2.36	3.58	RHAB	85

%Strain	m_1	m_2	M_1	M_2	GB type	Trace incl. (deg)
25	0.43	0.39	3.45	3.45	RHAB	65
25	0.44	0.46	2.42	2.35	RHAB	65
25	0.33	0.48	3.63	2.43	RHAB	89
25	0.48	0.43	2.66	3.29	RHAB	72
25	0.42	0.47	3.13	2.37	RHAB	79
25	0.42	0.31	3.13	3.66	RHAB	86
25	0.35	0.47	3.59	3.53	RHAB	84
25	0.48	0.49	2.72	2.53	RHAB	90
25	0.46	0.49	3.01	2.52	RHAB	79
25	0.46	0.36	3.01	3.52	RHAB	81
25	0.45	0.31	3.19	3.65	RHAB	80
25	0.50	0.39	2.56	3.43	RHAB	90
25	0.44	0.39	3.08	3.43	RHAB	74
25	0.45	0.39	3.50	3.43	RHAB	78
25	0.39	0.37	3.47	3.43	RHAB	89
25	0.43	0.41	3.18	3.30	RHAB	88
25	0.46	0.41	2.34	3.26	RHAB	77
25	0.46	0.43	2.34	3.05	RHAB	72
25	0.47	0.47	3.47	2.37	RHAB	70
25	0.41	0.37	3.30	3.54	RHAB	40
25	0.41	0.46	3.30	3.55	RHAB	85
25	0.48	0.37	2.81	3.48	RHAB	75
25	0.47	0.48	2.44	2.43	RHAB	80
25	0.48	0.47	2.81	2.90	RHAB	88
25	0.50	0.46	2.89	3.55	RHAB	77
25	0.48	0.37	2.81	3.54	Σ9	27
25	0.40	0.28	3.40	3.67	RHAB	46
25	0.41	0.28	3.39	3.67	RHAB	46
25	0.34	0.42	3.61	3.31	RHAB	49
25	0.33	0.42	3.62	3.31	RHAB	55
25	0.38	0.28	3.40	3.67	RHAB	65
25	0.38	0.28	3.39	3.67	RHAB	65
25	0.38	0.45	3.39	3.58	RHAB	55
25	0.48	0.42	2.61	3.31	RHAB	60
25	0.48	0.40	2.61	3.39	RHAB	67
25	0.34	0.40	3.61	3.18	RHAB	75
25	0.44	0.28	2.99	3.67	RHAB	67
25	0.46	0.45	2.32	3.58	Σ3	58
25	0.33	0.45	3.62	3.58	Σ9	44
25	0.45	0.34	2.37	3.61	RHAB	68
25	0.42	0.48	2.44	2.83	RHAB	77
25	0.45	0.41	2.37	3.23	RHAB	85
25	0.45	0.48	2.37	2.82	RHAB	44
25	0.45	0.43	2.37	3.05	RHAB	78
25	0.39	0.48	3.40	2.82	RHAB	69
25	0.34	0.48	3.61	2.82	RHAB	86

%Strain	m_1	m_2	M_1	M_2	GB type	Trace incl. (deg)
25	0.43	0.41	3.23	3.23	RHAB	59
25	0.43	0.48	3.23	2.82	RHAB	40
25	0.43	0.48	3.24	2.82	RHAB	62

Table E.2 Parameters measured for each cracked grain boundary of unirradiated 316LGBE stainless steel following straining to 15% and 25% strain in 500˚C SCW.

%Strain	m_1	m_2	M_1	M_2	GB type	Trace incl. (deg)
15	0.45	0.47	3.03	3.14	RHAB	77
15	0.32	0.44	3.64	3.34	RHAB	79
15	0.32	0.48	3.64	3.19	RHAB	66
15	0.35	0.48	3.56	3.19	RHAB	88
15	0.49	0.36	2.58	3.57	RHAB	85
15	0.44	0.44	3.63	3.22	RHAB	86
15	0.46	0.43	3.00	3.63	RHAB	83
15	0.4	0.45	3.39	2.29	RHAB	69
15	0.4	0.48	3.39	3.24	RHAB	73
15	0.47	0.49	3.44	3.29	RHAB	89
15	0.35	0.38	3.50	3.49	RHAB	87
25	0.45	0.47	3.03	3.14	RHAB	84
25	0.32	0.44	3.64	3.34	RHAB	76
25	0.32	0.43	3.64	2.44	RHAB	58
25	0.35	0.43	3.56	2.44	RHAB	84
25	0.32	0.48	3.64	3.19	RHAB	62
25	0.35	0.48	3.56	3.19	RHAB	87
25	0.49	0.36	2.58	3.57	RHAB	84
25	0.44	0.44	3.62	3.22	RHAB	84
25	0.44	0.44	3.63	3.22	RHAB	86
25	0.44	0.44	3.63	3.22	RHAB	90
25	0.46	0.43	3.00	3.63	RHAB	83
25	0.4	0.45	3.39	2.29	RHAB	65
25	0.4	0.48	3.39	3.24	RHAB	75
25	0.47	0.49	3.44	3.29	RHAB	90
25	0.35	0.38	3.50	3.49	RHAB	85
25	0.35	0.49	3.50	2.69	RHAB	77
25	0.44	0.38	2.41	3.49	RHAB	86
25	0.48	0.38	2.44	3.49	$\Sigma 3$	83
25	0.44	0.46	3.43	2.37	RHAB	83
25	0.48	0.49	3.25	2.52	RHAB	89
25	0.48	0.46	3.25	2.37	RHAB	89
25	0.48	0.47	3.25	2.96	RHAB	66
25	0.46	0.42	3.52	3.28	$\Sigma 3$	81
25	0.44	0.47	3.57	2.96	$\Sigma 9$	78
25	0.46	0.47	3.53	2.97	RHAB	82
25	0.37	0.44	3.52	3.55	RHAB	86
25	0.37	0.47	3.52	3.43	RHAB	82
25	0.43	0.46	3.62	3.54	RHAB	84
25	0.37	0.4	3.50	3.37	RHAB	78
25	0.37	0.5	3.50	2.60	RHAB	71
25	0.39	0.37	3.39	3.52	$\Sigma 27$	77
25	0.48	0.32	3.41	3.63	RHAB	82
25	0.45	0.48	3.36	3.35	RHAB	89

%Strain	m_1	m_2	M_1	M_2	GB type	Trace incl. (deg)
25	0.45	0.48	3.36	3.07	RHAB	78
25	0.48	0.5	2.89	2.79	RHAB	85
25	0.5	0.49	2.58	2.87	RHAB	79
25	0.5	0.49	3.01	2.86	RHAB	80
25	0.46	0.49	3.28	2.86	RHAB	75
25	0.46	0.49	3.28	2.86	RHAB	87
25	0.46	0.47	3.28	3.47	RHAB	85
25	0.5	0.47	2.57	2.95	RHAB	77
25	0.44	0.47	3.52	2.95	Σ27	88
25	0.47	0.49	3.32	2.96	RHAB	88
25	0.46	0.45	2.34	3.10	RHAB	84
25	0.43	0.45	3.22	3.34	RHAB	83
25	0.46	0.44	2.34	3.09	RHAB	55
25	0.47	0.5	2.70	2.93	RHAB	84
25	0.48	0.48	3.03	2.90	RHAB	78
25	0.45	0.49	3.09	3.20	RHAB	86
25	0.5	0.43	2.79	3.64	RHAB	68
25	0.48	0.46	2.90	3.02	RHAB	81
25	0.5	0.4	2.90	3.39	RHAB	81
25	0.47	0.4	2.42	3.39	RHAB	63
25	0.5	0.43	2.96	3.45	RHAB	81
25	0.42	0.43	3.26	3.45	RHAB	79
25	0.5	0.41	2.96	3.24	Σ9	71
25	0.43	0.49	3.45	3.30	RHAB	74
25	0.49	0.44	3.31	2.96	RHAB	76
25	0.49	0.44	3.28	2.96	RHAB	78
25	0.44	0.37	3.62	3.52	Σ9	78
25	0.38	0.38	3.44	3.48	RHAB	81
25	0.47	0.45	3.47	2.37	RHAB	86
25	0.45	0.43	3.03	3.19	Σ3	87
25	0.48	0.49	3.35	3.26	RHAB	74
25	0.43	0.43	3.35	2.43	Σ3	87
25	0.5	0.46	2.81	3.42	RHAB	89
25	0.48	0.39	3.35	3.35	Σ27	87
25	0.5	0.48	2.57	3.35	RHAB	87
25	0.44	0.48	3.07	3.35	RHAB	84
25	0.39	0.49	3.42	2.55	RHAB	78
25	0.41	0.45	3.30	3.02	RHAB	81
25	0.46	0.46	3.17	2.44	RHAB	85
25	0.46	0.44	3.17	3.09	RHAB	85
25	0.46	0.45	3.17	3.02	RHAB	82
25	0.39	0.46	3.42	3.26	RHAB	88
25	0.44	0.46	3.01	3.26	RHAB	83
25	0.44	0.4	3.56	3.34	RHAB	86
25	0.49	0.5	3.30	3.03	RHAB	89
25	0.44	0.45	3.62	2.85	RHAB	85

%Strain	m_1	m_2	M_1	M_2	GB type	Trace incl. (deg)
25	0.48	0.45	2.65	2.85	RHAB	80
25	0.5	0.46	2.60	2.37	RHAB	89
25	0.39	0.38	3.42	3.49	Σ9	82
25	0.36	0.46	3.57	3.58	Σ27	71
25	0.42	0.46	3.30	2.78	RHAB	82
25	0.42	0.44	3.29	3.10	Σ3	89
25	0.41	0.42	3.39	3.66	RHAB	76
25	0.47	0.42	3.50	3.66	RHAB	73
25	0.47	0.42	2.38	3.66	RHAB	80
25	0.46	0.42	2.38	3.66	RHAB	87
25	0.42	0.5	3.07	2.69	RHAB	86
25	0.47	0.49	2.77	2.76	RHAB	75
25	0.47	0.44	2.60	3.17	RHAB	90
25	0.4	0.42	3.41	3.27	Σ3	90
25	0.42	0.36	3.27	3.57	RHAB	89
25	0.48	0.5	3.27	2.69	RHAB	75
25	0.38	0.5	3.39	2.69	RHAB	80
25	0.3	0.47	3.65	2.86	Σ27	87
25	0.44	0.5	3.34	2.74	RHAB	85
25	0.44	0.44	3.34	3.06	RHAB	79
25	0.49	0.44	2.55	3.16	RHAB	87
25	0.45	0.49	3.58	3.20	RHAB	73
25	0.49	0.48	2.65	3.39	RHAB	81
25	0.48	0.48	3.21	2.47	RHAB	73
25	0.43	0.41	3.66	2.45	RHAB	79
25	0.49	0.43	2.55	3.66	RHAB	75
25	0.42	0.49	3.06	2.57	Σ3	83
25	0.46	0.46	3.01	3.58	RHAB	75
25	0.46	0.46	3.01	3.02	RHAB	88
25	0.44	0.49	3.30	2.55	RHAB	87
25	0.49	0.43	2.98	3.08	RHAB	89
25	0.44	0.43	3.30	3.08	RHAB	79
25	0.37	0.37	3.52	3.53	RHAB	82
25	0.49	0.34	2.86	3.59	RHAB	72
25	0.49	0.34	3.12	3.59	RHAB	69
25	0.43	0.48	2.44	2.55	RHAB	83
25	0.44	0.48	3.30	2.55	RHAB	87
25	0.39	0.41	3.47	3.35	RHAB	84
25	0.39	0.41	3.48	3.35	RHAB	89
25	0.49	0.41	2.83	3.35	RHAB	90
25	0.39	0.4	3.48	3.39	Σ3	78
25	0.47	0.39	2.43	3.44	RHAB	74
25	0.46	0.44	3.00	3.64	RHAB	81
25	0.43	0.45	3.23	3.47	RHAB	73
25	0.43	0.47	3.23	2.99	RHAB	56
25	0.47	0.47	3.03	2.99	RHAB	62

%Strain	m_1	m_2	M_1	M_2	GB type	Trace incl. (deg)
25	0.48	0.45	2.70	3.63	RHAB	74
25	0.48	0.47	2.70	2.80	RHAB	88
25	0.44	0.46	3.58	3.00	RHAB	81
25	0.41	0.49	3.31	3.27	RHAB	86
25	0.44	0.47	3.16	2.34	RHAB	83
25	0.47	0.47	2.99	2.34	RHAB	67
25	0.44	0.47	3.16	3.39	RHAB	75
25	0.44	0.46	3.16	3.52	RHAB	90
25	0.47	0.47	2.99	3.51	Σ9	74
25	0.45	0.47	3.05	3.38	RHAB	79
25	0.49	0.36	3.05	3.56	RHAB	82
25	0.44	0.47	2.36	2.41	RHAB	88
25	0.48	0.35	3.28	3.57	RHAB	86
25	0.45	0.35	3.16	3.57	RHAB	90
25	0.45	0.47	3.16	2.41	RHAB	77
25	0.47	0.4	3.51	3.30	RHAB	65
25	0.45	0.49	3.48	2.54	RHAB	79

Table E.3 Parameters measured for each NS cracked grain boundary of irradiated 316L stainless steel following straining to 2%, 5%, and 10% in 400˚C SCW.

%Strain	m_1	m_2	M_1	M_2	GB type	Trace incl. (deg)
2	0.50	0.35	2.71	3.59	RHAB	86
2	0.47	0.42	2.99	3.24	RHAB	87
2	0.47	0.50	2.54	2.71	RHAB	82
2	0.46	0.34	2.81	3.59	RHAB	72
2	0.44	0.49	3.17	2.98	RHAB	76
2	0.42	0.42	3.31	3.31	RHAB	90
2	0.42	0.46	3.25	3.29	RHAB	79
2	0.45	0.45	3.02	3.22	RHAB	85
2	0.46	0.38	2.60	3.45	RHAB	90
2	0.47	0.43	3.45	3.04	RHAB	87
2	0.41	0.49	3.33	3.10	RHAB	87
2	0.45	0.42	3.03	3.67	RHAB	88
2	0.37	0.43	3.50	3.05	RHAB	89
2	0.42	0.46	3.06	3.45	RHAB	75
2	0.44	0.46	2.93	3.49	RHAB	86
2	0.34	0.39	3.61	3.44	RHAB	90
2	0.36	0.49	3.57	2.75	RHAB	64
2	0.46	0.33	3.55	3.63	RHAB	86
2	0.33	0.41	3.64	3.37	RHAB	85
2	0.47	0.41	2.65	3.37	RHAB	78
2	0.48	0.37	2.89	3.53	RHAB	77
2	0.37	0.37	3.52	3.53	RHAB	56
2	0.49	0.34	2.89	3.59	RHAB	71
2	0.49	0.34	2.92	3.59	RHAB	72
2	0.49	0.34	2.94	3.59	RHAB	83
2	0.44	0.38	2.98	3.43	RHAB	87
2	0.46	0.36	3.00	3.54	RHAB	85
2	0.31	0.43	3.66	3.25	RHAB	83
2	0.42	0.33	3.28	3.63	RHAB	85
2	0.41	0.33	3.11	3.63	RHAB	59
2	0.37	0.34	3.48	3.59	RHAB	67
2	0.31	0.48	2.47	3.66	RHAB	74
2	0.36	0.34	3.57	3.55	RHAB	88
2	0.39	0.50	3.47	2.98	RHAB	83
2	0.39	0.42	3.47	3.30	RHAB	86
2	0.40	0.32	3.17	3.64	RHAB	83
2	0.44	0.38	2.97	3.49	RHAB	86
2	0.38	0.39	3.33	3.44	RHAB	73
2	0.39	0.37	3.40	3.52	RHAB	76
2	0.40	0.39	3.40	3.44	RHAB	64
2	0.45	0.41	2.98	3.31	RHAB	74
2	0.43	0.44	3.02	3.30	RHAB	60
2	0.39	0.44	3.35	3.30	RHAB	67

%Strain	m_1	m_2	M_1	M_2	GB type	Trace incl. (deg)
2	0.40	0.41	3.36	3.39	RHAB	82
2	0.39	0.40	3.36	3.41	RHAB	57
2	0.49	0.43	2.53	3.22	RHAB	76
2	0.50	0.42	2.71	3.67	RHAB	68
2	0.48	0.33	3.13	3.62	RHAB	67
2	0.48	0.47	3.42	3.39	RHAB	86
2	0.50	0.45	2.60	3.59	RHAB	63
2	0.48	0.44	2.94	3.63	RHAB	57
5	0.45	0.42	3.03	3.67	RHAB	88
5	0.44	0.43	3.03	3.66	RHAB	88
5	0.37	0.43	3.50	3.05	RHAB	86
5	0.37	0.42	3.50	3.11	RHAB	71
5	0.44	0.28	3.32	3.67	RHAB	71
5	0.49	0.28	3.02	3.67	RHAB	71
5	0.39	0.46	3.43	3.17	RHAB	83
5	0.46	0.50	3.02	2.80	RHAB	74
5	0.44	0.36	3.36	3.52	RHAB	75
5	0.44	0.39	3.11	3.45	RHAB	79
5	0.44	0.39	3.11	3.45	RHAB	80
5	0.49	0.39	2.65	3.48	RHAB	78
5	0.45	0.44	3.00	2.98	RHAB	80
5	0.48	0.45	3.27	3.63	RHAB	75
5	0.45	0.46	3.61	2.99	RHAB	44
5	0.47	0.48	3.54	3.35	RHAB	69
5	0.48	0.44	3.34	3.44	RHAB	77
5	0.45	0.46	3.04	2.97	RHAB	69
5	0.45	0.36	3.62	3.57	Σ9	87
5	0.48	0.44	2.61	3.65	RHAB	80
5	0.44	0.42	3.65	3.10	Σ9	80
5	0.44	0.47	3.64	2.41	RHAB	83
5	0.44	0.49	3.05	2.55	RHAB	83
5	0.48	0.39	3.25	3.44	RHAB	71
5	0.42	0.40	3.32	3.41	RHAB	74
5	0.48	0.47	3.11	3.50	RHAB	66
5	0.48	0.47	3.21	3.50	RHAB	66
5	0.40	0.45	3.35	3.62	RHAB	78
5	0.47	0.44	3.41	3.04	RHAB	84
5	0.47	0.44	2.98	3.04	RHAB	89
5	0.47	0.47	3.41	2.54	RHAB	88
5	0.42	0.45	3.20	3.37	RHAB	79
5	0.49	0.49	3.04	2.84	RHAB	53
5	0.43	0.49	3.02	2.97	RHAB	78
5	0.45	0.44	2.74	3.63	Σ9	84
5	0.46	0.48	3.56	3.26	RHAB	76
5	0.40	0.46	3.44	2.42	RHAB	65
5	0.39	0.50	3.44	2.59	RHAB	90

%Strain	m_1	m_2	M_1	M_2	GB type	Trace incl. (deg)
5	0.48	0.42	2.91	3.17	RHAB	87
5	0.48	0.48	2.91	2.85	RHAB	53
5	0.48	0.48	2.68	2.85	RHAB	85
5	0.42	0.47	3.17	3.46	RHAB	87
5	0.45	0.48	3.09	2.92	RHAB	58
5	0.45	0.43	3.60	3.18	RHAB	48
5	0.45	0.33	3.61	3.63	RHAB	87
5	0.47	0.45	3.34	3.36	RHAB	87
5	0.36	0.46	3.55	2.34	RHAB	67
5	0.39	0.43	3.46	3.22	RHAB	79
5	0.38	0.40	3.33	3.40	RHAB	53
5	0.43	0.44	3.28	3.55	RHAB	76
5	0.43	0.48	3.28	3.45	RHAB	76
5	0.46	0.37	3.05	3.39	RHAB	85
5	0.37	0.38	3.51	3.30	RHAB	72
5	0.37	0.49	3.51	2.49	RHAB	72
5	0.48	0.47	3.21	2.42	RHAB	87
5	0.46	0.44	3.57	3.56	RHAB	85
5	0.48	0.46	3.32	2.73	RHAB	80
5	0.41	0.49	3.36	3.00	RHAB	89
5	0.49	0.49	2.69	2.57	RHAB	82
5	0.49	0.47	2.55	3.29	RHAB	87
5	0.34	0.39	3.61	3.44	RHAB	89
5	0.36	0.49	3.57	2.75	RHAB	77
5	0.46	0.33	3.55	3.63	RHAB	84
5	0.48	0.37	2.89	3.53	RHAB	84
5	0.37	0.37	3.52	3.53	RHAB	61
5	0.49	0.34	2.92	3.59	RHAB	74
5	0.49	0.34	2.94	3.59	RHAB	79
5	0.49	0.34	2.89	3.59	RHAB	74
5	0.44	0.38	2.98	3.43	RHAB	69
5	0.37	0.38	3.44	3.43	RHAB	83
5	0.46	0.36	3.00	3.54	RHAB	89
5	0.46	0.37	3.00	3.53	RHAB	62
5	0.44	0.36	3.16	3.54	RHAB	70
5	0.31	0.43	3.66	3.25	RHAB	83
5	0.47	0.34	2.43	3.59	RHAB	78
5	0.37	0.46	3.48	2.81	RHAB	48
5	0.37	0.34	3.48	3.59	RHAB	76
5	0.36	0.45	3.57	2.88	RHAB	86
5	0.36	0.48	3.57	2.47	RHAB	25
5	0.45	0.45	2.39	2.88	RHAB	53
5	0.36	0.34	3.57	3.55	RHAB	88
5	0.39	0.42	3.45	3.30	RHAB	50
5	0.39	0.42	3.46	3.30	RHAB	65
5	0.39	0.42	3.47	3.30	RHAB	88

%Strain	m_1	m_2	M_1	M_2	GB type	Trace incl. (deg)
5	0.39	0.50	3.47	2.98	RHAB	88
5	0.46	0.42	2.38	3.30	RHAB	86
5	0.40	0.32	3.17	3.64	RHAB	83
5	0.44	0.38	2.97	3.49	RHAB	90
5	0.44	0.50	2.97	2.56	RHAB	81
5	0.38	0.39	3.33	3.44	RHAB	78
5	0.48	0.39	2.49	3.44	RHAB	78
5	0.39	0.37	3.40	3.52	RHAB	71
5	0.40	0.39	3.40	3.44	RHAB	62
5	0.45	0.41	2.98	3.31	RHAB	75
5	0.43	0.44	3.02	3.30	RHAB	59
5	0.39	0.44	3.35	3.30	RHAB	66
5	0.40	0.45	3.36	2.41	Σ3	90
5	0.40	0.41	3.36	3.39	RHAB	86
5	0.39	0.40	3.36	3.41	RHAB	57
5	0.42	0.39	3.23	3.42	RHAB	80
5	0.32	0.48	3.64	2.80	RHAB	73
5	0.32	0.38	3.64	3.50	RHAB	74
5	0.36	0.38	3.56	3.42	RHAB	80
5	0.43	0.35	2.43	3.58	RHAB	72
5	0.39	0.41	3.43	3.10	RHAB	69
5	0.43	0.44	2.43	3.04	RHAB	57
5	0.39	0.35	3.43	3.58	RHAB	78
5	0.47	0.29	2.82	3.67	RHAB	81
5	0.46	0.32	3.00	3.65	RHAB	63
5	0.47	0.32	2.82	3.65	RHAB	51
5	0.34	0.32	3.58	3.65	RHAB	86
5	0.37	0.43	3.46	3.14	RHAB	82
5	0.50	0.44	3.12	3.28	RHAB	59
5	0.37	0.44	3.46	3.28	RHAB	57
5	0.49	0.42	2.82	3.22	RHAB	69
5	0.41	0.48	3.34	3.04	RHAB	90
5	0.41	0.40	3.22	3.22	RHAB	90
5	0.48	0.34	2.47	3.62	RHAB	73
5	0.34	0.34	3.58	3.62	RHAB	73
5	0.34	0.34	3.58	3.62	RHAB	73
5	0.41	0.49	3.23	3.11	Σ9	71
5	0.43	0.47	2.41	2.75	RHAB	59
5	0.47	0.50	2.91	2.90	RHAB	71
5	0.44	0.38	3.41	3.49	RHAB	68
5	0.49	0.44	3.10	3.46	RHAB	55
5	0.50	0.44	2.96	3.05	RHAB	76
5	0.48	0.45	2.94	2.32	Σ9	50
5	0.45	0.33	2.94	3.59	RHAB	69
5	0.45	0.43	2.94	3.03	RHAB	84
5	0.45	0.45	2.94	2.83	RHAB	69

%Strain	m_1	m_2	M_1	M_2	GB type	Trace incl. (deg)
5	0.45	0.45	2.94	2.83	RHAB	69
5	0.47	0.49	2.98	2.73	RHAB	61
5	0.45	0.49	2.41	3.10	Σ27	76
5	0.31	0.47	3.66	2.86	RHAB	61
5	0.35	0.49	3.60	2.51	RHAB	71
5	0.30	0.29	3.66	3.67	RHAB	74
5	0.49	0.42	2.51	3.36	RHAB	59
5	0.47	0.44	3.49	3.05	RHAB	70
5	0.49	0.44	2.88	3.05	RHAB	70
5	0.36	0.47	3.56	2.77	RHAB	81
5	0.46	0.43	3.30	3.16	RHAB	85
5	0.46	0.45	3.30	3.04	RHAB	65
5	0.46	0.43	3.30	3.17	RHAB	78
5	0.42	0.48	3.14	2.44	RHAB	72
5	0.48	0.36	2.50	3.55	RHAB	83
5	0.36	0.30	3.54	3.67	RHAB	89
5	0.47	0.36	2.77	3.56	RHAB	65
5	0.48	0.44	2.49	3.05	RHAB	79
5	0.32	0.41	3.64	3.17	RHAB	76
5	0.40	0.41	3.33	3.34	Σ9	26
5	0.49	0.49	2.98	2.53	Σ3	76
5	0.46	0.49	2.35	2.73	RHAB	79
5	0.42	0.35	3.27	3.59	RHAB	63
5	0.42	0.46	3.27	2.35	RHAB	86
5	0.35	0.44	3.59	3.30	RHAB	62
5	0.48	0.37	3.40	3.54	RHAB	65
5	0.49	0.39	2.54	3.40	RHAB	74
5	0.42	0.37	3.28	3.52	RHAB	81
5	0.42	0.44	3.28	3.64	RHAB	62
5	0.31	0.44	3.65	3.08	RHAB	75
5	0.39	0.40	3.36	3.40	RHAB	69
5	0.42	0.39	3.07	3.37	RHAB	72
5	0.42	0.40	3.07	3.35	RHAB	77
5	0.42	0.40	3.07	3.36	RHAB	65
5	0.36	0.48	3.56	2.44	RHAB	77
5	0.39	0.45	3.36	2.41	RHAB	71
5	0.39	0.40	3.36	3.40	RHAB	71
5	0.46	0.41	2.30	3.37	RHAB	83
5	0.47	0.41	2.65	3.37	RHAB	83
5	0.33	0.41	3.64	3.37	RHAB	83
5	0.41	0.33	3.11	3.63	RHAB	58
5	0.42	0.33	3.28	3.63	RHAB	83
5	0.42	0.33	3.28	3.63	RHAB	84
5	0.42	0.33	3.28	3.63	RHAB	48
5	0.49	0.43	2.53	3.22	RHAB	77
5	0.49	0.43	2.53	3.27	RHAB	55

%Strain	m_1	m_2	M_1	M_2	GB type	Trace incl. (deg)
5	0.50	0.41	2.71	3.67	RHAB	47
5	0.50	0.42	2.71	3.67	RHAB	73
5	0.46	0.42	3.53	3.67	RHAB	60
5	0.48	0.33	3.13	3.62	RHAB	71
5	0.48	0.33	2.50	3.62	RHAB	66
5	0.48	0.47	3.42	3.39	RHAB	79
5	0.50	0.47	2.95	3.39	RHAB	36
5	0.44	0.47	3.52	3.39	RHAB	72
5	0.50	0.45	2.60	3.59	RHAB	59
5	0.47	0.44	3.45	3.63	RHAB	49
5	0.48	0.44	2.94	3.63	RHAB	62
5	0.47	0.44	3.47	3.63	RHAB	46
5	0.47	0.46	3.45	3.59	RHAB	54
5	0.36	0.43	3.57	3.27	RHAB	76
5	0.49	0.43	2.53	3.27	RHAB	56
5	0.47	0.44	3.54	3.60	RHAB	90
5	0.45	0.44	3.57	3.60	RHAB	87
5	0.44	0.42	3.60	2.44	RHAB	73
5	0.44	0.46	3.60	3.53	RHAB	87
5	0.42	0.49	3.29	2.56	RHAB	61
5	0.49	0.42	3.09	3.29	RHAB	64
5	0.43	0.44	2.43	3.64	RHAB	87
5	0.50	0.48	2.60	2.77	RHAB	71
5	0.46	0.48	3.51	3.44	Σ3	71
5	0.45	0.45	3.56	3.61	RHAB	87
5	0.46	0.45	3.49	3.61	RHAB	79
5	0.45	0.47	3.56	3.47	RHAB	45
5	0.46	0.44	2.33	3.35	RHAB	90
5	0.42	0.41	3.67	3.67	Σ3	90
5	0.41	0.50	3.21	2.80	RHAB	73
5	0.48	0.47	2.91	2.42	RHAB	79
5	0.49	0.42	3.22	3.09	RHAB	55
5	0.49	0.50	3.22	2.74	RHAB	55
5	0.48	0.46	3.42	3.08	RHAB	84
5	0.50	0.46	2.57	3.08	Σ27	71
5	0.50	0.46	2.57	3.25	RHAB	88
5	0.43	0.42	3.42	3.67	RHAB	89
5	0.43	0.41	3.52	3.67	RHAB	60
5	0.47	0.44	3.18	3.48	RHAB	65
5	0.43	0.45	3.65	3.60	RHAB	63
5	0.39	0.50	3.41	2.57	RHAB	75
5	0.43	0.45	3.25	3.04	RHAB	70
5	0.48	0.48	2.83	3.29	RHAB	55
5	0.43	0.47	3.16	2.40	RHAB	89
5	0.50	0.29	2.95	3.67	RHAB	70
5	0.46	0.47	2.89	3.54	RHAB	76

%Strain	m_1	m_2	M_1	M_2	GB type	Trace incl. (deg)
5	0.49	0.45	3.04	3.62	RHAB	45
5	0.48	0.42	2.95	3.06	Σ9	90
5	0.50	0.48	3.02	2.50	RHAB	33
5	0.45	0.49	3.57	3.25	RHAB	83
5	0.42	0.44	3.38	3.54	RHAB	56
5	0.46	0.50	3.20	2.74	RHAB	82
5	0.48	0.49	3.44	3.03	RHAB	60
5	0.46	0.45	3.20	2.36	RHAB	73
5	0.47	0.50	2.41	3.04	RHAB	72
5	0.47	0.42	2.41	3.30	RHAB	72
5	0.47	0.43	3.35	3.43	RHAB	69
5	0.40	0.48	3.37	3.15	RHAB	86
5	0.43	0.47	3.06	2.98	RHAB	41
5	0.43	0.49	3.06	2.79	RHAB	89
5	0.44	0.49	3.64	3.24	RHAB	54
5	0.45	0.47	3.56	3.50	Σ3	59
10	0.35	0.48	3.57	2.47	RHAB	22
10	0.45	0.45	2.39	2.88	RHAB	39
10	0.36	0.45	3.57	2.88	RHAB	87
10	0.36	0.34	3.57	3.55	RHAB	88
10	0.41	0.48	3.08	2.47	Σ9	86
10	0.36	0.48	3.57	2.47	RHAB	22
10	0.39	0.42	3.45	3.30	RHAB	49
10	0.39	0.42	3.46	3.30	RHAB	65
10	0.39	0.50	3.47	2.98	RHAB	83
10	0.46	0.42	2.38	3.30	RHAB	84
10	0.39	0.42	3.47	3.30	RHAB	85
10	0.39	0.50	3.45	2.98	RHAB	47
10	0.46	0.35	2.38	3.58	RHAB	64
10	0.40	0.32	3.17	3.64	RHAB	80
10	0.42	0.32	3.06	3.64	RHAB	87
10	0.40	0.35	3.17	3.58	RHAB	59
10	0.37	0.50	3.45	2.56	RHAB	78
10	0.44	0.50	2.97	2.56	RHAB	88
10	0.44	0.38	2.97	3.49	RHAB	89
10	0.37	0.46	3.45	2.99	RHAB	50
10	0.38	0.39	3.33	3.44	RHAB	84
10	0.48	0.39	2.49	3.44	RHAB	77
10	0.39	0.37	3.40	3.52	RHAB	73
10	0.40	0.37	3.38	3.52	RHAB	47
10	0.40	0.39	3.40	3.44	RHAB	60
10	0.47	0.41	2.82	3.31	RHAB	69
10	0.45	0.41	2.98	3.31	RHAB	70
10	0.45	0.41	3.37	3.31	RHAB	43
10	0.39	0.44	3.35	3.30	RHAB	64
10	0.43	0.44	3.02	3.30	RHAB	58

%Strain	m_1	m_2	M_1	M_2	GB type	Trace incl. (deg)
10	0.40	0.41	3.36	3.39	RHAB	77
10	0.40	0.45	3.36	2.41	Σ3	87
10	0.39	0.45	3.36	2.41	RHAB	66
10	0.39	0.45	3.36	2.41	RHAB	74
10	0.39	0.40	3.36	3.41	RHAB	56
10	0.30	0.29	3.66	3.67	RHAB	77
10	0.49	0.42	2.51	3.36	RHAB	56
10	0.47	0.44	3.49	3.05	RHAB	79
10	0.47	0.44	3.49	3.05	RHAB	86
10	0.49	0.44	2.88	3.05	RHAB	70
10	0.36	0.47	3.56	2.77	RHAB	79
10	0.36	0.47	3.56	2.91	RHAB	84
10	0.36	0.49	3.56	2.85	RHAB	29
10	0.46	0.44	3.30	3.04	RHAB	73
10	0.46	0.45	3.30	3.04	RHAB	74
10	0.46	0.43	3.30	3.17	RHAB	76
10	0.46	0.43	3.30	3.16	RHAB	87
10	0.46	0.44	3.30	3.30	RHAB	88
10	0.48	0.44	3.20	3.30	RHAB	89
10	0.50	0.44	2.56	3.30	RHAB	67
10	0.42	0.48	3.14	2.44	RHAB	65
10	0.43	0.41	3.12	3.20	RHAB	73
10	0.44	0.41	3.05	3.20	RHAB	88
10	0.44	0.48	3.05	2.44	RHAB	53
10	0.48	0.36	2.50	3.55	RHAB	81
10	0.32	0.36	3.65	3.55	Σ3	74
10	0.38	0.36	3.49	3.55	LAB	88
10	0.37	0.47	3.54	2.49	RHAB	44
10	0.45	0.46	2.39	2.58	RHAB	61
10	0.36	0.45	3.54	2.29	RHAB	76
10	0.36	0.30	3.54	3.67	RHAB	82
10	0.36	0.47	3.54	2.49	RHAB	82
10	0.37	0.46	3.54	2.58	RHAB	21
10	0.47	0.36	2.77	3.56	RHAB	65
10	0.48	0.36	2.83	3.56	RHAB	63
10	0.48	0.44	2.49	3.05	RHAB	74
10	0.32	0.41	3.64	3.17	RHAB	78
10	0.40	0.41	3.33	3.34	Σ9	27
10	0.49	0.49	2.98	2.53	Σ3	75
10	0.36	0.49	3.50	2.53	RHAB	68
10	0.46	0.49	2.35	3.09	RHAB	60
10	0.42	0.49	3.29	2.73	RHAB	63
10	0.46	0.49	2.35	2.73	RHAB	78
10	0.35	0.49	3.60	2.73	RHAB	79
10	0.42	0.49	3.29	3.09	RHAB	58
10	0.42	0.35	3.27	3.59	RHAB	65

%Strain	m_1	m_2	M_1	M_2	GB type	Trace incl. (deg)
10	0.42	0.46	3.27	2.35	RHAB	77
10	0.43	0.35	2.44	3.59	RHAB	60
10	0.35	0.44	3.59	3.30	RHAB	59
10	0.48	0.37	3.40	3.54	RHAB	59
10	0.49	0.39	2.54	3.40	RHAB	86
10	0.42	0.49	3.28	2.68	RHAB	81
10	0.42	0.37	3.28	3.52	RHAB	76
10	0.42	0.46	3.28	2.99	RHAB	58
10	0.42	0.44	3.28	3.64	RHAB	61
10	0.42	0.47	3.28	2.82	RHAB	63
10	0.42	0.50	3.28	2.71	RHAB	49
10	0.31	0.44	3.65	3.08	RHAB	74
10	0.31	0.46	3.65	2.31	RHAB	48
10	0.39	0.40	3.36	3.40	RHAB	66
10	0.42	0.39	3.07	3.37	RHAB	72
10	0.42	0.40	3.07	3.35	RHAB	79
10	0.42	0.40	3.07	3.36	RHAB	64
10	0.36	0.48	3.56	2.44	RHAB	80
10	0.39	0.40	3.36	3.40	RHAB	71
10	0.39	0.45	3.36	2.41	RHAB	65
10	0.44	0.40	3.07	3.40	RHAB	45
10	0.43	0.49	3.27	2.85	Σ9	71
10	0.45	0.29	3.37	3.67	RHAB	74
10	0.29	0.49	3.67	3.29	RHAB	73
10	0.48	0.43	3.07	3.23	RHAB	38
10	0.38	0.49	3.45	2.61	RHAB	70
10	0.41	0.49	3.35	2.54	RHAB	60
10	0.47	0.44	2.94	3.04	RHAB	70
10	0.40	0.42	3.38	3.27	RHAB	80
10	0.40	0.50	3.38	2.59	RHAB	88
10	0.40	0.49	3.38	2.83	RHAB	53
10	0.39	0.34	3.44	3.61	RHAB	78
10	0.47	0.33	2.95	3.62	RHAB	62
10	0.44	0.44	3.10	2.39	RHAB	71
10	0.44	0.41	3.21	3.34	RHAB	74
10	0.47	0.39	3.48	3.40	RHAB	59
10	0.45	0.35	2.38	3.51	RHAB	83
10	0.41	0.35	3.35	3.51	RHAB	80
10	0.49	0.49	2.55	3.15	RHAB	67
10	0.47	0.42	2.87	3.32	RHAB	70
10	0.47	0.37	2.87	3.54	RHAB	76
10	0.47	0.49	2.87	2.55	RHAB	41
10	0.38	0.49	3.32	2.54	RHAB	77
10	0.46	0.49	3.01	2.54	RHAB	39
10	0.39	0.30	3.44	3.67	LAB	79
10	0.45	0.44	3.28	3.30	RHAB	63

%Strain	m_1	m_2	M_1	M_2	GB type	Trace incl. (deg)
10	0.45	0.44	3.03	3.20	RHAB	84
10	0.45	0.41	3.03	3.34	RHAB	57
10	0.49	0.49	2.52	3.15	Σ3	87
10	0.49	0.45	2.52	3.03	RHAB	45
10	0.49	0.50	2.56	2.94	RHAB	73
10	0.38	0.49	3.35	2.61	RHAB	78
10	0.42	0.47	3.29	2.97	RHAB	57
10	0.47	0.31	2.76	3.66	RHAB	77
10	0.31	0.47	3.66	2.87	RHAB	79
10	0.47	0.42	2.81	3.19	RHAB	89
10	0.49	0.46	2.50	3.59	RHAB	36
10	0.32	0.47	3.64	2.40	RHAB	66
10	0.48	0.47	2.47	2.40	RHAB	74
10	0.32	0.47	3.64	2.40	RHAB	73
10	0.40	0.42	3.28	3.05	Σ3	71
10	0.47	0.42	2.35	3.05	RHAB	79
10	0.46	0.37	3.56	3.46	RHAB	67
10	0.47	0.38	3.51	3.32	RHAB	44
10	0.49	0.43	2.52	3.25	RHAB	62
10	0.35	0.46	3.59	2.35	Σ3	62
10	0.47	0.46	2.97	2.35	Σ9	73
10	0.47	0.46	2.97	2.35	Σ9	41
10	0.50	0.44	2.57	3.11	RHAB	82
10	0.46	0.42	2.44	3.06	RHAB	65
10	0.46	0.42	2.44	3.06	RHAB	72
10	0.28	0.42	3.67	3.06	RHAB	82
10	0.44	0.42	3.04	3.06	RHAB	51
10	0.48	0.48	3.11	2.93	RHAB	76
10	0.49	0.39	2.55	3.47	RHAB	61
10	0.41	0.41	3.20	3.34	LAB	67
10	0.35	0.36	3.59	3.58	RHAB	80
10	0.39	0.45	3.43	3.04	RHAB	86
10	0.36	0.39	3.55	3.43	RHAB	79
10	0.45	0.40	3.50	3.14	RHAB	74
10	0.46	0.40	2.37	3.14	RHAB	67
10	0.40	0.40	3.14	3.41	RHAB	85
10	0.49	0.45	2.74	2.99	RHAB	75
10	0.46	0.45	3.33	2.99	RHAB	41
10	0.48	0.35	2.61	3.57	RHAB	86
10	0.45	0.35	3.27	3.57	RHAB	69
10	0.33	0.37	3.63	3.53	RHAB	47
10	0.49	0.45	2.49	2.40	RHAB	60
10	0.35	0.37	3.56	3.53	RHAB	70
10	0.45	0.35	3.11	3.57	RHAB	86
10	0.48	0.33	2.63	3.63	RHAB	76
10	0.37	0.46	3.54	2.98	RHAB	88

%Strain	m_1	m_2	M_1	M_2	GB type	Trace incl. (deg)
10	0.37	0.46	3.54	3.59	RHAB	58
10	0.48	0.37	2.50	3.54	RHAB	46
10	0.48	0.37	2.49	3.54	RHAB	50
10	0.36	0.32	3.56	3.65	RHAB	71
10	0.47	0.38	2.91	3.47	Σ3	73
10	0.49	0.42	2.85	3.13	RHAB	69
10	0.49	0.44	2.85	3.05	RHAB	86
10	0.49	0.44	2.85	3.05	RHAB	59
10	0.50	0.46	2.95	2.35	RHAB	77
10	0.46	0.36	3.51	3.56	Σ9	72
10	0.36	0.38	3.56	3.34	RHAB	84
10	0.46	0.38	2.35	3.34	RHAB	80
10	0.47	0.36	2.80	3.56	Σ3	80
10	0.48	0.46	2.83	3.51	Σ9	81
10	0.44	0.46	2.40	3.01	RHAB	82
10	0.44	0.46	2.41	3.39	RHAB	64
10	0.38	0.38	3.45	3.46	RHAB	79
10	0.38	0.38	3.45	3.46	RHAB	81
10	0.40	0.38	3.41	3.46	RHAB	82
10	0.38	0.46	3.45	2.77	RHAB	64
10	0.48	0.38	2.43	3.46	RHAB	88
10	0.39	0.49	3.38	2.52	RHAB	63
10	0.50	0.41	2.76	3.07	RHAB	46
10	0.43	0.47	3.05	2.50	RHAB	82
10	0.43	0.43	3.05	3.05	RHAB	76
10	0.49	0.45	2.52	2.84	RHAB	52
10	0.37	0.42	3.47	3.29	RHAB	86
10	0.31	0.35	3.65	3.57	RHAB	73
10	0.31	0.48	3.65	2.48	RHAB	61
10	0.40	0.42	3.37	3.06	RHAB	80
10	0.47	0.31	2.40	3.66	RHAB	70
10	0.31	0.31	3.64	3.66	RHAB	64
10	0.34	0.45	3.61	2.39	Σ3	83
10	0.38	0.45	3.44	2.76	Σ9	67
10	0.45	0.38	2.96	3.45	Σ3	71
10	0.44	0.44	3.54	2.97	RHAB	87
10	0.44	0.37	3.54	3.45	RHAB	79
10	0.44	0.46	2.97	2.82	Σ3	64
10	0.48	0.37	2.43	3.45	RHAB	26
10	0.36	0.29	3.57	3.67	RHAB	81
10	0.47	0.48	3.07	3.45	RHAB	87
10	0.47	0.49	3.07	2.51	RHAB	58
10	0.45	0.45	3.04	2.99	RHAB	56
10	0.34	0.31	3.61	3.64	RHAB	70
10	0.48	0.47	2.46	2.40	RHAB	89
10	0.34	0.47	3.61	2.40	RHAB	58

%Strain	m_1	m_2	M_1	M_2	GB type	Trace incl. (deg)
10	0.46	0.42	3.53	3.67	RHAB	55
10	0.50	0.42	2.71	3.67	RHAB	73
10	0.50	0.41	2.71	3.67	RHAB	53
10	0.50	0.49	2.95	3.25	RHAB	32
10	0.42	0.47	3.30	3.38	RHAB	52
10	0.44	0.47	3.52	3.39	RHAB	78
10	0.48	0.47	3.42	3.39	RHAB	81
10	0.47	0.47	2.37	3.39	Σ3	36
10	0.50	0.47	2.95	3.39	RHAB	32
10	0.47	0.45	3.41	3.59	RHAB	78
10	0.50	0.45	2.60	3.59	RHAB	51
10	0.47	0.46	3.45	3.59	RHAB	55
10	0.47	0.48	3.45	3.23	RHAB	72
10	0.47	0.49	3.45	2.52	RHAB	54
10	0.45	0.44	3.57	3.60	RHAB	89
10	0.47	0.44	3.54	3.60	RHAB	84
10	0.44	0.42	3.60	2.44	RHAB	70
10	0.44	0.46	3.60	3.53	RHAB	76
10	0.42	0.49	3.29	2.56	RHAB	63
10	0.49	0.42	3.09	3.29	RHAB	60
10	0.46	0.44	2.33	3.35	RHAB	88
10	0.44	0.44	3.58	3.35	LAB	70
10	0.42	0.41	3.67	3.67	Σ3	87
10	0.41	0.50	3.21	2.80	RHAB	73
10	0.49	0.47	2.87	2.95	RHAB	66
10	0.48	0.47	2.91	2.42	RHAB	80
10	0.48	0.47	2.91	2.42	RHAB	85
10	0.43	0.47	3.27	2.42	RHAB	89
10	0.49	0.47	2.87	2.42	RHAB	51
10	0.49	0.42	3.22	3.09	RHAB	55
10	0.49	0.50	3.21	2.74	RHAB	60
10	0.49	0.50	3.22	2.74	RHAB	48
10	0.48	0.46	3.42	3.08	RHAB	88
10	0.50	0.46	2.57	3.08	Σ27	70
10	0.48	0.49	3.42	2.95	RHAB	46
10	0.48	0.46	3.41	3.25	RHAB	84
10	0.50	0.46	2.57	3.25	RHAB	81
10	0.43	0.42	3.42	3.67	RHAB	85
10	0.43	0.41	3.52	3.67	RHAB	58
10	0.47	0.44	3.18	3.48	RHAB	66
10	0.47	0.48	3.18	3.38	RHAB	72
10	0.47	0.47	3.18	3.49	RHAB	80
10	0.47	0.48	3.18	3.32	RHAB	63
10	0.43	0.45	3.65	3.60	RHAB	57
10	0.43	0.45	3.66	3.60	RHAB	87
10	0.43	0.43	3.66	3.64	RHAB	42

%Strain	m_1	m_2	M_1	M_2	GB type	Trace incl. (deg)
10	0.39	0.50	3.41	2.57	RHAB	79
10	0.45	0.50	3.00	2.57	RHAB	56
10	0.49	0.47	3.23	2.96	RHAB	70
10	0.44	0.47	3.36	2.96	RHAB	80
10	0.49	0.49	3.23	2.84	RHAB	69
10	0.46	0.46	3.57	3.41	RHAB	57
10	0.46	0.44	3.57	3.36	RHAB	34
10	0.43	0.50	3.62	2.84	RHAB	64
10	0.46	0.50	3.22	2.58	RHAB	77
10	0.46	0.48	3.22	3.43	RHAB	60
10	0.46	0.50	3.22	2.92	RHAB	57
10	0.50	0.49	2.92	3.23	RHAB	83
10	0.41	0.49	3.27	3.22	RHAB	87
10	0.47	0.47	3.47	3.40	RHAB	52
10	0.43	0.47	3.61	3.49	RHAB	80
10	0.49	0.45	2.60	3.25	RHAB	80
10	0.48	0.38	2.58	3.35	RHAB	84
10	0.45	0.50	2.35	2.80	RHAB	65
10	0.47	0.50	3.49	2.90	RHAB	51
10	0.48	0.48	3.42	3.13	RHAB	85
10	0.46	0.45	3.56	3.09	RHAB	84
10	0.47	0.45	3.53	3.60	RHAB	86
10	0.47	0.45	3.53	3.09	RHAB	78
10	0.45	0.49	3.60	2.96	RHAB	82
10	0.49	0.49	3.23	2.96	RHAB	42
10	0.48	0.49	3.43	3.23	RHAB	59
10	0.46	0.49	3.60	3.24	RHAB	81
10	0.50	0.49	2.56	3.22	RHAB	87
10	0.49	0.46	2.84	3.55	RHAB	15
10	0.49	0.40	3.13	3.41	RHAB	61
10	0.49	0.42	2.82	3.31	RHAB	77
10	0.42	0.48	3.31	2.47	RHAB	85
10	0.49	0.42	2.71	3.30	RHAB	64
10	0.49	0.42	2.81	3.30	RHAB	64
10	0.46	0.43	3.57	3.60	RHAB	77
10	0.43	0.46	3.60	3.59	RHAB	49
10	0.46	0.46	3.57	3.59	Σ3	85
10	0.47	0.49	3.49	3.33	RHAB	75
10	0.50	0.45	2.92	3.02	RHAB	77
10	0.47	0.46	2.36	3.50	RHAB	31
10	0.45	0.49	3.57	2.70	RHAB	74
10	0.50	0.47	2.86	3.47	RHAB	59
10	0.48	0.46	2.58	3.46	RHAB	74
10	0.48	0.47	2.58	2.36	RHAB	74
10	0.38	0.49	3.35	2.92	RHAB	71
10	0.38	0.50	3.35	2.84	Σ9	65

%Strain	m_1	m_2	M_1	M_2	GB type	Trace incl. (deg)
10	0.39	0.49	3.41	2.71	RHAB	64
10	0.50	0.49	2.65	3.25	RHAB	75
10	0.50	0.49	2.73	2.52	RHAB	55
10	0.42	0.43	3.67	3.05	RHAB	72
10	0.44	0.49	3.23	2.54	RHAB	85
10	0.45	0.39	3.19	3.36	RHAB	84
10	0.45	0.47	3.19	2.41	RHAB	78
10	0.50	0.44	2.58	3.13	RHAB	71
10	0.46	0.45	3.57	3.17	RHAB	75
10	0.43	0.45	3.60	3.16	RHAB	84
10	0.43	0.50	3.60	2.81	RHAB	73
10	0.45	0.49	3.16	3.02	RHAB	82
10	0.45	0.44	3.26	3.65	RHAB	90
10	0.48	0.44	2.43	3.03	RHAB	73
10	0.48	0.47	2.43	2.74	RHAB	80
10	0.48	0.44	2.43	3.03	RHAB	90
10	0.48	0.45	2.43	3.52	RHAB	64
10	0.50	0.48	2.90	2.43	RHAB	54
10	0.50	0.46	2.90	3.51	RHAB	67
10	0.49	0.41	3.24	3.33	RHAB	87
10	0.49	0.45	3.24	3.61	RHAB	75
10	0.48	0.39	3.13	3.48	RHAB	64
10	0.40	0.49	3.23	3.31	RHAB	82
10	0.39	0.48	3.48	3.36	RHAB	37
10	0.47	0.48	3.44	3.43	RHAB	83
10	0.50	0.46	2.92	3.54	RHAB	73
10	0.50	0.49	2.92	3.26	RHAB	62
10	0.49	0.50	3.26	2.57	RHAB	66
10	0.49	0.50	3.26	2.57	RHAB	78
10	0.49	0.48	3.26	3.42	RHAB	60
10	0.45	0.44	3.27	3.34	RHAB	78
10	0.45	0.49	3.27	3.26	RHAB	73
10	0.44	0.44	3.62	3.63	RHAB	87
10	0.49	0.44	3.32	3.65	RHAB	68
10	0.47	0.38	3.44	3.48	RHAB	65
10	0.46	0.47	3.57	3.44	RHAB	78
10	0.46	0.47	2.96	3.52	RHAB	78
10	0.37	0.47	3.52	3.52	RHAB	59
10	0.48	0.45	3.04	3.61	RHAB	87
10	0.48	0.46	3.04	3.57	RHAB	69
10	0.45	0.45	3.35	3.60	RHAB	47
10	0.48	0.46	3.26	2.33	RHAB	85
10	0.49	0.49	3.21	3.11	Σ3	64
10	0.40	0.50	3.41	2.82	RHAB	84
10	0.45	0.49	3.50	2.73	RHAB	87
10	0.48	0.49	3.40	2.73	RHAB	57

%Strain	m_1	m_2	M_1	M_2	GB type	Trace incl. (deg)
10	0.43	0.50	3.66	2.57	RHAB	80
10	0.47	0.50	3.48	2.85	RHAB	70
10	0.44	0.50	3.03	2.85	RHAB	63
10	0.42	0.48	3.67	3.37	RHAB	44
10	0.42	0.48	3.67	3.37	RHAB	48
10	0.39	0.44	3.44	3.35	RHAB	74
10	0.42	0.49	3.67	2.56	RHAB	82
10	0.46	0.49	3.46	2.56	RHAB	30
10	0.46	0.48	3.12	3.25	RHAB	28
10	0.41	0.47	3.67	3.18	RHAB	77
10	0.42	0.47	3.67	3.18	RHAB	82
10	0.41	0.47	3.67	3.18	RHAB	89
10	0.42	0.47	3.67	3.18	RHAB	77
10	0.41	0.41	3.16	3.67	RHAB	55
10	0.49	0.50	3.22	2.74	RHAB	54
10	0.49	0.42	3.22	3.09	RHAB	55
10	0.42	0.50	3.09	2.74	RHAB	15
10	0.48	0.42	2.86	3.09	RHAB	79
10	0.46	0.43	3.59	3.05	RHAB	83
10	0.48	0.49	2.86	3.22	RHAB	75
10	0.50	0.47	2.78	2.36	RHAB	76
10	0.45	0.50	3.04	2.74	RHAB	75
10	0.50	0.46	2.78	3.11	RHAB	79
10	0.48	0.50	2.91	2.80	RHAB	57
10	0.43	0.50	3.26	2.80	RHAB	61
10	0.48	0.50	2.90	2.80	RHAB	64
10	0.48	0.50	2.90	2.80	RHAB	68
10	0.48	0.50	2.91	2.80	RHAB	55
10	0.47	0.37	2.42	3.52	RHAB	63
10	0.37	0.50	3.52	2.79	RHAB	76
10	0.47	0.47	2.84	2.37	RHAB	84
10	0.47	0.47	2.84	3.06	RHAB	65
10	0.50	0.43	2.81	3.52	RHAB	84
10	0.50	0.49	2.57	2.95	RHAB	53
10	0.48	0.45	3.39	3.60	RHAB	68
10	0.46	0.45	2.75	3.60	RHAB	89
10	0.50	0.45	2.95	3.60	RHAB	52
10	0.44	0.44	3.26	3.60	RHAB	42
10	0.49	0.49	3.10	3.00	Σ9	66
10	0.44	0.49	3.60	3.00	RHAB	70
10	0.49	0.44	3.16	3.26	RHAB	82
10	0.50	0.44	2.79	3.26	RHAB	74
10	0.46	0.50	2.98	2.69	RHAB	65
10	0.49	0.50	3.11	2.69	RHAB	41
10	0.47	0.43	3.49	3.66	RHAB	69
10	0.47	0.45	3.49	3.60	RHAB	60

%Strain	m_1	m_2	M_1	M_2	GB type	Trace incl. (deg)
10	0.44	0.44	3.26	3.62	RHAB	82
10	0.49	0.44	3.00	3.62	RHAB	81
10	0.44	0.43	3.60	3.05	RHAB	60
10	0.45	0.50	3.47	2.93	RHAB	67
10	0.42	0.50	3.67	2.93	RHAB	87
10	0.45	0.50	2.77	2.93	RHAB	74
10	0.48	0.43	2.79	3.45	RHAB	69
10	0.49	0.44	3.28	3.27	RHAB	89
10	0.44	0.48	3.27	3.40	RHAB	72
10	0.45	0.49	3.59	2.84	RHAB	43
10	0.44	0.47	3.61	3.50	RHAB	53
10	0.47	0.45	3.50	3.59	RHAB	58
10	0.47	0.47	3.50	3.51	RHAB	65
10	0.49	0.47	2.60	3.51	RHAB	76
10	0.47	0.49	3.50	2.49	RHAB	84
10	0.47	0.45	3.50	3.59	RHAB	54
10	0.47	0.47	3.07	3.48	RHAB	82
10	0.44	0.42	3.64	3.29	RHAB	75
10	0.43	0.43	2.44	3.64	RHAB	90
10	0.46	0.42	3.46	3.25	RHAB	74
10	0.43	0.43	3.26	3.65	RHAB	82
10	0.45	0.46	2.99	3.56	RHAB	75
10	0.45	0.46	2.29	3.56	RHAB	67
10	0.47	0.49	3.48	2.93	RHAB	84
10	0.50	0.49	2.77	2.93	RHAB	70
10	0.46	0.45	3.56	3.61	RHAB	72
10	0.46	0.45	3.56	3.60	RHAB	80
10	0.45	0.45	3.58	3.61	RHAB	86
10	0.46	0.49	3.56	2.73	RHAB	60
10	0.45	0.42	3.59	3.67	RHAB	64
10	0.47	0.42	2.35	3.67	RHAB	48
10	0.48	0.49	2.95	2.55	RHAB	65
10	0.50	0.43	2.68	3.43	RHAB	73
10	0.50	0.50	2.68	2.98	RHAB	85
10	0.49	0.48	2.98	3.12	Σ9	67
10	0.45	0.50	3.29	2.96	LAB	64
10	0.49	0.49	2.98	2.60	RHAB	64
10	0.35	0.49	3.59	2.98	RHAB	22
10	0.44	0.47	3.34	3.48	RHAB	73
10	0.44	0.47	3.34	3.48	RHAB	64
10	0.43	0.48	3.47	3.17	RHAB	61
10	0.44	0.47	3.35	3.48	RHAB	88
10	0.49	0.49	2.50	3.21	RHAB	69
10	0.46	0.49	3.56	3.21	RHAB	61
10	0.48	0.46	3.39	2.89	RHAB	77
10	0.44	0.46	3.50	2.89	RHAB	66

%Strain	m_1	m_2	M_1	M_2	GB type	Trace incl. (deg)
10	0.47	0.48	2.98	3.33	RHAB	60
10	0.36	0.43	3.57	3.27	RHAB	76
10	0.49	0.43	2.53	3.22	RHAB	77
10	0.49	0.43	2.53	3.27	RHAB	49

Table E.4 Parameters measured for each GBC cracked grain boundary of irradiated 316L stainless steel following straining to 5% in 400˚C SCW.

%Strain	m_1	m_2	M_1	M_2	GB type	Trace incl. (deg)
5	0.42	0.50	3.29	2.76	RHAB	83
5	0.44	0.48	3.48	3.14	RHAB	81
5	0.48	0.46	3.21	3.28	RHAB	19
5	0.43	0.48	3.47	3.17	RHAB	82
5	0.42	0.48	3.67	3.37	RHAB	49
5	0.48	0.46	3.26	3.10	RHAB	42
5	0.49	0.43	3.30	3.05	RHAB	45
5	0.44	0.49	3.60	3.00	RHAB	70
5	0.44	0.49	3.19	3.04	RHAB	44
5	0.48	0.49	3.31	2.55	RHAB	30
5	0.48	0.47	2.42	3.54	RHAB	40
5	0.39	0.50	3.48	2.62	RHAB	25
5	0.47	0.49	3.44	3.02	RHAB	41
5	0.47	0.45	2.79	3.56	RHAB	48
5	0.44	0.45	3.04	3.43	RHAB	45
5	0.44	0.42	3.63	3.26	RHAB	82
5	0.47	0.46	3.26	3.32	RHAB	57
5	0.48	0.46	3.25	2.33	RHAB	60
5	0.48	0.50	2.87	2.83	RHAB	42
5	0.48	0.50	2.90	2.80	RHAB	57
5	0.43	0.50	3.26	2.80	RHAB	57
5	0.48	0.50	2.91	2.80	RHAB	57
5	0.47	0.45	3.41	3.59	RHAB	80
5	0.50	0.45	2.60	3.59	RHAB	49
5	0.50	0.45	2.95	3.00	RHAB	38
5	0.46	0.50	2.98	2.69	RHAB	66
5	0.49	0.50	3.11	2.69	RHAB	41
5	0.50	0.45	2.95	3.60	RHAB	45
5	0.49	0.44	2.58	3.60	RHAB	78
5	0.44	0.49	3.55	2.95	RHAB	62
5	0.43	0.49	3.19	2.95	RHAB	57
5	0.50	0.49	2.57	2.95	RHAB	38
5	0.48	0.49	3.42	2.95	RHAB	38
5	0.43	0.50	3.19	2.57	Σ3	37
5	0.42	0.47	3.67	3.18	RHAB	76
5	0.41	0.49	3.67	3.11	RHAB	21
5	0.39	0.44	3.44	3.35	RHAB	76
5	0.49	0.47	2.56	3.14	RHAB	57
5	0.44	0.43	3.35	3.10	RHAB	67
5	0.44	0.42	3.64	3.29	RHAB	82
5	0.44	0.44	3.26	3.60	RHAB	41
5	0.44	0.49	3.26	2.98	Σ9	51
5	0.44	0.43	3.60	3.05	RHAB	63
5	0.43	0.43	2.44	3.64	RHAB	89

%Strain	m_1	m_2	M_1	M_2	GB type	Trace incl. (deg)
5	0.46	0.42	3.46	3.25	RHAB	74
5	0.44	0.47	3.48	3.58	RHAB	0
5	0.46	0.49	3.56	3.21	RHAB	65
5	0.49	0.45	3.21	3.00	RHAB	44
5	0.49	0.47	2.49	3.33	RHAB	31
5	0.49	0.42	3.10	3.67	RHAB	54
5	0.46	0.42	2.55	3.67	Σ27	2
5	0.45	0.49	3.59	2.84	RHAB	47
5	0.48	0.49	2.95	2.55	RHAB	62
5	0.50	0.44	2.68	2.42	RHAB	69
5	0.47	0.48	3.52	3.32	RHAB	29
5	0.37	0.47	3.52	3.52	RHAB	63
5	0.47	0.38	3.44	3.48	RHAB	69
5	0.44	0.44	3.34	3.62	RHAB	40
5	0.47	0.49	3.44	3.26	RHAB	60
5	0.50	0.49	2.92	3.22	RHAB	50
5	0.40	0.48	3.31	3.36	RHAB	9
5	0.48	0.48	3.36	3.26	RHAB	41
5	0.44	0.50	3.03	2.85	RHAB	63
5	0.44	0.43	3.65	3.66	Σ3	76
5	0.44	0.47	3.65	3.52	RHAB	54
5	0.50	0.45	2.67	2.33	RHAB	41
5	0.50	0.44	2.67	3.58	RHAB	83
5	0.50	0.45	2.73	3.59	RHAB	36
5	0.49	0.50	2.58	2.58	RHAB	36
5	0.50	0.44	2.58	3.13	RHAB	70
5	0.47	0.50	2.89	2.90	RHAB	71
5	0.49	0.45	3.24	3.61	RHAB	77
5	0.49	0.41	3.24	3.33	RHAB	80
5	0.41	0.48	3.33	3.33	RHAB	34
5	0.48	0.49	3.33	2.73	RHAB	39
5	0.45	0.49	3.50	2.73	RHAB	88
5	0.40	0.50	3.41	2.82	RHAB	59
5	0.45	0.47	3.63	2.39	RHAB	33
5	0.50	0.40	3.06	3.41	RHAB	38
5	0.49	0.49	2.55	2.52	RHAB	28
5	0.47	0.48	3.43	2.44	RHAB	58
5	0.44	0.48	3.04	3.35	RHAB	45
5	0.47	0.40	3.47	3.38	RHAB	83
5	0.47	0.40	3.54	3.38	RHAB	84
5	0.33	0.46	3.63	3.58	RHAB	44
5	0.49	0.47	3.20	3.40	RHAB	72
5	0.47	0.42	3.49	3.54	RHAB	37
5	0.49	0.46	3.11	2.35	RHAB	57
5	0.49	0.49	3.26	2.96	RHAB	42
5	0.46	0.44	3.41	3.36	RHAB	16

%Strain	m_1	m_2	M_1	M_2	GB type	Trace incl. (deg)
5	0.46	0.44	3.00	3.36	Σ9	19
5	0.44	0.47	3.36	2.96	RHAB	81
5	0.49	0.47	3.23	2.96	RHAB	74
5	0.49	0.49	3.23	2.84	RHAB	69
5	0.46	0.47	3.00	2.96	RHAB	53
5	0.49	0.48	2.81	2.83	RHAB	41
5	0.43	0.49	3.41	3.23	Σ3	82
5	0.46	0.49	3.56	2.55	RHAB	33
5	0.46	0.49	2.74	2.55	RHAB	26
5	0.48	0.47	3.31	3.54	RHAB	57
5	0.45	0.46	3.35	3.57	RHAB	53
5	0.48	0.46	3.21	3.57	RHAB	47

Table E.5 Parameters measured for each GBC cracked grain boundary of irradiated 316L stainless steel following straining to 2%, 5%, and 10% in 400˚C argon.

Crack type	%Strain	m_1	m_2	M_1	M_2	GB type	Trace incl. (deg)
GBC	5	0.40	0.48	3.39	3.40	RHAB	70
GBC	5	0.36	0.42	3.58	3.29	RHAB	82
GBC	5	0.45	0.33	3.46	3.64	RHAB	73
GBC	5	0.43	0.47	3.43	2.64	RHAB	81
GBC	5	0.45	0.49	3.53	2.52	RHAB	50
GBC	5	0.32	0.49	3.64	2.92	RHAB	86
GBC	5	0.47	0.43	3.50	3.03	RHAB	76
GBC	5	0.47	0.43	3.47	3.03	RHAB	75
GBC	5	0.44	0.45	3.62	3.01	RHAB	65
GBC	5	0.45	0.47	3.46	3.17	RHAB	46
GBC	5	0.44	0.44	3.04	3.09	RHAB	68
GBC	5	NM	NM	NM	NM	NM	86
GBC	5	NM	NM	NM	NM	NM	87
GBC	5	NM	NM	NM	NM	NM	74
GBC	5	NM	NM	NM	NM	NM	90
GBC	5	NM	NM	NM	NM	NM	76
GBC	5	NM	NM	NM	NM	NM	76
GBC	5	NM	NM	NM	NM	NM	89
GBC	5	NM	NM	NM	NM	NM	75
GBC	5	NM	NM	NM	NM	NM	72
GBC	5	NM	NM	NM	NM	NM	87
GBC	5	NM	NM	NM	NM	NM	85
GBC	5	NM	NM	NM	NM	NM	80
GBC	5	NM	NM	NM	NM	NM	84
GBC	5	NM	NM	NM	NM	NM	67
NS	5	NM	NM	NM	NM	NM	86
NS	5	NM	NM	NM	NM	NM	87
NS	5	NM	NM	NM	NM	NM	86
NS	5	NM	NM	NM	NM	NM	68
NS	5	NM	NM	NM	NM	NM	84

*NM = Not Measured

APPENDIX F

IG Crack Micrographs in SCW and Argon

IG Cracks

500˚C SCW

316L, 500˚C SCW, unir

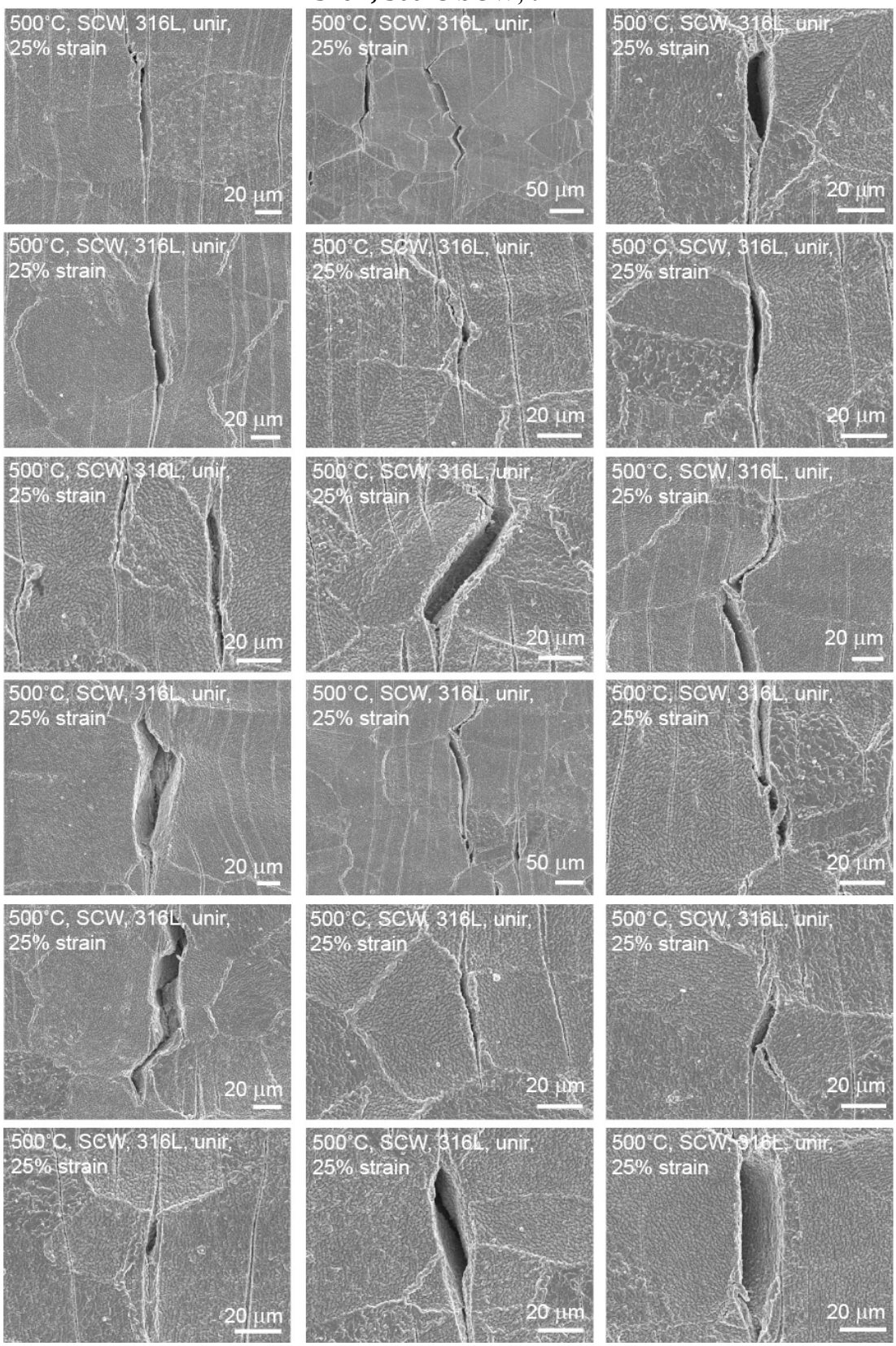

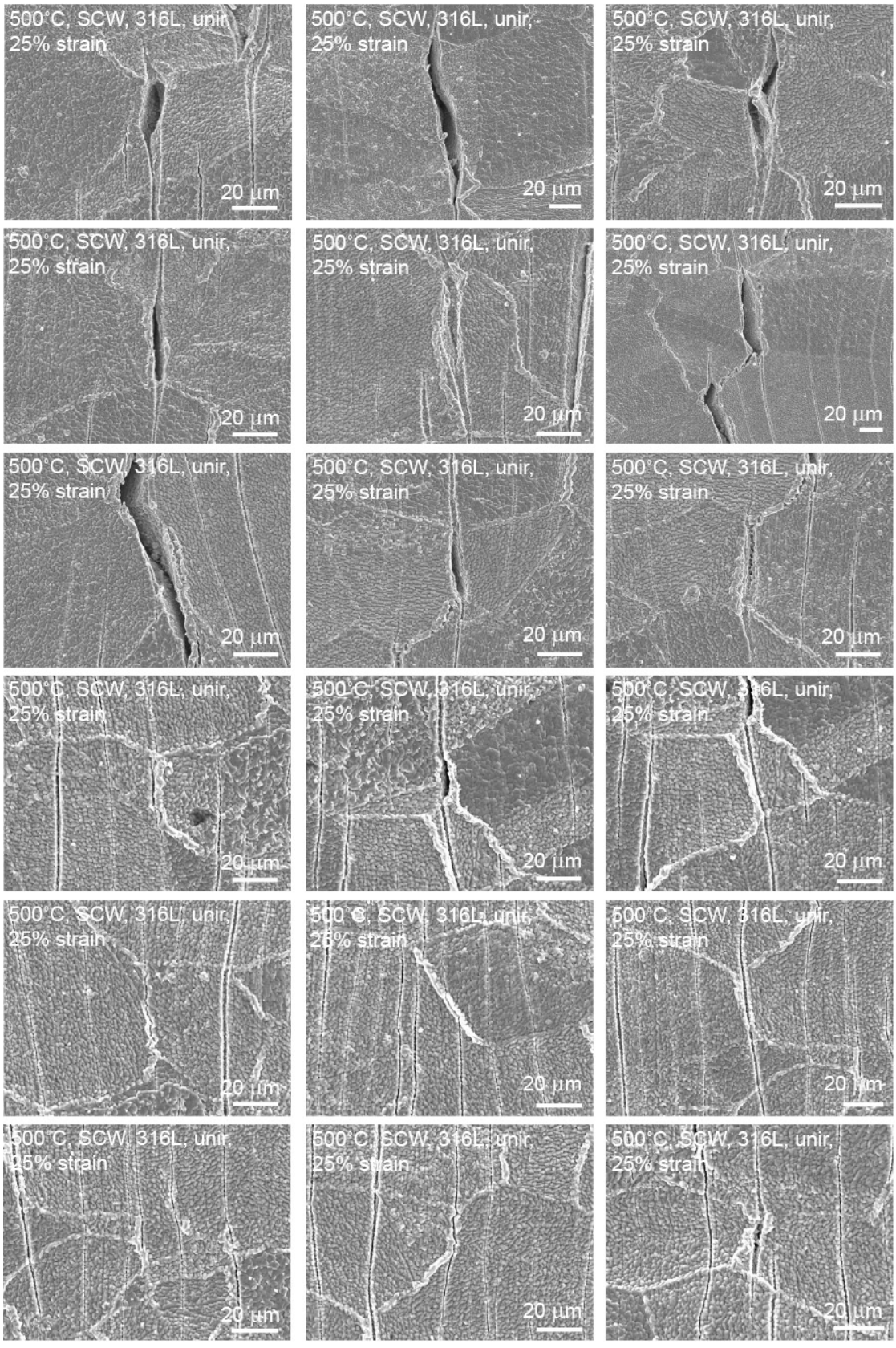
500˚C, SCW, 316L, unir,
25% strain
20 μm

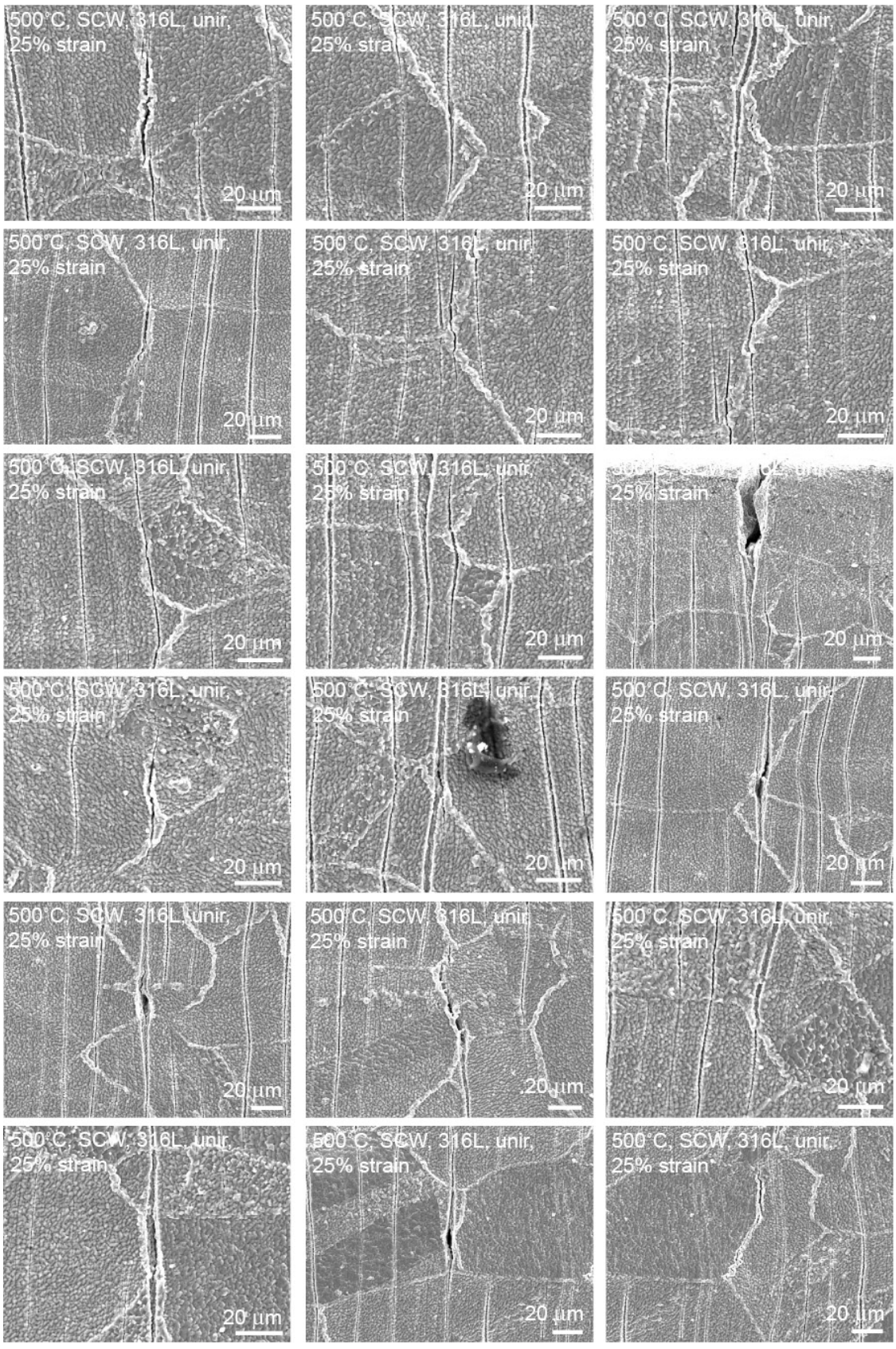
500 °C, SCW, 316L, unir,
25% strain
20 µm

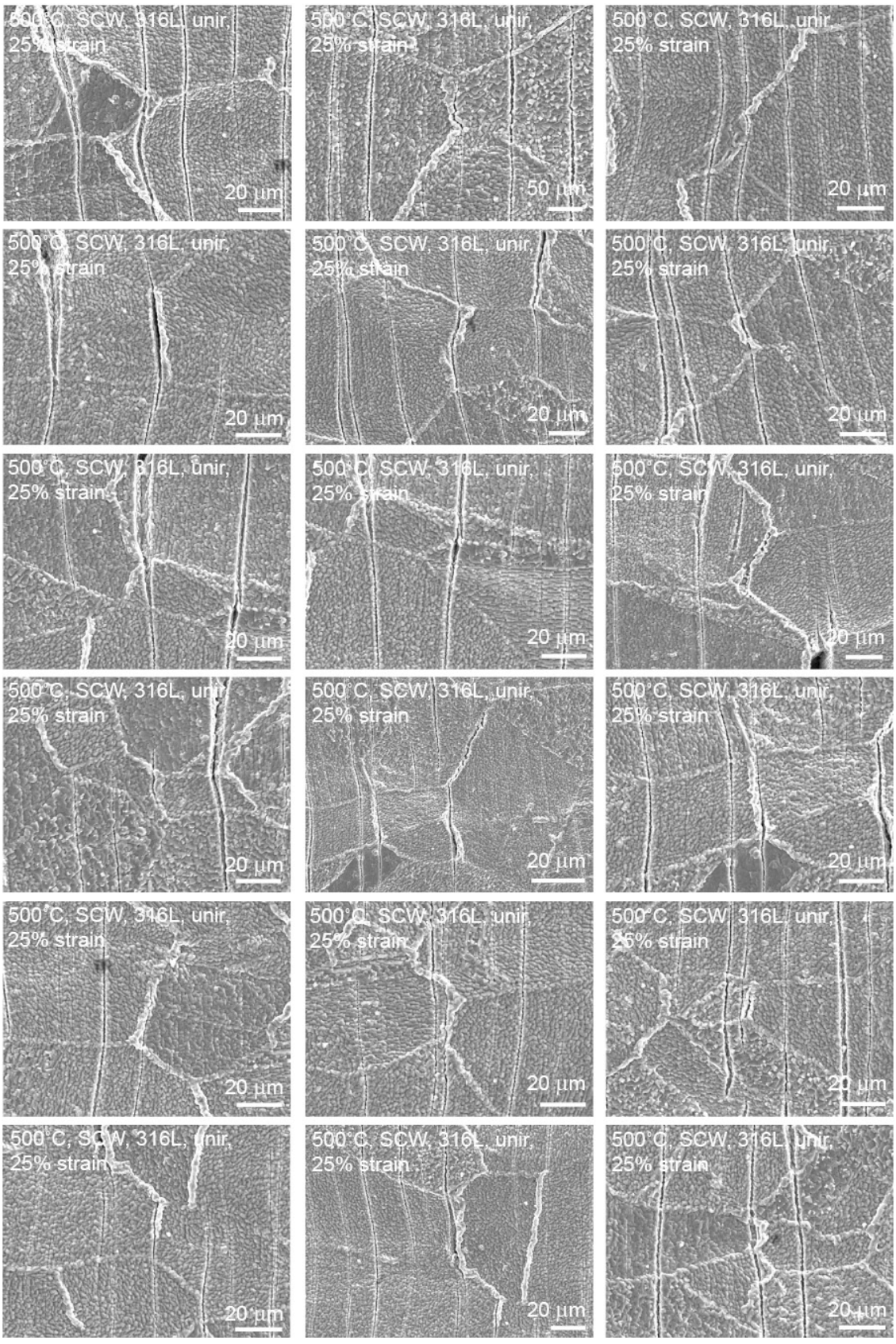
500°C, SCW, 316L, unir,
25% strain
20 µm
50 µm

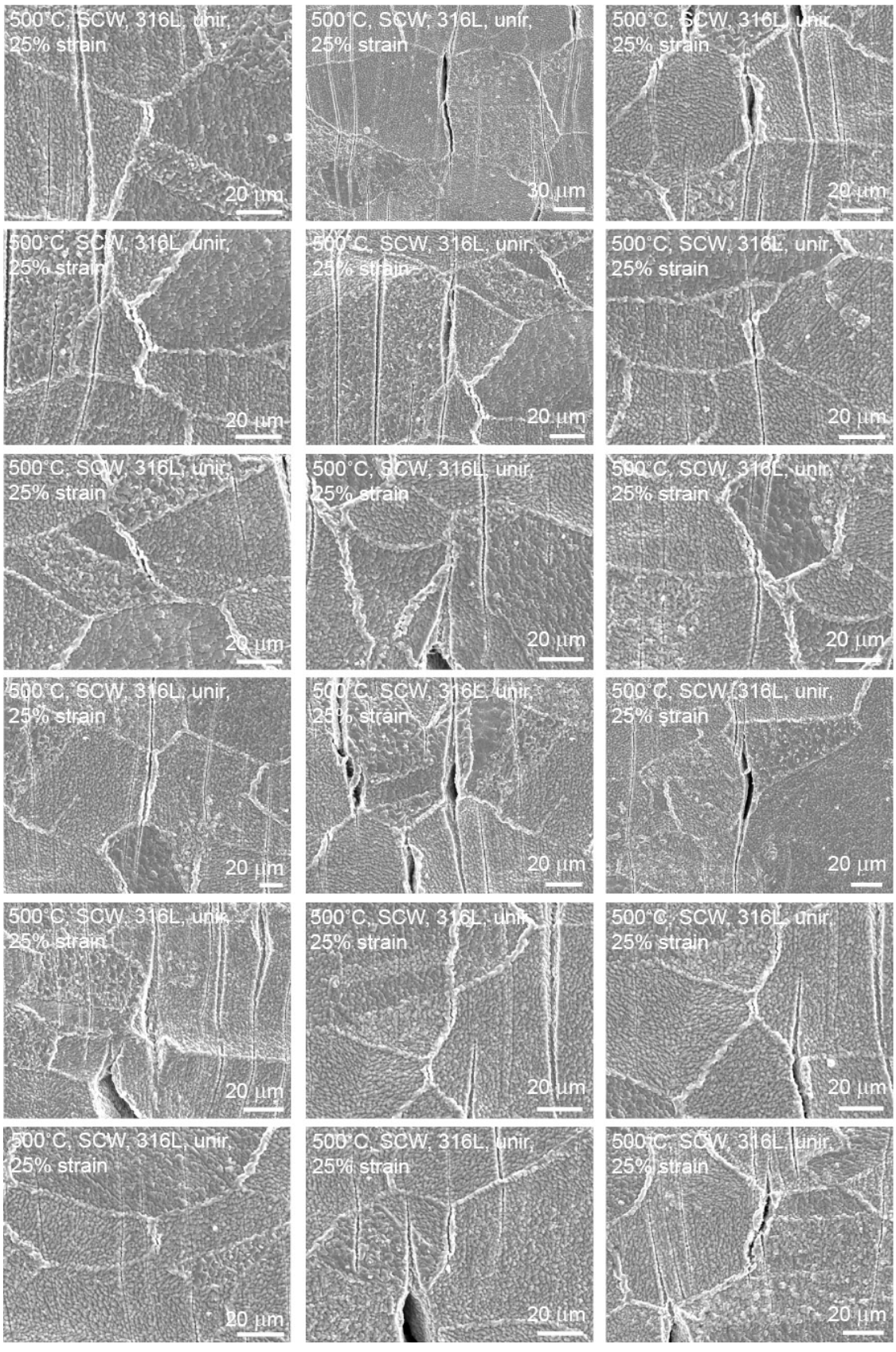
500°C, SCW, 316L, unir,
25% strain
20 μm
30 μm

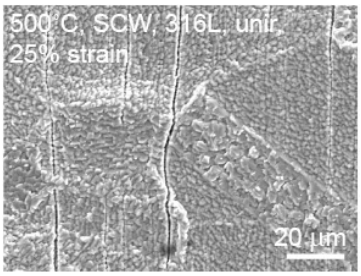
500 C, SCW, 316L, unir,
25% strain
20 µm

316LGBE, 500˚C SCW, unir

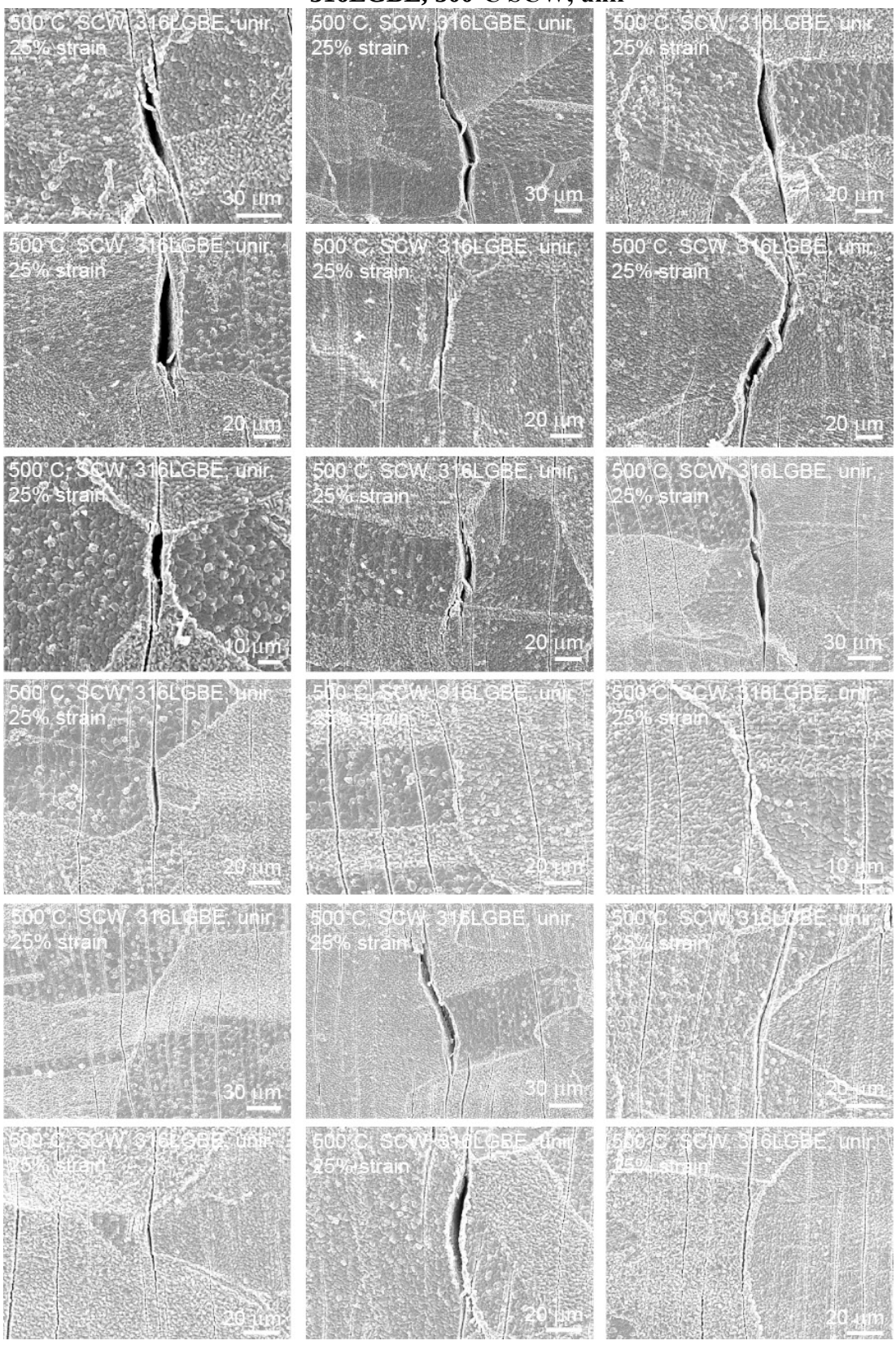

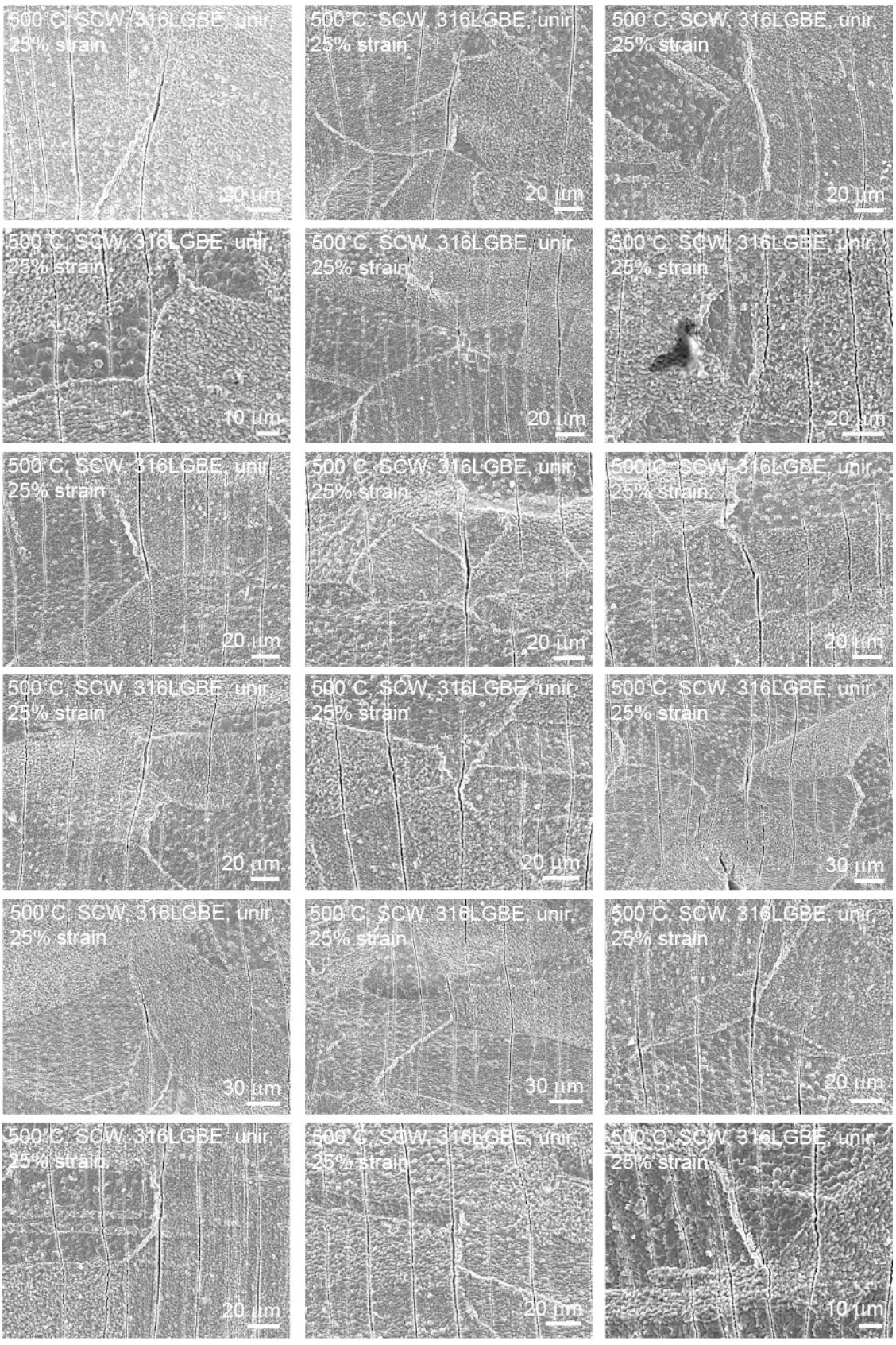
500 C, SCW, 316LGBE, unir,
25% strain
20 µm
500 C, SCW, 316LGBE, unir,
25% strain
20 µm
500 C, SCW, 316LGBE, unir,
25% strain
20 µm
500 C, SCW, 316LGBE, unir,
25% strain
10 µm
500 C, SCW, 316LGBE, unir,
25% strain
20 µm
500 C, SCW, 316LGBE, unir,
25% strain
20 µm
500 C, SCW, 316LGBE, unir,
25% strain
20 µm
500 C, SCW, 316LGBE, unir,
25% strain
20 µm
500 C, SCW, 316LGBE, unir,
25% strain
20 µm
500 C, SCW, 316LGBE, unir,
25% strain
20 µm
500 C, SCW, 316LGBE, unir,
25% strain
30 µm
500 C, SCW, 316LGBE, unir,
25% strain
30 µm
500 C, SCW, 316LGBE, unir,
25% strain
20 µm
500 C, SCW, 316LGBE, unir,
25% strain
20 µm
500 C, SCW, 316LGBE, unir,
25% strain
20 µm
500 C, SCW, 316LGBE, unir,
25% strain
10 µm

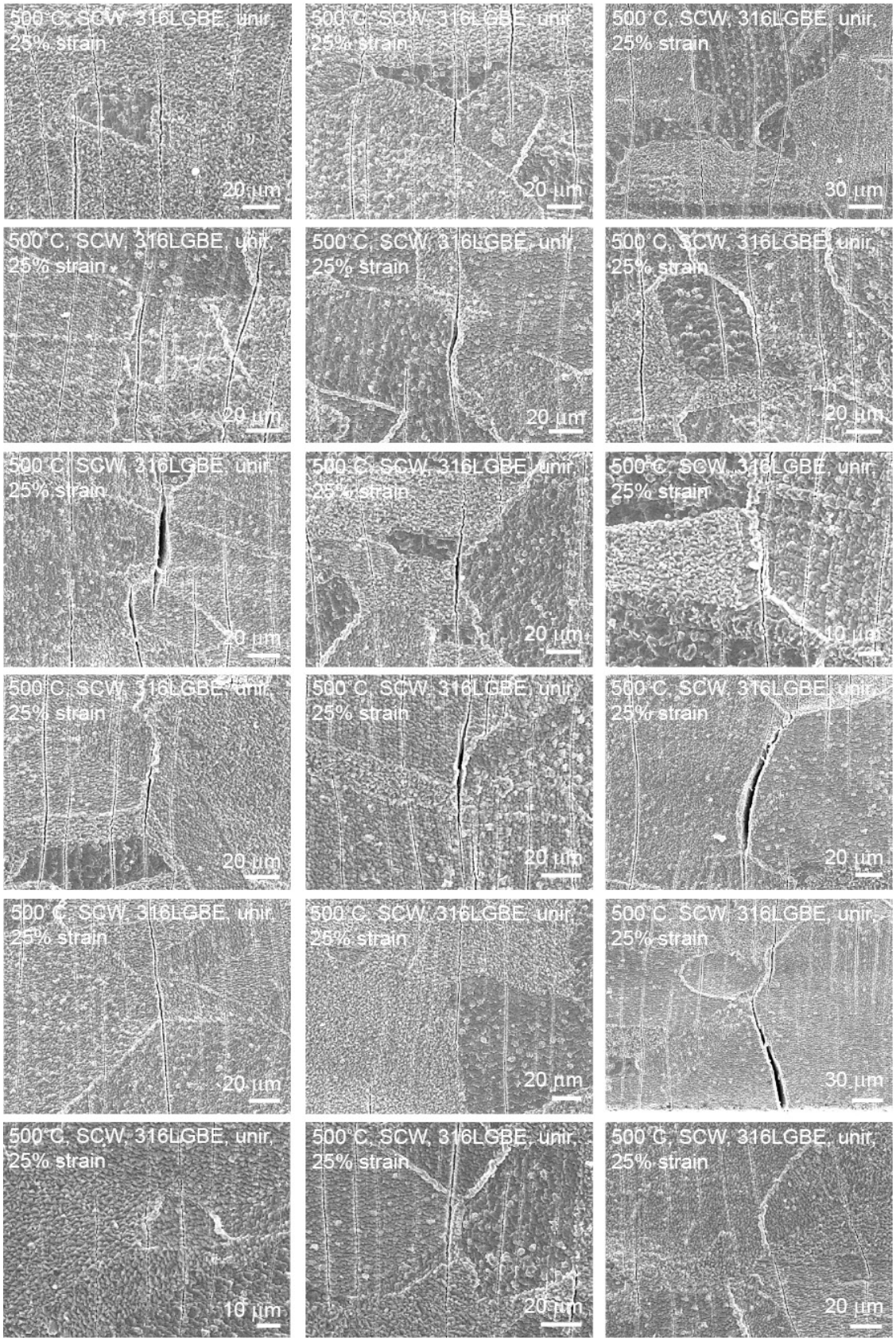
500 °C, SCW, 316LGBE, unir, 25% strain
20 µm
30 µm
10 µm

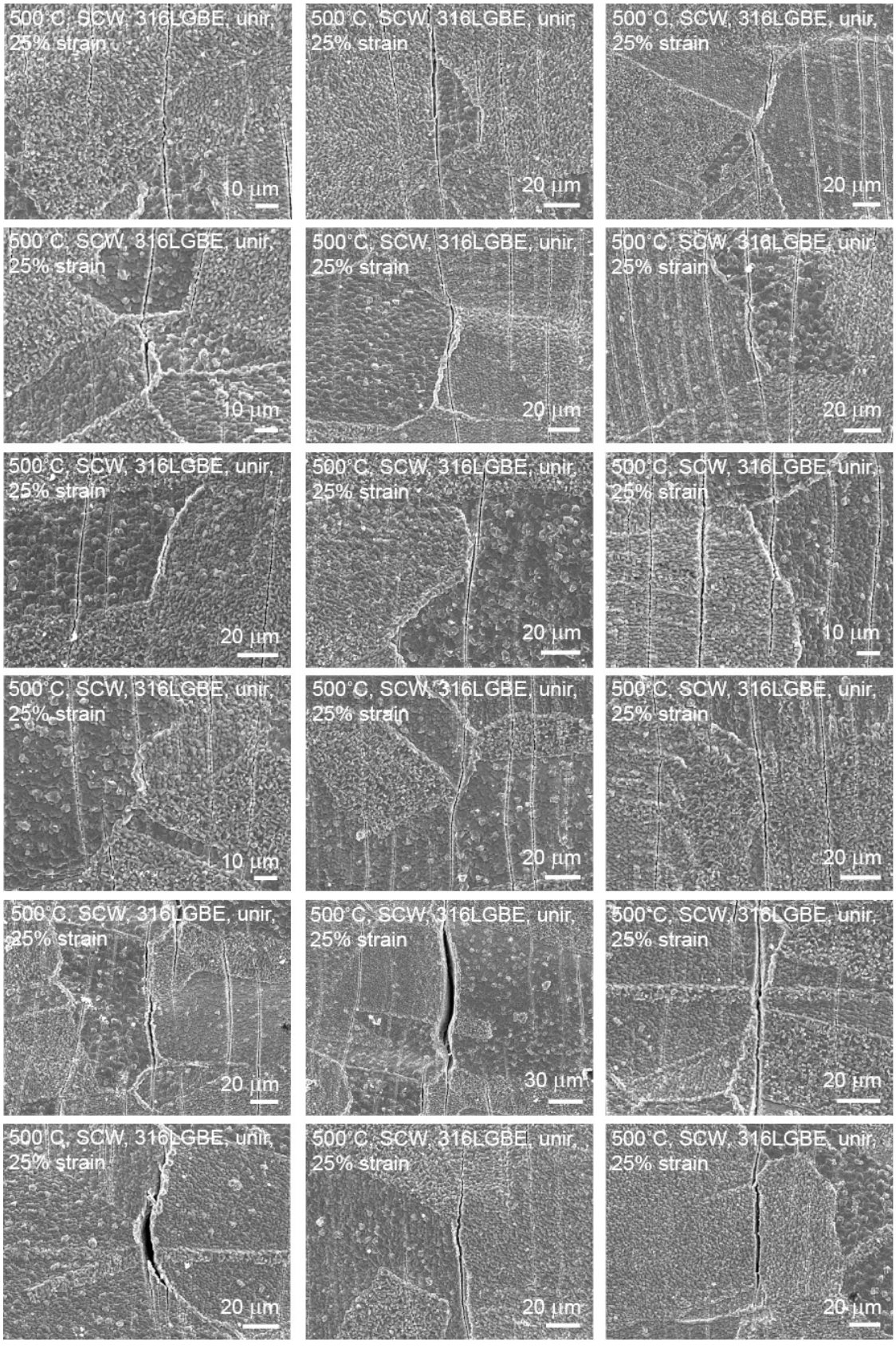
500 C, SCW, 316LGBE, unir, 25% strain
10 μm
500 C, SCW, 316LGBE, unir, 25% strain
20 μm
500 C, SCW, 316LGBE, unir, 25% strain
20 μm
500 C, SCW, 316LGBE, unir, 25% strain
10 μm
500 C, SCW, 316LGBE, unir, 25% strain
20 μm
500 C, SCW, 316LGBE, unir, 25% strain
20 μm
500 C, SCW, 316LGBE, unir, 25% strain
20 μm
500 C, SCW, 316LGBE, unir, 25% strain
20 μm
500 C, SCW, 316LGBE, unir, 25% strain
10 μm
500 C, SCW, 316LGBE, unir, 25% strain
10 μm
500 C, SCW, 316LGBE, unir, 25% strain
20 μm
500 C, SCW, 316LGBE, unir, 25% strain
20 μm
500 C, SCW, 316LGBE, unir, 25% strain
20 μm
500 C, SCW, 316LGBE, unir, 25% strain
30 μm
500 C, SCW, 316LGBE, unir, 25% strain
20 μm
500 C, SCW, 316LGBE, unir, 25% strain
20 μm
500 C, SCW, 316LGBE, unir, 25% strain
20 μm
500 C, SCW, 316LGBE, unir, 25% strain
20 μm

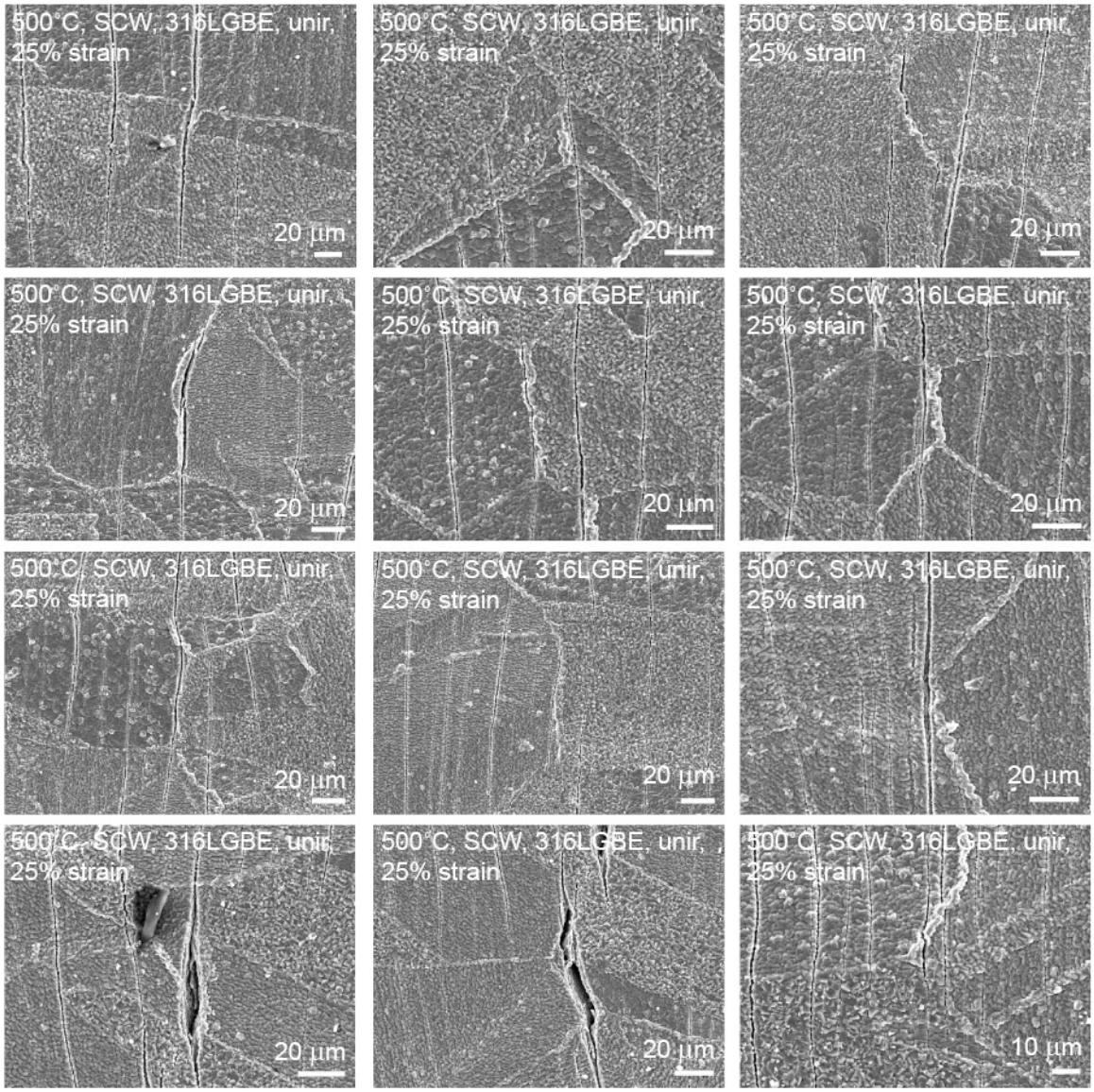
500°C, SCW, 316LGBE, unir, 25% strain
20 μm
500°C, SCW, 316LGBE, unir, 25% strain
20 μm
500°C, SCW, 316LGBE, unir, 25% strain
20 μm
500°C, SCW, 316LGBE, unir, 25% strain
20 μm
500°C, SCW, 316LGBE, unir, 25% strain
20 μm
500°C, SCW, 316LGBE, unir, 25% strain
20 μm
500°C, SCW, 316LGBE, unir, 25% strain
20 μm
500°C, SCW, 316LGBE, unir, 25% strain
20 μm
500°C, SCW, 316LGBE, unir, 25% strain
20 μm
500°C, SCW, 316LGBE, unir, 25% strain
20 μm
500°C, SCW, 316LGBE, unir, 25% strain
20 μm
500°C, SCW, 316LGBE, unir, 25% strain
10 μm

IG Cracks

400˚C SCW

NS CRACKS, 316L, 400˚C SCW, 7 dpa

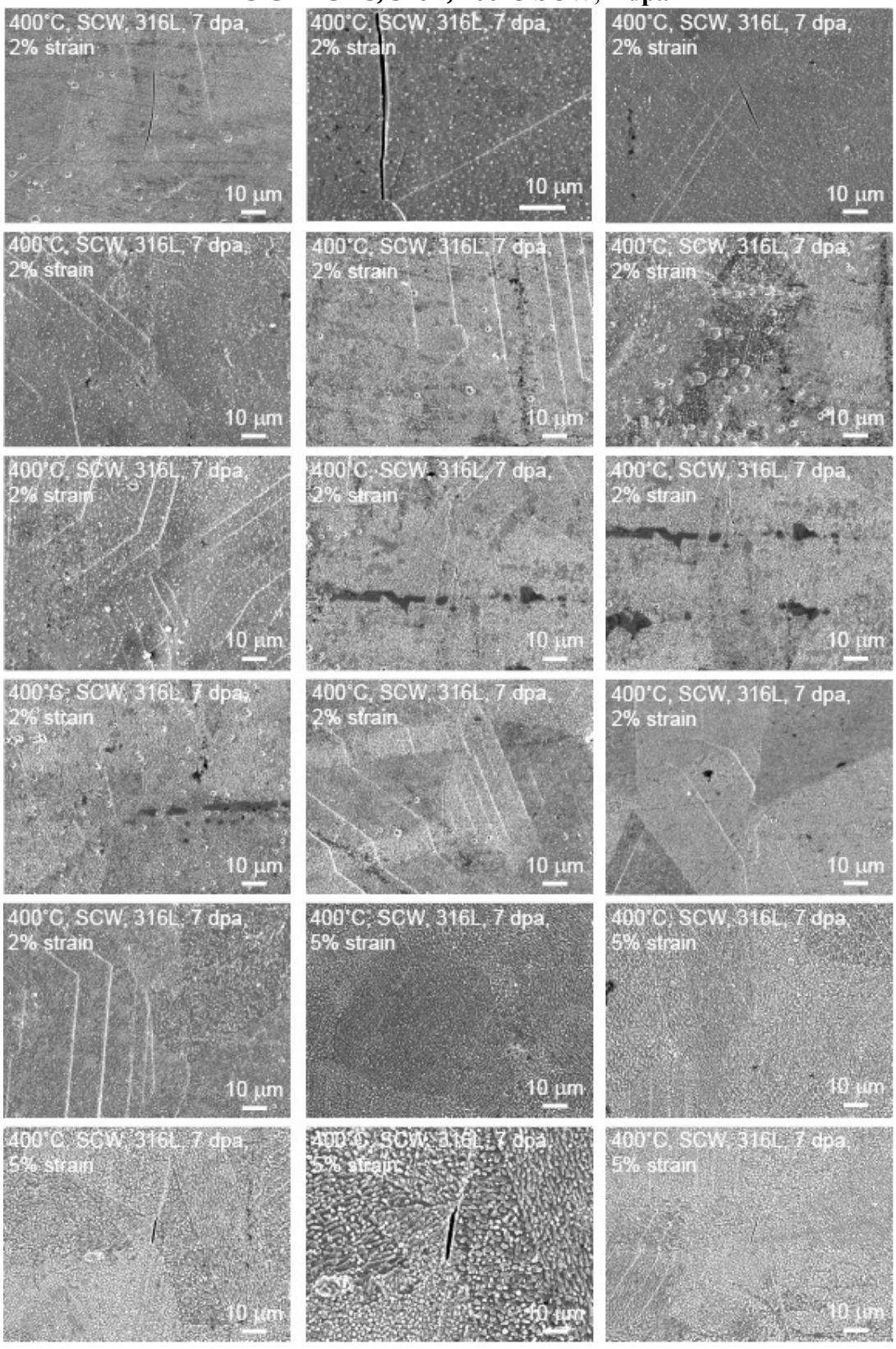

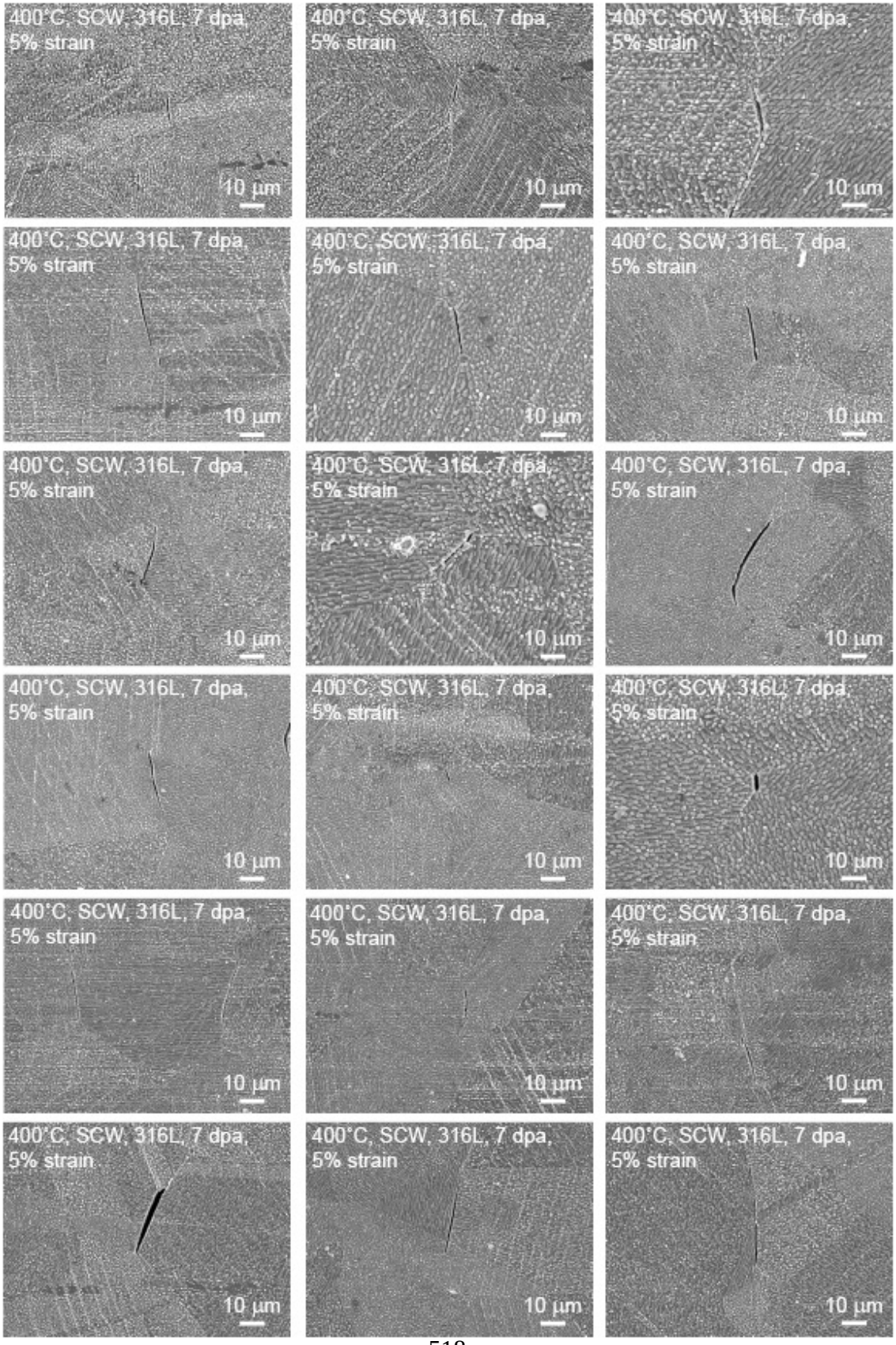
400°C, SCW, 316L, 7 dpa, 5% strain
10 µm

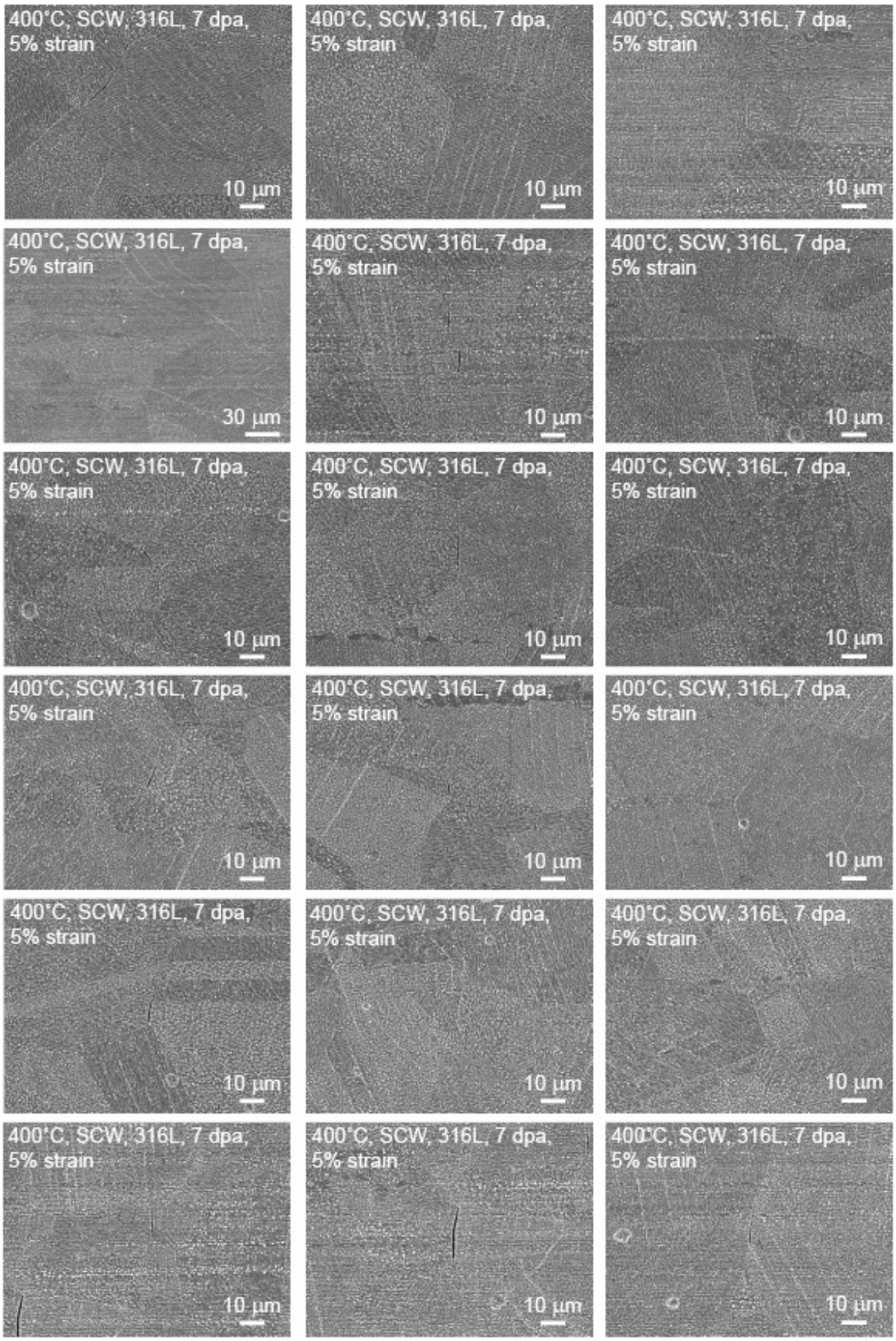
400°C, SCW, 316L, 7 dpa, 5% strain
10 μm
400°C, SCW, 316L, 7 dpa, 5% strain
10 μm
400°C, SCW, 316L, 7 dpa, 5% strain
10 μm
400°C, SCW, 316L, 7 dpa, 5% strain
30 μm
400°C, SCW, 316L, 7 dpa, 5% strain
10 μm
400°C, SCW, 316L, 7 dpa, 5% strain
10 μm
400°C, SCW, 316L, 7 dpa, 5% strain
10 μm
400°C, SCW, 316L, 7 dpa, 5% strain
10 μm
400°C, SCW, 316L, 7 dpa, 5% strain
10 μm
400°C, SCW, 316L, 7 dpa, 5% strain
10 μm
400°C, SCW, 316L, 7 dpa, 5% strain
10 μm
400°C, SCW, 316L, 7 dpa, 5% strain
10 μm
400°C, SCW, 316L, 7 dpa, 5% strain
10 μm
400°C, SCW, 316L, 7 dpa, 5% strain
10 μm
400°C, SCW, 316L, 7 dpa, 5% strain
10 μm
400°C, SCW, 316L, 7 dpa, 5% strain
10 μm
400°C, SCW, 316L, 7 dpa, 5% strain
10 μm
400°C, SCW, 316L, 7 dpa, 5% strain
10 μm

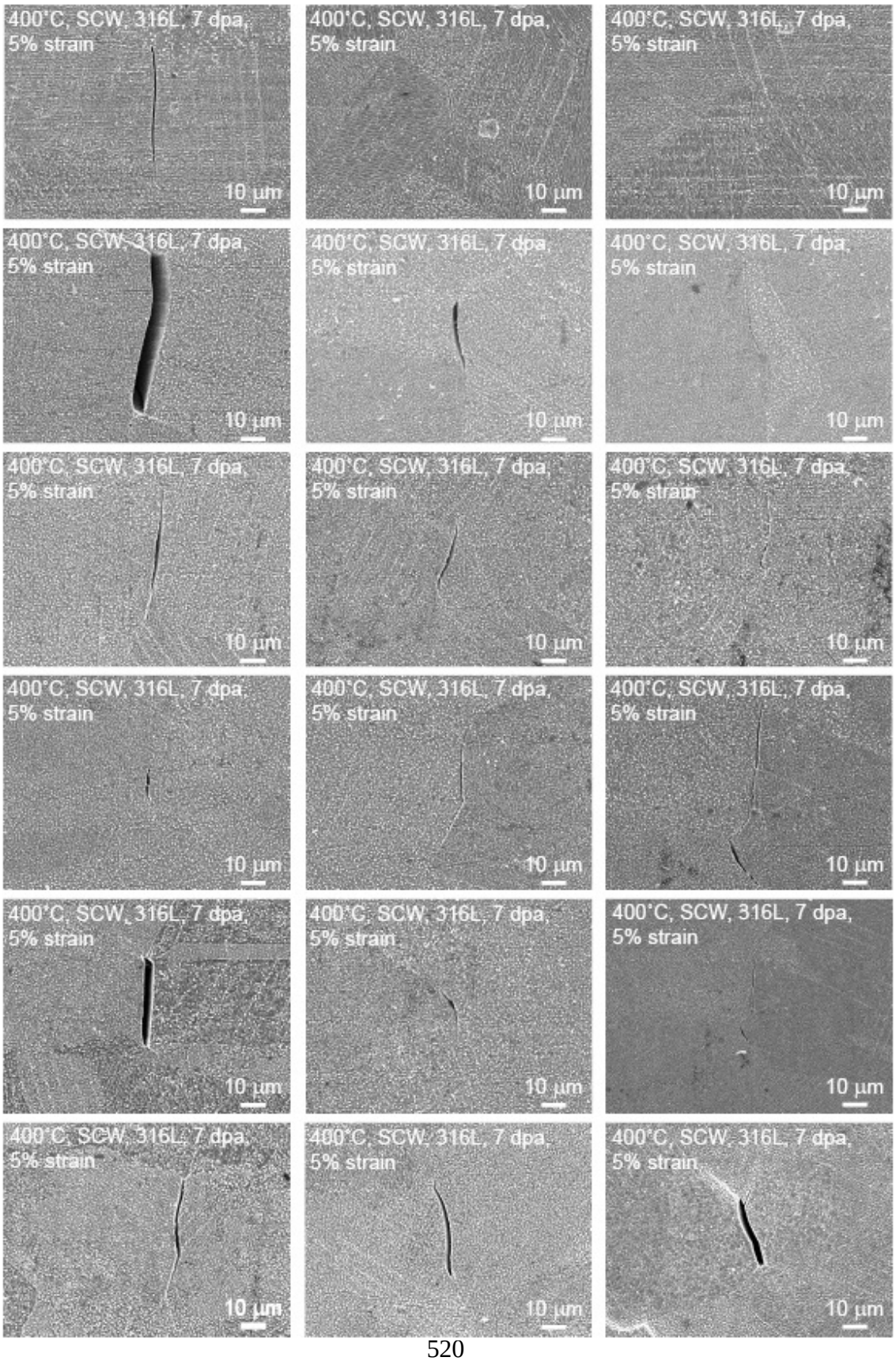
400°C, SCW, 316L, 7 dpa, 5% strain
10 µm

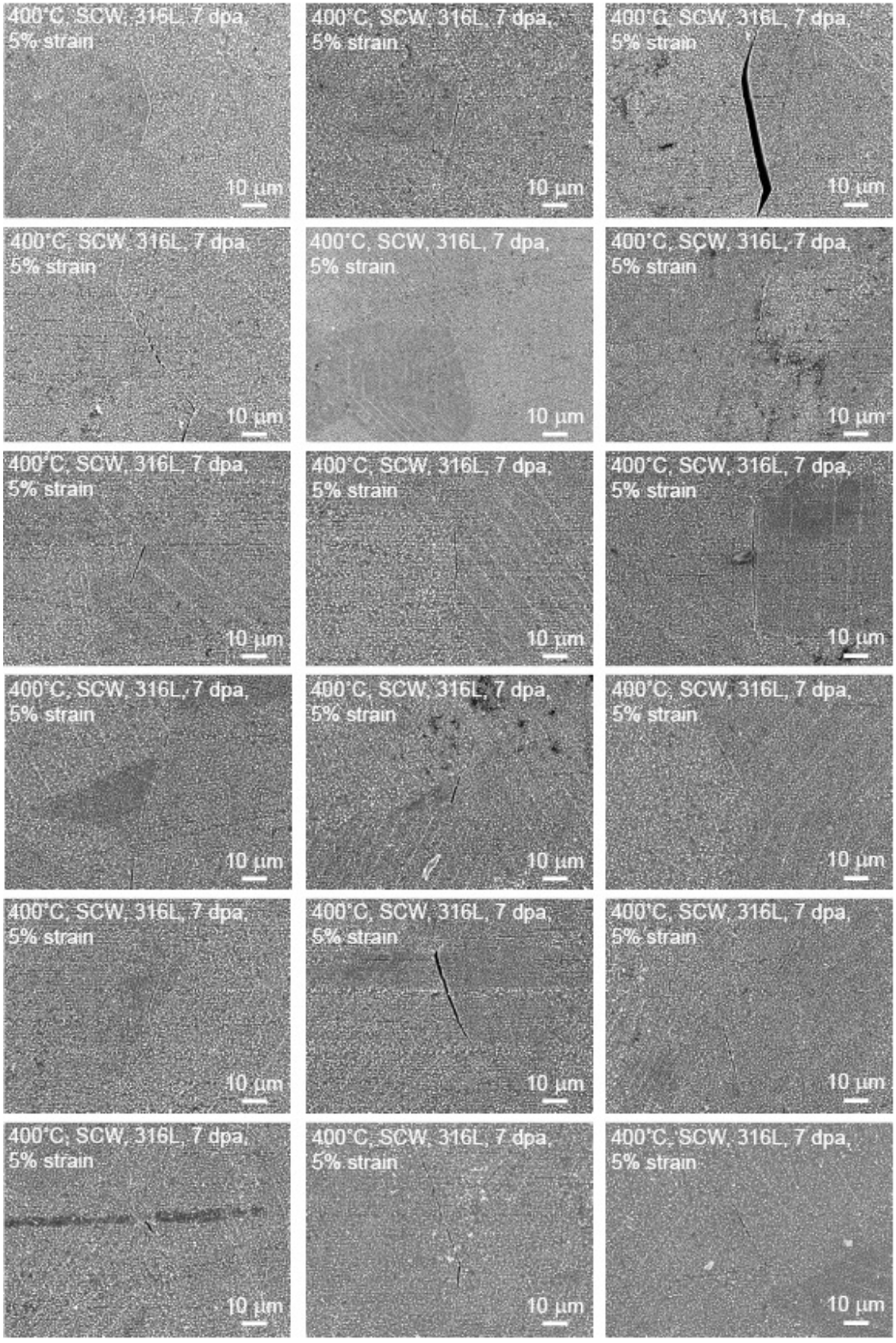
400°C, SCW, 316L, 7 dpa, 5% strain
10 µm

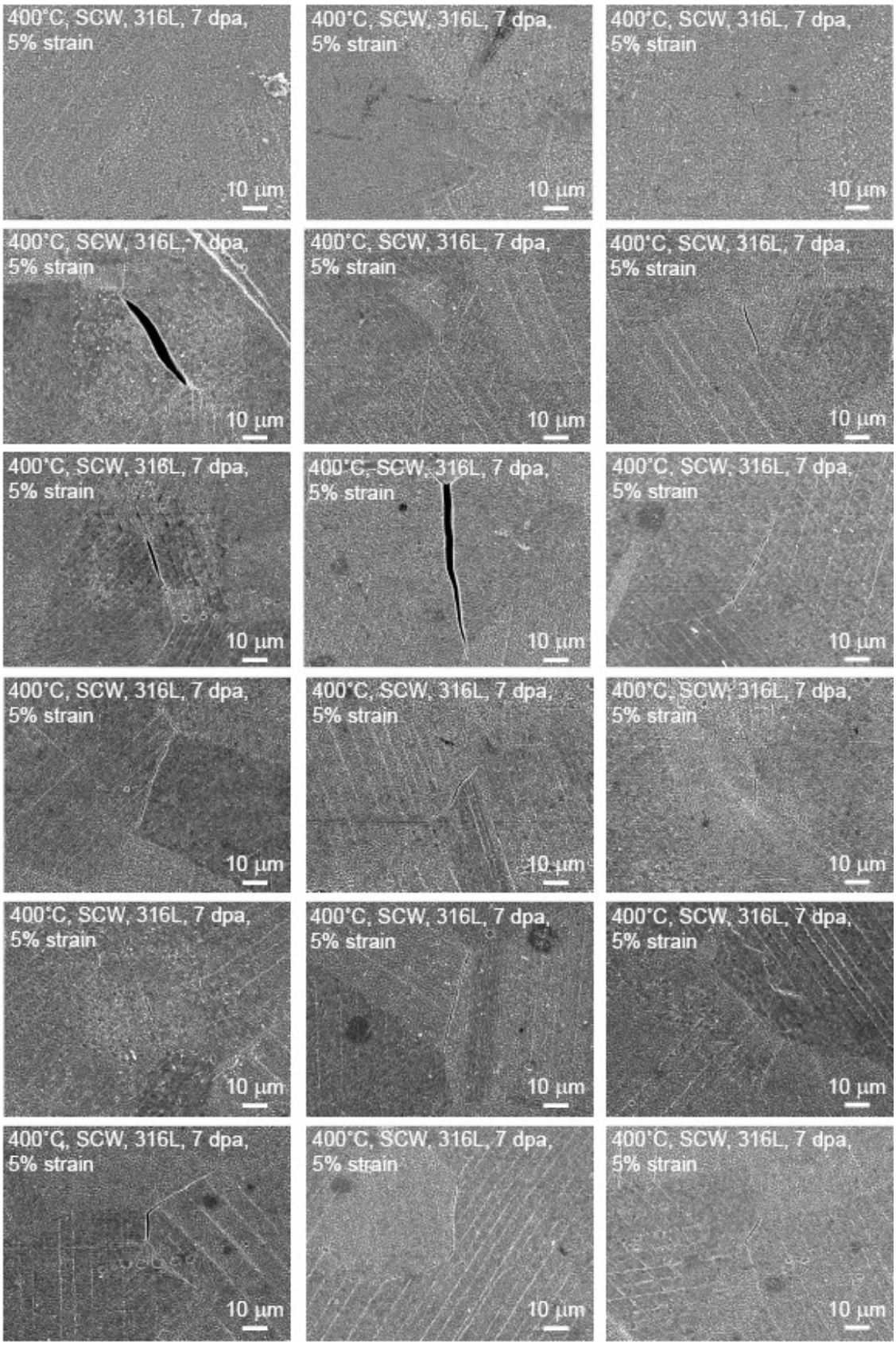
400°C, SCW, 316L, 7 dpa, 5% strain
10 µm

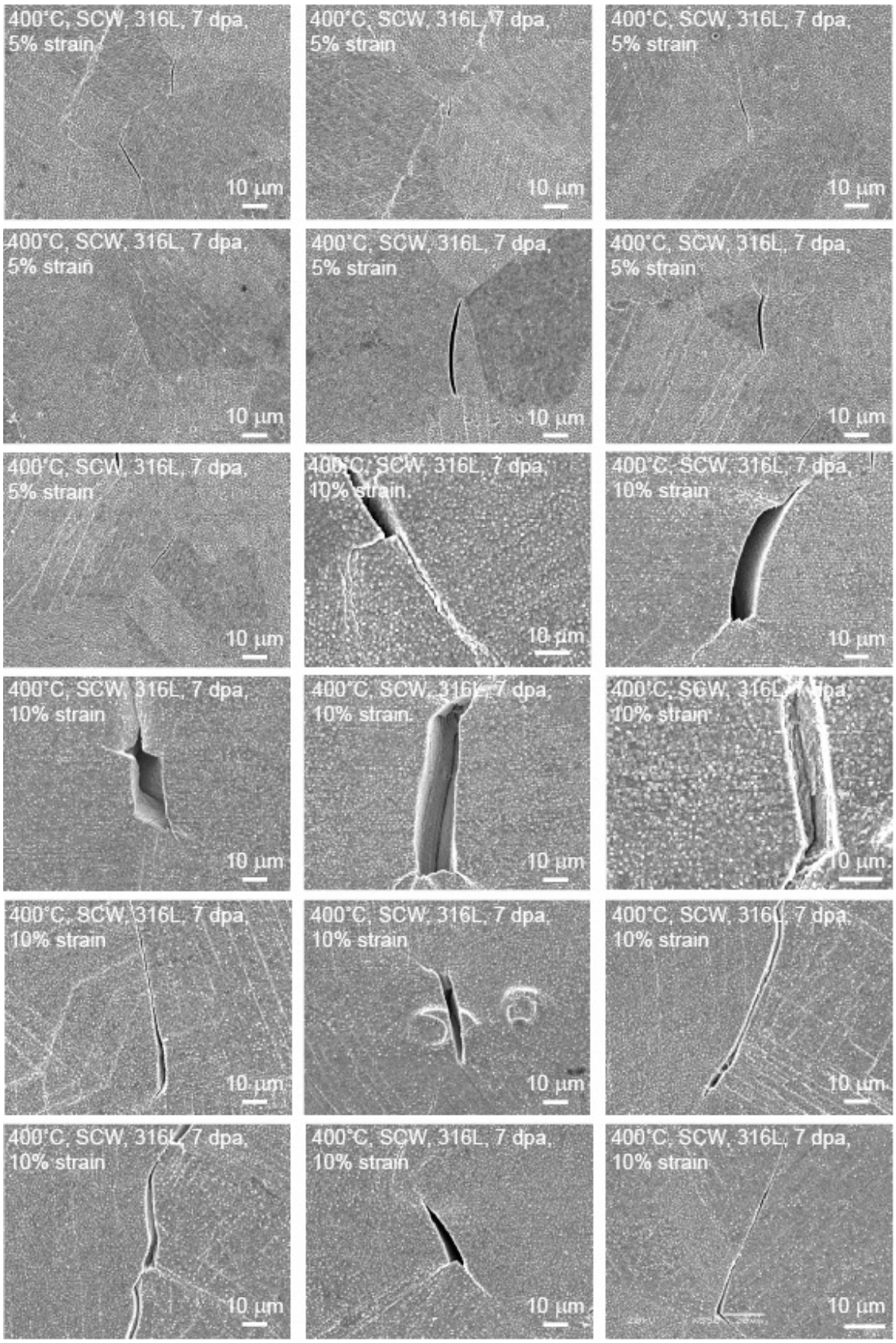
400°C, SCW, 316L, 7 dpa, 5% strain
10 μm
400°C, SCW, 316L, 7 dpa, 5% strain
10 μm
400°C, SCW, 316L, 7 dpa, 5% strain
10 μm
400°C, SCW, 316L, 7 dpa, 5% strain
10 μm
400°C, SCW, 316L, 7 dpa, 5% strain
10 μm
400°C, SCW, 316L, 7 dpa, 5% strain
10 μm
400°C, SCW, 316L, 7 dpa, 5% strain
10 μm
400°C, SCW, 316L, 7 dpa, 10% strain
10 μm
400°C, SCW, 316L, 7 dpa, 10% strain
10 μm
400°C, SCW, 316L, 7 dpa, 10% strain
10 μm
400°C, SCW, 316L, 7 dpa, 10% strain
10 μm
400°C, SCW, 316L, 7 dpa, 10% strain
10 μm
400°C, SCW, 316L, 7 dpa, 10% strain
10 μm
400°C, SCW, 316L, 7 dpa, 10% strain
10 μm
400°C, SCW, 316L, 7 dpa, 10% strain
10 μm
400°C, SCW, 316L, 7 dpa, 10% strain
10 μm
400°C, SCW, 316L, 7 dpa, 10% strain
10 μm

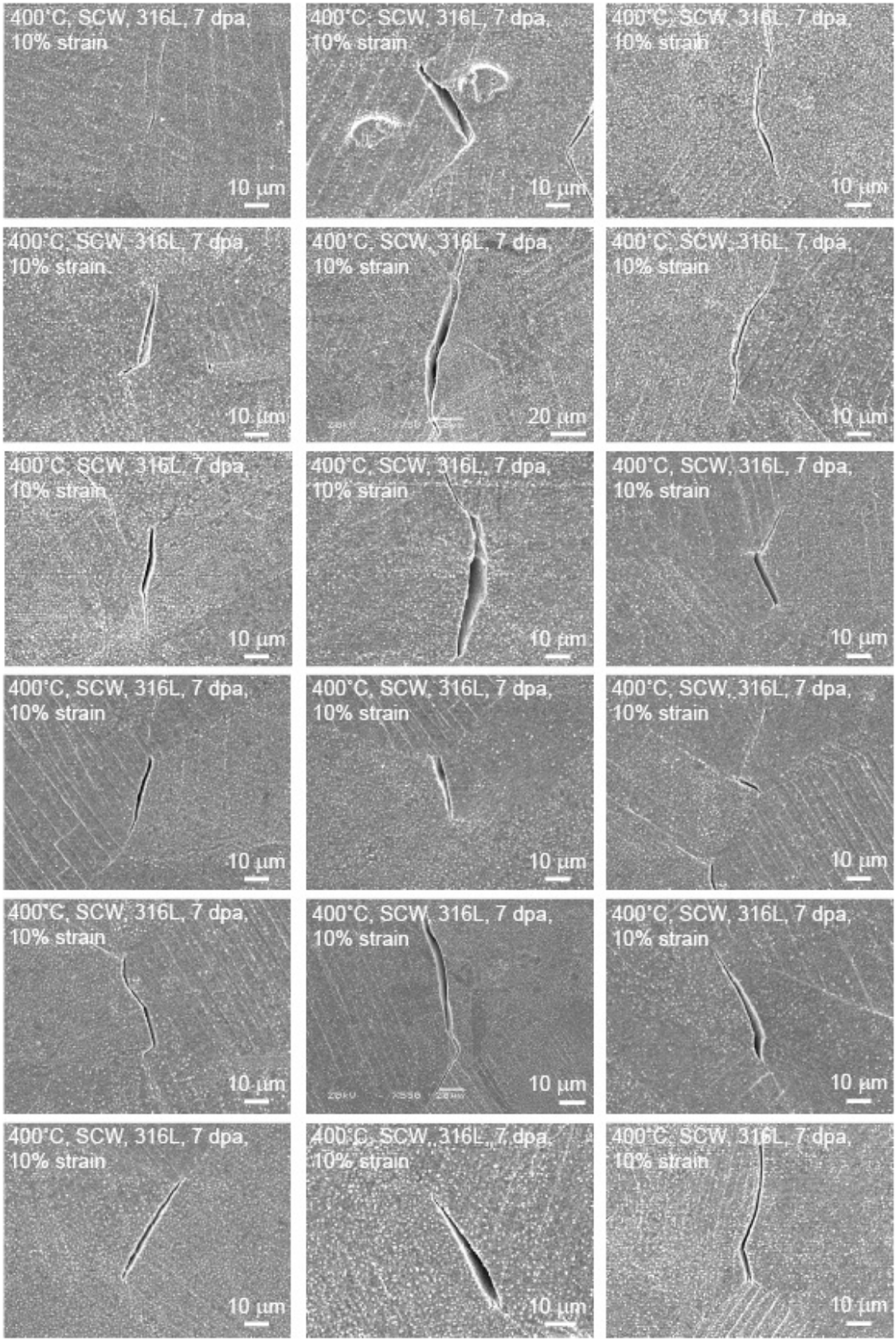
400°C, SCW, 316L, 7 dpa, 10% strain
10 μm
20 μm

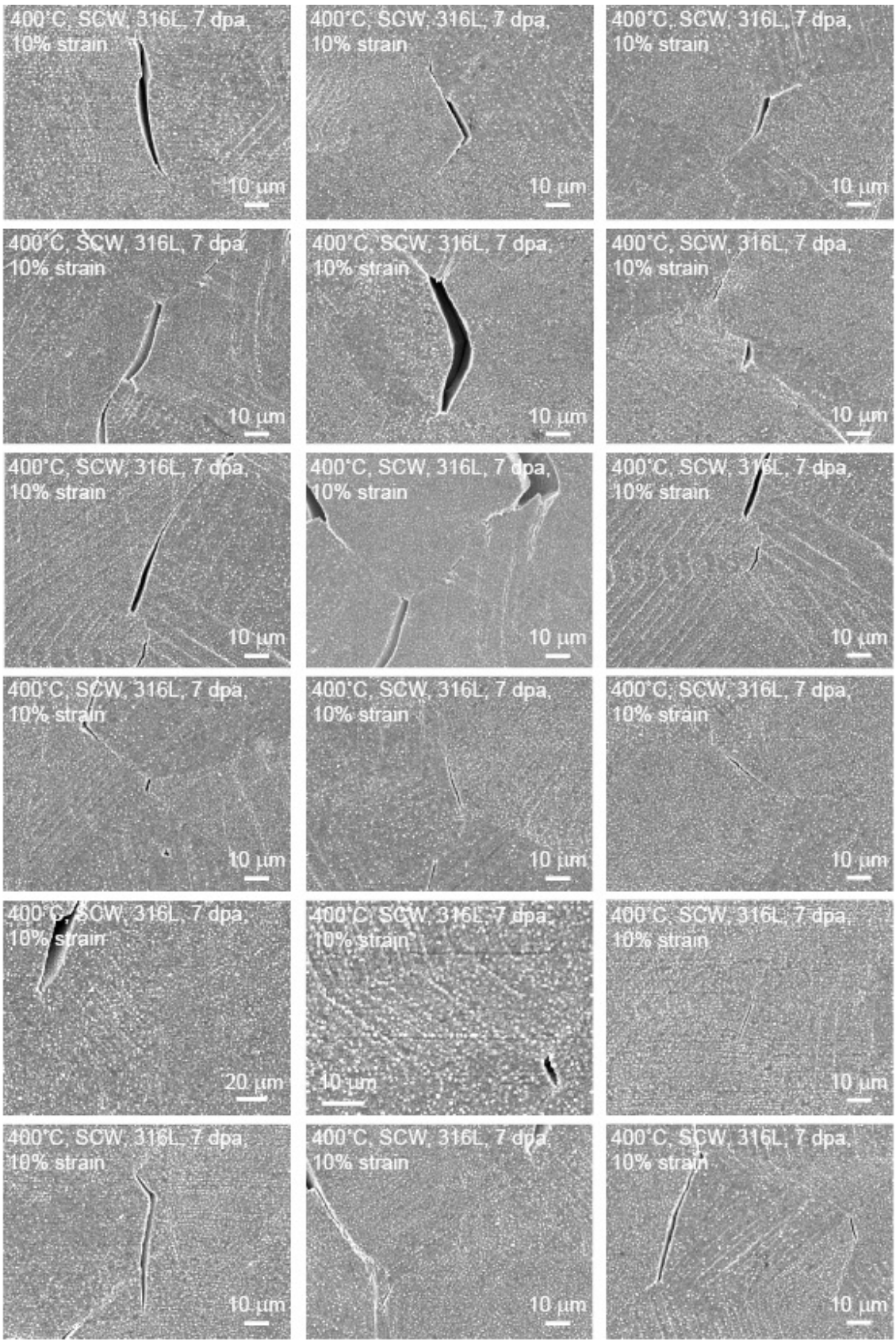
400°C, SCW, 316L, 7 dpa, 10% strain
10 μm
20 μm

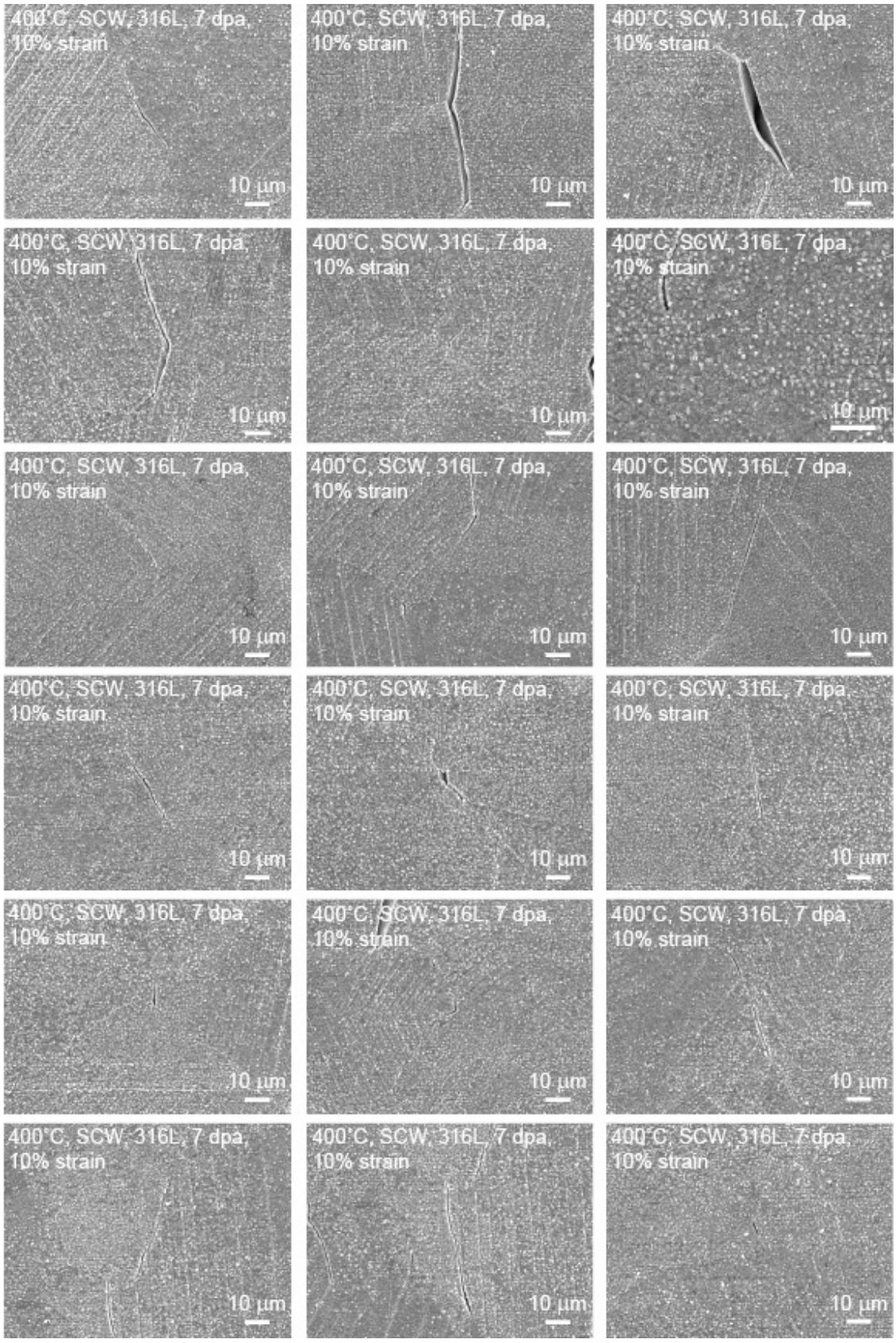
400°C, SCW, 316L, 7 dpa, 10% strain
10 μm

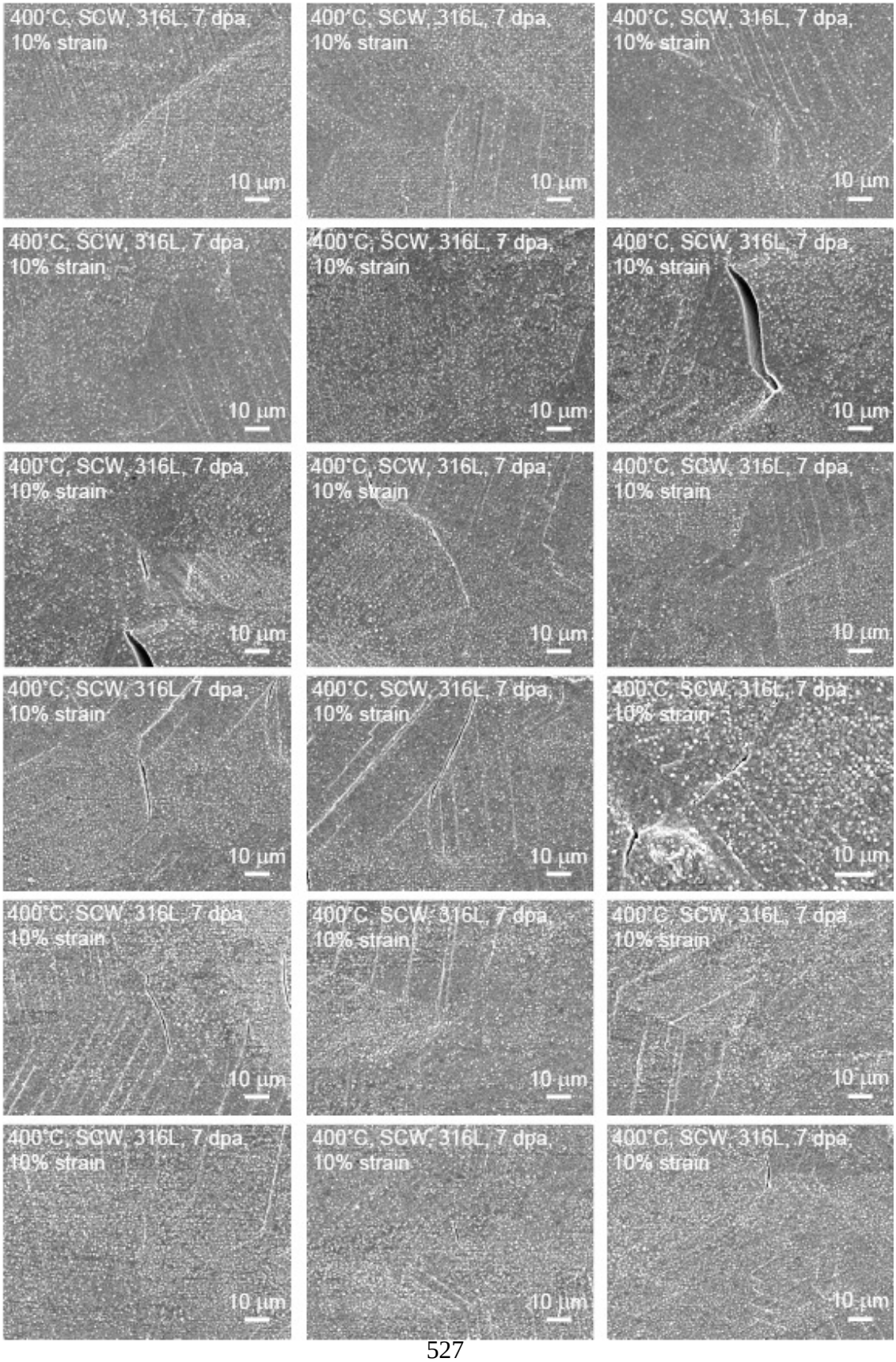
400°C, SCW, 316L, 7 dpa, 10% strain
10 μm

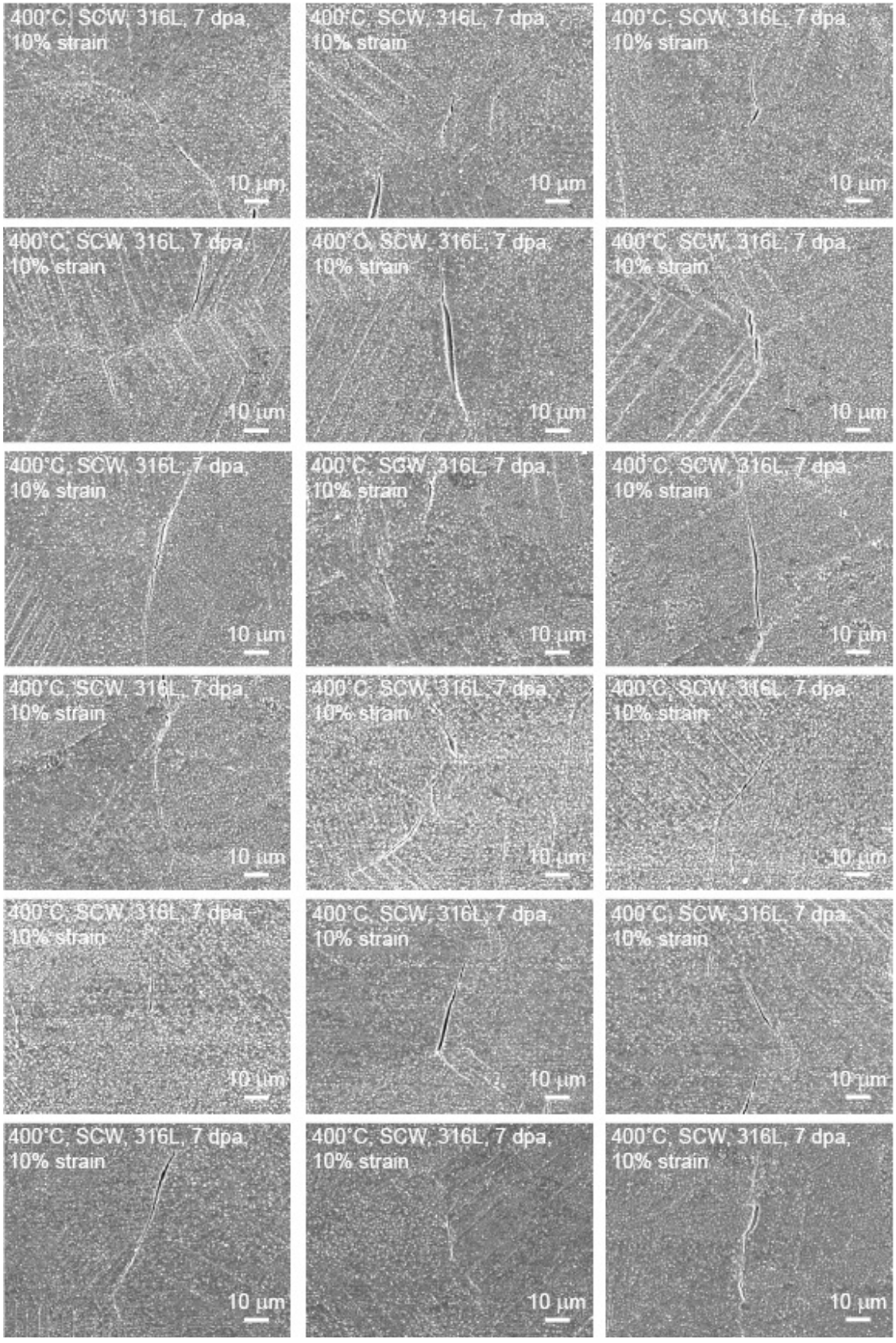
400°C, SCW, 316L, 7 dpa, 10% strain
10 µm

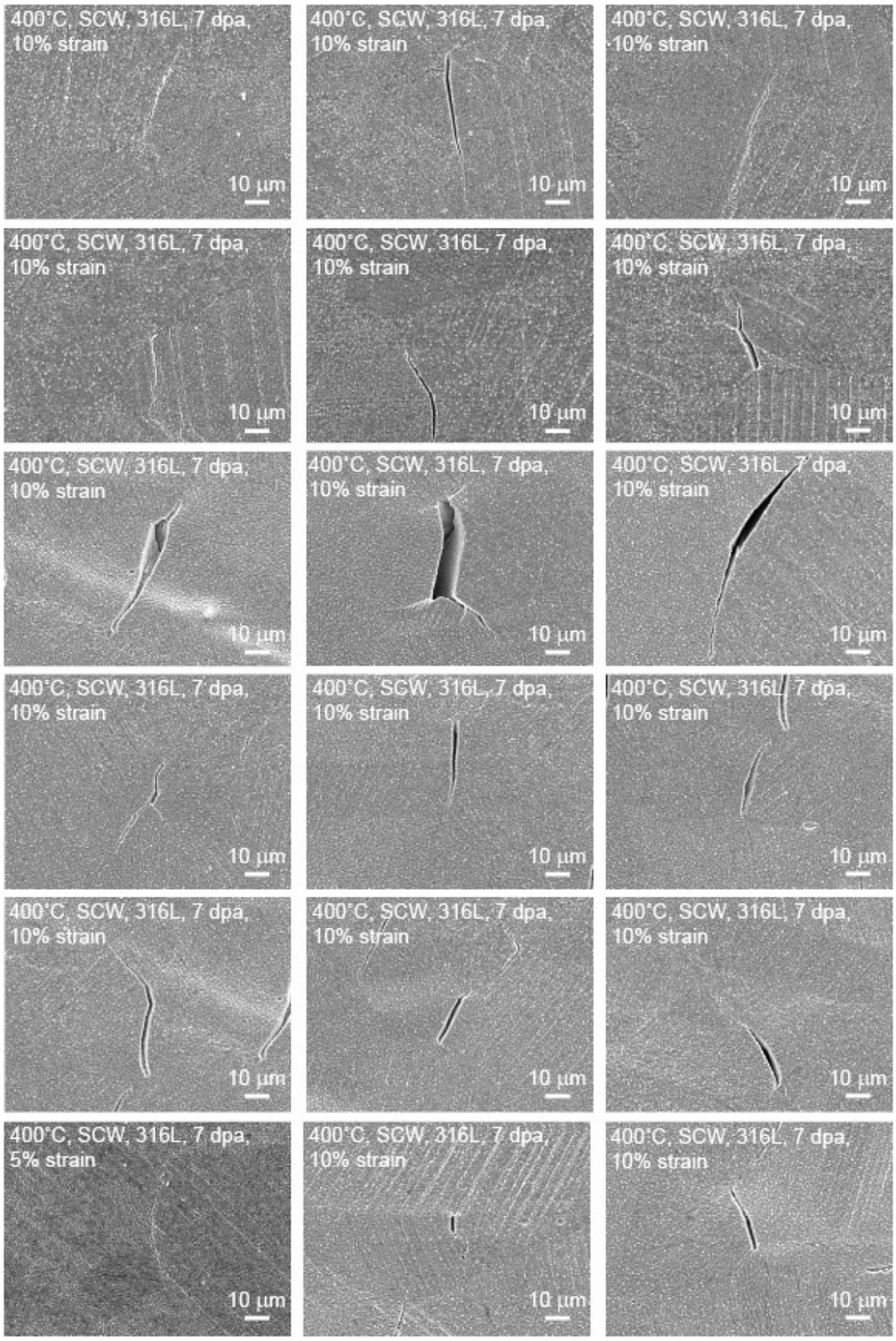
400°C, SCW, 316L, 7 dpa, 10% strain
10 µm
400°C, SCW, 316L, 7 dpa, 10% strain
10 µm
400°C, SCW, 316L, 7 dpa, 10% strain
10 µm
400°C, SCW, 316L, 7 dpa, 10% strain
10 µm
400°C, SCW, 316L, 7 dpa, 10% strain
10 µm
400°C, SCW, 316L, 7 dpa, 10% strain
10 µm
400°C, SCW, 316L, 7 dpa, 10% strain
10 µm
400°C, SCW, 316L, 7 dpa, 10% strain
10 µm
400°C, SCW, 316L, 7 dpa, 10% strain
10 µm
400°C, SCW, 316L, 7 dpa, 10% strain
10 µm
400°C, SCW, 316L, 7 dpa, 10% strain
10 µm
400°C, SCW, 316L, 7 dpa, 10% strain
10 µm
400°C, SCW, 316L, 7 dpa, 10% strain
10 µm
400°C, SCW, 316L, 7 dpa, 10% strain
10 µm
400°C, SCW, 316L, 7 dpa, 5% strain
10 µm
400°C, SCW, 316L, 7 dpa, 10% strain
10 µm
400°C, SCW, 316L, 7 dpa, 10% strain
10 µm

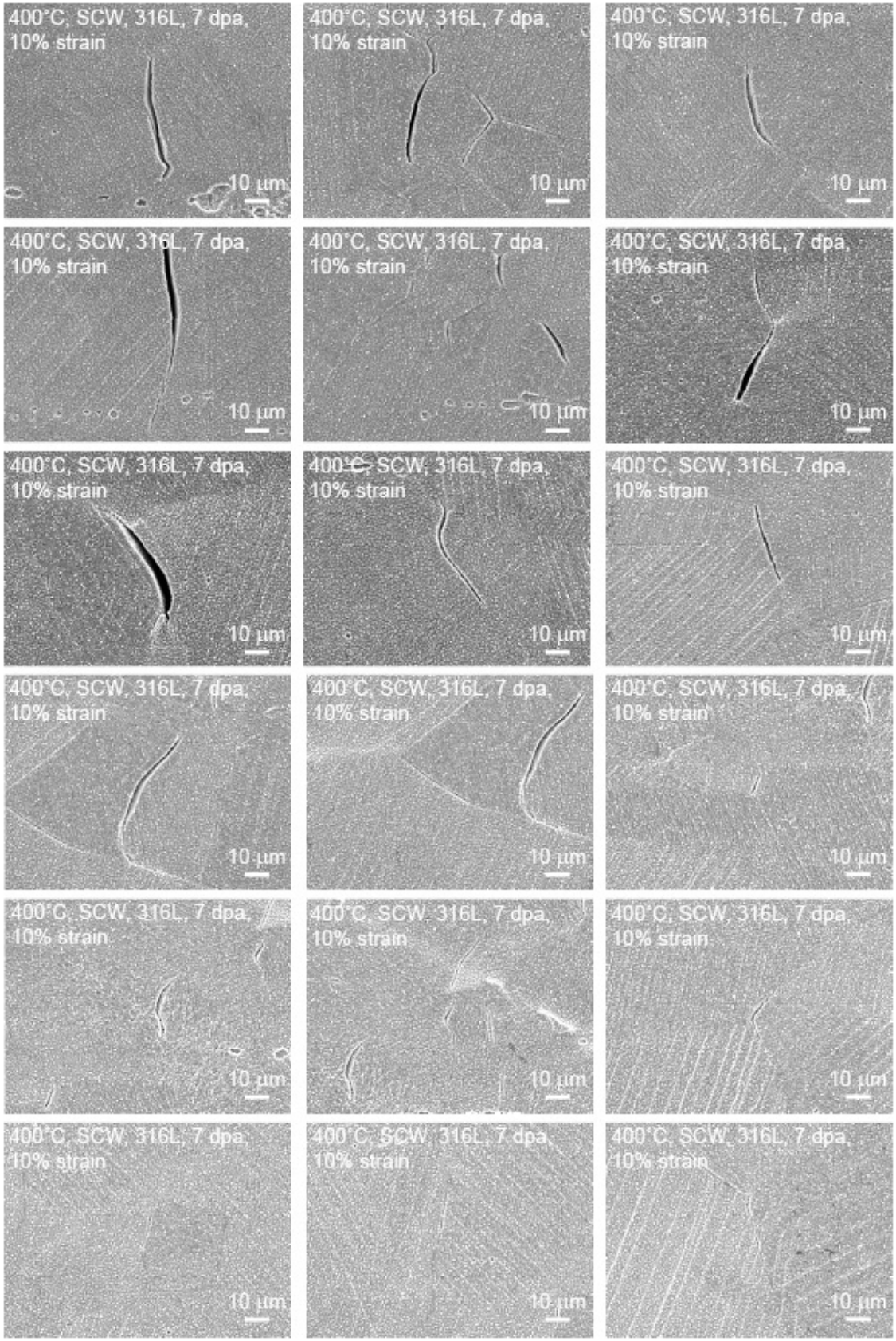
400°C, SCW, 316L, 7 dpa, 10% strain
10 µm

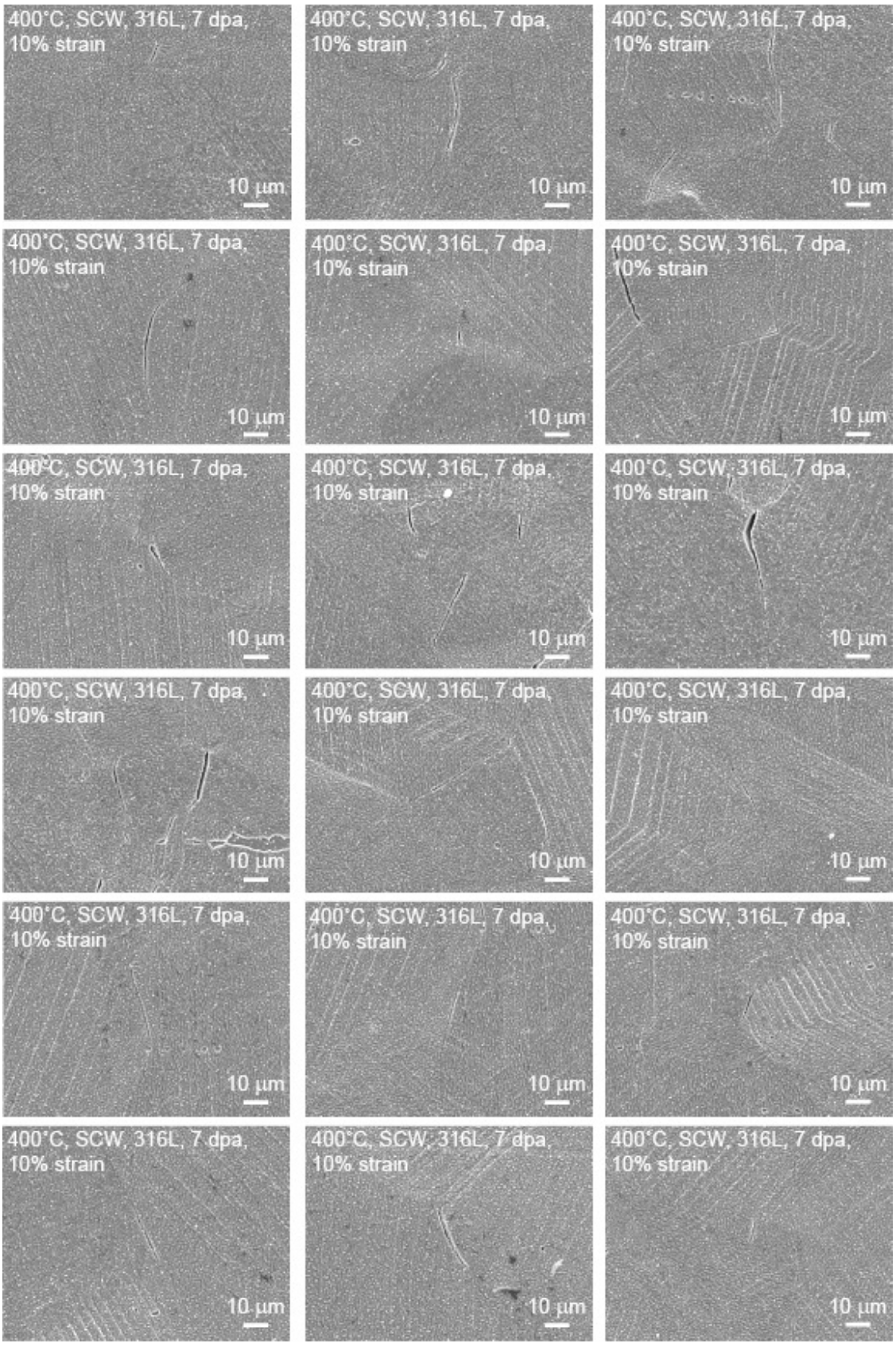
400°C, SCW, 316L, 7 dpa, 10% strain
10 µm

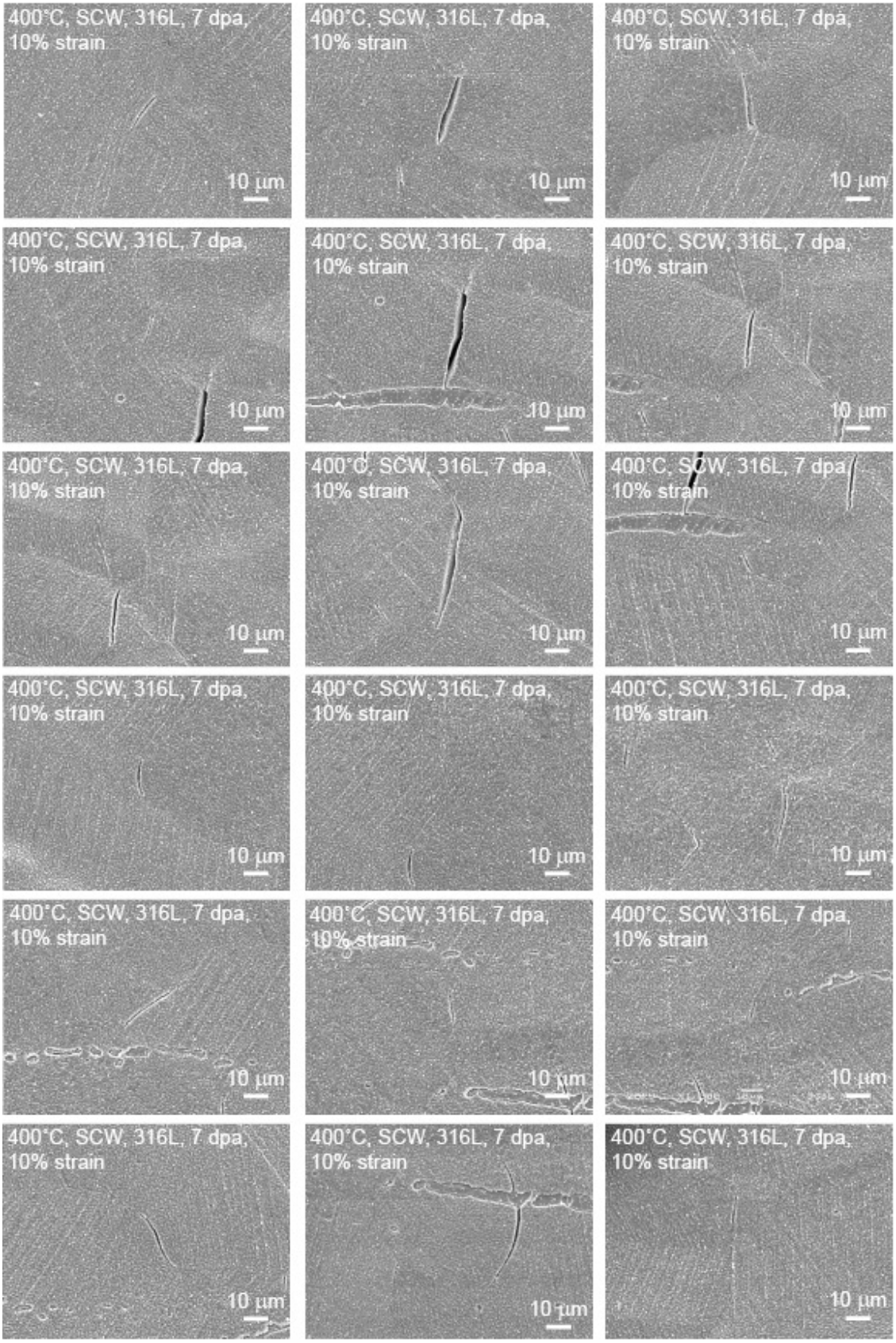
400°C, SCW, 316L, 7 dpa, 10% strain
10 µm

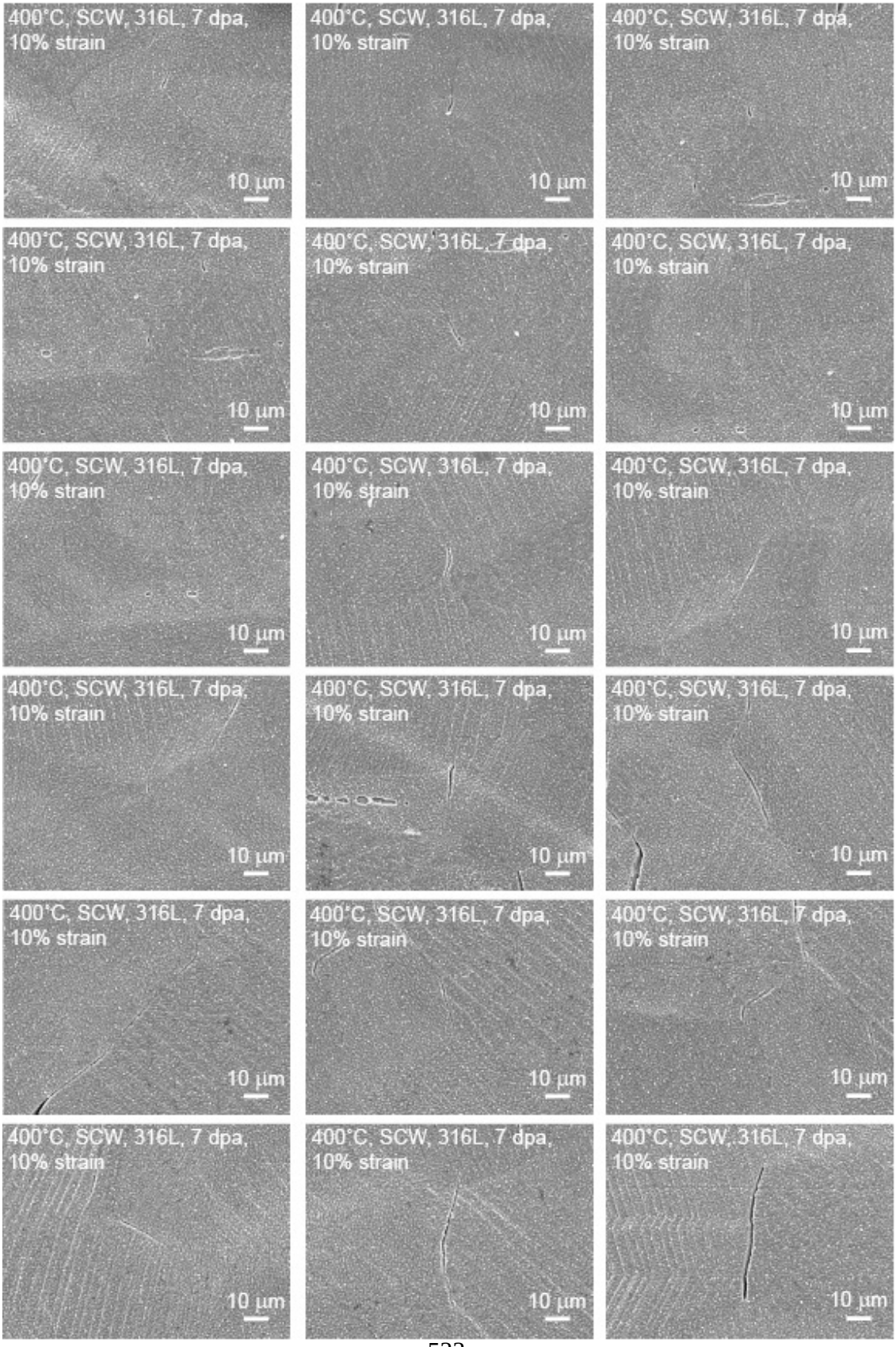
400°C, SCW, 316L, 7 dpa, 10% strain
10 µm

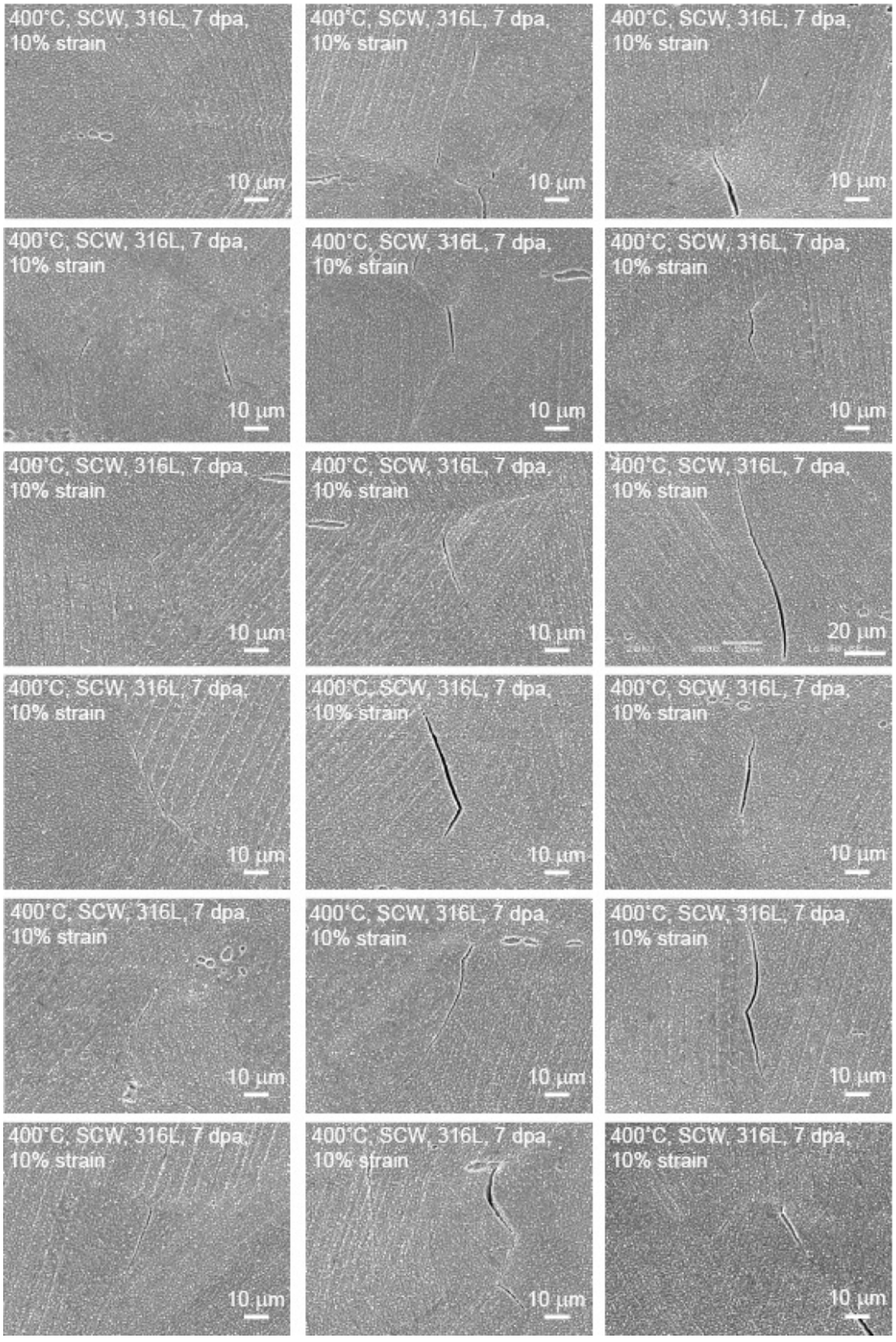
400°C, SCW, 316L, 7 dpa, 10% strain
10 μm
20 μm

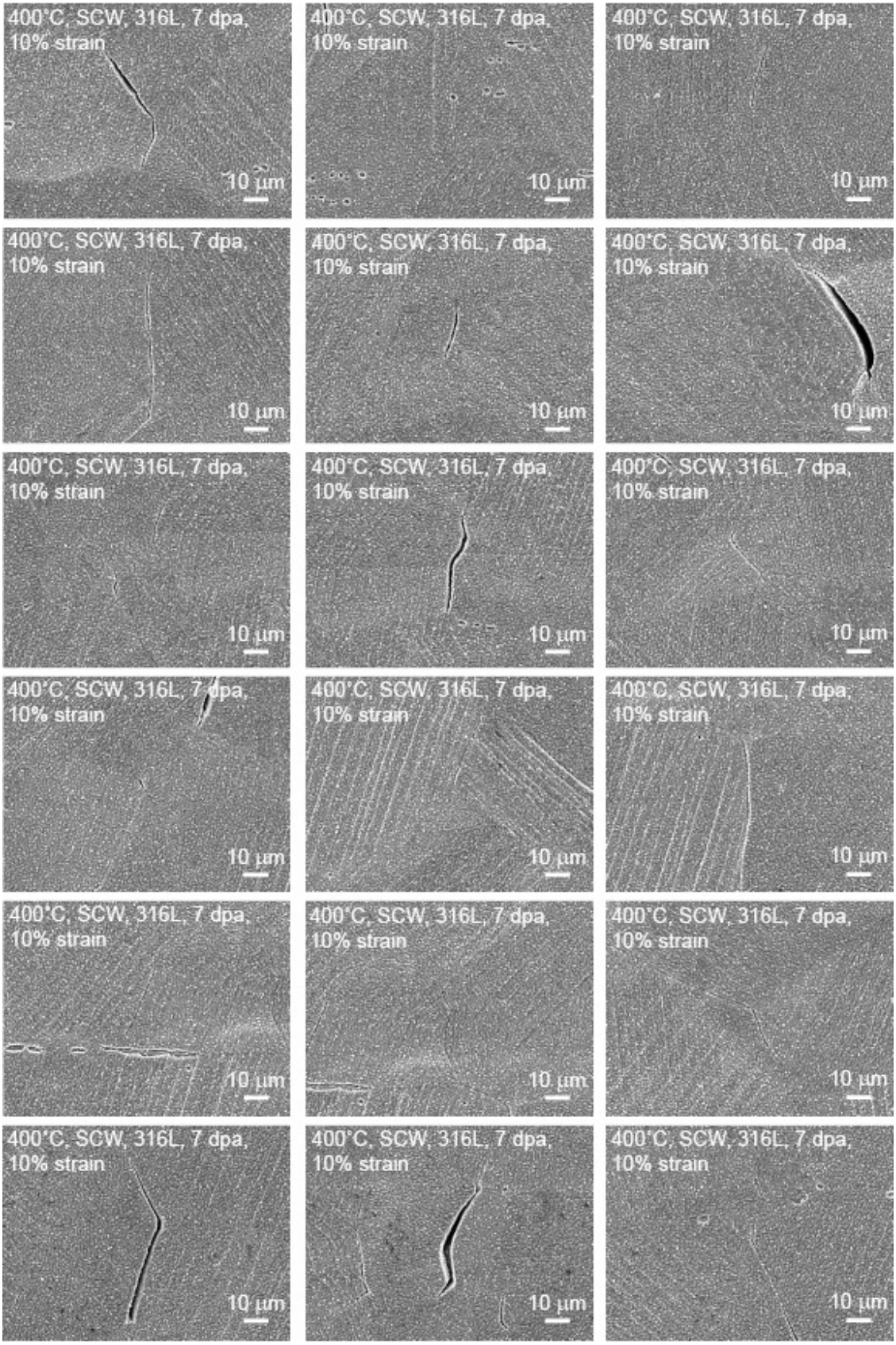
400°C, SCW, 316L, 7 dpa, 10% strain
10 µm

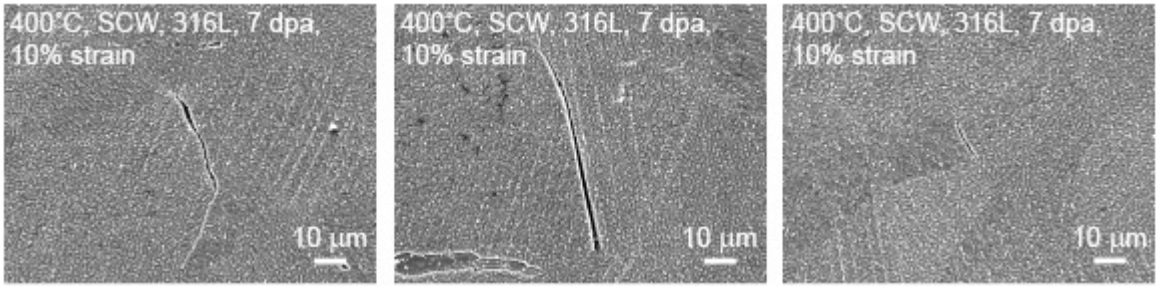
400°C, SCW, 316L, 7 dpa,
10% strain
10 μm
400°C, SCW, 316L, 7 dpa,
10% strain
10 μm
400°C, SCW, 316L, 7 dpa,
10% strain
10 μm

GBC CRACKS, 316L, 400˚C SCW, 7 dpa

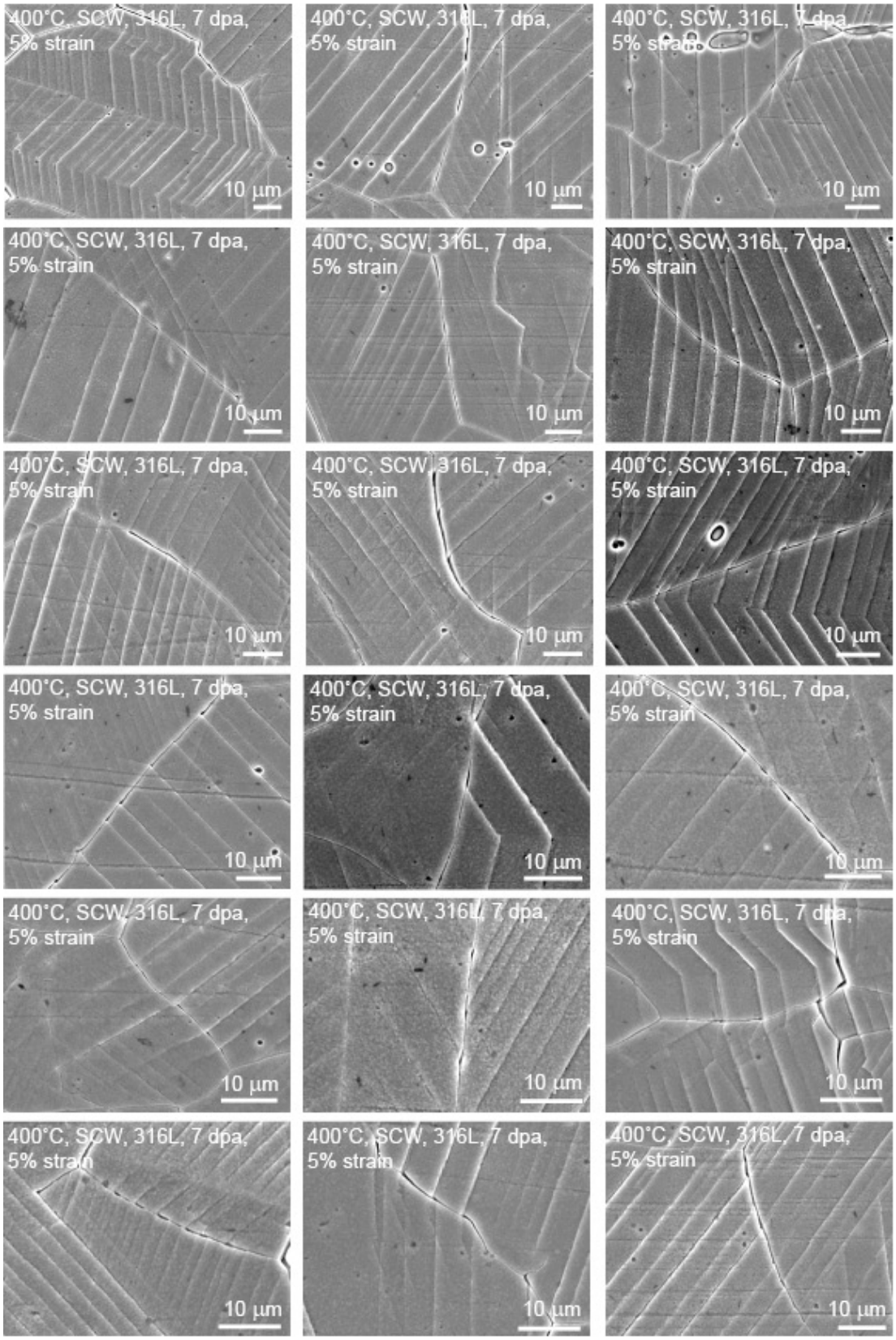

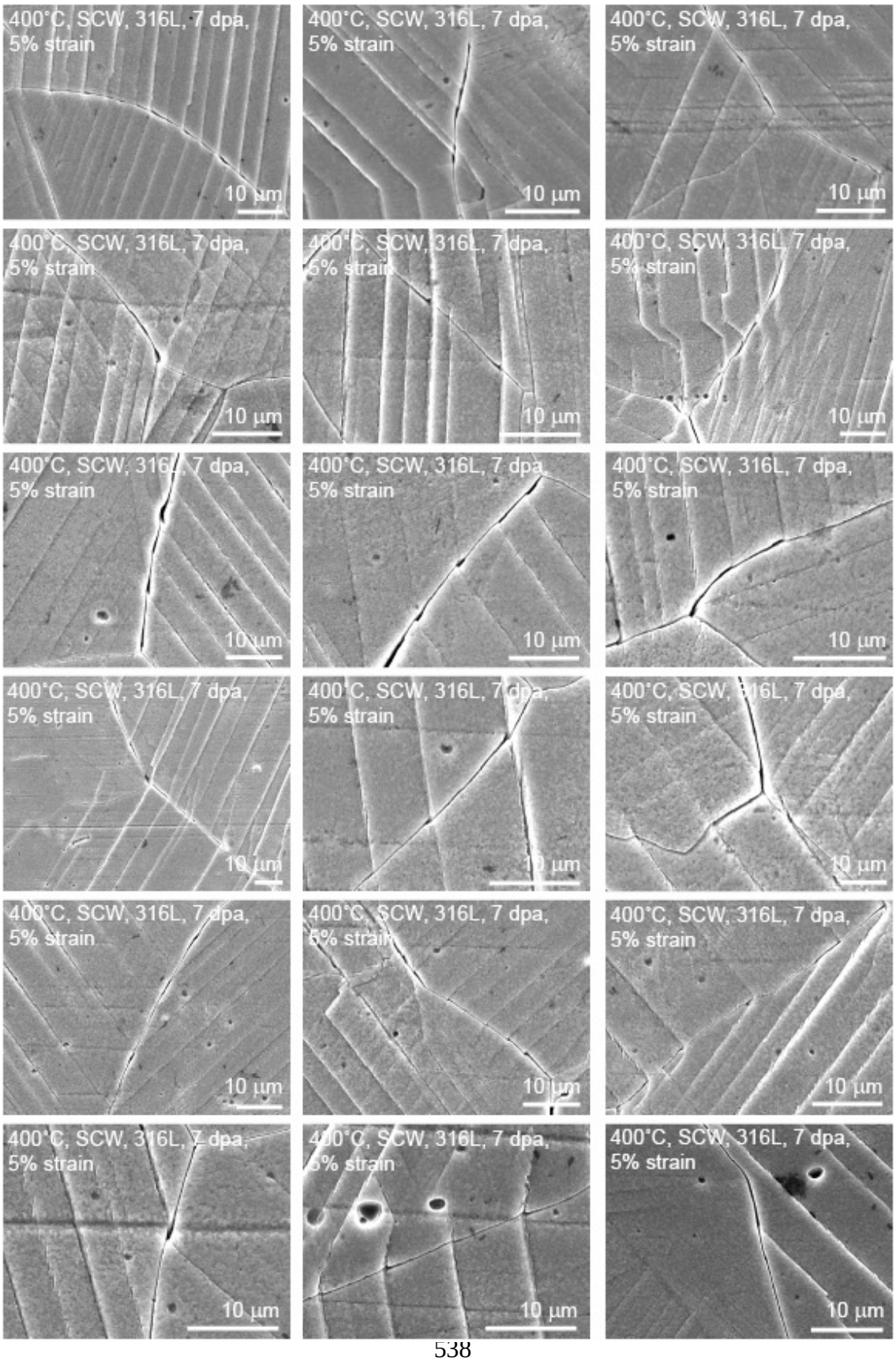
400°C, SCW, 316L, 7 dpa, 5% strain
10 μm

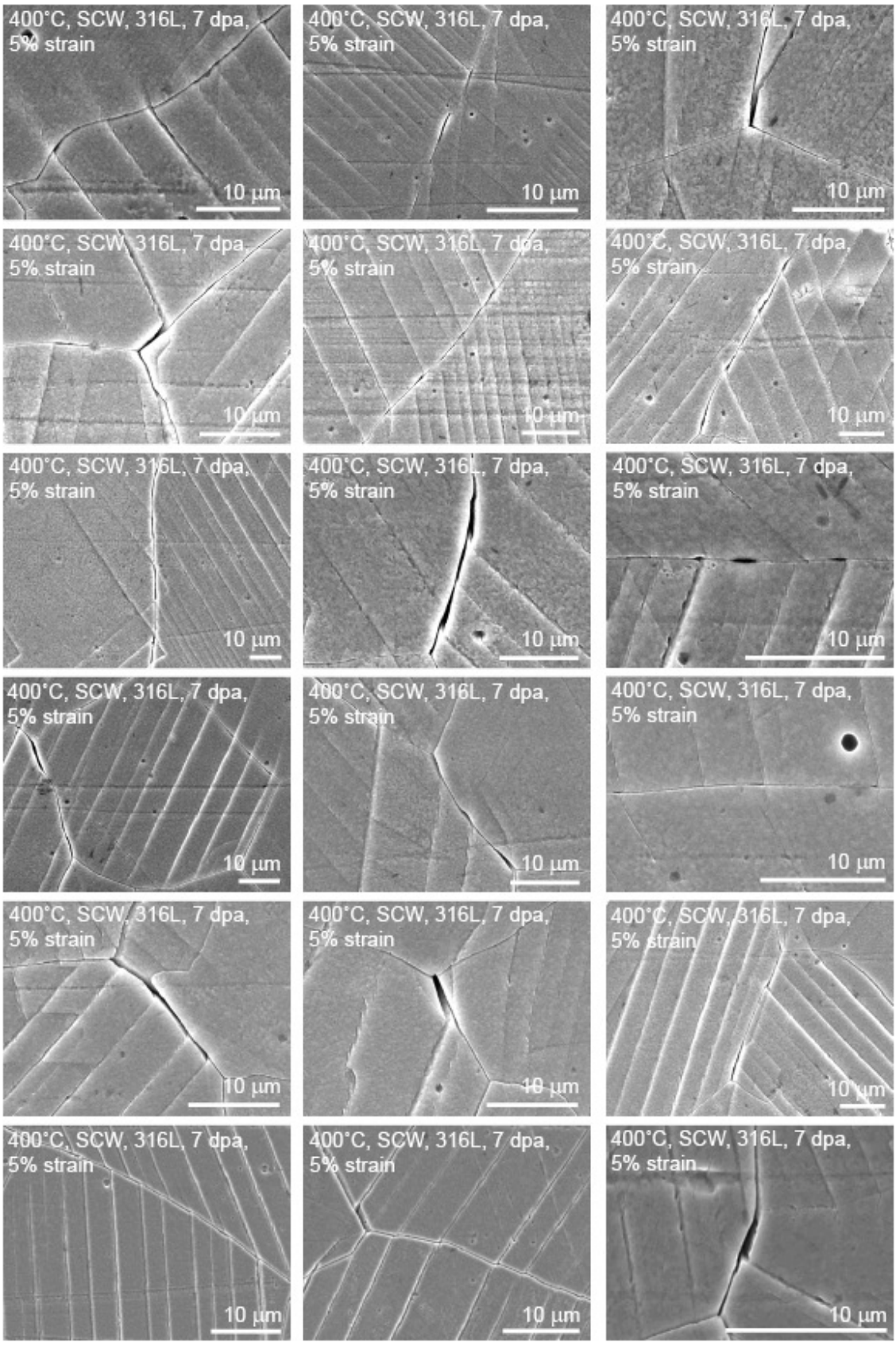
400°C, SCW, 316L, 7 dpa, 5% strain
10 μm

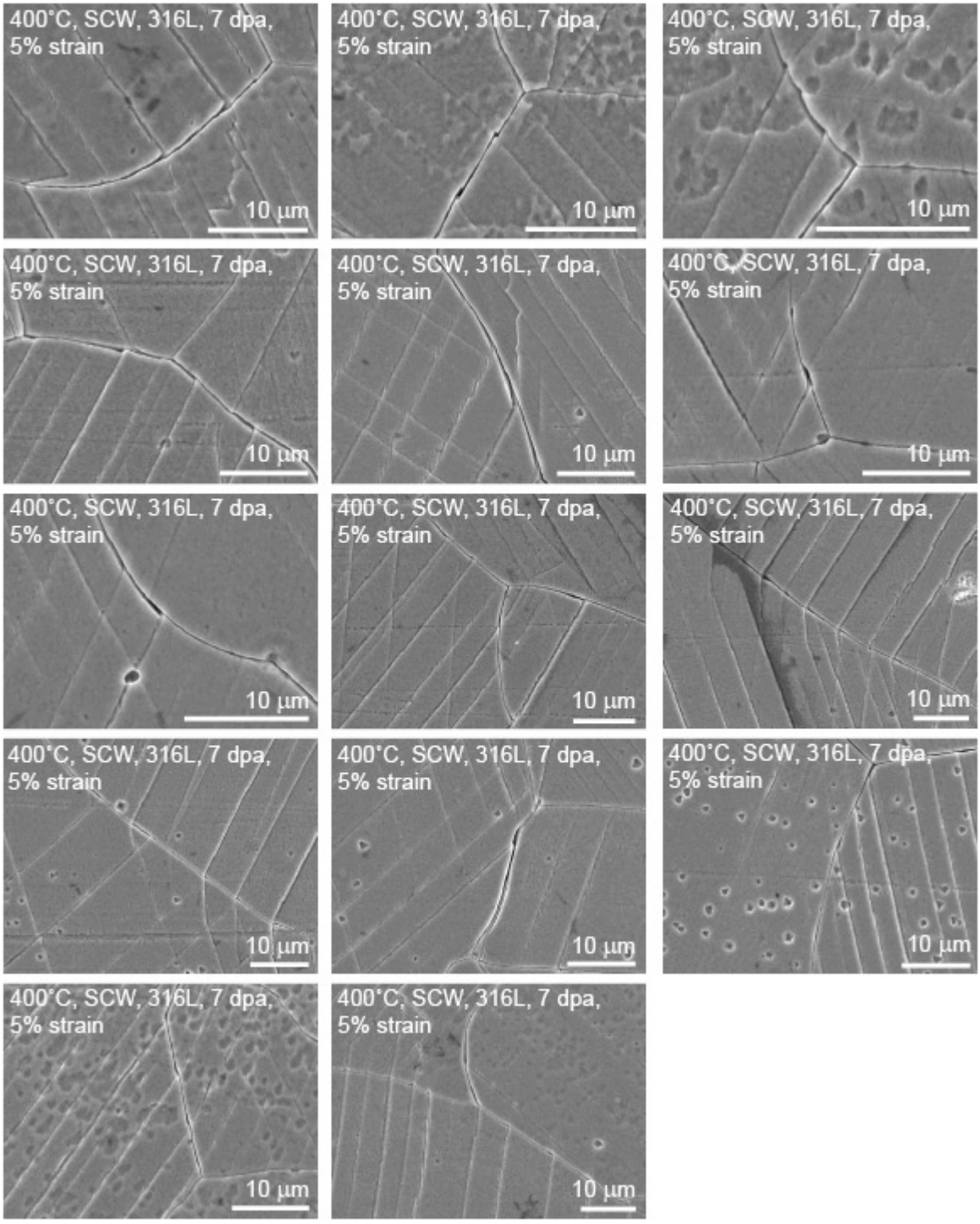
400°C, SCW, 316L, 7 dpa, 5% strain
10 μm

IG Cracks

400˚C Purified Argon

NS Cracks, 316L, 400˚C Argon, 7 dpa

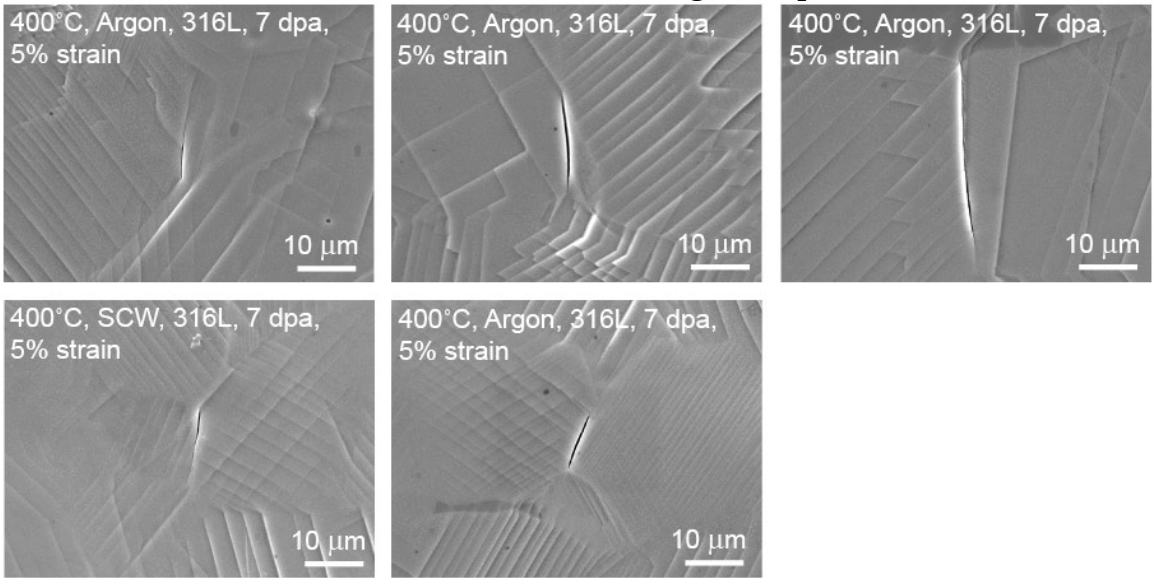

GBC Cracks, 316L, 400˚C Argon, 7 dpa

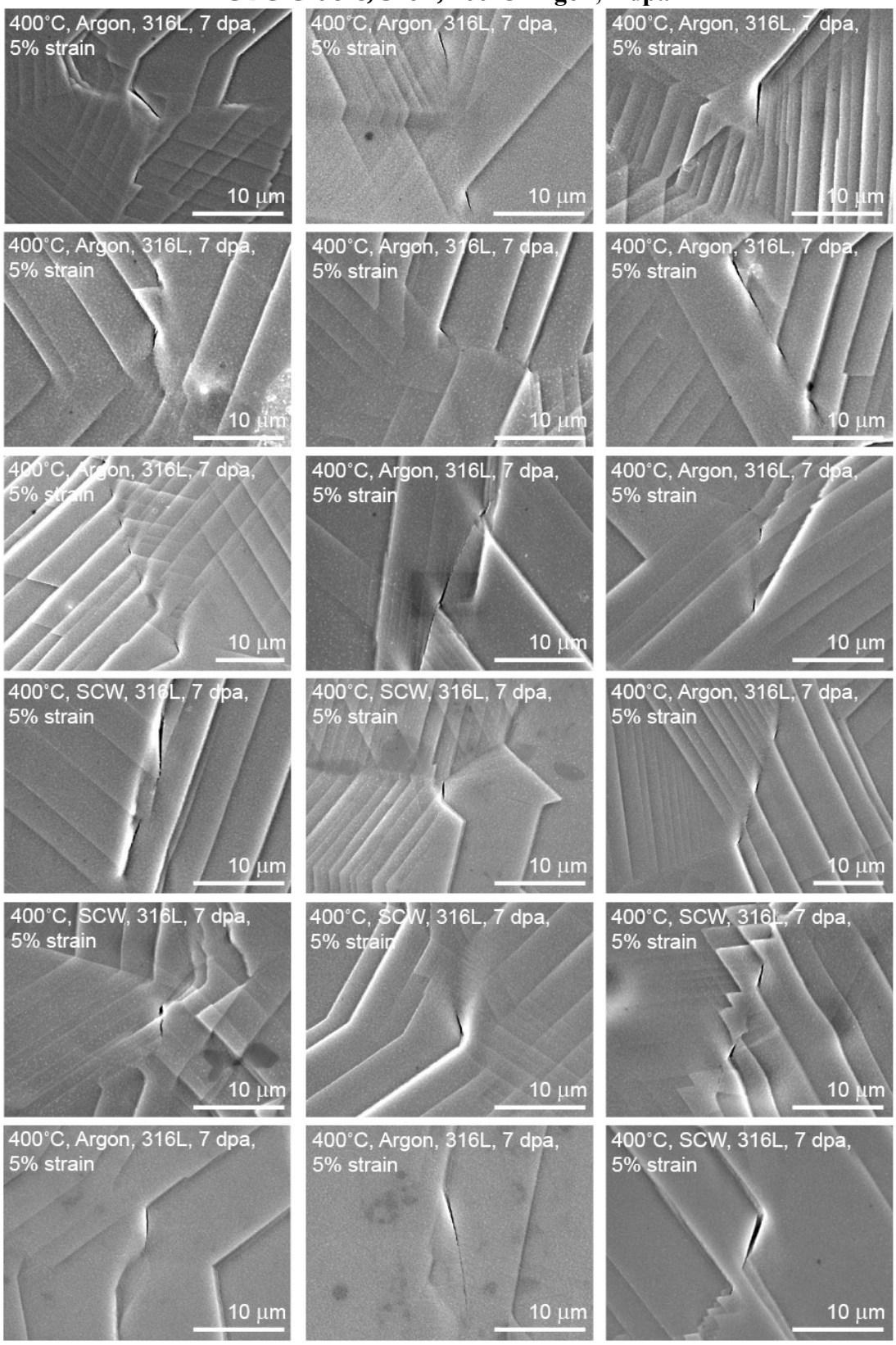

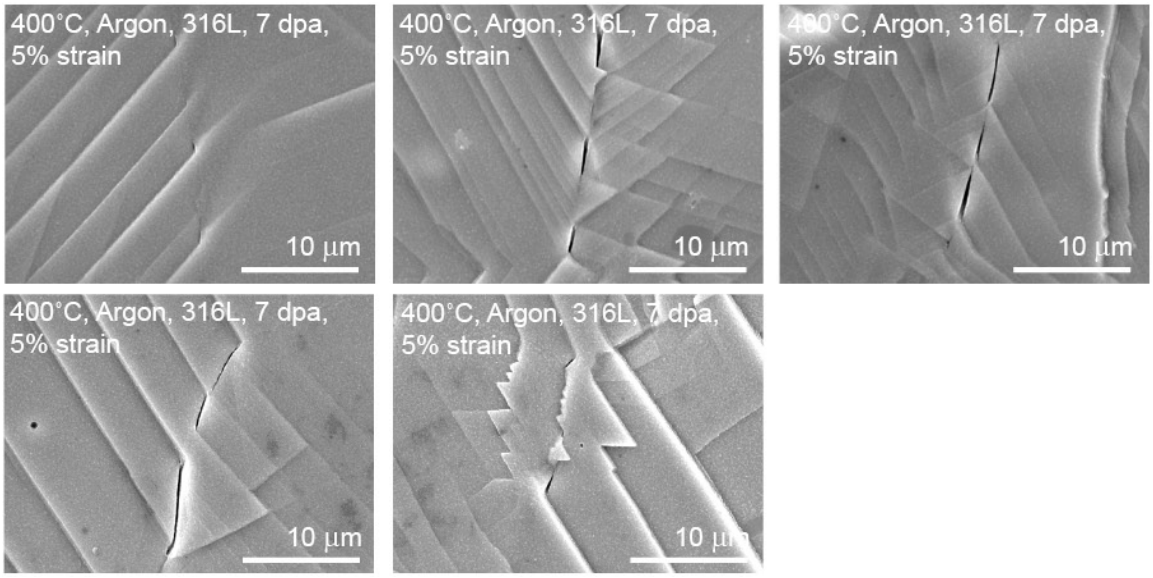
400˚C, Argon, 316L, 7 dpa, 5% strain
10 μm
400˚C, Argon, 316L, 7 dpa, 5% strain
10 μm
400˚C, Argon, 316L, 7 dpa, 5% strain
10 μm
400˚C, Argon, 316L, 7 dpa, 5% strain
10 μm
400˚C, Argon, 316L, 7 dpa, 5% strain
10 μm

APPENDIX G

Grain Boundary Plane Geometry

Derivation of expression for α

The desired angle, α, between the normal to the grain boundary plane and the tensile direction can be expressed as a function of their respective vectors, $\vec{n}$ and $\vec{z}$, respectively,

$$\alpha = \arccos\left(\frac{\vec{n}\cdot\vec{z}}{|n||z|}\right).$$

The normal to the grain boundary plane is the cross product of the grain boundary vectors along the sample surface, $\vec{v}_1$,and perpendicular surface, $\vec{v}_2$,

$$\vec{n} = \vec{v}_2 \times \vec{v}_1,$$

where these two vectors are expressed as,

$$\vec{v}_1 = (0,1,\tan(90-\theta))$$

and,

$$\vec{v}_2 = (1,0,\tan(90-\varphi)).$$

Thus, their cross product is,

$$\vec{n} = \begin{bmatrix} i & j & k \\ 1 & 0 & \dfrac{1}{\tan\varphi} \\ 0 & 1 & \dfrac{1}{\tan\theta} \end{bmatrix} = i\left(-\frac{1}{\tan\varphi}\right) + j\left(-\frac{1}{\tan\theta}\right) + k$$

and the derivation can then be completed,

$$\vec{z} = \langle 0,0,1 \rangle$$

$$\vec{n}\cdot\vec{z} = 0+0+1 = 1$$

$$|n| = \sqrt{\frac{1}{\tan^2\varphi} + \frac{1}{\tan^2\theta} + 1}$$

$$|z| = 1$$

$$\alpha = \arccos\left(\sqrt{\frac{1}{\tan^2\varphi} + \frac{1}{\tan^2\theta} + 1}\right)^{-1}.$$

Derivation of expression for β

The desired angle, β, between the specimen surface and the grain boundary plane can be expressed as a function of their normal vectors, $\vec{n}$ and $\vec{x}$, respectively,

$$\beta = \arccos\left(\frac{\vec{n}\cdot\vec{x}}{|n||x|}\right).$$

The normal to the grain boundary plane is the cross product of the grain boundary vectors along the sample surface, $\vec{v}_1$,and perpendicular surface, $\vec{v}_2$,

$$\vec{n} = \vec{v}_2 \times \vec{v}_1 ,$$

where these two vectors are expressed as,

$$\vec{v}_1 = (0,1,\tan(90-\theta))$$

and,

$$\vec{v}_2 = (1,0,\tan(90-\varphi)).$$

Thus, their cross product is,

$$\vec{n} = \begin{bmatrix} i & j & k \\ 1 & 0 & \dfrac{1}{\tan\varphi} \\ 0 & 1 & \dfrac{1}{\tan\theta} \end{bmatrix} = i\left(-\frac{1}{\tan\varphi}\right) + j\left(-\frac{1}{\tan\theta}\right) + k$$

and the derivation can then be completed,

$$\vec{x} = \langle -1,0,0 \rangle$$

$$\vec{n}\cdot\vec{x} = \left(-\frac{1}{\tan\varphi}\right)(-1) + 0 + 0 = \frac{1}{\tan\varphi}$$

$$|n| = \sqrt{\frac{1}{\tan^2\varphi} + \frac{1}{\tan^2\theta} + 1}$$

$$|x| = 1$$

$$\beta = \arccos\left(\frac{\dfrac{1}{\tan\varphi}}{\sqrt{\dfrac{1}{\tan^2\varphi}+\dfrac{1}{\tan^2\theta}+1}}\right),$$

or,

$$\varphi = \arctan\sqrt{\frac{\dfrac{1}{\cos^2\beta}-1}{\dfrac{1}{\tan^2\theta}+1}}\ .$$

Explanation of φ bias

As discussed in Chapter 5, when a grain boundary with a trace inclination, θ, is observed, any degree of rotation, β, around the surface trace vector is equally likely. Because of this relationship between θ and β, a bias exists for low values of φ that strengthens as θ decreases. As shown in the top row of images on the next page, when θ is large (~90˚) φ is approximately equal to β. When θ is small, however, as shown in the bottom row of images, there is a strong bias for low values of φ. Consider the case where θ=10˚, the degree of rotation β exceeds 60˚ before φ=20˚. Any values of β and φ are possible for any θ value, however, and when β=90˚, φ=90˚ and when β=0, φ=0. The figure below shows φ and a function of β when θ=10˚ and when θ=80˚, and clearly illustrates the bias for low values of φ when θ is low.

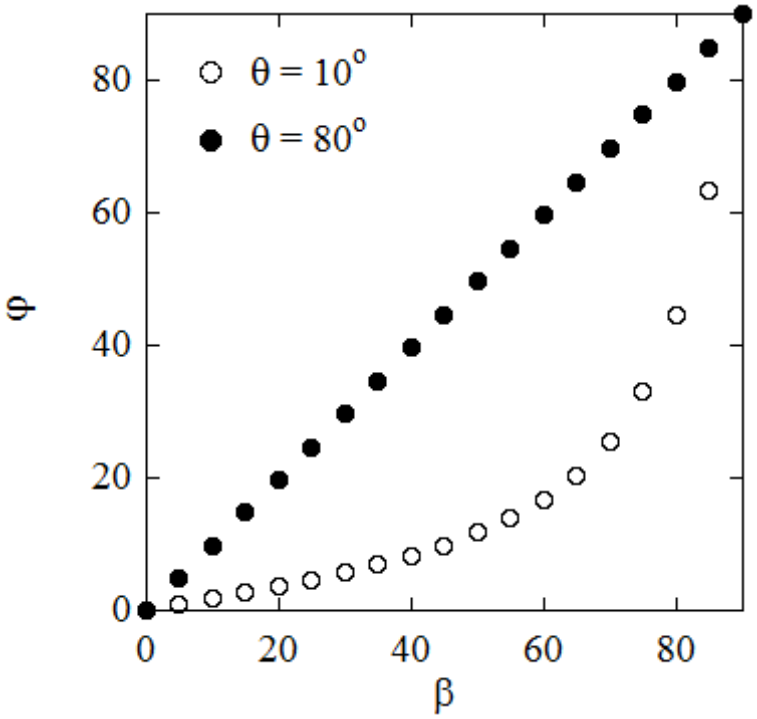

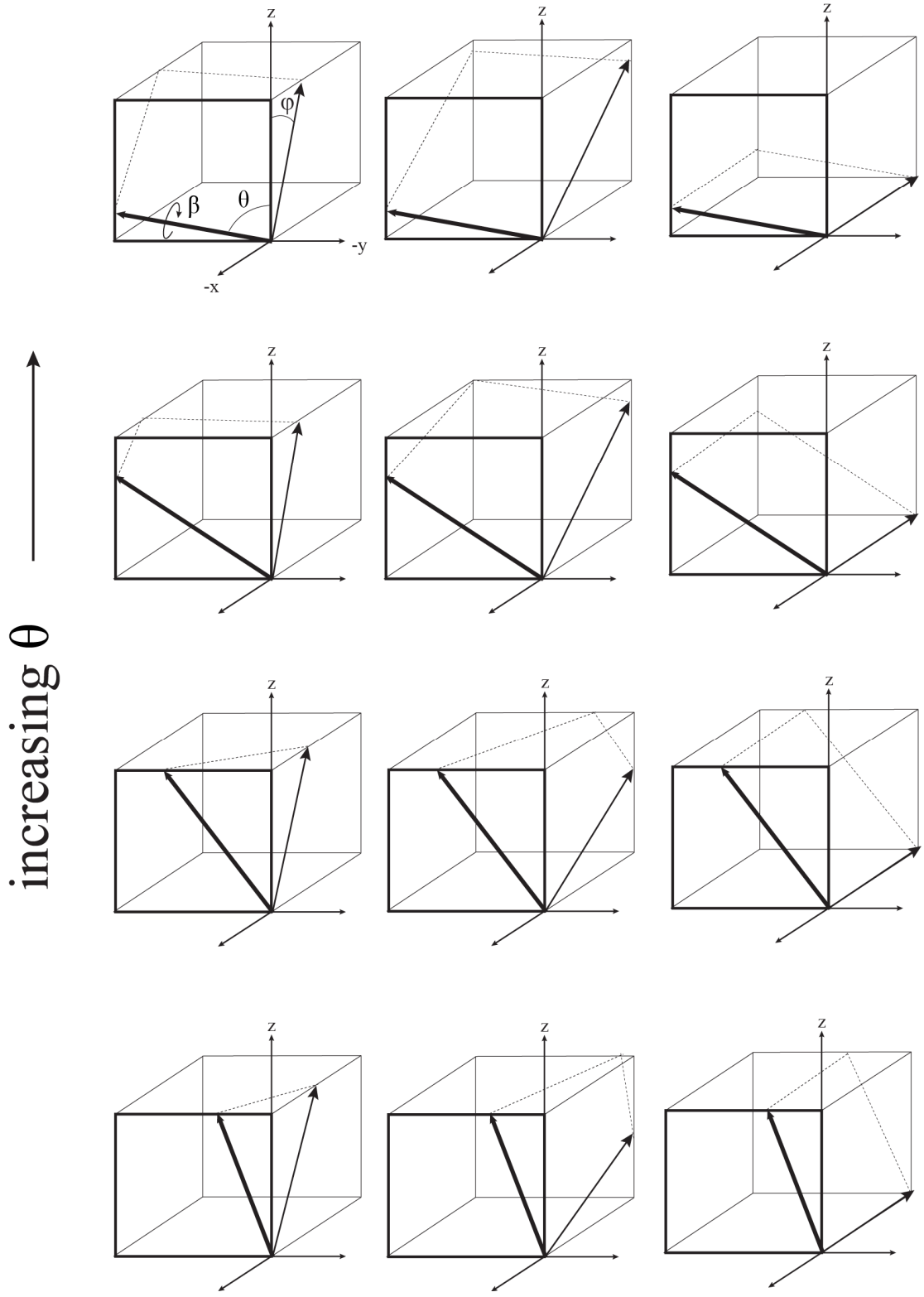
increasing β and φ
increasing θ
z
φ
β
θ
-y
-x

BIBLIOGRAPHY

1. U.S. DOE Nuclear Energy Research Advisory Committee and the Generation IV International Forum, System Research Plan for the Supercritical Water-Cooled Reactor (2004).
2. P. Scott, J. Nucl. Mater. 211 (1994) 101.
3. G. S. Was, P. Ampornrat, G. Gupta, S. Teysseyre, E. A. West, T. R. Allen, K. Sridharan, L. Tan, Y. Chen, X. Ren, C. Pister, J. Nucl. Mater. 371 (2007) 176.
4. S. Teysseyre, G. S. Was, Corrosion. 62 (2006) 1100.
5. R. Fujisawa, K. Nishimura, T. Nishida, M. Sakaihara, T. Kurata, Y. Watanabe, Corrosion, Paper 05395 (2005).
6. J. T. Busby, G. S. Was, E. A. Kenik, J. Nucl. Mater. 302 (2002) 20.
7. M. C. Hash, J. T. Busby, G. S. Was, Proc. Effects of Radiation on Materials: 21st International Symposium, American Society for Testing and Materials (2002).
8. T. Onchi, K. Dohi, N. Soneda, J. R. Cowan, R. J. Scowen, M. L. Castano, J. Nucl. Mater. 320 (2003) 194.
9. T. Onchi, K. Dohi, N. Soneda, M. Navas, M. L. Castano, J. Nucl. Mater. 340 (2005) 219.
10. G. S. Was, B. Alexandreanu, J. T. Busby, Proc. Advances in Fracture and Failure Prevention, Trans Tech Publications. (2004) 885.
11. C. Bailat, A. Almazouzi, N. Baluc, R. Schaublin, R. Groschel, M. Victoria, J. Nucl. Mater. 283-287 (2000) 446.
12. T. S. Byun, E. H. Lee, J. D. Hunn, J. Nucl. Mater. 321 (2003) 20.
13. Z. Jiao, J. T. Busby, R. Obata, G. S. Was, Proc. 12th Int. Conf. on Environmental Degradation of Materials in Nuclear Power Systems, Salt Lake City, UT. TMS (2005) 379.
14. Z. Jiao, J. T. Busby, G. S. Was, J. Nucl. Mater. 362 (2007) 218.
15. Z. Jiao, G. S. Was, J. Nucl. Mater. 382 (2008) 203.
16. Z. Jiao, G. S. Was, J. T. Busby, Proc. 13th Int. Conf. on Environmental Degradation of Materials in Nuclear Power Systems. Canadian Nuclear Society. Whistler, B.C. (2007) 529.
17. G. S. Was, B. Alexandreanu. J. T. Busby, Key Eng. Mat. 261-263 (2004) 885.
18. G. Alexandreanu, G. S. Was, Corrosion. 59 (2003) 705.
19. E. M. Lehockey, A. M. Brennenstuhl, S. Pagan, M. A. Clark, V. Perovic, Proc. 13th Int. Conf. on Environmental Degradation of Materials in Nuclear Power Systems. Canadian Nuclear Society. Whistler, B.C. (2007) 465.
20. W. H. Kim, C. Laird, Acta Met. 26 (1978) 789.
21. B. S. Rho, H. U. Hong, S. W. Nam, Scripta Mat. 43 (2000) 167.

22. J. Buongiorno, P. E. MacDonald, Supercritical Water Reactor: Progress Report for FY-03, INEEL (2003).
23. Y. Ikushima, Proc. Int. Symposium on Supercritical Water-Cooled Reactor Design Technology, Tokyo, Japan (2000).
24. Y. Watanabe, H. Abe, Y. Daigo, Proc. GENES4/ANP, Kyoto, Japan. (2003).
25. D. D. MacDonald, L. B. Kriksunov, Electrochimica Acta. 47 (2001) 775.
26. P. Kritzer, Proc. Int. Symposium on Supercritical Water-Cooled Reactor Design Technology, Tokyo, Japan (2000).
27. D. D. MacDonald, J. Supercritical Fluids. 30 (2004) 375.
28. T. Allen, D. Guzonas, G. S. Was, E. A. West, J. Nucl. Mater. (2010) submitted.
29. J. Kaneda, S. Kasahara, J. Kuniya, K. Moriya, F. Kano, N. Saito, A. Shiori, T. Shibayama, H. Takahashi, Proc. 12th Int. Conf. on Environmental Degradation of Materials in Nuclear Power Systems, Salt Lake City, UT. TMS (2005) 1409.
30. K. Sridharan, A. Zillmer, J. R. Licht, T. R. Allen, M. H. Anderson, L. Tan, Proc. ICAPP, Pittsburgh, PA (2004) Paper 4136.
31. Y. H. Jeong, J. Y. Park, H. G. Kim, J. T. Busby, E. Gartner, M. Atzmon, G. S. Was, R. J. Comstock, Y. S. Chu, M. Da Silva, A. Yilmazbayhan, A. T. Motta, Proc. 12th Int. Conf. on Environmental Degradation of Materials in Nuclear Power Systems, Salt Lake City, UT. TMS (2005) 1369.
32. Q. Peng, E. Gartner, J. T. Busby, A. T. Motta, G. S. Was, Corrosion. 63 (2007) 577.
33. A. T. Motta, A. D. Siwy, J. M. Kunkle, J. B. Bischoff, R. J. Comstock, Y. Chen, T. R. Allen, Proc. 13th Int. Conf. on Environmental Degradation of Materials in Nuclear Power Systems, Whistler, B.C., Canadian Nuclear Society. (2007) 1501.
34. A. T. Motta, Y. Aylin, M. Da Silva, R. J. Comstock, G. S. Was, J. T. Busby, E. Gartner, Q. Peng, Y. H. Jeong, J. Y. Park, J. Nucl, Mater. 371 (2007) 61.
35. S. Kasahara, J. Kuniya, K. Moriya, N. Saito, S. Shiga, GENES/ANP. Kyoto, Japan (2003) Paper 1132.
36. G. S. Was, S. Teysseyre, Z. Jiao, Corrosion 62 (2006) 989.
37. G. S. Was, T. R. Allen, Proc. American Nuclear Society – ICAPP. Seoul, Korea 6 (2005) 3460.
38. K. Sridharan, A. Zillmer, J. R. Licht, T. R. Allen, M. H. Anderson, L. Tan, Proc. ICAPP, Pittsburgh, PA (2004) Paper 4136.
39. T. R. Allen, Y. Chen, L. Tan, X. Ren, K. Sridharan, U. Shigeharu, Proc. 12th Int. Conf. on Environmental Degradation of Materials in Nuclear Power Systems, Salt Lake City, UT. TMS (2005) 1397.
40. Y. Chen, K. Sridharan, T. Allen, Proc. Corrosion 2005. NACE International (2005) Paper 05391.
41. I. Betova, M. Bojinov, P. Kinnunen, V. Lehtovuori, S. Peltonen, S. Penttila, T. Saario, Proc. ICAPP, Nice, Fance (2007).
42. J. Kaneda, S. Kasahara, J. Kuniya, K. Moriya, F. Kano, N. Saito, A. Shiori, T. Shibayama, H. Takahashi, Proc. 12th Int. Conf. on Environmental Degradation of Materials in Nuclear Power Systems, Salt Lake City, UT. TMS (2005).
43. A. G. Crouch, J. Robertson, Acta Met. 38 (1990) 2567.

44. H. Abe, Y. Watanabe, K. Sue, Proc. ICAPP, Pittsburgh, PA (2004) 1942.
45. Y. Tsuchiya, F. Kano, N. Saito, A. Shiori, S. Kasahara, K. Moriya, H. Takahashi, GENES/ANP. Kyoto, Japan (2003) Paper 1096.
46. Y. Tsuchiya, F. Kano, N. Saito, A. Shiori, K. Moriya, S. Kasahara, Corrosion 2004, New Orleans, LA. NACE International (2004) Paper No. 04485.
47. N. Saito, Y. Tsuchiya, F. Kano, M. Ookawa, J. Kaneda, K. Moriya, H. Matsui, Proc. American Nuclear Society Summer Meeting (2006) 2193.
48. Y. Watanabe, H. Abe, Y. Daigo, T. Nishida, Corrosion 2004, New Orleans, LA. NACE International (2004) Paper No. 04493.
49. S. Teysseyre, G. S. Was, Proc. 13th Int. Conf. on Environmental Degradation of Materials in Nuclear Power Systems, Whistler, B.C., Canadian Nuclear Society. (2007) 540.
50. Q. J. Peng, S. Teysseyre, P. L. Andresen, Corrosion. 63 (2007) 1033.
51. K. Arioka, T. Yamada, T. Terachi, T. Miyamoto, Corrosion. 64 (2008) 691.
52. C. Bosch, D. Delafosse, Corrosoion 2005, NACE International, Houston, TX (2005) Paper No. 05396.
53. R. Zhou, E. A. West, Z. Jiao, G. S. Was, J. Nucl. Mater. (2010) submitted.
54. R. Zhou, E. A. West, Z. Jiao, G. S. Was, Proc. 14th Int. Conf. on Environmental Degradation of Materials in Nuclear Power Systems, Virginia Beach, VA. American Nuclear Society (2009) in press.
55. S. Teysseyre, Z. Jiao, E. A. West, G. S. Was, J. Nucl. Mater. 371 (2007) 107.
56. E. A. West, S. Teysseyre, Z. Jiao, G. S. Was, Proc. 13th Int. Conf. on Environmental Degradation of Materials in Nuclear Power Systems, Whistler, B.C., Canadian Nuclear Society. (2007) 748.
57. P. R. Okamoto, L. E. Rehn, J. Nucl. Mater. 83 (1979) 2.
58. K. Arioka, T. Yamada, T. Terachi, T. Miyamoto, ICG-EAC, Sweden (2008).
59. K. Arioka, T. Yamada, T. Terachi, G. Chiba, Corrosion 63 (2007) 1114.
60. K. Arioka, T. Yamada, T. Terachi, R. W. Staehle, Corrosion 62 (2006) 74.
61. G. Gupta, P. Ampornrat, X. Ren, K. Sridharan, T. R. Allen, G. S. Was, J. Nucl. Mater. 361 (2007) 160.
62. G. E. Dieter, Mechanical Metallurgy, 3rd Edition, New York: McGraw-Hill, 1986.
63. J. Cadek, Creep in Metallic Materials, New York: Elsevier, 1988.
64. T. H. Courtney, Mechanical Behavior of Materials, Boston: McGraw-Hill, 2000.
65. M. E. Kassner, T. A. Hayes, Int. J. Plasticity, 19 (2003) 1715.
66. C. Gandhi, R. Raj, Met. Trans. A 12A (1981) 515.
67. R. W. Evans, B. Wilshire, Creep of Metals and Alloys, London: Institute of Metals, 1985.
68. I. S. Servi, N. J. Grant, J. of Met.. 3 (1951) 909.
69. B. F. Dyson, D. McLean, Met. Science. 11 (1977) 37.
70. B. F. Dyson, Scripta Met. 17 (1983) 31.
71. A. S. Argon, Scripta Met. 17 (1983) 5.
72. W. Beere, M. V. Speight, Met. Sci. 21 (1978) 172.
73. A. Needleman, J. R. Rice, Acta Met. 28 (1980) 1315.

74. W. F. Hosford, The Mechanics of Crystals and Textured Polycrystals, New York: Oxford University Press, 1993.
75. G. Sachs, Z. Ver. Dent. Ing. 72 (1928) 734.
76. G. I. Taylor, J. Inst. Met. 62 (1938) 307.
77. G. I. Taylor, Analysis of Plastic Strain in a Cubic Crystal, New York: Macmillan, 1938.
78. R. Von Mises, Z. Angew. Math. Mech. 8 (1928) 161.
79. J. F. Bishop, R. Hill, Phil. Mag. 42 (1951) 414.
80. J. F. Bishop, R. Hill, Phil. Mag. 42 (1951) 1298.
81. A. Kochendorfer, Plastische Eigenschaften von Kristallen und Metallischen Werkstoffen, Berlin: Springer, 1941.
82. M. F. Ashby, Phil. Mag. 21 (1970) 399.
83. Y. B. Chastel, P. R. Dawson, Switzerland: Trans. Tech. Pub. (1994) 1747.
84. U. F. Kocks, C. N. tome, H. R. Wenk, Texture and Anisotropy: Preferred Orientations in Polycrystals and their Effect on Material Properties, Cambridge: Cambridge University Press, 1998.
85. W. Yun, H. Kimura, Y. Akiniwa, K. Tanaka, Proc. Int. Symp. Micro-NanoMechatronics and Human Science, Piscataway, NJ. IEEE (2005) 223.
86. W. Yun, H. Kimura, Y. Akiniwa, K. Tanaka, Key Eng. Mat. (2007) 531.
87. B. Alexandreanu, O. K. Chopra, W. J. Shack, Proc. 12th Int. Conf. on Environmental Degradation of Materials in Nuclear Power Systems, Salt Lake City, UT. TMS (2005) 579.
88. D. L. Davidson, K. S. Chan, Acta Met. 37 (1989) 1089.
89. B. Alexandreanu, G. S. Was, Scripta Mat. 54 (2006) 1047.
90. W. H. Kim, D. Laird, Acta Met., 26 (1978) 777.
91. S. I. Wright, D. P. Field, Mat. Sci. Eng. A257 (1998) 165.
92. G. S. Was, Fundamentals of Radiation Materials Science: Metals and Alloys, Berlin: Springer, 2007.
93. American Society for Metals, the Inhomogeneity of Plastic Deformation, Metals Park, OH: American Society for Metals, 1973.
94. J. V. Sharp, Proc. 4th European Reg. Conf. on Electron Microscopy, Rome (1968) 417.
95. T. Miura, K. Fuji, K. Fukuya, Y. Ito, J. Nucl. Mat. 386-388 (2009) 210.
96. N. Hashimoto, T. S. Byun, J. Nucl. Mater. 367-370 (2007) 960.
97. K. Fukuya, K. Fujii, Y. Kitsunai, Proc. 12th Int. Conf. on Environmental Degradation of Materials in Nuclear Power Systems, Salt Lake City, UT. TMS (2005) 389.
98. M. P. Manahan, R. Kohli, J. Santucci, P. Sipush, Nucl. Eng. and Design, 113 (1989) 297.
99. F. Onimus, J. Bechade, C. Prioul, P. Pilvin, I. Monnet, S. Doriot, B. Verhaeghe, D. Gilbon, L. Robert, L. Legras, J. Mardon, J. ASTM Int. 2 (2005) 259.
100. S. J. Zinkle, Rad. Eff. Defect Solids, Switzerland, Gordon & Breach, 148 (1999) 447.

101. C. Zener, Fracturing of Metals, Cleveland, OH: American Society for Metals, 1948.
102. A. N. Stroh, Proc. Royal Society of London. 223 (1954) 404.
103. W. T. Read, W. Shockley, Phys. Rev. 78 (1950) 275.
104. V. Randle, The Measurement of Grain Boundary Geometry, Bristol, UK: Insitute of Physics, 1993.
105. H. Grimmer, W. Bollmann, D. H. Warrington, Acta. Cryst. A30 (1974) 197.
106. G. Palumbo, K. T. Aust, E. M. Lehockey. U. Erb, P. Lin, Scripta Mat. 38 (1998) 1685.
107. D. G. Brandon, Acta Met. 14 (1966) 1479.
108. E. A. West, G. S. Was, J. Nucl. Mat. 392 (2009) 264.
109. E. M. Lehockey, A. M. Brennenstuhl, I. Thompson, Corrosion Science, 46 (2004) 2383.
110. W. M. Kane, C. J. McMahon, Mat. Sci. & Amp. A. 507 (2009) 61.
111. V. Y. Gertsman, S. M. Bruemmer, Acta Mat. 49 (2001) 1589.
112. G. Palumbo, P. J. King, K. T. Aust, U. Erb, P. C. Lichtenberger, Scripta Met. 25 (1991) 1775.
113. K. T. Aust, U. Erb, G. Palumbo, Mat. Sci. Eng. A, A176 (1994) 329.
114. T. Watanabe, S. Tsurekawa, Acta Mat. 47 (1999) 4171.
115. B. Alexandreanu, B. Capell, G. S. Was, Mat. Sci. Eng. A, 300 (2001) 94.
116. D. C. Crawford, G. S. Was, Met. Trans. 23A (1992) 1195.
117. V. Y. Gertsman, K. Tangri, Acta Mat. 45 (1997) 4107.
118. Y. Pan, B. L. Adams, T. Olson, N. Panayotou, Acta Mat. 44 (1996) 4685.
119. G. S. Was, V. Thaveeprungsriporn, D. C. Crawford, JOM. 50 (1998) 44.
120. T. Watanabe, Mat. Sci. Eng. A176 (1994) 39.
121. V. Thaveeprungsriporn, G. S. Was, Met. And Mat. Trans. 23A (1997) 2101.
122. E. M. Lehockey, G. Palumbo, Mat. Sci. Eng. A37 (1997) 168.
123. E. M. Lehockey, G. Palumbo, P. Lin, Met. Mat. Trans. 29A (1998) 3069.
124. S. Watanabe, Y. Takamatsu, N. Sakaguchi, H. Takahashi, J. de Physique IV. 10 (2000) 173.
125. B. W. Bennett, H. W. Pickering, Met. Trans. 18A (1987) 1117.
126. T. S. Duh, J. J. Kai, F. R. Chen, L. H. Wang, J. Nucl. Mat. 294 (2001) 267.
127. J. J. Kai, F. R. Chen, T. S. Duh, Mat. Trans. 45 (2004) 40.
128. S. Watanabe, Y. Takamatsu, N. Sakaguchi, H. Takahashi, J. Nucl. Mat. 283-287 (2000) 152.
129. E. M. Lehockey, D. Limoges, G. Palumbo, J. Sklarchuk, K. Tomantschger, A. Vincze, J. Power Sources, 78 (1999) 79.
130. P. Lin, G. Palumbo, U. Erb, K. T. Aust, Scripta Met. 33 (1995) 1387.
131. H. M. Kim, J. A. Szpunar, Mat. Sci. Forum 157-6 (1994) 1997.
132. M. Michiuchi, H. Kokawa, Z. J. Wang, Y. S. Sato, K. Sakai, Acta Mat. 54 (2006) 5179.
133. M. Shimada, H. Kokawa, Z. J. Wang, Y. S. Sato, I. Karibe, Acta mat. 50 (2002) 2331.
134. G. Palumbo, K. T. Aust, Acta Met. 38 (1990) 2343.
135. L. Tan, K. Sridharan, T. R. Allen, J. Nucl. Mat. 348 (2006) 263.

136. L. Tan, K. Sridharan, T. R. Allen, R. K. Nanstad, D. A. McClintock, J. Nucl. Mat. 374 (2008) 270.
137. H. Kurishita, H. Yoshinaga, Mat. Forum, 13 (1989) 161.
138. S. Tsurekawa, T. Tanaka, H. Yoshinaga, Mat. Sci. Eng. A176 (1994) 341.
139. J. B. Brosse, R. Fillit, M. Biscondi, Scripta Met. 15 (1981) 619.
140. L. C. Lim, R. Raj, Acta Met. 32 (1984) 1183.
141. Y. S. Yi, J. S. Kim, Scripta Mat. 50 (2004) 855.
142. B. Alexandreanu, PhD Thesis, University of Michigan: Ann Arbor, (2002).
143. B. Alexandreanu, B. Capell, G. S. Was, Mat. Sci. Eng. A300 (2001) 94.
144. T. Watanabe, Res. Mech. 11 (1984) 47.
145. V. Thaveeprungsriporn, T. M. Angeliu, D. J. Paraventi, J. L. Hertzberg, G. S. Was, Proc. 6th Int. Conf. on Environmental Degradation of Materials in Nuclear Power Systems, TMS (1993) 721.
146. T. Watanabe, Met. Mat. Trans. A. 14 (1983) 531.
147. D. J. Dingley, R. C. Pond, Acta Met. 27 (1979) 667.
148. S. M. Bruemmer, B. W. Arey, L. A. Charlot, Corrosion, 48 (1992) 42.
149. T. R. Allen, Candidate Materials Evaluation for Supercritical Water-Cooled Reactor, Final Report (2008) 378.
150. Z. Jiao, G. S. Was, J. Nucl. Mat. (2010) submitted.
151. A. Kimura, H. Cho, N. Toda, R. Kasada, H. Kishimoto, N. Iwata, S. Ukai, M. Fujiwara, Proc. ICAPP 2005 3 (2005) 1737.
152. Y. Tsuchiya, F. Kano, N. Saito, M. Ookawa, J. Kaneda, N. Hara, Corrosion 2007, NACE International, (2007).
153. W. K. Boyd, H. A. Pray, Corrosion 13 (1957) 33.
154. S. Penttila, A. Toivonen, L. Heikinheimo, R. Novotny, 4th Int. Symp. Supercritical Water-Cooled Reactors, Heidelberg, Germany (2009) Paper No. 60.
155. L. Fournier, D. Delafosse, T. Magnin, Mat. Sci. Eng. A316 (2001) 166.
156. P. Ampornrat, G. S. Was, J. Nucl. Mat. 395 (2009) 30.
157. S. Kasahara, F. Kano, N. Saito, M. Ookawa, J. Kaneda, Workshop on fueled loop tests for SCWR R&D, Paris, OEDCD/NEA (2006).
158. J. Jang, PMB Meeting for the SCWR Mat. and Water Chem., Ann Arbor, MI (2006).
159. G. S. Was, S. Teysseyre, J. McKinley, Corrosion 2004, New Orleans, LA. NACE International (2004) Paper No. 04492.
160. L. Fournier, D. Delafosse, C. Bosch, T. Magnin, Corrosion 2001, Houston, TX. NACE International (2001) Paper No. 01361.
161. S. S. Hwang, B. H. Lee, J. G. Kim, J. Jang, J. Nucl. Mat. 372 (2008) 177.
162. J. Jang, S. S. Hwang, C. H. Han, B. H. Lee, Proc. ICAPP 2006, (2006) 2187.
163. G. Gupta, G. S. Was, Proc. 12th Int. Conf. on Environmental Degradation of Materials in Nuclear Power Systems, Salt Lake City, UT. TMS (2005) 1359.
164. P. Ampornrat, C. B. Bahn, G. S. Was, Proc. 12th Int. Conf. on Environmental Degradation of Materials in Nuclear Power Systems, Salt Lake City, UT. TMS (2005) 1387.
165. Y. Yi, B. Lee, S. Kim, J. Jang, Mat. Sci. Eng. A. 429 (2006) 161.

166. V. Randle, The Role of the Coincident Site Lattice in Grain boundary Engineering, London: Institute of Materials, 1996.
167. B. Ekmekci, A. Sayar, T. T. Opoz, A. Erden, J. Micromechanics and Microengineering 19(2009) 1.
168. S. I. Wright, B. L. Adams, Met. Trans. 23A (1992) 759.
169. J. F. Ziegler, SRIM 2006, Ed. J. P. Biersack, Yorktown, NY: IBM Corporation, (2006).
170. ASTM Designation E 521-89, Philadelphia, PA: American Society for Testing and Materials, (1989) D-9.
171. J. T. Busby, PhD Thesis, University of Michigan: Ann Arbor, (2001).
172. B. Wolf, Cryst. Res. Tech. 35 (2000) 377.
173. Scion Corporation, Scion Image, Frederick, MD (2005).
174. G. Cliff. G. W. Lorimer, J. Microscopy, 103 (1975) 203.
175. G. Gupta, PhD Thesis, University of Michigan: Ann Arbor, (2007).
176. Microset Website, http://www.microset.co.uk/media/121_forming_putty.html, cited September 16 (2009).
177. P. McPhail, Technical Support Engineer, Veeco Instruments, personal communication, (2009).
178. B. Alexandreanu, G. S. Was, Phil. Mag. A 81 (2001) 1951.
179. J. Cookson, PhD Thesis, University of Michigan: Ann Arbor, (1996).
180. M. J. Hackett, PhD Thesis, University of Michigan: Ann Arbor, (2008).
181. Kale Stephenson, University of Michigan, IM1 Schematic, personal communication, August 3 (2009).
182. J. T. Busby, M. C. Hash, G. S. Was, J. Nucl, Mat. 336 (2005) 267.
183. A. Seeger, Proc. 2nd UN Int. Conf. on Peaceful Uses of Atomic Energy, Geneva, 6 (1958) 250.
184. G. R. Odette, D. Frey, J. Nucl. Mat. 85&86, part B (1979) 817.
185. F. A. Garner, M. L. Hamilton, N. F. Panayotou, G. D. Johnson, J. Nucl Mat. 104 (1982) 803.
186. M. L. Grossbeck, P. J. Maziasz, A. F. Rowcliffe, J. Nucl. Mat. 191 (1992) 808.
187. L. Fournier, A. Serres, Q. Auzoux, D. Leboulch, G. S. Was, J. Nucl. Mat. 384 (2009) 38.
188. U. F. Kocks, Met. Trans. 1 (1970) 1121.
189. G. S. Was, Z. Jiao, J. T. Busby, Proc. 16th Euro. Conf. of Fracture, Alexandroupolis, Greece (2006).
190. W. Wu, X. Xiao, S. Zhang, H. Li, X. Zhou, C. Jiang, Nanoscale Res. Lett. 4 (2009) 926.
191. A. N. Stroh, Proc. Royal Soc. of London, 232 (1955) 548.
192. J. Tenbrink. R. P. Wahi, H. Wollenberger, J. Nucl. Mat. 155-157 (1988) 850.
193. M. Li, S. J. Zinkle, J. Nucl. Mat. 361 (2007) 192.
194. M. C. Marinelli, A. El Bartali, J. W. Signorelli, P. Evrard, V. Aubin, I. Alvarex-Armas, S. Degallaix-Moreuil, Mat. Sci. & Amp. A. 509 (2009) 81.
195. I. M. Robertson, T. C. Lee, H. K. Birnbaum, Ultramicroscopy, 40 (1992) 330.
196. T. C. Lee, I. M. Robertson, H. K. Birnbaum, Acta Met. 40 (1992) 2569.
197. L. C. Lim, R. Raj, Acta Met. 33 (1985) 1577.

198. T. C. Lee, I. M. Robertson, H. K. Birnbaum, Scripta Met. 23 (1989) 799.
199. T. C. Lee, I. M. Robertson, H. K. Birnbaum, Phil. Mag. A 62 (1990) 131.
200. T. C. Lee, I. M. Robertson, H. K. Birnbaum, Met. Trans. 21A (1990) 2437.
201. H. Kokawa, T. Watanabe, S. Karashima, J. Mat. Sci. 18 (1983) 1183.
202. R. C. Pond, D. A. Smith, P. W. J. Southerden, Phil. Mag. A 37 (1978) 27.
203. Z. Shen, R. H. Wagoner, W. A. T. Clark, Acta Met. 36 (1988) 3231.
204. W. A. T. Clark, R. H. Wagoner, Z. Y. Shen, T. C. Lee, I. M. Robertson, H. K. Birnbaum, Scripta Met. 26 (1992) 203.
205. M. P. Dwald, W. A. Curtin, Mat. Sci. Eng. 15 (2007) 193.
206. M. P. Dwald, W. A. Curtin, Phil. Mag. 87 (2007) 4615.
207. B. S. Rho, H. U. Hong, S. W. Nam, Scripta Mat. 43 (2000) 167.
208. S. L. Wong, P. R. Dawson, Acta Mat. 58 (2010) 1658.
209. E. Heripre, M. Dexet, J. Crepin, L. Gelebart, A. Roos, M. Bornert, D. Caldemaison, Int. J. Plasticity 23 (2007) 1512.
210. A. A. MacDowell, R. S. Celestre, N. Tamura, R. Spolenak, B. Valek, W. L. Brown, J. C. Bravman, H. A. Padmore, B. W. Batterman, J. R. Patel, Nucl. Inst. And Methods in Phys. Res. Sect. A 467-468 (2001) 936.
211. B. Clausen, T. Lorentzen, M. A. M. Bourke, M. R. Daymond, Mat. Sci. & Amp. A259 (1999) 17.
212. T. S. Byun, K. Farrell, E. H. Lee, J. D. Hunn, L. K. Mansur, J. Nucl. Mat. 298 (2001) 269.
213. B. J. Pestman, J. M. de Hosson, V. Vitek, F. W. Schapink, Scripta Met. 23 (1989) 1431.
214. H. Foell, University of Kiel, Web reference: http://www.tf.uni-kiel.de/matwis/amat/def_en/, (2007) cited March 28, 2010.
215. V. Randle, Scripta Mat. 54 (2006) 1011.
216. E. E. Badiyan, O. V. Shekhovtsov, Physics of Metals and Metallography 102 (2006) 181.
217. D. L. Olmsted, S. M. Foiles, E. A. Holm, Acta Mat. 57 (2009) 3694.
218. E. A. West, Z. Jiao, G. S. Was, Proc. 14th Int. Conf. on Environmental Degradation of Materials in Nuclear Power Systems, Virginia Beach, VA. American Nuclear Society (2009) in press.
219. P. Ampornrat, University of Michigan, Integranular cracking of austenitic alloys in 360˚C Water, personal communication (2009).
220. T. Magnin, Mat. Sci. Forum, 217-222 (1996) 83.
221. H. Leinonen, I. Virkkunen, H. Hanninen, Proc. of the Int. Conf. on Hydrogen Effects on Material Behavior and Corrosion Deformation Interactions (2003) 673.